UNIVERSITÀ DEGLI STUDI
DI MODENA E REGGIO EMILIA

PhD Course in
"Physics and Nanosciences"

XXXIII Cycle

Iron(II)-based Extended Metal Atom Chains (EMACs) as Nanoscale Magnets: Synthesis, Structure and Magnetic Behavior

Candidate: Alessio Nicolini

Supervisor: Prof. Andrea Cornia

Director of the PhD Course: Prof. Stefano Frabboni

Title

Iron(II)-based Extended Metal Atom Chains (EMACs) as Nanoscale Magnets: Synthesis, Structure and Magnetic Behavior

Submission Date

March 10, 2021

Final Revisions

June 18, 2021

Defence Date

July 8, 2021

Supervisor

Prof. Andrea Cornia

Opponents

Prof. Federico Boscherini, Università di Bologna

Prof.ssa Maurizia Palummo, Università “Tor Vergata” di Roma

Prof. Andrea Alessandrini, Università di Modena e Reggio Emilia

Contents

Abstract

The storage, transfer and elaboration of data are central targets in emerging fields such as **quantum technologies** and **spintronics** (spin electronics). A primary goal is the control of **magnetic properties** and **spin** at the atomic and molecular levels. Interesting are molecular nanostructures called **Single-Molecule Magnets** (**SMMs**), which possess similar magnetic properties to bulk magnets, but of pure molecular origin. Thanks to their **magnetic bistability** and **long relaxation times**, SMMs are attractive to be implemented as single bits, with the advantage that their physical properties can be tuned by chemical design.

Iron(II)-based **Extended Metal Atom Chains** (**EMACs**) are appealing synthetic targets as SMMs, because of the large spin and magnetic anisotropy of high-spin iron(II). EMACs are linear arrays of at least three metal ions wrapped together by polydentate organic ligands, which promote short separations between the metal centers and, sometimes, metal-metal bonds. However, these compounds proved to be very elusive, due to the exceedingly high tendency of iron(II) to undergo oxidation and hydrolysis processes. In fact, before our report of tetrairon(II) chain $[Fe_4(tpda)_3Cl_2]$ (**1Cl**) in 2018, the only known iron(II)-based EMAC was a triiron(II) complex with formamidinato ligands (**6**) described by Cotton *et al.* in 1998 (H_2tpda = N^2,N^6-di(pyridin-2-yl)pyridine-2,6-diamine). In 2020, Guillet *et al.* reported a new triiron(II) chain (**7**) supported by silylated diaminopyridines. Complexes **1Cl**, **6** and **7** display ferromagnetic interactions, but a metal-metal bond is only present in **7**.

The focus of this Thesis is on the design, the synthesis and the characterization of transition metal compounds potentially exhibiting highly magnetic electronic states as a result of ferromagnetic interactions and, possibly, metal-metal bonds. In particular, we describe a systematic study on a series of iron-based EMACs, obtained and handled in **strictly anaerobic and anhydrous conditions**. The molecular structures of the newly synthesized compounds were defined with atomic precision by **single-crystal X-ray diffraction**. Their chemical behavior and physical properties were extensively investigated in solution by **mass spectrometry**, **electronic** and **NMR spectroscopies** and **cyclic voltammetry**, and in the solid state by **Mössbauer spectroscopy** and **magnetic techniques** like DC/AC methods and micro-SQUID magnetometry.

The family of tetrairon(II) EMACs was expanded by preparing $[Fe_4(tpda)_3Br_2]$ (**1Br**), a compound structurally similar to **1Cl** but containing Br^- instead of Cl^- axial ligands. Mössbauer spectroscopy confirmed that both **1Cl** and **1Br** contain four high-spin iron(II) ions. The two

compounds, in which metal-metal distances range between 2.94 and 2.99 Å, are also close in terms of DC magnetic behavior, as they both exhibit **dominant ferromagnetic coupling** at room temperature. The electronic structure of each constituent ion was investigated through *ab-initio* calculations, which revealed that the main magnetic axis of all metals is directed close to the axis of the iron(II)-chain. The terminal ions (Fe1 and Fe4) have an easy-axis magnetic anisotropy, while the anisotropy of internal metal centers (Fe2 and Fe3) is of the hard-axis type and smaller in magnitude. Treatment of magnetic data using these *ab-initio* results showed that (a) super-exchange interactions are ferromagnetic within the (Fe1, Fe2) and (Fe3, Fe4) pairs but antiferromagnetic between Fe2 and Fe3, and that (b) super-exchange interactions compete with local anisotropies to give a weakly magnetic ground state. In spite of that, AC experiments pointed out that both **1Cl** and **1Br** display SMM behavior, with a significant difference: **slow magnetic relaxation** in **1Br** can be observed even in **zero static field**.

According to cyclic voltammetry, **1Cl** and **1Br** undergo multiple one-electron oxidations in solution. To attempt activating the **double-exchange mechanism**, which could strengthen the ferromagnetic interaction in mixed-valence compounds, the chemical oxidation of **1Cl** was carried out. Surprisingly, the isolated products were two linear triiron **mixed-valence species**, namely the one- and two-electron oxidized derivatives $[Fe_2^{II}Fe^{III}(tpda)_3]PF_6$ (**3**) and $[Fe^{II}Fe_2^{III}(tpda)_3Cl]PF_6$ (**3a**), respectively. In the former, structural data at 115 K indicate that valence states are localized and that the distance between the two neighboring iron(II) ions (2.73 Å) is slightly shorter than in **6** (2.78 Å). Variable temperature ^{57}Fe Mössbauer and electronic spectra indeed suggest that **3** is best classified as a **Robin-Day Class II mixed-valence system** at 298 K, while no delocalization occurs at 10 and 77 K. The DC magnetic response of the compound was analyzed with the aid of *ab-initio* calculations and provided evidence of ferromagnetic coupling between the two Fe^{2+} centers, while interaction with the Fe^{3+} ion was found antiferromagnetic and very anisotropic. As a result, the ground state is only weakly magnetic but shows an easy-axis anisotropy. Micro-SQUID measurements revealed a small opening of the hysteresis loop below 0.5 K, with some detectable remanent magnetization. Consistently, **3** exhibits zero-field SMM behavior in AC measurements, similarly to **1Br**. On the other hand, a further one-electron oxidation (to give **3a**) causes the loss of slow relaxation of the magnetization and the closure of magnetic hysteresis loop.

In order to attempt stabilizing these chain-like structures, a new tripodal ligand based on three covalently linked oligo-*α*-pyridylamine units, $N(CH_2CH_2NH\text{-}py\text{-}NH\text{-}py)_3$ (H_6L), was designed and synthesized from FHdpa, Cs_2CO_3 and tren (FHdpa = *N*-(6-fluoropyridin-2-yl)pyridin-2-amine; tren = tris(2-aminoethyl)amine). Its coordination chemistry towards

cobalt(II) and iron(II) was preliminary explored, although no new EMACs were obtained so far. The following mono-, di-, and polynuclear complexes were isolated in crystalline form: K[CoH_3L] (**CoL**), **CoL**·THF, [Fe_2ClH_3L] (**Fe_2L**) and [$Fe_6O_2(\mu_5\text{-}O)H_3L_2$] (**$Fe_6L_2$**). In **CoL**, which provided the first X-ray diffraction data on the new ligand, the metal ion occupies the octahedral coordination pocket defined by the inner pyridine rings and the outer amido groups. In **Fe_2L**, an iron(II) ion occupies the same octahedral coordination pocket as the cobalt(II) ion in **CoL**, while the second metal center is coordinated by the three outer pyridines and by a capping chlorido ligand. Compound **Fe_6L_2**, whose isolation was totally unexpected, contains a $Fe_5O_2(\mu_5\text{-}O)$ core encapsulated by two tripodal ligands and featuring two short Fe-Fe separations (2.63 Å). An additional metal center is present in one of the tren-like coordination pockets (the oxygen atoms are adventitious). **Fe_6L_2** possesses interesting redox properties, which suggest that it could be used as starting material for the preparation of new mixed-valence systems. Therefore, the coordination chemistry of H_6L proved to be extremely versatile, paving the way for a manifold of possible future studies.

Abstract (Italian)

Il trasferimento e l'elaborazione dei dati sono tra gli obiettivi primari in campi emergenti come le tecnologie quantistiche e la spintronica (spin elettronica). Un importante obiettivo è il controllo delle proprietà magnetiche e dello spin a livello atomico e molecolare. Interessanti, sono nanostrutture chiamate **Magneti a Molecola Singola** (**SMM**), che possiedono proprietà magnetiche simili a quelle dei magneti tradizionali, ma con origine puramente molecolare. La **bistabilità magnetica** e i **lunghi tempi di rilassamento** possono rendere i SMM applicabili come singoli bit. Le loro proprietà fisiche possono essere ottimizzate mediante design chimico.

Gli EMAC (**Extended Metal Atom Chains**) a base di ferro(II) sono potenziali SMM, per via del grande spin e anisotropia magnetica del Fe^{2+} ad alto spin. Gli EMAC sono catene lineari di almeno tre ioni metallici, avvolti da leganti organici polidentati, che promuovono corte distanze tra i metalli e, a volte, legami metallo-metallo. Tuttavia, è difficilissimo isolare questi composti per via della grande tendenza di Fe^{2+} a subire processi di ossidazione e idrolisi. Infatti, prima che nel 2018 noi pubblicassimo una catena di quattro ioni Fe^{2+}, $[Fe_4(tpda)_3Cl_2]$ (**1Cl**), con leganti oligo-α-piridilamminici, l'unico EMAC noto a base di ferro(II) era una catena di tre atomi di Fe (**6**, Cotton *et al.* nel 1998). Nel 2020, Guillet *et al.* ha riportato un nuovo complesso di tre atomi di Fe^{2+} (**7**) con leganti sililati. I complessi **1Cl**, **6** e **7** mostrano interazioni ferromagnetiche, mentre **7** contiene anche legami metallo-metallo.

L'obiettivo di questa Tesi è la progettazione, sintesi e caratterizzazione di composti di metalli di transizione con stati elettronici altamente magnetici, contenenti interazioni ferromagnetiche ed eventualmente legami metallo-metallo. In particolare, essa descrive uno studio sistematico di una serie di EMAC a base di ferro, ottenuti e maneggiati in **condizioni strettamente anaerobiche e anidre**. I nuovi composti sono stati caratterizzati con diffrazione di raggi X su cristallo singolo, definendo le loro strutture molecolari con precisione atomica. Poi, le loro proprietà sono state studiate in soluzione (**spettrometria di massa**, **spettroscopia elettronica** e **NMR**, **voltammetria ciclica**) e in stato solido (**spettroscopia Mössbauer**, e varie **tecniche magnetiche** come DC, AC e magnetometria micro-SQUID).

La famiglia degli EMAC tetrametallici di ferro(II) è stata espansa preparando $[Fe_4(tpda)_3Br_2]$ (**1Br**), un composto strutturalmente simile a **1Cl**, ma che contiene anioni Br^- invece di leganti Cl^-. La spettroscopia Mössbauer ha confermato che entrambi **1Cl** e **1Br** contengono solo ioni ferro(II) ad alto spin. Inoltre, i due composti, le cui distanze metallo-metallo spaziano tra 2.94 e 2.99 Å, hanno un comportamento magnetico simile, visto che entrambi esibiscono **interazioni**

ferromagnetiche dominanti a temperatura ambiente. La struttura elettronica di ognuno degli ioni ferro(II) è stata studiata tramite calcoli *ab-initio*, i quali hanno rivelato che l'asse magnetico principale di tutti i centri metallici è diretto verso una direzione simile a quella individuata dalla catena degli ioni ferro(II). Gli ioni terminali (Fe1 e Fe4) posseggono un'anisotropia di tipo asse-facile, mentre l'anisotropia dei centri metallici interni (Fe2 e Fe3) è asse-difficile, e più piccola in valore assoluto. Il trattamento dei dati magnetici tramite l'utilizzo dei risultati dei calcoli *ab-initio*, ha mostrato che: (a) le interazioni di super-scambio sono ferromagnetiche all'interno delle coppie (Fe1, Fe2) e (Fe3, Fe4), ma antiferromagnetiche tra Fe2 e Fe3, e che (b) le interazioni di super-scambio competono con le anisotropie locali per dare uno stato fondamentale debolmente magnetico. Nonostante questo, esperimenti di suscettometria AC hanno evidenziato che sia **1Cl** che **1Br** posseggono comportamento da SMM, mostrando però una notevole ed importante differenza: **il rilassamento lento della magnetizzazione** in **1Br**, è osservabile anche **senza l'applicazione di un campo magnetico esterno**.

Secondo gli studi di voltammetria ciclica, **1Cl** e **1Br** subiscono ossidazioni monoelettroniche multiple in soluzione. Per cercare di attivare il meccanismo del **doppio-scambio**, che può rafforzare le interazioni ferromagnetiche in **composti a valenza mista**, è stata eseguita l'ossidazione chimica di **1Cl**. Sorprendentemente, sono stati isolati due composti a valenza mista caratterizzati da una catena di tre atomi di ferro. I composti isolati hanno formula molecolare $[Fe_2^{II}Fe^{III}(tpda)_3]PF_6$ (**3**) e $[Fe^{II}Fe_2^{III}(tpda)_3Cl]PF_6$ (**3a**), ed essi rappresentano rispettivamente il derivato mono-ossidato e bi-ossidato. I dati strutturali del complesso **3** indicano che a 115 K le valenze dei centri metallici sono localizzate e che la distanza tra due ioni ferro(II) vicinali (2.73 Å) è leggermente più corta che in **6** (2.78 Å). Misure Mössbauer a temperatura variabile e studi di spettroscopia elettronica mostrano che a 298 K **3** è classificato come un **composto a valenza mista di tipo Robin-Day Classe II**, mentre non è presente delocalizzazione elettronica a 10 e 77 K. La risposta magnetica DC del complesso è stata analizzata tramite l'aiuto di calcoli *ab-initio*, fornendo prova della presenza di accoppiamenti ferromagnetici tra i due ioni ferro(II), mentre l'interazione con lo ione ferro(III) è risultata antiferromagnetica e molto anisotropa. Inoltre, misure micro-SQUID hanno rivelato una piccola apertura del ciclo di isteresi magnetica del composto **3**, al di sotto di 0.5 K, riuscendo anche a misurare una magnetizzazione residua in campo zero. Consistentemente a questa scoperta, misure AC hanno dimostrato che **3** mostra un comportamento da SMM anche in campo zero, allo stesso modo di **1Br**. Al contrario, un'ulteriore ossidazione monoelettronica per dare il composto **3a**, ha causato la completa perdita del rilassamento lento della magnetizzazione, e la chiusura del ciclo di isteresi magnetica.

Nel tentativo di cercare di stabilizzare queste strutture a catena, è stato progettato un nuovo legante tripodale costituito da tre unità oligo-*α*-piridilamminiche, legate covalentemente tra di loro tramite uno spaziatore alchilico. Questo nuovo legante, $N(CH_2CH_2NH\text{-}py\text{-}NH\text{-}py)_3$ (H_6L), è stato ottenuto utilizzando i seguenti reagenti: FHdpa, Cs_2CO_3 e tren (FHdpa = *N*-(6-fluoropiridin-2-il)piridin-2-ammina; tren = tris(2-amminoetil)ammina). La chimica di coordinazione di H_6L, è stata esplorata tramite studi preliminari con cobalto(II) e ferro(II), anche se nessun nuovo EMAC è stato ottenuto fino ad ora. I seguenti composti mono- bi- e polinucleari sono invece stati isolati in forma cristallina pura: $K[CoH_3L]$ (**CoL**), **CoL**·THF, $[Fe_2ClH_3L]$ (**Fe_2L**) e $[Fe_6O_2(\mu_5\text{-}O)H_3L_2]$ (**Fe_6L_2**). La struttura molecolare di **CoL** ha fornito i primi dati strutturali sul nuovo legante. Lo ione cobalto(II) presente in **CoL** occupa la tasca di coordinazione ottaedrica del legante, la quale è definita dagli anelli piridinici interni e dai gruppi ammidici esterni. Nel composto **Fe_2L** uno degli ioni ferro(II) occupa la stessa posizione del cobalto(II) in **CoL**, mentre il secondo ione ferro(II) è coordinato dalle tre piridine esterne e da un legante Cl^- terminale. L'ottenimento del composto **Fe_6L_2** è stato del tutto inaspettato. Esso contiene un nucleo $Fe_5O_2(\mu_5\text{-}O)$, incapsulato da due molecole del legante tripodale, ed è inoltre caratterizzato da due corte distanze ferro-ferro (2.63 Å). Il sesto centro metallico è situato in una delle tasche di coordinazione del tren, mente i tre atomi di ossigeno presenti nella struttura del complesso sono accidentali. **Fe_6L_2** possiede interessanti proprietà redox, le quali suggeriscono che esso può essere usato come reagente per sintetizzare nuovi composti a valenza mista. In conclusione, H_6L ha dimostrato di possedere una chimica di coordinazione estremamente versatile, aprendo la strada ad una moltitudine di studi futuri possibili.

List of acronyms and abbreviations

1Br	$[Fe_4(tpda)_3Br_2]$
1Cl	$[Fe_4(tpda)_3Cl_2]$
1ClBr	$[Fe_4(tpda)_3BrCl]$
2	$[Fe_2(Mes)_4]$
3	$[Fe_3(tpda)_3]PF_6$
3a	$[Fe_3(tpda)_3Cl]PF_6$
Mn_{12}	$[Mn_{12}O_{12}(OAc)_{16}(H_2O)_4]\cdot 2AcOH\cdot 4H_2O$
4	$[Cr_5(tpda)_4Cl_2]$
4a	$[Cr_3(dpa)_4Cl_2]$
5	$[Cr_5(tpda)_4(NCS)_2]$
5a	$[Cr_3(tpda)_4(NCS)_2]$
6	$[Fe_3(DPyF)_4][PF_6]_2$
7	$[Fe_3(tmsap)_3]$
8	$[Fe_4(\mu_4\text{-}O)(dpa)_6]$
9	$[Fe_2(dpa)_2(Mes)_2]$
9a	$[Fe_2(dpa)_3Cl][Fe_4(\mu_4\text{-}O)](dpa)_6]$
9b	$[Fe_2(dpa)_3Cl]$
10Br	$[Co_3(dpa)_4Br_2]$
10Cl	$[Co_3(dpa)_4Cl_2]$
10ClBr	$[Co_3(dpa)_4ClBr]$
11	$[Fe_2(dpa)_2(hmds)_2]$
12	[CoFeCl(py3tren)]
13	$[(Me_3TPya)_2Fe_2(A)](BAr^F{}_4)_3$
14	$[CFe^{III}Fe^{II}Fe^{III}C](BPh_4)_2$
15	$[CoCl_2H_3(py_3tren)]$
16	$K[Co(py_3tren)]$
17	$[Fe_5(\mu_5\text{-}O)(OEt)_{13}]$
18	$[Fe_5(\mu_5\text{-}O)(\mu\text{-}OPr^i)_8Cl_5]$
19	$[Os_3(CO)_8(\mu\text{-}OH)(\mu\text{-}H)(\mu\text{-}dppm)]$
AC	Alternating-current
ADP	Anisotropic displacement parameter
AILFT	Ab-Initio Ligand Field Theory

AOM	Angular-Overlap Model
B	*N*,*N*',*N*''-trimethyl-l,4,7-triazacyclononane
BAr^F_4	Tetrakis[3,5-bis(trifluoromethyl)phenyl]borate
Boc	Tert-butyloxycarbonyl
Br_2py	2,6-Dibromopyridine
BrHdpa	*N*-(6-bromopyridin-2-yl)pyridin-2-amine
Brpy	2-Bromopyridine
BVS	Bond-Valence Sum
C^{3-}	1,4,7-Tris(4-*tert*-butyl-2-mercaptobenzyl)-1,4,7-triazacyclononane
CAS	Complete Active Space
CASPT2	Complete Active-Space second-order Perturbation Theory
CASSCF	Complete Active Space Self-Consistent Field
CF	Crystal field
COSY	Correlated Spectroscopy
CV	Cyclic-Voltammetry
DC	Direct-current
DFT	Density Functional Theory
DLPNO	Domain-based local pair natural orbital
DMSO	Dimethyl sulfoxide
DMSO-d_6	Deuterated dimethyl sulfoxide
dppm	Bis(diphenylphosphino)methane
$DPyF^-$	*N*,*N*'-Di(2-pyridyl)formamidinate
EMAC	Extended Metal Atom Chain
EPR	Electron Paramagnetic Resonance
ESI-MS	Electrospray Ionization Mass Spectrometry
ET	Electron-transfer
F_2py	2,6-Difluoropyridine
Fc	Ferrocene
FC	Flash chromatography
FHdpa	*N*-(6-Fluoropyridin-2-yl)pyridin-2-amine
Fpy	2-Fluoropyridine
FWHM	Full-width at half-maximum
GC	Glassy carbon
H_2A	2,5-Di(2,6-dimethylanilino)-3,6-dibromo-1,4-benzoquinone
H_2tpda	N^2,N^6-Di(pyridin-2-yl)pyridine-2,6-diamine

$H_3(py_3tren)$	*N*,*N*,*N*-Tris(2-(2-pyridylamino)ethyl)amine
H_6L	$H_3tren(Hdpa)_3$
HBn	Toluene
Hdpa	Dipyridin-2-yl-amine
HEMAC	Heterometallic Extended Metal Atom Chain
Hhmds	1,1,1,3,3-Hexamethyldisilazane
HMBC	Heteronuclear Multiple-Bond Correlation
HMes	Mesitylene
HS	High-Spin
HSQC	Heteronuclear Single Quantum Coherence
IDP	Isotropic displacement parameter
IDS	International Data Corporation
INS	Inelastic Neutron Scattering
IVCT	Intervalence charge-transfer
LF	Ligand field
LUMO	Lowest unoccupied molecular orbital
M	Metal
$[M]^+$	Molecular ion peak
MALDI-TOF/TOF-MS (or MALDI-TOF-MS)	Matrix assisted laser desorption/ionization tandem time-of-flight mass spectrometry
MR	Molar ratio
MV	Mixed-valence
N.D.	Not determined
NEVPT2	Second-order *N*-electron Valence Perturbation Theory
NH_2py	2-Aminopyridine
$(NH_2)_2py$	2,6-Diaminopyridine
NMR	Nuclear magnetic resonance spectroscopy
py	Pyridine
QTM	Quantum tunnelling of the magnetization
RAS	Restricted Active Space
RASSCF	Restricted Active Space Self-Consistent Field
RASSI-SO	Restricted Active Space State Interaction-Spin Orbit coupling
SCE	Saturated calomel electrode
SC-XRD	Single-Crystals X-Ray Diffraction
SD	Slater Determinant

SH	Spin Hamiltonian
SMM	Single-Molecule Magnet
SO	Spin-orbit
SOF	Site occupation factor
SOMF	Spin-orbit mean-field
SOMO	Singly occupied molecular orbital
SPa	Side-product a
SPb	Side-product b
SQUID	Superconducting Quantum Interference Device
SRM	Slow relaxation of the magnetization
TBABr	Tetra-*n*-butylammonium bromide
TBACl	Tetra-*n*-butylammonium chloride
THF	Tetrahydrofuran
TIP	Temperature-independent paramagnetism
TLC	Thin-layer chromatography
$tmsap^{2-}$	2,6-Bis[(trimethylsilyl)amido]pyridine
TOCSY	Total correlation spectroscopy
TPya	Tris((6-methyl-2-pyridyl)methyl)amine
tren	Tris(2-aminoethyl)amine
UV-Vis-NIR	Ultraviolet-Visible-Near Infrared Spectroscopy
XRD	X-Ray Diffraction
ZFS	Zero-field splitting

Chapter 1

Introduction

The annual size of the Global DataSphere, which represents the total amount of data created, captured, and replicated across the world every year, has experienced an exponential increase during the last decade. In 2018, the IDC (International Data Corporation) predicted that it will exceed 170 trillion of gigabytes within 2025.[1] By consequence, the storage, transfer and elaboration of data became one of the most appealing targets in emerging fields such as **quantum technologies** and **spintronics** (spin electronics).[2] One of the primary goals in these areas is the control of magnetic properties and spin at the atomic and molecular level. In fact, molecular systems spanning over the nanometric or subnanometric scale can feature uncommon properties. For example, the quantum behavior of certain materials, such as high spin-coherence and long relaxation times, make them attractive for forefront applications in molecular spintronics, data storage and data elaboration.

Particularly interesting are molecules called **Single-Molecule Magnets** (SMMs),[3,4] which possess similar magnetic properties to those of bulk magnets, such as Fe_3O_4 (magnetite), but of different origin. The magnetic behavior of the latters arises from bulk cooperative phenomena, which reflect the long range magnetic order established in specific portions of the crystal lattice, called domains. Instead, magnetic hysteresis in SMMs is purely of intramolecular origin, and it thus persists also in solution or in polymeric matrices.[3,5] SMMs constitute a wide class of compounds, usually complexes of rare-earth elements or of transition metal ions, where the metal (M) centers are coordinated by polydentate organic ligands. They feature interesting quantum properties,[6–9] such as magnetic bistability and long relaxation times, which make them attractive in quantum technologies,[10,11] and for their implementation as single bits in ultra-high dense data storage devices. Furthermore, they can also find applications as potential materials for molecular spintronics,[12–17] or in molecular electronics, where they can be used as molecular spin-transistors, spin-valves, and other nanoscale devices.[16]

A major advantage of the use of single-molecules is that their physical properties can be tuned by chemical design strategies. Here, it is possible to operate on several factors, for example: the type and number of spin carriers, the spin value of the ground state, the type of ligands, the coordination geometry of each metal center, etc.[3] SMMs are favored over magnetic nanoparticles, which also feature nanoscale dimensions, since SMMs are fully monodisperse. Moreover, they usually crystallize in high-quality molecular crystals, paving the way for the use of numerous powerful characterization techniques, which allow to deeply investigate their structural, chemical and physical properties. Certain SMMs can also be deposited on surfaces,[18,19] for example to study how the magnetic state of the given SMM influences a current directly driven across it.

The aim of this Thesis is the design, the synthesis and the characterization of transition metal compounds with highly magnetic electronic states, containing ferromagnetic interactions and, possibly, metal-metal bonds. In particular, it describes a systematic study of a series of Fe-containing polynuclear high-spin molecules, obtained and handled in strictly anaerobic and anhydrous conditions, and which exhibit SMM behavior (the magnetic properties of Cr-based SMMs are also discussed). In addition, a new chelating organic ligand is presented, and its coordination chemistry to give mono- or polynuclear complexes of transition-metal ions is explored. This research work is highly multidisciplinary. In fact, it involves many different aspects of the design and chemical synthesis of new molecules, ranging from organic to inorganic and metal-organic chemistry. Moreover, many characterization techniques were used for studying the structural and physical properties of the novel compounds, as described below. Their molecular structures were characterized with atomic level precision in the solid state by Single-Crystal X-Ray Diffraction (SC-XRD) analysis. Their solution properties were investigated through many different techniques, such as mass spectrometry (ESI-MS, MALDI-TOF/TOF-MS), UV-Vis-NIR spectroscopy, NMR spectroscopy and Cyclic-Voltammetry (CV). The magnetic behavior of some of these molecules was explored in the solid-state by Direct-Current (DC) and Alternating-Current (AC) measurements, through SQUID (Superconducting Quantum Interference Device) and micro-SQUID magnetometry, and AC susceptometry. Fe-containing compounds were also investigated by variable temperature ^{57}Fe Mössbauer spectroscopy. Moreover, insight into the physical properties of some of the studied compounds was provided by *ab-initio* calculations or Angular-Overlap Model (AOM) treatment.

This Thesis is organized as follows. In **Chapter 2**, SMMs are presented in detail, along with some of their fundamental properties. **Chapter 3** introduces the family of compounds known

as Extended Metal Atom Chains (EMACs). In particular it focuses on the challenging aspects of the synthesis of iron(II)-based EMACs, and on their potential behavior as SMMs. A brief description of the tetrairon(II) chain $[Fe_4(tpda)_3Cl_2]$ (**1Cl**) is given. Complex **1Cl** was reported by some of us at the beginning of this work and was inspiring for this Thesis.[20] In fact, **Chapter 4** describes the effect of replacing axial chlorides in **1Cl** with Br^- ligands to afford derivative $[Fe_4(tpda)_3Br_2]$ (**1Br**). Special emphasis is placed on the magnetic properties of the two compounds. Subsequently, the effect of the stepwise oxidation of complex **1Cl** is reported in **Chapter 5**. Here, two mixed-valence (MV) species are described, $[Fe_3(tpda)_3]PF_6$ (**3**) and $[Fe_3(tpda)_3Cl]PF_6$ (**3a**), where double-exchange interaction mechanism can occur. **Chapter 6** is dedicated to the chemical design and synthesis of a novel tripodal ligand, $N(CH_2CH_2NH\text{-}py\text{-}NH\text{-}py)_3$ (H_6L), based on three covalently linked oligo-α-pyridylamine units (py = pyridine). Its acid-base properties and its coordination chemistry towards iron and cobalt were preliminary explored. **Chapter 7** contains a recently (2020) published paper[21] I co-authored on a topic not directly related to my main project, but relevant to the concepts covered in my Thesis. It presents an in-depth analysis of the magnetic properties of a series of tri- and pentachromium(II)-based EMACs, along with a detailed study of the symmetric or unsymmetric arrangement of the Cr ions along the metallic chain. Finally, **Chapter 8** presents the future perspectives and the general conclusions emerging from this Thesis.

Chapter 2

Single-Molecule Magnets (SMMs)

2.1 Introduction

In the early nineties, a cluster first synthesized in 1980[22] and containing twelve manganese atoms, $[Mn_{12}O_{12}(OAc)_{16}(H_2O)_4]\cdot 2AcOH\cdot 4H_2O$ (**Mn_{12}**), was identified as the first SMM.[23,24] it is composed by four Mn^{4+} and eight Mn^{3+} ions which confer to its ground state a high-spin (HS) value of S = 10. Despite the antiferromagnetic interactions between the metal ions, the **Mn_{12}** cluster showed magnetic bistability below ~4 K.[6] Since this discovery, SMMs and their quantum properties were deeply investigated by research groups all over the world, highlighting and progressively expanding the field of molecular magnetism.[25,26] As **Mn_{12}**, SMMs are usually polynuclear species, but many mononuclear ones are also known, and sometimes they are called Single-Ion Magnets.[27,28]

The biggest impediment to the practical application of SMMs is represented by their characteristic blocking temperature (T_B), above which the memory effect is lost.[3,4] In fact, T_B is normally very low, being close or lower to the boiling temperature of liquid helium. However, in recent years great advances have been made in the struggle to increase T_B values. In fact, nowadays SMMs can feature T_B up to 80 K, which is well-above the boiling temperature of liquid nitrogen (77 K).[29–31] These high- temperature SMMs are mononuclear dysprosium metallocene complexes, which were firstly simultaneously reported by Mills[31] and Layfield.[29,30] The main alternative to the use of rare-earth metals[32], which can possess a huge magnetic moment and a strong magnetic anisotropy, is represented by the stabilization of highly magnetic electronic states in transition-metal compounds, taking advantage of strong ferromagnetic interactions promoted by a super-exchange or direct-exchange mechanisms. Especially in the chemistry of Fe and Co, it is not uncommon to find compounds with a giant temperature-stable magnetic moment, as a consequence of the direct interaction between *d*-orbitals.[33,34]

2.2 Fundamental Properties of SMMs

The magnetic behavior of a SMM is usually interpreted within the Spin Hamiltonian (SH) formalism.[3] Eq. 2.1 represents a typical SH, composed by three fundamental terms, which take into account crystal field (CF) effects ($\widehat{H}_{CF}$), magnetic exchange interactions ($\widehat{H}_{EX}$) and Zeeman splitting ($\widehat{H}_{Z}$). The SH approach is particularly suitable for spin-only systems, with orbitally non-degenerate ground states and a quenched first-order orbital momentum.[3]

$$\widehat{H} = \widehat{H}_{CF} + \widehat{H}_{EX} + \widehat{H}_{Z} \quad (2.1)$$

2.2.1 Spin Hamiltonian Approach: Crystal Field and Zeeman Terms

To the ground electronic term of an isolated metal ion with *n* unpaired electrons and no orbital degeneracy correspond 2*S*+1 degenerate spin states, where $S = n/2$. For instance, the ^{6}S term of Fe^{3+} has $n = 5$, $S = 5/2$ and is six-fold degenerate. These states can be splitted by the application of an external magnetic field (**B**), as described by the Zeeman term in the SH:

$$\widehat{H}_{Z} = -\mathbf{B} \cdot \widehat{\mathbf{m}} = \mu_{\mathrm{B}} g_e \mathbf{B} \cdot \hat{\mathbf{S}} \quad (2.2)$$

where μ_{B} is the Bohr magneton, **m** is the magnetic moment, g_e is the free-electron *g*-factor and $\hat{\mathbf{S}}$ is the spin operator. The situation is different when a metal ion is surrounded by ligands and features an orbitally nondegenerate ground electronic term with *n* unpaired electrons (e.g., $n = 4$ and $S = 2$ in the $^5B_{1g}$ term of tetragonally-elongated octahedral Mn^{3+}). Depending on the arrangement of donor atoms, on CF strength and on spin-orbit (SO) coupling, the Zeeman term in the SH takes the form:

$$\widehat{H}_{Z} = -\mathbf{B} \cdot \widehat{\mathbf{m}} = \mu_{\mathrm{B}} \cdot \mathbf{B} \cdot \bar{\bar{g}} \cdot \hat{\mathbf{S}} \quad (2.3)$$

where $\bar{\bar{g}}$ is now a second-rank tensor (called *g*-tensor; formally only $\overline{\overline{g^2}}$ is a real second-rank tensor[3]) which connects the magnetic field and the spin vectors.

Furthermore, the 2*S*+1 fold degeneracy can be partially or totally lifted even in zero magnetic field. This splitting is thus called *zero-field splitting* (ZFS). The ZFS contributes to the SH with an additional term, which is in good approximation a quadratic form of the spin operators[3]:

$$\widehat{H}_{CF} = \hat{\mathbf{S}} \cdot \bar{\bar{D}} \cdot \hat{\mathbf{S}} \quad (2.4)$$

where $\overline{\overline{D}}$ is a symmetric second rank tensor called the ZFS tensor. When its three eigenvectors (called *principal directions*) lie along the *x*, *y*, and *z* reference axes, the CF term in the SH takes the form shown in Eq. 2.5. Without changing the physical meaning of the SH, Eq. 2.5 can be re-arranged into Eq. 2.6 by defining the *axial* (*D*) and *rhombic* (*E*) *anisotropy parameters* and subtracting a constant, so as to preserve the center of gravity of the multiplet:[3]

$$\hat{H}_{CF} = D_{xx}\hat{S}_x^2 + D_{yy}\hat{S}_y^2 + D_{zz}\hat{S}_z^2 \tag{2.5}$$

$$\hat{H}_{CF} = D\left[\hat{S}_z^2 - \frac{1}{3}S(S+1)\right] + E\left(\hat{S}_x^2 - \hat{S}_y^2\right);\ \overline{\overline{D}} = \begin{bmatrix} -\frac{1}{3}D + E & 0 & 0 \\ 0 & -\frac{1}{3}D - E & 0 \\ 0 & 0 & \frac{2}{3}D \end{bmatrix} \tag{2.6}$$

In Eq. 2.6, which represents the most used form of $\hat{H}_{CF}$, $\overline{\overline{D}}$ is now traceless (i.e., the sum of its diagonal elements is equal to zero). The $|E/D|$ ratio is usually not allowed to exceed 1/3, as this would be physically equivalent to redefining the reference frame. In addition, it is worth to note that the axial anisotropy term in $\hat{H}_{CF}$ is diagonal on the basis of projection states $|M_S\rangle$, which are eigenvectors of $\hat{S}_z$ with eigenvalues M_S (M_S takes $2S+1$ values, from $-S$ to $+S$ in integer steps). On the contrary, the rhombic term has no diagonal elements on the same basis. The denomination of the *D* and *E* parameters is easily explained using Eq. 2.6. In fact, when no rhombic distortion is present ($E = 0$), one has $\hat{H}_{CF} = D\hat{S}_z^2$ (omitting a constant). The energy of the spin states is then $E(M_S) = DM_S^2$ and is determined solely by the spin component along *z*, i.e. the system has an axial magnetic anisotropy and states with the same $|M_S|$ value have the same energy. When a non-zero rhombic distortion is present ($E \neq 0$), the energy is also dependent on the *x*- and *y*-components of the spin (Eq. 2.6). Because the rhombic SH term in Eq. 2.6 connects $|M_S\rangle$ states with $\Delta M_S = \pm 2$, when *S* is integer the states with the same value of $|M_S|$ are no longer degenerate. On the other hand, if *S* is half-integer, the degeneracy is preserved and the $\pm M_S$ pairs are called Kramers doublets.[35]

2.2.2 Spin Hamiltonian Approach: Magnetic Exchange Interaction

One of the most important phenomena in polynuclear SMMs is represented by the magnetic exchange interactions between different metal centers.[3,36] Their description depends on the nature of the molecular system and of the interacting spins, on the extent of electron delocalization, and on many other factors. Metal complexes are usually insulators, and the types

of magnetic interactions in which we are interested in are the following: *direct exchange*, *super-exchange* and *double-exchange*. Usually, in a mononuclear transition-metal complex the magnetic orbitals (i.e. the singly occupied molecular orbitals, SOMOs) mainly consist of the metal *d* orbitals.[37] However, in a polynuclear complex electron delocalization through intervening diamagnetic ligands (super-exchange) or by direct overlap between *d* orbitals (direct exchange) can occur. If we consider two different spin carriers (1 and 2) the interaction between electrons in their SOMOs is usually dominated by a term of the type:

$$\hat{H}_{EX} = J\hat{\mathbf{S}}_1 \cdot \hat{\mathbf{S}}_2 \qquad (2.7)$$

where $\hat{\mathbf{S}}_i$ (i = 1,2) is the spin angular momentum of each center and J is the (super)exchange coupling constant. Eq. 2.7 represents the *Heisenberg Hamiltonian*, also called *isotropic exchange Hamiltonian*. The sign of the J constant indicates the type of interaction between the two spins (see Fig. 2.1). When J is negative, energy is minimal for parallel $\mathbf{S}_1$ and $\mathbf{S}_2$ (ferromagnetic coupling). On the other hand, when J is positive energy is minimal if $\mathbf{S}_1$ and $\mathbf{S}_2$ are antiparallel (antiferromagnetic coupling). It is important to note that the sign and magnitude of J are strictly related to the convention used in Eq. 2.7 (considering $\hat{\mathbf{S}}_1 \cdot \hat{\mathbf{S}}_2 = a$, the other conventions are $-J{\cdot}a$, $2J{\cdot}a$ and $-2J{\cdot}a$).

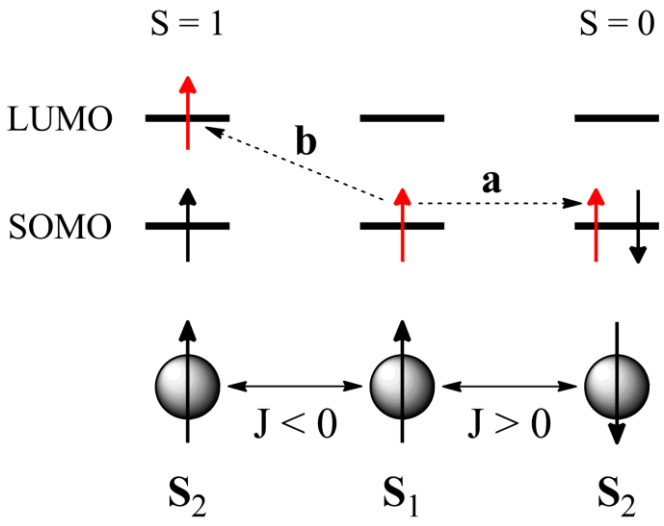

Figure 2.1. Ferromagnetic and antiferromagnetic contributions to the exchange interaction between $\mathbf{S}_1$ and $\mathbf{S}_2$. The red arrows represent the electron originally located in $SOMO_1$, which can be transferred to $SOMO_2$ (path **a**) or to $LUMO_2$ (path **b**), to originate antiferromagnetic and ferromagnetic coupling, respectively. LUMOs are the lowest unoccupied molecular orbitals.

Magnetic coupling between $\mathbf{S}_1$ and $\mathbf{S}_2$ is related to electron delocalization. This can occur in different ways, which are represented in Fig. 2.1. When the electron is transferred from $SOMO_1$ (mainly centered on 1) to $SOMO_2$ (mainly centered on 2), or vice versa, the excited state

so-formed is a singlet ($S = 0$), according to Pauli's exclusion principle (Fig. 2.1, path **a**). This singlet stabilizes the ground state spin-singlet over the spin-triplet state ($S = 1$). Therefore, this mechanism provides an antiferromagnetic contributions to the interaction. Alternatively, the electron can move from $SOMO_1$ to $LUMO_2$ (LUMO is the lowest unoccupied molecular orbital). The resulting excited state is more stable in triplet form, according to Hund's rules (Fig. 2.1, path **b**). Alternatively, electron-transfer (ET) can occur from a completely filled molecular orbital on one center to the SOMO of the other center. In both cases, the described mechanism stabilizes the ground state spin-triplet over the singlet and provides a ferromagnetic contribution to the interaction. Therefore, the nature of magnetic exchange interaction between the two spins is the outcome competing antiferromagnetic and ferromagnetic contributions. Typically the antiferromagnetic term prevails. However, when the magnetic orbitals on 1 and 2 are orthogonal to each other, the SOMO−SOMO ET is prevented, and ferromagnetic interaction predominates.[3,36]

When the M−M distance is sufficiently short, the d orbitals of 1 and 2 can overlap significantly, and a direct exchange mechanism can be operative. Instead, super-exchange mechanism involves one or more bridging diamagnetic atoms, which usually belong to ligand molecules. Here, the magnetic orbitals are delocalized also on the bridging ligand, which allows magnetic coupling between the metals.

The last interaction described in this Thesis is the double-exchange interaction. This electronic mechanism may become active in MV compounds,[38] which contain metal ions in different oxidation states. In these systems, which are deeply described in **Chapter 5**, the unpaired electrons can be localized onto specific M centers or delocalized and shared among ions in different oxidation states. For example, we can consider a Fe^{2+}−Fe^{3+} MV compound (a schematic representation of the *d* orbitals of the metals is given in Fig. 2.2). Here, the extra-electron can hop back and forth from the t_{2g} orbitals of Fe^{2+} to those of Fe^{3+}. This electron cannot change the direction of its spin during the ET. Because of Pauli principle, then, the double-exchange mechanism forces the two ions to align their spins parallel to each other, thereby strengthening the ferromagnetic contributions to magnetic interaction. Again, as for the two interaction mechanisms described above, double-exchange can occur by direct overlap of metal d orbitals, or through intervening diamagnetic ligands.[39,40]

When more than two spin centers are present, additional terms are simply added to the SH, and Eq. 2.7 can be rewritten as:

$$\widehat{H}_{EX} = \sum_{i<j} J_{ij} \hat{\mathbf{S}}_i \cdot \hat{\mathbf{S}}_j \qquad (2.8)$$

where *i* and *j* run over all the spin centers. Again, only isotropic interactions between true spins are considered in Eq. 2.8.

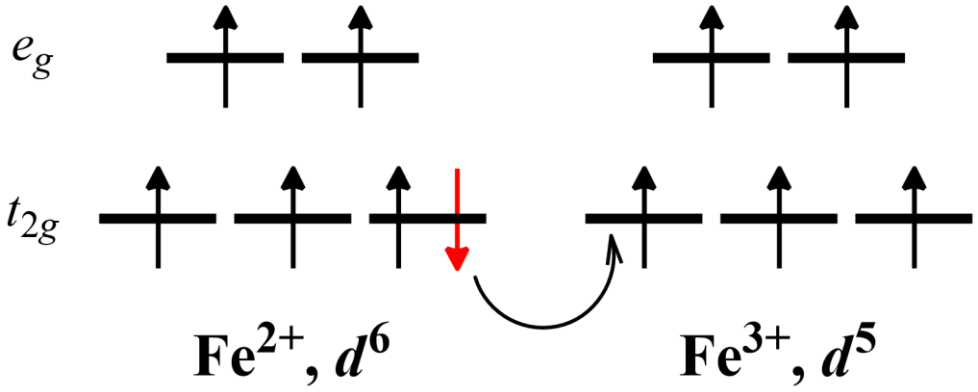

Fig. 2.2. Electronic configurations of HS iron(II) and iron(III) ions in octahedral coordination. The red arrow represents the hopping electron, whose movement originates the double-exchange mechanism, which forces the two metals to align parallel to each other.

2.2.3 Magnetic Anisotropy

Along with a high value of *S*, an SMM usually exhibits strong magnetic anisotropy, which arises from SO coupling and CF effects.[28,41] Magnetic anisotropy is described by the CF (or ZFS) Hamiltonian (see **Section 2.2.1**) and its nature depends on the sign of the *D* parameter. For simplicity, let us consider a purely axial system ($E = 0$) with anisotropy axis along *z*. From Eq. 2.6, it is evident that a positive value of *D* stabilizes the states with the smallest value of $|M_S|$, which corresponds to $M_S = 0$ for integer *S* or $M_S = \pm 1/2$ for half-integer *S*. Since the M_S's are the eigenvalues of $\hat{S}_z$, the magnetic moment lies preferentially in the *xy* plane, and the system exhibits the so-called *easy-plane* anisotropy. An opposite situation occurs when *D* is negative. Here, the states with the lowest energy have the largest $|M_S|$ value, i.e. $M_S = \pm S$. The magnetic moment then lies preferentially along the *z* direction, and the magnetic anisotropy is of the *easy-axis* type. Although some easy-plane systems showed SMMs behavior,[42,43] the vast majority of known SMMs exhibit a strong easy-axis anisotropy ($D < 0$). Here, the magnetic moment is preferentially oriented along the *z*-axis and the sign of M_S determines the direction of the magnetization. These two degenerate energy wells ($M_S = \pm S$) afford one of the most interesting properties of SMMs, namely *magnetic bistability*. In Fig. 2.3, panel **a**, the two energy minima are represented along with the energy distributions of the degenerate $\pm M_S$ pairs. The two minima are separated by an energy barrier, which is called *anisotropy barrier* and amounts to $U = |D|S^2$ for integer *S* and $U = |D|(S^2 - 1/4)$ for half-integer *S*.

The values of *D* and *E* are usually determined by Electron Paramagnetic Resonance (EPR)[44,45] spectroscopy, or less frequently, by Inelastic Neutron Scattering (INS).[46] They can also be estimated with good approximation from the fit of DC magnetic data, usually measured by SQUID magnetometry. Alternatively, *D* and *E* can be calculated with different theoretical techniques. For example, in this Thesis Ab-Initio Ligand Field Theory (AILFT)[47,48] and AOM[49] were used. AILFT calculation are parameterized using Complete Active Space Self-Consistent Field (CASSCF) method, or second-order *N*-electron Valence Perturbation Theory (NEVPT2). AOM is a semiempirical approach.

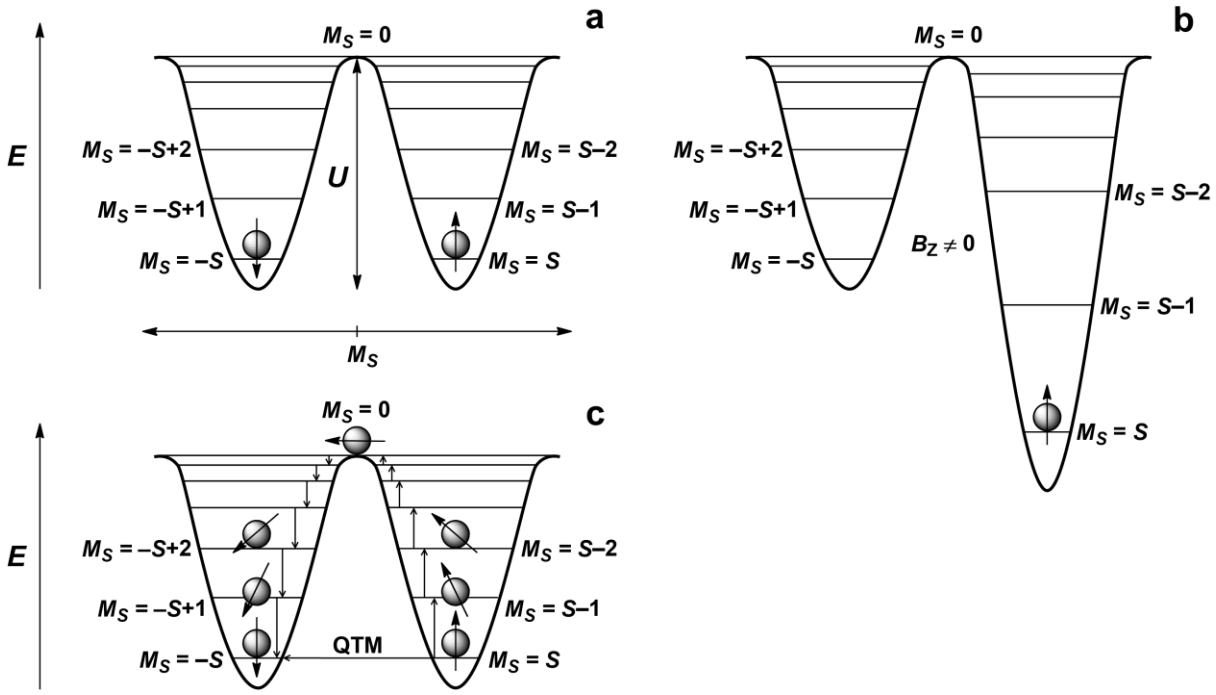

Figure 2.3. Energy levels of a uniaxial system with easy axis anisotropy ($D < 0$) and integer *S*. The negative and positive M_S values are located in the lefthand and righthand minima, respectively. Panel **a**: in zero field the two wells are equally populated and $\pm M_S$ states are degenerate. Panel **b**: when a magnetic field is applied along the $-z$ direction, only the favored minimum is populated ($M_S = S$, in this particular case). When B_z is removed (panel **c**), slow relaxation of the magnetization (SRM) occurs through subsequent steps, in order to restore the initial equilibrium of panel **a**. Quantum tunneling of magnetization (QTM) can also occur between degenerate levels.

2.2.4 Magnetization Dynamics

When an external magnetic field is applied along the *z* axis, the degeneracy between states with the same value of $|M_S|$ is removed by Zeeman splitting ($\widehat{H}_Z = \mu_B g_{zz} B_z \hat{S}_z$). This means that one of the two wells is stabilized over the other and becomes selectively populated. Since the two

wells correspond to opposite orientations of the magnetic moment, the molecule is magnetized by the applied field (see Fig. 2.3, panel **b**). When the field is brought to zero, the two wells become degenerate again. However, in a SMM the return to equilibrium (zero magnetization) may be an exceedingly slow process (Fig. 2.3, panel **c**). The molecule exhibits the so-called *slow relaxation of the magnetization* (SRM), which brings the magnetization to zero over very long timescales. Relaxation can occur with different mechanisms. When the decay of the magnetization over time is exponential, it is caused by the thermal energy. This thermally activated mechanism is called *Orbach relaxation*. Here, the magnetization reversal occurs through a multistep process involving successive $\Delta M_S = \pm 1$ transitions. For example, Fig. 2.3 (panel **c**) depicts all the transitions from the $+S$ to the $-S$ state ($S \rightarrow S-1$, $S-1 \rightarrow S-2$, …, $-S+2 \rightarrow -S+1$, $-S+1 \rightarrow -S$). These transitions, along with those where $\Delta M_S = \pm 2$, are principally caused by spin-phonon coupling,[7] which arises from the perturbation of the CF by the external environment (vibrations, rotations and geometrical strains of the lattice). In fact, during the steps from $M_S = +S$ to $M_S = 0$, the SMM absorbs phonons, which can be subsequently emitted in the transitions from the energy maximum to the state with $M_S = -S$. Due to the energy spacing implicit in Eq. 2.6, the rate-determining step of the process is the last one which allows reaching the top of the barrier. Moreover, when $k_B T << U$, the high-energy states are less and less populated.[7] Therefore, the relaxation rate exponentially decays upon cooling and the relaxation time τ follows the Arrhenius law, which is the signature of a thermally activated mechanism:

$$\tau = \tau_0 e^{(U_{\text{eff}}/k_B T)} \qquad (2.9)$$

In Eq. 2.9, τ_0 is a preexponential factor (or *characteristic time*) and U_{eff}/k_B is the *effective* barrier to magnetization reversal. Under-barrier relaxation processes, such as *quantum tunnelling of the magnetization* (QTM),[7] are also potentially operative, whereby the magnetic moment can flip its direction without climbing U. These under-barrier mechanisms contribute to speed up the magnetization dynamics and are responsible for a loss of magnetic information, leading to $U_{\text{eff}} < U$. QTM is a forbidden process for complexes which exhibit rigorously axial second-order anisotropy. In fact, here, the wavefunctions associated to the $\pm M_S$ pairs are orthogonal to each other and cannot overlap. Therefore, the electrons are not allowed to tunnel through the anisotropy barrier, from $-M_S$ to $+M_S$ state (or vice versa). When transverse anisotropies (such as rhombic distortion, or higher order perturbations) are present, the $\pm M_S$ wavefunctions are mixed together,[7,50–52] giving rise to new under-barrier mechanisms, which accelerate the relaxation process. The efficiency of QTM can be reduced by the application of an external DC field, which removes the degeneracy of the $\pm M_S$ levels (Fig. 2.3). However, at certain field

values the $-|M_S|$ and $+|M_S| - n$ (or $+|M_S|$ and $-|M_S| + n$, if the DC field has opposite sign) levels become degenerate again and the tunneling conditions are restored (n = 0, 1, 2, etc.).

SRM, which means long relaxation time, is an essential feature of SMMs. It is experimentally detected by AC susceptometry as a non-zero value of the out-of-phase component of the magnetic susceptibility (χ''). Both SRM[6] and QTM[8,53] were first observed in the **Mn12** cluster (see **Section 2.1**). Fig. 2.4 (from ref.[8]) shows the measured hysteresis loops upon application of an external magnetic field directed along the easy axis of a single crystal of **Mn12**. These loops proved the occurrence of QTM, which leads to characteristic magnetization "steps" at evenly-spaced field values. At these specific fields, the magnetization dynamics accelerates because the magnetic field restores the degeneracy condition between states lying on opposite sides of the barrier.

The performance of an SMM is related to the height of its energy barrier but also to the efficiency of QTM and other relaxation mechanisms. Figures of merit are the observation of zero-field SRM and the blocking temperature T_B, i.e. the temperature below which the magnetic moment is captured in one of the two energy minima, and magnetization reversal is inefficient. T_B can be used to compare different SMMs. It is conventionally defined as the temperature at which τ = 100 s.[3]

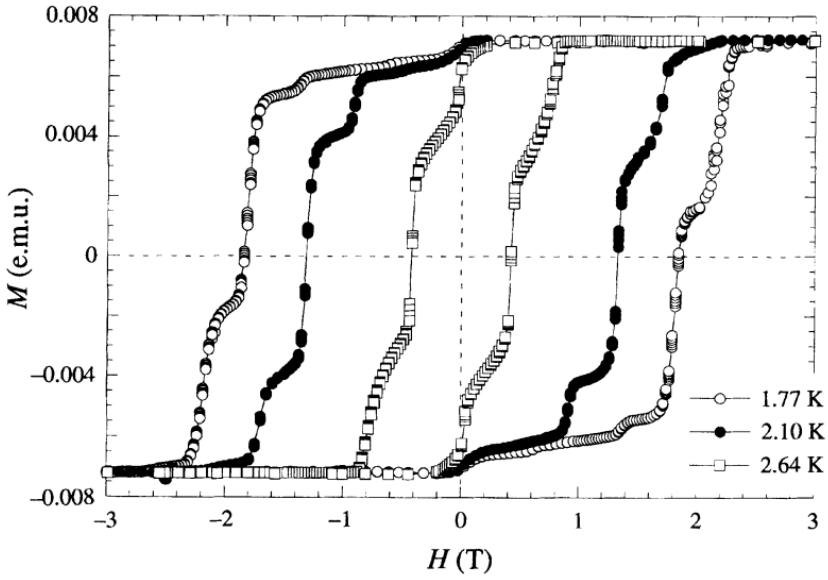

Figure 2.4. Hysteresis loops of the **Mn12** cluster, performed on a single crystal, with the magnetic field oriented along its easy axis. The image is taken from ref.[8].

In summary, in order to boost the performances of SMMs it is possible to play on several factors. For example, the anisotropy barrier can be raised, increasing the spin of the ground state and the easy-axis magnetic anisotropy. In addition, the efficiency of under-barrier

relaxation processes, such as QTM, must be suppressed as much as possible. However, accessing these high-temperature SMMs is not the only goal in molecular magnetism, where a variety of quantum effects are being studied deeply.

Chapter 3

Extended Metal Atom Chains (EMACs)

3.1 Introduction

Extended Metal Atom Chains (EMACs) are linear arrays of at least three metal ions, supported by polydentate organic ligands, which are wrapped along the metal chain.[54–57] They constitute a wide class of compounds. In fact, they can be homo- or heterometallic (HEMACs), homovalent or mixed valent species.[56,58] Oligo-*α*-pyridylamines or related proligands, like dipyridin-2-yl-amine (Hdpa) and N^2,N^6-di(pyridin-2-yl)pyridine-2,6-diamine (H_2tpda)[59,60] are the most widely used class of ligands in in this research area and are shown in Scheme 3.1. Sometimes they are helically twisted along the M chain, affording chiral molecules, which usually crystallize in racemic mixtures. Their geometry and multidentate nature enforce close distances between the metal centers, allowing for the formation of stringlike EMAC complexes. Sometimes the M−M distances are short enough for the establishment of M−M bonds, and/or strong magnetic interactions.[54,58] The metals can be arranged symmetrically or unsymmetrically along the chain, depending on several factors. In some EMACs, the metallic chains can be capped at their termini by axial ligands, which ensure charge balance. Without doubt, the family of EMACs played a key role in the understanding of M−M interactions.[54,56,57,61,62] Due to their unique structural, electronic and magnetic properties they have been examined as possible microscopic wires in molecular electronics.[58,61,63–65] Furthermore, EMACs attracted interest also in the field of SMMs, since the report that a series of penta- and trichromium(II) EMACs,[21,52] $[Cr_5(tpda)_4X_2]$ and $[Cr_3(dpa)_4X_2]$ ($X = Cl^-$, SCN^-), show an easy-axis anisotropy and low temperature SRM in their ground state ($S = 2$). Similar properties were found in related HEMACs, like Mo_2Cr and W_2Cr species.[66,67] The SMM behavior of EMACs will be better discussed in **Section 3.3**.

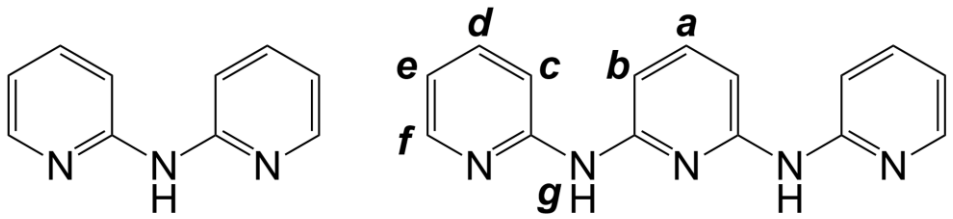

Scheme 3.1. Structures of oligo-*α*-pyridylamine proligands Hdpa and H_2tpda.

3.2 Ligands and Synthetic Strategies Towards EMACs

As mentioned above, oligo-*α*-pyridylamine ligands were widely used in the chemistry of EMACs.[54,55,59] In order to afford linear compounds, they must be fully deprotonated and adopt an *all-syn* conformation, where all N atoms act as donors Fig. 3.1 shows the two possible conformations for H_2tpda. Longer ligands afford chains which contain more M atoms, but the solubility of the compounds in organic solvents is decreased. For example, EMACs proved to be stable with up to 11 M ions, and the length record-holder is an undeca-nickel chain.[61,68] The coordination chemistry of Hdpa and H_2tpda was deeply studied in the field of EMACs. While the former is easily found on the market nowadays, H_2tpda was first synthesized in 1997 by Peng's group.[69] A much more efficient and reliable method was optimized and reported in 2018 by some of us.[70] Hdpa and H_2tpda can coordinate up to 3 and 5 metallic centers, respectively, and usually afford complexes with formula $[M_3(dpa)_4X_2]$ and $[M_5(tpda)_4X_2]$. Here, the M ions are most often in +2 oxidation state, while X are the axial ligands. They are usually halide ions (Cl^- and Br^-, rarely F^-), but also different anions can be present (NCS^-, CN^-, $^-C{\equiv}CPh$, $[Ag(CN)_2]^-$, etc.).[54,55] Even small neutral molecules, such as water, acetonitrile, etc., can sometimes act as axial ligands, towards neutral complexes or even cationic ones, whose extra-charge is then balanced by counteranions in the crystal lattice.[55]

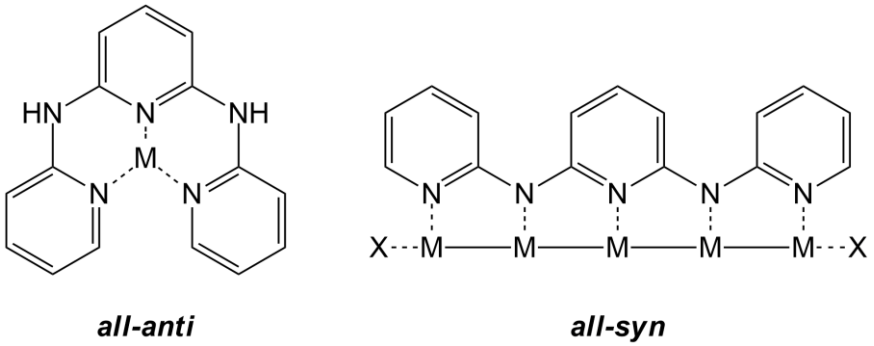

Figure 3.1. H_2tpda ligand in its two possible conformations.

A widely used strategy for the synthesis of EMACs consists in heating a mixture of MX_2 (X^- = halide ion, usually Cl^- o Br^-), Hdpa/H_2tpda and a strong base (usually ^{t}BuOK) in refluxing naphthalene.[56] Alternatively, the metal diacetate can be mixed with the ligand.[71] A great variety of EMACs were obtained with these two ligands. They are mainly constituted by first row transition metals (Cr, Co, Ni, Cu), but also by Ru and Rh.[55] Despite numerous attempts done in the past (see **Section 3.4.1**), iron(II)-based EMACs were absent in this series until 2018, when we reported complex $[Fe_4(tpda)_3Cl_2]$ (**1Cl**), which is described in **Section 3.4.2**.[20]

3.3 EMACs as Single-Molecule Magnets

As mentioned in **Chapter 2**, new classes of SMMs are being sought which feature thermally-persistent HS ground states resulting from strong ferromagnetic interactions. An easy-axis magnetic anisotropy is also desirable for SRM. Some polynuclear complexes of transition metals proved to satisfy these criteria, showing large spin values up to $S = 11$ for an octahedral hexairon MV compound reported by Betley and co-workers in 2018.[72] Similar characteristics can be encountered in EMACs, since they are polymetallic compounds with potentially strong M−M interactions. Their linear geometry is excellent to favor strong magnetic anisotropy of the easy-axis type, aligned along the metal chain. Moreover, the magnetic properties of EMACs are usually interesting, since the majority of them contains unpaired electrons. Therefore, EMACs seems to possess all the crucial factors to behave as SMMs. In fact, SMM behavior was first observed in the pentachromium(II) complex $[Cr_5(tpda)_4Cl_2]$ (**4**), by Cornia *et al.* in 2014.[52] Complex **4** showed SRM in an applied field of 2.5 kOe. Similar behavior was found in the shorter analogue $[Cr_3(dpa)_4Cl_2]$ (**4a**), and in the isothiocyanato derivatives

$[Cr_5(tpda)_4(NCS)_2]$ (**5**) and $[Cr_3(dpa)_4(NCS)_2]$ (**5a**), which (along with complex **4**) were deeply studied by some of us in a recent paper, that is presented in this Thesis in **Chapter 7**.[21] These chromium(II)-based EMACs exhibit a well-isolated ground state with $S = 2$, and feature similar easy-axis anisotropies. They behave as SMMs, displaying barriers to magnetization reversal (U_{eff}/k_B) ranging from 8.6 to 12.4 K, only observable in an applied static field of H = 2.0–3.5 kOe.[21]

Iron(II)-based EMACs were indicated as appealing synthetic targets in molecular magnetism, because of the large magnetic anisotropy and spin value of high-spin Fe^{2+}.[73,74] Moreover, it is not uncommon that polynuclear iron(II) compounds exhibit ferromagnetic interactions. In the following sections (**Section 3.4**, **3.4.1** and **3.4.2**) the challenging chemistry of iron(II) EMACs is examined. Some insights about their magnetic behaviour are also given.

3.4 Iron(II)-Based EMACs

Albeit Fe^{2+} was incorporated in some HEMACs,[58,75–79] homometallic iron(II)-based EMACs proved to be extremely challenging synthetic targets, because of the exceeding tendency of Fe^{2+} to undergo oxidation and/or hydrolysis processes. In fact, only two homometallic iron(II)-based EMACs have been reported prior to the beginning of this work. In 1998, Cotton *et al.* described the trinuclear complex $[Fe_3(DPyF)_4][PF_6]_2$ (**6**) ($DPyF^-$ = *N*,*N*'-di(2-pyridyl)formamidinate).[80] The first Fe^{2+} EMAC supported by oligo-*α*-pyridylamido ligands, $[Fe_4(tpda)_3Cl_2]$ (**1Cl**), was only recently reported by us,[20] although various attempts were done in the past (**Section 3.4.1**). Both complexes **1Cl** and **6** exhibit strong ferromagnetic interactions at room temperature, even if no M−M bonds are present. Finally, in 2020, Guillet *et al.* reported a new triiron(II) chain supported by silylated diaminopyridines, $[Fe_3(tmsap)_3]$ (**7**), which contains M−M bonds ($tmsap^{2-}$ = 2,6-bis[(trimethylsilyl)amido]pyridine).

3.4.1 Attempts Towards Iron(II)-based EMACs with Hdpa

Although complex **1Cl** was synthesized in 2018, many attempts towards iron(II)-based EMACs supported by oligo-*α*-pyridylamido ligands were done in the past. Two of them are here reported

to exemplify the synthetic difficulties in accessing this class of compounds. In 2000, the group of F. A. Cotton reported the tetrairon cluster $[Fe_4(\mu_4\text{-}O)(dpa)_6]$ (**8**), which was indicated as very unstable towards oxygen.[81] Compound **8** (Fig. 3.2) was isolated by mixing anhydrous iron(II) chloride with Lidpa, which was obtained by treatment of Hdpa with MeLi. This procedure failed to afford the desired iron(II) chain, probably due to traces of oxygen and/or water in the reaction environment. These impurities are reflected by the occurrence of the oxide anion in the structure. More recently, in 2015, Sundberg *et al.* explored the chemistry of Hdpa admixed with the organometallic reagent $[Fe_2(Mes)_4]$ (**2**) in hot toluene (HMes = mesitylene). They could only isolate the dinuclear complex $[Fe_2(dpa)_2(Mes)_2]$·toluene (**9**·toluene) and the longer analogue $[Fe_3(dpa)_4(Mes)_2]$ was apparently inaccessible (complexes **2** and **9** are represented in Fig. 3.2). They also highlighted some irreproducibility in the synthesis, which on one occasion afforded a different compound: $[Fe_2(dpa)_3Cl][Fe_4(\mu_4\text{-}O)](dpa)_6]$·3toluene (**9a**·3toluene). Compound **9a**·3toluene is composed by a first molecule, $[Fe_2(dpa)_3Cl]$ (**9b**), containing a Fe···Fe···Cl chain (Fig. 3.2), which co-crystallizes with the above-described complex **8** also isolated by Cotton *et al.* Therefore, the synthesis of iron(II)-based EMACs likely requires very strictly anaerobic and anhydrous conditions.

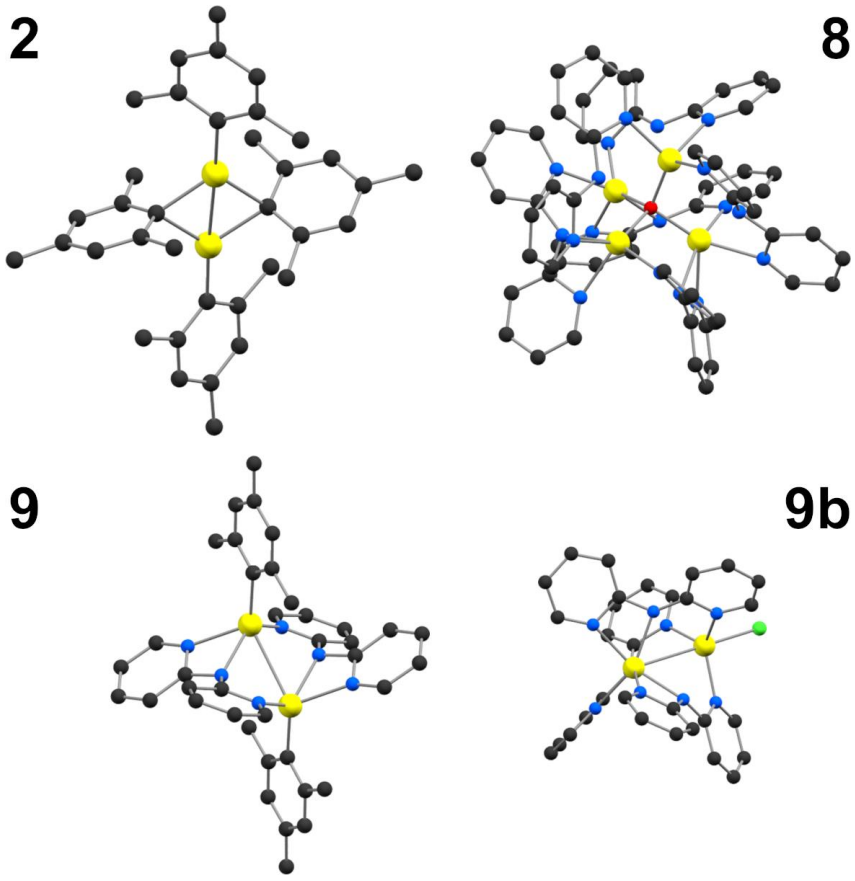

Fig. 3.2. Molecular structures of **2**, **8**, **9** and **9b** (ball and stick models). Color code: yellow, Fe; green, Cl; red, O; blue, N; black, C. H atoms are omitted for clarity.

3.4.2 The First Homometallic Iron(II)-based EMAC with Oligo-α-pyridylamido ligands: $[Fe_4(tpda)_3Cl_2]$ (**1Cl**)

Complex **1Cl** was reported by us at the beginning of this work, inspiring and laying the foundations for this Thesis. Fig. 3.3 shows the molecular structure of **1Cl** and represents in a simplified way its magnetic behavior. Compound $[Fe_4(tpda)_3Cl_2]\cdot 2.6CH_2Cl_2\cdot 0.84Et_2O$ (**1Cl**$\cdot 2.6CH_2Cl_2\cdot 0.84Et_2O$) was synthesized refluxing **2** with $Fe_4Cl_8\cdot 6THF$[82] (0.5 equiv of Fe) and H_2tpda (2 equiv) in toluene.[20] Compound **2** was identified as the key ingredient to success in the synthesis. In fact, it acts both as a deprotonating agent for H_2tpda, and as Fe^{2+} source, affording only HMes (an inert hydrocarbon) as a byproduct. Both **2** and **1Cl** are extremely air-sensitive compounds, and they were handled in a strictly controlled atmosphere of N_2. Complex **1Cl** is a tetrairon(II) string, where the M ions are held together by three $tpda^{2-}$ molecules, helically wrapped along the metallic chain. This chain is capped at its termini by two axial Cl^- ligands, whose presence balances the surplus of positive charges. The magnetic behavior of **1Cl** is interesting, since it presents strong ferromagnetic interactions at room temperature, even if M−M separations are too large for M−M bonds, as confirmed by Density Functional Theory (DFT) calculations. It was modeled as two ferromagnetic Fe_2 dimers, weakly antiferromagnetically coupled to each other at low temperature. In addition, **1Cl** showed weak SMM behavior below 2.8 K, only observable in a small applied magnetic field of 2 kOe.

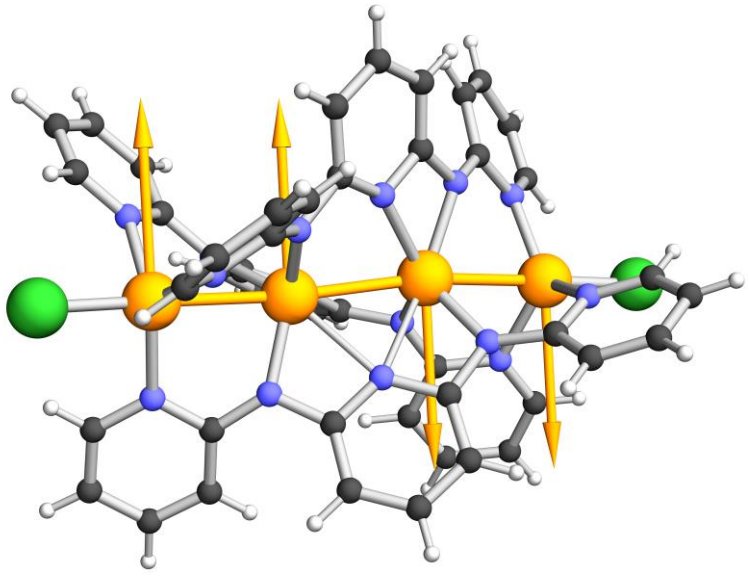

Figure 3.3. Molecular structure of **1Cl**, viewed approximately normal to the Cl−Fe···Fe···Fe···Fe−Cl chain. Color code: orange, Fe; green, Cl; blue, N; dark gray, C; light grey, H. The orange lines connecting the Fe ions do not correspond to chemical bonds, but provide a better representation only. The orange arrows pictorially represent the Fe spins, which interact to give two ferromagnetic Fe_2 dimers, antiferromagnetically coupled to each other.

Chapter 4

Tetrairon(II)-based Extended Metal Atom Chains as Single-Molecule Magnets

4.1 Introduction

The wide class of EMACs and their possible role as SMMs are deeply introduced in **Chapter 3**, were also the singular family of iron(II)-based EMACs is presented in detail (**Section 3.4**).

In this Chapter, we have used the same synthetic technique that allowed to access **1Cl** (see **Section 3.4.2**) to prepare its bromo analogue, $[Fe_4(tpda)_3Br_2]$ (**1Br**). We herein present a detailed comparison of the structural, electrochemical, and magnetic properties of the two congeners. In addition, to aid the analysis of DC magnetic data, the electronic structures of the constituent iron(II) ions were investigated by *ab-initio* (CASSCF-NEVPT2-SO) methods, considerably improving over our previous analysis of **1Cl** by AOM calculations.[20] We have found large single-ion anisotropies, whose competition with super-exchange interactions gives rise to a pseudo-doublet (non-Kramer doublet) ground state featuring a noncollinear spin arrangement. This weakly magnetic ground state can explain the observation of SMM behavior in AC magnetic studies conducted on both derivatives, SRM of **1Br** being detectable even at $H_{DC} = 0$.

4.2 Synthesis and Solution Studies

Compound **1Br** was synthesized by a procedure similar to that reported for its chloro analogue **1Cl**.[20] Refluxing $FeBr_2 \cdot 2THF$, $[Fe_2(Mes)_4]$ (**2**) and H_2tpda in 1:2:4 molar proportions in toluene under strictly anaerobic and anhydrous conditions gives an orange precipitate. This solid is likely to contain the tetrairon(II) EMAC (Scheme 4.1), which is only sparingly soluble in toluene but highly soluble in CH_2Cl_2. In fact, extraction of the solid with CH_2Cl_2 gives a red solution whose ESI-MS spectrum is similar to that recorded on a solution of pure **1Br** (*vide infra*). Concentration and cooling of these CH_2Cl_2 extracts affords crude **1Br** in moderate yield as an orange powder. MALDI-TOF/TOF-MS (positive ion mode), MALDI-TOF-MS for simplicity, shows one strong peak at m/z = 952.2 and a much weaker one at m/z = 1087.3, whose isotopic envelopes are consistent with $[Fe_3(tpda)_3+H]^+$ and $[Fe_4(tpda)_3Br+H]^+$, respectively (Figure 4.1). In addition, two weak signals are also present at m/z = 1031.3 and 1043.3, which are assigned to $[Fe_3(tpda)_3Br+H]^+$ and $[Fe_4(tpda)_3Cl+H]^+$, respectively (Figure 4.2). Traces of chloride salts may be present as contaminants in the reactant **2**, but the CH_2Cl_2 solvent may also represent a source of chloride ions during workup. This crude product can be recrystallized by vapour diffusion of Et_2O in a CH_2Cl_2 solution to give **1Br**$\cdot 2.3CH_2Cl_2 \cdot Et_2O$ as large dark red prisms.

These results confirm that iron amides are accessible via **2**,[83] which performs a dual role in the reaction. It not only acts as a source of iron(II) ions, but also serves as a strong base for deprotonation of H_2tpda, giving an inert hydrocarbon (HMes) as the only by-product. Because of their higher solubility in organic solvents compared to FeX_2, the THF adducts of iron(II) halides are used as additional sources of iron(II) and of the axial halide ligands. In spite of the favourable molar ratios of the reactants, $[Fe_5(tpda)_4Br_2]$ was not observed or isolated in these experimental conditions.

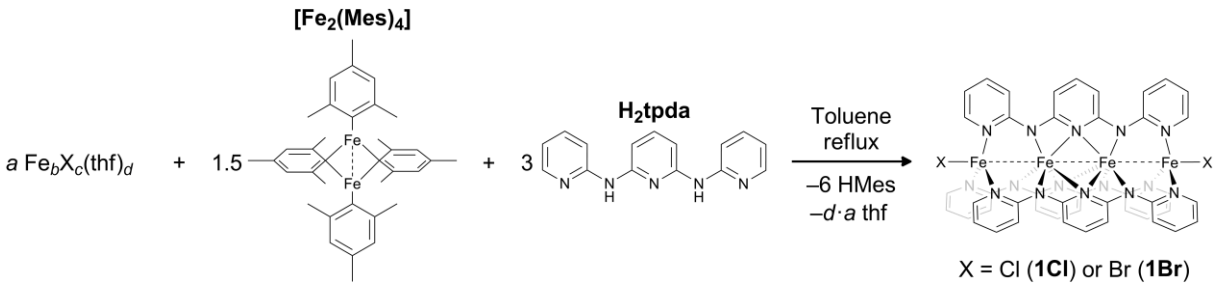

Scheme 4.1. Synthesis of tetrairon(II) EMACs $[Fe_4(tpda)_3X_2]$, where X = Cl (a = 1/4, b = 4, c = 8, d = 6) or Br (a = b = 1, c = d = 2).

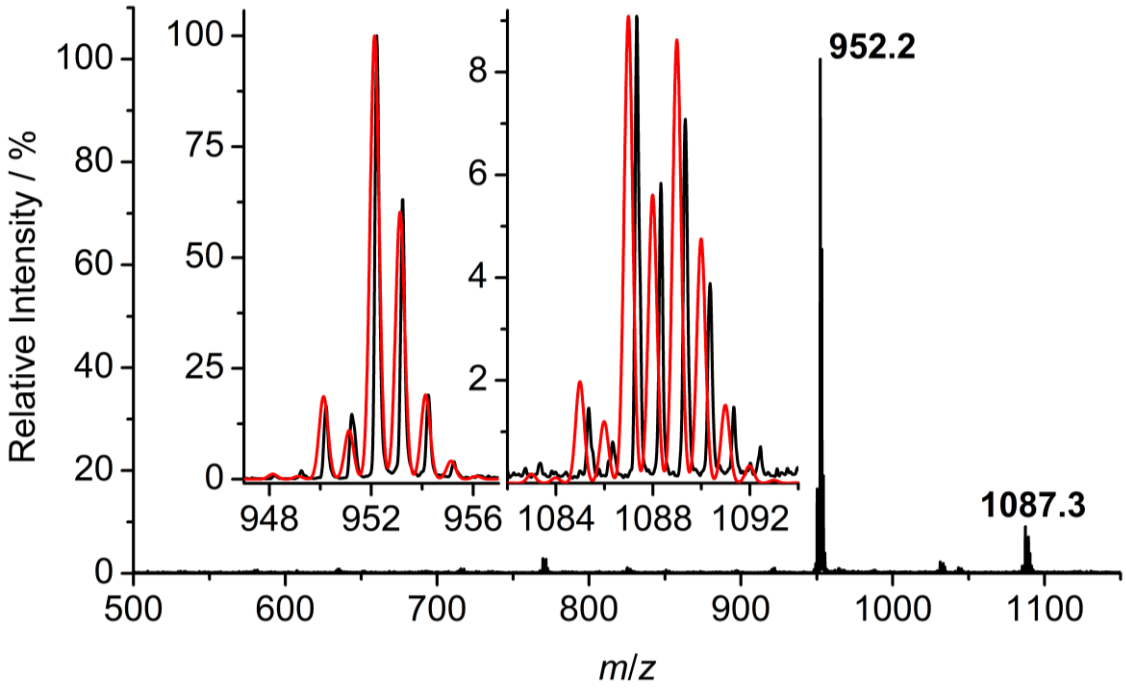

Figure 4.1. MALDI-TOF-MS spectrum of crude **1Br** in positive ion mode. The inset shows the experimental (black line) and simulated (red line) isotopic patterns of the peaks at *m*/*z* = 952.2 ($[Fe_3(tpda)_3+H]^+$) and 1087.3 ($[Fe_4(tpda)_3Br+H]^+$).

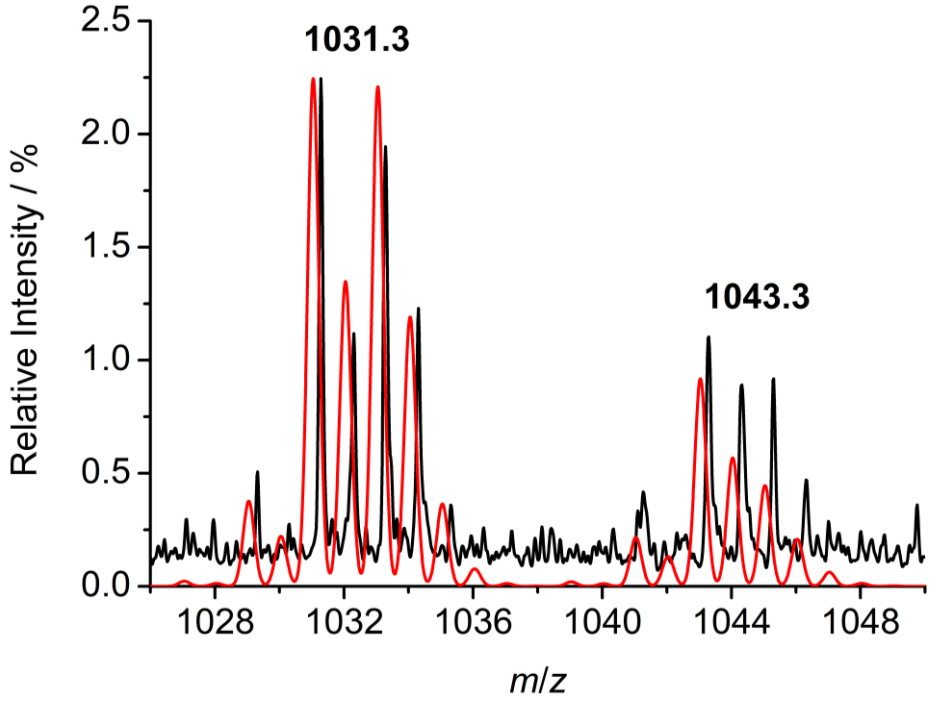

Figure 4.2. Magnification between *m*/*z* = 1026 and 1050 of the MALDI-TOF-MS spectrum of crude **1Br** in positive ion mode (black line). The red line represents the simulated isotopic pattern of the peaks at *m*/*z* = 1031.3 ($[Fe_3(tpda)_3Br+H]^+$) and 1043.3 ($[Fe_4(tpda)_3Cl+H]^+$).

The ESI-MS spectrum of **1Br** in CH_2Cl_2 (positive ion mode) shows no molecular ion peak (Fig. 4.3). Instead, two well resolved signals are present at *m*/*z* = 1030.1 (100%) and 986.1 (25%), whose isotopic patterns are consistent with the ionic species $[Fe_3(tpda)_3Br]^+$ and $[Fe_3(tpda)_3Cl]^+$, respectively. The same peaks are detected in the ESI-MS spectrum of chloro derivative **1Cl**, but with reversed relative intensity (13:100).[20] While formation of $[Fe_3(tpda)_3Br]^+$ in electrosprayed solutions of **1Cl** can only be explained assuming that traces of bromide ions remain from the synthesis of $[Fe_2(Mes)_4]$ (**2**), the origin of $[Fe_3(tpda)_3Cl]^+$ peak in the spectra of the bromo derivative is less clear. Chloride traces are already present in crude **1Br**, as shown by its MALDI-TOF-MS spectra (see above), but might also be generated by chloride abstraction from CH_2Cl_2 under ESI-MS ionization conditions, as found for other chlorinated solvents.[84,85]

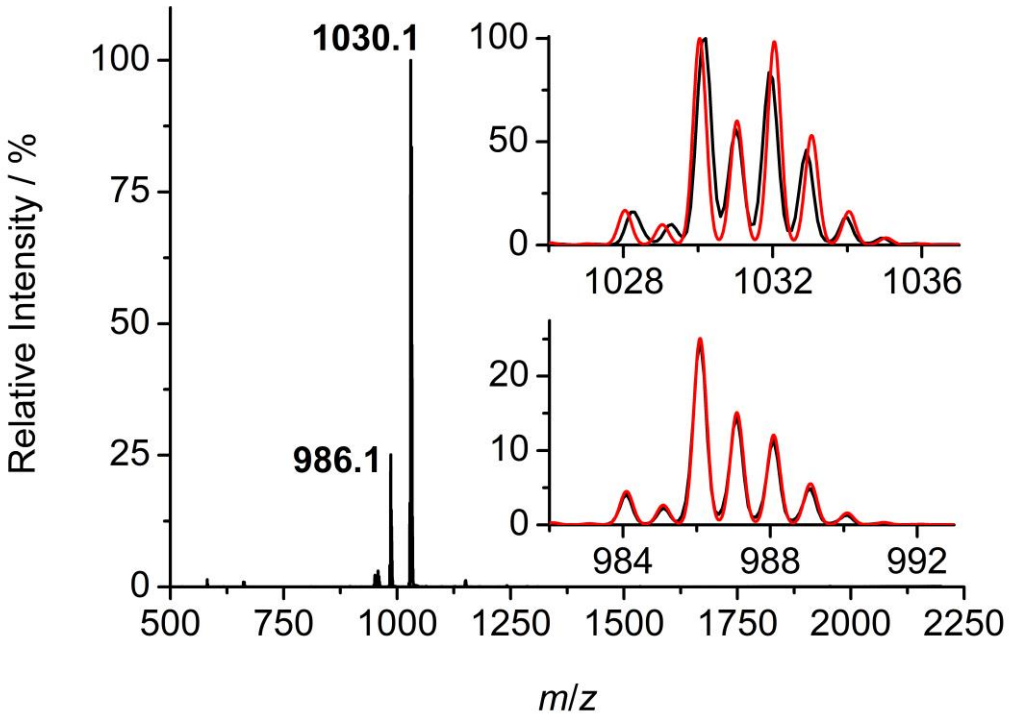

Figure 4.3. ESI-MS spectrum of **1Br** (direct infusion, CH_2Cl_2, positive ion mode). The inset shows the experimental (black line) and simulated (red line) isotopic patterns of the peaks at *m*/*z* = 1030.1 ($[Fe_3(tpda)_3Br]^+$) and 986.1 ($[Fe_3(tpda)_3Cl]^+$).

The room-temperature ^1H NMR spectrum of **1Br** in CD_2Cl_2 is displayed in Fig. 4.4 along with that of **1Cl** for comparison. In the two compounds, six paramagnetically shifted singlets (labelled from I to VI) are spread over a range of ~120 ppm with integrated areas in a 2:1:2:2:2:2 ratio (peak I in **1Br** partially overlaps with the CH_2 quartet of residual Et_2O). All signals except one (I) undergo downfield shifts compared to the signals of the free ligand in CD_2Cl_2 (Fig. A.1,

see **Appendix**). The three lowest-field signals (IV, V and VI) are approximately in the same position in the two compounds. However, significant differences occur in the high-field portion of the spectrum, since the half-intensity resonance (II) is the second highest-field signal in **1Cl** but the third in **1Br**.

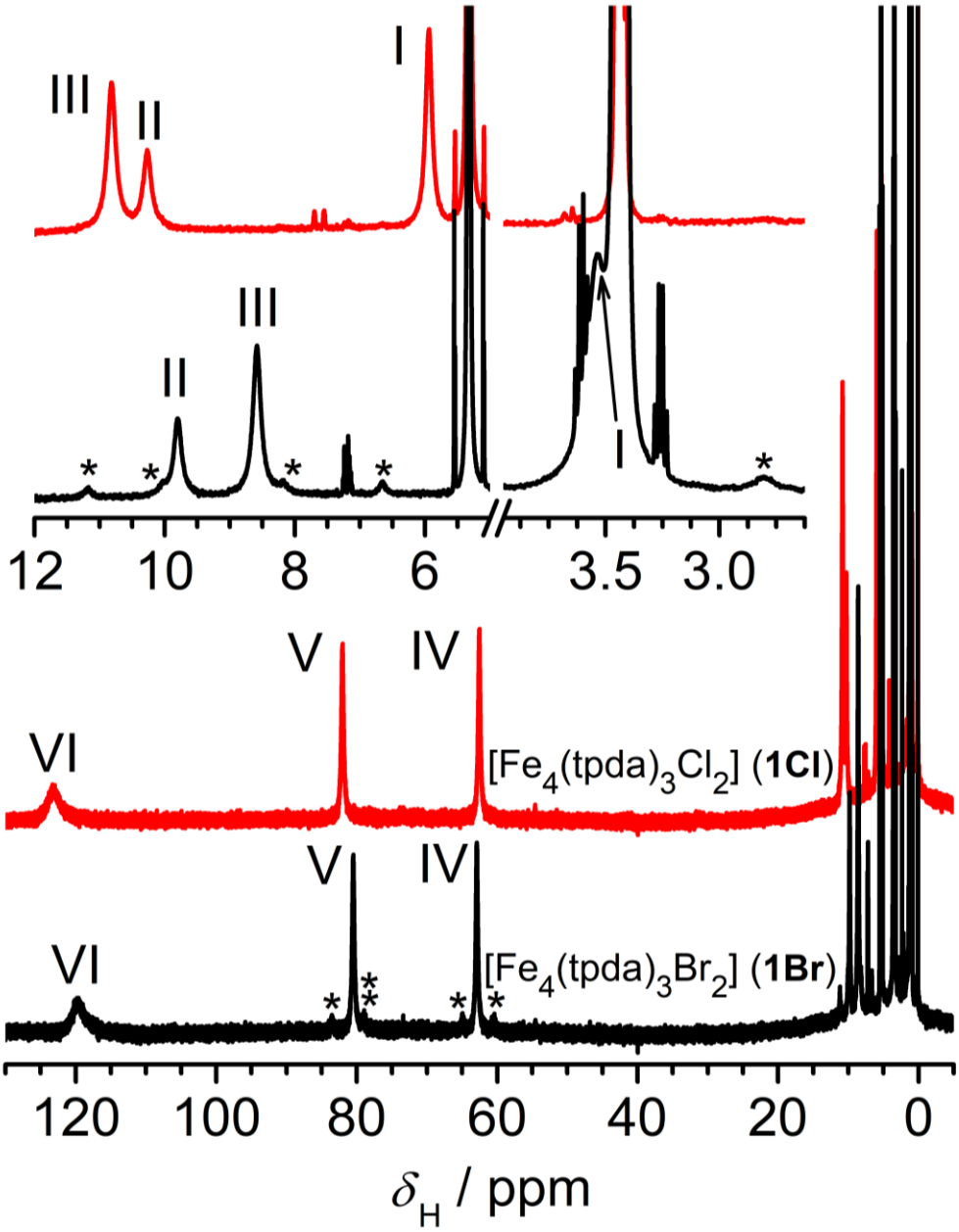

Figure 4.4. ^{1}H NMR spectra of **1Cl** (red line) and **1Br** (black line) in CD_2Cl_2 (298 K, 400.13 MHz). Signals of **1Cl** are labelled from I to VI in order of decreasing field; the same scheme is used for **1Br**, except that II still labels the half-intensity signal corresponding to H*a*. The inset shows a magnification of the spectra between 12.0 and 2.6 ppm (no peaks are present between 5.0 and 3.8 ppm). Processing parameters (TopSpin 4.0.6[86]): SI = TD, LB = 1.00 Hz. δ_H (ppm) = 3.43 (Et_2O, CH_2, q, ^3J = 7 Hz), 5.32 (residual protons in CD_2Cl_2), 7.15 (toluene, CH(2,4,6), m), 7.24 (toluene, CH(3,5), m). The spectral region between 2.6 and 0 ppm features no peaks from the compound (Figure A.2). The spectrum of **1Cl** is taken from Ref.[20]

This is a consequence of the fact that signals I and III are shifted upfield by 2.2-2.4 ppm in **1Br** vs **1Cl**. In both compounds, the observed spectra indicate that - in solution and over the NMR time scale - the molecules adopt the highest possible symmetry for a helical structure (D_3), implying three equivalent $tpda^{2-}$ ligands with C_2 symmetry and six chemically inequivalent H atoms. A similar behavior is displayed by pentachromium(II) EMAC $[Cr_5(tpda)_4Cl_2]$ (**4**), which exhibits its maximum possible symmetry (D_4) in CH_2Cl_2 solution over the NMR time scale, while it is much less symmetric in the solid state.[70] The half-intensity signal II can be firmly assigned to the *p*-H atom of the central pyridine ring (H*a* in Scheme 3.1). Among the remaining signals, the most downfield-shifted one (VI) is presumably due to *o*-H atoms (H*f*), which lie closest to the terminal iron(II) ions (Fe···H*f* = 2.98−3.16 Å in **1Br**, and 2.97−3.13 Å in **1Cl**). Though selective gradient-enhanced 1D-TOCSY (Total correlation spectroscopy) on **1Cl** exhibited no signal, a 2D-TOCSY experiment without gradients evidenced only a very weak cross peak between singlets I and III, which likely arise from the terminal pyridyl groups (H*c*-*e*). Isotopic-labelling experiments[70] would be required for a complete assignment of the spectrum.

It is important to note that neither the six peaks of **1Br** nor the set of eleven signals expected for a C_3-symmetric hetero-dihalide derivative are detected in the spectrum of **1Cl**. Since the intermolecular exchange of axial ligands is likely to be slow over the NMR timescale,[87] ^{1}H NMR data indicate that the species with axial bromido ligands found in the ESI-MS spectra of **1Cl** are trace impurities undetectable by NMR. However, the spectrum of **1Br** contains an additional set of ten weak singlets with roughly equal intensities, marked with asterisks in Figure 4.4. Considering that one signal may be broadened beyond detection or hidden, we tentatively ascribe this pattern to the hetero-dihalide species $[Fe_4(tpda)_3ClBr]$ (**1ClBr**), which is the likely source of chloro complexes found in ESI-MS and MALDI-TOF-MS spectra of **1Br** (see above). Hetero-dihalide tricobalt(II) EMACs were reported by Clérac *et al.*, who identified the species $[Co_3(dpa)_4Cl_2]$ (**10Cl**), $[Co_3(dpa)_4ClBr]$ (**10ClBr**) and $[Co_3(dpa)_4Br_2]$ (**10Br**) in ^{1}H NMR spectra and reported a strong tendency of Cl^- impurities to replace Br^- in pure **10Br**.[87] While the D_4-symmetric species **10Cl** and **10Br** give rise to four proton NMR signals, **10ClBr** has C_4 symmetry and eight ^{1}H NMR signals.[87] With the proposed assignment, the integrated signal intensities indicate a ~8% mole fraction of **1ClBr**, implying a 96:4 proportion of Br^- and Cl^- ligands. This low fraction is consistent with the results of the X-ray structure refinement, which provides no evidence for mixed Br/Cl axial ligands in **1Br**·2.3CH_2Cl_2·Et_2O (*vide infra*).

UV-Vis-NIR spectroscopy data were previously reported for the free ligand in THF solution.[20] The spectra show two intense absorptions bands, which are assigned to $\pi \rightarrow \pi^*$

transitions and are observed at 262 and 336 nm in H_2tpda, and at 320 and 390 nm tpda^{2-} (Fig. 4.5).[20] The electronic spectra of **1Cl** and **1Br** in CH_2Cl_2 solution both present two strong $\pi \rightarrow \pi^*$ transitions, with a slightly lower molar absorptivity (ε) in the latter (Fig. 4.5). The two peaks are red shifted as compared with those of H_2tpda and appear at 288 and 374 nm in **1Cl** and at 286 and 370 nm in **1Br**. In addition, they feature a shoulder at 448 nm. The electronic spectra of **1Cl** and **1Br** do not vary over time, but admission of air in the cuvette causes an immediate blueshift of the two main peaks and the disappearance of the shoulder at 448 nm, the final spectrum being superimposable to that of H_2tpda. Interestingly, the single strong band in the UV-Vis spectra of **10Cl** and **10Br** also has a lower ε and a higher energy in the bromo derivative.[87] This behavior can be explained considering the softer character of the bromido ligands, which promote better donation of electron density from the tpda^{2-} molecules and cause a smaller red shift.

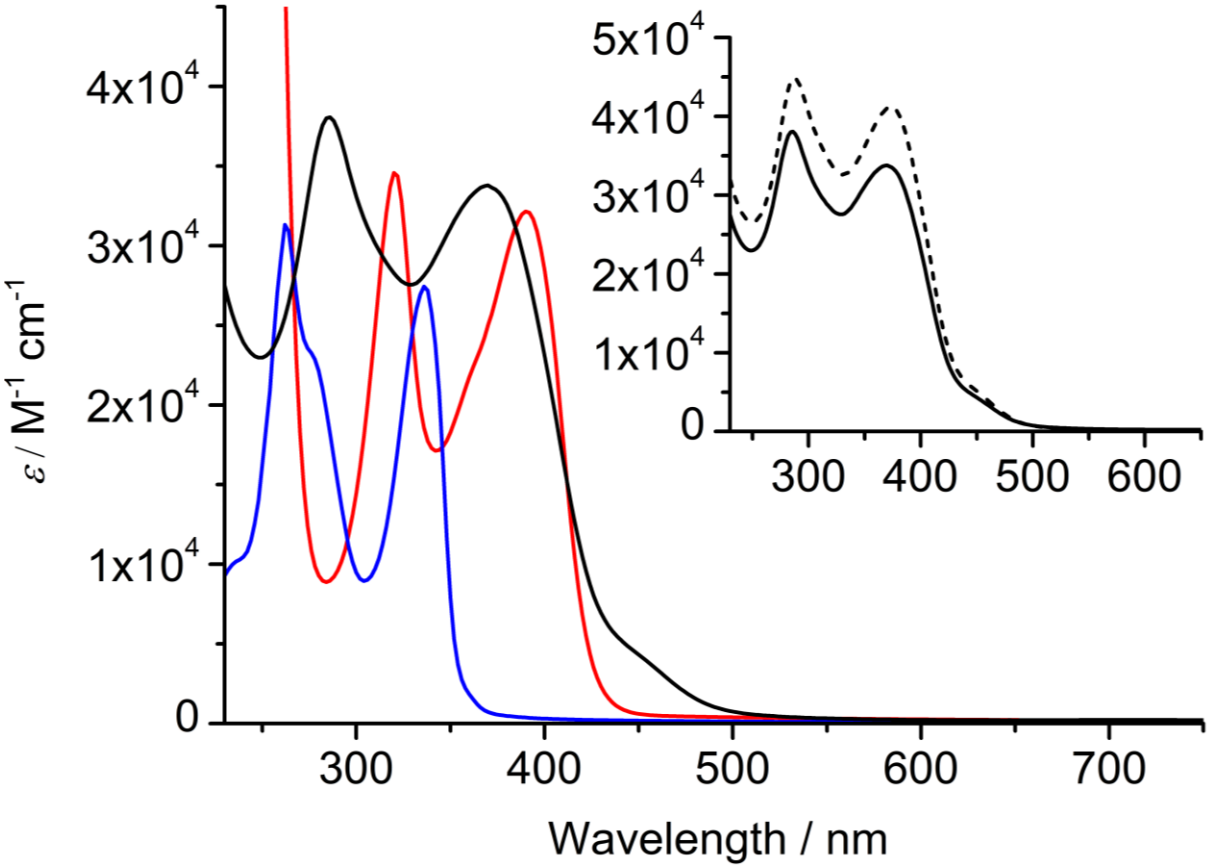

Figure 4.5. UV-Vis-NIR spectrum of **1Br** in CH_2Cl_2 (black line) and of H_2tpda in THF before (blue line) and after (red line) the addition of excess *t*BuOK. The inset shows a comparison between the spectra of **1Br** (solid line) and its chloro analogue **1Cl** (dashed line) in CH_2Cl_2. All the spectra were recorded up to 1500 nm, but only the characteristic portion of them is reported. The spectra of H_2tpda and **1Cl** are taken from Ref.[20]

4.3 X-Ray Structure of 1Br·2.3CH_2Cl_2·Et_2O

The molecular structure of **1Br**, as determined by SC-XRD on **1Br**·2.3CH_2Cl_2·Et_2O at 115(2) K, is displayed in Figure 4.6. The molecule has no crystallographically imposed symmetry and is partially disordered over two positions with 88:12 occupancies; the disorder is only resolvable on one $tpda^{2-}$ ligand, on the four metals, and on the terminal bromido ligands. We herein discuss only the highest-occupancy portion, whose crystal data and main geometric features are listed in Table 4.1 and Table 4.2, respectively.

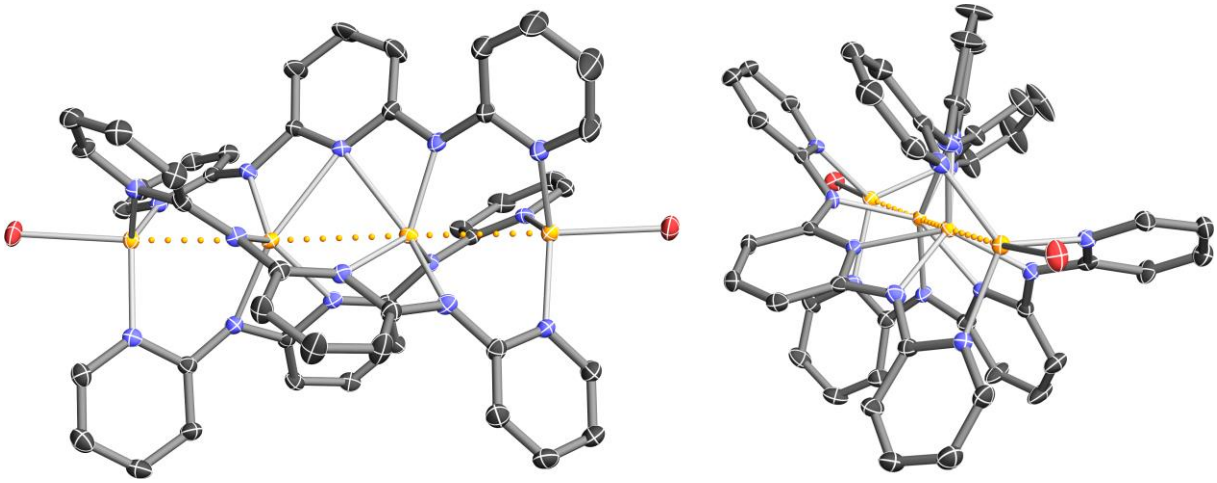

Figure 4.6. Molecular structure of **1Br** (right-handed enantiomer), viewed approximately normal to the Br–Fe···Fe···Fe···Fe–Br chain (left) and at ~25° from it (right). Color code: orange, Fe; red, Br; blue, N; dark gray, C. Hydrogen atoms and the minority disordered component are omitted for clarity. The dotted lines connecting the Fe centers are a guide to the eye and do not indicate chemical bonds. Thermal ellipsoids are drawn at the 60% probability level.

Complex **1Br** is a stringlike species formed by a chain of four metals arranged in a slightly helical *zig-zag* fashion (Fe···Fe···Fe = 167.7–172.1°, Fe···Fe···Fe···Fe torsion angle = 168.1°) and wrapped together by three all-*syn* $tpda^{2-}$ anions (Fig. 4.6). Each end of the chain is capped by one bromido ligand, with no crystallographic evidence for a detectable fraction of terminal chlorides (see experimental **Section 4.10.3**). **1Br** is indeed the first $tpda^{2-}$-based EMAC with bromido capping ligands.

Charge neutrality considerations and Bond-Valence Sum (BVS) calculations (Table 4.3) demonstrate that all four metal centers are HS iron(II), as confirmed by Mössbauer spectra (*vide infra*). The structure is almost superimposable to that of chloro analogue **1Cl** in **1Cl**· 2.6$CH_2Cl_2$0.84Et_2O, as shown in Fig. 4.7. The main difference is represented by the Fe–X (X = Br, Cl) distances, which are about 6% longer for Br (2.510–2.531 Å) vs Cl (2.358–2.386 Å).[20]

Table 4.1. Crystal data and refinement parameters for **1Br**·2.3CH_2Cl_2·Et_2O.

Identification code	201117na_7_work3bis_complete
Empirical formula	$C_{51.29}H_{47.58}Br_2Cl_{4.63}Fe_4N_{15}O$
Formula weight	1437.22
Temperature (K)	115(2)
Crystal system	monoclinic
Space group	$P2_1/c$
a (Å)	19.6801(16)
b (Å)	16.4420(14)
c (Å)	18.6092(14)
α (deg)	90
β (deg)	104.979(3)
γ (deg)	90
Volume (Å^3)	5817.0(8)
Z	4
ρ_{calcd} (g cm^{-3})	1.641
μ (mm^{-1})	2.616
F(000)	2884.0
Crystal size (mm^3)	0.710 × 0.530 × 0.390
Radiation	Mo-Kα (λ = 0.71073 Å)
$2\theta_{min}/2\theta_{max}$ (deg)	4.286/56.072
Index ranges	$-24 \le h \le 26$, $-21 \le k \le 20$, $-24 \le l \le 24$
Reflections collected	61609
Independent reflections	14013 [R_{int} = 0.0245, R_{sigma} = 0.0202]
Data/restraints/parameters	14013/134/829
Goodness-of-fit on F^2	1.214
Final R indexes ($I \ge 2\sigma(I)$)	R_1 = 0.0606, wR_2 = 0.1489
Final R indexes (all data)	R_1 = 0.0664, wR_2 = 0.1520
Largest diff. peak/hole (e Å^{-3})	2.60/−0.99

Table 4.2. Selected interatomic distances (Å) and angles (deg) for **1Br**·2.3CH_2Cl_2·Et_2O.

Fe1−Fe2	2.9747(12)
Fe2−Fe3	2.9711(11)
Fe3−Fe4	2.9551(12)
Fe1−Br1	2.5314(11)
Fe4−Br2	2.5100(12)
Fe1−N1	2.089(4)
Fe1−N2	2.067(4)
Fe1−N3	2.096(4)
Fe2−N4	2.108(4)
Fe2−N5	1.993(4)
Fe2−N6	2.011(4)
Fe2−N7	2.175(4)
Fe2−N8	2.492(4)
Fe3−N8	2.500(4)
Fe3−N9	2.234(4)
Fe3−N10	2.042(4)
Fe3−N11	2.036(4)
Fe3−N12	2.087(4)
Fe4−N13	2.088(4)
Fe4−N14	2.088(4)
Fe4−N15	2.071(5)
Br1−Fe1−Fe2	177.01(6)
Fe1−Fe2−Fe3	172.08(4)
Fe2−Fe3−Fe4	167.67(6)
Fe3−Fe4−Br2	178.62(8)

To the best of our knowledge, no other EMACs containing $tpda^{2-}$ and different axial halides are known. However, a comparison can be made with trimetallic chains supported by dpa^{-}, the shorter congener of $tpda^{2-}$ (Scheme 3.1). The structures of $[M_3(dpa)_4Cl_2]$ and $[M_3(dpa)_4Br_2]$ are

reported for M = Cr^{2+} (213 K),[88] Co^{2+} (109-111 K),[87,89] and Cu^{2+} (295 K).[90,91] In these complexes the M−X bond distance also increases by 5−8% when replacing Cl with Br.

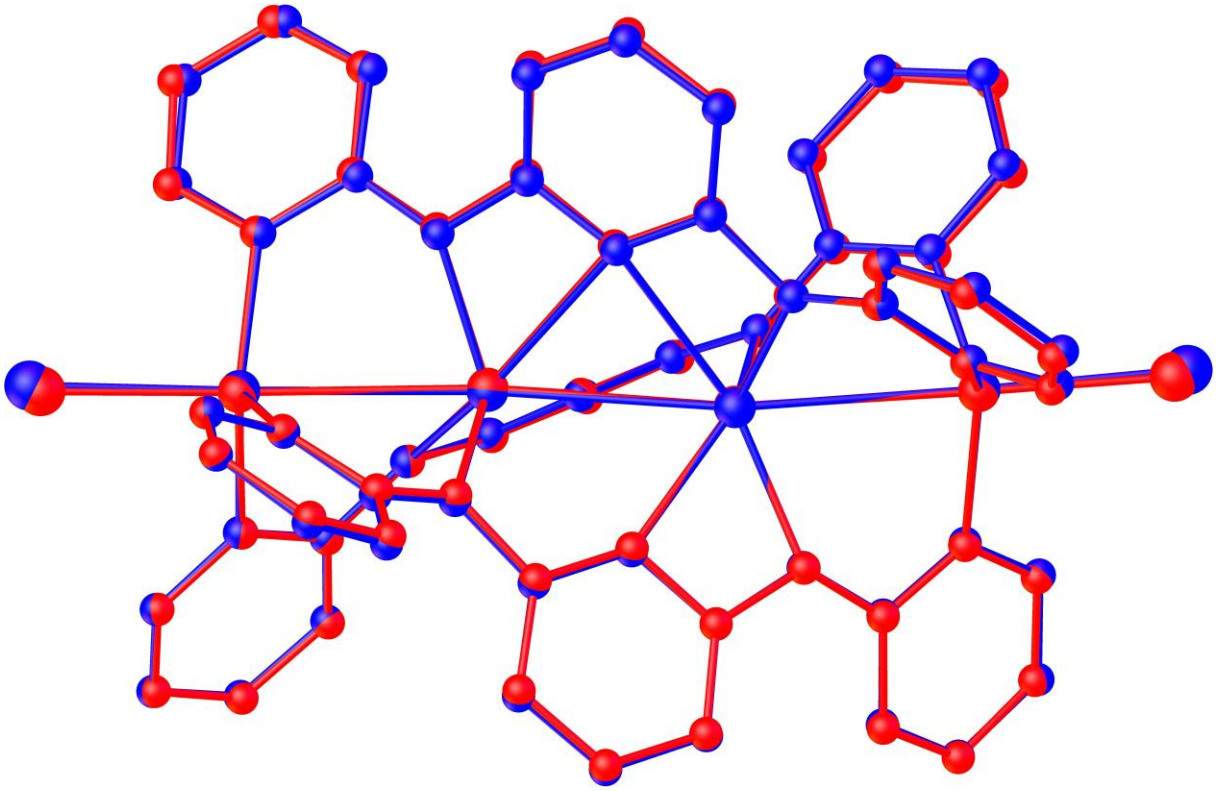

Figure 4.7. Superimposed molecular structures of **1Cl** (red) and **1Br** (blue) drawn using a ball-and-stick model (right-handed enantiomers). The minority disordered component in **1Br** and hydrogen atoms in both **1Cl** and **1Br** are omitted for clarity. The lines connecting the Fe centers do not indicate chemical bonds.

Table 4.3. Bond-Valence Sum calculations on **1Br**·2.3CH_2Cl_2·Et_2O.[a]

Atom	Fe^{2+}	Fe^{3+}
Fe1	1.650	1.902
Fe2	1.895	2.228
Fe3	1.767	2.078
Fe4	1.680	1.933

[a]Bond-valence parameters (R_0; B) were taken from file bvparm2016.cif available at https://www.iucr.org/resources/data/datasets/bond-valence-parameters: Fe^{2+}–N^{-3} (1.76; 0.37), Fe^{3+}–N^{-3} (1.82; 0.37), Fe^{2+}–Br^{-1} (2.21; 0.35), Fe^{3+}–Br^{-1} (2.22; 0.37).

The Fe···Fe distances in **1Br** range from 2.955 to 2.975 Å and are hence comparable with those found in **1Cl** (2.941 to 2.991 Å). They are far too large for a M−M bond, but shorter than

in dpa^- based diiron(II) complexes, such as $[Fe_2(dpa)_2(Mes)_2]$[83] (**9**; 3.104(2) Å), $[Fe_2(dpa)_3Cl]$[83] (**9b**; 3.043(1) Å), and $[Fe_2(dpa)_2(hmds)_2]$[92] (**11**; Hhmds = 1,1,1,3,3,3-hexamethyldisilazane; 3.3609(1) Å). Triiron(II) complexes $[Fe_3(DPyF)_4][PF_6]_2$ (**6**) and $[Fe_3(tmsap)_3]$ (**7**) present considerably shorter Fe···Fe distances of 2.782(1)−2.783(1) and 2.4416(5) Å, respectively, consistent with the presence of M−M bonds in the latter.[80,93]

The coordination geometry of the metal centers is highlighted in Fig. 4.8. The terminal iron centers (Fe1 and Fe4) possess a distorted trigonal-pyramidal coordination environment, afforded by three pyridyl N atoms (N_{py}) and one terminal bromido ligand (Fe−N_{py} = 2.067−2.096 Å, N_{py}−Fe−N_{py} = 110.8−125.7°, Br−Fe−N_{py} = 95.1−98.4°). The internal iron centers (Fe2 and Fe3) are pentacoordinated, with a very distorted geometry. Each of them is primarily involved in three short contacts with amido N atoms (N4, N5, N6 and N10, N11, N12, Fe−N = 1.993−2.108 Å). In addition, Fe2 and Fe3 have a slightly longer contact with the central N_{py} atoms of two different $tpda^{2-}$ ligands (N7 and N9, Fe−N = 2.175−2.234 Å). The central N_{py} atom (N8) of the third $tpda^{2-}$ ligand is involved in a longer coordination bond with both Fe2 and Fe3, thus completing their coordination spheres (Fe−N8 = 2.492−2.500 Å). It is worth noting that only this $tpda^{2-}$ ligand is almost symmetrically bonded to the metal chain (Fe2−N8 ≈ Fe3−N8). The remaining two ligands are asymmetrically positioned, so that in the solid state **1Br** does not achieve the maximum possible symmetry for a helical structure (D_3) but approaches twofold symmetry perpendicular to the metal chain. Each $tpda^{2-}$ ligand is helically wrapped around the linear array of metal ions, due to steric interactions between pyridyl *β*-H atoms (H*b* and H*c* in Scheme 3.1). As a result of this twisting, the dihedral angle between neighboring pyridine rings of the same $tpda^{2-}$ ligand ranges from 36° to 53° (Fig. 4.6, on the right). The molecule is thus chiral, but both enantiomers are found in a 1:1 ratio in the centrosymmetric crystal structure.

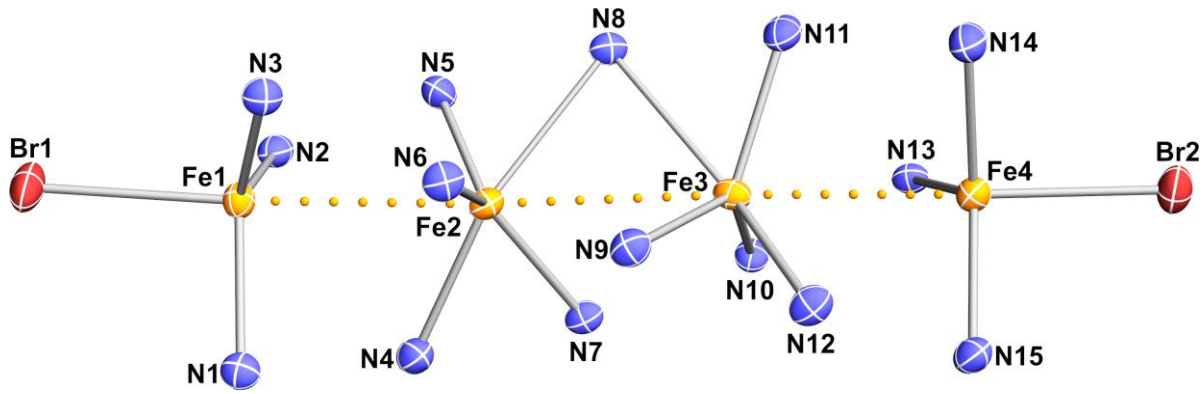

Figure 4.8. Coordination geometry of the four Fe centers in **1Br** (right-handed enantiomer), drawn using the same color code as in Figure 4.6. The dotted lines connecting the Fe centers do not indicate chemical bonds. Thermal ellipsoids are drawn at the 60% probability level.

For comparison, the other $tpda^{2-}$-based homometallic EMACs reported in the past (Ni_5,[94] Cr_5[95,96], Co_5[97] and Ru_5[98]), are *penta*metallic chains wrapped by *four* ligands and thus contain one more metal center and one more ligand. Quite remarkably, a similar situation is encountered in iron(II) complexes of tridentate dpa^-. Only two iron(II) centers are incorporated,[83,92] whereas with different metals the coordination capacity of the ligand is fully exploited to give Ni_3,[99,100] Cr_3,[88] Co_3,[87,89] Cu_3[90,91] and Ru_3[101] species. This behavior is difficult to understand on purely structural grounds, e.g. on the basis of ionic radii. One adverse factor might be the tendency of iron(II) to undergo facile oxidation and hydrolysis processes in the adopted experimental conditions.

4.4 Electrochemistry

Extensive, temperature dependent electrochemical measurements were carried out on **1Cl** and **1Br** in CH_2Cl_2 solution. The cyclic voltammogram of **1Cl** at −10°C using 0.1 M TBACl as supporting electrolyte was presented previously in Ref.[20] and shows four quasi-reversible signals spanning a potential range of 0.80 V (Fig. 4.9 and Table 4.4). **1Br** behaves similarly: its cyclic voltammogram at −13°C (Fig. 4.9) consists of four consecutive redox signals (hereafter indicated as signals I, II, III, and IV at increasing potential values). The curves are stable and do not change with time using 0.1 M tetra-*n*-butylammonium bromide (TBABr) as supporting electrolyte. As found in **1Cl**, the peak-to-peak separation increases from signal I to IV and with the potential scan rate. The peak currents of all the signals are proportional to the square root of the scan rate (not shown). The electrochemistry of the complex consists of four quasi-reversible and diffusion controlled redox processes spanning a potential window of only 0.75 V, whereby the **1Br** complex shuttles between five oxidation states (Table 4.4). These four reversible ET processes will be hereafter indicated as ET-I, ET-II, ET-III and ET-IV and correspond to the ETs: $(Fe_4)^{8+} \leftrightarrows (Fe_4)^{9+}$, $(Fe_4)^{9+} \leftrightarrows (Fe_4)^{10+}$, $(Fe_4)^{10+} \leftrightarrows (Fe_4)^{11+}$, $(Fe_4)^{11+} \leftrightarrows (Fe_4)^{12+}$. The $E°'$ values of corresponding ET steps (from ET-I to ET-IV) are much more negative in **1Cl**[20] than in **1Br**. The difference amounts to 0.110-0.235 V, depending on the redox step. Thus, from a thermodynamic point of view, chlorido ligands allow an easier oxidation of the Fe^{2+} ions than bromido ligands. This agrees with the higher Fe^{3+}-binding affinity of Cl^- with respect to Br^- and is consistent with experimental evidence gained during

the syntheses (i.e., **1Br** is less air-sensitive). The $E°'$ values of all redox steps in both complexes show a monotonic linear increase with increasing temperature from −13 to +3 °C (Figures 4.10 and 4.11). The calculated values of $\Delta S°'_{rc}$ and $\Delta H°'_{rc}$ are reported in Table 4.5.

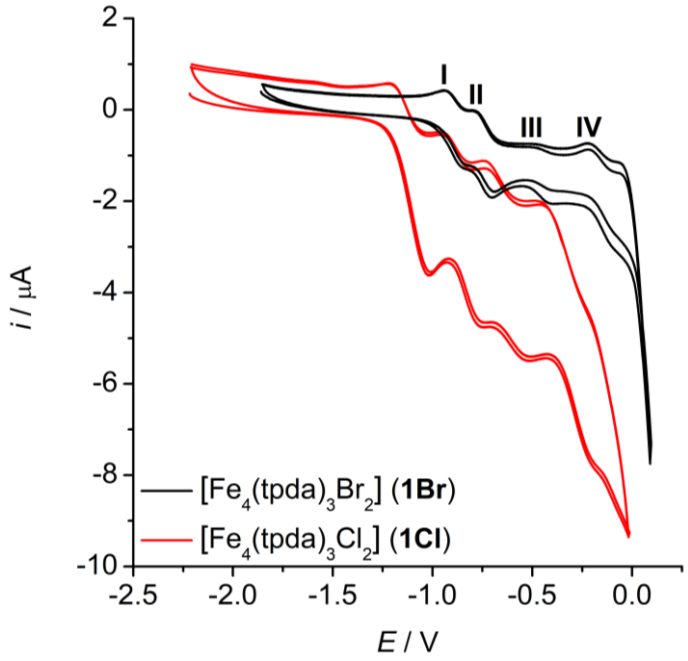

Figure 4.9. Cyclic voltammogram of **1Br** (black line) and **1Cl** (red line). Conditions for **1Br**: glassy carbon (GC) working electrode, 0.1 M TBABr in CH_2Cl_2, scan rate 0.05 V s^{-1}, ferrocenium/ferrocene reference, T = −13 °C. Conditions for **1Cl**: GC working electrode, 0.1 M TBACl in CH_2Cl_2, scan rate 0.05 V s^{-1}, ferrocenium/ferrocene reference, T = −10 °C (Data for **1Cl** are taken from Ref.[20]).

Table 4.4. Electrochemical data from CV for the consecutive ET processes of **1Br** (**1Cl**) in CH_2Cl_2 at −13 °C, using TBABr (TBACl) 0.1 M as base electrolyte.[a]

	$E°'$ / V	$\Delta E°'$ / V	K_c	k_{ET} / cm s^{-1}
ET-I	−0.890 (−1.125)			0.00952 (0.00418)
		0.145 (0.270)	$0.65\cdot10^3$ ($1.73\cdot10^5$)	
ET-II	−0.745 (−0.855)			0.0102 (0.00341)
		0.302 (0.216)	$7.21\cdot10^5$ ($1.55\cdot10^4$)	
ET-III	−0.443 (−0.639)			0.00721 (0.00225)
		0.301 (0.316)	$6.89\cdot10^5$ ($1.35\cdot10^6$)	
ET-IV	−0.142 (−0.323)			0.00514 (0.00192)

[a] $E°'$ = formal reduction potential (referred to ferrocenium/ferrocene redox couple), $\Delta E°'$ = separation in $E°'$ values of consecutive ET processes, K_c = comproportionation constant, k_{ET} = heterogeneous ET rate constant. The average errors on $E°'$, $\Delta E°'$, K_c and k_{ET} are ±0.002 V, ±0.004 V, ±12% and ±6%, respectively.

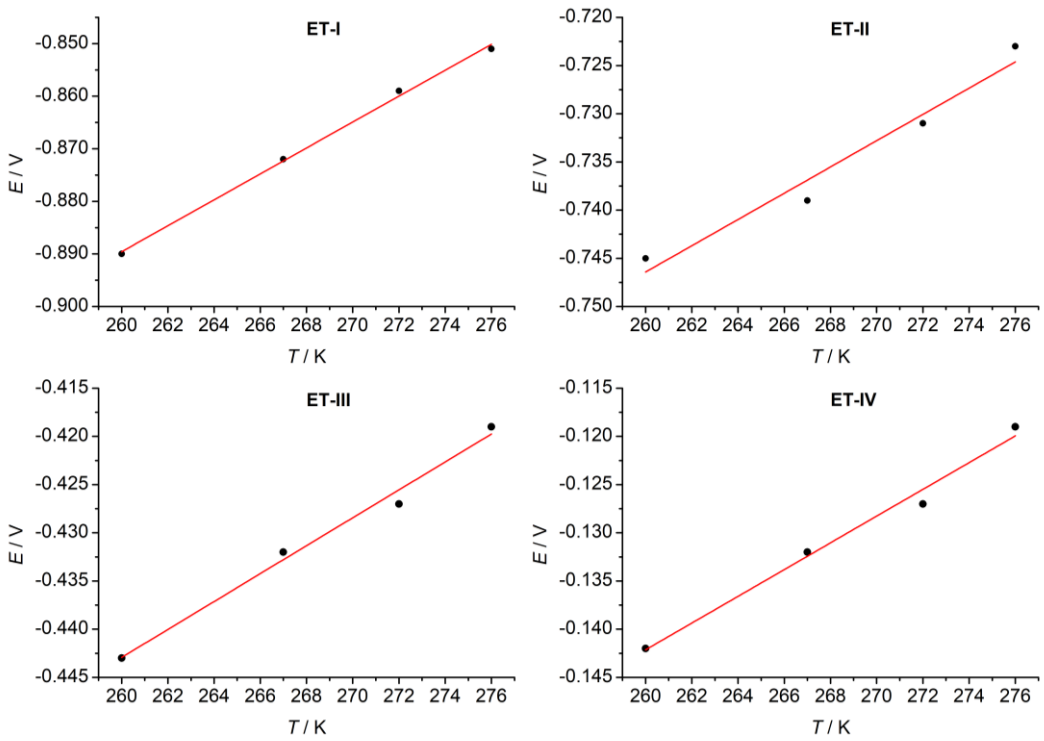

Figure 4.10. Plot of $E°'$ versus temperature for the different ET steps of $[Fe_4(tpda)_3Br_2]$ (**1Br**). Conditions: working electrode, GC; 0.1 M TBABr in CH_2Cl_2; scan rate, 0.05 V s^{-1}; reference, ferrocenium/ferrocene. The red lines represent the linear fits to the experimental datapoints.

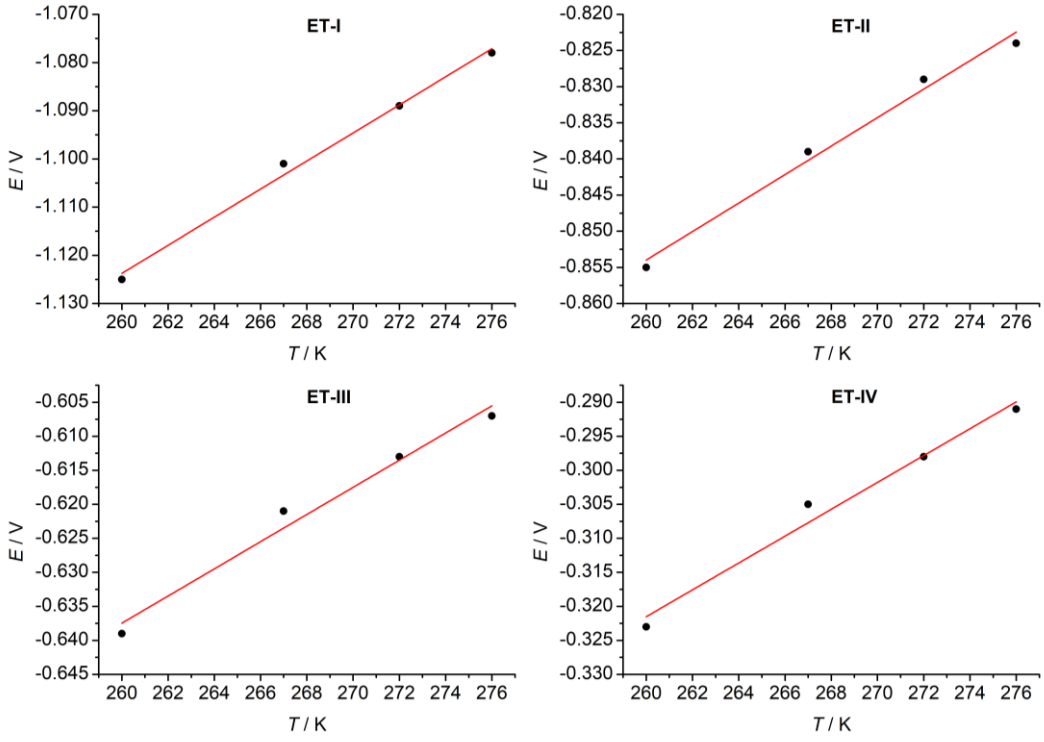

Figure 4.11. Plot of $E°'$ versus temperature for the different ET steps of $[Fe_4(tpda)_3Cl_2]$ (**1Cl**). Conditions: working electrode, GC; 0.1 M TBACl in CH_2Cl_2; scan rate, 0.05 V s^{-1}; reference, ferrocenium/ferrocene. The red lines represent the linear fits to the experimental datapoints.

Table 4.5. Thermodynamic contributions to $E^{\circ\prime}$ for **1Br** and **1Cl** in CH_2Cl_2 solution at −13 °C, using 0.1 M TBABr and TBACl (tetra-*n*-butylammonium chloride), respectively, as supporting electrolytes.[a]

1Br	$E^{\circ\prime}$ / V (±0.002)	$\Delta S^{\circ\prime}_{rc}$ / J K^{-1} mol^{-1}	$\Delta H^{\circ\prime}_{rc}$ / kJ mol^{-1}	$T\Delta S^{\circ\prime}_{rc}$ / F	$-\Delta H^{\circ\prime}_{rc}$ / F
I	−0.890	233±11	147.2±2.2	0.606±0.029	−1.525±0.022
II	−0.745	136±8	107.7±2.1	0.366±0.021	−1.116±0.021
III	−0.443	140±7	79.6±1.9	0.377±0.019	−0.825±0.019
IV	−0.142	134±12	48.5±1.7	0.348±0.032	−0.701±0.017
1Cl					
I	−1.125	281±12	181.5±2.1	0.757±0.032	−1.881±0.021
II	−0.855	190±9	131.8±2.2	0.512±0.024	−1.366±0.022
III	−0.639	193±10	111.6±1.8	0.520±0.027	−1.156±0.018
IV	−0.323	190±12	80.5±1.1	0.512±0.032	−0.834±0.011

[a]Potential values and thermodynamic parameters are referenced to ferrocenium/ferrocene redox couple.

$E^{\circ\prime}$ is made up of two opposite contributions: an enthalpic term which is negative and predominant, and an entropic term which is positive and smaller in magnitude. The enthalpic contribution decreases progressively in magnitude from ET-I to ET-IV, although the $\Delta H^{\circ\prime}_{rc}$ values are markedly different in **1Cl** and **1Br**. The entropic contribution $\Delta S^{\circ\prime}_{rc}$ in ET-I is much higher than in the remaining ET steps, which conversely entail very similar entropic contributions. This is probably related to the fact that the reorganization effect of the solvent around the complex is much more extensive in ET-I than in the other ET steps. In fact, the first oxidation (ET-I) transforms a neutral species into a monopositive one, while ET-II to ET-IV increase the charge of an already charged species. Other related iron complexes exhibit similar electrochemical behavior.[102,103]

In **1Br** the observed differences in $E^{\circ\prime}$ values for consecutive ET processes ($\Delta E^{\circ\prime}$) correspond to moderate (ET-I/ET-II) or large (ET-II/ET-III and ET-III/ET-IV) comproportionation constants $K_c = \exp[nF(E^{\circ\prime}_1 - E^{\circ\prime}_2)/RT]$, whose values are shown in Table 4.4.[104,105] The order of magnitude of K_c in **1Br** spans the range 10^3-10^6 as compared with 10^4-10^6 in **1Cl**. The data indicate high thermodynamic stability toward disproportionation for the mixed valence species $(Fe_4)^{10+}$ and $(Fe_4)^{11+}$ derived from **1Br**, which might become synthetically accessible,[106] whereas $(Fe_4)^{9+}$ is much less stable. Interestingly, replacing Cl^- axial ligands with Br^- affects

to the largest extent the stability of the monooxidized $(Fe_4)^{9+}$ species, whose K_c value undergoes a more than 200-fold decrease from **1Cl** to **1Br**.

The enthalpic ($\Delta H^{\circ\prime}_c$) and entropic ($\Delta S^{\circ\prime}_c$) contributions to K_c were determined by recording the temperature dependence of K_c and applying the van't Hoff equation (Fig. 4.12). The results, presented in Table 4.6, reveal that in both **1Br** and **1Cl** the major contribution to K_c is of enthalpic origin, although a significant, albeit minor, entropic contribution is observed for the species $(Fe_4)^{9+}$. The other mixed valent species show negligible entropic contributions to K_c. The observed difference is due to the very positive value of $\Delta S^{\circ\prime}_{rc}$ of ET-I (see above).

The heterogeneous k_{ET} values for signals I and II of **1Br** are rather similar, but then progressively decrease from signal II to IV (i.e., with increasing oxidation state and charge of the complex, see Table 4.4) probably due to a progressive increase in the reorganization energy λ, as already observed for other mixed valence complexes.[107] A similar behavior is shown by the chloro derivative **1Cl**, although the differences in k_{ET} values are much less noticeable. The k_{ET} values of corresponding ET steps are always higher in **1Br** than in **1Cl**, suggesting different reorganization energies.

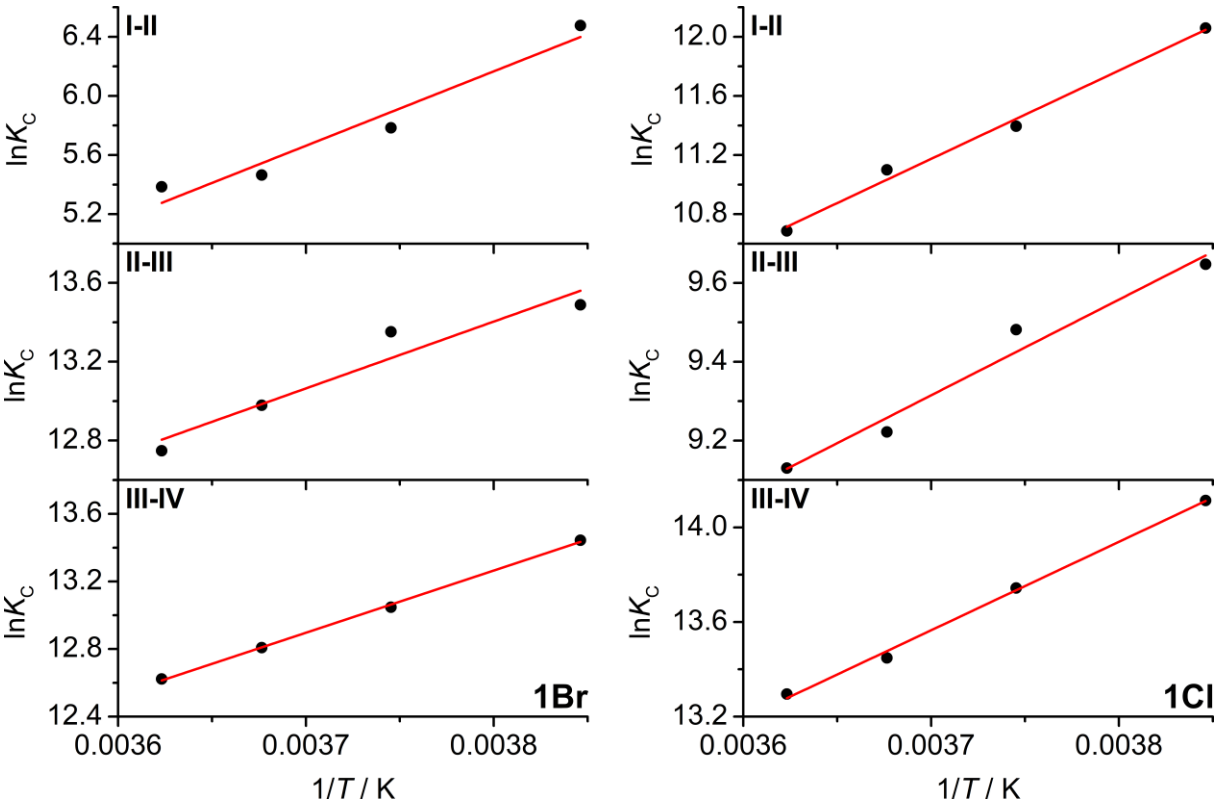

Figure 4.12. $\ln K_c$ vs $1/T$ (van't Hoff plot) for the mixed valence species derived from $[Fe_4(tpda)_3Br_2]$ (**1Br**, left panels) and $[Fe_4(tpda)_3Cl_2]$ (**1Cl**, right panels). The red lines represent the linear fits to the experimental datapoints.

Table 4.6. Comproportionation constants (T = −13 °C) and the corresponding enthalpic and entropic components for mixed oxidation states of **1Br** (**1Cl**) in CH_2Cl_2 solution, using 0.1 M TBABr (TBACl) as supporting electrolyte.[a]

	K_c	$\Delta H°_c$ / kJ mol^{-1}	$\Delta S°_c$ / J K^{-1} mol^{-1}
$(Fe_4)^{9+}$	$0.65\cdot10^3$ ($1.73\cdot10^5$)	−41.8 (−49.7)	−107.7 (−90.9)
$(Fe_4)^{10+}$	$7.21\cdot10^5$ ($1.55\cdot10^4$)	−28.2 (−20.2)	4.3 (2.8)
$(Fe_4)^{11+}$	$6.89\cdot10^5$ ($1.35\cdot10^6$)	−30.6 (−31.1)	−6.0 (−2.3)

[a]The average errors on K_c, $\Delta H°'_c$, and $\Delta S°'_c$ are ±12%, ±0.8 kJ mol^{-1} and ±1.6 J K^{-1} mol^{-1}, respectively.

4.5 Mössbauer Spectroscopy

Mössbauer spectra collected on **1Cl** and **1Br** at 10 and 77 K (Fig. 4.13) suggest similar electronic structures in the two complexes. Since all four Fe centers are crystallographically independent in the solid state, it is expected that each of them would exhibit a quadrupole doublet. However, the Mössbauer spectra of **1Cl** and **1Br** allowed the resolution of only two distinct quadrupole doublets (sub-spectrum 1 and 2), with equal intensities and spectral parameters (isomer shift = δ; quadrupole splitting = ΔE_Q; and linewidth, calculated as full-width at half-maximum = FWHM) consistent with HS Fe^{2+} (Table 4.7).[108] Hence, the four Fe sites can be partitioned into two chemically distinct pairs, with unresolvable differences in Mössbauer parameters within each pair. The much increased linewidth of sub-spectrum 1 at 10 vs 77 K may actually hint at enhanced chemical inequivalence within the pair at 10 K. In fact, lowering temperature has been shown to lead to lower-symmetry structures in related Fe-containing chain compounds.[76] Such a structural change, or more likely small differences in the second order Doppler effect for these Fe sites, may be responsible or contribute to the observed broadness of the sub-spectrum 1 at 10 K. The best-fit parameters to the 10 and 77 K datasets are otherwise similar, suggesting that the Fe centers undergo no gross changes in geometry, oxidation or spin state in the explored temperature range. We propose that sub-spectrum 1 arises from the internal Fe sites (Fe2 and Fe3), whereas the doublet with the higher ΔE_Q (sub-spectrum 2) is due to the terminal Fe sites (Fe1 and Fe4). Our assignment is supported by the Mössbauer behavior of the

bimetallic Co^{2+}-Fe^{2+} complex [CoFeCl(py$_3$tren)] (**12**), which features an FeN_3Cl chromophore and no M–M bond (H_3(py$_3$tren) = *N*,*N*,*N*-tris(2-(2-pyridylamino)ethyl)amine). At 80 K, the HS Fe^{2+} ion in **12** has $\delta = 0.88$ mm/s, $\Delta E_Q = 2.62$ mm/s and FWHM = 0.35 mm/s.[109] The quadrupole splitting is thus practically identical to that of sub-spectrum 2 in **1Cl** at 77 K (Table 4.7), although the isomer shift is roughly intermediate between sub-spectra 1 and 2. The diiron(II) complex [Fe_2Cl(py$_3$tren)], also reported in Ref.[109], unfortunately cannot be used to support our assignment, because the Fe–Fe bond strongly modifies its Mössbauer behavior. Importantly, no Fe^{3+} impurities are detectable by Mössbauer spectroscopy in either **1Cl** or **1Br**. Therefore, our synthetic procedure (see above), in addition to being reproducible and well tested, is successful in preventing any oxidation of the Fe^{2+} ions.

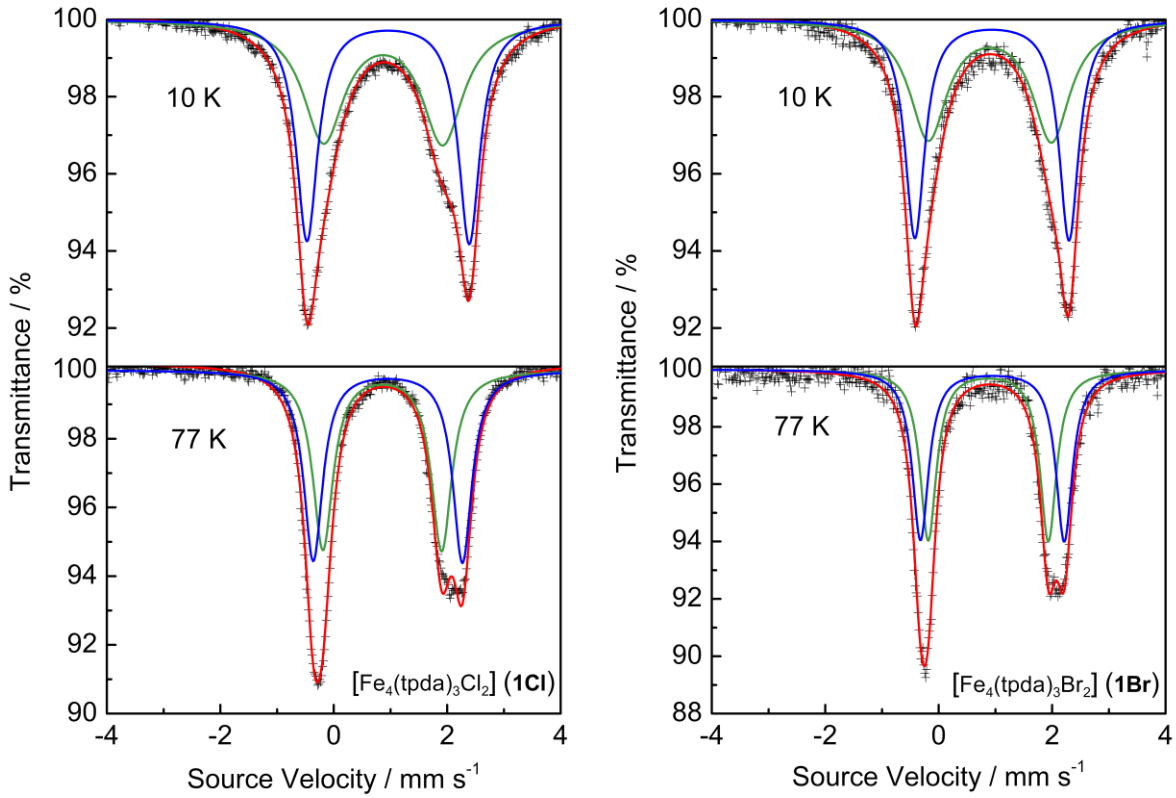

Figure 4.13. Mössbauer data for [Fe_4(tpda)$_3Cl_2$] (**1Cl**, left) and [Fe_4(tpda)$_3Br_2$] (**1Br**, right) at 10 K (top) and 77 K (bottom). The green line corresponds to sub-spectrum 1, the blue line to sub-spectrum 2, the red line to the overall fit, and the black crosses to the experimental data. Best-fit parameters for both temperatures are listed in Table 4.7.

Table 4.7. Best-fit Mössbauer parameters for **1Cl** and **1Br** at 77 K (10 K).[a] Standard deviations are estimated to be ~0.01 mm s^{-1}.

	Sub-spectrum	δ (mm s^{-1})	ΔE_Q (mm s^{-1})	FWHM (mm s^{-1})
$[Fe_4(tpda)_3Cl_2]$ (**1Cl**)	1	0.86 (0.87)	2.09 (2.10)	0.43 (0.88)
	2	0.95 (0.96)	2.63 (2.86)	0.41 (0.46)
$[Fe_4(tpda)_3Br_2]$ (**1Br**)	1	0.87 (0.90)	2.12 (2.17)	0.35 (0.80)
	2	0.95 (0.94)	2.54 (2.72)	0.35 (0.42)

[a]Reduced χ^2: 1.677 (0.793) for **1Cl** and 0.577 (0.747) for **1Br**.

4.6 DC Magnetic Properties and AOM Calculations

The DC magnetic response of a polycrystalline sample of **1Br**·2.3CH_2Cl_2·Et_2O is presented in Fig. 4.14(a). The value of $\chi_M T$ (χ_M = molar magnetic susceptibility) at 300 K is 16.4 emu K mol^{-1}. Because of the absence of M−M bonds, it is meaningful to compare this value with the cumulative Curie constant for four localized and noninteracting S = 2 spins, which is significantly lower (12.0 emu K mol^{-1} with g = 2.00). On lowering temperature, the $\chi_M T$ product undergoes a small increase up to its maximum value at 100 K (17.3 emu K mol^{-1}). With further cooling, it drops rapidly to 2.4 emu K mol^{-1} at 2 K, signaling a weakly magnetic ground state. This is also reflected by isothermal M_M vs H curves recorded at 2, 4 and 8 K (M_M is molar magnetization). At the highest available field (H = 70 kOe), the average value of M_M reaches 9.3 $N_A\mu_B$, which is about 60% of the saturation value of 16.0 $N_A\mu_B$ expected for four noninteracting S = 2 spins with g = 2.00 (N_A is Avogadro's constant).

This behavior closely mirrors that found in **1Cl**·2.6CH_2Cl_2·0.84Et_2O (Fig. 4.14(b)), which was recently analyzed by us using a local-site model and treating ligand field (LF) effects in a simplified fashion within the AOM.[20] At this level of theory, the approximately C_{3v} coordination geometry of Fe1 and Fe4 yields an unquenched first-order orbital momentum and a large easy-axis anisotropy roughly parallel to the axis of the chain (Z).

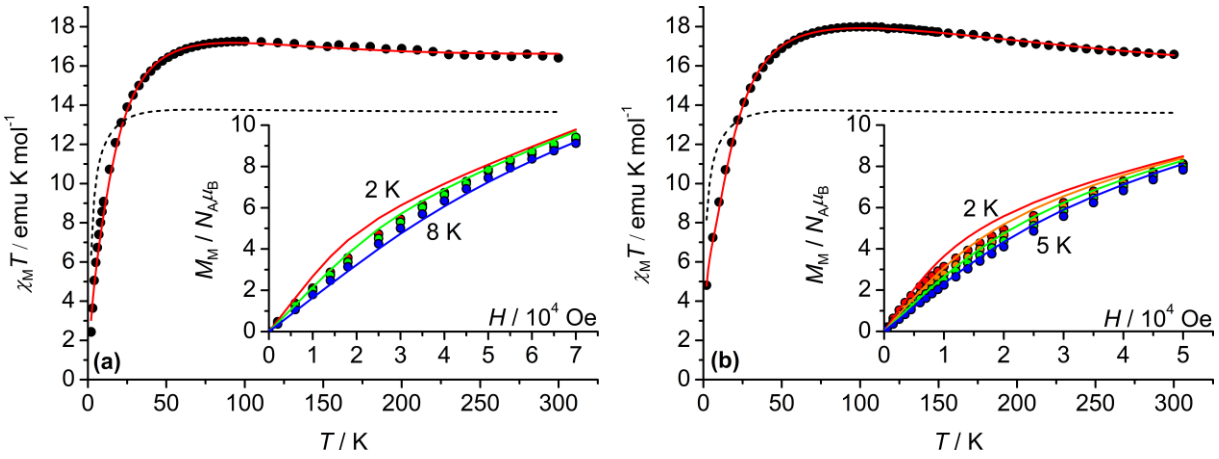

Figure 4.14. DC magnetic response of polycrystalline samples of **1Br**·2.3CH_2Cl_2·Et_2O (a) and **1Cl**·2.6CH_2Cl_2·0.84Et_2O (b). The black dots in the main panels are the experimental temperature-dependent $\chi_M T$ data measured at H = 1 T (a) or 0.1 T (b). The insets show isothermal M_M vs H data recorded (a) at 2, 4, and 8 K (red, green and blue dots, respectively), and (b) at 2, 3, 4, and 5 K (red, orange, green and blue dots, respectively). The solid curves provide the best-fit with *ab-initio* approach using model m**1Br**D in (a) and model m**1Cl**D in (b). The dashed lines are the simulated magnetic responses of four uncoupled HS iron(II) ions, with single-ion parameters fixed at the values obtained by *ab-initio* calculations. Experimental data in (b) are taken from Ref.[20]

By contrast, Fe2 and Fe3 have a well-isolated S = 2 orbital singlet and an easy-axis anisotropy directed roughly normal to Z. This analysis showed that the measured $\chi_M T$ vs T curve is substantially different from the predicted response of four uncoupled Fe^{2+} centers and can only be modelled by introducing super-exchange interactions. Using $J\hat{\mathbf{S}}_i \cdot \hat{\mathbf{S}}_j$ convention for the Heisenberg Hamiltonian, the best model entails (a) ferromagnetic interactions (J < 0) within the Fe1-Fe2 and Fe3-Fe4 pairs, which dominate around room temperature, and (b) weaker antiferromagnetic coupling (J_{eff} > 0) between the two pairs (treated in the mean-field approximation) to reproduce the $\chi_M T$ drop at low T.[20] For comparison, exactly the same strategy was applied to **1Br**·2.3CH_2Cl_2·Et_2O, as detailed in **Sections 4.6.1**. The best-fit parameters so obtained are as follows: J = −14.1(3) cm^{-1}, J_{eff}/g_{av}^2 = 0.315(4) cm^{-1} and TIP = 3.39(16)·10^{-3} emu mol^{-1} (g_{av} is the temperature-independent average g-factor of the Fe_2 unit and TIP is the temperature-independent paramagnetism). The best-fit curve is drawn in Fig. 4.15. As compared with **1Cl**·2.6CH_2Cl_2·0.84Et_2O (J = −21.4(4) cm^{-1}, J_{eff}/g_{av}^2 = 0.345(7) cm^{-1} and TIP = 2.1(2)·10^{-3} emu mol^{-1}), the interdimer interaction is similar, while the intradimer ferromagnetic coupling is ~35% weaker.

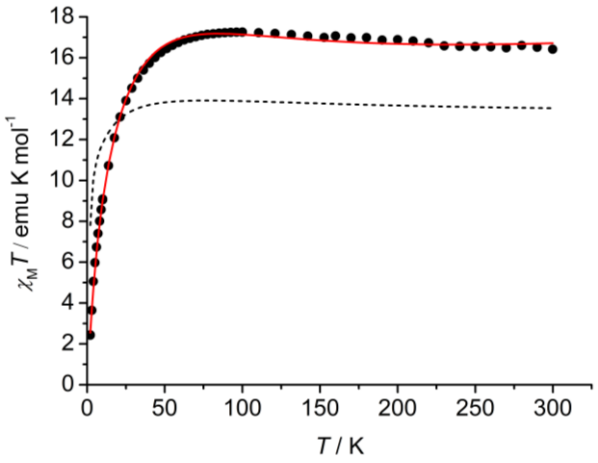

Figure 4.15. Experimental susceptibility data at H = 1 T (black dots) and best-fit curve (from AOM calculations, red line) for **1Br**·2.3CH_2Cl_2·Et_2O. The dashed line represents the simulated magnetic response of four uncoupled HS iron(II) ions, where LF parameters and g-values are fixed at the values obtained from AOM calculations.

4.6.1 Details on AOM Calculations

AOM calculations on **1Br** were carried out with the AOMX program package,[110] following the same approach used in Ref.[20] for chloro derivative **1Cl**. Since Fe1 and Fe4 exhibit very similar coordination environments (see Fig. 4.8), their X-ray coordination geometries were averaged and, additionally, C_{3v} symmetry was enforced on the resulting average FeN_3Br chromophore to give Fe−N = 2.0832 Å, Fe−Br = 2.5207 Å and N−Fe−Br = 97.445°. This choice is justified by the observation that the magnetic response predicted by the AOM for the average C_{3v} chromophore in **1Cl** is within 0.5% from those of the real Fe1(N1,N2,N3,Cl1) and Fe4(N13,N14,N15,Cl2) chromophores.[20] Regarding the internal Fe centers Fe2 and Fe3 (see Fig. 4.8), the X-ray coordination geometries of the chromophores Fe2(N4,N5,N6,N7,N8) and Fe3(N8,N9,N10,N11,N12) were directly used.

LF parameters e_σ and e_π that account for σ and π interactions, respectively,[111] were inferred from the values reported for *trans*-$[Fe(py)_4Br_2]$ and *trans*-$[Fe(py)_4(NCS)_2]$, which possess a tetragonally-elongated octahedral geometry. Based on spectroscopic data at 23 K, Little and Long[112] found e_σ(py) = 4050 cm^{-1} and e_σ(Br) = 2400 cm^{-1} in *trans*-$[Fe(py)_4Br_2]$ (Fe−N = 2.2059−2.270 Å, Fe−Br = 2.6753 Å).[113] In addition, anisotropic π interactions perpendicular to the aromatic plane, described by parameter $e_{\pi\perp}$(py), must be taken into account for pyridine ligands. $e_{\pi\perp}$(py) is usually very small in iron(II) complexes and a value of only ~100 cm^{-1} is reported in *trans*-$[Fe(py)_4(NCS)_2]$.[114] For the terminal Fe centers (Fe1 and Fe4) the nodal planes

of pyridine π orbitals were taken to coincide with the Fe1–N1–C1, Fe1–N2–C16, Fe1–N3–C31, Fe4–N13–C15, Fe4–N14–C30 and Fe4–N15–C45 planes (Ψ = 155.917° in the idealized C_{3v} chromophore). It was assumed that π interactions for the axial bromide ligands, e_π(Br), are isotropic in the plane perpendicular to the Fe−Br bond and amount to 30% of the corresponding σ contribution.[111]

For each ligand, the LF parameters were calculated from the above reference values assuming an r^{-6} dependence on metal-ligand distance r,[112–114] as given by:

$$e_t(\mathrm{X})' = e_t(\mathrm{X})\left(\frac{r}{r\prime}\right)^6 \qquad (4.1)$$

where $t = \sigma$ or π and X is the type of ligand. In our previous AOM analysis of **1Cl** we used *trans*-[Fe(py)$_4$Cl$_2$] as a reference compound with Fe−N = 2.229 Å.[115] In their paper, Little and Long[112] assumed the same e_σ(py) value for *trans*-[Fe(py)$_4$Br$_2$] and *trans*-[Fe(py)$_4$Cl$_2$]. Since the average Fe−N distances in the two compounds differ by 0.4% only (2.238 vs 2.229 Å), for the sake of simplicity and for a better comparison between **1Cl** and **1Br** we used Fe−N = 2.229 Å as reference distance for **1Br** as well, yielding e_σ(py) = 6078 cm^{-1} and $e_{\pi\perp}$(py) = 150 cm^{-1}. From the value of e_σ(Br) = 3430 cm^{-1} we finally calculated e_π(Br) = 0.3e_σ(Br) = 1029 cm^{-1}.

Racah parameters for the interelectronic repulsion were fixed at B = 850 cm^{-1} and C = 3100 cm^{-1}, hence ~20% lower than in free Fe^{2+}.[116] To assess the effects of SO coupling, the effective one-electron SO coupling constant (ζ_{3d}) was either neglected or fixed at 350 cm^{-1} in separate calculations for each chromophore, while the orbital reduction factor (k) was taken isotropic and unitary.[114]

AOM calculations on the terminal C_{3v} chromophore in zero magnetic field were performed both with and without the inclusion of SO coupling. In the first case (ζ_{3d} = 0), the ground ^{5}D Russell-Saunders term of the free Fe^{2+} ion (L = 2, S = 2) is split by the LF of three py and one bromido ligands into the three spin-quintet terms listed in Table 4.8. The ground ^{5}E term is well-isolated from the excited ones (> 6200 cm^{-1}) and consists in a 0.920:0.080 mixture of $(xz,yz)^3(xy,x^2–y^2)^2(z^2)^1$ and $(xz,yz)^2(xy,x^2–y^2)^3(z^2)^1$ configurations. The excited ^{5}E term corresponds to the complementary 0.080:0.920 mixture. Finally, the ^{5}A$_1$ term coincides with the pure $(xz,yz)^2(xy,x^2–y^2)^2(z^2)^2$ configuration. When SO coupling is included in the calculation (ζ_{3d} = 350 cm^{-1}), the spin-quintet terms give the $(2L+1)(2S+1)$ = 25 zero-field levels listed in Table 4.8. The first ten low-lying levels are well-isolated (> 6000 cm^{-1}) from the remaining ones, and originate primarily from the ground orbital doublet term ^{5}E. Using PHI v3.0.6 code[117]

and Simplex minimization algorithm, these levels were mapped onto the Griffith-Figgis Hamiltonian for the terminal irons (i = 1, 4):

$$\widehat{H}_i = \widehat{H}_{CF,i} + \lambda_i k_i \hat{\mathbf{L}}_i \cdot \hat{\mathbf{S}}_i + \mu_{\mathrm{B}} \mathbf{B} \cdot \left(k_i \hat{\mathbf{L}}_i + g_e \hat{\mathbf{S}}_i\right) \quad (4.2)$$

$$\widehat{H}_{CF,i} = B^0_{2,i}\hat{O}^0_{2,i} + B^0_{4,i}\hat{O}^0_{4,i} + B^3_{4,i}\hat{O}^3_{4,i} \quad (4.3)$$

where $\hat{\mathbf{L}}_i$ and $\hat{\mathbf{S}}_i$ are the orbital and spin angular momenta (L_i = 2, S_i = 2), **B** is the applied magnetic field, k_i is the orbital reduction factor, and $\lambda_i = -\zeta_{3d}/2S_i$ is the effective many-electrons SO coupling constant. In accordance with the treatment in Ref.[114] we set k_i = 1 and $\lambda_i = -\zeta_{3d}/2S_i$ = –87.5 cm^{-1}. In the CF Hamiltonian in Eq. 4.3, $B^0_{2,i}$, $B^0_{4,i}$ and $\left|B^3_{4,i}\right|$ are the CF parameters appropriate for C_{3v} symmetry, while $\hat{O}^0_{2,i}$, $\hat{O}^0_{4,i}$, and $\hat{O}^3_{4,i}$ are the operator equivalents.

Table 4.8. Energy levels (cm^{-1}) obtained by AOM calculations on the idealized terminal chromophore with C_{3v} symmetry in **1Br**, with and without SO coupling.[a]

ζ_{3d} = 0 cm^{-1}		ζ_{3d} = 350 cm^{-1}			
^{5}E	0.000	1	0.000	14	6266.736
^{5}E	6277.700	2	0.042	15	6404.264
^{5}A$_1$	6526.556	3	56.274	16	6404.264
		4	56.274	17	6547.284
		5	118.480	18	6547.284
		6	118.480	19	6699.387
		7	171.469	20	6699.387
		8	205.604	21	6703.197
		9	261.633	22	6703.197
		10	261.633	23	6703.325
		11	6094.128	24	6722.306
		12	6094.128	25	6723.303
		13	6238.276		

[a]Interelectronic repulsion and SO coupling parameters: B = 850 cm^{-1}, C = 3100 cm^{-1}, ζ_{3d} = 0 or 350 cm^{-1} (see column headers), k = 1.0. LF parameters for C_{3v} chromophore: e_σ(py) = 6078 cm^{-1}, $e_{\pi\perp}$(py) = 150 cm^{-1}, e_σ(Br) = 3430 cm^{-1}, e_π(Br) = 1029 cm^{-1}.

The resulting best-fit CF parameters for the terminal C_{3v} chromophore are: $B^0_{2,i}$ = 212.3(12) cm^{-1}, $B^0_{4,i}$ = 55.32(10) cm^{-1} and $\left|B^3_{4,i}\right|$ = 577(4) cm^{-1}. The presence of other

minima was excluded prior to the fit, performing an explorative survey over values of $B^0_{2,i}$, $B^0_{4,i}$, and $\left|B^3_{4,i}\right|$ between ±1000 cm^{-1}.

In AOM calculations on the inner Fe centers (Fe2 and Fe3), all N-donor atoms were treated as pyridine-type donors, with e_σ(N) values estimated from Fe−N distances using Eq. 4.1 and setting e_π(N)/e_σ (N) = 0.[20] As found in **1Cl**, both Fe2 and Fe3 have a well-isolated $S_i = 2$ orbital singlet, the first-order orbital momentum being quenched by the highly-distorted pentacoordinate environment.[20] Excited states lie at >1800 and >2300 cm^{-1}, respectively, and the $S_i = 2$ manifolds span an energy range of 35−46 cm^{-1} (Table 4.9). The pattern of energy levels indicates an easy-axis anisotropy, with a small or moderate rhombic distortion. Using PHI v3.0.6 code,[117] the five low-lying levels of Fe2 and Fe3 (i = 2, 3) were mapped on a giant SH:

$$\widehat{H}_i = \hat{\mathbf{S}}_i \cdot \bar{\bar{D}}_i \cdot \hat{\mathbf{S}}_i + \mu_B \mathbf{B} \cdot \bar{\bar{g}}_i \cdot \hat{\mathbf{S}}_i \qquad (4.4)$$

The fit of the zero-field levels gave the axial (D_i) and rhombic (E_i) ZFS parameters. D_i is negative and large ($|D_i|$ = 8.8−11.3 cm^{-1}), while rhombic distortion is moderate in Fe2 ($|E_2/D_2|$ = 0.11) and small in Fe3 ($|E_3/D_3|$ = 0.02). The values of D_i and E_i along with the principal directions of $\bar{\bar{D}}_i$ for each Fe center are listed in Table 4.10. The angle between the easy axis of Fe2 (Fe3) and the Fe2−Fe1 (Fe3−Fe4) direction is 82.4° (104.5°) and indicates that the easy direction of Fe2 (Fe3) is approximately perpendicular to the metal chain. In the same Table we also list the g-values along the principal directions of the $\bar{\bar{D}}_i$ tensor, which were obtained from the field-dependence of the five low-lying levels. For simplicity, in all subsequent calculations the $\bar{\bar{D}}_i$ and $\bar{\bar{g}}_i$ tensors of Fe2 and Fe3 were assumed to be axial, with identical D_i parameters and principal g-factors, obtained as average values over the data in Table 4.10. Furthermore, the easy axes of Fe2 and Fe3 were taken as perpendicular to the threefold-symmetry axes of Fe1 and Fe4, respectively.

Based on these single-ion properties, the magnetic behaviour of complex **1Br** was analyzed with the same procedure used for the chloro analogue **1Cl**.[20] The molecule was modelled in PHI v3.0.6[117] as two identical ferromagnetic Fe_2 pairs (Fe1,Fe2 and Fe3,Fe4) weakly antiferromagnetically coupled with each other. The Hamiltonians for the two pairs:

$$\widehat{H}_{\mathrm{Fe1,Fe2}} = J\hat{\mathbf{S}}_1 \cdot \hat{\mathbf{S}}_2 + \widehat{H}_1 + \widehat{H}_2 \qquad (4.5)$$

$$\widehat{H}_{\mathrm{Fe3,Fe4}} = J\hat{\mathbf{S}}_3 \cdot \hat{\mathbf{S}}_4 + \widehat{H}_3 + \widehat{H}_4 \qquad (4.6)$$

contain the intradimer ferromagnetic interaction ($J < 0$), which was treated following Lines' approach,[117,118] and the single-ion Hamiltonians $\widehat{H}_i$ defined in Eqs. 4.2-4.4. The single-ion parameters used in Eqs. 4.5 and 4.6 were as follows: for Fe1 and Fe4, $S_i = 2$, $L_i = 2$, $B^0_{2,i} = 212.3$ cm^{-1}, $B^0_{4,i} = 55.32$ cm^{-1}, $B^3_{4,i} = 577$ cm^{-1}, $\lambda_i = -87.5$ cm^{-1}; for Fe2 and Fe3: $S_i = 2$, $L_i = 0$, $B^0_{2,i} = D_i/3 = -3.359$ cm^{-1}, $B^2_{2,i} = E_i = 0$, $g_{x,i} = g_{y,i} = 2.03$, $g_{z,i} = 2.21$. The antiferromagnetic interdimer interaction ($J_{\text{eff}} > 0$) was treated in the mean-field approximation,[26] which is valid for $J_{\text{eff}} << |J|$. Thanks to this simplification, the size of Hilbert space collapses from 15625 × 15625 to 125 × 125, allowing for diagonalization of the Hamiltonian matrix and calculation of accurate powder averages with our computational resources. However, only susceptibility vs temperature data could be fitted, based on mean-field correction given by Eq. 4.7:

$$\chi = \frac{\chi_0}{1+\frac{zJ_{\text{eff}}}{N_{\text{A}}\mu_{\text{B}}^2 g_{\text{av}}^2}\chi_0} \qquad (4.7)$$

where χ and χ_0 are the corrected and uncorrected susceptibility, respectively, $z = 1$ is the number of interacting nearest neighbors, and g_{av} is the temperature independent average g-factor of the Fe_2 unit. Notice that Eq. 4.7 differs slightly from that used in PHI v3.0.6[117] and that the best-fit zJ parameter appearing in PHI corresponds to $-zJ_{\text{eff}}/g_{\text{av}}^2$ in our treatment. TIP was also included to accurately reproduce high-temperature data.

Table 4.9. Energy (cm^{-1}) of the low-lying levels obtained by AOM calculations on Fe2 and Fe3 in **1Br**.[a] Separations to the nearest excited levels are listed at the bottom of each column.

	Fe2 [b]		Fe3 [c]
1	0.000	1	0.000
2	0.465	2	0.104
3	30.518	3	25.956
4	38.043	4	27.101
5	46.158	5	35.443
	(>1800)		(>2300)

[a]Interelectronic repulsion and SO coupling parameters: $B = 850$ cm^{-1}, $C = 3100$ cm^{-1}, $\zeta_{3d} = 350$ cm^{-1}, $k = 1.0$. [b]LF parameters for Fe2: e_σ(N4) = 5661 cm^{-1}, e_σ(N5) = 7926 cm^{-1}, e_σ(N6) = 7510 cm^{-1}, e_σ(N7) = 4692 cm^{-1}, e_σ(N8) = 2074 cm^{-1}, $e_\pi/e_\sigma = 0$. [c]LF parameters for Fe3: e_σ(N8) = 2035 cm^{-1}, e_σ(N9) = 3996 cm^{-1}, e_σ(N10) = 6851 cm^{-1}, e_σ(N11) = 6974 cm^{-1}, e_σ(N12) = 6012 cm^{-1}, $e_\pi/e_\sigma = 0$.

Table 4.10. Magnetic parameters of Fe2 and Fe3 in **1Br** derived from AOM calculations and Eq. 4.4.

	Easy axis (z)[a]	Hard axis (x)[a]	Intermed. axis (y)[a]	D_i, E_i (cm^{-1})	$g_{x,i}$, $g_{y,i}$, $g_{z,i}$[b]
Fe2	82.41, 34.80	73.40, −57.48	161.66, −31.51	−11.31, 1.26	1.99, 2.06, 2.24
Fe3	104.52, 1.35	34.07, 68.83	59.94, −80.03	−8.85, 0.19	2.04, 2.03, 2.18

[a]Polar angles θ and ϕ (°) of the principal directions of the $\overline{\overline{D}}_i$ tensor (x,y,z) in a local reference frame (X,Y,Z) defined as follows: for Fe2, the Z axis is taken along Fe2–Fe1, with X along the projection of Fe2–N4 on the plane normal to Z; for Fe3, the Z axis is taken along Fe3–Fe4 direction, with X along the projection of Fe3–N12 on the plane normal to Z; in both cases Y is chosen so as to give a right-handed orthogonal coordinate system. [b]Values of the g-factor along the principal directions of the $\overline{\overline{D}}_i$ tensor.

4.7 Ab-initio Calculations

The single-ion properties in complexes **1Cl** and **1Br** were investigated at a more sophisticated theoretical level by CASSCF-NEVPT2-SO calculations (see experimental **Section 4.10.8**), performed by Benjamin Cahier at the Max-Planck-Institut für Kohlenforschung (Mülheim an der Ruhr, Germany). The treatment showed that, at variance with AOM results, quenching of first-order orbital momentum is substantial even for the terminal centers Fe1 and Fe4. Deviations from threefold symmetry in their coordination environment are in fact sufficient to split the ^{5}E term by a few hundreds of wavenumbers. Upon application of SO coupling, the five lowest-lying states are separated from excited states by at least 300-350 cm^{-1} except for Fe4 in **1Cl** (240 cm^{-1}) (Table A.2 and A.3). The situation is similar to that encountered in mononuclear iron(II) pyrrolide complexes, featuring a quasi-threefold symmetric FeN_3N coordination environment.[50,51,119] The five lowest-lying levels of the i-th metal ion were then mapped onto the single-ion SH in Eq. 4.4. This showed that the anisotropy of Fe1 and Fe4 is of the *easy-axis* type ($D_i < 0$) with $|D_i|$ = 11-19 cm^{-1} (Table 4.11). A significant rhombic anisotropy is predicted, with $|E_i/D_i|$ = 0.05-0.18 and the intermediate direction lying close to the Fe1-N1 and Fe4-N13 bonds. The two inner metals (Fe2 and Fe3) display a very distorted coordination environment and attain an orbitally nondegenerate S_i = 2 electronic state as well. However, their anisotropy

is of the *hard-axis* type ($D_i > 0$) with D_i = 8-10 cm^{-1} and $|E_i/D_i|$ = 0.06-0.21 in Eq. 4.4 (Table 4.11). Interestingly, all four metal ions have their main anisotropy axes directed close to the chain axis, as pictorially shown in Fig. 4.16. Therefore, the terminal and internal Fe^{2+} ions have approximately collinear main anisotropy axes, but opposite anisotropies, with a preference of the spins at terminal (internal) sites to align parallel (perpendicular) to *Z*. Notice that the AOM also predicted a qualitatively similar tendency, but with a different origin: an orbitally degenerate ground term for Fe1 and Fe4, and an easy-axis anisotropy normal to *Z* for Fe2 and Fe3.

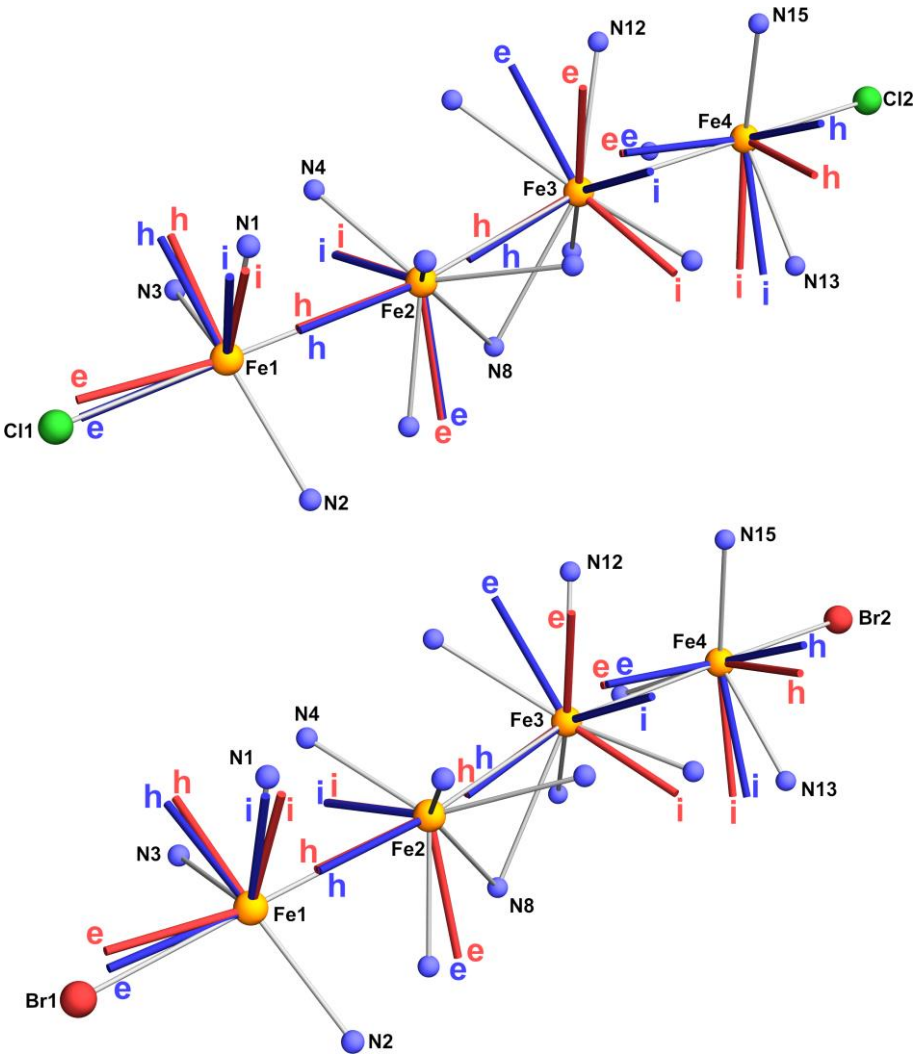

Figure 16. Principal directions of single-ion $\bar{\bar{D}}_i$ (blue) and $\bar{\bar{g}}_i$ (red) tensors obtained by *ab-initio* calculations on **1Cl** (upper panel) and **1Br** (lower panel). e = easy, i = intermediate, h = hard direction.

Overall, Tables 4.11 and 4.12 and Fig. 4.16 indicate that the single-ion $\bar{\bar{D}}_i$ and $\bar{\bar{g}}_i$ tensors are very similar in the two derivatives, in terms of both magnitude and orientation. Knowledge of these single-ion properties allowed modelling the magnetic behavior of **1Cl** and **1Br** without risk of overparameterization. First, PHI v3.1.5 software[117] was used to calculate the $\chi_M T$ vs T

response for the four noninteracting HS Fe^{2+} ions with single-ion parameters fixed at the values obtained by *ab-initio* calculations. The result (dashed lines in Fig. 4.14) is very far from experimental data and further confirms the existence of magnetic interactions among metal ions.

Table 4.11. Single-ion ZFS parameters and *g*-factors of **1Cl** and **1Br** from *ab-initio* calculations.

	$[Fe_4(tpda)_3Cl_2]$ (**1Cl**)		$[Fe_4(tpda)_3Br_2]$ (**1Br**)	
	D_i, E_i (cm^{-1})[a]	$g_{1,i}$, $g_{2,i}$, $g_{3,i}$[b]	D_i, E_i (cm^{-1})[a]	$g_{1,i}$, $g_{2,i}$, $g_{3,i}$[b]
Fe1	−11.32, −1.94	1.998, 2.125, 2.311	−12.02, −2.18	1.994, 2.134, 2.324
Fe2	9.61, 1.95	2.000, 2.101, 2.201	9.62, 2.05	2.001, 2.099, 2.203
Fe3	7.81, 0.50	2.007, 2.111, 2.131	7.68, 0.51	2.007, 2.108, 2.132
Fe4	−18.97, −0.92	1.934, 2.067, 2.425	−17.43, −1.49	1.962, 2.100, 2.406

[a]Axial and rhombic ZFS parameters of Fe*i*. [b]Principal values of the $\bar{\bar{g}}_i$ tensor of Fe*i*, listed in order of increasing magnitude.

Table 4.12. Angles (°) between the easy (e), intermediate (i) and hard (h) principal directions of the $\bar{\bar{D}}_i$ and $\bar{\bar{g}}_i$ tensors for each iron(II) ion in **1Cl** and **1Br**. Values for the main anisotropy axes are marked in bold.

	$[Fe_4(tpda)_3Cl_2]$ (**1Cl**)			$[Fe_4(tpda)_3Br_2]$ (**1Br**)		
	$i_{D,i}$, $i_{g,i}$	$h_{D,i}$, $h_{g,i}$	$e_{D,i}$, $e_{g,i}$	$i_{D,i}$, $i_{g,i}$	$h_{D,i}$, $h_{g,i}$	$e_{D,i}$, $e_{g,i}$
Fe1	6.07	4.05	**7.29**	5.70	3.61	**6.45**
Fe2	1.01	**1.16**	0.58	1.21	**1.22**	0.38
Fe3	43.20	**1.18**	43.19	44.14	**1.18**	44.13
Fe4	20.45	20.84	**4.07**	10.79	11.43	**3.79**

We then wrote a new SH ($\hat{H}$, Eq. 4.8) as the sum of single-ion Hamiltonians $\hat{H}_i$ (Eq. 4.4) and of a Heisenberg Hamiltonian, which accounts for super-exchange interaction between the *i*- and *j*-th localized spin centers through isotropic coupling constant J_{ij} (Scheme 4.2), with positive and negative values of J_{ij} corresponding to antiferromagnetic and ferromagnetic coupling, respectively. Both nearest-neighbor (J_{12}, J_{23}, J_{34}) and next-nearest-neighbor (J_{13}, J_{24}) couplings were included, setting $J_{13} = J_{24} = J'$ for simplicity.

$$\hat{H} = \sum_{i=1}^{4} \hat{H}_i + J_{12}\hat{\mathbf{S}}_1 \cdot \hat{\mathbf{S}}_2 + J_{34}\hat{\mathbf{S}}_3 \cdot \hat{\mathbf{S}}_4 + J_{23}\hat{\mathbf{S}}_2 \cdot \hat{\mathbf{S}}_3 + J'\left(\hat{\mathbf{S}}_1 \cdot \hat{\mathbf{S}}_3 + \hat{\mathbf{S}}_2 \cdot \hat{\mathbf{S}}_4\right) \quad (4.8)$$

Several models, labelled as m**1X**A, m**1X**B, etc. (X = Cl, Br), were tested for their ability to simultaneously account for $\chi_M T$ vs T and M_M vs H data. The models differ in the constraints applied to J_{ij} values as well as in the refinement of a TIP correction. The best-fit parameter sets so obtained are listed in Tables A.4 and A.5. We also carried out some fits on the susceptibility data only, as given in Table A.6. The most important results are gathered in Table 4.13 (entries are labelled as m**1X**A, m**1X**B, etc. where X = Cl, Br). Graphical material for selected models is available in Figures 4.17-4.19, A.5, and A.6.

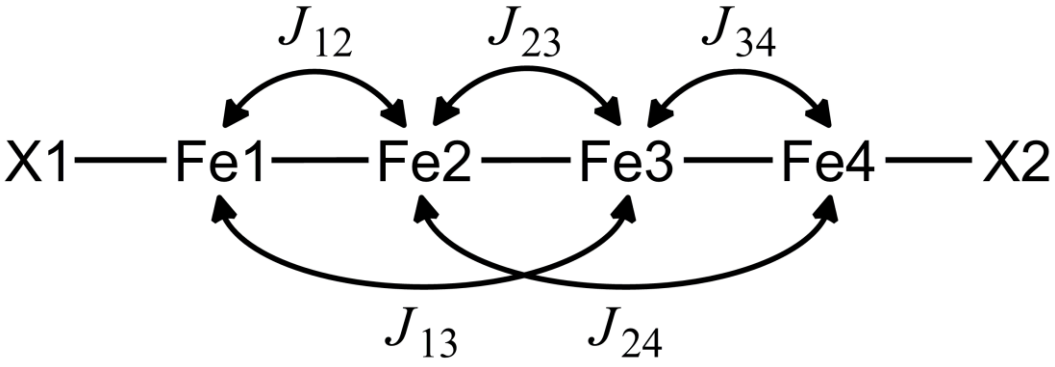

Scheme 4.2. Definition of super-exchange coupling constants J_{ij} in complexes **1Cl** and **1Br**. Terminal ligands X1 and X2 can be either Cl (**1Cl**) or Br (**1Br**).

Table 4.13. Best-fit parameters from the simultaneous fit of susceptibility and magnetization data of **1Cl**·2.6CH_2Cl_2·0.84Et_2O and **1Br**·2.3CH_2Cl_2·Et_2O.[a]

Model	J_{12}	J_{34}	J_{23}	TIP	R
m**1Cl**A	−14.0(2)		4.404(17)	$8.0(2)\cdot10^{-3}$	322.4
m**1Cl**D	−51.4(10)	−9.43(5)	4.319(7)	$1.9(15)\cdot10^{-4}$	19.1
m**1Cl**E	−4.87(13)	−35.1(10)	4.48(3)	$5.7(2)\cdot10^{-3}$	325.8
m**1Br**A	−9.31(16)		4.11(3)	$8.9(3)\cdot10^{-3}$	54.2
m**1Br**D	−26.8(14)	−4.61(15)	4.19(3)	$4.7(4)\cdot10^{-3}$	25.4
m**1Br**E	−3.61(3)	−38.6(11)	4.292(13)	$2.5(2)\cdot10^{-3}$	4.9

[a] J values are expressed in cm^{-1}, TIP in emu mol^{-1}.

In the simplest treatment, only nearest-neighbor super-exchange interactions were retained ($J' = 0$), and interactions within the Fe1,Fe2 and Fe3,Fe4 pairs were constrained to be equal ($J_{12} = J_{34}$). This model converges to ferromagnetic Fe1-Fe2 and Fe3-Fe4 couplings and to an

antiferromagnetic Fe2-Fe3 interaction, and is thus qualitatively consistent with the results of DFT calculations.[20] However, even with the refinement of TIP correction, the magnetic response of both complexes on a high-energy scale ($\chi_M T$ vs T data) cannot be accurately reproduced (entries m**1X**A). As a cross check, this model remains unsatisfactory when M_M vs H data are excluded from the fit (entries m**1X**A'). Allowing nonzero J' (while setting TIP = 0 to avoid overparameterization) gives two minima in the least-squares procedure, for either $J_{23} < 0$ and $J' > 0$, or vice versa. Both solutions have quite large $|J'|$ values (1.5-4.8 cm^{-1}) and are regarded as physically unlikely (entries m**1X**B, m**1X**C, m**1X**B' and m**1X**C').

The condition $J_{12} = J_{34}$ was then relaxed. For **1Cl**, the improvement over m**1Cl**A is considerable with $J_{12} < J_{34} < 0$, $J_{23} > 0$ and a negligible TIP correction (entry m**1Cl**D). For **1Br**, both $J_{12} < J_{34} < 0$ and $J_{34} < J_{12} < 0$ (in either case with $J_{23} > 0$) give much improved fits as compared with m**1Br**A (entries m**1Br**D and m**1Br**E). Allowing J_{12} and J_{34} to be different while introducing next-nearest neighbor interactions (J') with TIP = 0 gives four distinct minima depending on the ordering of J_{12} and J_{34} and on the signs of J_{23} and J'. In **1Cl** (**1Br**) three (two) of these minima are regarded as physically unlikely ($|J'|$ = 1.8-3.9 cm^{-1}); the remaining ones (entries m**1Cl**G, m**1Br**G and m**1Br**I) have negligible $|J'|$ values and afford a comparable fit quality to the corresponding models with J' = 0 and TIP correction (entries m**1Cl**D, m**1Br**D and m**1Br**E, respectively).

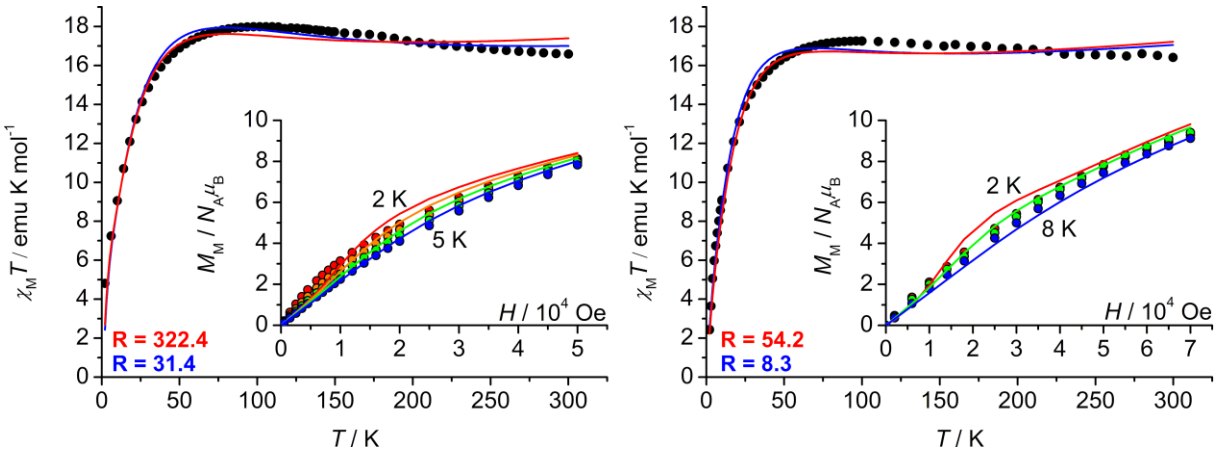

Figure 4.17. Best-fit curves (red lines) to the experimental data in Fig. 4.14 based on model m**1Cl**A (left) and model m**1Br**A (right) (see Tables A.4 and A.5). The blue lines in the main panels are the best-fit curves from the treatment of $\chi_M T$ vs T data only, based on model m**1Cl**A' (left) and model m**1Br**A' (right) (see Table A.6).

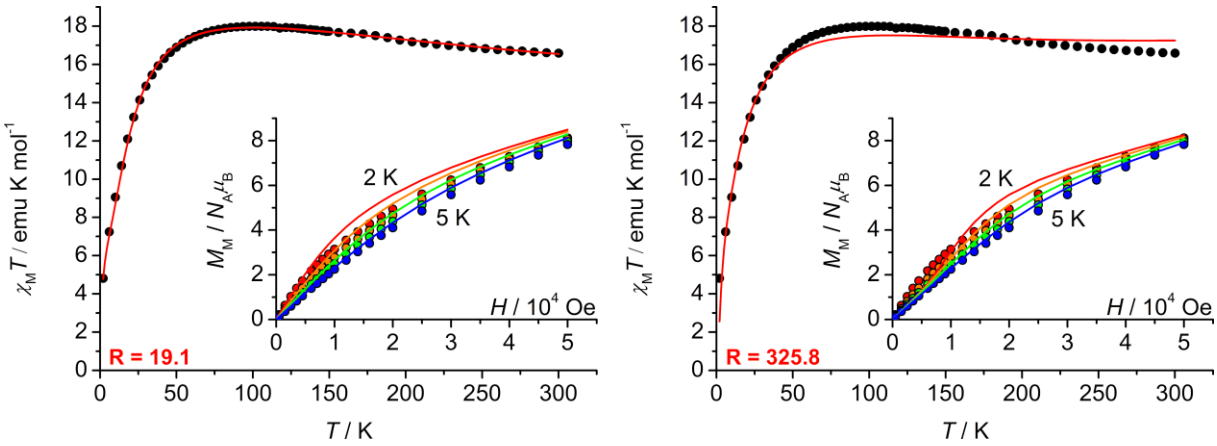

Figure 4.18. Best-fit curves to the experimental data in Fig. 4.14(b) based on models m**1Cl**D (left) and m**1Cl**E (right) (see Table A.4).

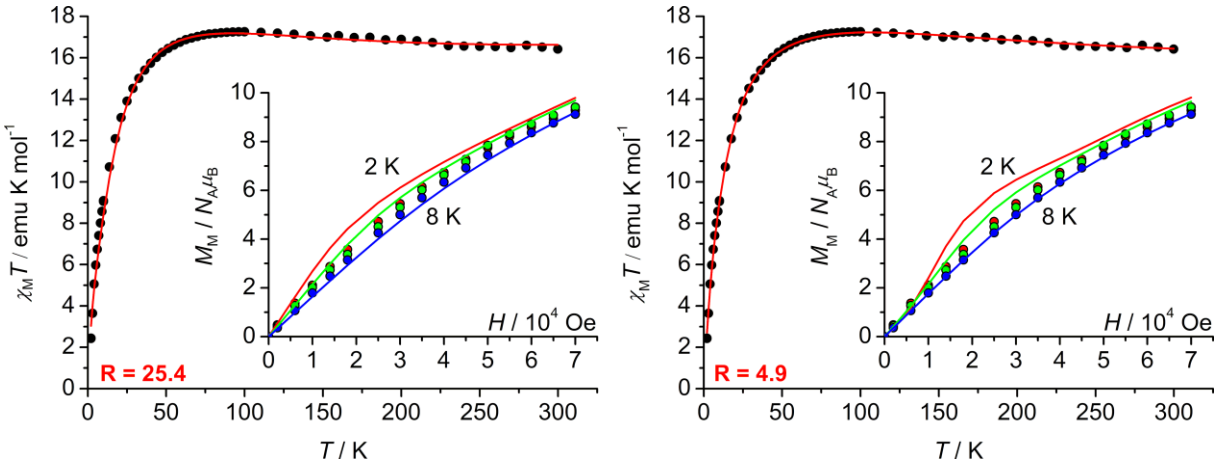

Figure 4.19. Best-fit curves to the experimental data in Fig. 4.14(a) based on models m**1Br**D (left) and m**1Br**E (right) (see Table A.5).

It is important to note that the net coupling between the ferromagnetic Fe1,Fe2 and Fe3,Fe4 pairs, estimated as $J_{23}+2J'$, is invariably antiferromagnetic and remarkably constant across the explored models (3.7-5.1 cm^{-1} in **1Cl** and 2.9-4.6 cm^{-1} in **1Br**). The low temperature decrease of the $\chi_M T$ product is in fact primarily sensitive to this combined coupling term, and much less to the separate values of J_{23} and J'. Therefore, in what follows we disregard next-nearest neighbor interactions and further scrutinize models m**1Cl**D, m**1Br**D and m**1Br**E. Model m**1Cl**D unequivocally identifies the ordering of J_{12} and J_{34} in **1Cl**, namely $|J_{12}| > |J_{34}|$. Models m**1Br**D and m**1Br**E show that both orderings yield a good reproduction of experimental data for **1Br**, the best mathematical solution being obtained with $|J_{34}| > |J_{12}|$ (m**1Br**E). On structural grounds, a reversed ordering of J_{12} and J_{34} in the two complexes is very unlikely. We thus contend that m**1Cl**D and m**1Br**D are the most plausible models for the two derivatives, with a J_{12} constant 5-6 times more ferromagnetic than J_{34} (Fig. 4.14). Notice that the average

magnitude of the two coupling constants is smaller in **1Br** (–15.7 cm^{-1}) than in **1Cl** (–30.4 cm^{-1}), as found in our simplified treatment based on AOM. Furthermore, the two models entail remarkably similar values of J_{23} (4.2-4.3 cm^{-1}), again in accordance with the almost superimposable structures of the two derivatives and with AOM-based treatment.

We now analyze in detail the lowest-lying spin levels in the two complexes, as resulting from the parameters ($\bar{\bar{D}}_i$ and $\bar{\bar{g}}_i$ tensors, and best-fit J_{ij} values) of models m**1Cl**D and m**1Br**D. At $H = 0$, the lowest-energy states are closely-spaced non-Kramers doublets (hereafter referred to as *pseudo-doublets*), which however do not follow the pattern typical of a well-isolated total spin state undergoing predominantly axial ZFS (Figures 4.20 and 4.21). Each of these pseudo-doublets can be approximated to an $\tilde{S} = 1/2$ *pseudo*-spin with an anisotropic *g*-tensor (principal components g_1, g_2 and g_3 in order of increasing magnitude).[117] Notice that in non-Kramers systems pseudo-doublets have vanishing values of g_1 and g_2. The ground doublet in **1Cl** (**1Br**) has g_3 ~ 7.6 (6.4) in a direction (z_3) at about 29° (44°) from *Z*. This g_3 value corresponds to magnetic moment projections of $\pm 3.8\mu_B$ ($\pm 3.2\mu_B$) and the ground doublet is thus only weakly magnetic. The first-excited doublet lies about 2.5 (4.6) cm^{-1} higher in energy. It has g_3' ~ 9.1 (11.3) in a direction (z_3') that forms an angle of about 26° (17°) with *Z* and is consequently more magnetic than the ground doublet. Figures 4.20 and 4.21 present the expected Zeeman splittings when a magnetic field up to 10 kOe is applied along z_3.

The local spin components in the four lowest-lying states (1 to 4, in order of increasing energy) have been computed for $H = 1$ kOe directed along z_3 and z_3', respectively. The results for the ground doublet of **1Cl** and **1Br** are presented in vectorial form and superimposed to the X-ray molecular structures in Figures 4.22 and 4.23, respectively. Similar views for the first-excited doublet are available as Figures 4.24 and 4.25.

The states comprised in each doublet have roughly opposite components of the local spins, as expected; furthermore, spin components are substantial and reveal a noncollinear spin arrangement (Table 4.14).

Table 4.14. Spin moduli ($\hbar$), inter-spin angles (°) and angles between the spins and the chain axis *Z* (°) in state 1 of models m**1Cl**D and m**1Br**D.

Model	$\mathbf{S}_1$	$\mathbf{S}_2$	$\mathbf{S}_3$	$\mathbf{S}_4$	$\widehat{\mathbf{S}_1\mathbf{S}_2}$	$\widehat{\mathbf{S}_2\mathbf{S}_3}$	$\widehat{\mathbf{S}_3\mathbf{S}_4}$	$\widehat{\mathbf{S}_1 Z}$	$\widehat{\mathbf{S}_2 Z}$	$\widehat{\mathbf{S}_3 Z}$	$\widehat{\mathbf{S}_4 Z}$
m1ClD	1.53	1.61	1.82	1.99	6.1	162.8	34.9	66.7	71.0	121.7	155.9
m1BrD	1.63	1.74	1.77	1.97	14.5	171.1	47.2	56.3	69.7	113.5	159.1

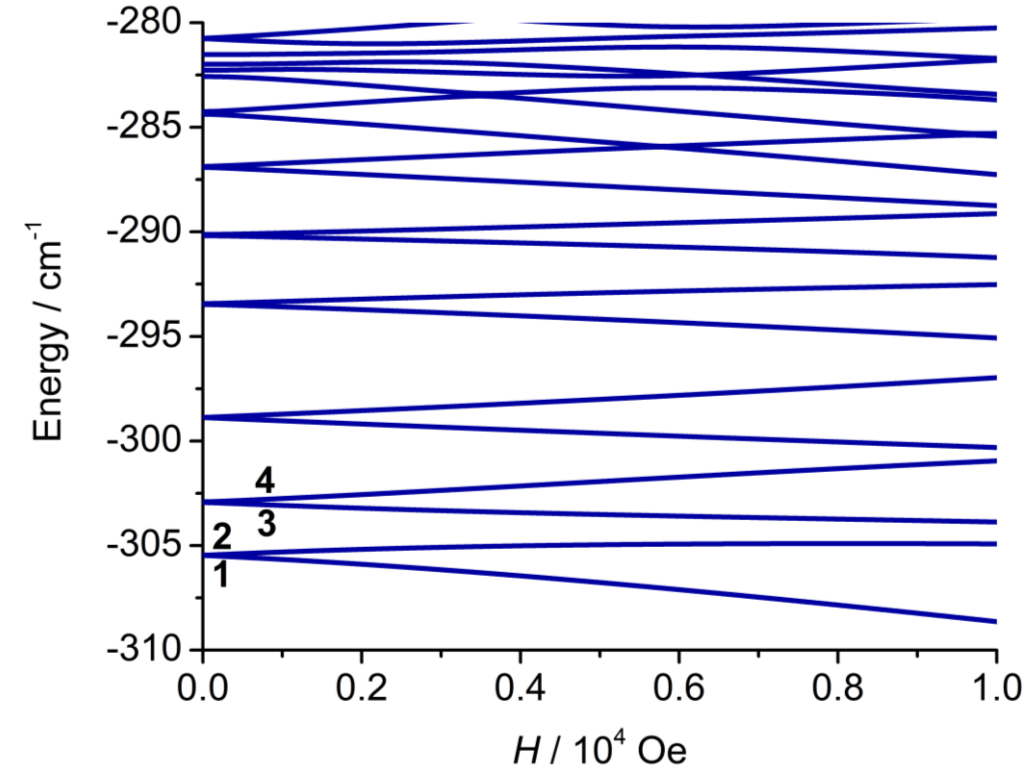

Figure 4.20. Zeeman diagram for **1Cl** when the magnetic field is applied along the direction of maximum splitting for the ground doublet (z_3).

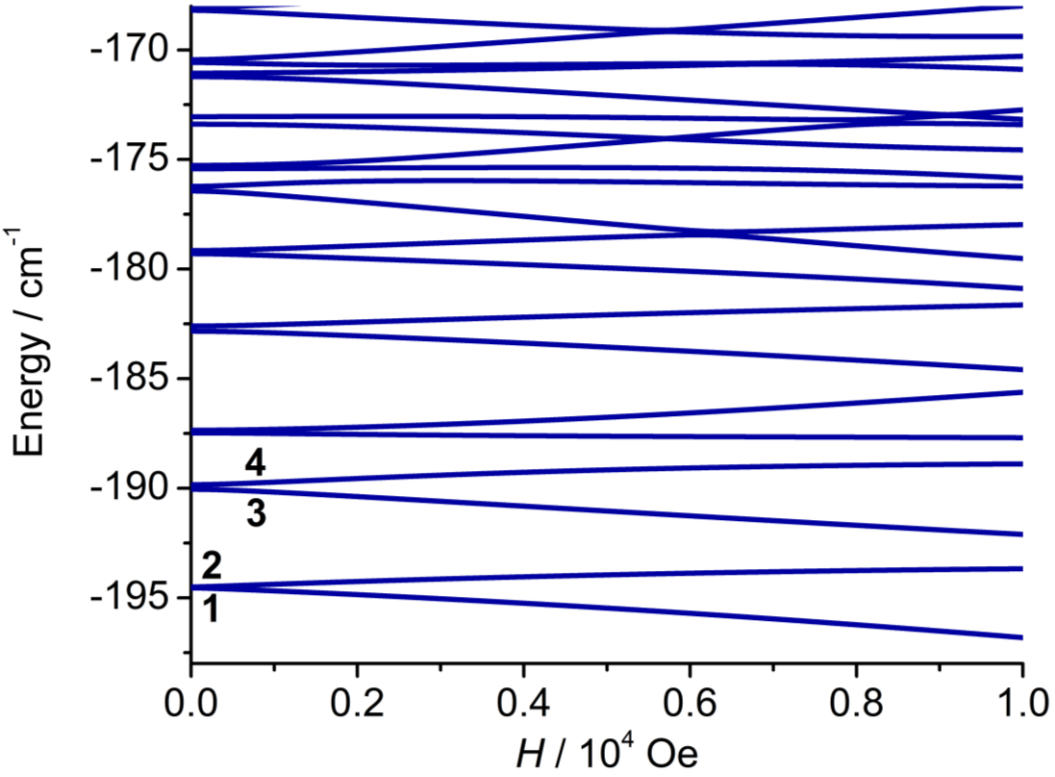

Figure 4.21. Zeeman diagram for **1Br** when the magnetic field is applied along the direction of maximum splitting for the ground doublet (z_3).

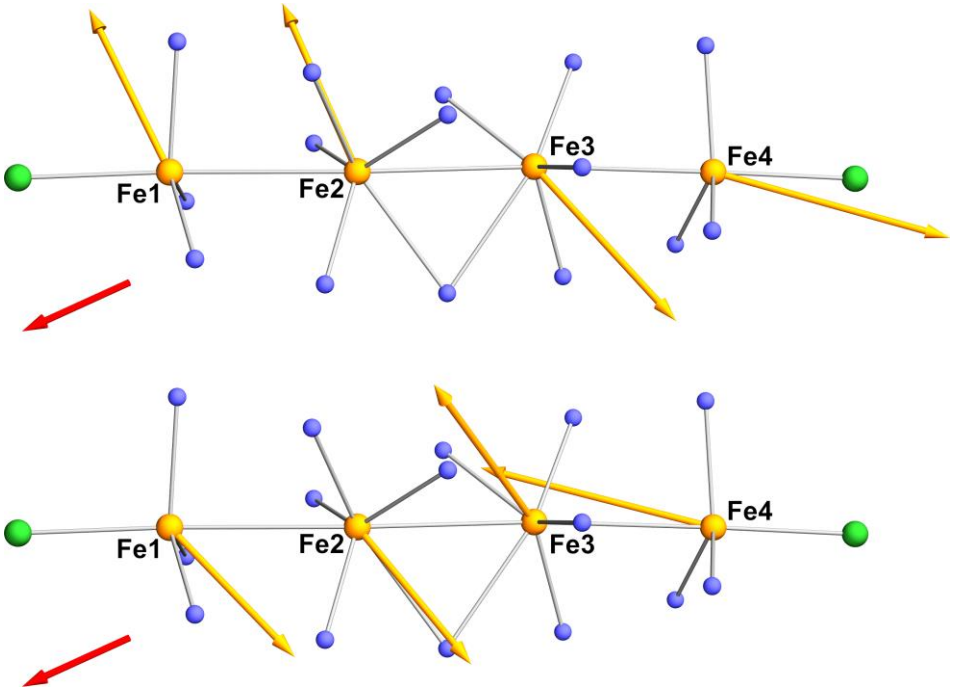

Figures 4.22. Local spin components (orange arrows, drawn on an arbitrary scale) in the ground doublet of **1Cl** when a 1-kOe magnetic field (red arrow) is applied along the direction of maximum Zeeman splitting (z_3). The upper and lower panels picture states 1 and 2, respectively. Color code: orange, Fe; blue, N; green, Cl.

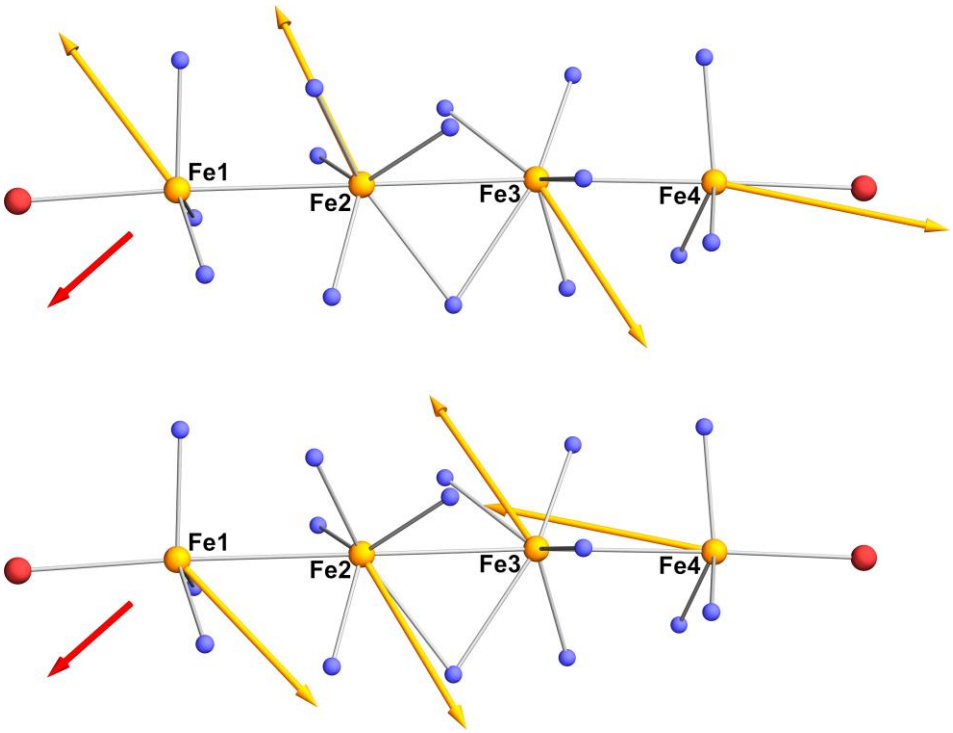

Figures 4.23. Local spin components (orange arrows, drawn on an arbitrary scale) in the ground doublet of **1Br** when a 1-kOe magnetic field (red arrow) is applied along the direction of maximum Zeeman splitting (z_3). The upper and lower panels picture states 1 and 2, respectively. Color code: orange, Fe; blue, N; red, Br.

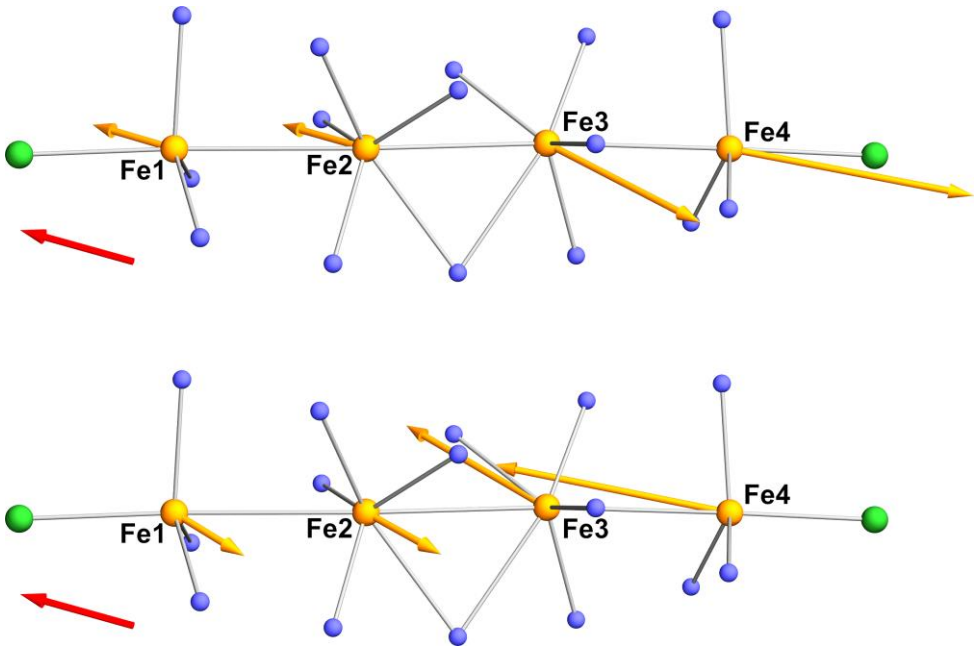

Figure 4.24. Local spin components (orange arrows, drawn on an arbitrary scale) in the first-excited doublet of **1Cl** when a 1-kOe magnetic field (red arrow) is applied along the direction of maximum Zeeman splitting (z_3'). The upper and lower panels picture states 3 and 4, respectively. Same color code as in Fig. 4.22.

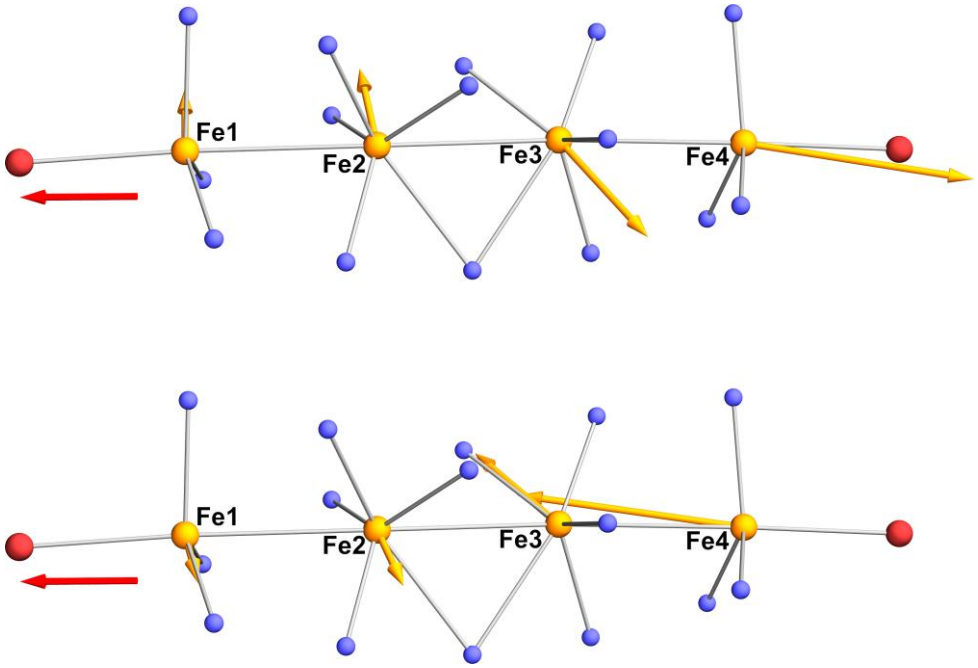

Figure 4.25. Local spin components (orange arrows, drawn on an arbitrary scale) in the first-excited doublet of **1Br** when a 1-kOe magnetic field (red arrow) is applied along the direction of maximum Zeeman splitting (z_3'). The upper and lower panels picture states 3 and 4, respectively. Same color code as in Fig. 4.23.

Looking at state 1 (upper panels in Figures 4.22 and 4.23), the large ferromagnetic coupling between Fe1 and Fe2 and the antiferromagnetic coupling of Fe2 to Fe3 limit noncollinearities between neighboring spins to less than 20°. Moreover, spins at these sites form large angles with the chain axis (Table 4.14). This arrangement is understood as a consequence of the fact that the magnetic anisotropies of Fe1 and Fe2 are comparable in magnitude, roughly collinear but opposite in sign. The coupled state of the pair is thus only weakly anisotropic and the spins are torqued away from Z under the influence of hard-axis Fe3 and of the antiferromagnetic J_{23} interaction. Due to the large $|D|$ value of the terminal metal Fe4 and the weak ferromagnetic interaction between Fe3 and Fe4, the spin on Fe4 lies close to its local easy direction and forms a substantial angle with the spin on Fe3 (Figures 4.22 and 4.23, and Table 4.14). Notice that noncollinearities within the Fe1,Fe2 and Fe3,Fe4 pairs are enhanced in **1Br**, which features smaller $|J_{12}|$ and $|J_{34}|$ values. As a final observation, the spins on Fe1, Fe2, and Fe3 are roughly orthogonal to z_3 and contribute only marginally to the magnetic moment in state 1, which is primarily determined by Fe4.

In state 3 (Figures 4.24 and 4.25), the spins on Fe1 and Fe2 are also approximately parallel with each other, and antiparallel to Fe3; this state however entails a much decreased spin on Fe1 and Fe2, in such a way that Fe1, Fe2 and Fe3 roughly cancel each other and the magnetic moment of state 3 is primarily determined by Fe4.

The origin of the weakly magnetic pseudo-doublet ground state is clearly the competition between the large, noncollinear single-ion anisotropies and super-exchange interactions. For dominant super-exchange couplings, the alternating signs of J_{ij} constants across the molecule (Scheme 4.2) would afford a nonmagnetic ground state with $S = 0$ total spin, irrespective of local anisotropies. In the complexes under study, this strong-exchange regime[3] is not reached and the ground state is magnetic - albeit weakly. To ascertain the role of noncollinear anisotropies, test calculations were performed using the best-fit J_{ij} values of model m**1Cl**D but averaging all $\bar{\bar{D}}_i$ and $\bar{\bar{g}}_i$ tensors to axial symmetry and aligning their main axes with Z. With this operation, the g_3 value for the ground pseudo-doublet drastically decreases from 7.6 to 0.62. The new zero-field wavefunctions are predominantly (>50%) constituted by the pairs of product states $|-2,-1,+1,+2\rangle$, $|+2,+1,-1,-2\rangle$ and $|-2,-2,+2,+2\rangle$, $|+2,+2,-2,-2\rangle$, with equal weights within each pair (product states are labelled with the M_S quantum numbers of the four ions). The unequal g-factors along Z are the reason for the residual magnetic response of the ground pseudo-doublet, which would otherwise be perfectly nonmagnetic ($g_3 = 0$). The occurrence of a magnetic ground state is consistent with the observation of SMM properties in both derivatives, as presented in the next Section.

4.8 AC Magnetic Studies

A crystalline sample of **1Cl**·2.6CH_2Cl_2·0.84Et_2O, investigated up to ν = 1500 Hz, showed the onset of SRM below 2.8 K when a small static field (H_{DC} = 2 kOe) was applied, but no detectable out-of-phase signal at H_{DC} = 0.[20] AC susceptibility measurements were also performed on a polycrystalline sample of **1Br**·2.3CH_2Cl_2·Et_2O up to ν = 9980 Hz. Preliminary scans at 2.0 K for H_{DC} values between 0 and 2.5 kOe revealed that the compound features SRM even in zero DC field (Fig. 4.26).

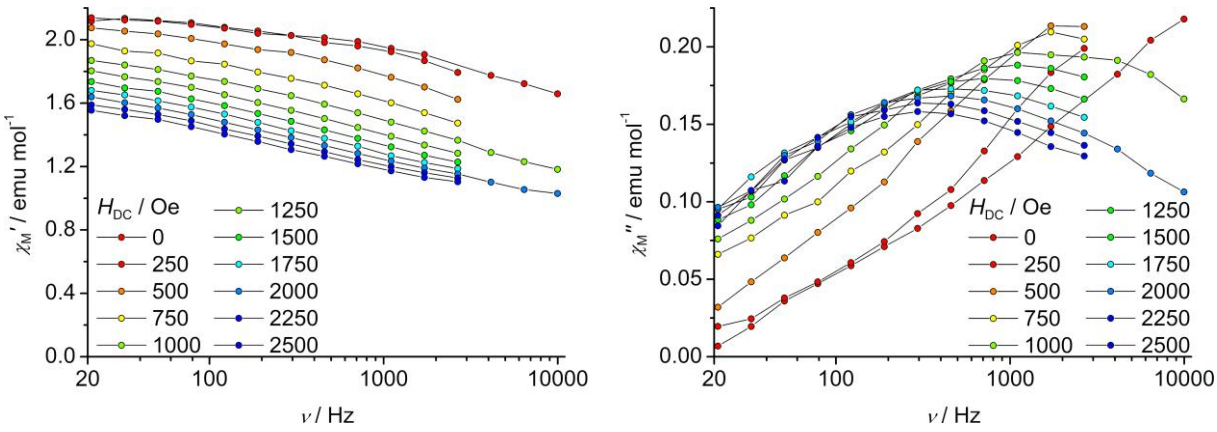

Figure 4.26. DC-field dependence of the in-phase (χ_M', left panel) and out-of-phase (χ_M'', right panel) components of molar magnetic susceptibility of **1Br**·2.3CH_2Cl_2·Et_2O at T = 2.0 K.

The frequency dependence of the in-phase (χ_M') and out-of-phase (χ_M'') components of molar magnetic susceptibility does not change significantly above 2 kOe. Complete sets of frequency-dependent data were then recorded at 0, 1 and 2 kOe for temperatures between 2.0 and 8.0 K. In zero DC field, the onset of SRM was clearly detected below 4.0 K, where each isothermal $\chi_M''(\nu)$ curve is a monotonic increasing function (Fig. 4.27), with no detectable maximum in our accessible frequency range. Therefore the χ_M'' vs ν curves could not be fitted with the generalized Debye model.[3] An alternative method,[120,121] employed also to fit the AC data of **1Cl**·2.6CH_2Cl_2·0.84Et_2O[20] was used, which allows a rough estimate of U_{eff}/k_B and τ_0 by applying Eq. 4.9:

$$\ln(\chi_M''/\chi_M') = \ln(\omega\tau_0) + E_a/(k_BT) \qquad (4.9)$$

where $\omega = 2\pi\nu$ and $E_a \approx U_{eff}$. Eq. 4.9 is valid assuming that only one characteristic Debye relaxation process is present, with one time constant and one energy barrier. A linear regression on $\ln(\chi_M''/\chi_M')$ vs $1/T$ data between 2.0 and 4.0 K was then performed for each ν value ranging from 78.7 to 9980 Hz (Fig. 4.28). The values U_{eff}/k_B = 5.4(4) K and $\tau_0 = 1.1(8)\cdot10^{-6}$ s were

obtained by averaging the best-fit slopes (E_a/k_B) and intercepts ($\ln(\omega\tau_0)$), respectively, at different frequencies (the numbers in parentheses are the associated standard deviations).

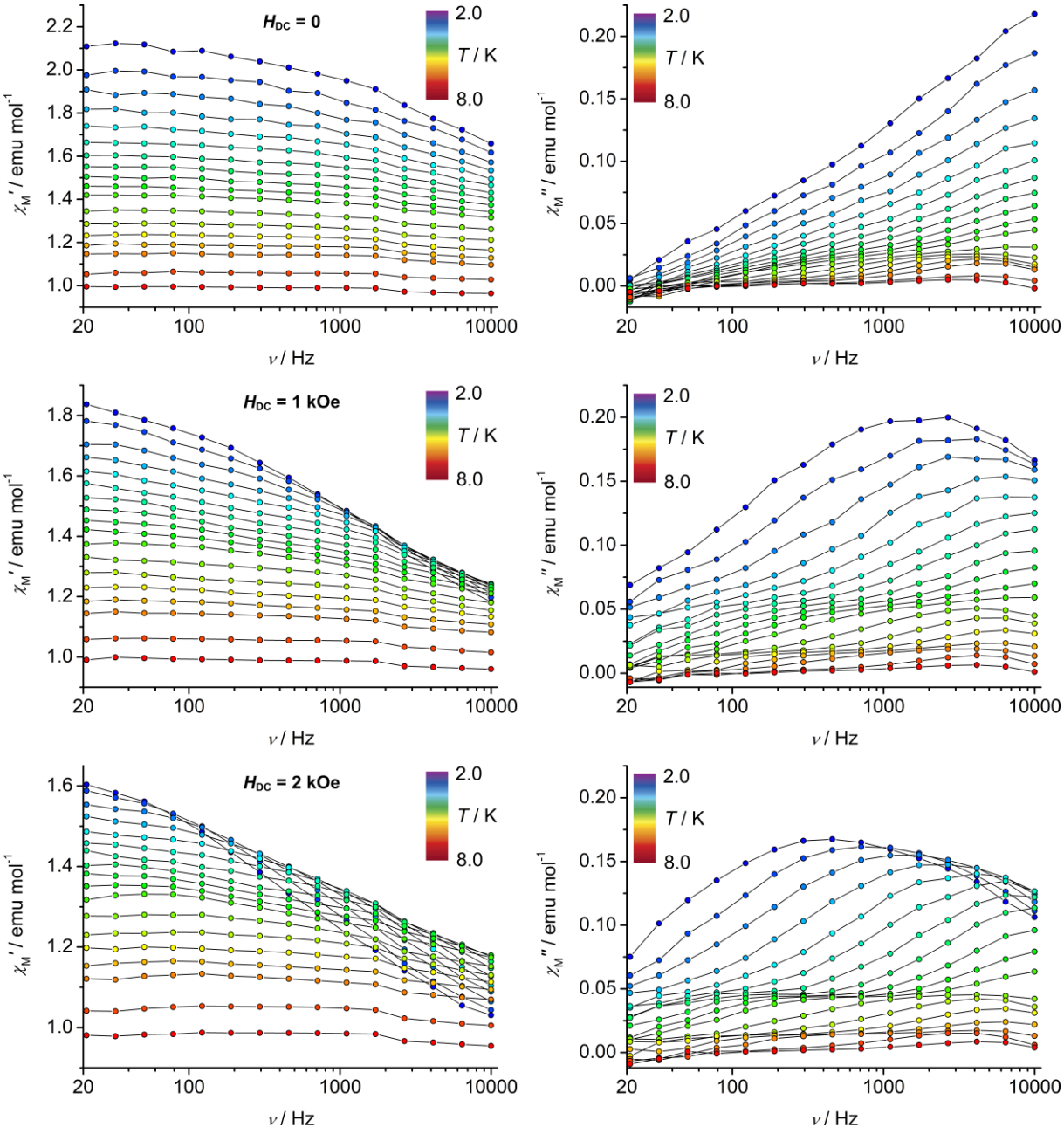

Figure 4.27. Frequency dependence of the in-phase (χ_M', left panels) and out-of-phase (χ_M'', right panels) components of molar magnetic susceptibility for **1Br**·2.3CH_2Cl_2·Et_2O at T = 2.0, 2.2, 2.4, 2.6, 2.8, 3.0, 3.2, 3.4, 3.6, 3.8, 4.0, 4.4, 4.8, 5.2, 5.6, 6.0, 7.0 and 8.0 K. Measurements were carried out with a DC field of 0 (top), 1 (middle) and 2 kOe (bottom).

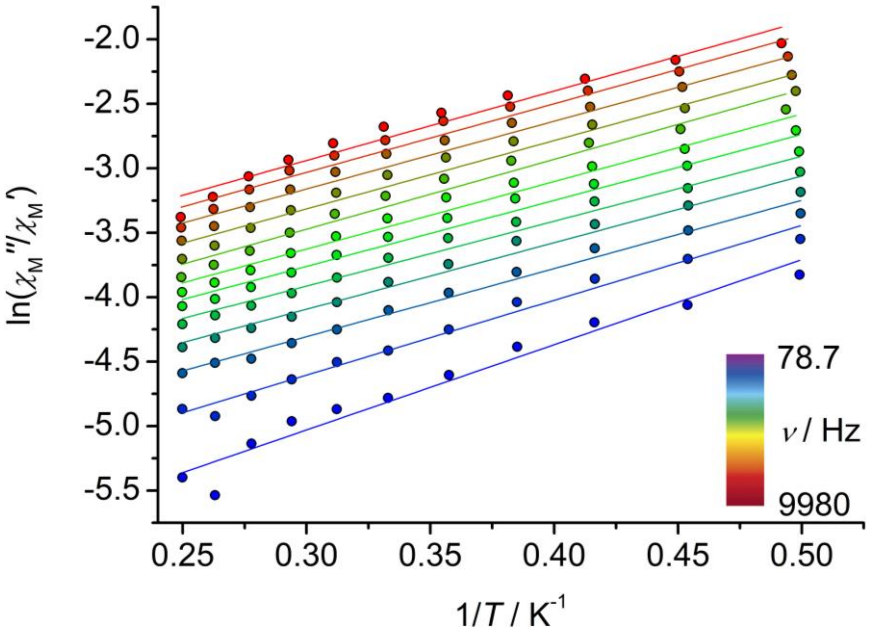

Figure 4.28. Frequency-dependent $\ln(\chi_M''/\chi_M')$ vs $1/T$ plots for **1Br**·2.3CH_2Cl_2·Et_2O (coloured dots) in zero DC field. The coloured lines represent the linear regression fits at each specific frequency (Eq. 4.9).

Upon application of a DC field, magnetic relaxation slows down and clear maxima appear in isothermal χ_M'' vs ν curves recorded at $T \leq 3.0$ K (Fig. 4.27). The nonzero H_{DC} is likely to reduce the efficiency of under-barrier relaxation processes, such as QTM, which are expected because of the significant rhombicity of the structure.[3,7] The standard treatment is then applicable, based on extended Debye model[3,122,123] and on Eqs. 4.10-4.12.

$$\chi_M(\omega) = \chi_{M,S} + \frac{(\chi_{M,T}-\chi_{M,S})}{1+(i\omega\tau)^{1-\alpha}} \quad (4.10)$$

$$\chi_M''(\omega) = (\chi_{M,T} - \chi_{M,S}) \frac{(\omega\tau)^{1-\alpha}\cos(\pi\alpha/2)}{1+2(\omega\tau)^{1-\alpha}\sin(\pi\alpha/2)+(\omega\tau)^{2-2\alpha}} \quad (4.11)$$

$$\chi_M'(\omega) = \chi_{M,S} + (\chi_{M,T} - \chi_{M,S}) \frac{1+(\omega\tau)^{1-\alpha}\sin(\pi\alpha/2)}{1+2(\omega\tau)^{1-\alpha}\sin(\pi\alpha/2)+(\omega\tau)^{2-2\alpha}} \quad (4.12)$$

where $\chi_{M,T}$ and $\chi_{M,S}$ are the isothermal and adiabatic susceptibilities, respectively, τ is the average relaxation time and α determines the width of the distribution of relaxation times (α = 0 corresponds to a single relaxation process, while α = 1 to an infinitely wide distribution). Isothermal χ_M'' and χ_M' vs ν curves were simultaneously fitted with Eqs. 4.11 and 4.12, in order to cross-check the two experimental datasets and obtain more reliable results. The best-fit parameters (τ, α, $\chi_{M,T}$ and $\chi_{M,S}$) for the two different static fields are reported in Table 4.15 and 4.16. In both cases, the relaxation times decrease with increasing temperature, presumably due to the progressive enhancement of thermally activated relaxation processes. The use of a 2-kOe static field leads to approximately three times slower relaxation than at H_{DC} = 1 kOe. The α

parameter does not follow a straightforward trend, but for H_{DC} = 1 kOe (2 kOe) it ranges between 0.51−0.63 (0.44−0.51). Its substantial value (≈0.5) highlights a very broad distribution of relaxation times. From Fig. 4.29 it is evident that the ln(τ) vs 1/T plots at 1 and 2 kOe do not follow a linear trend. Therefore, slow relaxation of the magnetization cannot be described solely by a multistep thermally activated relaxation processes (Orbach mechanism), where τ exponentially increases with decreasing T and follows the expression $\tau = \tau_0 \exp[U_{eff}/(k_B T)]$. The temperature dependences of ln(τ) at 1 and 2 kOe were simultaneously fitted to Eq. 4.13, which accounts for Orbach and QTM relaxation mechanisms but disregards Raman relaxation:

$$\tau = \{\tau_0^{-1} \exp[-U_{eff}/(k_B T)] + \tau_{QTM}^{-1}\}^{-1} \quad (4.13)$$

In Eq. 4.13, τ_{QTM} is the relaxation time associated to QTM mechanism and only U_{eff} is assumed to be independent of H_{DC}. The calculated best-fit parameters are: at H_{DC} = 1 kOe, τ_0 = 1.9(6)·10^{-8} s, τ_{QTM} = 1.44(11)·10^{-4} s; at H_{DC} = 2 kOe, τ_0 = 5.2(16)·10^{-8} s, τ_{QTM} = 4.4(4)·10^{-4} s; U_{eff}/k_B = 18.9(8) K. This value of U_{eff} is ~3.5 times larger than that estimated in zero DC field, and is also larger than found in **1Cl** at 2 kOe (10.1(1.3) K).[20]

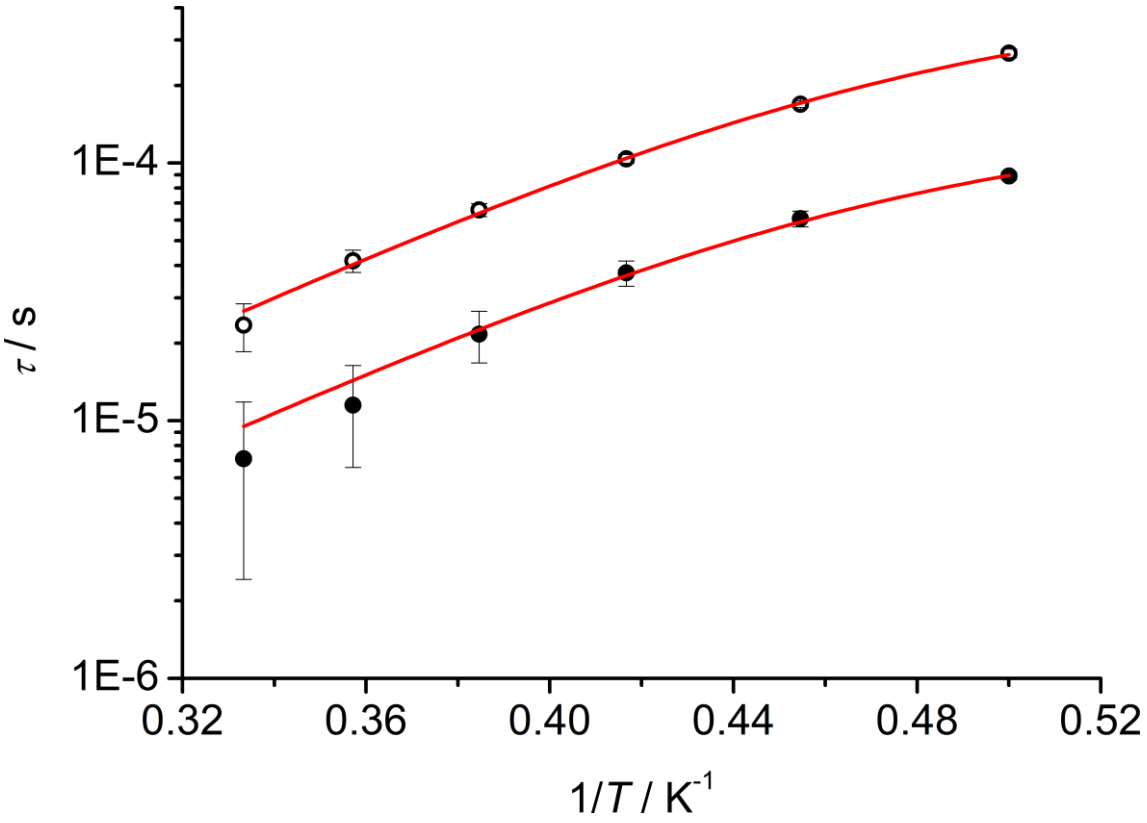

Figure 4.29. Temperature dependence of the relaxation time of **1Br**·2.3CH_2Cl_2·Et_2O (τ, in $\log_{10}$ scale) at H_{DC} = 1 kOe (solid dots) and 2 kOe (open dots), along with the best-fit curve (red lines).

Table 4.15. Best-fit parameters obtained from the simultaneous treatment of χ_M'' and χ_M' vs ν data with the extended Debye model (Eqs. 4.11 and 4.12) for compound **1Br**·2.3CH_2Cl_2·Et_2O (H_{DC} = 1 kOe).

T / K	$\chi_{M,T}$ / emu mol^{-1}	$\chi_{M,S}$ / emu mol^{-1}	τ / μs	α
2.0	1.914(4)	0.904(11)	89(3)	0.514(7)
2.2	1.846(6)	0.89(2)	61(4)	0.526(11)
2.4	1.760(7)	0.88(3)	37(4)	0.530(15)
2.6	1.706(9)	0.83(5)	22(5)	0.56(2)
2.8	1.661(11)	0.77(9)	11(5)	0.61(3)
3.0	1.615(12)	0.75(13)	7(5)	0.63(3)

Table 4.16. Best-fit parameters obtained from the simultaneous treatment of χ_M'' and χ_M' vs ν data with the extended Debye model (Eqs. 4.11 and 4.12) for compound **1Br**·2.3CH_2Cl_2·Et_2O (H_{DC} = 2 kOe).

T / K	$\chi_{M,T}$ / emu mol^{-1}	$\chi_{M,S}$ / emu mol^{-1}	τ / μs	α
2.0	1.726(8)	0.886(10)	267(10)	0.513(10)
2.2	1.662(5)	0.902(7)	169(5)	0.474(8)
2.4	1.612(4)	0.903(9)	104(4)	0.465(9)
2.6	1.559(4)	0.906(13)	66(4)	0.450(12)
2.8	1.512(5)	0.90(2)	42(4)	0.443(18)
3.0	1.481(6)	0.86(4)	24(5)	0.48(3)

4.9 Conclusions

In this Chapter we have described and compared the solution and solid-state properties of two tetrairon-based EMACs supported by oligo-*α*-pyridylamido ligands and capped by halide ligands: **1Cl** and **1Br**. The complexes contain exclusively iron(II) centers, as most directly supported by Mössbauer spectroscopy, and undergo four consecutive quasi-reversible one-electron oxidations in dichloromethane solution. The DC magnetic properties indicate a weakly magnetic ground state in both derivatives. SRM is nevertheless detected in AC measurements, with **1Br** displaying SMM behavior even in zero static field. To aid the analysis of magnetic data, a local-site model was assumed and the single-ion properties were evaluated by *ab-initio* (CASSCF-NEVPT2-SO) methods. The results showed that in these stringlike complexes the terminal metal centers (Fe1 and Fe4) have a *negative D* parameter, whereas the internal ones (Fe2 and Fe3) have a *positive D*, corresponding to predominantly easy- and hard-axis magnetic anisotropies, respectively. Due to the significant deviations from D_3 molecular symmetry, however, different anisotropies are predicted for the two terminal metals and, to a lesser extent, for the internal ones. In addition, single-ion magnetic anisotropies display significant rhombic distortions with $|E/D|$ up to 0.2 and noncollinear principal axes. These local anisotropies compete with super-exchange interactions, which turn out to be ferromagnetic within the Fe1,Fe2 and Fe3,Fe4 pairs and antiferromagnetic between Fe2 and Fe3. Since the strong-exchange regime[3] typical of most polynuclear molecular magnets is not attained, the ground state is a non-Kramers doublet featuring a highly noncollinear spin arrangement.

In conclusion, the large Fe···Fe separations and the super-exchange patterns found in **1Cl** and **1Br** yield weak-to-moderate ferromagnetic couplings accompanied by antiferromagnetic contributions that severely plague SMM behavior. Additionally, the different coordination pockets available in these EMACs lead to opposite and partially cancelling local anisotropies. Therefore, the formation of M−M bonds seems requisite to stabilize well-isolated ground spin states in iron(II)-based EMACs.[93] Instilling a negative *D* parameter in the ground state is a second mandatory task for the design of M−M bonded SMMs. A recent study[124] on a dimeric system has clearly shown that local-site models are of limited utility to accomplish this task. In fact, the reorganization of molecular orbital energies upon M−M bond formation can trigger a strikingly different anisotropy as compared with that predicted by a localized model. An alternative strategy to strengthen ferromagnetic interactions in iron-based EMACs without Fe–Fe bonds is the design of MV species, in which double-exchange coupling is operative.[3,36,40] The rich electrochemistry of the herein reported iron(II) derivatives suggests that

partially-oxidized congeners may be chemically accessible. In fact, we were able to isolate two new MV species from the chemical oxidation of **1Cl**, $[Fe^{II}_2Fe^{III}(tpda)_3]PF_6$ (**3**) and $[Fe^{II}Fe^{III}_2(tpda)_3Cl]PF_6$ (**3a**), to which **Chapter 5** is dedicated.

4.10 Experimental Section

4.10.1 Materials and Methods

All synthetic operations involving iron(II) complexes were carried out inside an MBraun UniLAB glovebox under an inert and controlled dinitrogen atmosphere (H_2O and O_2 < 1 ppm), continuously purified over activated charcoal, molecular sieves, and copper as a dioxygen scavenger. All chemicals were of reagent grade and used as received, unless otherwise noted. Dichloromethane, toluene, acetone and 1,4-dioxane were purchased anhydrous. THF and Et_2O were pre-dried over KOH[125] and $CaCl_2$,[126] respectively, and subsequently distilled from their sodium diphenylketyl solutions before use. With the exception of acetone, all solvents (including CD_2Cl_2) were deoxygenated through three freeze-pump-thaw cycles and stored over 4Å molecular sieves. [$Fe_2(Mes)_4$] (**2**) was synthesized from Fe_4Cl_8·6THF[82] and MesMgBr in THF/1,4-dioxane.[103,127] H_2tpda was prepared refluxing 2,6-diaminopyridine, 2-fluoropyridine and LiH in toluene/pyridine, following the high-yield procedure that some of us recently reported.[70] The compound [$Fe_4(tpda)_3Cl_2$]·2.6CH_2Cl_2·0.84Et_2O (**1Cl**·2.6CH_2Cl_2·0.84Et_2O) was prepared as previously described.[20] TBACl and TBABr were recrystallized twice from acetone/Et_2O, washed with Et_2O and dried under vacuum.[126]

Elemental analysis was performed using a ThermoFisher Scientific Flash 2000 analyzer, following brief exposure of the sample to the air (30-60 s). All other characterization data were collected with strict exclusion of dioxygen and water. ESI-MS measurements were conducted on a 6310A Ion Trap LC-MS(n) instrument (Agilent Technologies) by direct infusion of dichloromethane solutions and working in positive ion mode. MALDI-TOF-MS measurements were performed at the University of Wisconsin-Madison with a Bruker ULTRAFLEX^{TM} III instrument (equipped with a SmartBeam^{TM} laser) using a powdery sample finely milled with a large excess of pure anthracene and working in positive ion mode. The *m*/*z* values in the MALDI-TOF-MS spectrum are expressed by setting the isotopic peak of anthracene ($C_{14}H_{10}$) at *m*/*z* = 178.08. The electronic spectrum in dichloromethane solution was recorded up to 2000 nm on a Jasco V-570 double beam UV-Vis-NIR spectrometer, using a quartz cuvette sealed with an airtight Teflon® cap (optical path length *l* = 0.1 cm). The ^{1}H NMR spectrum was recorded at 298 K in CD_2Cl_2 with a Bruker Avance400 FT-NMR spectrometer (400.13 MHz). The chemical shifts are expressed in ppm downfield from Me_4Si as external standard, by setting

the residual ^{1}H signal of CD_2Cl_2 at 5.32 ppm. Spectrum processing and analysis were carried out with TopSpin 4.0.6 software[86] (SI = TD, LB = 1.00 Hz).

4.10.2 Synthesis of $[Fe_4(tpda)_3Br_2]\cdot 2.3CH_2Cl_2\cdot Et_2O$ (**1Br**$\cdot 2.3CH_2Cl_2\cdot Et_2O$)

Iron(III)-free $FeBr_2\cdot 2THF$[128,129] was prepared by stirring $FeBr_2$ (19.6 mg, 0.0909 mmol) with a five-fold molar excess of Fe^0 powder in THF at room temperature (5 mL). Excess Fe^0 was removed with a magnet and the solution was evaporated to dryness to give $FeBr_2\cdot 2THF$ as a very light green solid, which was treated with a dark red solution of $[Fe_2(Mes)_4]$ (105.5 mg, 0.1793 mmol) in toluene (3 mL). A suspension of H_2tpda (94.20 mg, 0.3578 mmol) in toluene (4 mL) was then added dropwise under stirring, yielding a light brown suspension. After 5 min, the reaction mixture was gently heated to reflux for 165 min, whereupon it initially turned orange, then gradually darkened to dark orange-brown. After cooling to room temperature, an orange solid was separated from the dark liquid phase by filtration through a fritted glass funnel (porosity G3 or G4) and extracted with CH_2Cl_2 (2 × 25 mL), to give a red solution (for each extraction the solid and the solvent were stirred together for 90 min). The solvent was evaporated under vacuum until only ~2 mL remained, and an orange precipitate had formed. The suspension was cooled down to −35 °C and the liquid phase was carefully removed using a very narrow bore pipette. The solid was thoroughly dried under vacuum to give **1Br** as an orange powder (50 mg, 48%), from which we measured Mössbauer and MALDI-TOF-MS spectra. For all other characterizations the product was crystallized by slow vapour diffusion of Et_2O (75 mL) into the CH_2Cl_2 extract (50 mL). Dark red prisms were obtained and separated easily by flotation from a powdery residue and from minority crystal phases (see **Supplementary Note 1**, **Appendix**) and vacuum-dried to remove lattice solvent (30−35% overall yield).

Anal. Calcd for **1Br** ($C_{45}H_{33}Br_2Fe_4N_{15}$): C, 46.31; H, 2.85; N, 18.00. Found: C, 45.86; H, 2.92; N, 18.40. ESI-MS (*m*/*z*): 1030.1 ($[Fe_3(tpda)_3Br]^+$, 100); 986.1 ($[Fe_3(tpda)_3Cl]^+$, 25). MALDI-TOF-MS (*m*/*z*): 952.2 ($[Fe_3(tpda)_3+H]^+$, 100); 1087.3 ($[Fe_4(tpda)_3Br+H]^+$, 9); 1031.3 ($[Fe_3(tpda)_3Br+H]^+$, 2); 1043.3 ($[Fe_4(tpda)_3Cl+H]^+$, 1). UV-Vis-NIR (CH_2Cl_2, $4.3\cdot 10^{-4}$ M): λ_{max} (ε) = 286 nm ($3.81\cdot 10^4$ M^{-1} cm^{-1}), 370 nm ($3.38\cdot 10^4$ M^{-1} cm^{-1}), 448 nm (sh). ^{1}H NMR (CD_2Cl_2, 400.13 MHz): δ_H (ppm) = 3.53 (6H, s), 8.58 (6H, s), 9.80 (3H, s, H*a*), 62.91 (6H, s), 80.50 (6H, s), 119.7 (6H, s).

4.10.3 X-ray Crystallography of **1Br**·2.3CH_2Cl_2·Et_2O

A prismatic crystal of the compound was removed from the mother liquor under nitrogen, rapidly cooled down in a cold dinitrogen stream and mounted on a Bruker-Nonius X8APEX diffractometer equipped with Mo-Kα generator, area detector and Kryoflex liquid dinitrogen cryostat for data collection at 115(2) K. Acquisition of matrix frames and data collection were carried out using APEX2 software[130] while data reduction used SAINT program.[130] Multi-scan absorption correction was applied with SADABS.[130] Programs SIR92[131] and SHELXL-2014/7,[132] both implemented in the WINGX v2014.1 suite,[133] were used for structure solution and refinement on F_o^2, respectively. Although the molecule has no crystallographically-imposed symmetry, two $tpda^{2-}$ ligands (those containing N7 and N8) are almost perfectly related by a twofold axis normal to the metal chain. The third $tpda^{2-}$ ligand, the metal ions and the terminal bromido ligands lift such local symmetry and are disordered over two unequally populated positions (0.88:0.12) related by a 180° rotation around the above-mentioned dyad. As a consequence of this, the minority component is structurally similar to its majority counterpart. All attempts to model the terminal ligands as mixed Br/Cl scatterers with complementary occupancies gave unphysically low (< 0.01 $Å^2$) displacement parameters for the minority (Cl) components. Lattice solvent molecules (CH_2Cl_2 and Et_2O) also show severe positional disorder, with shared occupation of crystallographic sites, which makes their modelling extremely challenging. Non-hydrogen atoms were refined anisotropically, but isotropic displacement parameters had to be used for most disordered portions of the structure. These were refined with further restraints/constraints on geometry and displacement parameters. In particular, similarity restraints were applied to the geometry of CH_2Cl_2 molecules, whereas Et_2O molecules were restrained to the geometry found in CCDC 973959. Hydrogen atoms were treated isotropically and refined using a riding model with U(H) = 1.2U_{eq}(C) for methylene and U(H) = 1.5U_{eq}(C) for methyl hydrogens, which were set in a staggered conformation. Crystal data and refinement parameters are gathered in Table 4.1 while an exhaustive listing of interatomic distances and angles as well as further details on structural analysis are available in Table A.1 and in **Supplementary Note 2**.

4.10.4 Electrochemistry

CV measurements were carried out using a PARSTAT model 2273 potentiostat-galvanostat. Experiments were performed at different scan rates (0.02−5 V s^{-1}) using a cell for small volume

samples (0.5 mL). A 1-mm diameter glassy carbon (GC) disk, a Pt wire, and an Ag wire were used as working, counter, and quasi-reference (Ag/AgCl or Ag/AgBr) electrodes, respectively. The GC electrode was cleaned following a previously reported procedure.[20,134] For all the experiments, the potential of the quasi-reference electrode was calibrated against the ferrocenium/ferrocene redox couple (in dichloromethane, $E°$ = 0.460 V vs KCl saturated calomel electrode, SCE).[135] All the reported potential values $E°'$ are referenced to the ferrocenium/ferrocene redox couple. The formal potential value ($E°'$) corresponding to each ET process was calculated as the semi-sum of the cathodic and anodic peak potentials, $E°' = (E_{pc}+E_{pa})/2$. The dependence of $\Delta E_p = E_{pa}-E_{pc}$ on scan rate yielded the standard heterogeneous ET rate constant (k_{ET}),[136] which is the ET rate constant measured at the formal potential $E°'$. Due to the instability of **1Cl** and **1Br** in the presence of O_2 or H_2O, the experiments were performed in the above-described MBraun UniLAB glovebox at temperatures ranging between −15 and +5 °C.[20] Variable temperature experiments were conducted using an isothermal cell configuration, in which the temperature of the reference and working electrodes was varied. For this experimental configuration, the reduction entropy referenced to the ferrocenium/ferrocene redox couple ($\Delta S°'_{rc}$) is given by:

$$\Delta S°'_{rc} = S°'_{red} - S°'_{ox} = nF\left(\frac{\partial E°'}{\partial T}\right)_P \qquad (4.14)$$

Thus, $\Delta S°'_{rc}$ can be calculated from the slope of the $E°'$ vs T plot, which is linear under the assumption that $\Delta S°'_{rc}$ is constant over the limited temperature range investigated. With the same assumption, the enthalpy change (also referenced to the ferrocenium/ferrocene redox couple, $\Delta H°'_{rc}$) was obtained from the Gibbs-Helmholtz equation, namely as the negative slope of the $E°'/T$ vs $1/T$ plot. All measurements were made on ~0.2 mM solutions of **1Cl** and **1Br** prepared by dissolving vacuum-dried crystals in CH_2Cl_2 and using 0.1 M TBACl and TBABr, respectively, as supporting electrolytes. The ohmic drop between the working and the reference electrodes was minimized through a careful feedback correction. The experiments were repeated at least five times; $E°'$ and k_{ET} values were found to be reproducible within ±0.002 V and ±6%, respectively.

4.10.5 Magnetic Measurements

Magnetic measurements were made on a Quantum Design PPM cryogenic system with a two-coil susceptometer. A polycrystalline sample of **1Br**·2.3CH_2Cl_2·Et_2O (20.41 mg) and a small amount of its mother liquor (24.08 mg, CH_2Cl_2:Et_2O 54:46) were introduced into a quartz tube,

which was subsequently flame-sealed. The presence of the mother liquor was necessary to prevent field-induced torquing at low temperature. The diamagnetic contributions of the sample and of the mother liquor were evaluated using Pascal's constants.[137] The magnetic response of an identical quartz tube was previously measured to correct for the diamagnetic contributions of the quartz.[20] DC measurements were based on extraction magnetometry technique. Magnetic susceptibility was obtained as $\chi = M/H$ from magnetization (M) measurements in a static magnetic field H = 10 kOe from 300.0 to 2.0 K. The isothermal field dependence of M was also measured at 2, 4 and 8 K, scanning the field up to 70 kOe. AC measurements were performed using a small oscillating magnetic field of 10 Oe (for frequencies v between 21 and 1715 Hz) or 5 Oe (for v between 2664 and 9980 Hz) to minimize self-heating of the sample. The influence of a static magnetic field (H_{DC}) on the out-of-phase component of the magnetic susceptibility (χ'') was explored with preliminary χ'' vs v scans at 2 K for H_{DC} values ranging from 0 to 2.5 kOe. Afterwards, χ'' vs v scans between 2.0 and 8.0 K were carried out for H_{DC} = 0, 1, and 2 kOe.

4.10.6 Mössbauer Spectroscopy

Mössbauer spectra of **1Cl** and **1Br** encased in an eicosane matrix were collected at 10 and 77 K with a 1024 channel See Co model W304 resonant gamma-ray spectrometer using ^{57}Co on Rh foil as a gamma-ray source (initial strength = 25 mCi, obtained from Ritverc Isotope Products) at the University of Wisconsin-Madison. The source velocity range used was ±4 mm/s and measurements were conducted under vacuum. Cryogenic temperatures were achieved using a Lakeshore model 336 temperature controller in conjunction with a Janis model SHI-850 cryostat. Mössbauer data were fitted with the WMOSS4F software package,[138] using an adaptive nonlinear least-squares algorithm developed by Dennis *et al.* (available within WMOSS4F) was used to fit each doublet (see **Supplementary Note 3** for further details).[139] Refined parameters for each quadrupole doublet were δ, ΔE_Q, and the linewidth, calculated as FWHM. Errors associated with δ, ΔE_Q, and FWHM are estimated to be ~0.01 mm s^{-1}. All reported isomer shifts are referenced to α-Fe foil at room temperature (294 K). At both temperatures the spectra could be satisfactorily fitted using two doublets with fixed 1:1 relative areas (sub-spectrum 1 and 2). Attempts to fit more quadrupole doublets to the data did not lead to convergence due to overparameterization. Alternative fits to the 77 K spectra are included in the **Appendix** (Fig. A.3 and A.4); while numerically sound, these alternative parameter sets are

less consistent with those extracted from the 10 K spectra, which could only be modeled with the parameters reported in Table 4.7.

The reduced χ^2 value was used to assess the fit quality. The reduced χ^2 is defined as the χ^2 statistic per degree of freedom, where a degree of freedom is defined as the difference between the number of measured datapoints (n) and the number of parameters (p) fit to the data. The reduced χ^2 statistic is given by:

$$\text{reduced } \chi^2 = \frac{1}{n-p}\sum_{k=1}^{n}\frac{(O_k-E_k)^2}{E_k} \qquad (4.15)$$

where O_k is the kth observed value for the signal intensity at a given source velocity and E_k is the kth expected value for the signal intensity at the same source velocity.[140]

4.10.7 Angular Overlap Model (AOM) Calculations

The electronic structure of the iron(II) centers in **1Br** was studied using AOM calculations, carried out with the program package AOMX.[110] Following the same approach developed for the chloro derivative **1Cl**,[20] the X-ray coordinates of Fe1(N1,N2,N3,Br1) and Fe4(N13,N14,N15,Br2) were averaged to C_{3v} symmetry. As for Fe2(N4,N5,N6,N7,N8) and Fe3(N8,N9,N10,N11,N12), the X-ray coordinates were directly used in the calculations. The LF parameters accounting for σ and π interactions[111] were obtained from the values reported for *trans*-[Fe(py)$_4$Br$_2$] and *trans*-[Fe(py)$_4$(NCS)$_2$], assuming an r^{-6} dependence on metal-ligand distance r and treating all the N-donor atoms as pyridine-type donors for simplicity.[112–114] Racah parameters for the interelectronic repulsion were fixed at B = 850 cm^{-1} and C = 3100 cm^{-1}, hence ~20% lower than the free ion values.[116] The effective one-electron SO coupling constant was fixed at ζ_{3d} = 350 cm^{-1}, while the orbital reduction factor (k) was taken as isotropic and unitary.[114] Further details can be found in **Section 4.6.1**.

4.10.8 Ab-initio Calculations

All calculations have been done with the Orca 4.2 package.[141] To extract the local anisotropy of the i-th Fe center, the remaining iron(II) ions were replaced by diamagnetic zinc(II) ions. The ZFS D_i and E_i parameters were evaluated following the procedure developed in ref.[142] A state average CASSCF calculation was performed; dynamical correlation was taken into account with the domain-based local pair natural orbital 2nd-order N-electron valence state

perturbation theory (DLPNO-NEVPT2) method.[143] Finally, SO coupling was accounted for by quasi-degenerate perturbation theory with the spin-orbit mean-field (SOMF) Hamiltonian.[144] The complete active space (CAS) is composed of the five mainly-3d orbitals of the Fe centers and the six associated electrons, i.e. CAS(6,5). Averaging of the molecular orbitals was done over all five quintet and 45 triplet spin states generated by the CAS(6,5)SCF optimization. The SO coupling was considered between all M_S components of these spin states, the spin-free energy (diagonal elements of the SO matrix) being evaluated at the DLPNO-NEVPT2 level. In CASSCF, NEVPT2, and SO calculations, the relativistic Karlsruhe basis sets using a Douglas-Kroll-Hess (DKH) Hamiltonian were used (DKH-def2-TZVP for Fe atoms, DKH-def2-TZVP(-f) for bonding N, Br and Cl atoms and for first neighbor Zn atoms, and DKH-def2-SVP for H atoms).[145] The corresponding def2/JK auxiliary basis was used.[146] Preliminary calculations on various truncated complexes have shown little influence of the truncation on both electronic structure and magnetic properties of the Fe centers. We nevertheless considered the complete structure to avoid any bias.

The principal directions of $\bar{\bar{D}}_i$ and $\bar{\bar{g}}_i$ tensors do not in general coincide.[147] However, the $\bar{\bar{D}}_i$ tensors of three over four metal centers in both **1Cl** and **1Br** have their easy, intermediate, and hard principal axes at small angles from the corresponding principal directions of $\bar{\bar{g}}_i$, i.e. the easy direction of $\bar{\bar{D}}_i$ is close to the easy direction of $\bar{\bar{g}}_i$, etc. (Table 4.12). For Fe1 and Fe2, misalignments in **1Cl** (**1Br**) are in the range 0.58−7.29° (0.38−6.45°). For Fe4 the misalignment is larger, with angles ranging from 4.07 to 20.84° (3.79° to 11.43°). For Fe3, the hard directions of $\bar{\bar{D}}_i$ and $\bar{\bar{g}}_i$ are both approximately along the metal chain, but the two remaining principal axes are strongly misaligned, with offsets close to 45°. This behavior is probably related to the very small rhombic anisotropy of Fe3.

4.10.9 Spin Hamiltonian Calculations

The fitting of magnetic data utilized PHI v3.1.5 software.[117] Since PHI allows only one set of Euler angles to be defined for each spin center, the orientation of the $\bar{\bar{g}}_i$ tensor was assumed to coincide with that of the $\bar{\bar{D}}_i$ tensors for i = 1, 2, and 4, a reasonable approximation considering the data in Table 4.12. The $\bar{\bar{g}}_3$ tensor is severely misaligned with respect to $\bar{\bar{D}}_3$ in the *XY* plane. However, its easy and intermediate components are equal to within 0.025 and were averaged to give an axial $\bar{\bar{g}}_3$ tensor. When susceptibility and magnetization data were simultaneously fitted, the minimized quantity was the total residual *R* defined as:

$$R = \left[\sum_{p=1}^{n}\left(M_{\mathrm{exp},p} - M_{\mathrm{calc},p}\right)^2\right]\left[\sum_{p=1}^{m}\left(\chi_{\mathrm{exp},p} - \chi_{\mathrm{calc},p}\right)^2\right] \qquad (4.16)$$

where n and m are the number of magnetization (M) and susceptibility (χ) datapoints, respectively, while "exp" and "calc" represent experimental and calculated values, respectively. Refined parameters were isotropic coupling constants J_{ij} and TIP. The TIP correction was introduced to better reproduce high-temperature susceptibility data and compensate for possible systematic errors. For each model, the variable space was surveyed prior to the fit, in order to exclude the presence of additional minima in the R hypersurface. Models with anisotropic super-exchange interactions were also tested but did not improve the fit quality. Although magnetic measurements were performed on uncrushed polycrystalline samples restrained in the frozen mother liquor, the crystals were considered small enough to give rise to a powder average. Therefore, calculated susceptibility and magnetization data were integrated over 377 and 233 different directions, respectively, following the Zaremba-Conroy-Wolfsberg scheme as presented by Levitt (Field Powder 6 and 5 in PHI v3.1.5).[117,148] Local spin components were computed using in-house developed software based on ZHEEV routine for matrix diagonalization.[149]

Chapter 5

Fe^{II}/Fe^{III} Mixed-Valence EMACs: Effect of Stepwise Oxidation of $[Fe_4(tpda)_3Cl_2]$

5.1 Introduction

Systems where at least two atoms of the same metal are present in different oxidation states, are called MV compounds.[38] Although the term "valence" was progressively replaced by "oxidation state" many decades ago, the definition *mixed-valency* is still used by chemists nowadays.[150] The word "mixed" reflects a paramount characteristic of MV systems, namely the extent of electronic delocalization between ions in different oxidation states, which can significantly vary within this class of compounds.[151,152] However, this term is indiscriminately used also for MV systems where the valence electrons are trapped on their original M centers, and where no delocalization occurs. Not by chance, more than one century ago, one of the first concepts associated to MV molecules was "oscillating valency".[153]

MV compounds constitute a very large family of systems, which were firstly classified by Robin and Day, two important pioneers in this field, in 1968.[154] The chemical and physical properties of MV systems were deeply investigated in the last 50 years.[38,150–152,154–156] Robin and Day ranked these systems into three main categories, depending on the degree of electron delocalization.[154] Let us consider a complex with two M ions in different oxidation states. When the crystallographic sites occupied by the metals are very different from each other, the valence electrons are localized onto the respective center and the compounds belong to the *Robin-Day Class I* category. On the other hand, when the two sites are crystallographically indistinguishable, the valence electrons are completely delocalized over the metals, which thus assume non-integer oxidation states (when one, or an odd number of electrons are delocalized between the ions). These are *Robin-Day Class III* MV compounds. Between these two cases,

lie various intermediate situations, where the two crystallographic centers are neither coincident nor very different. Here, electron hopping somewhat occurs, to give *Robin-Day Class II* systems, which were theoretically studied in detail by Allen and Hush, two other important pioneers of the field.[151,152] To get more into details, sometimes MV compounds are placed in Class II category when their ground states are localized onto the vibrational time scale, while Class III systems are delocalized on the same timescale.[150]

Electron delocalization is directly related to the electronic mechanism of double-exchange (see **Section 2.2.2**), which can be triggered on in Class II and III compounds, and which favors a parallel alignment of the interacting spins. The higher is the double-exchange coupling between these spins, the more they are propense to interact ferromagnetically.[39,157–159] In this sense, double-exchange may be competitive with Heisenberg interactions of antiferromagnetic nature and may even itself rule the magnetic behavior.

The presence of electron delocalization in MV compounds was firstly inferred from their usually deep-intense colors, compared to the paler and milder colors of many homovalent transition metal complexes. In fact, there are many examples of MV systems whose electronic spectrum turns out to be a superposition of the fully reduced and fully oxidized form, but where at least a new band arises.[150–152,160–162] These intense absorption bands are usually in the visible region, and they are called *intervalence charge-transfer* (IVCT) bands. They are responsible of the unusual and intense colors frequently assumed by MV compounds and have triggered a considerable interest for MV systems in the past. The IVCT bands arise from a phonon coupled, inner- or outer-sphere M to M electronic transition.[151,152] Robin-Day Class II systems are the ones which exhibit the most evident IVCT band, usually characterized by energies ranging from 14000 to 27000 cm^{-1} (714−370 nm).[154] For example, $[KFe^{II}Fe^{III}(CN)_6]$ (Prussian blue), which is probably the first ever synthesized MV compound (by Woodward in 1724),[163] possesses a deep blue color, although Fe^{2+} and Fe^{3+} complexes are usually light orange, light green, or even colorless. In fact, the IVCT transition around 14100 cm^{-1} in the electronic spectrum of $[KFe^{II}Fe^{III}(CN)_6]$ features a molar absorptivity (ε) of ~10^4, although Fe^{2+} and Fe^{3+} ions alone undergo only weak spin-forbidden transitions in this energy range.[162] Therefore, a most appealing feature of MV compounds is that their physical properties are not simply the sum of those of the constituting M ions. This opens a multitude of new pathways for tuning the physical properties of molecules by chemical design.

Probably, Fe-containing MV systems constitute the largest sub-group of this family of compounds. This is due to the fact that their physical properties can be more easily investigated in detail compared to other transition-metal complexes, thanks to ^{57}Fe Mössbauer

spectroscopy.[108,164] In fact, this technique is able to distinguish between Fe ions in different oxidation states, chemical environment, spin state, and so on. Therefore, Mössbauer spectroscopy also provides a measurement of the degree of electron delocalization in a MV compound, which is essential for a proper classification using Robin-Day scheme. In addition, Fe^{2+}–Fe^{3+} MV systems can be interesting as SMMs. There is a number of $Fe^{II}Fe^{III}$ MV dimers in which double-exchange interactions stabilize an S = 9/2 ground state as a result of ferromagnetic coupling.[40,159,165–168] When double-exchange is very strong, it is able to ferromagnetically align two M centers very far away from each other. For example, the MV diiminobenzoquinone-bridged $Fe^{II}Fe^{III}$ complex $[(Me_3TPya)_2Fe_2(A)](BAr^F_4)_3$ (**13**) the Fe···Fe distance is > 8 Å and exchange interactions between the M centers are much stronger than in the fully reduced analogue (TPya = tris((6-methyl-2-pyridyl)methyl)amine, H_2A = 2,5-di(2,6-dimethylanilino)-3,6-dibromo-1,4-benzoquinone, BAr^F_4 = tetrakis[3,5-bis(trifluoromethyl)phenyl]borate).[40]

In order to attempt strengthening the ferromagnetic interactions found in complex $[Fe_4(tpda)_3Cl_2]$ (**1Cl**), the one-electron oxidation of **1Cl** was carried out with $FcPF_6$ (Fc = ferrocene). The reaction, however, afforded crystals of $[Fe^{II}_2Fe^{III}(tpda)_3]PF_6$ (**3**), a MV species with one metal center less than expected. In **3** partial electron delocalization between the Fe centers was observed at room temperature. Complex **3** shows predominant ferromagnetic interactions and easy-axis anisotropy. In addition, it exhibits weak SMM behavior and magnetic hysteresis, SRM being observable even without application of a static magnetic field. The doubly-oxidized MV species $[Fe^{II}Fe^{III}_2(tpda)_3Cl]PF_6$ (**3a**) was isolated as a byproduct of the preparation of **3**. This further oxidation causes, however, the complete loss of SMM behavior.

5.2 Synthesis and Solution Studies

$[Fe_3(tpda)_3]PF_6$ (**3**) was synthesized from the direct chemical oxidation of **1Cl** with $FcPF_6$ (0.95 eq) in CH_2Cl_2. Complex **1Cl** was preferred over **1Br** since the idealized one-electron oxidized species $[Fe_4(tpda)_3Cl_2]PF_6$ turned out to be more stable towards disproportionation compared to $[Fe_4(tpda)_3Br_2]PF_6$ (see **Section 4.4**). The reaction was carried out in glovebox, in order to avoid unwanted overoxidation processes. Surprisingly, compound **3** is air-stable in the solid state, whereas its CH_2Cl_2 solutions react quickly with dioxygen and water. Cuboidal

crystals of the product (yield = 36−54%) were obtained by liquid diffusion of hexanes into a concentrated CH_2Cl_2 solution of **3**. In addition to the dominant one, two more crystalline phases (hexagonal rods and needles) were found in erratic amounts (~0−10% in total) in different synthetic batches. When necessary, these impurities were removed by flotation in CCl_4, exploiting differences in density (see Table 5.2 in **Section 5.3**). X-ray data collection (100(2) K) showed that hexagonal rod-like crystals are the two-electron oxidized complex $[Fe_3(tpda)_3Cl]PF_6$ (**3a**). The needle-like crystals were obtained in minor quantity, and they showed the same unit cell parameters as the hexagonal rods. Notwithstanding the strictly anaerobic and anhydrous conditions, X-ray analysis demonstrated that some additional adventitious oxidation processes occur. In order to minimize them, the stoichiometry of the reaction was tuned using a small defect (~5%) of $FcPF_6$.

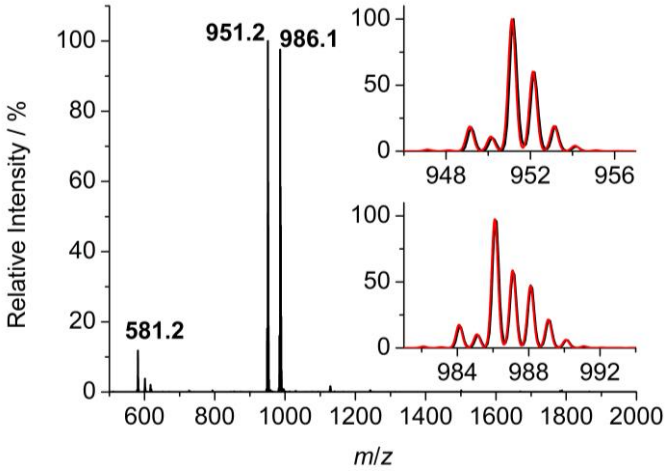

Figure 5.1. ESI-MS spectrum of **3** (direct infusion, CH_2Cl_2, positive ion mode). The inset shows the experimental (black line) and simulated (red line) isotopic patterns of the peaks at *m*/*z* = 951.2 ($[Fe^{II}_2Fe^{III}(tpda)_3]^+$) and 986.1 ($[Fe^{II}Fe^{III}_2(tpda)_3Cl]^+$).

The ESI-MS spectrum of a solution prepared by dissolving crystals of **3** in CH_2Cl_2 (Fig. 5.1) presents two well resolved signals, with *m*/*z* = 951.2 (100%) and 986.1 (98%), and a much weaker one with *m*/*z* = 581.2 (12%). Their isotopic patterns are consistent with the ionic species $[Fe^{II}_2Fe^{III}(tpda)_3]^+$, $[Fe^{II}Fe^{III}_2(tpda)_3Cl]^+$ (Fig. 5.1, inset) and $[Fe^{II}(H_2tpda)(Htpda)]^+$, respectively. $[Fe^{II}_2Fe^{III}(tpda)_3]^+$ ion was not systematically found in the spectrum of **3**, and when present it was replaced over time by $[Fe^{II}Fe^{III}_2(tpda)_3Cl]^+$. Instead, the ESI-MS spectrum of a CH_2Cl_2 solution prepared from carefully separated crystals of **3a** exhibits only one signal (*m*/*z* = 986.1), corresponding to $[Fe^{II}Fe^{III}_2(tpda)_3Cl]^+$ ion. The spectra of both **3** and **3a** exhibit the molecular ion peak ($[M]^+$) minus one PF_6^- anion, in accordance with the monocharged cationic nature of the two complexes. Significantly, both **3** and **3a** are triiron species according to SC-XRD analysis, even if they were prepared from tetrairon(II) complex **1Cl**. This agrees

with the ESI-MS measurements on **1Cl** and **1Br** where $[M]^+$ was never detected, but only $[M]^+$ minus a FeX moiety (X = Cl or Br, respectively). Thus, when **1Cl** is subject to oxidizing conditions, such as direct chemical oxidation, ESI-MS ionization, or the chemical manipulations required by mass spectrometry, a structural rearrangement probably occurs, which leads to the expulsion of a $FeCl_2$ or FeCl moiety, as applicable. This confirms the exceedingly elusive behavior of this family of polyiron string-like complexes. X-ray structural data and MALDI-TOF-MS measurements suggest the presence of 9.2 and 11.5 mol% of chlorinated species in **3**, respectively (see below). However, the molar percentage of $[Fe^{II}Fe^{III}_2(tpda)_3Cl]^+$ is much higher in the ESI-MS data (49.5 mol%). Here, the ionization solvent, (CH_2Cl_2) may be responsible of an oxidative addition of Cl^- ions to $[M-PF_6]^+$. In fact, $CHCl_3$ and CCl_4 are known to be able to promote chloride-attachment ions in negative ion ESI-MS.[84,85] Thus, the MV $[Fe^{II}_2Fe^{III}(tpda)_3]^+$ ion undergoes additional oxidation processes during its ESI-MS analysis, probably due to small air admissions and/or ionization conditions.

MALDI-TOF/TOF-MS (MALDI-TOF-MS for simplicity) spectrum of **3** in solid anthracene (Fig. 5.2) is consistent with the ESI-MS results. It exhibits one intense peak with *m*/*z* = 951.9 ($[Fe_3(tpda)_3+H]^+$, 100) and a much weaker one with *m*/*z* = 986.9 ($[Fe_3(tpda)_3Cl+H]^+$, 13). Here, the intensity ratio between the two signals (100:13) more closely mirrors the structural disorder found in $[Fe_3(tpda)_3Cl_{0.094}](PF_6)_{0.953}$ (**3**), compared to the ESI-MS spectrum (100:98). Thus, for the detection of this elusive compound, MALDI-TOF-MS spectrometry seems to be a more suitable analytic technique than ESI-MS, due to different ionization conditions and/or better protection from the air (sample embedded in a solid matrix instead of dissolved in an organic solvent).

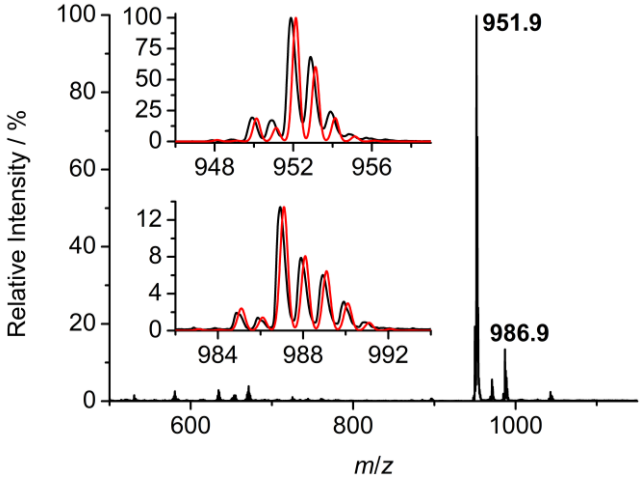

Figure 5.2. MALDI-TOF-MS spectrum of **3** in solid anthracene (positive ion mode). The inset shows the experimental (black line) and simulated (red line) isotopic patterns of the peaks at *m*/*z* = 951.9 ($[Fe^{II}_2Fe^{III}(tpda)_3+H]^+$) and 986.9 ($[Fe^{II}Fe^{III}_2(tpda)_3Cl+H]^+$).

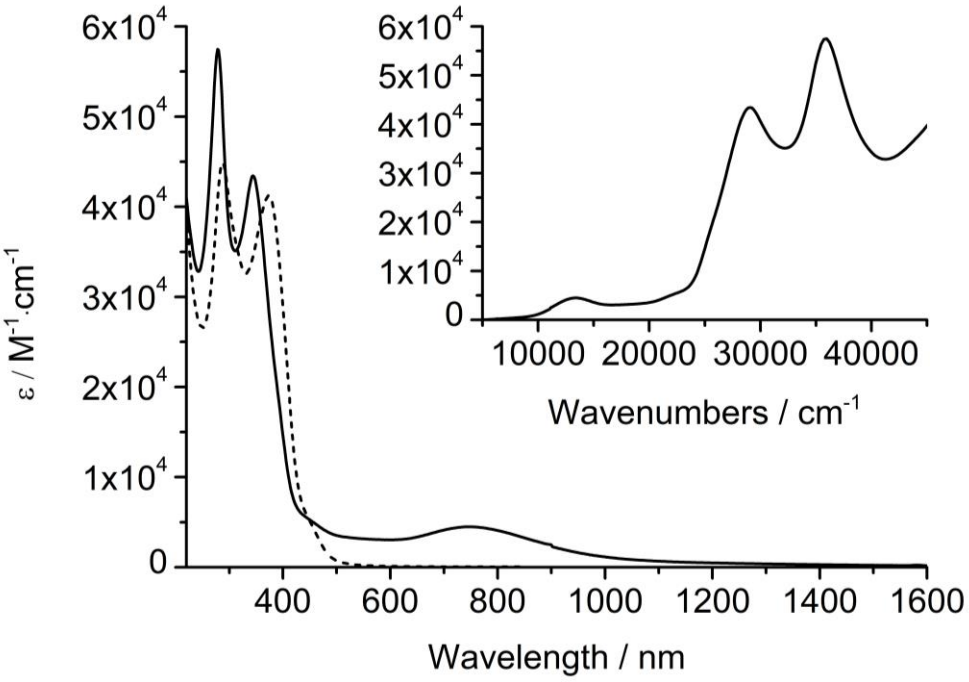

Figure 5.3. UV-Vis-NIR spectrum of a CH_2Cl_2 solution of **3** (solid line) and of **1Cl** (dashed line). The inset shows the spectrum of **3** reported in wavenumbers. All the spectra were recorded up to 2000 nm, but only the characteristic portion of them is reported.

Crystals of **3** dissolved in CH_2Cl_2 afford a dark emerald green solution, whose electronic spectrum is presented in Fig. 5.3. The intense and characteristic color of this solution is an important hint of a potential electronic delocalization in **3**, since many $Fe^{II}Fe^{III}$ MV compounds of Class II and III are described as green or dark green. Below 500 nm, the UV-Vis-NIR spectrum of **3** resembles that of the completely reduced species, **1Cl** (which is also shown in Fig. 5.3). In fact, it features two strong $\pi \rightarrow \pi^*$ transitions at 278 and 344 nm, along with a weak shoulder at 453 nm. However, unlike complexes **1Br** and **1Cl** (see **Section 4.2**), the absorption spectrum of **3** contains a new broad band at λ_{max} = 744 nm (13441 cm^{-1}). This band is attributable to an IVCT transition, which is responsible of the dark emerald green color of a CH_2Cl_2 solution of **3**. The energy of this IVCT band is found consistent with those of many $Fe^{II}Fe^{III}$ MV compounds of Robin-Day Class II, with reported IVCT bands ranging from ~680−780 nm.[159,167,169–171] In addition, a similar band can be found in Robin-Day Class III systems also, as in the completely delocalized MV species $[A_2Fe_2(\mu\text{-}OH)_3](ClO_4)_2 \cdot 2MeOH \cdot 2H_2O$, which exhibits a IVCT transition at λ_{max} = 758 nm (B = *N*,*N*',*N*''-trimethyl-l,4,7-triazacyclononane).[165,172] A Gaussian fit to the IVCT band of **3** yields a FWHM of 4266 cm^{-1}. Typically, the Hush equation[152,155] (Eq. 5.1) is employed to obtain the expected width for the IVCT band (FWHM'):

$$\mathrm{FWHM}' = \sqrt{2310 \cdot \nu_{\max}} \qquad (5.1)$$

where ν_{max} is the energy of the maximum of the IVCT band. Particularly narrow bands indicate a Robin-Day Class III compound. For a Robin-Day Class II system, the observed FWHM is expected to be greater than or equal to FWHM'. For complex **3**, FWHM' = 5572 cm^{-1}. While the narrow IVCT band suggests that **3** may belong to Robin-Day type III, it should be noted that the Hush equation was derived from measurements on bimetallic compounds that contain an inversion center, which is not the case for **3**, meaning that the Hush analysis should not be taken at face value. In fact, limitations to the use of the Hush equation for classifying compounds into Robin-Day classes are well documented in the literature; notably, contradictions in classification often originate from different spectroscopic timescales.[173] Therefore, UV-Vis-NIR data for **3** at room temperature support Robin-Day Class II or III behavior, and confirm that **3** is a MV complex in solution. More detailed considerations on the Robin-Day classification of **3** are found in **Section 5.5,** where variable temperature Mössbauer measurements support a Robin-Day Class II behavior for **3**, excluding full electron delocalization among the Fe ions.

5.3 X-ray Structure of $[Fe_3(tpda)_3]PF_6$ (3)

The molecular structure of $[Fe_3(tpda)_3]PF_6$ (**3**) determined at 115 K (dataset: *130818NA_11_work3.hkl*) is shown in Fig. 5.4. Compound **3** crystallizes in centric space group $R\bar{3}$ and the asymmetric unit contains a third of a complex molecule, which develops around a threefold axis. The crystal structure is composed by an alternation of $[Fe_3(tpda)_3]$ molecules and PF_6^- anions along the *c* axis, all of them lying on a 3-fold axis, with no lattice solvent. The PF_6^- ions are found on $\bar{3}$ sites. Tri-iron complex in **3** is constituted by a linear chain of three iron ions, wrapped together by three molecules of $tpda^{2-}$ (relevant bond distances and angles are listed in Table 5.1, while crystal data are in Table 5.2). Metal ions are not symmetrically arranged along the chain, which conveys to the molecule C_3 rather than D_3 symmetry in the solid state.

According to BVS calculations (Table 5.3), the tri-iron chain comprises a solitary Fe^{3+} ion (Fe1) and a pair of Fe^{2+} ions (Fe1···Fe2 = 3.5912 Å, Fe2···Fe3 = 2.7324 Å). These oxidation states for the Fe ions, along with the occurrence of three completely deprotonated H_2tpda proligands and one PF_6^- anion per molecule, are consistent with electroneutrality principle. This

valence-localized description at 115 K is supported by Mössbauer spectra at 10 and 77 K (Figure 5.6, **Section 5.5**) and proves that oxidation is metal-centered rather than ligand-centered.

The $Fe^{2+}\cdots Fe^{2+}$ distance is significantly shorter than in the reduced complexes **1Br** and **1Cl** (from 2.941 to 2.991 Å). It is also slightly shorter than in Cotton's triiron(II) complex **6** (2.782(1)−2.783(1) Å).[80] On the contrary, the Fe···Fe distance in **3** turned out to be longer than in the recently reported trinuclear iron(II) complex, **7**, which exhibits M−M bonds.[93] The $Fe^{2+}\cdots Fe^{3+}$ distance in **3** is significantly longer than those found in many examples of $Fe^{II}Fe^{III}$ MV dinuclear complexes, where it ranges from 2.509 to 3.155 Å.[159,165–172,174] Although a number of examples of dinuclear Fe-based MV compounds are reported, to the best of our knowledge a MV triiron chain is not a common system. For example, in 1999 Glaser *et al.* reported the linear thiophenolate-bridged complex $[CFe^{III}Fe^{II}Fe^{III}C](BPh_4)_2$ (**14**), where C^{3-} = 1,4,7-tris(4-*tert*-butyl-2-mercaptobenzyl)-1,4,7-triazacyclononane.[175] Complex **14** features a Fe^{2+}−Fe^{3+} distance of 2.99(3) Å, and the extra-electron is found fully delocalized over all three Fe centers, to give a Robin-Day Class III compound.

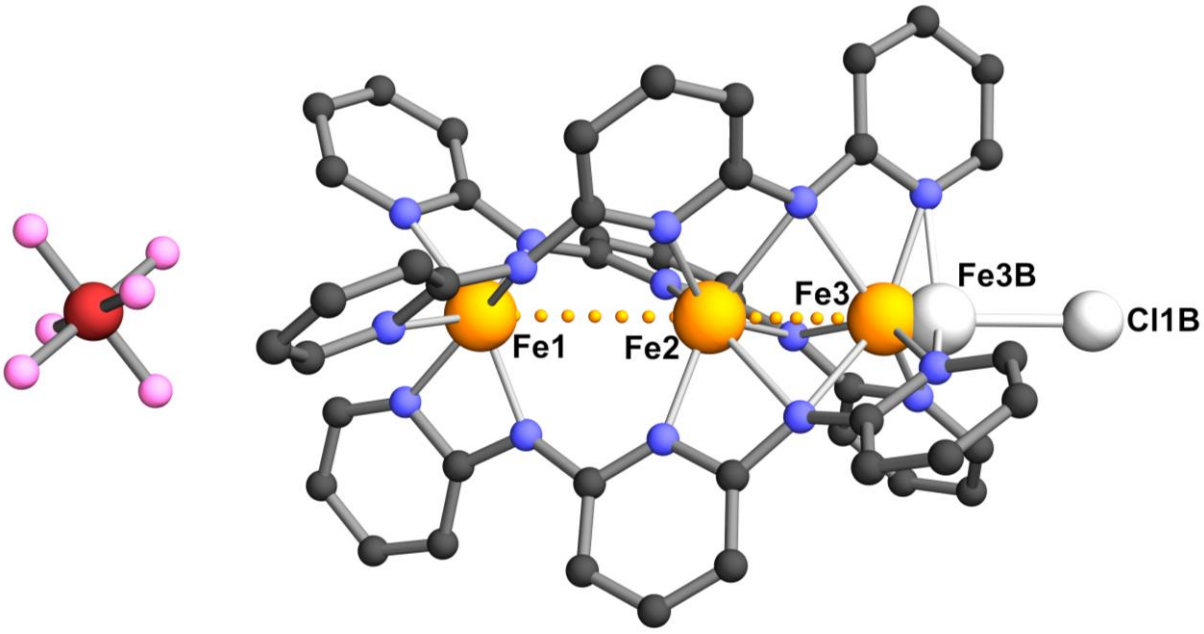

Figure 5.4. Molecular structure of **3** (left-handed enantiomer), viewed approximately normal to the 3-fold axis (ball-and-stick model). Only one of the two PF_6^- anions is shown for simplicity. Color code: orange, Fe; red, P; pink, F; blue, N; dark gray, C. The disordered minor component, $[Fe_3(tpda)_3Cl](PF_6)_{0.5}$ (9.2%), is represented in light grey. H atoms are omitted for clarity. The dotted lines connecting the Fe ions do not correspond to chemical bonds, but provide a better representation only.

Table 5.1. Selected Interatomic Distances (Å) for **3**.

	130818NA_11_work3	*truef_a*
Fe(1)−Fe(2)	3.5912(11)	3.5964(19)
Fe(2)−Fe(3)	2.7324(17)	2.714(3)
Fe(2)−Fe(3B)	3.599(18)	3.70(2)
Fe(1)−N(1)	2.170(2)	2.166(4)
Fe(1)−N(2)	2.035(2)	2.030(4)
Fe(2)−N(3)	2.084(3)	2.078(4)
Fe(2)−N(4)	2.374(3)	2.363(4)
Fe(3)−N(4)	2.346(3)	2.334(4)
Fe(3)−N(5)	2.103(3)	2.099(4)
Fe(3B)−N(5)	2.006(3)	2.011(6)
Fe(3B)−Cl(1)	2.39(3)	2.34(4)

Table 5.3. Bond-Valence Sum calculations on **3**, dataset: *130818NA_11_work3.hkl* (*truef_a.hkl*).[a]

Atom	Fe^{2+}	$Fe3^{+}$
Fe(1)	2.417 (2.447)	2.843 (2.878)
Fe(2)	1.820 (1.858)	2.141 (2.185)
Fe(3)	1.803 (1.836)	2.120 (2.159)

[a]Bond-valence parameters (Fe^{2+}–N^{-3} (1.76; 0.37), Fe^{3+}–N^{-3} (1.82; 0.37), Fe^{2+}–Cl^{-1} (2.06; 0.37), Fe^{3+}–Cl^{-1} (2.09; 0.37), for R_0 and B respectively) were taken from file bvparm2016.cif available at https://www.iucr.org/resources/data/datasets/bond-valence-parameters.

Table 5.2. Crystal data and refinement parameters for **3** and **3a**.

Compound	**3**	**3**	**3a**
Dataset (*.hkl*)	*130818NA_11_work3*	*truef_a*	cu_b46bruker1_0m_a
Empirical formula	$C_{45}H_{33}Cl_{0.09}F_{5.72}Fe_3N_{15}P_{0.95}$	$C_{45}H_{33}Cl_{0.1}F_{5.71}Fe_3N_{15}P_{0.95}$	$C_{45}H_{33}ClF_6Fe_3N_{15}P$
Molecular formula	$[Fe_3(tpda)_3Cl_{0.094}](PF_6)_{0.953}$	$[Fe_3(tpda)_3Cl_{0.097}](PF_6)_{0.952}$	$[Fe_3(tpda)_3Cl]PF_6$
Formula weight (g/mol)	1092.90	1092.80	1131.83
T (K)	115(2)	100(2)	100(2)
Radiation	Mo-Kα (λ = 0.71073 Å)	Cu-Kα (λ = 1.54178 Å)	Cu-Kα (λ = 1.54178 Å)
Crystal system	trigonal	trigonal	trigonal
Space group	$R\bar{3}$	$R\bar{3}$	$P3c1$
a (Å)	14.5340(4)	14.4979(5)	13.8961(5)
b (Å)	14.5340(4)	14.4979(5)	13.8961(5)
c (Å)	36.0874(11)	36.0575(14)	28.4118(12)
α (deg)	90	90	90
β (deg)	90	90	90
γ (deg)	120	120	120
V (Å^3)	6601.7(4)	6563.5(5)	4751.3(4)
Z	6	6	4
ρ_{calcd} (g cm^{-3})	1.649	1.659	1.582
$2\theta_{min}/2\theta_{max}$ (deg)	6.55/55.99	7.354/130.926	6.222/131.84
Reflections collected/independent	22479/3541	13033/2468	19846/5295
R_{int}	0.0401	0.0394	0.0825
No. of parameters/restraints	231/19	231/19	458/106
$R1/wR2$ (all data)	0.0701/0.1401	0.0723/0.1411	0.0996/0.2030
$R1/wR2$ ($I \geq 2\sigma(I)$)	0.0528/0.1308	0.0667/0.1378	0.0705/0.1826
GOF	1.079	1.190	1.033
Largest diff. peak/hole (e Å^{-3})	2.39/−0.85	0.91/−0.52	0.75/−0.51

Unlike its precursor **1Cl**, **3** contains no axial capping ligands. Thus, each external Fe ion (Fe1 and Fe3) is located quite far from the plane defined by the outer N_{py} atoms (metal···plane: Fe1, 1.273 Å; Fe3, 1.996 Å) and Fe3 is significantly more "internal" than Fe1. All metal ions are hexacoordinated by three amide (N_{am}) and three N_{py} atoms. Fe1 possesses a distorted octahedral geometry, while the coordination environment of Fe2 and Fe3 is even more distorted. Fe1 forms short contacts with its N_{am} donors (2.035 Å) and slightly longer bonds with the N_{py} ones (2.170 Å). On the contrary, for Fe2 and Fe3 the Fe−N_{py} distances are much more elongated (2.346−2.374 Å), while the Fe-N_{am} ones are only slightly longer (2.084−2.103 Å) than Fe1−N_{am}. The average Fe−N distance is 5.6% shorter for Fe1 than for Fe2 and Fe3 (2.1025 vs. 2.2268 Å), consistent with a valence-localized description. Interestingly, in complex **13** the average Fe−N bond distance undergoes an almost identical decrease (5.2%) upon one-electron chemical oxidation.[40] These considerations about Fe−N distances are only rough evaluations, but they endorse the results given by BVS calculations. The average twisting of the ligands (average angle between the mean planes defined by two neighboring pyridine rings = 36.8°) is less pronounced than in its reduced analogues **1Br** and **1Cl** (45.2°), and in **3a** (44.9°, see below).

Disorder effects in the structure of **3** suggest the occurrence of 9.2 mol% of $[Fe_3(tpda)_3Cl](PF_6)_{0.5}$, i.e. a species with one axial chlorido ligand (Cl1b) and a significant displacement of Fe3 (Fe3B), as shown in Fig. 5.4. Fe3B now lies only 0.203 Å from the plane defined by N_{py} atoms, towards Cl1b. Fe3B possesses a trigonal-pyramidal coordination geometry (Fe3B−N_{py} = 2.006 Å, Fe3B−Cl1 = 2.39 Å, Cl1−Fe3B−N_{py} = 95.8°), which is almost identical to that found in **1Cl** (Fe−N_{py} = 2.07−2.09 Å, Fe−Cl = 2.36−2.39 Å, N_{py}−Fe−N_{py} = 111.9−125.4°, Cl−Fe−N_{py} = 95.2−98.3°).

Due to the presence of chlorido ligands, one PF_6^- is found every other molecule of $[Fe_3(tpda)_3Cl](PF_6)_{0.5}$, onto the 3-fold axis. Thus, $[Fe_3(tpda)_3Cl](PF_6)_{0.5}$ is a MV species formulated as $[Fe_2^{II}Fe^{III}(tpda)_3Cl][Fe^{II}Fe_2^{III}(tpda)_3Cl]PF_6$. Accordingly, compound **3** is composed by mono- and di-oxidized species, at 95.3% and 4.7% respectively. The di-oxidized contribution in **3** was found to be almost identical (4.85%) in another crystal from a different synthetic batch (dataset: *truef_a.hkl*).

5.4 X-ray Structure of $[Fe_3(tpda)_3Cl]PF_6$ (3a)

Compound **3a**, $[Fe_3(tpda)_3Cl]PF_6$, crystallizes in the form of air-stable hexagonal rods (acentric space group *P*3*c*1). Relevant bond distances and angles are listed in Table 5.4, while crystal data are in Table 5.2. Two crystallographically different molecules of **3a** (MOL1 and MOL2) occur in the lattice and develop around 3-fold axes. Two crystallographically independent PF_6^- ions also lie on a separate 3-fold axis. The asymmetric unit thus contains one third of each triiron molecule and of each PF_6^- anion. At variance with **3**, separate chains of triiron EMACs and PF_6^- anions run along the *c* axis. The molecular chain is disordered over two position in both MOL1 (81:19) and MOL2 (58:42), but disorder can only be resolved at the metal sites and axial ligands. Only the X-Ray structure of MOL1 is shown in Fig. 5.5, since it is very similar to that of MOL2. Complex **3a** closely resembles the minor component of **3**. In fact, $[Fe_3(tpda)_3Cl]PF_6$ is constituted by a chain of three Fe ions, wrapped by three $tpda^{2-}$ molecules and capped at one end by a chlorido ligand.

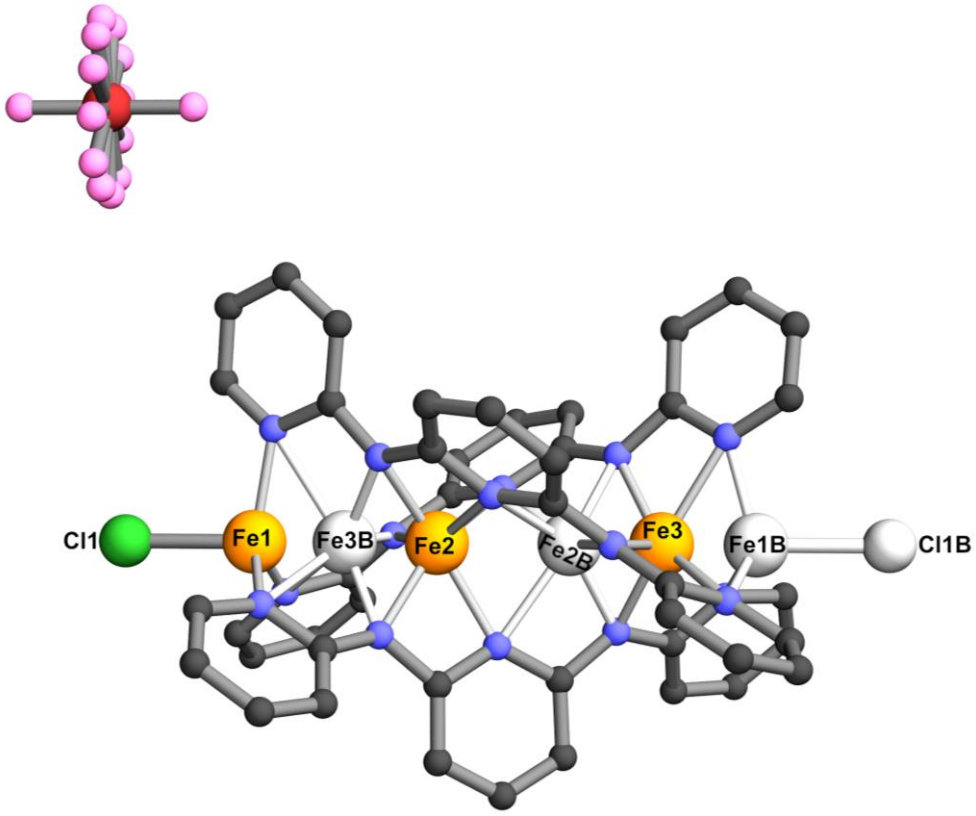

Figure 5.5. Molecular structure of **3a** (MOL1, right-handed enantiomer), viewed approximately normal to the 3-fold axis of the molecule (ball-and-stick model). Only one of the two PF_6^- anions is shown for simplicity, and it is disordered on a 3-fold axis. Color code: orange, Fe; green, Cl; red, P; pink, F; blue, N; dark gray, C. The disordered minor component of MOL1 (19%), is represented in light grey. H atoms are omitted for clarity.

Table 5.4. Selected Interatomic Distances (Å) for **3a**.

MOL1 (81:19)		MOL2 (58:42)	
Cl(1)−Fe(1)	2.343(7)	Cl(2)−Fe(4)	2.349(12)
Fe(1)−Fe(2)	3.292 (5)	Fe(4)−Fe(5)	3.329(7)
Fe(2)−Fe(3)	4.020(4)	Fe(5)−Fe(6)	4.046(6)
Fe(1)−N(1)	2.060(12)	Fe(4)−N(6)	2.018(14)
Fe(2)−N(2)	2.053(11)	Fe(5)−N(7)	1.966(12)
Fe(2)−N(3)	2.142(11)	Fe(5)−N(8)	2.177(12)
Fe(3)−N(4)	2.020(11)	Fe(6)−N(9)	1.968(13)
Fe(3)−N(5)	2.236(13)	Fe(6)−N(10)	2.319(14)
Cl(1B)−Fe(1B)	2.35(2)	Cl(2B)−Fe(4B)	2.404(16)
Fe(1B)−Fe(2B)	3.31(2)	Fe(4B)−Fe(5B)	3.31(1)
Fe(2B)−Fe(3B)	4.04(2)	Fe(5B)−Fe(6B)	4.03(1)
Fe(1B)−N(5)	1.988(13)	Fe(4B)−N(10)	2.008(13)
Fe(2B)−N(4)	2.014(14)	Fe(5B)−N(9)	1.982(13)
Fe(2B)−N(3)	2.254(15)	Fe(5B)−N(8)	2.222(13)
Fe(3B)−N(2)	1.954(14)	Fe(6B)−N(7)	1.916(13)
Fe(3B)−N(1)	2.411(17)	Fe(6B)−N(6)	2.378(17)

In order ensure electroneutrality, compound **3a** should be a MV species formulated as $Fe^{II}Fe_2^{III}$. BVS calculations on **3a** support this hypothesis. Moreover, BVS demonstrates that in both MOL1 and MOL2 the Fe^{2+} ion is always the one bounded to the chlorido ligand (Table 5.5). The $Fe^{3+}\cdots Fe^{3+}$ distance (4.020−4.046) is much longer than the $Fe^{3+}\cdots Fe^{2+}$ separation (3.292−3.329). The Fe^{2+} ions (Fe1, Fe1B, Fe4, Fe4B) adopt the same coordination geometry as Fe3B in compound **3** (see above). They lie in a trigonal-pyramidal environment, afforded by three short contacts with N_{py} atoms and by the axial coordination of the chloride ion (Fe^{2+}–N_{py} = 1.988−2.060 Å, Fe^{2+}–Cl = 2.343−2.404 Å, Cl–Fe^{2+}–N_{py} = 99.4−105.3°). The

central (Fe2, Fe2B, Fe5, Fe5B) and the external (Fe3, Fe3B, Fe6, Fe6B) Fe^{3+} ions possess a distorted octahedral coordination geometry. Each central Fe^{3+} ion forms three short contacts with its N_{am} donors (Fe−N_{am} = 1.966−2.053 Å) and three slightly longer ones with as many N_{py} atoms (N3,N8: Fe−N_{py} = 2.142−2.254 Å). The terminal Fe^{3+} ions follow the same coordination pattern, with longer Fe−N_{py} bonds (Fe−N_{am} = 1.916−2.020 Å, Fe−N_{py} = 2.236−2.411 Å). The average angle between the mean planes defined by two neighboring pyridine rings (44.9°) is similar with the one of **1Br** and **1Cl** (45.2°), but larger than in **3** (36.8°).

Table 5.5. Bond-Valence Sum calculations on **3a**.[a]

Atom	Fe^{2+}	$Fe3^{+}$
Fe(1)	1.799	2.073
Fe(2)	2.427	2.855
Fe(3)	2.314	2.722
Fe(4)	1.952	2.253
Fe(5)	2.691	3.165
Fe(6)	2.372	2.790
Fe(4B)	1.929	2.233
Fe(5B)	2.507	2.948
Fe(6B)	2.533	2.978

[a]Bond-valence parameters (Fe^{2+}–N^{-3} (1.76; 0.37), Fe^{3+}–N^{-3} (1.82; 0.37), Fe^{2+}–Cl^{-1} (2.06; 0.37), Fe^{3+}–Cl^{-1} (2.09; 0.37), for R_0 and B respectively) were taken from file bvparm2016.cif available at https://www.iucr.org/resources/data/datasets/bond-valence-parameters. BVS calculations on Fe ions of the minority components (Fe4B, Fe5B and Fe6B) are here reported only for MOL2, whose contribution to the structure is 42%, compared to 19% for MOL1.

5.5 Mössbauer Studies

The Mössbauer data collected on **3** suggest marked differences in the electronic structure compared to compounds **1Br** and **1Cl**. Data collected at temperatures of 10 K, 77 K, and 294 K are displayed in Fig. 5.6. At all three temperatures, the profiles suggest three distinct chemical environments for the Fe ions in the complex, in agreement with X-ray crystallography. The data at each temperature were fitted with three quadrupole doublets, whose best-fit parameters are listed in Table 5.6. The relative areas for the three signals were fixed at 0.333, assuming the same recoil-free fraction for each Fe center. It should be noted that the linewidth for the first quadrupole doublet, $FWHM_1$, was fixed at 0.650 mm/s to obtain a reasonable fit to the data. The broadening of two of the quadrupole doublets is less likely due to symmetry lowering than in the cases of **1Br** and **1Cl**, but could be due to slow magnetic relaxation, a phenomenon well observable on the Mössbauer timescale.[80] This magnetic relaxation is evident from the AC susceptibility measurements on the compound, which shows zero-field SMM behavior, with an anisotropy barrier of U_{eff}/k_B = 8.4(6) K (see **Section 5.7**).

^{57}Fe Mössbauer spectroscopy is a well-founded technique for Robin-Day classifications.[154,176,177] The best-fit parameters for the quadrupole doublets of the 10 K and 77 K datasets are consistent with two of the Fe centers being HS Fe^{2+} and the third being HS Fe^{3+}, thereby suggesting valence localization on Mössbauer timescale, or classification in Robin Day Class I (Table 5.6). For the 294 K dataset, the best-fit parameters suggest a different description. At 77 K, the difference between δ_2 and δ_1 is 0.355 mm/s, while the difference between the quadrupole splittings, ΔE_{Q2} and ΔE_{Q1}, is 1.555 mm/s. At 294 K, the difference between δ_2 and δ_1 is 0.393 mm/s, while the difference between ΔE_{Q2} and ΔE_{Q1} dramatically decreases to 0.139 mm/s. This suggests charge transfer between one Fe^{2+} and the terminal Fe^{3+} center, because the normal temperature dependence for the quadrupole splittings would not cause such a small difference between ΔE_{Q2} and ΔE_{Q1} values at room temperature, with only a modest increase in the difference between the isomer shifts.[108] Most likely, the charge transfer involves the proximal central Fe^{2+} rather than the terminal Fe^{2+}. Therefore, the yellow and blue sub-spectra in Fig. 5.6 can be tentatively assigned to the terminal and the central Fe^{2+} center, respectively. At room temperature, then, one of the Fe^{2+} centers remains as HS Fe^{2+}; the other two observed signals suggest oxidation states in between +2 and +3. This observation shows that at room temperature the compound should be classified as a Robin-Day Class II or Class III complex. Since the Mössbauer parameters of two HS $Fe^{2.5+}$ centers should be closer than observed, a classification in Robin-Day Class II is proposed.[154] The presence of an IVCT band

in the UV-Vis-NIR spectrum of **3** (see **Section 5.2**) further argues against classification as a Robin-Day Class I compound at room temperature, as IVCT bands are only exhibited by Class II and III complexes.[154]

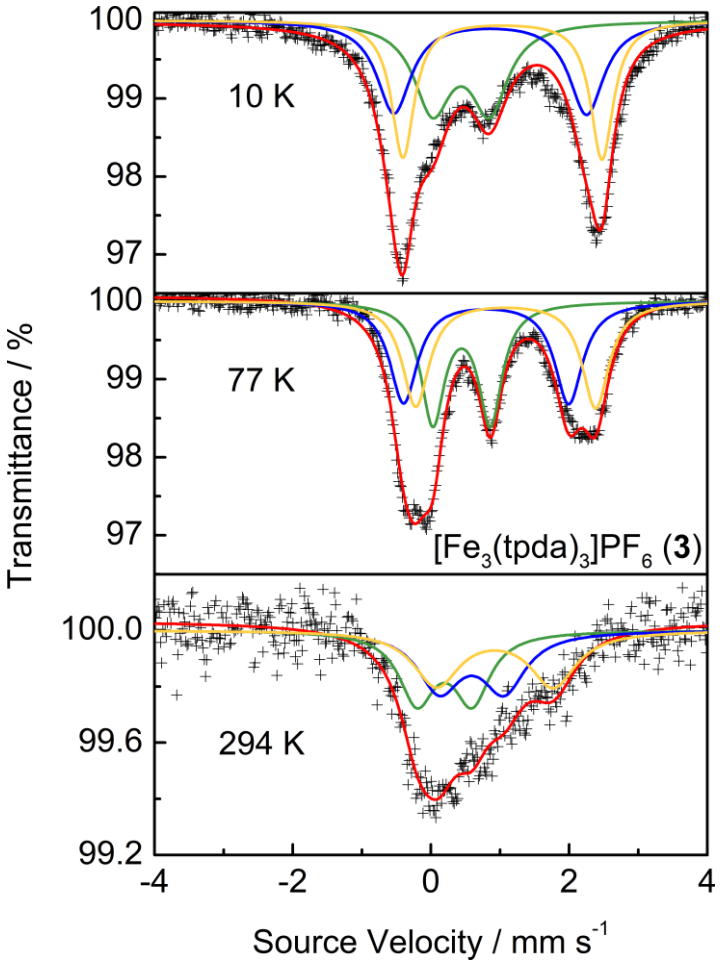

Figure 5.6. Mössbauer data for **3** at 10 K (top), 77 K (middle) and 294 K (bottom). The green line corresponds to sub-spectrum 1, the blue line to sub-spectrum 2, the yellow line to sub-spectrum 3, the red line to the overall fit, and the black crosses to the raw data.

Table 5.6. Fitted Mössbauer parameters for **3**, at 10, 77 and 294 K.[a]

Sub-spectrum	δ (mm s^{-1})			ΔE_Q (mm s^{-1})			FWHM (mm s^{-1})		
	10 K	77 K	294 K	10 K	77 K	294 K	10 K	77 K	294 K
1	0.436	0.445	0.297[b]	0.824	0.833	0.797	0.650	0.416	0.627
2	0.859	0.800	0.690[b]	2.788	2.388	0.936	0.607	0.493	0.756
3	1.036	1.083	1.026[b]	2.880	2.602	1.689	0.402	0.474	0.803

[a]Reduced χ^2 for the fit at 10, 77 and 294 K respectively: 1.315, 1.011 and 0.536. [b] The values $\delta'_1 = 0.197$, $\delta'_2 = 0.590$, and $\delta'_3 = 0.926$ mm/s obtained from the fit were corrected assuming a second-order Doppler shift of approximately −0.100 mm/s at room temperature.[108]

5.6 DC Magnetic Studies and *Ab-Initio* Calculations

The DC magnetic response of a polycrystalline sample of **3** is presented in Figure 5.7. The value of $\chi_M T$ at 300 K (12.6 emu K mol^{-1}) is well above the cumulative Curie constant for three noninteracting spins with S_1 = 5/2, S_2 = S_3 = 2 (C_{tot} ~10.38 emu K mol^{-1}, with g = 2.00). This behaviour can be ascribed to either dominant ferromagnetic coupling at room temperature, or orbital momentum. On lowering temperature, the $\chi_M T$ product undergoes a small increase up to its maximum value at 220−210 K (13.0 emu K mol^{-1}). With further cooling the $\chi_M T$ value slowly decreases until 50−40 K (12.3 emu K mol^{-1}), and then rises again to reach a local maximum at 12 K (12.8 emu K mol^{-1}). Below this temperature the $\chi_M T$ product rapidly drops to 6.3 emu K mol^{-1} at 2 K. This low-temperature decrease indicates a weakly magnetic ground state, in agreement with the isothermal M_M vs H curves recorded at 2, 4 and 8 K (M_M is molar magnetization). In fact, at the highest available field (H_{max} = 70 kOe), the average value of M_M reaches only 9.4 $N_A\mu_B$, which corresponds to 72% of the saturation value expected for three noninteracting spins with S_1 = 5/2, S_2 = S_3 = 2 (~13 $N_A\mu_B$, with g = 2.00). Also magnetic saturation, promoted by the 10 kOe applied field, can provide a contribution to the drop of the $\chi_M T$ product.

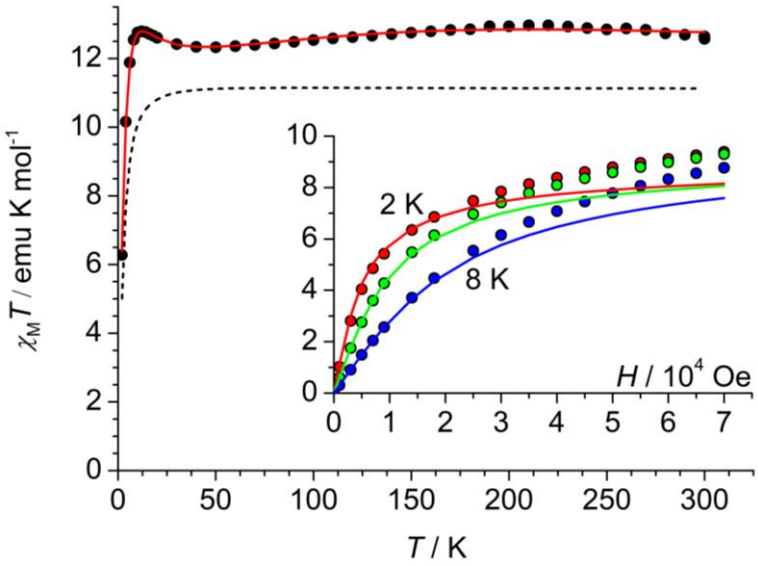

Figure 5.7. DC magnetic response of a polycrystalline sample of **3**. The black dots in the main panel are the experimental temperature-dependent $\chi_M T$ data measured at H = 10 kOe. The inset shows isothermal M_M vs H data recorded at 2, 4 and 8 K (red, green and blue dots, respectively). The solid curves provide the best-fit with *ab-initio* approach using model m**3**B. The dashed line is the simulated magnetic response of three noninteracting HS Fe ions (two Fe^{2+} and one Fe^{3+}), with single-ion parameters fixed at the values obtained by *ab-initio* calculations.

The single-ion properties of complex **3** were theoretically investigated through CASSCF/RASSI-SO calculations (**Sections 5.6.1**, **5.6.2** and **5.10.8**), which were performed by Simone Calvello and Alessandro Soncini at the University of Melbourne (RASSI-SO = Restricted Active Space State Interaction-Spin Orbit coupling). This study indicates that orbital momentum is substantially quenched for the two Fe^{2+} centers (Fe2 and Fe3), which can be treated as pure spins. In fact, the Russell-Saunders ^5D term of the free Fe^{2+} ion ([Ar]$3d^6$) is split (Fig. 5.11 in **Section 5.6.1**) by the distorted octahedral coordination geometry (C_3 point group) to give a ^5A ground term ($S = 2$) well separated from excited ones (1840−1850 cm^{-1} for Fe2 and 1100−1290 cm^{-1} for Fe3). Both Fe2 and Fe3 display a hard-axis magnetic anisotropy, i.e. positive axial ZFS parameters with $D_3 > D_2$ (ZFS parameters and g-values of the three Fe centers are gathered in Table 5.7). This result is consistent with the hard-axis magnetic anisotropy (D_i = 7.7−9.6 cm^{-1}, E_i = 0.5−2.0 cm^{-1}) exhibited by the central iron(II) ions in tetrairon(II) EMACs **1Cl**[20] and **1Br** (Section 4.7). These internal Fe centers indeed possess distorted octahedral coordination geometries (see ref.[20] and Section 4.3) which are very similar to those displayed by Fe2 and Fe3 in complex **3**. Here, as opposed to **1Cl** and **1Br**, the rhombic anisotropy (E) is suppressed by the crystallographically imposed 3-fold symmetry of complex **3**, to give a purely axial anisotropy. The *ab-initio* calculations provided not only $D_i = 3B^0_{2,i}$, but also the fourth-order CF parameters allowed by the symmetry of complex **3**: $B^0_{4,i}$, $B^3_{4,i}$ and $B^{-3}_{4,i}$ (these CF parameters for Fe2 and Fe3 are listed in Table 5.8). The *ab-initio* calculations performed on the Fe^{2+} ions are described in detail below, in **Section 5.6.1**.

Table 5.7. Single-ion ZFS parameters and g-factors of **3** from *ab-initio* calculations.

	D_i (cm^{-1})[a]	$g_\perp$, $g_\parallel$[b]
Fe1	−0.97	*c*
Fe2	7.10	2.135, 1.994
Fe3	12.21	2.220, 1.989

[a]Axial ZFS parameters of Fe*i* ($D_i = 3B^0_2$, from Table 5.8). [b]Principal values of the $\bar{\bar{g}}_i$ tensor of Fe*i*, where $g_x = g_y = g_\perp$, and $g_z = g_\parallel$ (the z axis coincides with the 3-fold axis). [c]The g-factor of the Fe^{3+} ion was considered 2.000.

On the other hand, in the distorted octahedral coordination geometry (C_3 point group) of Fe1, the ^6S Russell-Saunders term of the free Fe^{3+} ion affords a ^6A ground term (S = 5/2) well separated (≈1700 cm^{-1}) from the excited ones (S = 3/2 and 1/2). Although the HS Fe^{3+} ion ([Ar]$3d^5$) is often considered "isotropic", the calculations highlighted a small and negative D for Fe1, which thus exhibits easy-axis anisotropy (purely-axial), albeit much smaller in

magnitude than for the two Fe^{2+} ions. The *ab-initio* calculations on Fe1 are described in detail below, in **Section 5.6.2**.

Table 5.8. CF parameters for the Fe^{2+} ions in complex **3**, from *ab-initio* calculations.

	B_2^0	B_4^0	B_4^3	B_4^{-3}
Fe2	2.367	$1.028 \cdot 10^{-3}$	$-1.076 \cdot 10^{-7}$	$1.236 \cdot 10^{-9}$
Fe3	4.071	$4.578 \cdot 10^{-3}$	$2.480 \cdot 10^{-7}$	$-3.947 \cdot 10^{-9}$

Knowledge of the single-ion properties allowed modelling the magnetic behavior of **3** without risk of overparameterization. Since the orbital momentum is substantially quenched for all the Fe centers, Fe1, Fe2 and Fe3 were treated as pure spins ($S_1 = 5/2$, $S_2 = S_3 = 2$). First, PHI v3.1.5 software[117] was used to calculate the $\chi_M T$ vs T response for the three noninteracting Fe centers with single-ion parameters held fixed at the values obtained by *ab-initio* calculations. The resulting curve (dashed line in Fig. 5.7) is well below the experimental data, indicating the existence of magnetic interactions between the metal ions, which are likely to be predominantly ferromagnetic. As described for complexes **1Cl** and **1Br**, a new SH was written by adding an isotropic exchange Hamiltonian to the sum of single-ion Hamiltonians ($\widehat{H}_i$, Eq. 4.4). The isotropic exchange Hamiltonian accounts for super-exchange interaction between the *i*- and *j*-th localized spin centers through isotropic coupling constants J_{ij} (only nearest neighbor interactions were considered):

$$\widehat{H} = \sum_{i=1}^{3} \widehat{H}_i + J_{12}\hat{\mathbf{S}}_1 \cdot \hat{\mathbf{S}}_2 + J_{23}\hat{\mathbf{S}}_2 \cdot \hat{\mathbf{S}}_3 \qquad (5.2)$$

Simultaneous fits of susceptibility and magnetization data were performed varying exchange coupling constants only, while CF parameters and *g*-factors were taken from *ab-initio* calculations and held fixed for each spin center. All tested models based on Eq. 5.2 totally failed to reproduce the experimental data, and the best result obtained (entry m**3**A) is presented in Fig. 5.8 (left panel). The best-fit parameters related to this and other models discussed below are gathered in Table 5.9.

The SH was thus refined as follows, introducing anisotropic contributions to the *J* couplings:

$$\widehat{H} = \sum_{i=1}^{3} \widehat{H}_i + J_{\perp,12}\left(\hat{S}_{1,x}\hat{S}_{2,x} + \hat{S}_{1,y}S_{2,y}\right) + J_{||,12}\hat{S}_{1,z}\hat{S}_{2,z} + J_{\perp,23}\left(\hat{S}_{2,x}\hat{S}_{3,x} + \hat{S}_{2,y}\hat{S}_{3,y}\right) + J_{||,23}S_{2,z}\hat{S}_{3,z} \qquad (5.3)$$

where $J_{\perp,ij}$ and $J_{||,ij}$ embed both isotropic and anisotropic exchange interactions, and $\hat{S}_{i,x}$, $\hat{S}_{i,y}$, and $\hat{S}_{i,z}$ are the three components of the spin angular momentum (the *z* axis coincides with the C_3 axis).

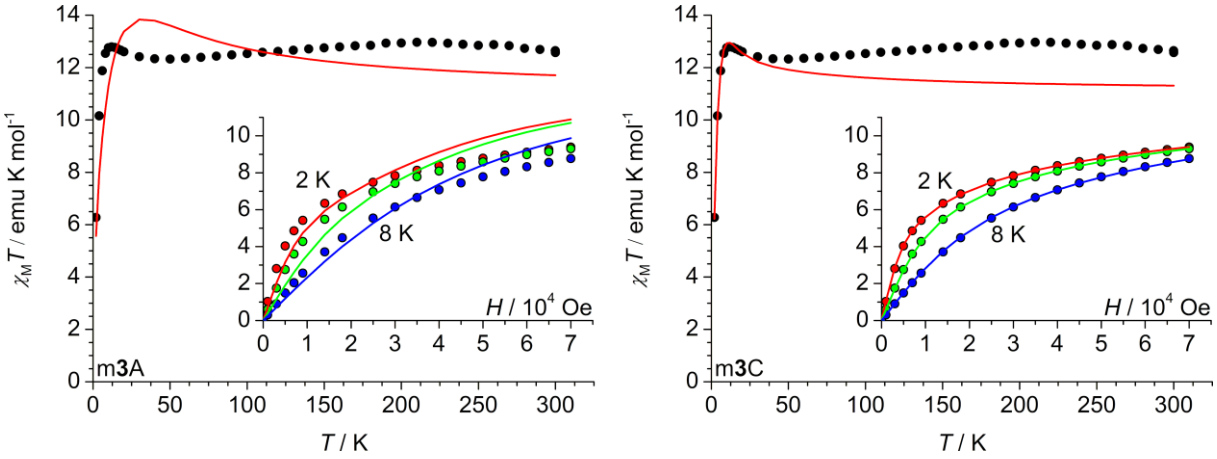

Fig. 5.8. Best-fit curves to the experimental data in Fig. 5.7, based on models m**3**A (left) and m**3**C (right) (see Table 5.9).

Table 5.9. Best-fit parameters from the simultaneous fit of susceptibility and magnetization data of **3**.[a]

Model	J_{12}	$J_{xx,12}$ / $J_{yy,12}$	$J_{zz,12}$	$J_{\perp 12}$	$J_{\|12}$	J_{23}	$J_{xx,23}$ / $J_{yy,23}$	$J_{zz,23}$	$J_{\perp 23}$	$J_{\|23}$	R
m**3**A	−7.8(6)	/	/	/	/	1.25(6)	/	/	/	/	1375
m**3**B	5.7(5)	35.0(9)	−70.0(11)	**40.7(4)**	**−64.2(6)**	−55.6(7)	−4.7(15)	9.4(13)	**−60.4(8)**	**−46.2(6)**	**3.7**
m**3**C	−1.72(4)	5.02(10)	−10.04(7)	3.30(5)	−11.76(3)	−1.19(4)	1.16(8)	−2.32(8)	−0.04(4)	−3.51(4)	1.3[b]

[a] J values are expressed in cm^{-1}. [b] This lower R value is only a mathematical artifact, since model m**3**C totally failed to reproduce susceptibility data.

Each pairwise interaction between spins in **3** can be described in a more compact way using diagonal second-rank tensor $\bar{\bar{J}}$, with $J_\perp$ and $J_\parallel$ constants as diagonal elements (for simplicity we drop the *ij* indices). On its turn, $\bar{\bar{J}}$ can be expressed as the sum of an isotropic exchange tensor $\bar{\bar{J}}_{\text{iso}}$ (i.e. the isotropic coupling constant J times the 3 × 3 identity matrix) and of a traceless diagonal tensor $\bar{\bar{J}}_{\text{anis}}$ that describes the anisotropic part of the interaction:

$$\bar{\bar{J}} = \bar{\bar{J}}_{\text{iso}} + \bar{\bar{J}}_{\text{anis}}; \quad \begin{bmatrix} J_\perp & 0 & 0 \\ 0 & J_\perp & 0 \\ 0 & 0 & J_{||} \end{bmatrix} = \begin{bmatrix} J & 0 & 0 \\ 0 & J & 0 \\ 0 & 0 & J \end{bmatrix} + \begin{bmatrix} J_{xx} & 0 & 0 \\ 0 & J_{yy} & 0 \\ 0 & 0 & J_{zz} \end{bmatrix} \qquad (5.4)$$

where $J = (1/3)\cdot\mathrm{Tr}(\bar{\bar{J}})$ and $\mathrm{Tr}(\bar{\bar{J}}_{\mathrm{anis}}) = 0$. Therefore $J_{\perp} = J_{xx} + J = J_{yy} + J$ and $J_{\parallel} = J_{zz} + J$.

We neglect other interaction terms such as antisymmetric exchange and we do not explicitly include the double-exchange interaction, which is likely to occur in a MV complex like **3** (**Sections 5.2** and **5.5**).

In order to fully explore the hypersurface of the residuals (R), several anisotropic models differing in the constraints applied to $J_{\perp,ij}$ and $J_{\parallel,ij}$ values were tested. However, only one model (entry m**3**B in Table 5.9 and Fig. 5.7) accurately accounted for the magnetic response of **3** on a high-energy scale (susceptibility vs. T data) through substantial couplings between Fe centers. By contrast, it is not completely satisfactory in reproducing the details of low-temperature magnetism, as it underestimates M_{M} vs H curves by about ≈10% (for $H > 20$ kOe). Other tested models that reached convergence accurately reproduced the low temperature magnetic response of **3**, but completely failed to account for susceptibility data. Therefore, they are not reported here. However, one of these models (entry m**3**C) was found particularly interesting, since the pattern of its exchange constants is similar to that of m**3**B, but pairwise interactions are much weaker (Fig. 5.8, right panel).

Model m**3**B gives a very accurate fit of susceptibility data and a rough reproduction of low temperature magnetization with only four adjustable parameters. It is characterized by a strong and very anisotropic interaction between Fe^{3+} (Fe1) and the central Fe^{2+} ion (Fe2), with $J_{\perp 12}$ and $J_{\parallel 12}$ of comparable magnitude but opposite sign (Table 5.9). This means that Fe1 and Fe2 are ferromagnetically coupled along the molecular axis (z), while they interact antiferromagnetically in the plane perpendicular to it (xy). The net coupling is given by the isotropic coupling constant $J_{12} = 5.7$ cm^{-1} and it is antiferromagnetic. On the other hand, the two Fe^{2+} ions (Fe2 and Fe3) are strongly ferromagnetically coupled ($J_{23} = -55.6$ cm^{-1}). This is reasonable considering that the two ions are only 2.732 Å away from each other.[109] Furthermore, the interaction is much less anisotropic than between Fe1 and Fe2. Therefore, predominant ferromagnetic interactions are present in complex **3** and the room temperature value of the $\chi_{\mathrm{M}}T$ product is well above that of the three non-interacting spins. However, at low temperature, the competitive antiferromagnetic interactions and/or single ion anisotropy effects cause a drop in the magnetism of **3**.

Despite the prevalent hard-axis anisotropies of the Fe^{2+} ions, complex **3** shows weak SMM behaviour below 3.0 K, which persists in zero static field also (see **Section 5.7**). Therefore, we calculated the energy levels that result from the parameters (CF parameters, g-values, and best-fit $J_{\perp,ij}$ and $J_{\parallel,ij}$ values) of model m**3**B (Fig. 5.9). At $H = 0$, the lowest-energy states are

closely-spaced Kramers doublets, which do not follow the pattern typical of a well-isolated total spin state undergoing predominantly axial ZFS. These doublets are substantially split (Fig. 5.9) by a magnetic field of 10 kOe applied along the molecular axis *z*. The splitting is instead negligible when the same field is applied along the *x* and *y* directions (except for the sixth excited doublet, Fig. 5.9). This behaviour clearly indicates that complex **3** possesses a magnetic ground state with easy-axis anisotropy along the 3-fold axis. In fact, the calculated susceptibility (2 K and 10 kOe) along *z* is ~4.5 times greater than orthogonal to it (Fig. 5.10). Very important, the presence of easy-axis anisotropy in complex **3** was experimentally established by micro-SQUID measurements, as detailed in **Section 5.8**.

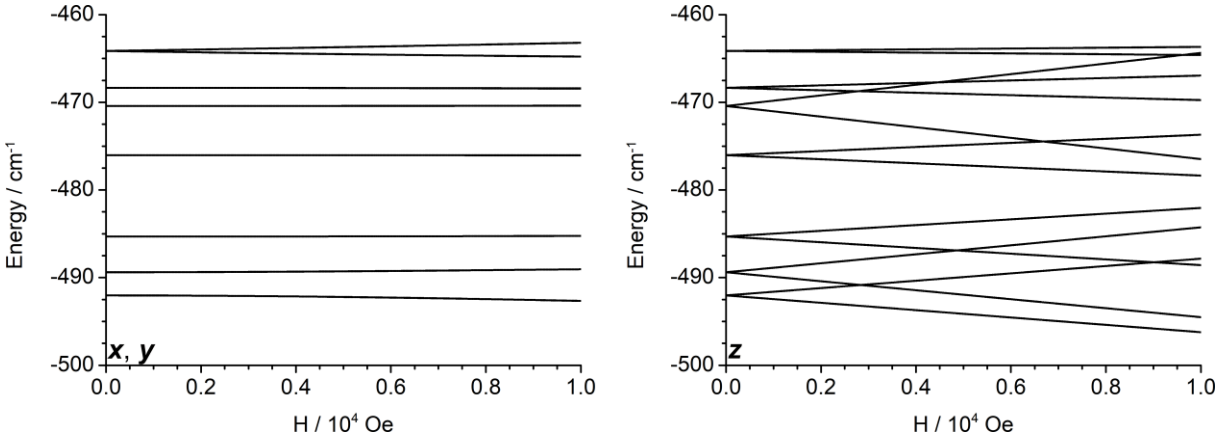

Figure 5.9. Zeeman diagram for **3** (model m**3**B) when the magnetic field is applied along the chain axis *z* (right panel) or perpendicular to it (left panel).

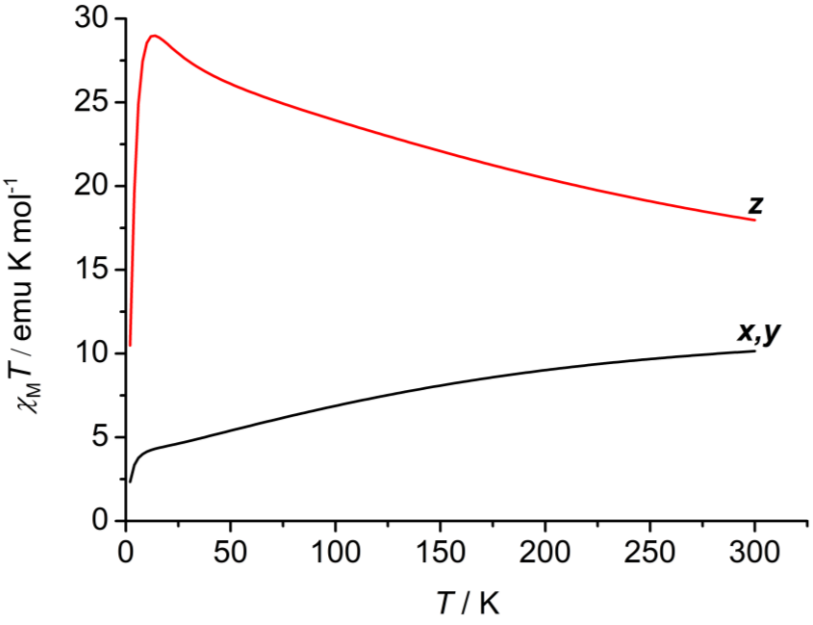

Figure 5.10. Temperature dependent $\chi_M T$ product calculated with the best-fit parameters of model m**3**B when H = 10 kOe is applied along the chain axis *z* (red line) or perpendicular to it (black line).

5.6.1 Details on *Ab-Initio* Calculations: Fe^{2+} ions (Fe2 and Fe3)

In the set of *ab initio* calculations performed, the first step is the RASSCF calculation, where electron-electron repulsion and CF energy contributions are introduced. In an octahedral coordination environment, the ^5D Russell-Saunders term of the free ion is split into $^5T_{2g}$ and ^5E_g terms, with the former being the ground state. Furthermore, if trigonal distortion is present as in **3**, the symmetry lowering will further split the $^5T_{2g}$ term into an orbital singlet and an orbital doublet, the ground term being determined by the nature of the distortion. Since the octahedral splitting gap (Δ) is $\Delta >> k_BT$, in the calculations only the wave functions for the three $^5T_{2g}$-derived states were optimized, as they are the ones that contribute most to the electronic properties of the complex. Dynamic correlation is a very important contribution to correctly describe the electronic properties of **3**. Therefore, we have also performed CASPT2 (complete active-space second-order perturbation theory) calculations on the wave functions of the three $^5T_{2g}$-derived states optimized in the RASSCF step. SO coupling was subsequently introduced in the RASSI calculation, which causes the mixing the CASPT2-optimized $^5T_{2g}$ -derived states and further splits them.

For the central (Fe2) and the terminal (Fe3) Fe^{2+} ions, the results of the RASSCF calculation (Fig. 5.11 and Table 5.10) show that, in the ground term, the doubly occupied orbital is the $3d_{z^2}$ orbital, where the *z* axis is along the chain of three Fe ions. The inclusion of dynamic correlation reduces the trigonal splitting gap of Fe3, although the RASSCF ground state is retained after the CASPT2 calculation. On the other hand, the trigonal splitting of Fe2 is not significantly perturbed. After inclusion of SO coupling in the RASSI step of the calculation, the ground ^5A crystal field term of both Fe^{2+} ions splits into five SO states with $M_L \approx 0$ (M_L is the quantum number associated with the *z*-projection of orbital momentum). The ZFS parameters for the five-state manifold were computed by Molcas[178] using Eq. 2.6. It can be noted that, throughout the entire set of calculations, an almost perfectly axial magnetic anisotropy for both Fe^{2+} ions was found, as expected for the crystallographically imposed 3-fold symmetry of complex **3**. This set of *ab-initio* calculations consistently indicates that both Fe^{2+} ions possess a hard-axis magnetic anisotropy (Table 5.7), which is stronger for the terminal Fe center (Fe3).

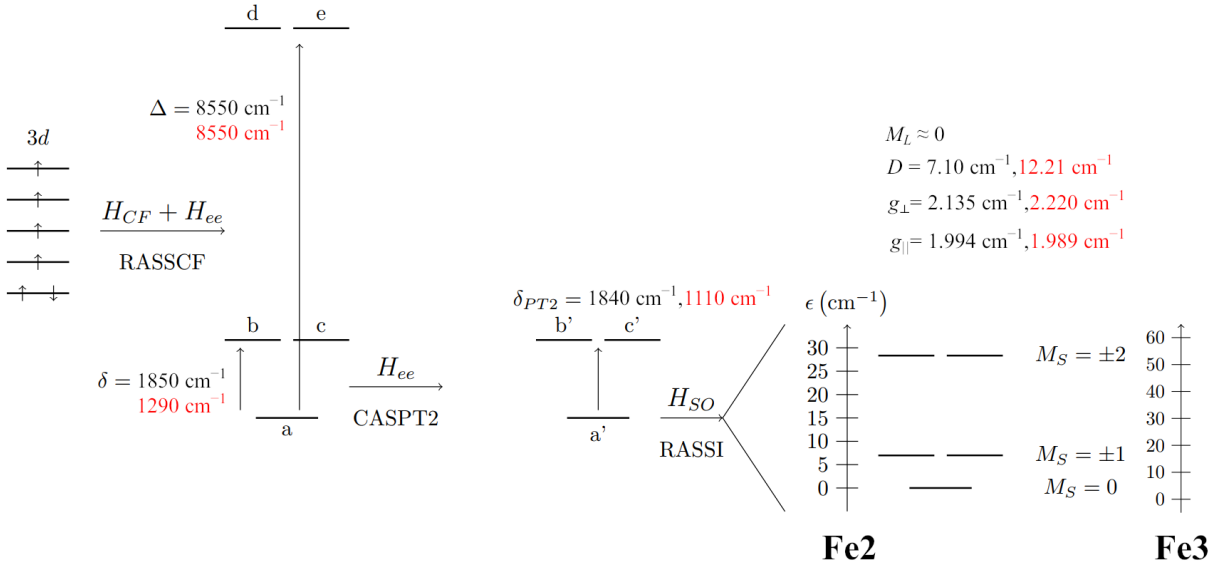

Figure 5.11. From left to right: sketch of 3d orbitals for a free Fe^{2+} ion; multiconfigurational crystal-field-split states (labeled a-e), with octahedral (Δ, $^5T_{2g}$–^5E_g) and trigonal (δ) energy separations; multiconfigurational crystal-field-split states (labeled a'-c') after inclusion of dynamic correlation contributions (trigonal energy separations provided as δ_{PT2}); ZFS states labeled according to their M_S quantum numbers, with ZFS parameters and principal g-values. The values reported in black and red are referred to Fe2 and Fe3, respectively (Figure kindly provided by S. Calvello).

Table 5.10. Composition of the RAS(12,16) states from Fig. 5.11 in terms of Slater Determinants (SDs). For each SD, the occupation of the 3d orbitals is displayed in black for Fe2 and in red for Fe3 (Table kindly provided by S. Calvello).

RASSCF State	SD Composition
a	$3d_{xy}$ ↑↑ $3d_{x^2-y^2}$; $3d_{xz}$ ↑↑ $3d_{yz}$; 97.4% 97.4% ↑↓ $3d_{z^2}$
b	$3d_{xy}$ ↑↑ $3d_{x^2-y^2}$; $3d_{xz}$ ↑↓ $3d_{yz}$; 95.0% 97.0% ↑ $3d_{z^2}$ — $3d_{xy}$ ↑↑ $3d_{x^2-y^2}$; $3d_{xz}$ ↑↓ $3d_{yz}$; 2.4% 0.4% ↑ $3d_{z^2}$
c	$3d_{xy}$ ↑↑ $3d_{x^2-y^2}$; $3d_{xz}$ ↑↓ $3d_{yz}$; 2.4% 0.4% ↑ $3d_{z^2}$ — $3d_{xy}$ ↑↑ $3d_{x^2-y^2}$; $3d_{xz}$ ↑↓ $3d_{yz}$; 95.0% 97.0% ↑ $3d_{z^2}$
d	$3d_{xy}$ ↑↓ $3d_{x^2-y^2}$; $3d_{xz}$ ↑↑ $3d_{yz}$; 71.5% ↑ $3d_{z^2}$ — $3d_{xy}$ ↑↓ $3d_{x^2-y^2}$; $3d_{xz}$ ↑↑ $3d_{yz}$; 97.3% 25.9% ↑ $3d_{z^2}$
e	$3d_{xy}$ ↑↓ $3d_{x^2-y^2}$; $3d_{xz}$ ↑↑ $3d_{yz}$; 97.3% 25.9% ↑ $3d_{z^2}$ — $3d_{xy}$ ↑↓ $3d_{x^2-y^2}$; $3d_{xz}$ ↑↑ $3d_{yz}$; 71.5% ↑ $3d_{z^2}$

5.6.2 Details on *Ab-Initio* Calculations: Fe^{3+} ion (Fe1)

With the observed coordination geometry, the $t_{2g}^3e_g^2$ configuration of HS Fe^{3+} ion (Fe1) is expected to lead to a ^{6}A electronic term, well separated in energy from CF terms with lower spin (S = 3/2 and S = 1/2). While in first approximation (which we have employed in this work) SO coupling within the ^{6}A term would not induce ZFS, excited terms with S = 3/2 and S = 1/2 are expected to weakly couple with the ground term, leading to a ZFS. We have calculated the entity of this splitting by performing a sample CAS(5,5)SCF calculation on the ground Russell-Saunders term for each possible spin, subsequently mixing these terms via SO coupling in the RASSI step. The results of the calculation (Fig. 5.12) show that, indeed, the Fe^{3+} ion possesses a ^{6}A ground term well separated from any excited term. It has to be noted, however, that the lowest-lying S = 3/2 term only lies approximately 1700 cm^{-1} higher in energy. Therefore, in order to accurately describe the properties of this ion the inclusion of this CASSCF-optimized state in the RASSI SO mixing might have to be performed, as well as including dynamic correlation contributions through CASPT2 calculations. Within the framework of this sample calculation, the ZFS is about one order of magnitude smaller than that of Fe^{2+} ions and indicates that Fe1 possesses weak easy-axis anisotropy.

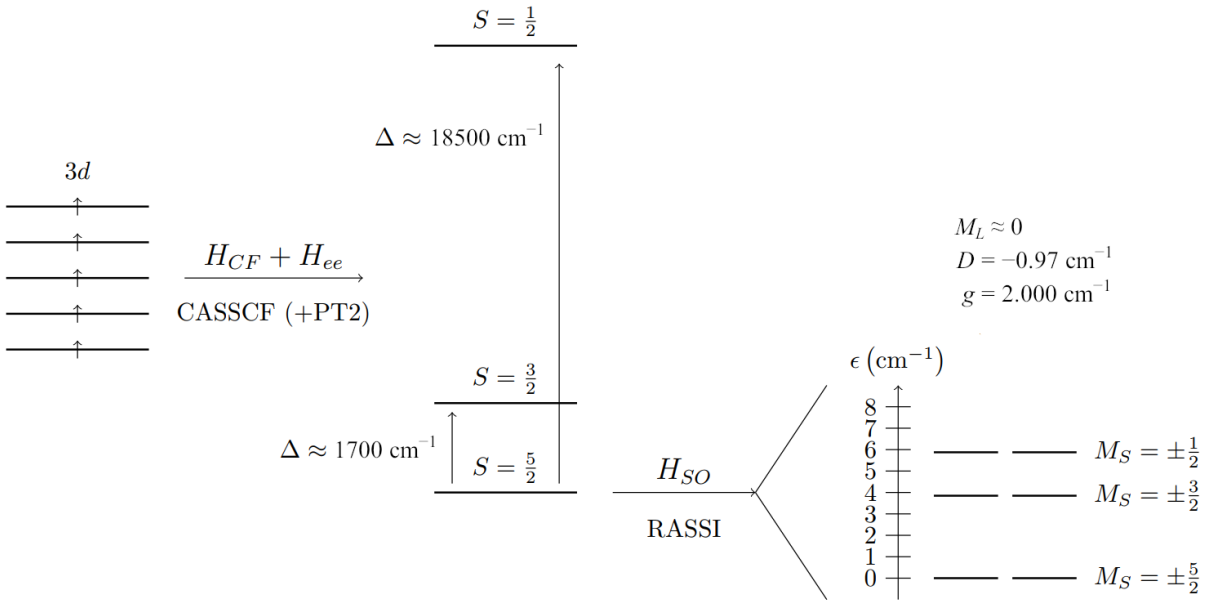

Figure 5.12. From left to right: sketch of 3d orbitals for a free Fe^{3+} ion; lowest CF state for each spin value in Fe1, with spin energy separations provided as Δ; ZFS states labeled according to their M_S quantum numbers, with ZFS parameters and principal g-values (Figure kindly provided by S. Calvello).

5.7 AC Magnetic Studies

A polycrystalline sample of **3** was tested for SRM with AC susceptibility measurements. Preliminary scans of χ_M'' vs ν (from 21 to 2664 Hz) at 2.0 K and for H_{DC} values between 0 and 2.5 kOe revealed that **3** features SRM even in zero DC field (Fig. 5.13). The largest χ_M'' values were detected at H_{DC} = 750 Oe and complete sets of isothermal χ_M'' vs ν curves (from 21 to 9980 Hz) were thus collected both in zero-field (between 1.95 and 10.0 K) and with H_{DC} = 750 Oe (between 2.1 and 10.0 K). Unfortunately, some of the high-frequency data had to be removed due to self-heating of the sample. As suggested by the preliminary scans at 2.0 K, the SMM behavior of **3** does not differ much in zero-field and at 750 Oe. In both cases, the onset of SRM is clearly observed below 3.0 K, although no maximum was detected in our accessible frequencies range (Fig. 5.14). Thus, the isothermal curves could not be fitted with the generalized Debye model (Eqs. 4.10-4.12).[3] Instead, both datasets were fitted following the same approach employed for the zero-field isothermal χ_M'' vs ν curves of complex **1Br** (see **Section 4.8**). The anisotropy barrier and the characteristic time were extrapolated applying Eq. 4.9[120,121] to frequency values from 79 to 6426 Hz, for temperatures up to 2.9 K. The best-fit curves are represented in Fig. 5.15. The following values of U_{eff}/k_B and τ_0 were obtained by averaging the best-fit slopes (E_a/k_B) and intercepts ($\ln(\omega\tau_0)$), respectively, at different frequencies (the numbers in parentheses are the standard deviations of the average values): H_{DC} = 0 Oe, U_{eff}/k_B = 8.4(6) K and $\tau_0 = 1.4(9)\cdot10^{-7}$ s; H_{DC} = 750 Oe, U_{eff}/k_B = 8.5(6) K and $\tau_0 = 1.8(10)\cdot10^{-7}$ s. Complex **3** thus exhibits improved SMM behavior compared to its fully reduced precursor, **1Cl**, which showed detectable SRM only in an applied DC field (U_{eff}/k_B = 10.1(13) K and $\tau_0 = 2.6(2)\cdot10^{-7}$ s).[20] Interestingly, the replacement of Cl^- with Br^- axial ligands (**Section 4.8**) has similar consequences on SMM behavior, as **1Br** also exhibits measurable SRM in zero-field, with comparable activation parameters (U_{eff}/k_B = 5.4(4) K and $\tau_0 = 1.1(8)\cdot10^{-6}$ s).

One difference with respect to **1Br** is that the activation parameters of **3** remain the same (within experimental error) in zero and nonzero applied DC field, suggesting that either under-barrier relaxation mechanisms are not efficient here or the application of H_{DC} is not sufficient to inhibits non-Orbach mechanisms. At variance with this, in complex **1Br** the application of H_{DC} leads to an anisotropy barrier of 18.9(8) K, which is ~3.5 times greater than in zero-field (**Section 4.8**).

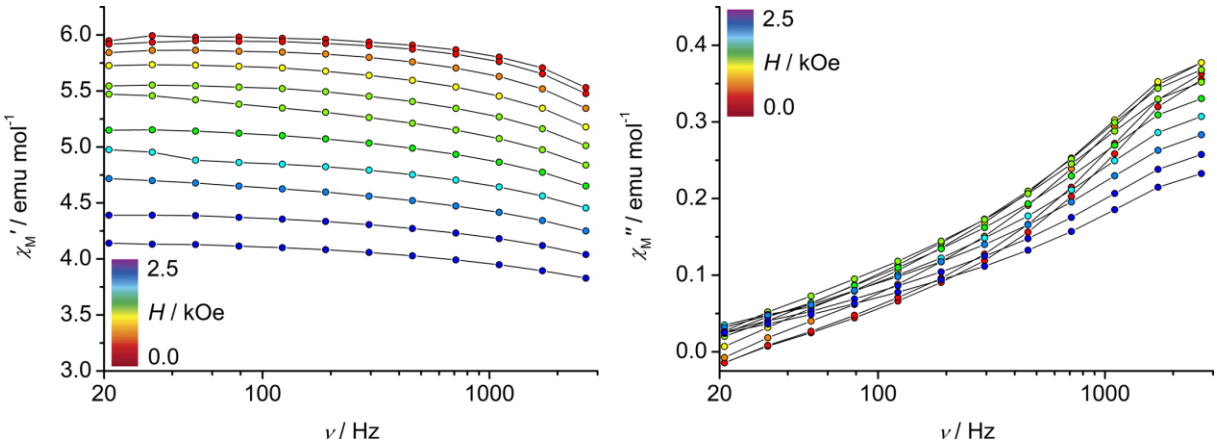

Fig. 5.13. Field dependence of the in-phase (χ_M', left panel) and out-of-phase (χ_M'', right panel) components of molar magnetic susceptibility of **3** at T = 2.0 K.

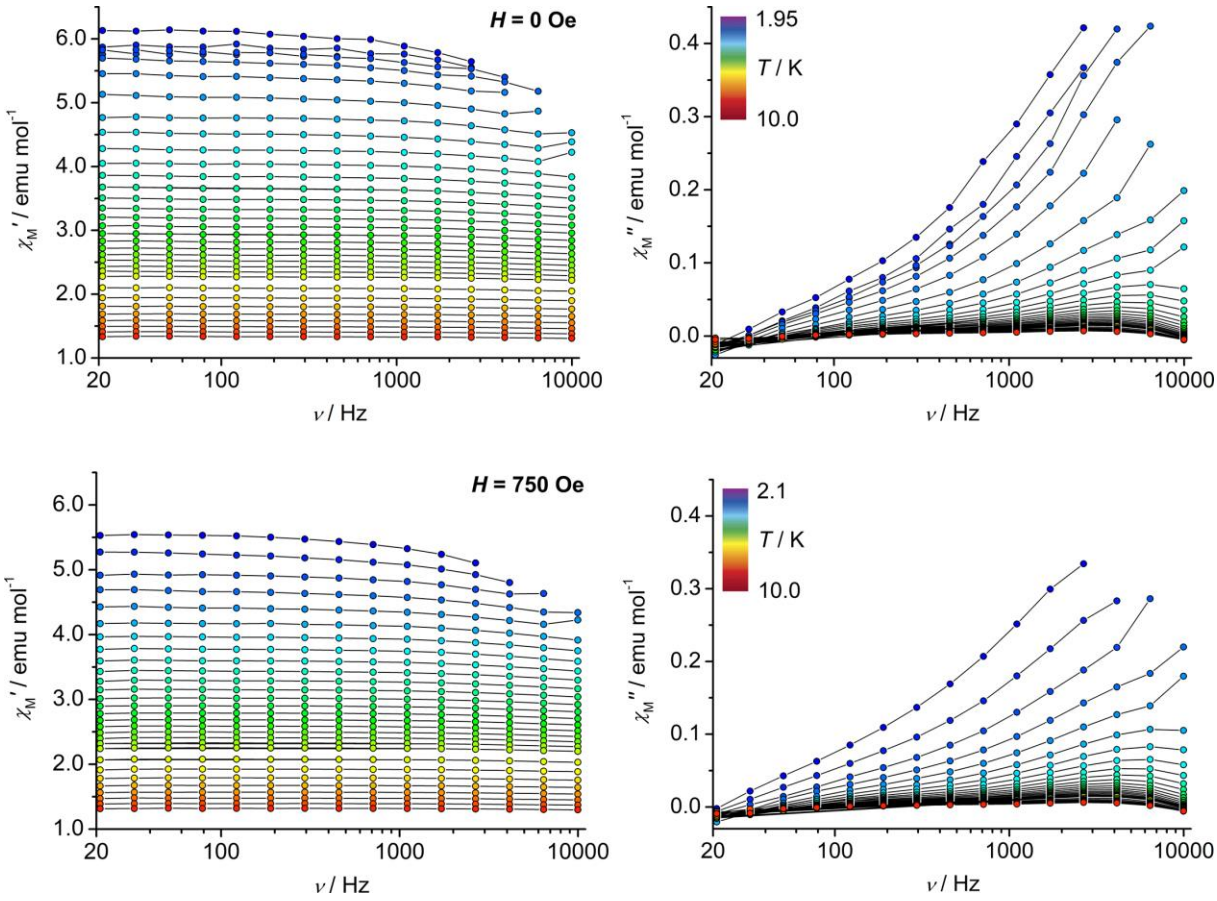

Fig. 5.14. Frequency dependence of the in-phase (χ_M', left panels) and out-of-phase (χ_M'', right panels) components of molar magnetic susceptibility of **3** at T ranging from 1.95 (or 2.1) to 10 K. Measurements were carried out with a static DC field of 0 (top) and 750 Oe (bottom). The isothermal curves at H_{DC} = 0 Oe (750 Oe) were measured at 1.95, 2.05, 2.1, 2.2, 2.3, 2.5, 2.7, 2.9, 3.1, 3.3, 3.5, 3.7, 3.9, 4.05, 4.25, 4.45, 4.65, 4.85, 5.0, 5.2, 5.4, 5.6, 5.8, 6.0, 6.5, 7.0, 7.5, 8.0, 8.5, 9.0, 9.5, 10 K (2.1, 2.3, 2.5, 2.7, 2.9, 3.1, 3.3, 3.5, 3.7, 3.9, 4.05, 4.25, 4.45, 4.65, 4.85, 5.05, 5.25, 5.4, 5.6, 5.8, 6.0, 6.5, 7.0, 7.5, 8.0, 8.5, 9.0, 9.5, 10 K).

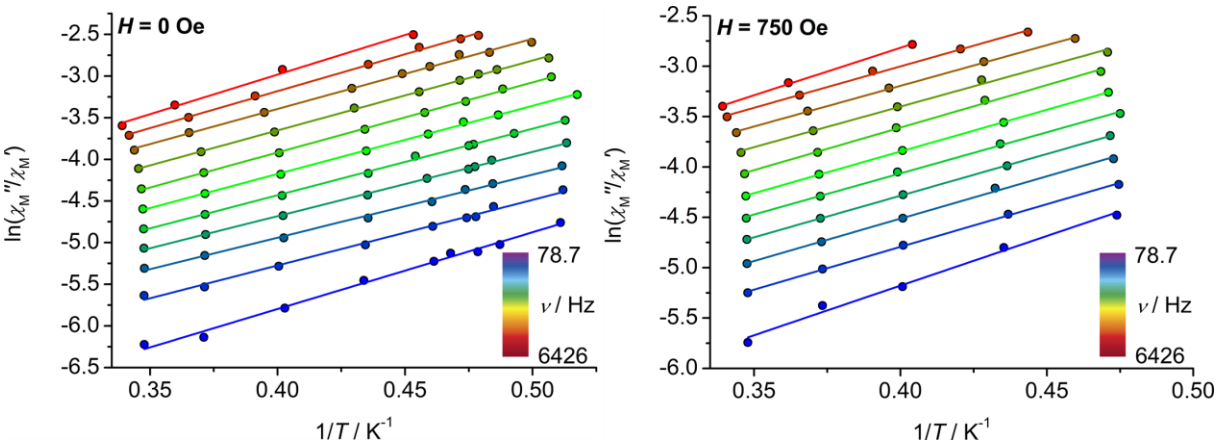

Fig. 5.15. Frequency-dependent $\ln(\chi_M''/\chi_M')$ vs $1/T$ plots for **3** (colored dots) at H_{DC} = 0 and 750 Oe. The colored lines represent the linear regression fits at each specific frequency.

5.8 Micro-SQUID Measurements

The micro-SQUID measurements were performed by Michael Schulze and Wolfgang Wernsdorfer at the Karlsruhe Institute of Technology (Karlsruhe, Baden-Wuerttemberg, Germany).

This measurement technique provides a tool to measure flux changes through a superconducting loop down to 10^{-4} Φ_0 from mK-temperatures up to 6 K.[179] For manipulation of magnetic objects, magnetic fields up to 1.4 T can be applied, using sweeping rates up to 1 T/s. The high sensitivity to magnetic fields allows to investigate samples with size down to the μm region, like magnetic nanoparticles and ensembles of SMMs. Substituting the constrictions of superconducting Nb with single-walled carbon nanotubes allows to extend the investigation down to the molecular level.[179–182] The micro-SQUID method was here used to measure single crystals of complexes $[Fe_3(tpda)_3]PF_6$ (**3**) and $[Fe_3(tpda)_3Cl]PF_6$ (**3a**).

Consistent with the outcome of SH calculations (**Section 5.6**), the crystal of **3** was found to have an easy magnetic axis, along which the external magnetic field was applied. Due to the crystal symmetry, such easy axis must coincide with the 3-fold molecular axis *z* (**Section 5.6**). The isothermal magnetic hysteresis loops measured at T = 4.5−0.03 K, in fields up to 10 kOe and with a field-scan rate up to 128 mT/s are represented in Fig. 5.16, along with their first derivatives (M is magnetization and M_S is saturation magnetization). We found that complex **3**

exhibits a small opening of the hysteresis loop at temperatures ≤ 0.5 K. In particular, SRM is detectable even in zero field, and this observation is in agreement with AC magnetic measurements. As expected, the remanent magnetization is larger when higher field-scan rates are used (Fig. 5.16).

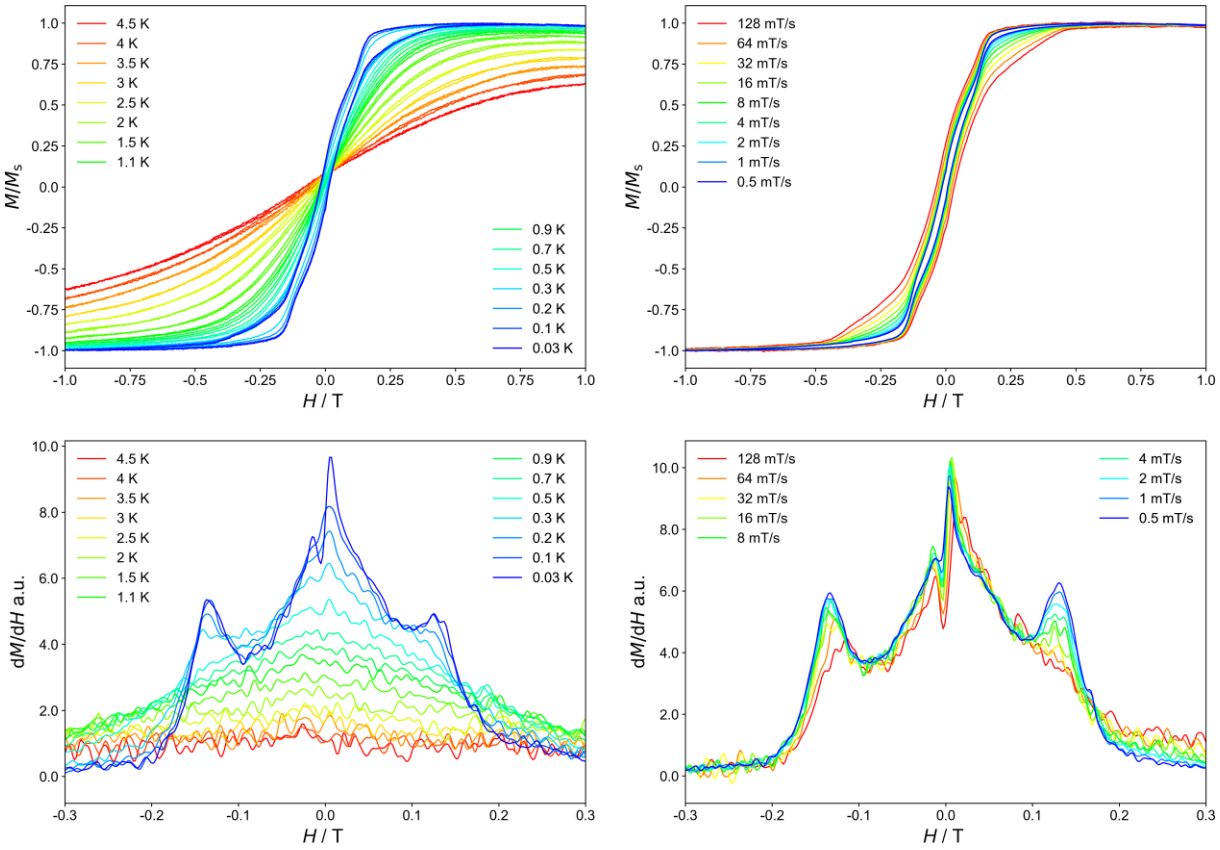

Fig. 5.16. Hysteresis loops of $[Fe_3(tpda)_3]PF_6$ (**3**) and their low-field first derivatives from micro-SQUID measurements on a single crystal. The panels on the left-hand side show isothermal measurements at 8 mT/s (4.5−0.03 K). The panels on the right-hand side show measurements at 0.03 K and different field-scan rates (0.5−128 mT/s).

On the other hand, similar measurements performed on a single crystal of **3a** at T = 4.5−0.03 K, in fields up to 14 kOe and with a field-scan rate up to 128 mT/s highlighted a very different behaviour. Complex **3a** displays simple paramagnetic properties, with no opening in its low-temperature hysteresis loops even at 0.03 K and with the highest field-scan rate (Fig. 5.17). This indicates that further one-electron oxidation of $[Fe_2^{II}Fe^{III}(tpda)_3]PF_6$ (**3**) to give $[Fe^{II}Fe_2^{III}(tpda)_3Cl]PF_6$ (**3a**) suppresses SMM behaviour, at least within the timescale of the available magnetic techniques.

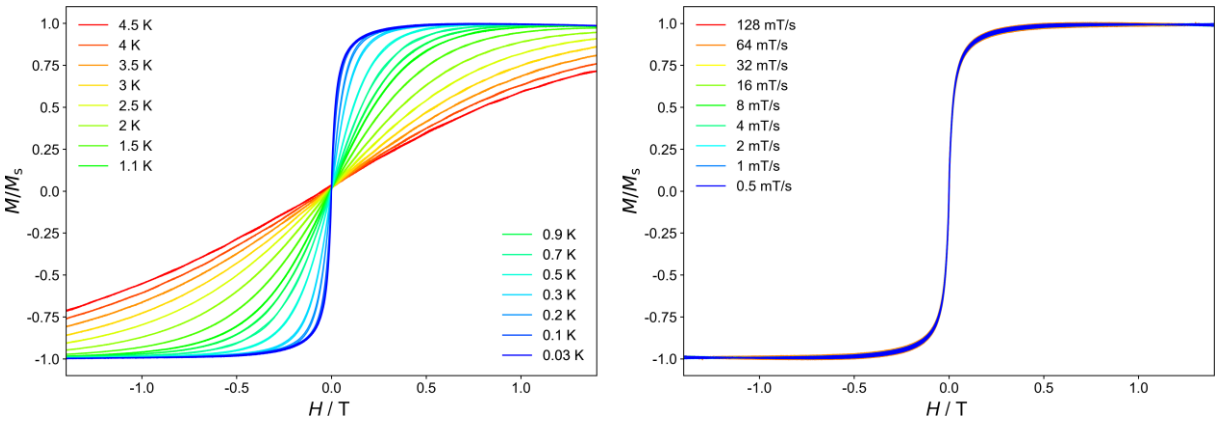

Fig. 5.17. Hysteresis loops of $[Fe_3(tpda)_3Cl]PF_6$ (**3a**) from micro-SQUID measurements on a single crystal. The panel on the left-hand side shows isothermal measurements at 8 mT/s (4.5−0.03 K). The panel on the right-hand side shows measurements at 0.03 K and different field-scan rates (0.5−128 mT/s).

5.9 Conclusions

In this Chapter, we have described and analyzed the effect of the stepwise oxidation of the tetrairon(II) EMAC **1Cl**[20] to give the one- and two-electron oxidized MV species **3** and **3a**, respectively (complex **3a** was obtained as a byproduct during the preparation of **3**). These oxidations cause a rearrangement of the molecular structure, leading to the extrusion of a $FeCl_2$ or FeCl fragment (see **Chapter 4** and ref.[20]). In fact, both compounds feature one metal less than expected and are triiron chains with 3-fold symmetry. According to BVS calculations, and as experimentally confirmed by Mössbauer spectroscopy at 10, 77 and 298 K, complex **3** contains a pair of nearby HS Fe^{2+} ions, and a terminal HS Fe^{3+} ion, with localized valence states below 77 K. However, electron delocalization is clearly observed at room temperature, indicating that **3** is a Robin-Day Class II MV species. UV-Vis-NIR spectroscopy confirms Mössbauer findings, with an intense IVCT absorption whose FWHM is on the threshold of Robin-Day Class II and III classification. The DC magnetic properties indicate predominant ferromagnetic interactions but a weakly magnetic ground state. In order to facilitate the treatment of magnetic data, a local site model has been adopted and the single-ion properties of **3** have been evaluated by *ab-initio* (CASSCF/RASSI-SO) calculations. This theoretical approach suggests hard-axis anisotropy for the Fe^{2+} ions (Fe2 and Fe3), and a weak easy-axis anisotropy for the Fe^{3+} ion (Fe1). These local anisotropies compete with super-exchange interactions, which turned out to be strongly anisotropic and predominantly antiferromagnetic for the Fe1,Fe2 pair, and much less anisotropic and strongly ferromagnetic for the Fe2,Fe3 pair of Fe^{2+} ions. The strong ferromagnetic coupling within the Fe2,Fe3 pair is consistent with the short $Fe^{2+}\cdots Fe^{2+}$ separation.[109] Our analysis indicates that the hard-axis anisotropies of the Fe^{2+} ions are overriden by exchange anisotropy to give an easy-axis overall anisotropy. This is in line with the SRM detected in AC measurements even in zero static field. Micro-SQUID measurements confirm that **3** is characterized by easy-axis anisotropy and reveal a small opening of magnetic hysteresis loop below 0.5 K, with a small but detectable remanent magnetization. Finally, micro-SQUID technique indicates no detectable SMM behaviour in single crystals of **3a**.

Thus, while **1Cl** exhibits detectable SMM behaviour only in an applied static field, its one-electron oxidation product **3** behaves as a SMM even in zero field. On the other hand, complex **3a** obtained by further one-electron oxidation shows simple paramagnetic behaviour, probably due to the greater Fe···Fe separations and to the lower anisotropy of Fe^{3+}. In both complexes double-exchange mechanisms are expected to be operative among metal centers in different

oxidation states. The presence of both exchange mechanisms will be investigated by theoretical calculations in a future work. Another future perspective is to access tetrairon, one-electron oxidized MV congener of **1Cl**, without rearrangement of molecular structure to give triiron species.

5.10 Experimental Section

5.10.1 Materials and Methods

All synthetic operations were carried out inside an MBraun UniLAB glovebox under an inert and controlled dinitrogen atmosphere, continuously purified over activated charcoal, molecular sieves and a copper dioxygen scavenger (H_2O and O_2 < 1 ppm). All chemicals were of reagent grade and used as received, unless otherwise noted. Dichloromethane was purchased anhydrous. Et_2O was pre-dried over $CaCl_2$,[126] respectively, and subsequently distilled from their sodium benzophenone ketyl solutions before use. All solvents were deoxygenated through three freeze-pump-thaw cycles and stored over 4A molecular sieves. Compound $[Fe_4(tpda)_3Cl_2]\cdot 2.6CH_2Cl_2\cdot 0.84Et_2O$ (**1Cl**$\cdot 2.6CH_2Cl_2\cdot 0.84Et_2O$) was prepared as previously described.[20]

All the characterization data were collected with strict exclusion of dioxygen and water. ESI-MS measurements were conducted on a 6310A Ion Trap LC-MS(n) instrument (Agilent Technologies) by direct infusion of dichloromethane solutions and working in positive ion mode. MALDI-TOF-MS measurements were performed at the University of Wisconsin-Madison with a Bruker ULTRAFLEX™ III instrument (equipped with a SmartBeam™ laser) using a powdery sample finely milled with a large excess of pure anthracene and working in positive ion mode. The *m*/*z* values in the MALDI-TOF-MS spectrum are expressed by setting the isotopic peak of anthracene ($C_{14}H_{10}$) at *m*/*z* = 178.08. The electronic spectrum in dichloromethane solution was recorded up to 2000 nm on a double beam UV-Vis-NIR Jasco V-570 spectrometer, using a quartz cuvette sealed with an airtight Teflon® cap (optical path length *l* = 0.1 cm).

5.10.2 Synthesis of $[Fe_3(tpda)_3Cl]PF_6$ (**3**) and $[Fe_3(tpda)_3Cl]PF_6$ (**3a**)

In order to remove the crystallization solvent, crystals of **1Cl**$\cdot 2.6CH_2Cl_2\cdot 0.84Et_2O$ were dried under vacuum, to give an orange powder (37.7 mg, 0.0350 mmol). At room temperature, the solid was dissolved in 25 mL of CH_2Cl_2 and a blue solution of $FcPF_6$ (10.99 mg, 0.03320 mmol) in CH_2Cl_2 (8 mL) was carefully added dropwise, with stirring, using a dropping funnel. After

few drops of the oxidant were added, the initially red solution rapidly turned into a dark emerald green solution, which was stirred for additional 30 min. The CH_2Cl_2 solution was concentrated to half of its volume in vacuum, and carefully layered with hexanes (~1.5 times by volume). Slow liquid diffusion afforded small dark green crystals of the product, with a cuboidal shape (20.5 mg, 0.0188 mmol, 53.7%). Prismatic or needle-shaped crystals of **3a** were found in erratic amounts. Crystals of **3** were separated from those of **3a** by flotation in CCl_4, and cleaned with few drops of Et_2O. After evaporation of the cleaning solvent under gentle vacuum, they were used for DC, AC and micro-SQUID magnetic characterizations (see **Sections 5.6**, **5.7** and **5.8**). For all the other subsequent characterizations, crystals of **3** (or **3a**) were separated from any powdery residue by flotation, cleaned with few drops of Et_2O and dried under vacuum.

3. ESI-MS (*m*/*z*): 951.2 ($[Fe_3(tpda)_3]^+$, 100); 986.1 ($[Fe_3(tpda)_3Cl]^+$, 98); 581.2 ($[Fe(H_2tpda)(Htpda)]^+$, 12). MALDI-TOF-MS (*m*/*z*): 951.9 ($[Fe_3(tpda)_3+H]^+$, 100); 987.0 ($[Fe_3(tpda)_3Cl+H]^+$, 13). UV-Vis-NIR (CH_2Cl_2, $3.04\cdot10^{-4}$ M): λ_{max} (ε) = 278 nm ($5.75\cdot10^4$ M^{-1} cm^{-1}), 344 nm ($4.34\cdot10^4$ M^{-1} cm^{-1}), 453 nm (sh), 744 nm ($4.49\cdot10^3$ M^{-1} cm^{-1}).

3a. ESI-MS (*m*/*z*): 986.1 ($[Fe_3(tpda)_3Cl]^+$, 100). UV-Vis-NIR (CH_2Cl_2, $7.76\cdot10^{-5}$ M): λ_{max} (ε) = 276 nm ($5.75\cdot10^4$ M^{-1} cm^{-1}), 344 nm ($4.70\cdot10^4$ M^{-1} cm^{-1}), 570 nm ($4.23\cdot10^3$ M^{-1} cm^{-1}), 730 nm ($6.31\cdot10^3$ M^{-1} cm^{-1}).

5.10.3 X-ray Crystallography of $[Fe_3(tpda)_3]PF_6$ (**3**)

Compound $[Fe_3(tpda)_3]PF_6$ (**3**, dataset: *130818NA_11_work3.hkl*) grows as trigonally-distorted cubes, which were measured at 115(2) K on a four-circle Bruker-Nonius X8APEX diffractometer equipped with Mo-Kα radiation (0.71073 Å) and a Kryo-Flex N_2 flow cryostat. The data collection ($<I/\sigma(I)>$ = 11.08) was extended to 0.76 Å resolution and gave a good R(merge) = 0.040 in Laue class $\bar{3}$, consistent with the unit cell metrics. Systematic absences were only those associated to a rhombohedral lattice (extinction symbol R– –), indicating $R\bar{3}$ (centric) and $R3$ (acentric) as possible space groups. Structure solution and full-matrix least-squares refinement on F_o^2 with SIR92[131] and SHELXL-2014/7[132] programs, respectively (both implemented in the WINGX suite [133]), were straightforward and successful in the centric space group. The triiron complex develops around a 3-fold axis, while two independent PF_6^- ions are located with their P atoms (P1, P2) on $\bar{3}$ sites, resulting in an alternation of EMACs and anions along the threefold crystal axis (Z = 6). One of the two PF_6^- ions (P2) lies with two F atoms (F2, F2') on the 3 axis and is consequently disordered. A careful examination of Fourier maps

(Fig. 5.18) around the linear Fe3-F2-P2 array showed a large electron density residual (4.3 eÅ^{-3}) on the 3-fold axis at ca. 0.9 Å from Fe3 towards F2; the electron density of F2 was found distinctly elongated towards Fe3, while P2 had an essentially spherical electron density. This strongly suggests that the Fe3 metal site is disordered over two positions (90.6 : 9.4), with the minority component axially coordinated by a chlorido ligand; therefore, the neighboring PF_6^- ion must be only partially occupied. Disorder on the organic ligand was however unresolvable. All non hydrogen atoms were refined anisotropically, with the exception of Cl atom. Additional restraints were introduced on geometry and displacement parameters of disordered PF_6^- anion using DFIX, SADI and RIGU[183] instructions. Hydrogen atoms were set in idealized positions with isotropic displacement parameters constrained to those of the attached carbon atoms. Crystal data and refinement parameters are available in Table 5.2.

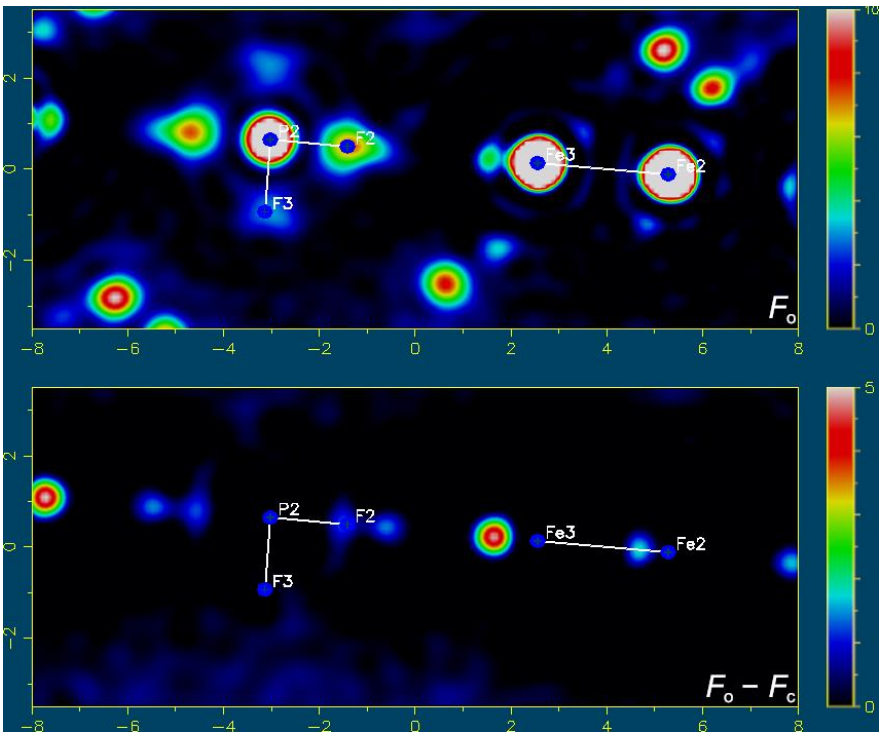

Figure 5.18. Slant Fourier maps on the plane defined by atoms Fe2, Fe3, P2, F2 and F3 (resolution 0.1 Å). The *x* and *y* axis of the maps represents lengths in Å. The color code on the right defines the electron density (in number of electrons). Above (F_o): *F*(observed) map, with phases from *F*(calculated). Below (F_o–F_c): Fourier difference map, with phases from *F*(calculated).

A second data collection on a crystal from a different synthesis (dataset: *truef_a.hkl* from Tobias Rüffer, at the "Institute of Chemistry, Faculty of Natural Sciences, Technische Universität Chemnitz", in Chemnitz, Germany) was carried out at 100(2) K on a Bruker D8 Venture diffractometer equipped with Cu-Kα radiation (1.54178 Å). This new dataset (<I/σ(I)> = 10.02) was extended to 0.81 Å resolution and had R(merge) = 0.040 in Laue class $\bar{3}$. The structure solution (up to 0.85 Å resolution) was performed as described above. It

confirmed the same space group and the disordered Fe3 atom seen in the first data collection (90.3 : 9.7 occupancies). Crystal data and refinement parameters are available in Table 5.2.

5.10.4 X-ray Crystallography of $[Fe_3(tpda)_3Cl]PF_6$ (**3a**)

Compound $[Fe_3(tpda)_3Cl]PF_6$ (**3a**) grows as weakly-diffracting hexagonal green-black rods, which were measured on a Bruker D8 Venture diffractometer equipped with Cu-Kα radiation (1.54178 Å) at 100(2) K, by Tobias Rüffer ("Institute of Chemistry, Faculty of Natural Sciences, Technische Universität Chemnitz", Chemnitz, Germany). The data collection ($<I/\sigma(I)>$ = 4.49) was extended to 0.84 Å and gave a reasonable *R*(merge) = 0.090 in Laue class $\bar{3}m1$, consistent with the unit cell metrics. Systematic absences ($h\bar{h}l$ for odd *l*) pointed clearly to extinction symbol *P*–*c*–corresponding to possible space groups $P\bar{3}c1$ (centric) and $P3c1$ (acentric). Structure solution was straightforward in both space groups using the SIR92 program[131]. Full-matrix least-squares refinement on F_o^2 with SHELXL-2014/7 program[132], implemented in the WINGX suite[133], converged to *R*1 ~ 0.16 in the centric space group, with a triiron complex and a disordered PF_6^- ion both developing around 3-fold axes (*Z* = 4). Residual electron density peaks revealed that the EMAC is itself partially disordered, with about 65% of the chains oriented in one direction and 35% in the opposite direction. However, anisotropic refinement of the minority component proved problematic, with some displacement ellipsoids going non-positive definite. The *R*1 factor was halved working in the acentric space group, with two crystallographically independent EMACs and two PF_6^- ions developing around 3-fold axes. The two triiron molecules are disordered to a significantly different extent (0.81:0.19 for Cl1-Fe1-Fe2-Fe3 and 0.58:0.42 for Cl2-Fe4-Fe5-Fe6). Disorder on the organic ligand was unresolvable. Axial chlorido ligands in neighboring molecules overlap extensively and a split-atom model was preferred. Most non hydrogen atoms were refined anisotropically, but isotropic treatment was applied to: (a) the minority components of Fe1, Fe2 and Fe3, which were refined with a common isotropic displacement parameter (IDP); (b) the minority component of Cl1; (c) both components of Cl2, which were refined with the same IDP; (d) one of the two independent PF_6^- ions; for best refinement, its P atom (P2) was allowed to move from the special position and a common IDP was assigned to its F atoms.

Additional constraints/restraints were introduced on geometry and/or displacement parameters using DFIX, SADI, EADP and RIGU[183] instructions. Hydrogen atoms were set in idealized positions with IDPs constrained to those of the attached carbon atoms. Final

refinement was carried out as a quasi-perfect racemic twin (0.48:0.52). Crystal data and refinement parameters are available in Table 5.2.

5.10.5 Mössbauer measurements

Mössbauer spectra were collected with a 1024 channel See Co model W304 resonant gamma-ray spectrometer using ^{57}Co on Rh foil as a gamma-ray source (obtained from Ritverc Isotope Products) at the University of Wisconsin-Madison. The source velocity range used was ±4 mm/s for each data collection. Inside a glovebox, each sample was mixed with eicosane in the sample holder, to protect it from the reaction with dioxygen and/or water in the air. Each measurement was conducted with the sample under vacuum. Cryogenic temperature measurements were achieved using a Lakeshore model 336 temperature controller in conjunction with a Janis model SHI-850 cryostat.

Mössbauer data were fitted using the WMOSS4F software package.[138] Mössbauer data were fitted with the minimum necessary number of quadrupole doublets, each doublet corresponding to a distinct Fe chemical environment. An adaptive nonlinear least-squares algorithm developed by Dennis *et al.* (available within WMOSS4F) was used to fit each doublet.[139] The parameters fit for each quadrupole doublet were their δ, ΔE_Q, and linewidths, calculated as FWHM. Relative areas were fixed to account appropriately for contributions of given Fe centers within the compounds to the total integration of the area-under-the-curve. Reduced χ^2 values for each fit were used to assess the quality of the fits to the data. The reduced χ^2 is defined as the χ^2 statistic per degree of freedom, where a degree of freedom is defined as the difference between the number of measured datapoints and the number of parameters fit to the data. The reduced χ^2 statistic is given by Eq 4.15.[140]

5.10.6 Magnetic Measurements

Magnetic measurements were made on a Quantum Design PPM cryogenic System with a two-coils susceptometer. DC magnetic measurements were made using extraction magnetometry technique. A polycrystalline sample of **3** (19.36 mg) was admixed with eicosane (17.13 mg), in a White Delrin® sealed bucket holder. The presence of the eicosane was necessary in order to prevent field-induced torqueing at low temperature and to protect the sample from the reaction with dioxygen and/or water in the air. The magnetic response of the sample holder was

previously measured. The diamagnetic contributions of the sample and the mother liquor were evaluated using Pascal's constants.[137] Magnetic susceptibility was obtained as $\chi = M/H$ from magnetization (M) measurements in a static magnetic field H = 10 kOe from 300.0 to 2.0 K. The isothermal field dependence of M was also measured at 2, 4 and 8 K, scanning the field up to 70 kOe. AC measurements were performed using a small oscillating magnetic field of 10.0 Oe for ν between 21 and 9980 Hz. The field dependence of the out-of-phase component of the magnetic susceptibility (χ'') was explored with preliminary scans of χ'' vs ν at 2 K with H in the range from 0 to 2.5 kOe. Afterwards, scans of χ'' vs ν, between 1.95 and 10.0 K were carried out in zero field. Alternatively, the same scans were carried out in a static field of 750 Oe, between 2.1 and 10.0 K. Unfortunately, some of the high-frequency data had to be removed due to self-heating of the sample.

5.10.7 Micro-SQUID Measurements

The micro-SQUID measurements were performed on single crystals of **3** and **3a**. The isothermal M/M_S vs field (M_S = saturation magnetization) hysteresis loops of complex **3** (**3a**) were recorded from 4.5 K to 0.03 K, scanning the field back and forth between −1.0 T and +1.0 T (−1.4 T and +1.4 T), at 8 mT/s. Additional hysteresis loops were recorded on both complexes at 0.03 K, by varying the field-scanning rate from 0.5 to 128 mT/s.

Center piece of the setup is the name-giving micro-SQUID, a DC-SQUID made out of Nb on a sapphire substrate using small constrictions as Josephson Junctions. A low height of 7 nm helps to protect the SQUID against magnetic fields in the plane of the SQUID. The sapphire substrate provides the platform for mounting the investigated sample as well. The process of using electron beam lithography and Reactive Ion Etching as a top-down approach for device fabrication allows for huge flexibility in design, providing easy tuning of the coupling to magnetic objects. The micro-SQUIDs are mounted inside a 3D-vector coil providing the magnetic fields required to manipulate the sample and the feedback loop used for magnetization measurement. The compact design allows for high flexibility in application of the magnetic field in speed and amplitude, while the usage of superconducting NbTi wires and thermalization to the 4 K-stage of the Sionludi dilution cryostat, prevents thermal disturbances. To reach the required cryogenic temperatures, a Sionludi dilution cryostat, developed at the CNRS (*centre national de la recherche scientifique*) in Grenoble, is used for these measurements. For the measurement of magnetization, the switching current I_s of the micro-SQUID is determined in the kHz range using a custom measurement electronic. The periodicity of the I_s dependence on

the external flux through the SQUID loop prevents a simple conversion from I_s to flux, which is proportional to the magnetization of a nearby magnetic object. Therefore, a feedback loop is implemented, which aims to keep the I_s at a constant value. Changes in the external flux due to magnetization changes can be counterbalanced by applying a compensating magnetic field. These compensation fields can be neglected compared to the fields in the plane of the SQUID used to manipulate the magnetic sample, which gets reduced to a 2D plane due to this measurement system. The control of the feedback is done by a ADwin Gold II by Jäger Computergesteuerte Messtechnik GmbH, which provides the interface between the I_s measurement electronic, the current sources for the 3D vector coils and the measurement PC.

5.10.8 Ab-initio Calculations

All the CASSCF/RASSI-SO calculations were performed by Simone Calvello and Alessandro Soncini at the University of Melbourne, using the software Molcas 8.2.[178] To extract the local anisotropy of the *i*-th Fe center, the remaining Fe^{2+} (Fe^{3+}) ions were replaced by diamagnetic Zn^{2+} (Ga^{3+}) ions. For all the calculations the experimental geometry of complex **3** was directly used, without any geometry optimization. In the SEWARD step, we have computed all integrals using the following basis sets: ANO-RCC-PVTZ for Fe, Ga and Zn, ANO-RCC-VTZ for N, ANO-RCC-VDZ for C and ANO-RCC-MB for H. In order to speed up the reading and writing of the electronic integrals, Cholesky decomposition has been employed, with Medium option. In the CASSCF calculations, given the quasi-octahedral coordination environment the two Fe^{2+} ions, we have performed state-averaging among 3 roots for $S = 2$ which would correspond to the $^5T_{2g}$ states, but the wave function for all five $S = 2$ states, thus including ^5E_g, have been computed. All the Fe ions were considered HS, according with Mössbauer spectroscopy measurements. For this reason, we have chosen not to include any $S = 1$ or $S = 0$ states in these calculations. In the CASPT2 step, we have elected to freeze (i.e., avoid including contributions from these orbitals to the electron correlation) only the deep core orbitals (i.e., 1*s*, 2*s*, 2*p* and 3*s* for Fe, 1*s*, 2*s*, 2*p*, 3*s* and 3*p* for Ga and Zn, 1*s* for N and C, and none for H), since they will not provide a significant correlation contribution, and calculated the dynamic correlation for the three $^5T_{2g}$ states. In the RASSI step, finally, the optimized CASSCF states have been mixed through the SO Hamiltonian. In order to include electron correlation from the ligands, we have performed calculations using two different active spaces: CASSCF(6,5)/CASPT2(6,5)/RASSI-SO, where only the five 3d orbitals of the Fe ions are included; and RASSCF(12,16)/CASPT2(12,16)/RASSI-SO, where the occupation of the three

RAS spaces is (i) RAS1: 3p orbitals of Fe; (ii) 3d orbitals of Fe; and (iii) 4d and 5p orbitals of Fe. One additional calculation, RASSCF(14,17)/CASPT2(14,17)/RASSI-SO, in which the 3s orbital was added to the RAS1 space, was attempted but failed to converge for one of the tested system. It has to be noted that CASPT2 calculations require a significant amount of RAM to be performed, and the CASPT2(12,16) calculation already utilized almost the entire RAM available to our virtual machines. For this reason, it would not be feasible to attempt calculations with much larger active spaces than the ones investigated in this work.

5.10.9 Spin Hamiltonian Calculations

The fitting of magnetic data utilized PHI v3.1.5 software.[117] Susceptibility and magnetization data were simultaneously fitted and the minimized quantity was the total residual R defined by Eq. 4.16. Refined parameters were anisotropic coupling constants $J_{\perp,ij}$ and $J_{||,ij}$. For each model, the variables space was surveyed prior to the fit, in order to exclude the presence of additional minima in the R hypersurface. Although magnetic measurements were performed on uncrushed polycrystalline samples restrained in eicosane, the crystals are considered small enough to give rise to a powder average. Therefore, calculated susceptibility and magnetization data were integrated over 377 and 233 different directions, respectively, following the Zaremba-Conroy-Wolfsberg scheme as presented by Levitt (Field Powder 6 and 5 in PHI v3.1.5).[117,148]

Chapter 6

Design of a Novel Tridecadentate Tripodal Ligand and Investigation of its Coordination Chemistry

6.1 Introduction

Chapter 4 and **Chapter 5** report detailed studies of tetrairon(II) and MV triiron chains, supported by $tpda^{2-}$ ligands. The investigated complexes showed very interesting physical properties, such as ferromagnetic interactions and SMM behavior. They proved to be very elusive compounds. For example, in the tetrairon(II) complexes **1Br** and **1Cl** the coordinating ability of the $tpda^{2-}$ ligand, which is capable to coordinate up to 5 metal centers, is not fully exploited. Similarly, one-electron oxidation on **1Cl** failed to afford a MV tetranuclear chain of Fe atoms, since a $FeCl_2$ fragment is expelled to give the MV species $[Fe_2^{II}Fe^{III}(tpda)_3]PF_6$ (**3**).

In order to better stabilize these string-like molecules, the design of a new ligand was taken into account as a possible solution. In 2014, Tereniak *et al.* reported a series of homo- and heterobimetallic complexes containing Fe(II), Co(II) and Mn(II).[109] Varying the structure of an eptadentate tris(amidinato)amine ligand,[184] which formed dimeric complexes (Co_2 and FeCo) with short M−M bonds, they designed and synthesized a new organic ligand, *N*,*N*,*N*-tris(2-(2-pyridylamino)ethyl)amine ($H_3(py_3tren)$), represented in Fig. 6.1. $H_3(py_3tren)$ is constituted by three pyridyl moieties (py), each one attached to a branch of the tren ligand (tren = tris(2-aminoethyl)amine). Upon full deprotonation with benzyl potassium (KBn, where HBn = toluene), py_3tren^{3-} was able to chelate up to two divalent M ions (M^1 and M^2) with its seven available N donors, to give a series of $[M^1M^2Cl(py_3tren)]$ complexes, where Cl^- acts as

an axial ligand towards the external M ion (Fig. 6.1). This series of dinuclear complexes feature short M−M separations (2.287−2.531 Å), and a metal-metal bond in the diiron(II) species. Therefore, $H_3(py_3tren)$ exhibits interesting ligating properties, such as structural rigidity and aptitude in forcing short distances between two M ions placed in its coordination pockets. In addition, its intrinsic threefold symmetry can lead to structurally axial complexes, a feature that preludes well for SMM behavior provided that an easy-axis anisotropy is achieved.

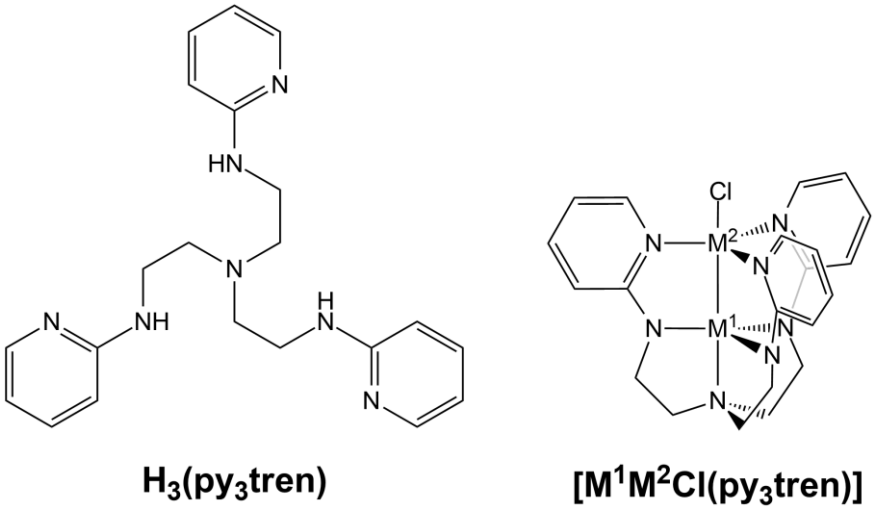

Figure 6.1. Structures of $H_3(py_3tren)$ proligand (left) and of the related dimetallic complexes reported in ref.[109] (right).

Due to its structural and coordinating properties, $H_3(py_3tren)$ was inspirational for the design of a new organic ligand, based on oligo-*α*-pyridylamido units. Since our goal was the stabilization of chain-like complexes with three or more M ions, the design of the appropriate ligand implied extending each branch of $H_3(py_3tren)$ by a NHpy unit, to obtain the $H_3tren(Hdpa)_3$ (H_6L) ligand, as depicted in Scheme 6.1d (L^{6-} = $tren(dpa)_3$).

6.1.1 Synthetic Design of H_6L

Different synthetic patterns towards $H_3(py_3tren)$ are described in Scheme 6.1. This ligand was obtained in a one-step nucleophilic aromatic substitution reaction, by heating under inert atmosphere the tren ligand with an excess of K_2CO_3 and 2-bromopyridine (Brpy) in DMSO (Scheme 6.1a).[109] The product was isolated as a tan solid after purification by silica gel chromatography (yield = 56%). Alternatively, 2-fluoropyridine (Fpy) can be used as electrophile (Scheme 6.1b).[185] Since Fpy is a liquid, the solvent can be avoided here, thus simplifying the synthetic work-up. Moreover, the yield is strongly improved (86%), due to the

higher reactivity of fluorinated pyridines towards nucleophilic substitution. A similar reaction pattern was almost simultaneously reported by Tsai *et al.*, who used Cs_2CO_3 as a base and worked in acetonitrile (Scheme 6.1c).[186] However, this method led to an inferior yield (72%).

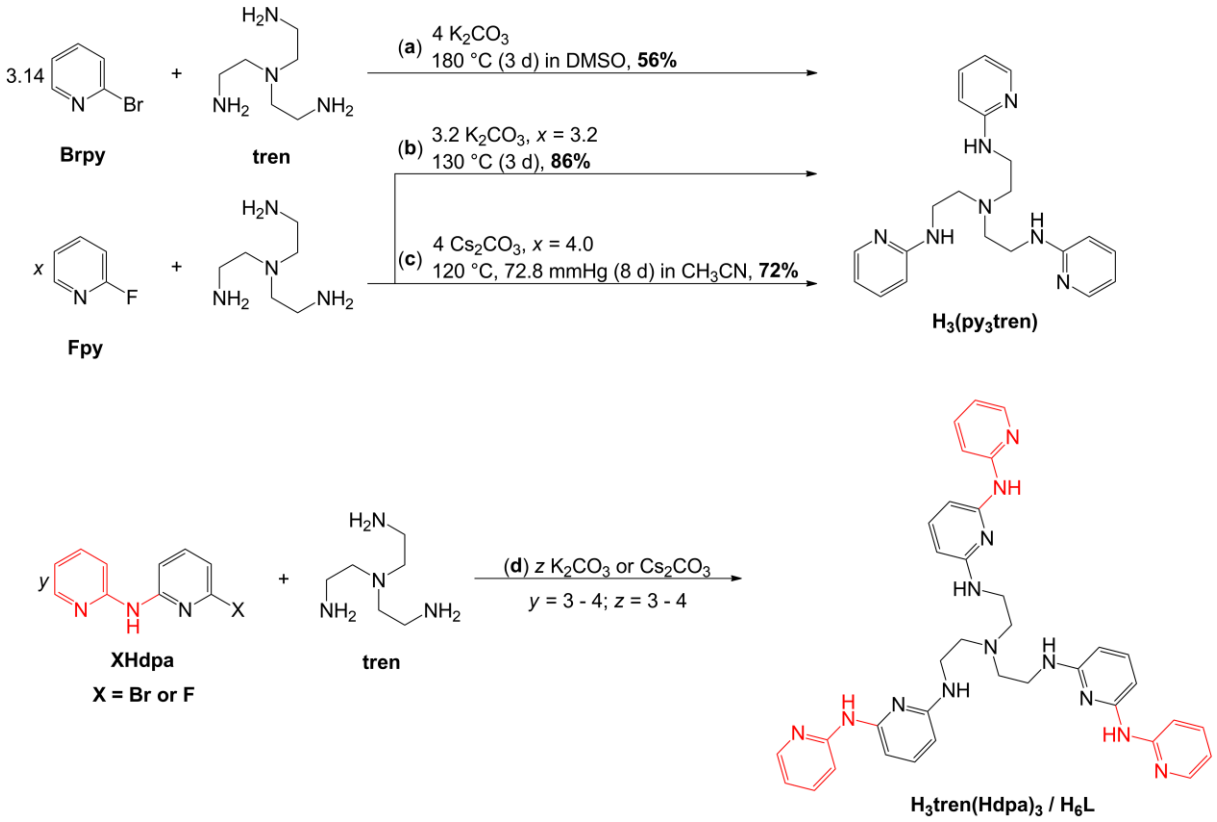

Scheme 6.1. Syntheses of the ligand $H_3(py_3tren)$ (Schemes a,[109] b[185] and c[186]). Scheme d shows a hypothetical reaction path to achieve the novel tripodal ligand H_6L (the experimental conditions are not specified here).

Analogous reactions can be in principle used for the preparation of H_6L. Here, the electrophilic reagent is extended by one −NHpy moiety, to give XHdpa (where X = Br or F) as described in Scheme 6.1d. One of these halogenated substrates, *N*-(6-bromopyridin-2-yl)pyridin-2-amine (BrHdpa), is a well-known molecule.[187,188] On the other hand *N*-(6-fluoropyridin-2-yl)pyridin-2-amine (FHdpa) was not reported prior to this work.

In this Chapter we report an optimized synthetic procedure for H_6L based on full exploration of different reaction patterns and on a comparison of BrHdpa and FHdpa as electrophiles. First, an optimized synthesis of the two halogenated diaminopyridines is presented. They were obtained by nucleophilic substitution reaction of 2-aminopyridine (NH_2py) with 2,6-dibromopyridine (Br_2py) or 2,6-difluoropyridine (F_2py). Even if palladium catalyzed

amination of 2-halopyridines, the so called Buchwald-Hartwig reaction,[189,190] possesses great advantages, it can result in inefficient cross-couplings when N-containing heterocycles are involved.[191] However, this reaction was widely applied in the synthesis of oligo-*α*-pyridylamines and related ligands.[61,192–199] More recently, an improved and Pd-free synthesis of H_2tpda was reported by some of us, which involves the coupling of 2,6-diaminopyridine ($(NH_2)_2$py) and Fpy.[70] This procedure results in a much better yield (~90%) compared to previous reports.[94,97,200,201] Therefore, in this work a metal-free approach was followed for the synthesis of BrHdpa and FHdpa. In particular, while the former was prepared through a slightly modified literature method,[188] the latter was synthesized following the same approach mentioned above for H_2tpda.

6.2 Optimized Synthesis of BrHdpa

The synthesis of BrHdpa was reported by Deng *et al.* in 2014. Under a nitrogen atmosphere, NH_2py, Br_2py, and ^{t}BuOK were heated together (1:1:1.6 MR; MR = molar ratio) in benzene for three days (80 °C). After purification by silica-gel chromatography they obtained the desired product in 65% yield.

In this work, replacing benzene with toluene as a much safer solvent gave the product with the same yield (Scheme 6.2a). The use of a mechanical overhead stirrer was necessary to ensure the homogeneity of the reaction environment, since a very dense solid mass formed around 70 °C. The progress of the reaction was monitored through thin-layer chromatography (TLC) on silica plates (one drop of reaction mixture in 0.5 mL of CH_2Cl_2; eluent Et_2O : *n*-hexane, 1:1; r.f. NH_2py, 0.02; r.f. BrHdpa, 0.31; r.f. Br_2py, 0.55) and ^{1}H NMR spectroscopy in deuterated dimethyl sulfoxide (DMSO-d_6). After evaporation of the solvent, the crude solid reaction product was dissolved in CH_2Cl_2 and washed with water. The organic phase was dried and the solid obtained was purified by silica-gel flash chromatography (FC), to give pure BrHdpa with 65% yield (eluent petroleum ether : Et_2O, further details can be found in experimental **Section 6.9.2**). In an attempt to avoid chromatography, trituration of the crude reaction product in *n*-hexane was attempted. Unfortunately, the triturated solid was shown to contain NH_2py, Br_2py, and BrHdpa in ~2:2:10 MR. Therefore, chromatography proved to be essential in order to obtain a clean product.

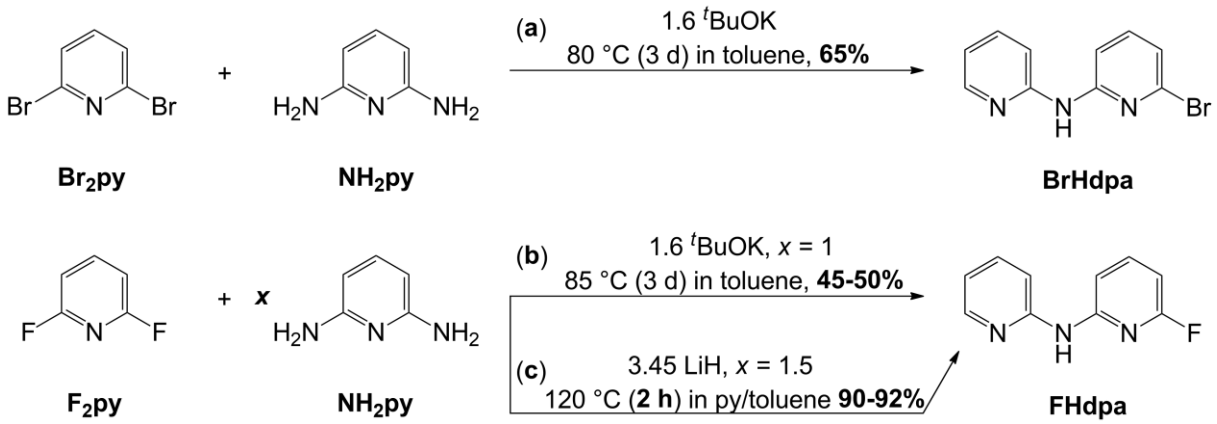

Scheme 6.2. Syntheses of BrHdpa (above, Scheme a) and of FHdpa (below, Schemes b and c).

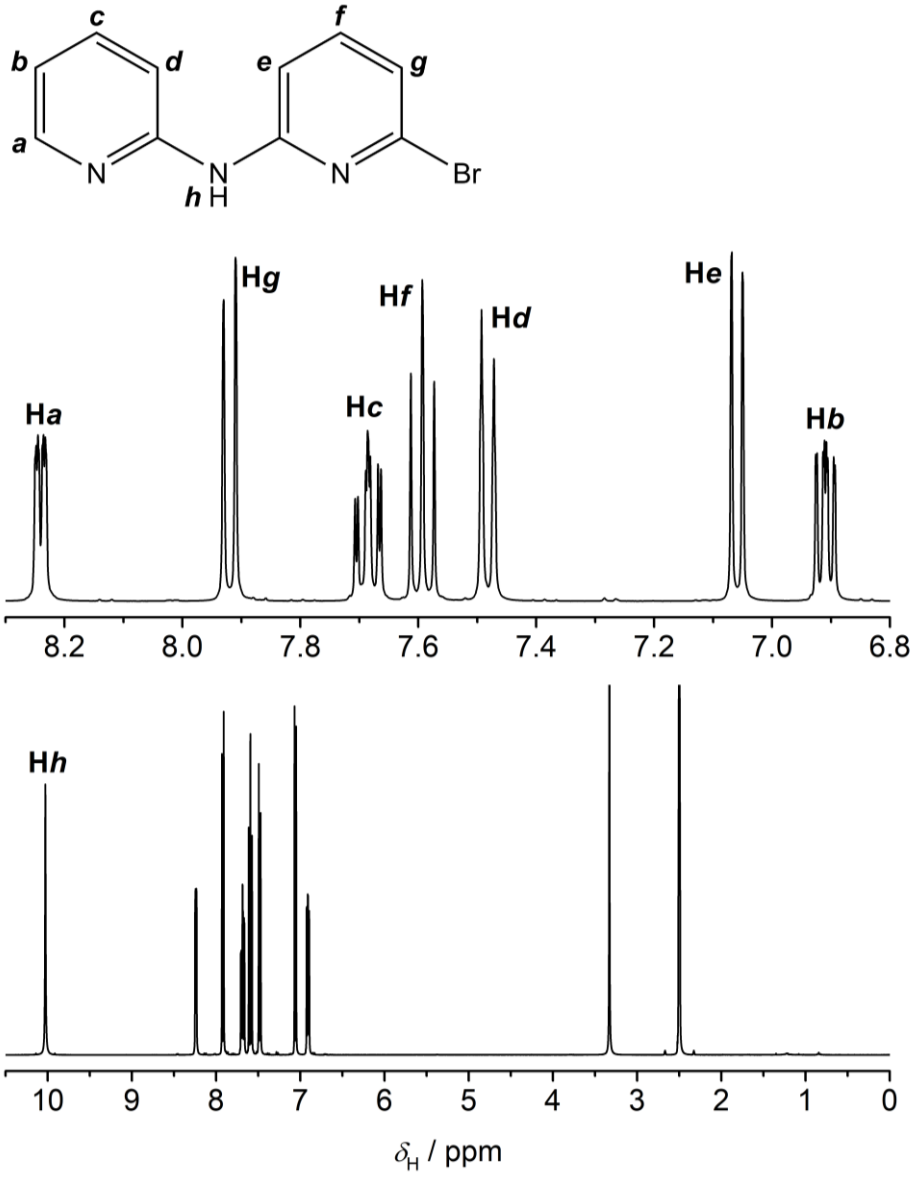

Fig. 6.2. Bottom: ^{1}H NMR spectrum of BrHdpa in DMSO-d_6 (298 K, 400.13 MHz). Top: structure of BrHdpa and magnification of the spectrum between 8.3 and 6.8 ppm. Processing parameters (TopSpin 4.0.6[86]): SI = TD, LB = 0.30 Hz. δ_H (ppm) = 2.50 (residual protons in DMSO-d_6), 3.33 (water, OH, s).

The ^{1}H NMR spectrum of pure BrHdpa in DMSO-d_6 is reported in Fig. 6.2. It presents eight well-resolved signals, with identical integrated intensities. The spectrum highlights the high purity of the product, since no additional peaks are present apart from those of water traces and of residual protons in the deuterated solvent. Because of the high degree of structural similarity between BrHdpa and FHdpa, the assignment shown in Fig. 6.2 is based on the results of an extensive investigation of FHdpa by mono- and bidimensional NMR spectroscopy (see below, **Section 6.3**).

Finally, it is important to notice that another synthetic path for BrHdpa was reported by Bolliger *et al.* in 2011, where Br_2py, NH_2py, and $KN(SiMe_3)_3$ (1: 1.1 : 1.5 MR) were stirred together in 1,4-dioxane for 15 min at room temperature. The authors claim that the product was isolated with 87% of yield after FC. We replicated this synthesis at the beginning of our work, but no significant quantity of BrHdpa was obtained.

6.3 Optimized Synthesis of FHdpa

Two different metal-free pathways for the synthesis of FHdpa were explored in this Thesis. They are compared in Scheme 6.2, where the experimental conditions are detailed.

First, an analogous approach to that employed in the synthesis of BrHdpa (see **Section 6.2**) was attempted (Scheme 6.2b). Here, the higher reactivity of fluorinated vs. brominated pyridines towards nucleophilic substitution was expected to favor the reaction, as described for $H_3(py_3tren)$.[109,185] Mixing NH_2py, F_2py, and $^{t}BuOK$ in a 1:1:1.6 MR afforded initially a "cleaner" reaction environment, since no very dense solid mass formed. As opposed to the synthesis of BrHdpa, the use of a mechanical overhead stirrer could thus be avoided (see **Section 6.2**). Unexpectedly, the reaction proved to be less efficient with F_2py than with Br_2py. In fact, after 80 h of heating in hot toluene (85 °C) conversion was inferior, as was the yield after work-up (~45−50%). The use of a larger excess of base (2.2 equiv) did not lead to any improvement.

Although this procedure showed FHdpa to be synthetically accessible, the yield was not satisfying and a second approach was attempted (Scheme 6.2c). As mentioned in **Section 6.1.1**, the new procedure was inspired by the improved synthesis of the H_2tpda ligand, whereupon

$(NH_2)_2$py and Fpy are reacted in a 1:3 MR in py/toluene solution, using a strong excess of LiH as base.[70] Similarly, NH_2py, F_2py and LiH were here mixed in a 1:1.5:3.45 MR. After only two hours of heating in py/toluene, full conversion of NH_2py into FHdpa was observed. The evolution of the reaction was monitored through TLC on silica plates (one drop of reaction mixture in 0.5 mL of CH_2Cl_2; eluent petroleum ether : Et_2O, 1:1; r.f. NH_2py, 0.02; r.f. FHdpa, 0.26; F_2py is not detectable) and ^{1}H NMR spectroscopy in CD_3CN. After work-up, the pure product was reproducibly obtained with 90−92% yield, corresponding to a twofold increase with respect to previously reported method. However, this synthetic pathway proved to be much more convenient not only in terms of conversion, yield and reaction time. In fact, work-up is much simpler and less time-consuming, since purification by chromatography can be avoided here. The non-reacted F_2py is easily removed under vacuum, while the remaining traces of NH_2py are eliminated through extensive washings with water. The product can be further purified with a filtration on a short silica plug, to afford very pure FHdpa. The assignment of the proton and carbon NMR spectra of FHdpa was based on a detailed characterization by 1D and 2D methods. In particular, the following NMR experiments were performed: ^{1}H, ^{13}C, ^{1}H−^{1}H Correlated Spectroscopy (COSY), ^{1}H−^{13}C Heteronuclear Single Quantum Coherence (HSQC), and ^{1}H−^{13}C Heteronuclear Multiple-Bond Correlation (HMBC). The spectra obtained in the relevant experiments are reported in Figures 6.3−6.6.

The ^{1}H NMR spectrum of pure FHdpa in CD_3CN is reported in Fig. 6.3. It presents eight well-resolved signals, which identical integrated areas. The spectrum highlights the high purity of the product, since no additional peaks are present, apart from those of water traces and of residual protons in the deuterated solvent. Despite the slightly lower solubility of FHdpa in this solvent, CD_3CN was preferred over DMSO-d_6 in order to avoid overlap between the signals of H*c* and H*g* around δ = 7.7 ppm. The protons on the non-halogenated ring (H*a*, H*b*, H*c*, and H*d*) possess the same hyperfine pattern and similar *J*-couplings as in BrHdpa. On the other hand, each of the three proton on the fluorinated pyridine ring (H*g*, H*h*, H*i*) undergoes one significant additional splitting, due to the heteronuclear ^{1}H–^{19}F coupling. A similar situation is observed in the ^{13}C NMR spectrum of FHdpa (Fig. 6.4), where the resonances corresponding to the five carbons of the fluorinated ring (C*f*, C*g*, C*h*, C*i*, and C*j*) are split into doublets by the ^{13}C–^{19}F coupling. Such heteronuclear couplings were crucial for assigning the signals to these five C atoms. The NMR peaks of protons directly bounded to each of them were in turn individuated by HSQC analysis, while the signals of the nuclei in the non-halogenated pyridine ring were assigned by cross-checking the data from all the NMR experiments.

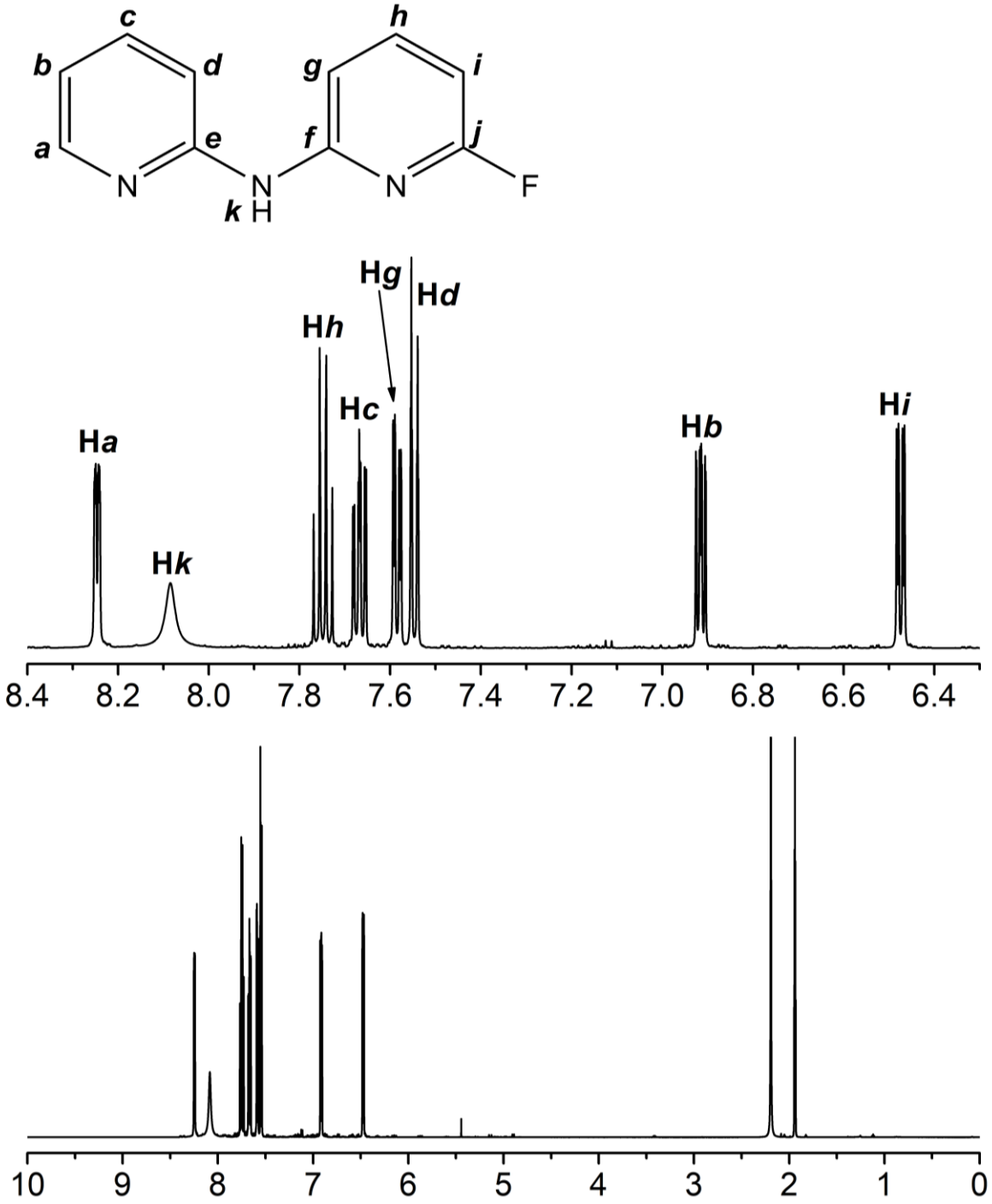

Fig. 6.3. Bottom: ^{1}H NMR spectrum of FHdpa in CD_3CN (298 K, 600.13 MHz). Top: structure of FHdpa and magnification of the spectrum between 8.4 and 6.3 ppm. Processing parameters (TopSpin 4.0.6[86]): SI = TD, LB = 0.30 Hz. δ_H (ppm) = 1.94 (residual protons in CD_3CN), 2.19 (water, OH, s), 5.44 (dichloromethane, CH_2, s).

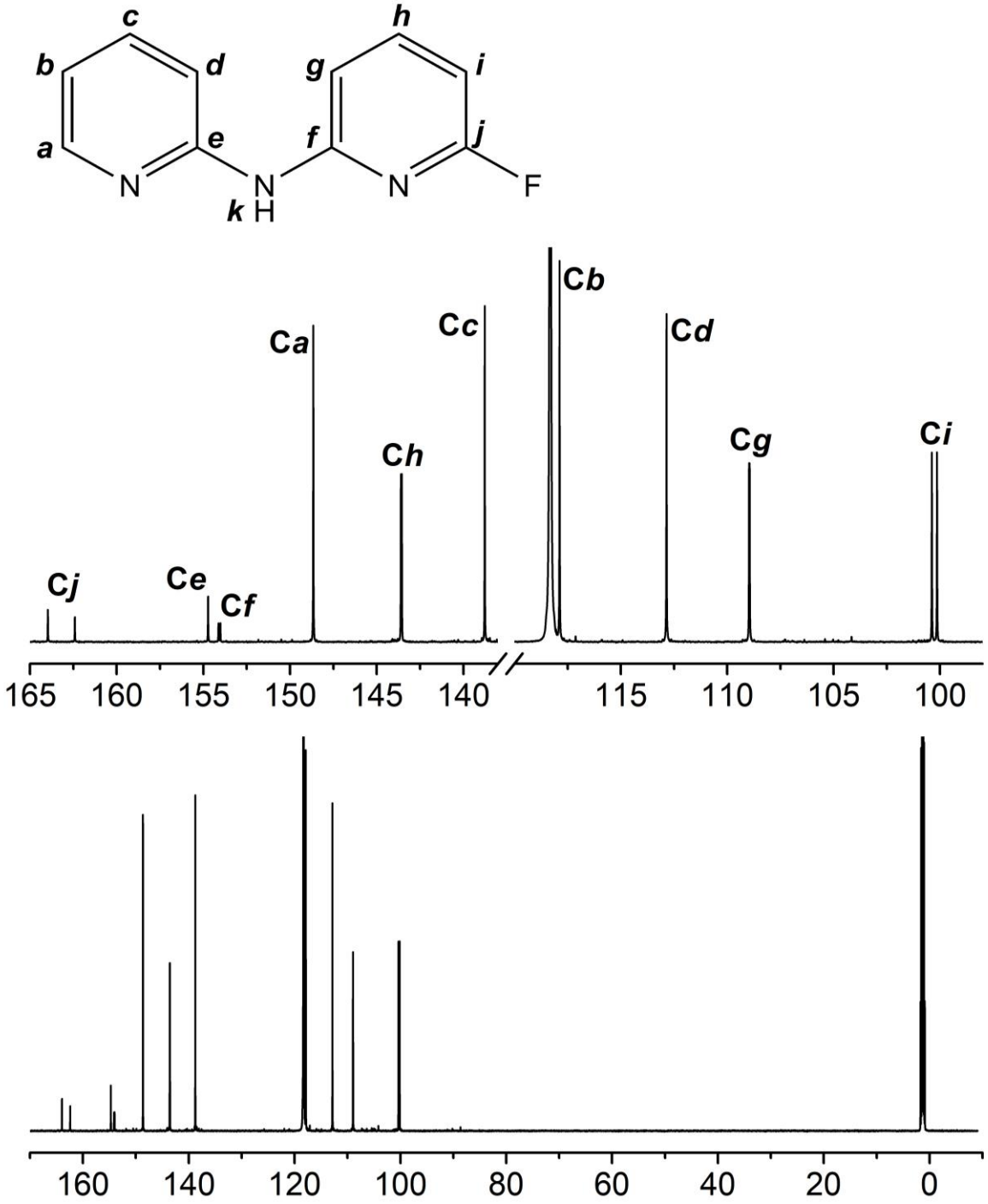

Fig. 6.4. Bottom: ^{13}C NMR spectrum of FHdpa in CD_3CN (298 K, 600.13 MHz). Top: structure of FHdpa and magnification of the spectrum between 165 and 98 ppm (the region from 138 to 120 ppm is not shown since no peaks are present). Processing parameters (TopSpin 4.0.6[86]): SI = TD, LB = 2.00 Hz. δ_C (ppm) = 1.32 (CD_3CN, CD_3, septet), 118.32 (CD_3CN, CN, s).

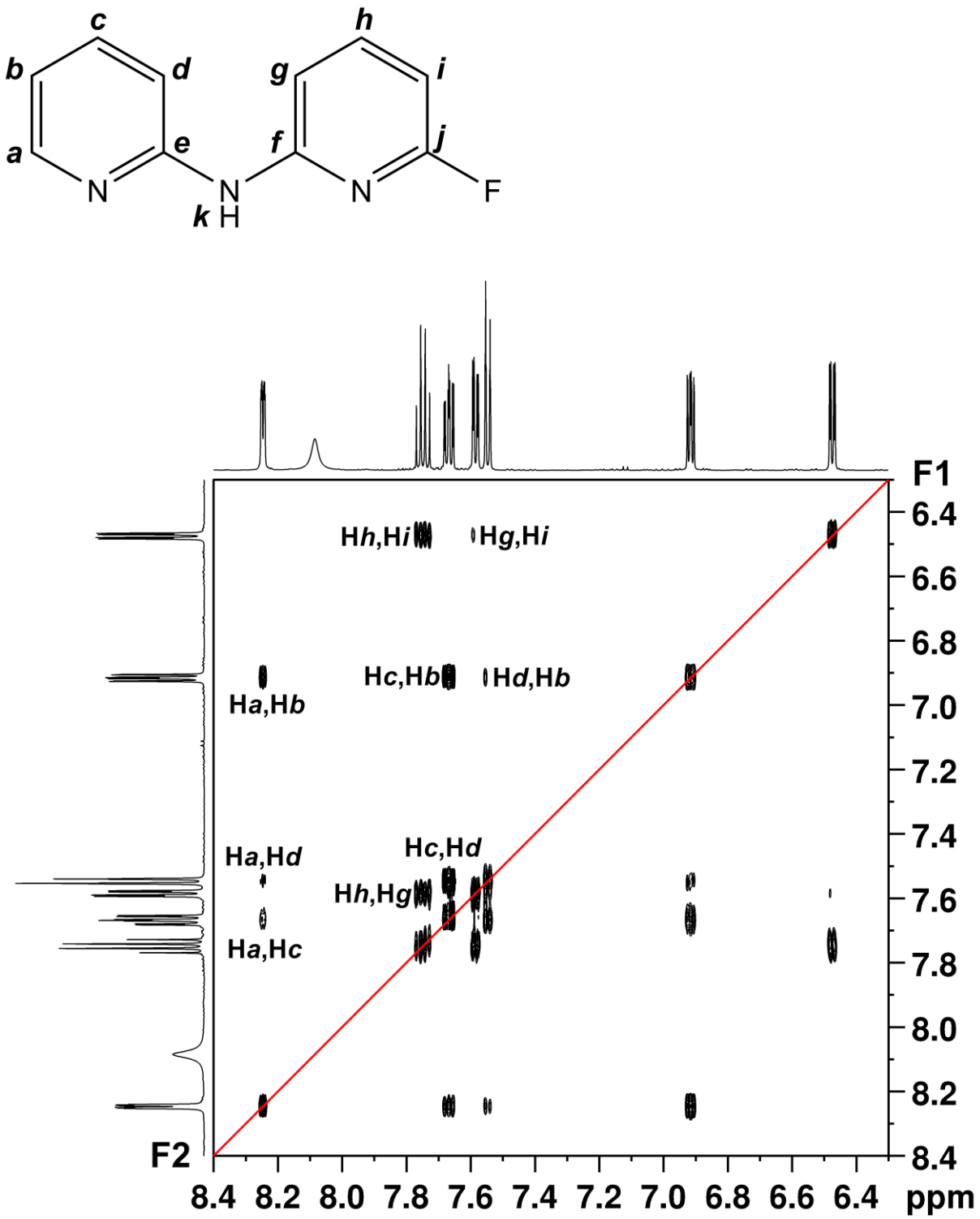

Fig. 6.5. Structure and $^{1}H–^{1}H$ COSY spectrum of FHdpa in CD_3CN between 8.4 and 6.3 ppm (298 K, 600.13 MHz). The labelling of the cross-peaks indicates the $^{1}H–^{1}H$ coupling (F2,F1). The red line highlights the diagonal peaks. Processing parameters (TopSpin 4.0.6[86]) for F2 (*x* axis): SI = TD, LB = 1.00 Hz. Processing parameters for F1 (*y* axis): SI = 2·TD, LB = 0.30 Hz.

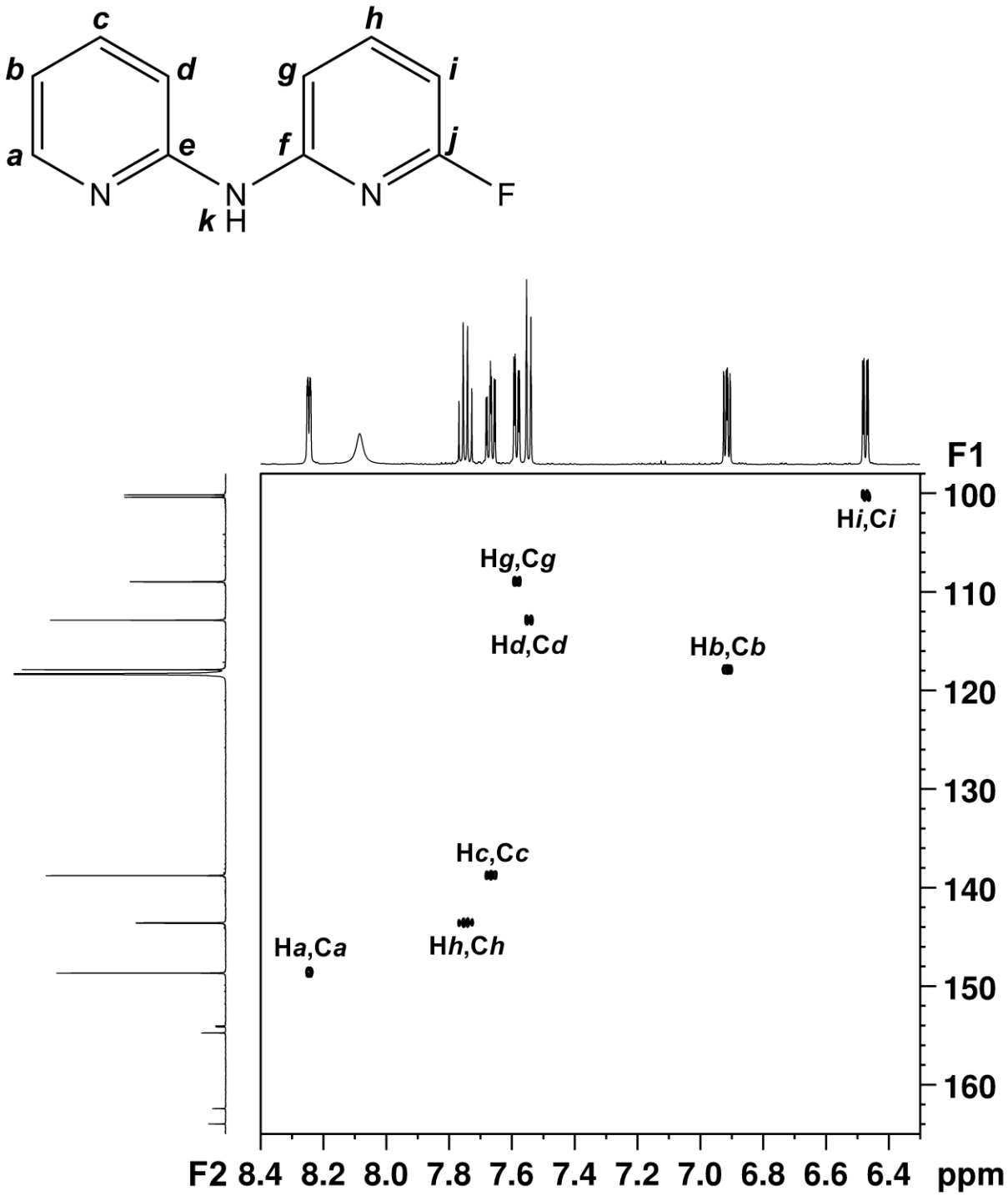

Fig. 6.6. Structure and $^{1}H-^{13}C$ HSQC spectrum of FHdpa in CD_3CN for δ_H = 8.4−6.3 ppm and δ_C =165−98 ppm (298 K, 600.13 MHz). The labelling of the cross-peaks indicates the $^{1}H-^{13}C$ coupling (F2,F1). Processing parameters (TopSpin 4.0.6[86]) for F2 (*x* axis): SI = 2·TD, LB = 1.00 Hz. Processing parameters for F1 (*y* axis): SI = 3·TD, LB = 0.30 Hz.

6.4 Optimized Synthesis of H_6L

As introduced in **Section 6.1.1**, different synthetic pathways were reported for the synthesis of the shorter analogue of H_6L, $H_3(py_3tren)$ (Scheme 6.1). These literature reports were inspirational for the synthesis of H_6L by aromatic nucleophilic substitution, whereupon each of the primary amine terminations of tren replaces the halogen atom of a molecule of XHdpa (where X = Br or F). Both BrHdpa and FHdpa were tested as electrophilic reagents and the base chosen for the reaction was K_2CO_3 or Cs_2CO_3. LiH was also tested as base in one synthetic attempt. All the syntheses were performed under N_2 atmosphere. These synthetic attempts are reported in Scheme 6.3. The evolution of the reactions was monitored through TLC on aluminum oxide cards (one drop of reaction mixture in 0.5 mL of CH_2Cl_2; eluent Et_2O : EtOH, 10:0.4; r.f. tren, 0.00; r.f. H_6L, 0.20; r.f. X_2py, 0.70 for X = F, 0.68 for X = Br) and ^1H NMR spectroscopy in CD_3CN. The work-up procedures used in conjunction with the various synthetic approaches reported below (**Section 6.4.1** and **6.4.2**) are similar to that used in the optimized synthesis of H_6L, which is detailed in the experimental **Section 6.9.4**. In general, it consists in the dissolution of the reaction mixture into CH_2Cl_2, followed by washings with $NaHCO_3$ (saturated solution) and water. The organic phases were then dried over $MgSO_4$ and evaporated under reduce pressure, to give a dark orange solid, which was then purified by gradient FC (basic Al_2O_3, eluent Et_2O : EtOH, from 1:0 to 1:1). In the final optimized procedure FC was replaced by a different purification method (see **Section 6.4.2**).

Before entering into the details of the syntheses of H_6L, it is helpful to present and explain its ^1H NMR spectrum. Despite lower solubility in this solvent, CD_3CN was preferred over DMSO-d_6 to avoid the complete or partial overlap of the signals of aliphatic H atoms with those of water and of residual protons in the deuterated solvent. Moreover, CD_3CN allowed to better separate the signals of H_6L (especially the ones of aliphatic H atoms) from those of the reaction's side-products (see below, **Section 6.4.1** and **6.4.2**). The assignment of the ^1H and ^{13}C spectra was based on a detailed characterization by 1D and 2D NMR spectroscopy (^1H, ^{13}C, ^1H–^1H COSY, ^1H–^{13}C HSQC, and ^1H–^{13}C HMBC), aided by the completely assigned spectra of one of its precursors, FHdpa. The spectra obtained in the relevant experiments are reported in Figures 6.7−6.10. These experiments were performed on a sample of H_6L purified through FC, and synthesized following reaction Scheme 6.3e.

The ^1H NMR spectrum of pure H_6L is reported in Fig. 6.7. It presents nine well-resolved signals with identical integrated areas and whose chemical shift ranges from 5.21 to 8.15 ppm. Seven out of nine of these signals (H*a*, H*b*, H*c*, H*d*, H*g*, H*h*, and H*i*) correspond to the aromatic

H atoms, while the two remaining resonances at δ = 5.21 and 7.77 ppm arise from the amino protons H*k* and H*n*. The high-field region shows one quartet and one triplet which have identical integrated areas but are twice as intense as each of the other nine resonances at $\delta \geq 5.21$ ppm. They correspond to the aliphatic H atoms H*l* and H*m*, respectively. These two signals are both shifted downfield with respect to the triplets of the tren ligand, which are found at δ = 2.40 and 2.61 ppm in CD_3CN.

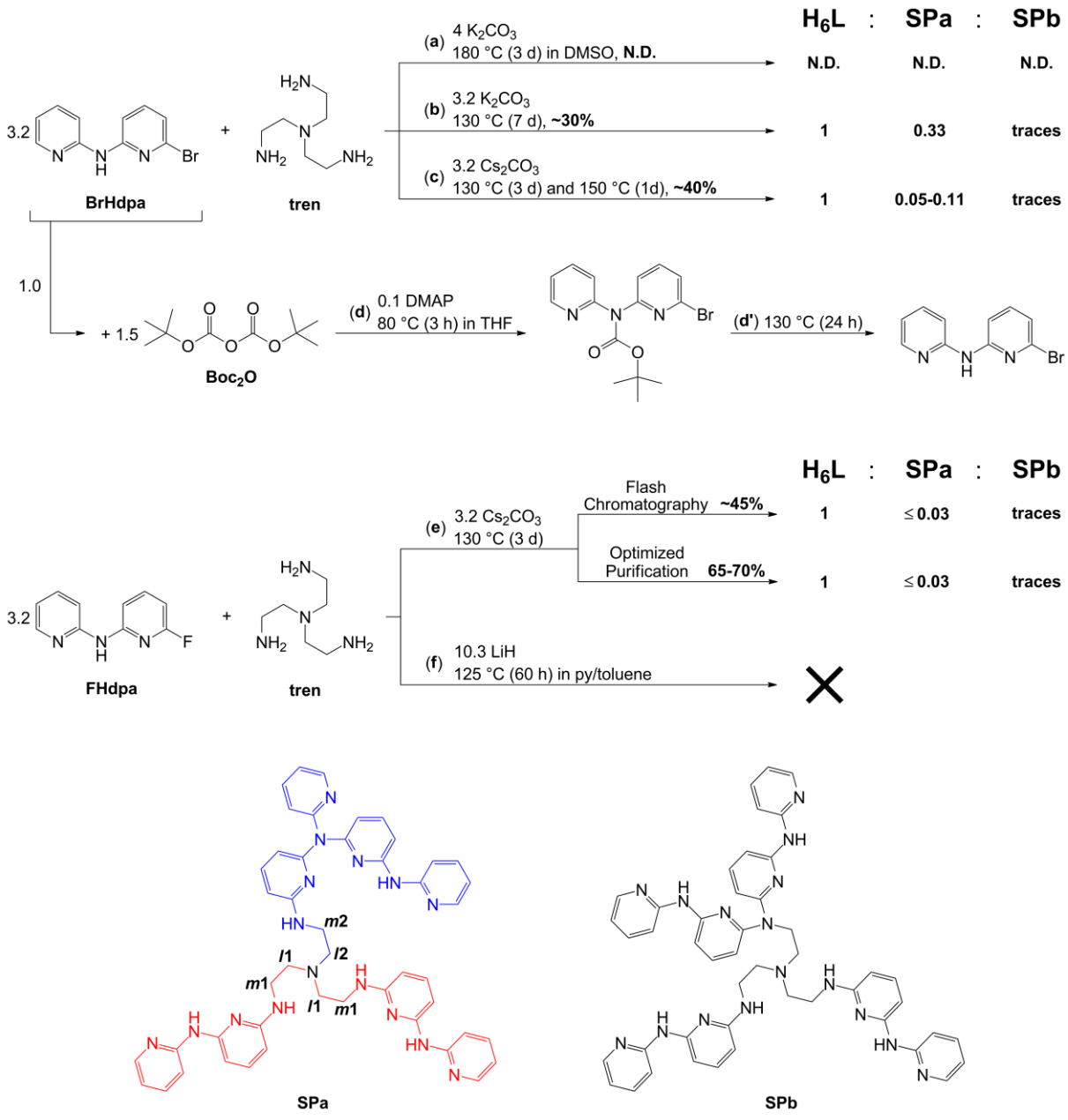

Scheme 6.3. Syntheses of H_6L, starting from BrHdpa (Schemes a, b, c, d and d') or from FHdpa (Schemes e and f). Bottom: structures of the overarylation side-products **SPa** and **SPb**. The red (blue) region of **SPa** generates the ^1H NMR signals marked with red (blue) circles in Fig. 6.11 (below). N.D. = not determined.

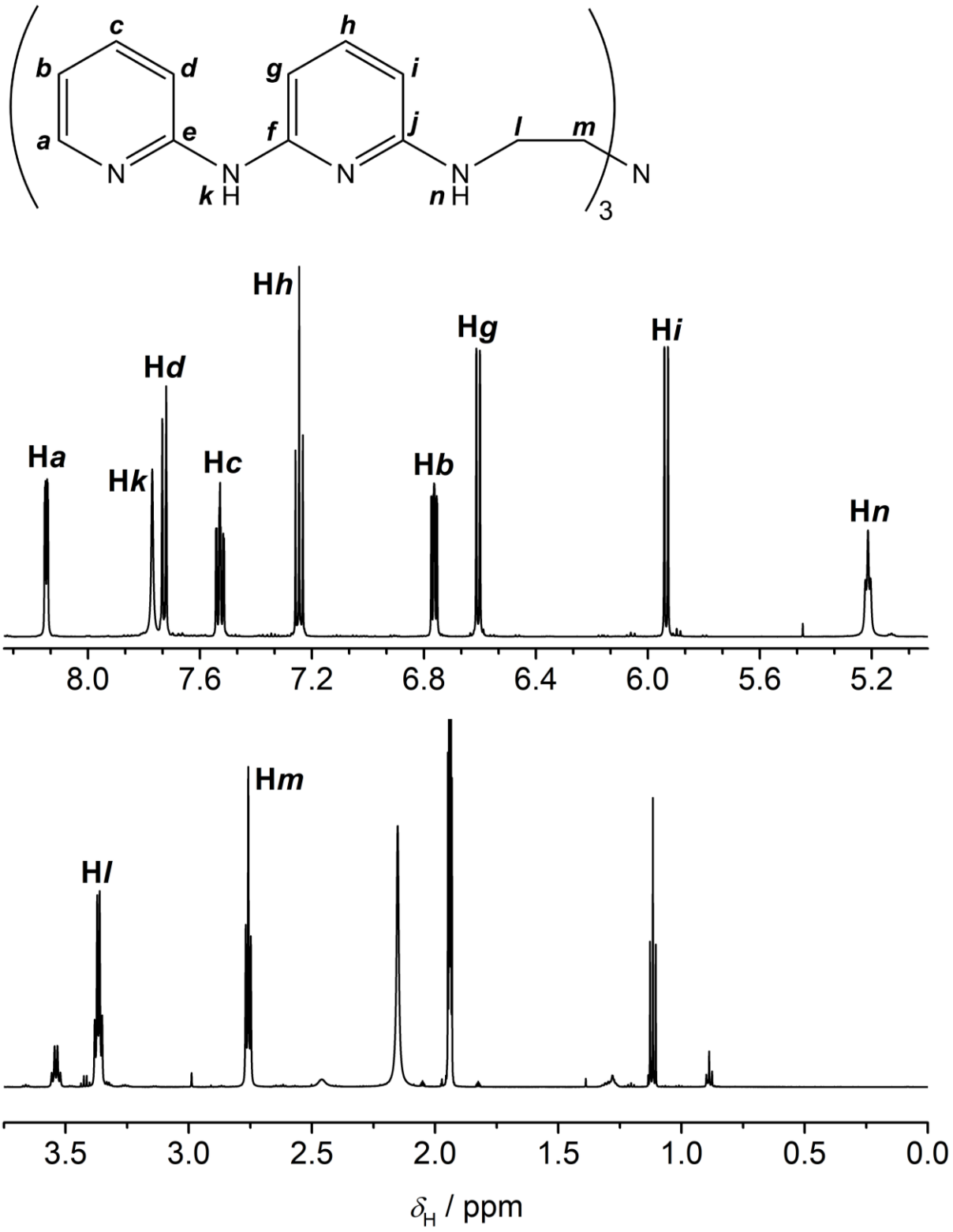

Fig. 6.7. Structure and ^{1}H NMR spectrum of H_6L in CD_3CN (298 K, 600.13 MHz) for δ_H = 3.75−0.0 ppm (bottom) and for δ_H = 8.3−5.0 ppm (top). Processing parameters (TopSpin 4.0.6[86]): SI = TD, LB = 0.30 Hz. δ_H (ppm) = 0.89 (*n*-hexane, CH_3, t, ^3J = 7 Hz), 1.12 (ethanol, CH_3, t, ^3J = 7 Hz), 1.28 (*n*-hexane, CH_2, m), 1.94 (residual protons in CD_3CN), 2.15 (water, OH, s), 2.46 (ethanol, OH, s), 3.54 (ethanol, CH_2, q, ^3J = 7 Hz), 5.44 (dichloromethane, CH_2, s).

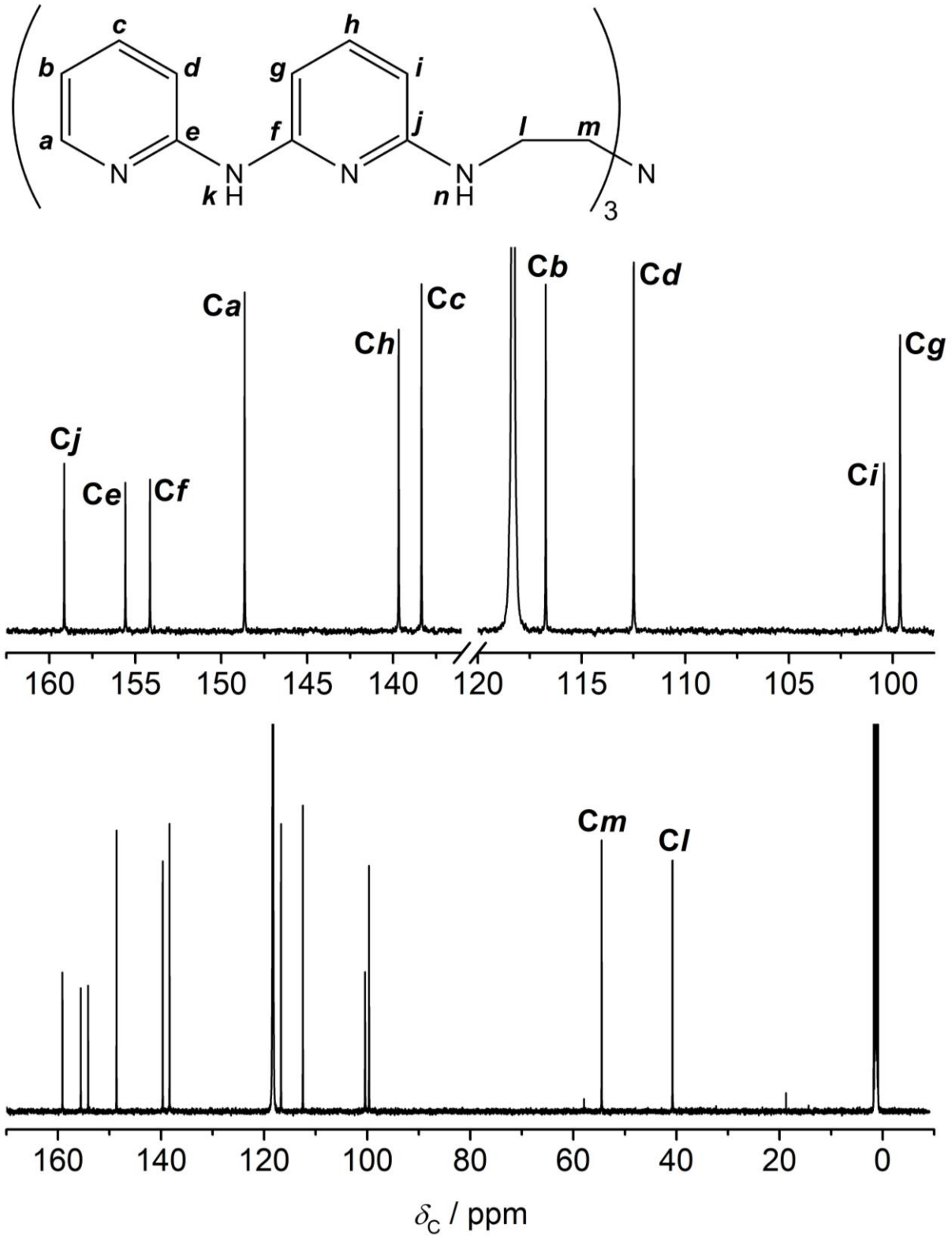

Fig. 6.8. Bottom: ^{13}C NMR spectrum of H_6L in CD_3CN (298 K, 600.13 MHz). Top: structure of H_6L and magnification of the spectrum between 162.5 and 98 ppm (the region from 136 to 120 ppm is not shown since no peaks are present). Processing parameters (TopSpin 4.0.6[86]): SI = TD, LB = 2.00 Hz. δ_C (ppm) = 1.32 (CD_3CN, CD_3, septet), 18.76 (ethanol, CH_3, s), 57.96 (ethanol, CH_2, s), 118.31 (CD_3CN, CN, s).

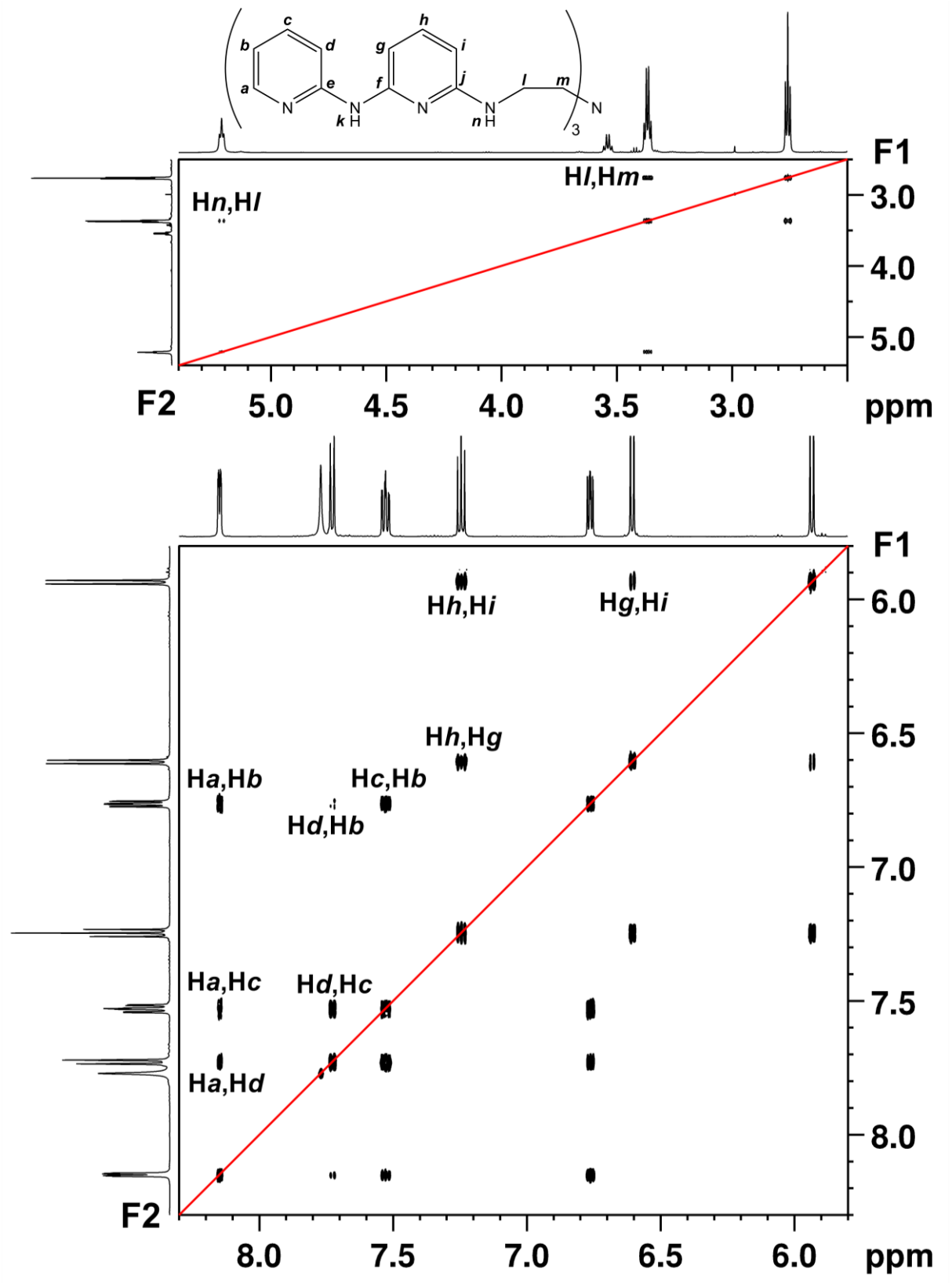

Fig. 6.9. Structure and $^{1}H–^{1}H$ COSY spectrum of H_6L in CD_3CN (298 K, 600.13 MHz) for δ_H = 8.3−5.8 ppm (bottom), and δ_H = 5.4−2.5 ppm (top). The labelling of the cross-peaks indicates the $^{1}H–^{1}H$ coupling (F2,F1). The red line highlights the diagonal peaks. Processing parameters (TopSpin 4.0.6[86]) for F2 (*x* axis): SI = TD, LB = 1.00 Hz. Processing parameters for F1 (*y* axis): SI = 2·TD, LB = 0.30 Hz.

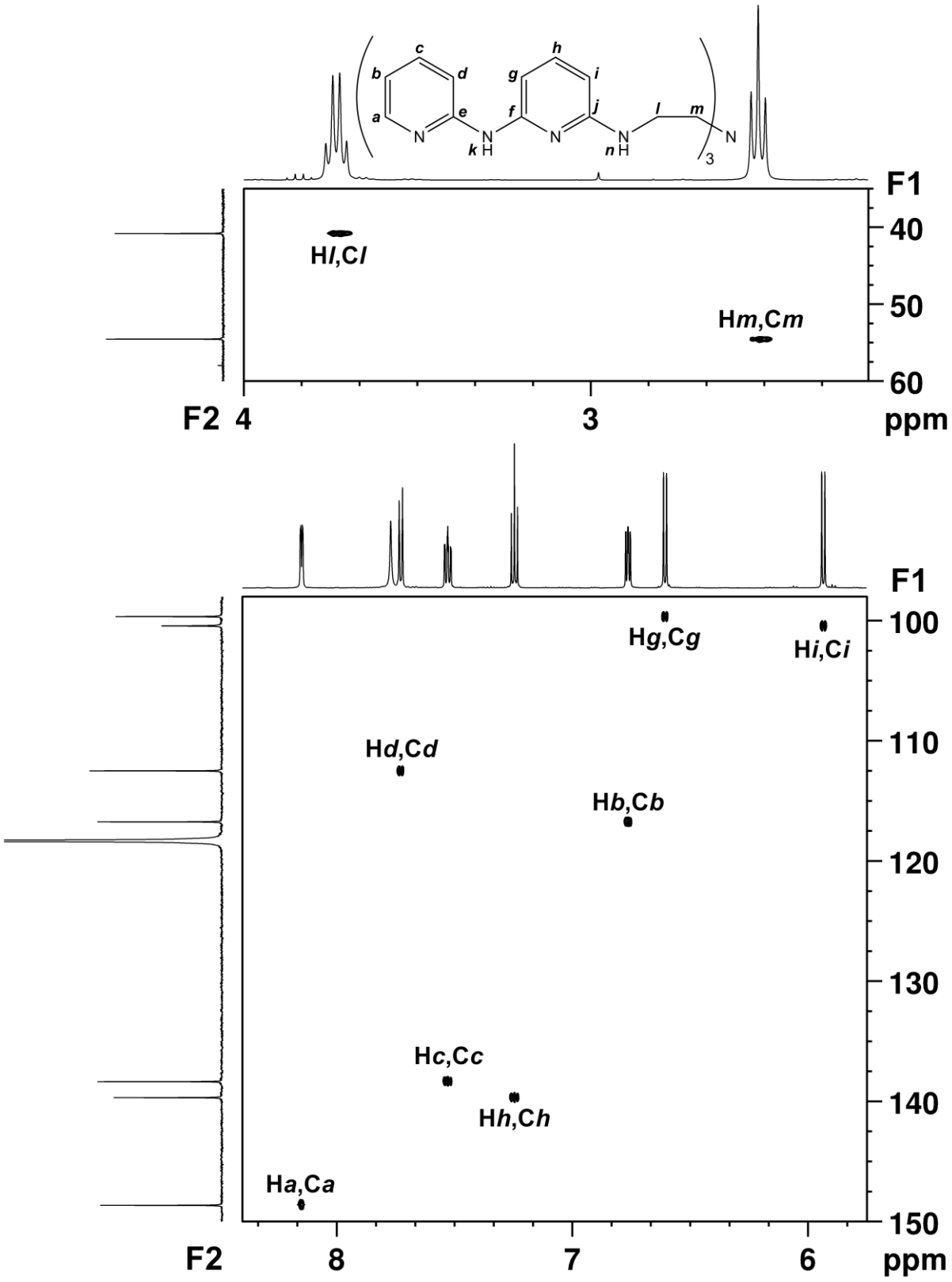

Fig. 6.10. Structure and $^{1}H–^{13}C$ HSQC spectrum of H_6L in CD_3CN (298 K, 600.13 MHz) for δ_H = 8.4−5.75 ppm, δ_C = 150−98 ppm (bottom), and δ_H = 4.0−2.2 ppm, δ_C = 60−35 ppm (top). The labelling of the cross-peaks indicates the $^{1}H–^{13}C$ coupling (F2,F1). Processing parameters (TopSpin 4.0.6[86]) for F2 (*x* axis): SI = 2·TD, LB = 1.00 Hz. Processing parameters for F1 (*y* axis): SI = 3·TD, LB = 0.30 Hz.

6.4.1 Synthesis of H_6L from BrHdpa

The synthesis of H_6L was initially investigated employing BrHdpa as electrophilic reagent. The approach reported by Tereniak *et al.*[109] was first followed, heating at 180 °C tren, BrHdpa and K_2CO_3 in a 1 : 3.2 : 4 MR in DMSO for three days under N_2 atmosphere (Scheme 6.3a). The yellow solution progressively turned black in 10-15 hours. Here, unlike in the synthesis of $H_3(py_3tren)$, one or more side-reactions are likely to occur, since during the work-up we isolated an untractable black material, insoluble in $CHCl_3$ and in water. However, this first attempt demonstrated the formation of H_6L (according to ^1H NMR spectroscopy), although the product was admixed with other unknown species. Moreover, the conversion of BrHdpa into H_6L was low (< 60%).

To improve conversion, and try to limit the occurrence of possible side-reactions, a DMSO-free synthesis was carried out at the lower temperature of 130 °C for three days (Scheme 6.3b), following the reaction scheme reported by Hohloch *et al.*,[185] where Fpy (liquid at room temperature) ensured the homogeneity of the reaction mixture. Similarly, BrHdpa is liquid at 130 °C. In this case, the reaction proceeded without the formation of insoluble black materials. The conversion of liquid BrHdpa into solid products, however, led to a progressive thickening of the reaction mixture and blocked the magnetic stirring bar after 10-15 hours. Despite this, H_6L formed in significant amounts. After work-up and separation from the intermediate bipodal ligand $H_4tren(Hdpa)_2$ by gradient FC, the product was isolated as a yellow oil in ~30% yield. However, NMR spectroscopy showed that the purity of the chromatographed material was unsatisfactory. H_6L was found admixed in a ~3:1 MR with a side-product of the reaction, which co-eluted during the FC purification. This side-product (**SPa**), whose structure is represented in Scheme 6.3, arises from a further nucleophilic substitution reaction between H_6L and BrHdpa. Due to its low symmetry, **SPa** introduces many extra peaks in the ^1H NMR spectrum of the chromatographed mixture (Fig. 6.11). In particular, the spectrum shows a new set of eleven signals, indicated in Fig. 6.11 by red circles, which are similar to those found in H_6L in terms of hyperfine splitting and relative integrated areas, and arise from the two "non-modified" branches of **SPa** (also colored in red in Scheme 6.3). The chemical shifts of seven of these signals are significantly different from those of H_6L, and they were easily identified in the ^1H NMR spectrum. On the other hand, the remaining four are hidden by the corresponding peaks of H_6L (H*a*, H*b*, H*c* and H*h*). However, their presence was clearly demonstrated by 2D NMR spectroscopy analysis ($^1H-^1H$ COSY). The branch of **SPa** undergoing the "extra" nucleophilic substitution (colored in blue in Scheme 6.3) should be responsible for a set of eighteen peaks (indicated in Fig. 6.11 by blue circles). However, in Fig. 6.11 seventeen over

the eighteen expected peaks were detected, and their presence was confirmed by ^{1}H-^{1}H COSY spectroscopy.

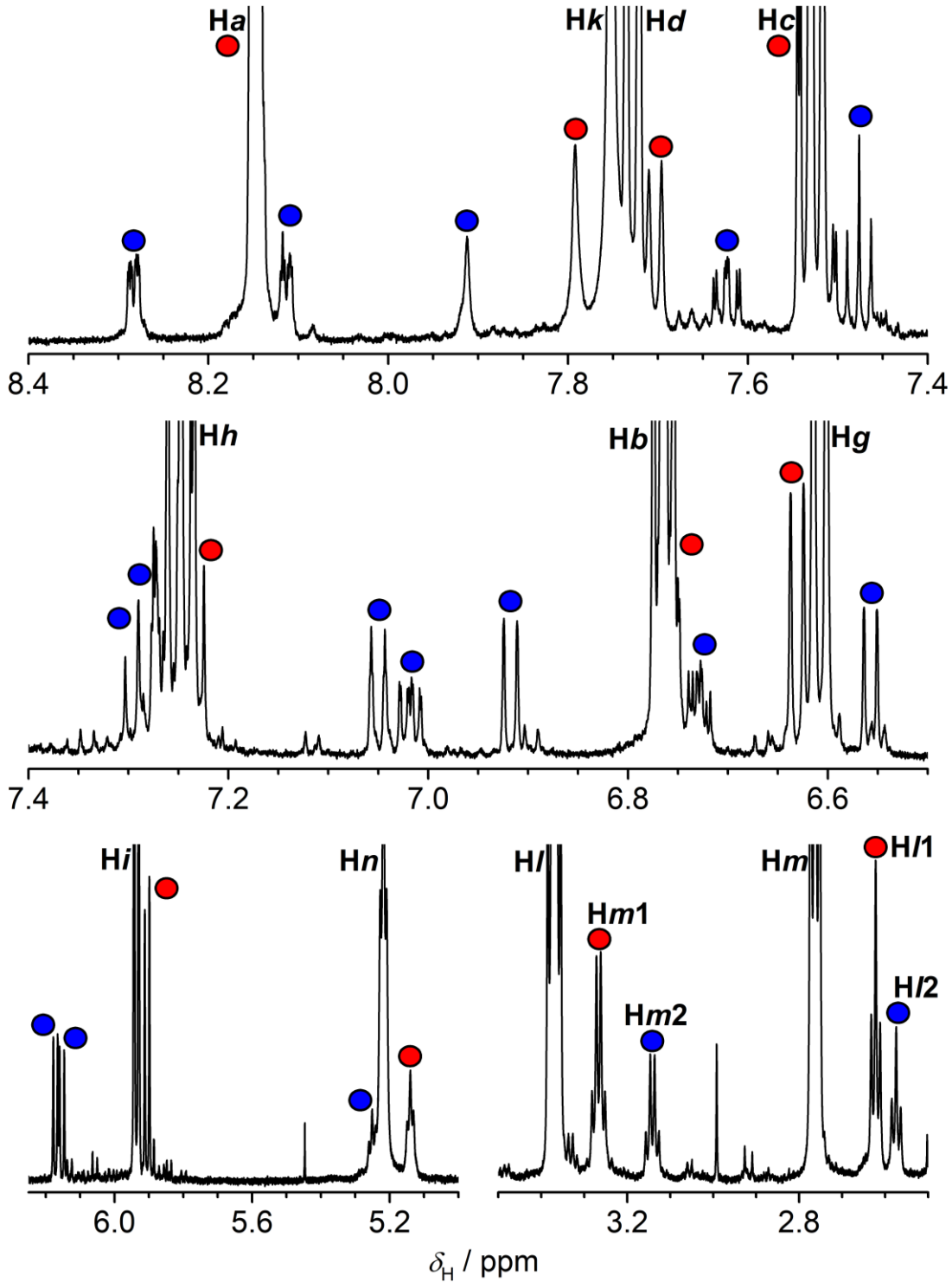

Fig. 6.11. ^{1}H NMR spectrum of the chromatographed mixture containing H_6L and **SPa**, in CD_3CN (298 K, 600.13 MHz), for δ_H = 3.5−2.5 ppm (bottom right), δ_H = 6.25−5.0 ppm (bottom left), δ_H = 7.4−6.5 ppm (middle), and δ_H = 8.4−7.4 ppm (top). The labels show the proton's assignments for H_6L. The red and blue circles indicate the signals originating from the different branches of **SPa**, which are marked with the same colors in Scheme 6.3. Processing parameters (TopSpin 4.0.6[86]): SI = TD, LB = 0.30 Hz.

Unfortunately, due to the complexity of the spectra, the remaining peak was not spotted. This hidden signal is part of a set of sixteen peaks (with identical integrated areas), which arise from fourteen pyridyl and two amino protons. The fifteen spotted peaks are in the correct 1:2 intensity ratio with the nine aromatic signals marked with red circles. The two remaining peaks correspond to the aliphatic H atoms and their integrated intensity is in fact in the expected 2:1 and 1:2 ratio with respect to the fifteen aromatic peaks (sixteen expected) and the aliphatic signals marked with red circles, respectively. All the aliphatic protons of **SPa** were assigned with good confidence, following the same scheme adopted for H_6L, while the assignment of the aromatic resonances is not straightforward due to many overlapping peaks. Therefore, the high-field region is the most informative one to understand which species are present in a sample, and to estimate their MR. For this reason, in the discussion below the ^{1}H NMR spectra were only analyzed and presented between 3.45 and 2.45 ppm.

These NMR spectroscopy findings are in accordance with ESI-MS spectrometry measurements. The ESI-MS spectrum of the chromatographed mixture containing H_6L and **SPa** is shown in Fig. 6.12. Two intense and well resolved peaks are present at m/z = 654.4 (100%) and 823.5 (41%), which are well simulated by the ionic species $[H_6L+H]^+$ and $[H_5L(dpa)+H]^+$ ($[\mathbf{SPa}+H]^+$). The intensity ratio between these two signals (~2.4:1) is lower than observed with ^{1}H NMR spectroscopy (~3:1). However, a minority peak well simulated by $[H_4L(dpa)_2+H]^+$ is well visible at m/z = 992.5 (8%), even if the species $H_4L(dpa)_2$ was not detected in the ^{1}H NMR spectrum of the same mixture. Since NMR is a better quantitative technique than ESI-MS spectrometry, these findings suggest that the signals related to $[H_5L(dpa)+H]^+$ and $[H_4L(dpa)_2+H]^+$ are enhanced by 5−10% here, probably due to ionic collision phenomena.

A possible countermeasure to avoid unwanted nucleophilic substitution side-reactions consists in protecting the secondary amino group of BrHdpa. Tert-butyloxycarbonyl (Boc) was employed here, since it is probably the most common protecting group for primary and secondary amines, and it endures towards basic and nucleophilic attacks.[202] The protection of BrHdpa was carried out with quantitative yield, following a reported literature procedure (Scheme 6.3d).[203] Unfortunately, the protecting group was cleaved at 130 °C over long times and BrHdpa was recovered. Thermolytic deprotection of a Boc-olefin at higher temperature (185 °C) was previously reported,[204] while deprotection of Boc-amines at 100 °C in presence of water is well known.[205,206] Therefore, the deprotection of Br(Boc(dpa)) is likely due to our working temperature and possible traces of moisture in the starting substrate. Since the nucleophilic substitution reaction towards the formation of H_6L does not proceed significantly below 130 °C, this synthetic strategy was abandoned.

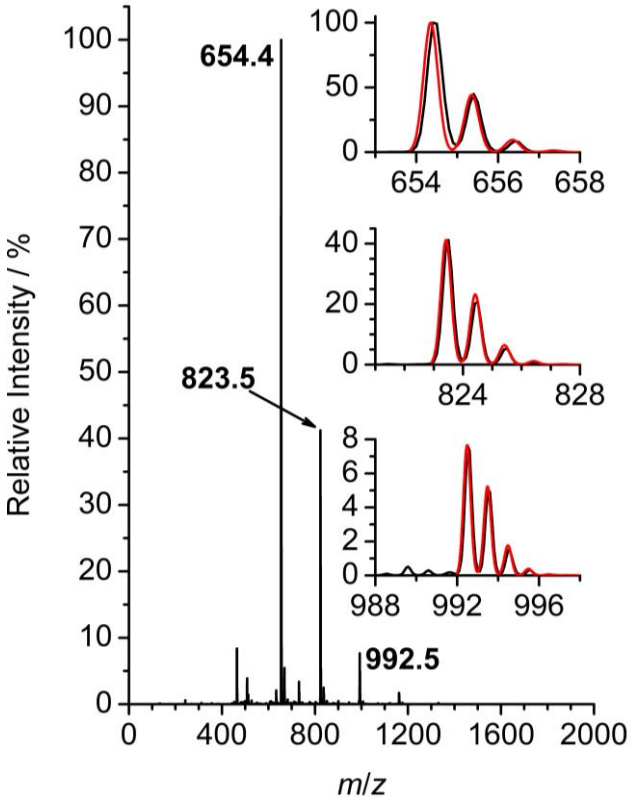

Fig. 6.12. ESI-MS spectrum of the chromatographed mixture containing H_6L and **SPa** (direct infusion, CH_2Cl_2, positive ion mode). The insets shows the experimental (black line) and simulated (red line) isotopic patterns of the peaks at *m*/*z* = 654.4 ($[H_6L+H]^+$), 823.5 ($[H_5L(dpa)+H]^+$) and 992.5 ($[H_4L(dpa)_2+H]^+$). The peak at *m*/*z* = 464.3 (8%) was not assigned.

The solution to this problem was found replacing K_2CO_3 with Cs_2CO_3. In fact, cesium bases such as CsOH, $CsHCO_3$, Cs_2CO_3 and CsF, are known to promote alkylation of primary amines, suppressing overalkylation.[207,208] In particular, these bases eliminate any need of chemical protection, since they possess high chemoselectivity to favor mono-N-alkylation over dialkylation of amines upon reaction with alkyl bromides and alkyl sulfonates. A preliminary investigation was done performing two parallel syntheses, where tren, BrHdpa and X_2CO_3 (1 : 3.2 : 3.2 MR) were heated together at 130 °C for 3 d (reaction **A**: X = Cs; reaction **B**: X = K). The different effect of the two carbonates is evident comparing the ^{1}H NMR spectra of reaction mixtures **A** and **B** (Fig. 6.13). Here, only the high-field region of the spectra is shown, since it contains the most informative and best resolved peaks. Both spectra exhibit the characteristic set of eleven signals of H_6L, which is the main product of the reaction. The second most abundant species is the bipodal ligand H_4tren(Hdpa)$_2$, whose structure is shown on the top of Fig. 6.13. It exhibits two pairs of aliphatic signals, H*l*3-H*m*3 (quartet-triplet) and H*l*4-H*m*4 (triplet-triplet), with H*l*3 extensively overlapping with H*l*. These four peaks (H*l*3,H*m*3,H*l*4,H*m*4) are in a 2:2:1:1 intensity ratio.

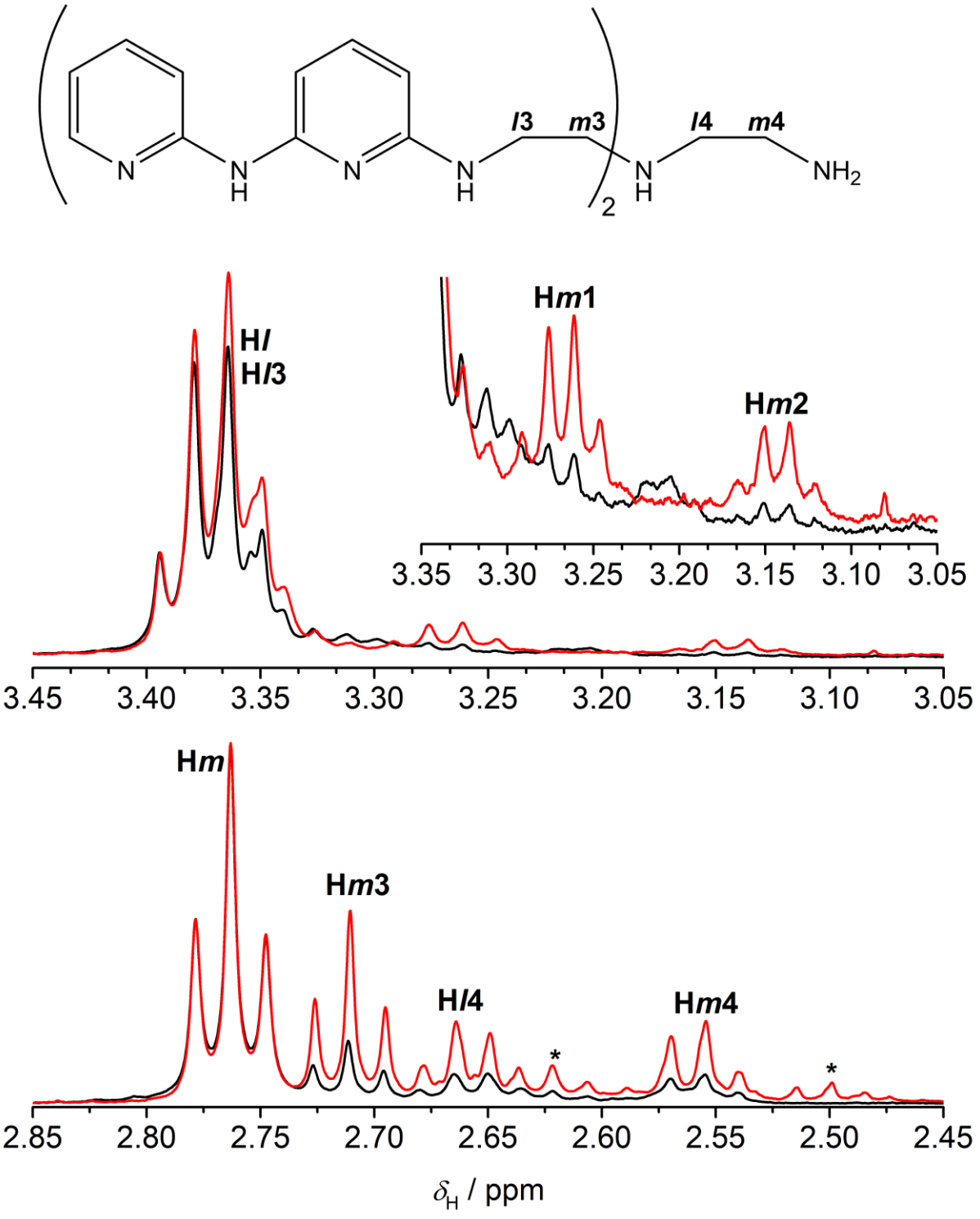

Fig. 6.13. ^{1}H NMR spectra (high-field region) of reaction mixture **A** (black line, Cs_2CO_3 as base), and **B** (red line, K_2CO_3 as base), in CD_3CN (298 K, 400.13 MHz), for δ_H = 2.85−2.45 ppm (bottom) and δ_H = 3.45−3.05 ppm (top). The inset of the top panel shows a magnification of the spectrum between 3.35 and 3.05 ppm. The intensities of the two spectra were normalized with respect to H*m* (δ_H = 2.76 ppm). The structure of the bipodal ligand, H_4tren(Hdpa)$_2$, is shown at the top of the Figure. H*m*1 and H*m*2 arise from **SPa**. The very weak peaks marked with the asterisks arise from the monopodal ligand, H_5tren(Hdpa). Processing parameters (TopSpin 4.0.6[86]): SI = TD, LB = 0.30 Hz.

SPa is also present as impurity, and its two aliphatic quartets (H*m*1 and H*m*2) are well visible in the spectra, while H*l*1 and H*l*2 (triplets) are hidden by other signals. From Fig. 6.13 it is evident that the MR between H_6L and H_4tren(Hdpa)$_2$ is much higher when Cs_2CO_3 is used (reaction **A**), reflecting a more efficient conversion into the desired product. Furthermore, these conditions yield a significantly smaller amount of **SPa**, which is only present in trace quantities in the spectrum of mixture **A** (Fig. 6.13, inset, black line). It is worth to note that the two spectra also feature some very feeble aliphatic signals, which are likely to arise from a second side-product, probably **SPb** (see Scheme 6.3) and from the monopodal ligand, H_5tren(Hdpa). However, their protons could not be assigned, since the corresponding aromatic signals were never found with detectable intensity. In any case **SPb** and H_5tren(Hdpa), if present, can be considered trace impurities.

Tren, BrHdpa and Cs_2CO_3 (1 : 3.2 : 3.2, Scheme 6.3c) were thus heated at 130 °C for three days and afterwards at 150 °C for 1 day. After work-up and purification by FC, H_6L was isolated as a yellow oil with ~40% yield, and in 90−95% purity. Therefore, the replacement of K_2CO_3 with Cs_2CO_3 not only inhibits undesired side-reactions, but also increments the yield by ~10%. Moreover, the non-occurrence of side reactions was proven up to 150 °C, allowing shorter reaction times (4 d) than with K_2CO_3 (7 d) (Scheme 6.3b).

In conclusion, the tripodal ligand H_6L was synthesized from tren, BrHdpa and Cs_2CO_3 with decent conversion, good yield and purity. However, as described in the next Section, the synthetic procedure was strongly improved using FHdpa as arylating agent, and replacing FC with a simpler purification method.

6.4.2 Synthesis of H_6L from FHdpa

Since fluorinated electrophiles are usually more reactive than brominated ones towards nucleophilic substitution reactions, the new compound FHdpa was synthesized (see **Section 6.3**) and tested as substrate for the synthesis of H_6L. Here, the optimized conditions of the reaction with BrHdpa were employed. Therefore, tren, FHdpa and Cs_2CO_3 (1 : 3.2 : 3.2 MR) were heated together at 130 °C for three days (Scheme 6.3e). In Fig. 6.14, we compare the ^{1}H NMR spectra of the crude reaction mixtures obtained from the syntheses described in Schemes 6.3c and 6.3e. It is clear that much smaller amounts of overarylated side products **SPa** and **SPb** are formed when the fluorinated electrophile is used. Additionally, the reaction with FHdpa does not proceed any further after 3 days at 130 °C and the procedure is thus faster than with BrHdpa. After work-up and purification by FC, H_6L was isolated in ~45% yield, which is

slightly higher (5%) than with BrHdpa. The same yield was reproducibly obtained in two different syntheses.

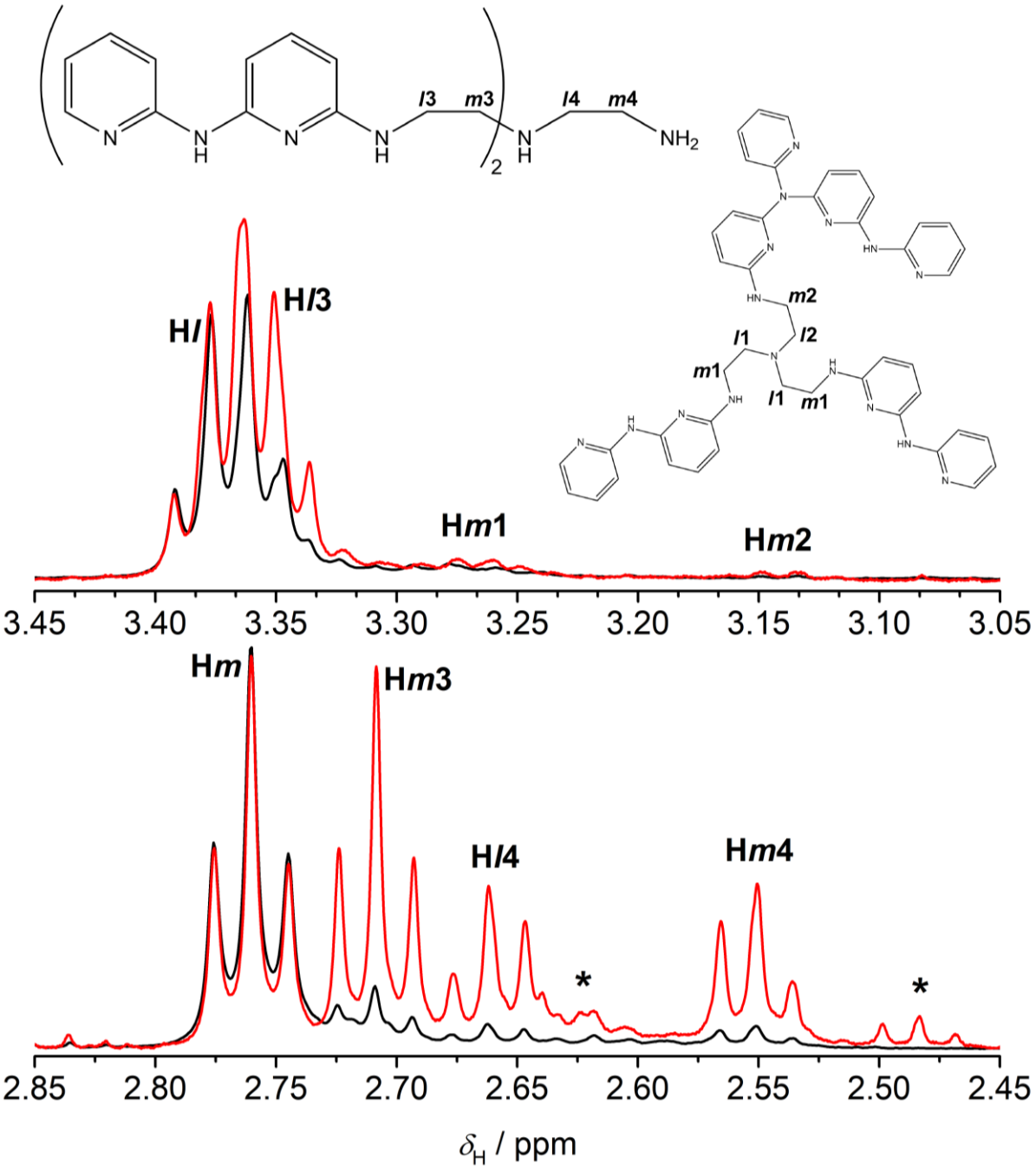

Fig. 6.14. ^{1}H NMR spectra (high-field region) of the reaction mixtures from syntheses 6.3e (black line, FHdpa as substrate), and 6.3c (red line, BrHdpa as substrate) after 3 d at 130 °C, in CD_3CN (298 K, 400.13 MHz), for δ_H = 2.85−2.45 ppm (bottom), δ_H = 3.45−3.05 ppm (top). The intensities of the two spectra were normalized with respect to H*m* (δ_H = 2.76 ppm). The structures of H_4tren(Hdpa)$_2$ (top left) and of **SPa** (top right) are shown at the top of the Figure. The very weak peaks marked with the asterisks arise from H_5tren(Hdpa). Processing parameters (TopSpin 4.0.6[86]): SI = TD, LB = 0.30 Hz.

The ^{1}H NMR spectrum of the isolated product (Fig. 6.7) indicates good purity of H_6L, with a total molar fraction of the overarylated side-products (**SPa** and **SPb**) ≤ 3%. The superior quality of the product is endorsed by its physical state, a beautiful lightweight yellow solid, compared to the oils obtained in the previous syntheses (see **Section 6.4.1**). Unfortunately, despite many attempts we were unable to grow XRD-quality crystals of H_6L.

Since H_6L is a polyamine, during the purification by FC its chromatographic band undergoes strong broadening and streaks along the column. This leads to an important loss of product, which is retained by the stationary phase at the end of the process. Moreover, after evaporation, the elution solvents are easily retained by the product. In particular, 0.44 molecules of EtOH were reproducibly detected per molecule of H_6L, as shown in Fig. 6.7. The main goal of this purification is the separation of H_6L from unreacted FHdpa, from H_4tren(Hdpa)$_2$, and from possible traces of H_5tren(Hdpa). Due to their free $-NH_2$ moieties H_4tren(Hdpa)$_2$ and H_5tren(Hdpa) do not run over Al_2O_3 or SiO_2. Therefore, to avoid the FC, a simple filtration over a very short silica plug (~2 cm high) was performed after the work-up. Silica was preferred over basic aluminum oxide, since in the latter case the separation was not complete. Afterwards, a 24 h trituration in Et_2O was carried out at room temperature, to remove all the unreacted FHdpa, which is very soluble in these conditions. After a further trituration in *n*-hexane (2 h, room temperature), the product was isolated as a yellow powder in 65−70% yield. H_6L is only slightly soluble in Et_2O, and insoluble in *n*-hexane. Therefore, the loss of product is much lower here, compared to the FC process, and explains the much higher yield. Rewardingly, the ^{1}H NMR purity is not worse than that of the chromatographed material. Considering that three nucleophilic substitutions must occur to give H_6L, the total yield of the reaction is quite high, since it reflects an efficiency of 87−89% for each nucleophilic attack. It is worth to note that all the reported yields are underestimated, since a fraction of tren unavoidably escapes from the reaction flask, during the first hours of reaction.

Finally, since the optimized procedure for the synthesis of FHdpa (Scheme 6.2c) and H_2tpda[70] gave excellent results, it was mandatory to test it for the synthesis of H_6L. Unfortunately, heating tren, FHdpa and LiH (1 : 3.2 : 10.3 MR) in py/toluene (125 °C, 60 h), did not lead to the formation of H_6L (Scheme 6.3f). This synthetic path is probably effective only for the arylation of aromatic amines and was thus abandoned.

6.5 Acid Properties of H_6L

The acid-base properties of the novel tripodal ligand, H_6L, were investigated through UV-Vis-NIR spectroscopy. A THF solution of the ligand was titrated through consecutive additions of a THF solution of ^{t}BuOK. The electronic spectra of H_6L before and upon deprotonation are presented in Fig. 6.15.

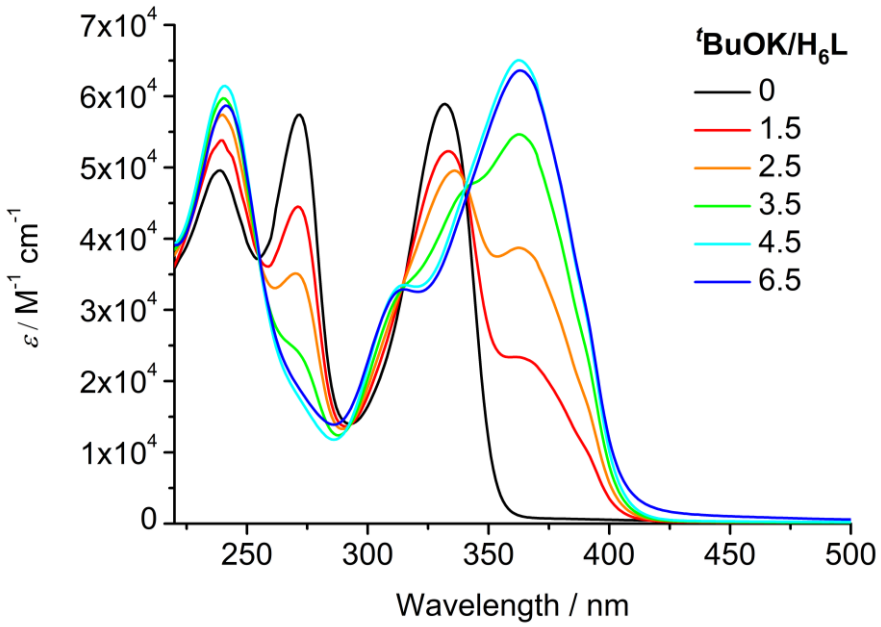

Figure 6.15. UV-Vis-NIR spectrum of a THF solution of H_6L before (black line) and after (colored lines) subsequent additions of ^{t}BuOK (THF solution). The legend shows the MR between ^{t}BuOK and H_6L at each step of the titration. All the spectra were recorded up to λ = 1000 nm, but only the characteristic portion of them is reported here.

The electronic spectrum of the tripodal ligand exhibits three very intense absorption bands with λ_{max} = 239, 272 and 332 nm. Upon deprotonation with ^{t}BuOK, a new intense band with λ_{max} = 363 nm progressively appears, along with a much weaker one around 313−314 nm, which is not well-resolved. Simultaneously, the original bands at 272 and 332 nm decrease in intensity, with the latter undergoing a small red-shift, until they completely disappear. Contrariwise, the most energetic band of H_6L (239 nm) increases in intensity during the titration. Since the addition of 4.5 or 6.5 moles of base per mole of H_6L gave essentially the same spectrum, ^{t}BuOK is clearly unable to remove six NH protons per molecule. Furthermore, the two isosbestic points at λ = 255 and 340 nm indicate that upon addition of ^{t}BuOK the solution contains only two different chromophores in equilibrium with each other. Most likely, these are the Hdpa-like branch of the ligand and its conjugated base obtained upon removal of the aromatic secondary amine proton H*k*, which is certainly more acidic than H*n* (see Fig. 6.7). The final product of the

titration is thus the triply deprotonated form of the ligand, H_3L^{3-} (or K_3H_3L). It is important to note that a stoichiometric amount of base is not sufficient to remove the three H*k* atoms, since the deprotonation process only reaches completeness with 3.5−4.5 moles of ^{t}BuOK per mole of H_6L. From the value of ε_{336} as a function of the ^{t}BuOK : H_6L MR, we estimate that a MR of ~4:1 is necessary for the virtually complete removal of H*k* atoms.

In order to achieve full deprotonation of H_6L to give L^{6-} a stronger base is probably needed. A good candidate is represented by KBn, which was employed for the deprotonation of $H_3(py_3tren)$.[109] Unfortunately, but not surprisingly, the instability of KBn at room temperature in THF over short times made it impossible to study the acid properties of H_6L through UV-Vis-NIR analysis.

6.6 Coordination Chemistry of H_6L: Co(II)

The new tripodal ligand was designed and synthesized with the aim of better stabilizing chain-like structures containing 3−5 metal centers, with particular interest towards the synthesis of new iron(II)-based EMACs. Preliminary studies of the coordination chemistry of H_6L were however conducted using Co^{2+}. This metal ion was chosen because it is a better UV-Vis chromophore and is also "easier to handle" as compared with Fe^{2+}. For instance, it possesses lower tendency to undergo oxidation and/or hydrolysis processes. All the syntheses and the procedures discussed below were nevertheless executed inside a glovebox, in a strictly anaerobic and anhydrous environment.

6.6.1 Synthesis and Solution Studies

The first synthetic attempt was performed following a classical procedure for the synthesis of EMACs. Anhydrous $CoCl_2$, ^{t}BuOK and H_6L were mixed together (5 : 6.8 : 1 MR) and heated in naphthalene at 200 °C for 6 hours. These severe reaction conditions were chosen in a try to achieve full deprotonation of H_6L, which does not occur at room temperature in THF (see **Section 6.5**). Unfortunately, this reaction did not lead to positive results, affording only a black material which was completely insoluble in CH_2Cl_2. Therefore, in these high-temperature

conditions the tripodal ligand is likely to undergo degradation, which prevents the formation of tractable materials. Milder experimental conditions were thus tested.

To simplify these preliminary studies, our efforts were focused on the synthesis of mononuclear cobalt(II)-based complexes, in order to find a repeatable and reliable synthetic approach, which might be afterwards extended to polynuclear systems of cobalt and of other transition metals. To prevent any possible degradation of H_6L, strong heating was avoided. The reaction between H_6L and cobalt(II) at room temperature was tested and monitored by UV-Vis-NIR spectroscopy. H_6L and ^{t}BuOK were dissolved in THF in 1 : 3.8 MR, to give a clear yellow solution (see **Section 6.5**). A deep blue THF solution of $CoCl_2$ (1:1 MR with H_6L) was then added, causing the solution to turn dark red. Clearly, this color change cannot be due to the superimposed colors of the two admixed solutions (yellow and deep blue) and a complexation reaction has likely occurred. In Fig. 6.16 we compare the electronic spectra of THF solutions of $CoCl_2$, of H_6L before and after adding ^{t}BuOK (both taken from **Section 6.5**, Fig. 6.15), and of the final dark red solution. The spectrum of this solution exhibits three very intense absorption bands with λ_{max} = 239, 306 and 364 nm, whose energies are close to those of the bands of H_6L after deprotonation (λ_{max} = 239, 314−315 and 363 nm, see **Section 6.5**). Two shoulders are also present. One of them is centered at ~272 nm, where H_6L possesses one of its bands, while the other one is found around ≈420 nm.

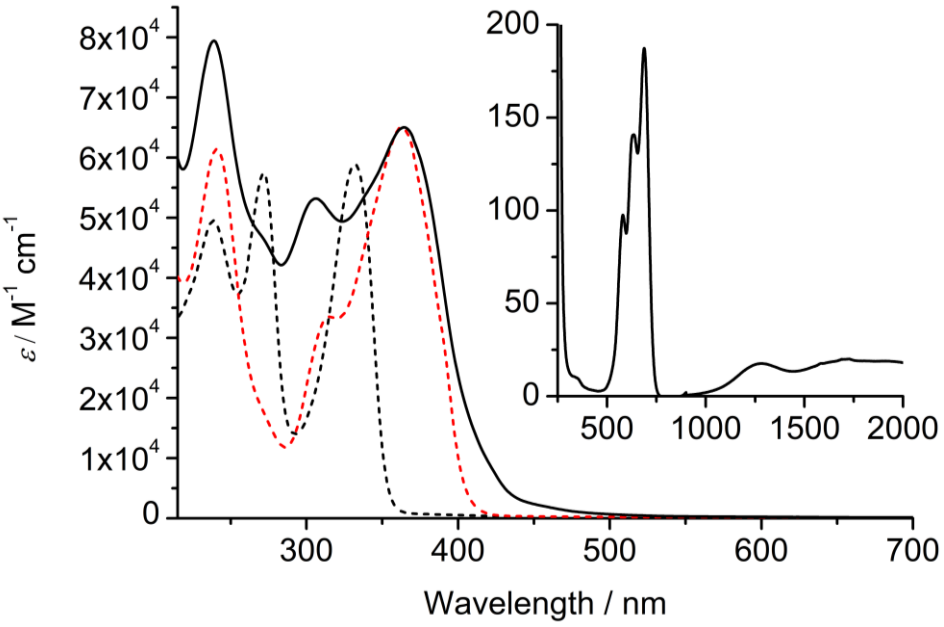

Figure 6.16. UV-Vis-NIR spectrum of the dark red THF solution containing H_6L, ^{t}BuOK and $CoCl_2$ (solid line). The main panel also shows the spectrum of H_6L before (black dashed line) and after (red dashed line) the addition of ^{t}BuOK (extracted from Fig. 6.15). The inset shows the spectrum of a THF solution of $CoCl_2$. All the spectra were recorded up to λ = 2000 nm, but only the characteristic portion of them is reported here.

This analysis indicates that upon addition of ^{t}BuOK and $CoCl_2$ to H_6L, the formation of a cobalt-containing coordination complex has occurred, in which the ligand is present in its triply deprotonated form. In this complex the coordination geometry of the Co^{2+} ion is likely to be octahedral (O_h), since tetrahedral (T_d) Co^{2+} complexes are usually described as green or deep blue.[186,209,210] Moreover, the intensities of the CF absorptions allows to distinguish between O_h and T_d complexes, as discussed below. In T_d complexes, three CF transitions are expected in the electronic spectrum: ν_1 ($A_2(F) \rightarrow T_2(F)$), ν_2 ($A_2(F) \rightarrow T_1(F)$) and ν_3 ($A_2(F) \rightarrow T_1(P)$). The intensity of these absorptions is usually of the order of $\varepsilon \approx 10^1-10^3$ M^{-1} cm^{-1}.[116] The CF bands of O_h complexes (usually found between ~625 and ~1250 nm) are much less intense ($\varepsilon \approx 10^1$ M^{-1} cm^{-1}), since they are related to the following symmetry-forbidden transitions: ν_1 ($T_{1g}(F) \rightarrow T_{2g}(F)$), ν_2 ($T_{1g}(F) \rightarrow A_{2g}(F)$) and ν_3 ($T_{1g}(F) \rightarrow T_{1g}(P)$).[116,211] These CF bands are not detectable in the spectrum of the dark red solution obtained during this test (Fig. 6.16, main panel), strongly suggesting O_h coordination. On the other hand, the electronic spectrum of $CoCl_2$ in THF (Fig. 6.16, inset) presents three bands at λ_{max} = 580, 635 and 688 nm (ε = 98−187 M^{-1} cm^{-1}). In addition a very weak and broad band is found at ≈1280 nm ($\varepsilon \sim 20$ M^{-1} cm^{-1}), extensively overlapped with a much broader absorption located at greater wavelengths. This spectrum strongly resembles that of an acetone solution of $CoCl_2$ (575, ~630(sh), 674, 1330, 1610 and 1960 nm).[212] These spectral features clearly indicate a T_d coordination environment for the Co^{2+} ion. Many tetrahedral Co^{2+} complexes with pyridine-type ligands (py or amino-pyridines) are known, and their ν_2 and ν_3 are reported to be in the NIR (around ≈1250−2200 nm) and in the visible range (around ≈590−670 nm), respectively.[209,210,213] The lowest energy transition (ν_1) was not detectable in our frequency range (0−2000 nm). The splitting of the ν_2 absorption can be ascribed to SO coupling, as described by Cotton at al., for tetrahalogenocobaltate(II) complexes.[211]

The crucial role of the base was proven in a second test, where H_6L and $CoCl_2$ (1:1) were dissolved in THF, without ^{t}BuOK, to give a green suspension. The formation of a significant quantity of precipitate suggests that the green color of the liquid phase is due to a chemical reaction rather than to the superimposed colors of the combined solutions (yellow and blue). This conclusion was confirmed by the UV-Vis-NIR spectrum of the green solution (Fig. 6.17). The spectrum presents three very intense bands at λ_{max} = 239, 270 and 334 nm, which closely replicate those of H_6L, along with a shoulder around 363 nm, and a very broad and much weaker absorption at ~430 nm. The absorptions found at λ > 500 nm, are consistent in energy and intensity with the ν_3 (λ_{max} = 553, 610(sh) and 640 nm; ε = 251−456 M^{-1} cm^{-1}) and ν_2 (λ_{max} ~1210 nm; ε = 56 M^{-1} cm^{-1}) crystal field transitions of Co^{2+} T_d complexes. Therefore, admixing H_6L and $CoCl_2$ in THF with no added base is likely to afford a coordination complex

of Co^{2+} with a T_d coordination environment. The structure of this complex is probably similar to that of the monocobalt(II) complex reported by Tsai *et al.* in 2017 (Fig. 6.18), $[CoCl_2H_3(py_3tren)]$ (**15**). Complex **15** was also obtained by simply mixing the shorter analogue of H_6L, $H_3(py_3tren)$, with $CoCl_2$ in THF, in a 1:1 MR. Here, the Co^{2+} ion is coordinated by two chlorido ligands and two pyridine-type N donors. This indicates that addition of a base has a profound influence on the coordination mode of H_6L towards Co^{2+}.

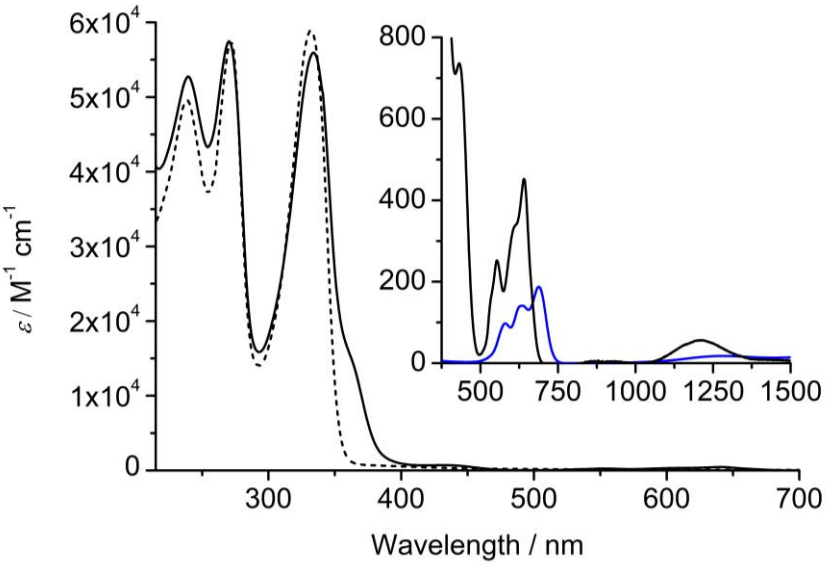

Figure 6.17. UV-Vis-NIR spectra of H_6L (dashed line) and of the green THF solution containing H_6L and $CoCl_2$ (solid line). The inset shows a magnification of the spectra between 375 and 2000 nm, along with the spectrum of a THF solution of $CoCl_2$ (blue line).

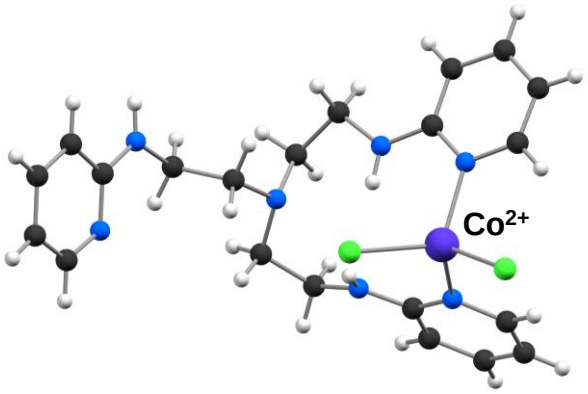

Figure 6.18. Molecular structure of $[CoCl_2H_3(py_3tren)]$ (**15**), drawn using a ball-and stick model. Color code: purple, Co; green, Cl; blue, N; black, C; light grey, H.

Therefore, synthetic attempts were made in order to isolate the presumably octahedral cobalt(II) complex formed upon addition of ^{t}BuOK. The general scheme consisted in the deprotonation of the ligand in THF using ^{t}BuOK (THF solution) followed by addition of

anhydrous $CoCl_2$. The form in which $CoCl_2$ was used turned out to be critically important for the success of the synthesis. In fact, powdered $CoCl_2$ does not completely dissolve in the reaction environment, even after stirring overnight, significantly lowering the yield of the reaction. Additional heating to reflux in THF (3 h) does not afford any significant improvement. On the other hand, when $CoCl_2$ was added as a clear THF solution (deep blue in color) it caused an immediate change of color of the reaction mixture from yellow to dark red, which persisted in time. The dark red solution was separated from a very fine solid by filtration, and was then concentrated and layered with Et_2O. The crystallization afforded two different crystalline phases, in erratic proportions. All crystals are dichroic, looking green or red depending on the angle of observation. The crystallization step also produced a significant amount of powder, which was separated from the crystals by flotation. The UV-Vis-NIR spectrum of the crystals dissolved in THF is similar to that recorded during the preliminary test (see above), as shown in Fig. 6.19. SC-XRD analysis revealed that the product is the O_h monocobalt(II) complex $K[CoH_3L]$ (**CoL**) obtained as two different solvatomorphs: **CoL** (small parallelogram plates) and **CoL**·THF (big hexagonal prisms). Both crystalline phases feature a Co^{2+} ions with distorted octahedral coordination geometry, consistent with UV-Vis-NIR analysis. The molecular structure of **CoL** is explained in detail in **Section 6.6.2**.

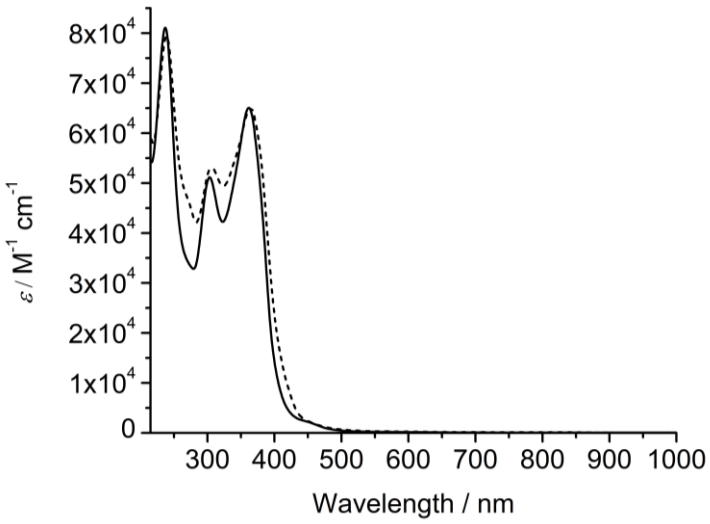

Figure 6.19. UV-Vis-NIR spectra of **CoL** in THF (solid line) and of a THF solution of H_6L, ^{t}BuOK and $CoCl_2$ (dashed line). The latter spectrum is taken from Fig. 6.16.

The ESI-MS spectra of complex **CoL** were recorded dissolving crystals of the product in THF:CH_2Cl_2 (1:4). Figures 6.20 and 6.21 show the spectra recorded in positive and in negative ion mode, respectively. The positive ion spectrum is dominated by the molecular ion peak ($[M]^+$) of **CoL** ($K[CoH_3L]^+$) at m/z = 748.3, probably generated by the one electron oxidation of Co^{2+}. Two much weaker signals are also present at m/z = 692.4 (8%) and 787.2 (4%), which

arise from the ionic species $K[H_6L]^+$ and $K_2[CoH_3L]^+$, respectively. At variance with $K[CoH_3L]^+$, $K_2[CoH_3L]^+$ is likely to contain a Co^{2+} ion. In negative ion mode, only one significant peak is present, at m/z = 709.3. It arises from the loss of one K ion by the $[M]^+$, to give the anionic species $[CoH_3L]^-$.

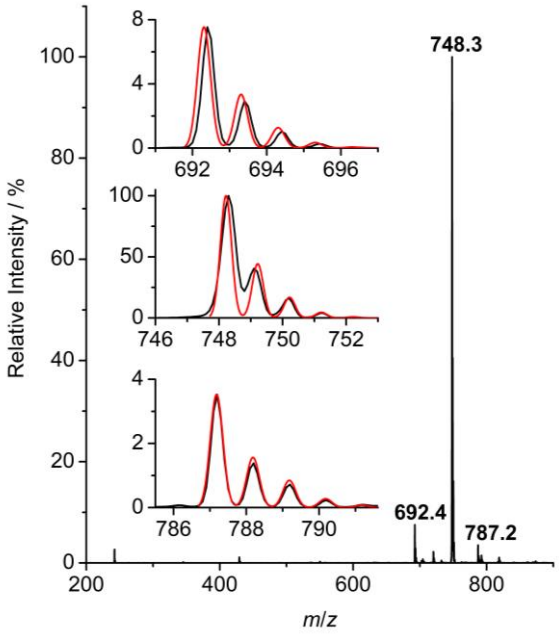

Figure 6.20. ESI-MS spectrum of **CoL** (direct infusion, THF:CH_2Cl_2 1:4, positive ion mode). The insets show the experimental (black line) and simulated (red line) isotopic patterns of the peaks at m/z = 692.4 ($[KH_6L]^+$), 748.3 ($K[CoH_3L]^+$) and 787.2 ($K_2[CoH_3L]^+$).

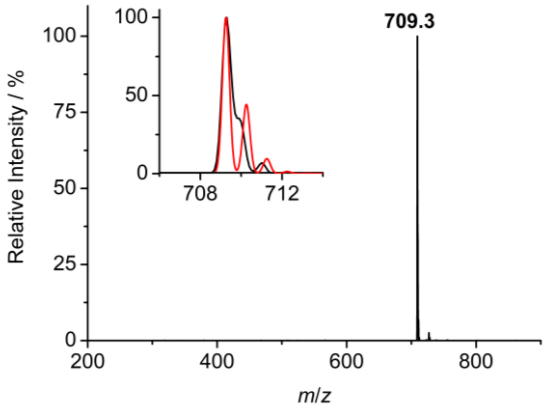

Figure 6.21. ESI-MS spectrum of **CoL** (direct infusion, THF:CH_2Cl_2 1:4, negative ion mode). The inset shows the experimental (black line) and simulated (red line) isotopic patterns of the peak at m/z = 709.3 ($[CoH_3L]^-$).

The same synthesis was attempted replacing ^{t}BuOK with the stronger base KBn, earlier used by Tereniak *et al.* for the deprotonation of $H_3(py_3tren)$.[109] KBn is a convenient base since it affords only toluene as byproduct, which is an inert hydrocarbon. On the other hand, KBn is

unstable in THF at room temperature. Therefore, a cold THF solution of KBn (red in color) was added to H_6L (THF solution) at −50 °C. The color of the solution changed from yellow to green upon deprotonation of the ligand. Then, the deep blue THF solution of $CoCl_2$ was added, and the reaction mixture rapidly turned into light brown/beige. The system was slowly allowed to reach room temperature, to give a dark red solution. The UV-Vis-NIR spectrum of this solution is superimposable (within the experimental error) to that obtained using ^{t}BuOK (Fig. 6.22). After the same work-up and crystallization step described for the previous reaction, crystals of **CoL** and **CoL**·THF were isolated with ~70% of yield. This high yield depends on the fact that crystallization produced only traces of powdery residues. Therefore, although the same crystalline phases were obtained, the use of KBn is more convenient. Moreover, KBn is a very strong base, and might be used for the full deprotonation of H_6L, in order to extend this synthetic approach towards the preparation of polynuclear complexes of Co and of other transition metals.

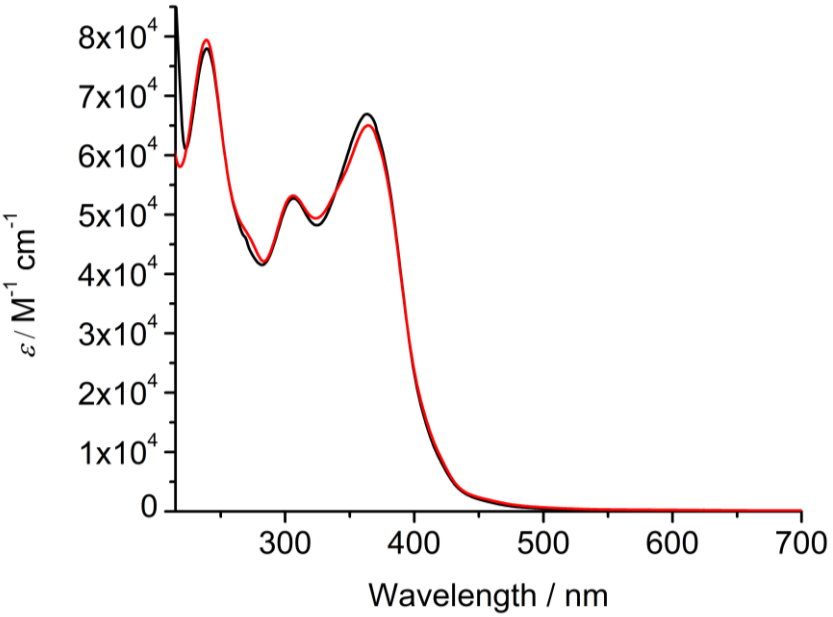

Figure 6.22. UV-Vis-NIR spectra of the dark red THF solutions containing H_6L, $CoCl_2$ and KBn (black line) or ^{t}BuOK (red line).

6.6.2 X-Ray Structures of K[CoH_3L] (**CoL**) and **CoL**·THF

A very important aspect of the herein presented preliminary investigations is that they provided the first crystallographic structural data on the novel tripodal ligand. The crystal and molecular structures of **CoL** and **CoL**·THF were determined at room temperature by SC-XRD analysis and are represented in Figures 6.23 and 6.24, respectively. Crystal data and refinement

parameters are gathered in Table 6.1, while relevant bond distances and angles are found in Table 6.2. Since they are solvatomorphs of the same coordination complex, K[CoH$_3$L], the two structures are very similar to each other. Compound **CoL** is discussed first. It is a monocobalt complex, with the M ion encapsulated by the triply deprotonated form of H$_6$L, H$_3$L^{3-}. The molecule does not possess any imposed crystallographic symmetry, since **CoL** crystallizes in the triclinic system. The aliphatic part of one branch of H$_3$L^{3-} (CH$_2$−CH$_2$−N6H) is disordered over two positions, with 0.63:0.37 occupancies. Only the highest-occupancy portion is here considered. All three branches of the ligand are folded towards the Co ion, in order to provide the highest possible number of N donors for coordination. In agreement with UV-Vis-NIR spectroscopy (see **Section 6.6.1**), the Co^{2+} ion is settled in an octahedral pocket comprising three aromatic amido-type nitrogen atoms (N$_{am}$) and three pyridine-type N donors (N$_{py}$) from the internal pyridyl moieties.

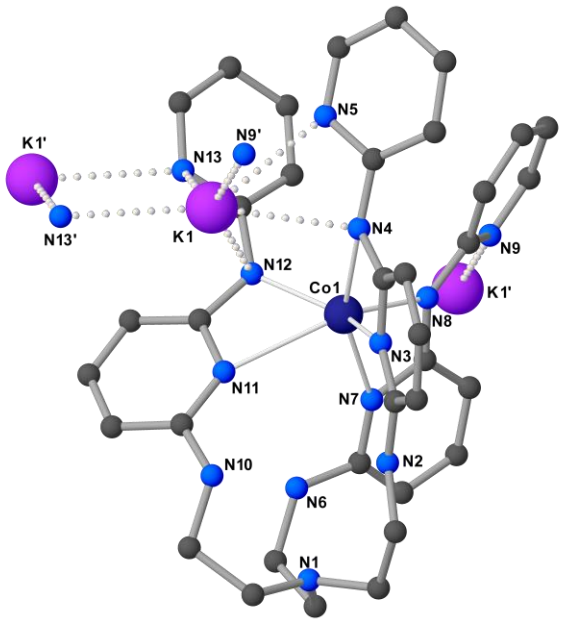

Figure 6.23. Molecular structure of **CoL** (right-handed enantiomer), drawn using a ball-and-stick model. Atoms K1', N9' and N13' belong to neighboring asymmetric units. The dotted lines represent the K−N coordination bonds. Color code: dark blue, Co; violet, K; blue, N; dark gray, C. Hydrogen atoms and the minority disordered component are omitted for clarity.

Thus, an important structural difference emerges in comparison with monocobalt(II) complex K[Co(py$_3$tren)] (**16**) reported by Tereniak *et al.*[109] In **16**, the Co^{2+} ion sits in the trigonal pyramidal coordination pocket afforded by the aliphatic moiety of the ligand. In **CoL**, the structurally similar site defined by N1, N2, N6 and N10 is not occupied and an octahedral coordination site unavailable in **16** is preferred. Bond-Valence Sum (BVS) calculations clearly

indicate that the Co ion is in a +2 oxidation state (Table 6.3), so that the complex can be formulated as $[CoH_3L]^-$. Furthermore, BVS also suggests that the Co^{2+} ion is in a HS state.

Table 6.1. Crystal data and refinement parameters for **CoL** and **CoL**·THF.

Compound	**CoL**	**CoL**·THF
Empirical formula	$C_{36}H_{36}CoKN_{13}$	$C_{40}H_{44}CoKN_{13}O$
Molecular formula	$K[CoH_3L]$	$K[CoH_3L]\cdot THF$
Formula weight (g/mol)	748.81	820.91
T (K)	298(2)	298(2)
Radiation	Mo-Kα (λ = 0.71073 Å)	Mo-Kα (λ = 0.71073 Å)
Crystal system	triclinic	triclinic
Space group	$P\bar{1}$	$P\bar{1}$
a (Å)	9.2943(7)	11.552(2)
b (Å)	13.5586(12)	11.5803(16)
c (Å)	15.2137(14)	16.730(3)
α (deg)	65.925(3)	89.437(7)
β (deg)	88.643(3)	85.811(6)
γ (deg)	78.900(4)	63.871(6)
V (Å^3)	1714.4(3)	2003.4(6)
Z	2	2
ρ_{calcd} (g cm^{-3})	1.451	1.361
$2\theta_{min}/2\theta_{max}$ (deg)	6.126/50.994	6.672/51.966
Reflections collected/independent	17317/6189	19983/7765
R_{int}	0.0721	0.0547
No. of parameters/restraints	488/49	494/26
$R1/wR2$ (all data)	0.1589/0.2022	0.1063/0.1588
$R1/wR2$ ($I \geq 2\sigma(I)$)	0.0647/0.1695	0.0543/0.1350
GOF	1.004	1.034
Largest diff. peak/hole (e Å^{-3})	0.46/−0.42	0.60/−0.41

Table 6.2. Selected interatomic distances (Å) and angles (°) in **CoL** and **CoL**·THF.

Distances (Å)	**CoL**	**CoL**·THF	Angles (°)	**CoL**	**CoL**·THF
Co1···N1	5.211(6)	5.159(3)	N3−Co1−N4	60.72(18)	61.48(11)
Co1−N3	2.075(5)	2.080(3)	N3−Co1−N7	107.57(18)	104.18(10)
Co1−N4	2.332(5)	2.239(3)	N3−Co1−N8	109.31(18)	107.38(11)
Co1−N7	2.233(5)	2.217(3)	N3−Co1−N11	90.83(17)	90.31(10)
Co1−N8	2.075(5)	2.068(3)	N3−Co1−N12	133.17(19)	137.71(12)
Co1−N11	2.591(5)	2.625(3)	N4−Co1−N7	158.35(17)	155.17(10)
Co1−N12	2.024(5)	2.027(3)	N4−Co1−N8	102.76(18)	100.41(11)
Co1···K1	3.8613(17)	3.6196(11)	N4−Co1−N11	106.00(16)	105.59(10)
K1−N4	2.887(5)	2.822(3)	N4−Co1−N12	93.57(18)	100.08(11)
K1−N5	2.918(6)	2.815(3)	N7−Co1−N8	62.21(19)	62.85(10)
K1−N9	3.060(5)	/	N7−Co1−N11	91.63(17)	94.02(9)
K1−O1A	/	2.756(8)	N7−Co1−N12	106.70(18)	103.47(11)
K1−N12	3.109(5)	2.970(3)	N8−Co1−N11	150.43(18)	153.35(10)
K1−N13	2.960(5)	3.039(3)	N8−Co1−N12	114.5(2)	113.55(12)
K1−N13’	2.926(5)	2.920(3)	N11−Co1−N12	57.26(2)	56.35(10)

Table 6.3. Bond-Valence Sum calculations on **CoL** and **CoL**·THF.[a]

Atom Co1	Co^{2+} (HS)	Co^{2+} (LS)	Co^{3+}
CoL	1.742	1.260	1.606
CoL·THF	1.798	1.300	1.658

[a]Bond-valence parameters (R_0; B) were taken from file bvparm2020.cif available at https://www.iucr.org/resources/data/datasets/bond-valence-parameters: Co^{2+}(HS)−N^{-3} (1.72; 0.37), Co^{2+}(LS)−N^{-3} (1.60; 0.37), Co^{3+}−N^{-3} (1.69; 0.37).

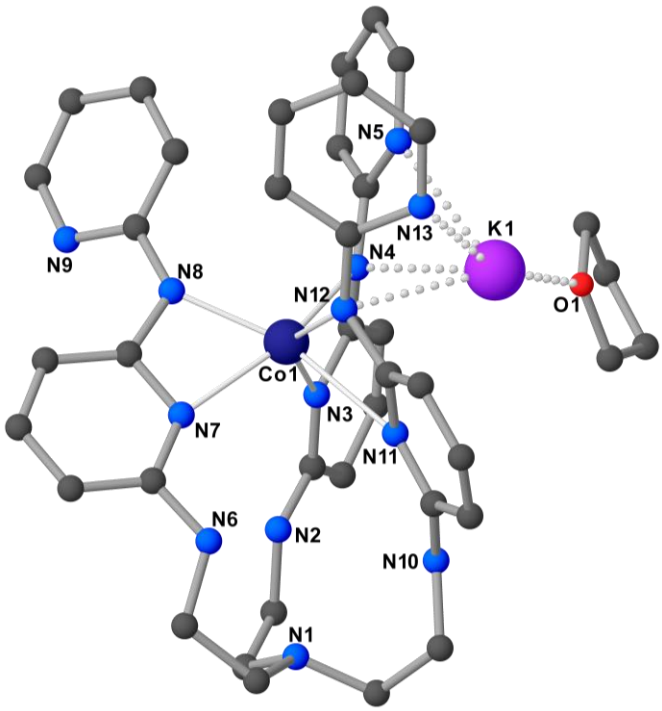

Figure 6.24. Molecular structure of **CoL**·THF (right-handed enantiomer), drawn using a ball-and-stick model. The dotted lines represent the K−E coordination bonds (where E = N or O). Color code: dark blue, Co; violet, K; red, O; blue, N; dark gray, C. Hydrogen atoms and the minority disordered component of THF are omitted for clarity.

Consistent with electroneutrality considerations, the lattice contains one K^+ counterion per $[CoH_3L]^-$ complex. This K ion is coordinated by two N_{am} (N4 and N12) and two N_{py} (N5 and N13) donors, which belong to two branches of the same ligand (N−K = 2.887−3.109 Å). In addition, the K ion interacts with two more N_{py} donors (N9' and N13') from as many neighboring asymmetric units (2.926−3.060 Å). Notice that N_{py} donors N13 and N13' bridge two K counterions related by an inversion center, with N13, K1, N13' and K1' roughly lying at the vertices of a square (internal angles = 88−92°, K1−N13 = 2.960(5), K1−N13' = 2.926(5)). While N9' belong to a molecule generated by the translation of the asymmetric unit along the *a* axis, N13' is part of another one generated by the inversion with respect to the center of the N13,K1,N13',K1' square. Interestingly, the **CoL** molecules form centrosymmetric dimers which are assembled in chains along the *a* axis, due to the interaction through the N9 atoms. Interaction with K^+ through N9 and N13 requires these two dpa^--like terminations to adopt a *syn-anti* conformation. In a perfect all-*syn* conformation (see Fig. 3.1, **Section 3.2**), the dihedral angles between neighboring pyridine rings are equal to 0°. Here, rotation of the terminal pyridines amounts to 132 and 148°. On the contrary, the remaining branch (N2, N3, N4, N5) of the tripodal ligand is in the all-*syn* conformation, and the angle formed by its two pyridines is of 46° only. This value is comparable with those reported in **Chapter 4** (**Section 4.3**) for the

tpda^{2-} ligand in complex **1Br** (36−56°). Due to the torsions of the ligand's branches, **CoL** becomes chiral; however, the space group is centrosymmetric ($P\bar{1}$) and both enantiomers are found in the lattice in a 1:1 ratio.

The molecular structure of **CoL**·THF (Fig. 6.24) is very similar to that of **CoL**, as shown in Fig. 6.25. Bond distances and angles resemble those of **CoL**, and a direct comparison can be found in Table 6.2. The main differences lie in the coordination environment of the K counterion: in **CoL**·THF, the O atom of a solvent molecule replaces N9 in the coordination sphere of K^+ (the THF molecule is found disordered over two position with 0.63:0.37 occupancies, but only the highest-occupancy portion is considered here). This replacement causes the isolation of the centrosymmetric dimers of **CoL**·THF, which cannot assemble in chains here. It is interesting that the N9-containing termination of the ligand still adopts an *anti* conformation although it is not engaged in a coordination bond. However, the N9-containing pyridines in **CoL** and **CoL**·THF differ substantially in orientation and form a dihedral angle as large as ~70° (Fig. 6.25).

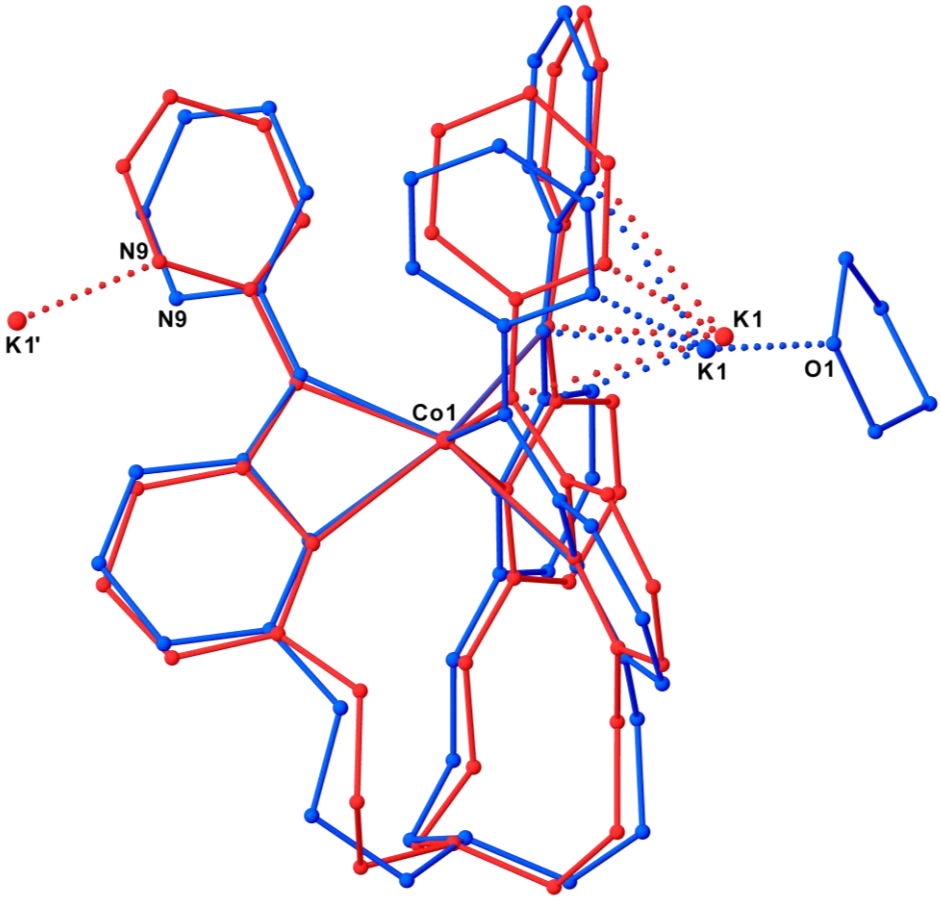

Figure 6.25. Superimposed molecular structures of **CoL** (red) and **CoL**·THF (blue), drawn using a ball-and-stick model (right-handed enantiomers). The dotted lines represent the K−E coordination bonds (where E = N or O). Hydrogen atoms and the minority disordered components are omitted for clarity.

6.7 Coordination Chemistry of H_6L: Fe(II)

After exploring the coordination chemistry of the novel tripodal ligand (H_6L) with cobalt(II), the reactivity of H_6L towards Fe(II) was investigated. The first attempts targeted the synthesis of simple mono- and dinuclear iron(II)-based complexes, following the same approach used for the preparation of **CoL** and **CoL**·THF. In parallel, the synthesis of polynuclear compounds with 3 or more iron(II) centers was tried. Here, in an effort to generate new iron(II) EMACs, the procedure was similar to that used for the syntheses of $[Fe_4(tpda)_3Br_2]$ (**1Br**) and $[Fe_4(tpda)_3Cl_2]$ (**1Cl**), which are described in **Chapter 4** and in ref.[20]

6.7.1 Preliminary Studies Towards Mono and Dinuclear Complexes of H_6L

Compound $K[CoH_3L]$ (**CoL**) was isolated reacting H_6L, ^{t}BuOK (or KBn) and $CoCl_2$ in THF. In a similar fashion, H_6L and ^{t}BuOK (1:3.1 MR) were dissolved together in THF, and subsequently a colorless THF solution of Fe_4Cl_8·6THF was added (1:1 Fe:H_6L MR). The color of the solution rapidly turned from yellow to orange, potentially indicating the formation of a coordination complex. In addition, a precipitate formed progressively over time, while the suspension darkened to dark orange. After 1 h of reaction time, no additional macroscopic changes were observed. Then, the suspension was concentrated, filtered, and layered with Et_2O. Unfortunately, the liquid diffusion failed to afford crystals, but only a yellow material. A further recrystallization by liquid diffusion (THF/Et_2O or CH_3CN/Et_2O) was attempted without success.

The MALDI-TOF-MS spectrum of the reaction mixture before the work-up is shown in Fig. 6.26. It exhibits five intense peaks at *m*/*z* = 454.8 (100%), 508.9 (57%), 707.9 (73%), 746.0 (70%) and 785.1 (45%), along with many other minority signals. The last three peaks can be assigned to the ionic species $[FeH_4L+H]^+$, $K[FeH_3L+H]^+$, and $K_2[FeH_3L+H]^+$, respectively. Since the resolution of the isotopic patterns was poor, these assignments were only based on the matching with the theoretical *m*/*z* values (708.3, 746.2, and 785.2, respectively). The three signals are consistent with the formation of a coordination compound $K[FeH_3L]$ analogous to **CoL**, which also gives rise to ESI-MS peaks attributed to the ionic species $K[CoH_3L]^+$ and $K_2[CoH_3L]^+$ (see **Section 6.6.1**). The remaining two main peaks in Fig. 6.26 are at *m*/*z* values (454.8 and 508.9) lower than the isotopic mass of the free ligand (653.34 g/mol). They are likely

to arise from fragmentation and/or collision processes, probably involving the ionic species which were tentatively assigned above.

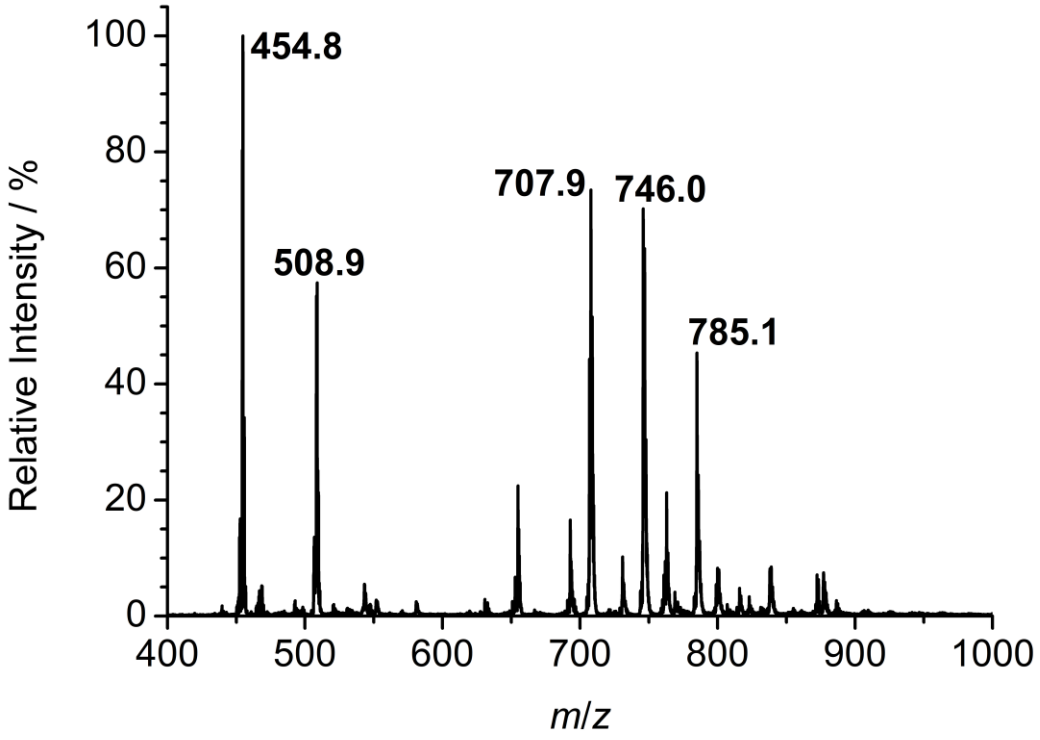

Figure 6.26. MALDI-TOF-MS spectrum of the reaction mixture (H_6L : ^tBuOK : $Fe_4Cl_8{\cdot}6THF$, 1:3.1:0.25 MR) prior to work-up (positive ion mode, solid matrix = anthracene).

In parallel, the same reaction was carried out doubling the relative amount of $Fe_4Cl_8{\cdot}6THF$ (2:1 Fe:H_6L MR). The reaction mixture underwent the same macroscopic changes described above to give an orange suspension which was analyzed by MALDI-TOF-MS and ESI-MS spectrometry, as described below. The suspension was filtered to give a yellow solid and a pale yellow solution. Complete evaporation of the solvent from the liquid phase gave only traces of non-crystalline material. Attempts to recrystallize the yellow solid by either vapor or liquid diffusion (CH_2Cl_2/Et_2O) afforded an insignificant quantity of non-crystalline material. However, some very interesting results were obtained from mass spectrometry.

The MALDI-TOF-MS spectrum of the reaction mixture is shown in Fig. 6.27. It presents two intense peaks at *m*/*z* = 762.3 (100%) and 797.3 (77%), which arise from the ionic species $[Fe_2H_3L]^+$ and $[Fe_2ClH_3L]^+$, respectively. The most intense peak overlaps extensively with other signals that probably originate from ionic species differing from $[Fe_2H_3L]^+$ in the number of H atoms. Therefore, the assignment was only based on the matching with the theoretical *m*/*z* value (762.2). On the other hand, the signal at *m*/*z* = 797.3 is well resolved and its isotopic pattern is satisfactorily simulated by $[Fe_2ClH_3L]^+$ (Fig. 6.27, inset).

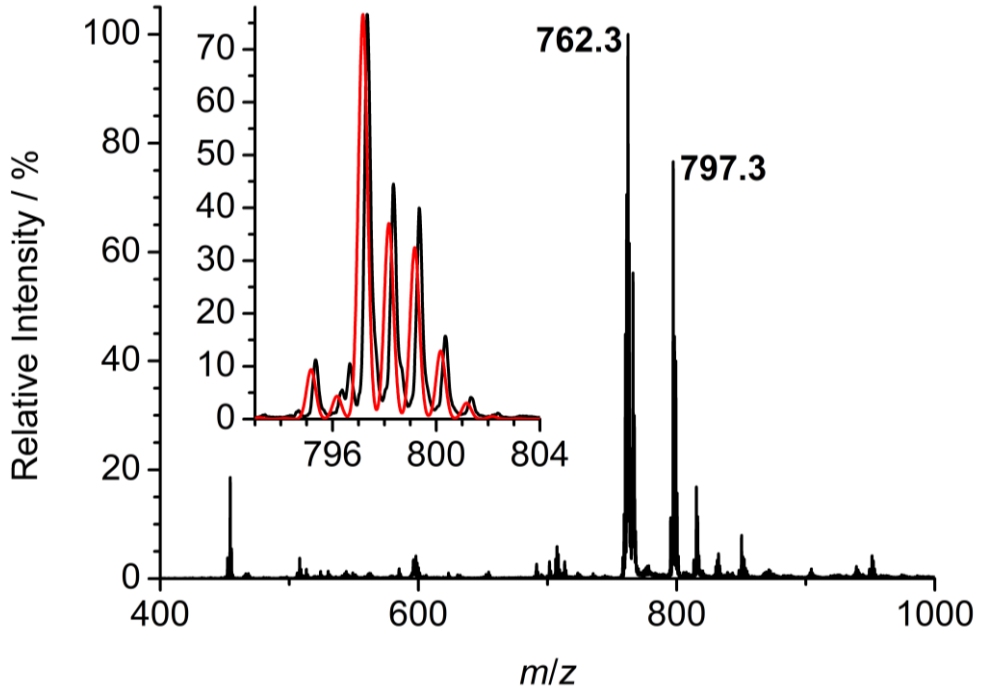

Figure 6.27. MALDI-TOF-MS spectrum of the reaction mixture (H_6L : ^tBuOK : Fe_4Cl_8·6THF, 1:3.1:0.5 MR) prior to work-up (positive ion mode, solid matrix = anthracene). The inset shows the experimental (black line) and simulated (red line) isotopic patterns of the peak at *m*/*z* = 797.3 ($[Fe_2ClH_3L]^+$).

The ESI-MS spectrum of the same mixture, dissolved in CH_2Cl_2, is shown in Fig. 6.28. It is characterized by two intense and well resolved signals at *m*/*z* = 797.1 (100%) and 762.2 (37%), which are very well simulated by the ionic species $[Fe_2ClH_3L]^+$ and $[Fe_2H_3L]^+$, respectively. Other minority peaks (<10%) are present, but only that at *m*/*z* = 744.2 (9%) was assigned straightforwardly to $[FeClH_6L]^+$. During the measurements, the signals of the dinuclear species disappear over time and the peak of $[FeClH_6L]^+$ dominates the spectrum after 3−4 minutes from the beginning of the infusion. This evolution of the ESI-MS profile may be due either to the occurrence of side-reactions with CH_2Cl_2 and/or to ionization conditions. In addition, the CH_2Cl_2 solution is very air-sensitive and when exposed to the atmosphere it immediately turns from yellow to dark grey/dark brown. Therefore, the change of the spectrum over time can also be due to unavoidable traces of oxygen and/or water during the ESI-MS measurement.

The synthetic attempts reported so far failed to produce crystalline material or any tractable solid. However, crystals of $[Fe_2ClH_3L]$ (**Fe_2L**) were accidentally recovered from an attempt to synthesize a polyiron compound of H_6L starting from $[Fe_2(Mes)_4]$ (**2**) as an iron(II) source (see **Section 6.7.3**). The molecular structure of **Fe_2L** is described in detail in the next Section.

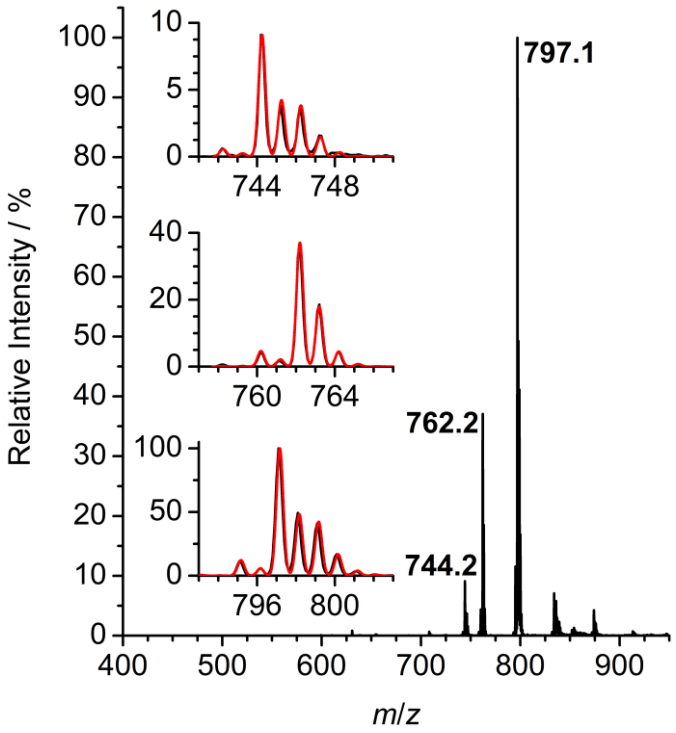

Figure 6.28. ESI-MS spectrum of the reaction mixture (H_6L : ^tBuOK : Fe_4Cl_8·6THF, 1:3.1:0.5 MR) prior to work-up (direct infusion, CH_2Cl_2, positive ion mode). The inset shows the experimental (black line) and simulated (red line) isotopic patterns of the peaks at *m*/*z* = 797.1 ($[Fe_2ClH_3L]^+$), 762.2 ($[Fe_2H_3L]^+$) and 744.2 ($[FeClH_6L]^+$).

6.7.2 X-Ray Structure of $[Fe_2ClH_3L]$·0.36Et_2O (**Fe_2L**·0.36Et_2O)

Refluxing $[Fe_2(Mes)_4]$ with H_6L in toluene, and extracting the obtained solid with CH_2Cl_2, led to a green solution. Slow liquid diffusion of Et_2O into this solution afforded small yellow plates, with trapezoidal shape. Based on a SC-XRD study, the compound was identified as $[Fe_2ClH_3L]$ (**Fe_2L**) and its molecular structure is represented in Fig. 6.29. Crystal data and refinement parameters are gathered in Table 6.4, while relevant bond distances and angles can be found in Table 6.5. **Fe_2L** contains two HS Fe^2 ions, as shown by BVS calculations (Table 6.6) and in accordance with electroneutrality considerations. The metal centers are wrapped by the tripodal ligand in its triply deprotonated form (H_3L^{3-}). Here, at difference with the monocobalt(II) complex **CoL** (see **Section 6.6.2**), all the ligand's branches are in their all-*syn* form, and their twisting leads to a 41.5° angle between the mean planes of adjacent pyridine rings. One chlorido axial ligand caps the complex at its open end. Complex **Fe_2L** possesses crystallographically imposed C_3 symmetry, and N1, Fe1, Fe2 and Cl1 lie on a 3-fold axis. Along the same C_3 axis,

all **Fe$_2$L** molecules are oriented towards the same direction but have alternating handedness, so that a racemic molecular crystal is obtained.

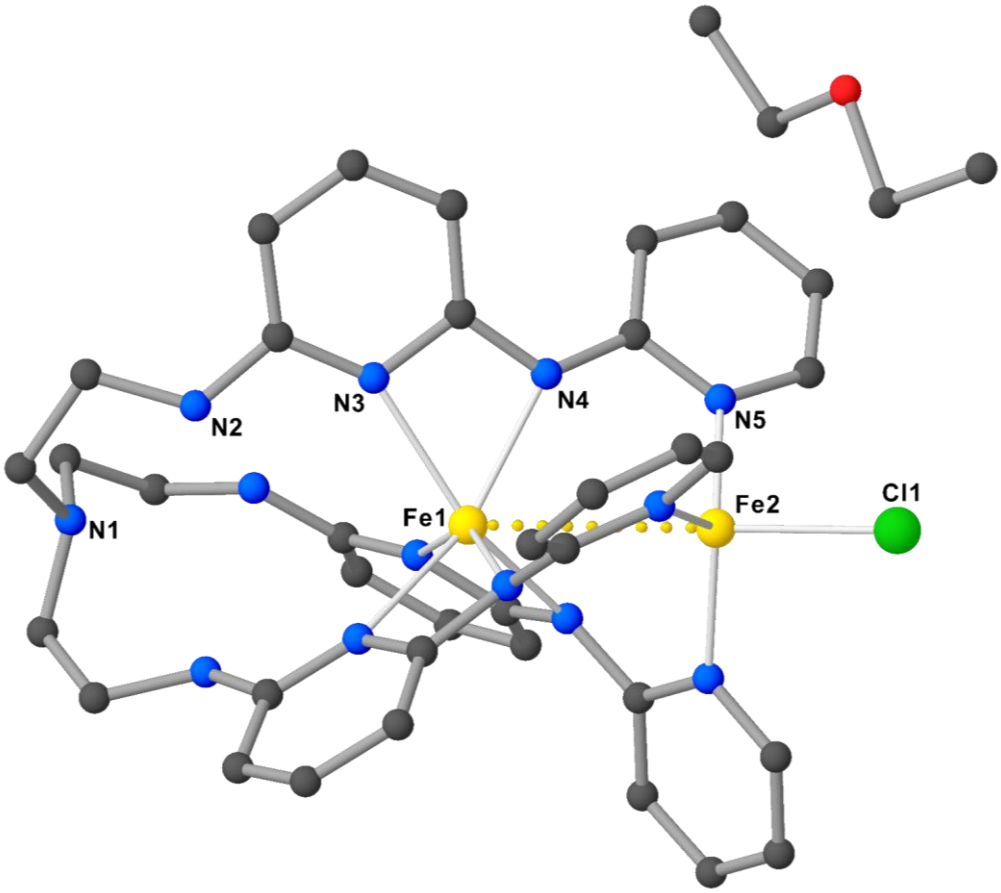

Figure 6.29. Molecular structure of **Fe$_2$L**, drawn using a ball-and-stick model (left-handed enantiomer). The dotted line connecting the Fe^{2+} ions does not correspond to a chemical bond, but provides a better representation only. Color code: orange, Fe; green, Cl; red, O; blue, N; dark gray, C. Hydrogen atoms and the minority disordered component of Et_2O are omitted for clarity.

The distance between the tertiary N atom of tren (N1) and the chlorido ligand of the adjacent molecule is equal to ~7.0 Å. Finally, a partially occupied Et_2O molecule is present as crystallization solvent. It is disordered over two sites (0.25:0.11 occupancies) near to a D_3 special position (only the high-occupancy portion is shown in Fig. 6.29). At first sight, it is evident that **Fe$_2$L** resembles half of the structure of complex $[Fe_4(tpda)_3Cl_2]$ (**1Cl**),[20] as depicted in Fig. 6.30. The main difference is that the Fe1···Fe2 separation (3.2242(12) Å) is 8.7% longer than the average distance between terminals and internals Fe centers in **1Cl** (2.966 Å). Fe1 has a similar coordination environment to the internal Fe ions in complex **1Cl**. In fact, Fe1 forms three short contacts with as many N_{am} donors, and three slightly longer bonds with the N_{py} atoms, resulting in a very distorted octahedral geometry (Fe−N_{am} = 2.156(3) Å, Fe−N_{py} = 2.240(3) Å, N3−Fe1−N4 = 60.60(10)°). It is worth to note that the position of the

metal inside the octahedral pocket of the ligand is almost the same in mononuclear and dinuclear complexes. Fe1 is found at 5.174(5) Å from N1, while in **CoL** and in **CoL**·THF the average Co···N1 separation is 5.185 Å. On the other hand, Fe2 possesses the same trigonal-pyramidal coordination geometry (F−N_{py} = 2.073(3) Å, Fe2−Cl1 = 2.3618(18) Å, Cl1−Fe2−N_{py} = 97.17(9)°, N_{py}−Fe−N_{py} = 118.47(4)°) as the terminal Fe ions in **1Cl** (Fe−N_{py} = 2.07−2.09 Å, Fe−Cl = 2.358−2.386 Å, Cl−Fe−N_{py} = 95.2−98.3°, N_{py}−Fe−N_{py} = 111.9−125.4°).

Despite synthetic attempts that followed its first isolation, complex **Fe_2L** could not be prepared again. However, the preliminary results described in **Section 6.7.1** are promising for optimizing an affordable method towards its deliberate preparation. The similarity between the molecular structure of **Fe_2L** and "half" complex **1Cl** might help to better understand the magnetic behaviour of **1Cl**, which was described as two ferromagnetic Fe_2 dimers, weakly antiferromagnetically coupled to each other.[20] Interesting is also the crystallographically-imposed 3-fold symmetry of **Fe_2L**, which is expected to leave an unquenched orbital momentum on Fe2.

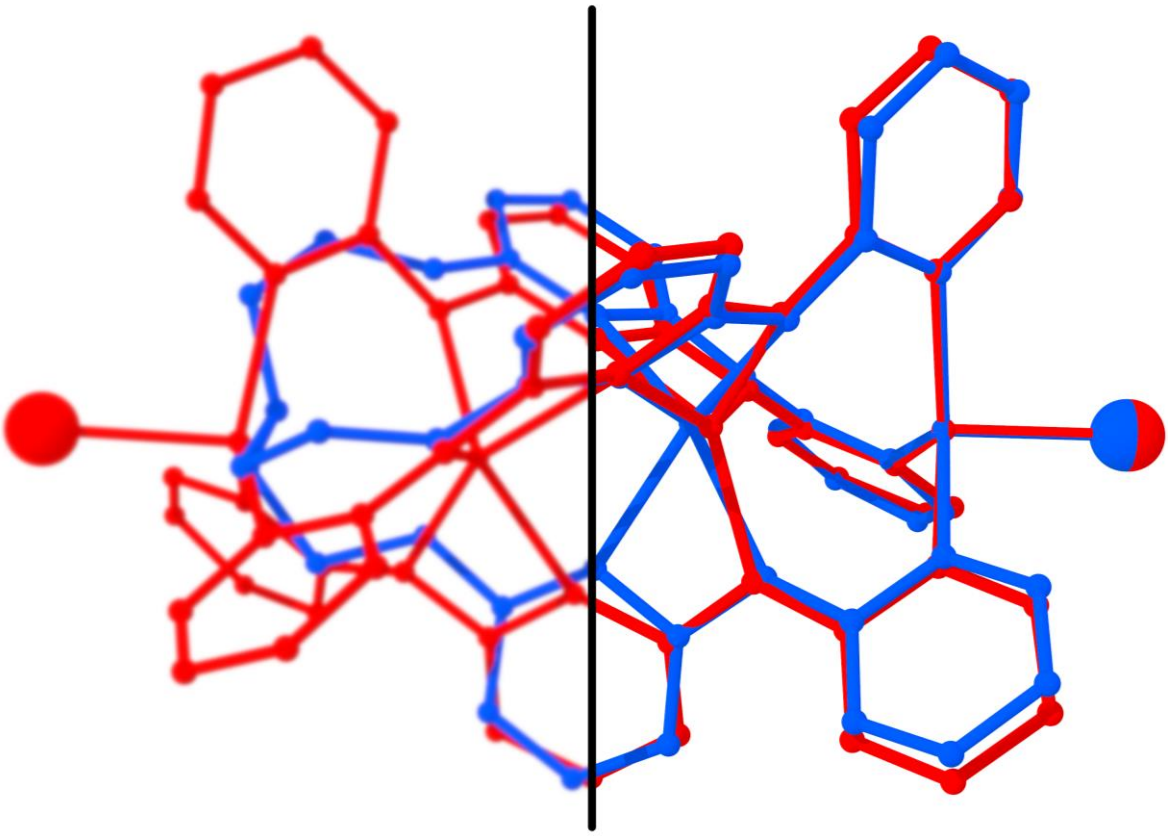

Figure 6.30. Superimposed molecular structures of **Fe_2L** (blue) and **1Cl** (red) drawn using a ball-and-stick model (left-handed enantiomers). Crystallization solvents and hydrogen atoms are omitted for clarity. The right part of the figure shows the region where the two complexes have almost superimposable structures.

Table 6.4. Crystal data and refinement parameters for **Fe_2L**·0.36Et_2O.

Empirical formula	$C_{37.43}H_{39.57}ClFe_2N_{13}O_{0.36}$
Molecular formula	$[Fe_2ClH_3L]\cdot 0.36Et_2O$
Formula weight (g/mol)	824.39
T (K)	100(2)
Radiation	Mo-Kα (λ = 0.71073 Å)
Crystal system	trigonal
Space group	$P\bar{3}c1$
a (Å)	11.42020(10)
b (Å)	11.42020(10)
c (Å)	35.5543(11)
α (deg)	90
β (deg)	90
γ (deg)	120
V (Å^3)	4015.78(14)
Z	4
ρ_{calcd} (g cm^{-3})	1.364
$2\theta_{min}/2\theta_{max}$ (deg)	2.29/52.74
Reflections collected/independent	29392/2762
R_{int}	0.0671
No. of parameters/restraints	193/13
$R1/wR2$ (all data)	0.0767/0.1405
$R1/wR2$ ($I \geq 2\sigma(I)$)	0.0521/0.1276
GOF	1.065
Largest diff. peak/hole (e Å^{-3})	1.75/−0.67

Table 6.5. Selected interatomic distances (Å) and angles (°) in **Fe$_2$L**·0.36Et$_2$O.

Fe1···Fe2	3.2242(12)
Fe2−Cl1	2.3618(18)
Fe1···N1	5.174(5)
Fe1−N3	2.240(3)
Fe1−N4	2.156(3)
Fe2−N5	2.073(3)
N3−Fe1−N4	60.60(10)
Cl1−Fe2−N5	97.17(9)
N5−Fe2−N5^2	118.47(4)

Table 6.6. Bond-Valence Sum calculations on **Fe$_2$L**·0.36Et$_2$O.[a]

Atom	Fe^{2+}	Fe^{3+}
Fe1	1.846	2.171
Fe2	1.732	1.997

[a]Bond-valence parameters (R_0; B) were taken from file bvparm2020.cif available at https://www.iucr.org/resources/data/datasets/bond-valence-parameters: Fe^{2+}−N^{-3} (1.76; 0.37), Fe^{3+}−N^{-3} (1.82; 0.37), Fe^{2+}−Cl^{-1} (2.06; 0.37), Fe^{3+}−Cl^{-1} (2.09; 0.37).

6.7.3 Synthesis and Solution Studies of a Polynuclear Compound of H_6L: $[Fe_6O_2(\mu_5\text{-}O)H_3L_2]$ (**Fe$_6$L$_2$**)

The new tripodal ligand was designed with the idea of preparing stable arrays of three or more metal ions, wrapped by the three branches of H_6L and perhaps arranged linearly to form new EMACs. The synthesis of such polyiron(II) complexes was undertaken in parallel to the investigations towards mono- and diiron(II) complexes of H_6L (see **Section 6.7.1**).

Here, we slightly modified the synthetic method that led to the successful isolation of iron(II)-based EMACs supported by H_2tpda, namely complexes **1Cl** and **1Br** (see ref.[20] and **Chapter 4**). This approach involves refluxing Fe_4Cl_8·6THF (or $FeBr_2$·2THF), [$Fe_2(Mes)_4$] and the ligand in toluene, in strictly anaerobic and anhydrous environment, and in the right MR to achieve full deprotonation of the ligand and to provide a specific number of iron(II) ions inside the complex. Here, the chosen Fe:H_6L MR was 3:1, to design a triiron(II) neutral complex where the ligand is completely deprotonated. To simplify the reaction environment, Fe_4Cl_8·6THF was excluded since neither chlorides nor additional iron sources are required. Therefore, inside a glovebox, H_6L was admixed with a slight excess of [$Fe_2(Mes)_4$] (1:1.6 MR) in toluene, and the mixture was heated to reflux for 3h. The orange solid obtained after filtration was extracted with THF. Evaporation of the solvent led to a red, powdery solid in 56% yield, which was characterized by mass spectrometry and UV-Vis-NIR spectroscopy (see below). Obtaining XRD-quality single crystals of this material proved extremely challenging. A manifold of recrystallization attempts was conducted based on slow liquid diffusion of Et_2O or *n*-hexane into THF, CH_2Cl_2, 1,4-dioxane or CH_3CN solutions, which mostly gave only spherulites of a very dark microcrystalline material. However, very slow liquid diffusion of Et_2O into a THF solution afforded beautiful very dark red plates in 48% total yield. They were characterized by SC-XRD analysis, which identified the product as the hexairon complex [$Fe_6O_2(\mu_5\text{-}O)H_3L_2$] (**$Fe_6L_2$**). Its molecular structure is described in **Section 6.7.4** and represented in Fig. 6.35. Elemental analysis (Table 6.7) indicated C, H, N and Fe contents in accordance with the above formula. The small observed deviations can be easily explained considering residual traces of THF and/or Et_2O, which can be retained by **Fe_6L_2** even after prolonged treatment in vacuum. Moreover, this compound is exceedingly air-sensitive and immediately turns from red to black upon exposure to air (crystals of **Fe_6L_2** are instead stable when covered by immersion oil). Before elemental analysis the sample was unavoidably exposed to the air (~30−60 s).

Table 6.7. Calculated and experimental elementary content of **Fe_6L_2**. The values are expressed in %.

	C	H	N	O	Fe
Calculated ($C_{72}H_{69}Fe_6N_{26}O_3$)	51.43	4.14	21.66	2.85	19.93
Experimental	52.11	4.12	21.24	/	19.7

The ESI-MS spectra (direct infusion, THF solution) of **Fe_6L_2**, as crystals or powder, are shown in Fig. 6.31. They result similar, suggesting that the content of the powdery sample is

substantially analogous to that of the crystalline one, in accordance with electronic spectroscopy (see below). They are both dominated by a strong peak around *m*/*z* = 1680, whose isotopic pattern can be well simulated as a linear combination of signals from the molecular ion peak, $[Fe_6O_3H_3L_2]^+$ (*m*/*z* = 1681.2), and from species differing for the loss or addition of one or more H atoms, namely $[Fe_6O_3H_2L_2]^+$ (*m*/*z* = 1680.2), $[Fe_6O_3H_4L_2]^+$ (*m*/*z* = 1682.2) and $[Fe_6O_3H_5L_2]^+$ (*m*/*z* = 1683.2). Different combination coefficients are required to reproduce the isotopic patterns observed in the spectra of the crystalline and powdery material. Two minority signals at *m*/*z* = 1626.3−1627.3 (10%) and 850.1 (<3%) are present in the spectrum of crystalline **Fe_6L_2** (Fig. 6.31, left panel). They are well simulated by the species $[Fe_5O_3H_4L_2]^+$ + $[Fe_5O_3H_5L_2]^+$, and $[Fe_3ClL]^+$, respectively. The latter presumably originates from residual chloride impurities in $[Fe_2(Mes)_4]$, as described for compound **1Br** in **Section 4.2**. An interesting result is that the spectrum of the powdery sample (Fig. 6.31, right panel) contains two additional signals at *m*/*z* = 1735.2 (6%) and 815.2 (5%) assigned to the heptairon species $[Fe_7O_3HL_2]^+$ and to the targeted triiron complex $[Fe_3L]^+$.

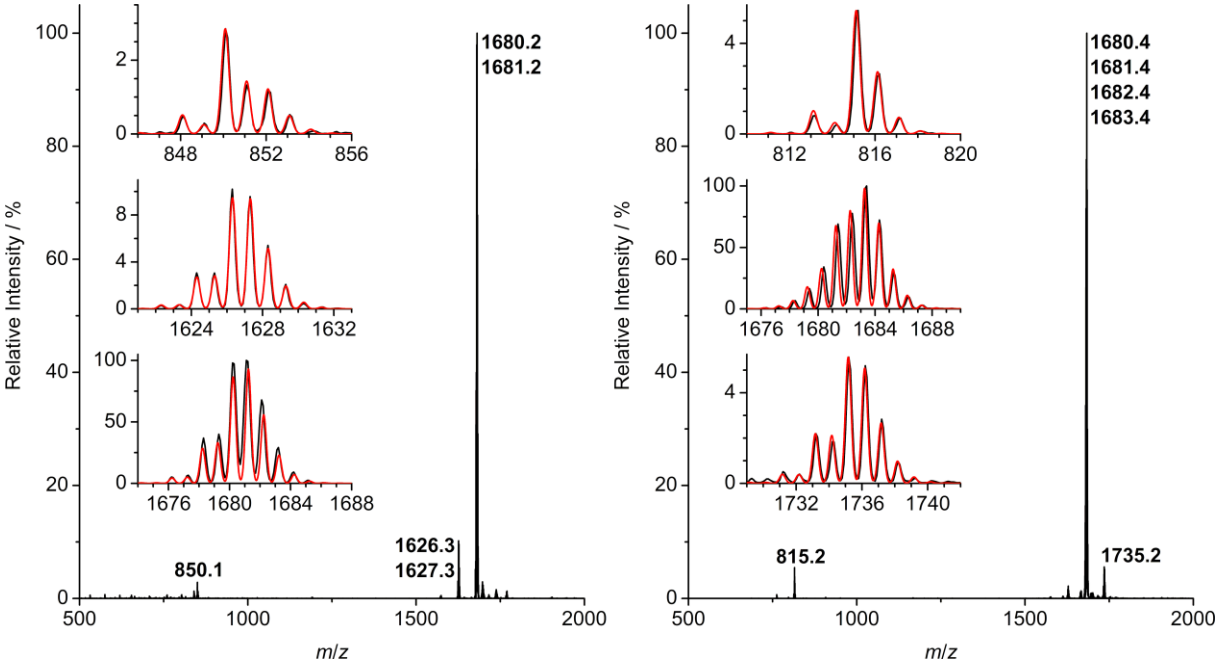

Fig. 6.31. ESI-MS spectrum of **Fe_6L_2**, in crystalline (left panel) and powdery (right panel) form (direct infusion, THF, positive ion mode). The insets shows the experimental (black line) and simulated (red line) isotopic patterns of the peaks, assigned as follows. Left panel: *m*/*z* = 850.1 ($[Fe_3ClL]^+$), 1626.3−1627.3 ($[Fe_5O_3H_4L_2]^+$ and $[Fe_5O_3H_5L_2]^+$, 0.9:0.1 ratio), 1680.2−1681.2 ($[Fe_6O_3H_2L_2]^+$ and $[Fe_6O_3H_3L_2]^+$, 0.8:0.2 ratio). Right panel: *m*/*z* = 815.2 ($[Fe_3L]^+$), 1680.4−1681.4−1682.4−1683.4 ($[Fe_6O_3H_2L_2]^+$, $[Fe_6O_3H_3L_2]^+$, $[Fe_6O_3H_4L_2]^+$ and $[Fe_6O_3H_5L_2]^+$, 0.08:0.24:0.24:0.44 ratio) and 1735.2 ($[Fe_7O_3HL_2]^+$).

The UV−Vis−NIR spectrum of crystals of **Fe$_6$L$_2$**, dissolved in THF, is shown in Fig. 6.32. It presents two intense absorptions at λ_{max} = 242 and 341 nm, along with 3 shoulders around 268, ~380 and ~500 nm. Fig. 6.32 (solid lines) shows that the crystalline material and the powdery sample give the same electronic absorption spectrum. Together with ESI-MS data (Fig. 6.31,), this is a strong indication that the powdery material is also **Fe$_6$L$_2$**. Furthermore, the spectrum does not change over time, suggesting high stability of the complex in THF solution. This stability is retained until the air-tight cuvette employed for the measurements is unsealed to allow diffusion of air into the THF solution. Upon admittance of air, the yellow solution immediately turns green/light grey and gives a quite different electronic spectrum, which is shown in Fig. 6.32 (dashed lines). The final spectrum is stable over time and again very similar when starting from crystalline or powdery material. The two peaks and the shoulder at λ_{max} < 350 nm are not significantly shifted compared to the original spectrum, but they gain intensity. Most important, the shoulder at ~380 disappears, and a new weak and very broad band arises. It is centered around ~520 nm and extends up to ~1000 nm. The position and the width of this absorption may suggest oxidation of **Fe$_6$L$_2$** to a Fe^{2+}/Fe^{3+} MV system with electron delocalization (Robin-Day Class II or III), as extensively discussed in **Chapter 5**.

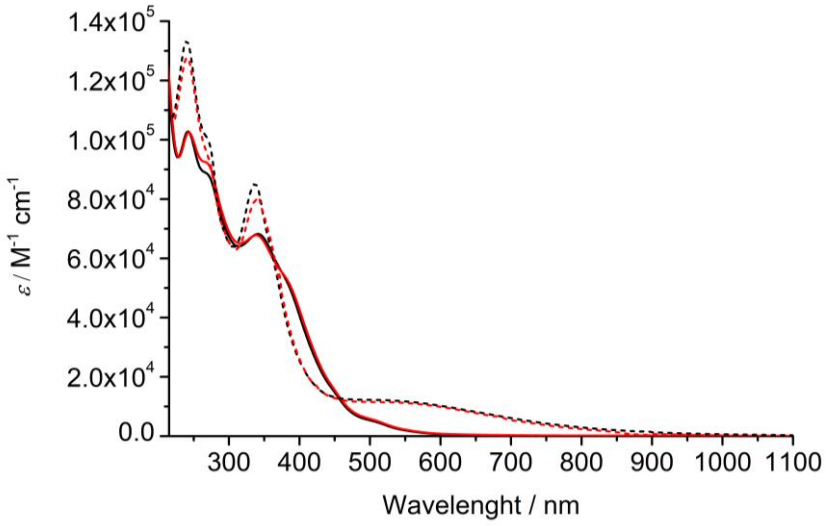

Figure 6.32. UV-Vis-NIR spectra of THF solutions of **Fe$_6$L$_2$**, prepared starting from crystals (black lines) or powders (red lines), before (solid lines) and after (dashed lines) unsealing the air-tight cuvette.

In order to understand if this transformation only involves two species (**Fe$_6$L$_2$** and the oxidation product), the conversion was followed over time. Since the process was otherwise instantaneous, the air-tight cuvette was unsealed for ~2 seconds, but the solution was left undisturbed. In this way, the free surface of the sample captured oxygen and immediately turned green/light grey, but diffusion was sufficiently slow to allow recording the set of spectra gathered in Fig. 6.33. The presence of two isosbestic points at 367 and 458 nm clearly indicates

that **Fe$_6$L$_2$** is converted into another definite species upon exposure to the air. This new species might be chemically accessible using **Fe$_6$L$_2$** as starting material.

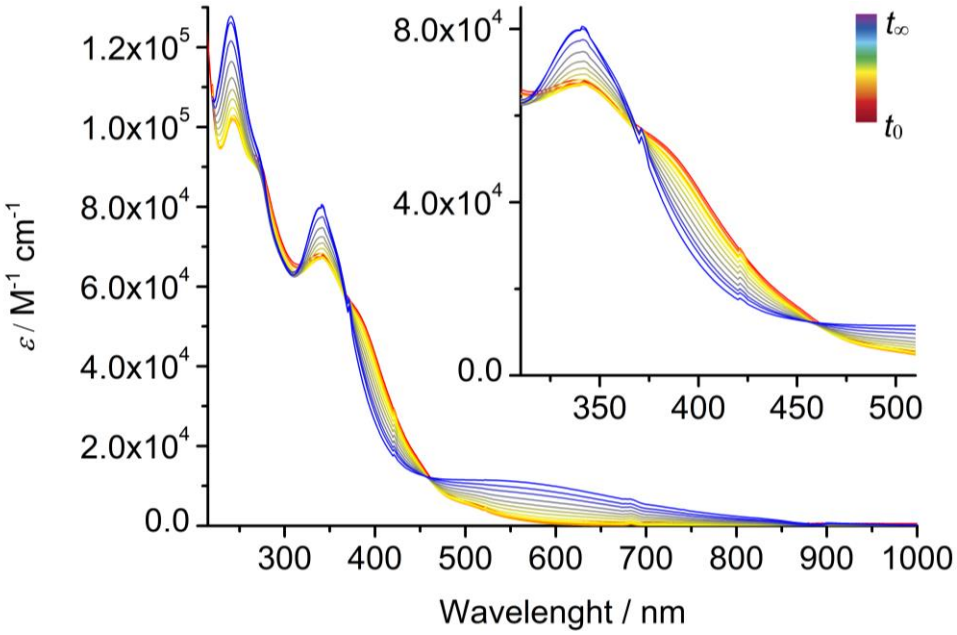

Figure 6.33. Time-evolution of the UV-Vis-NIR spectrum of **Fe$_6$L$_2$** (powder) in THF, after exposure of the solution to the air (time interval between the spectra = 2 min.). The red and the blue lines are the spectra at t_0 (initial spectrum, with the sample in the air-tight cuvette) and at t_∞ (final spectrum), respectively. The inset shows a magnification of the spectrum in the region between 310−510 nm. Scan rate = 2000 nm/min.

It is worth to note that when CH_2Cl_2 (rather than THF) was used to extract the orange solid produced by the reaction, it immediately gave a dark green solution, which strongly resembles that of the MV species $[Fe_2^{II}Fe^{III}(tpda)_3]PF_6$, (**3**, see **Section 5.2**). This color could suggest the formation of a Fe^{2+}/Fe^{3+} MV compound, as widely discussed in **Chapter 5**. Unexpectedly, the MALDI-TOF-MS spectrum of the extract (Fig. 6.34) contains two peaks at *m*/*z* = 815.0 (100%, $[Fe_3L]^+$) and 850.0 (50%, $[Fe_3ClL]^+$). The observed color change and the presence of a significant amount of ionic chlorinated species in the MALDI-TOF-MS spectrum may suggest a possible reduction of CH_2Cl_2 by **Fe$_6$L$_2$**. However, a very negative reduction potential would be required to reduce CH_2Cl_2, since its electroreduction to higher hydrocarbons was reported to occur between −2.2 and −2.5 V (vs SCE, in CH_3CN).[214] To get more insight into the redox activity of **Fe$_6$L$_2$**, CV studies would be desirable.

Finally, we recall that slow liquid diffusion of Et_2O into the green CH_2Cl_2 extract occasionally gave few crystals of $[Fe_2ClH_3L]$ (**Fe$_2$L**), which is described in **Sections 6.7.1** and **6.7.2**.

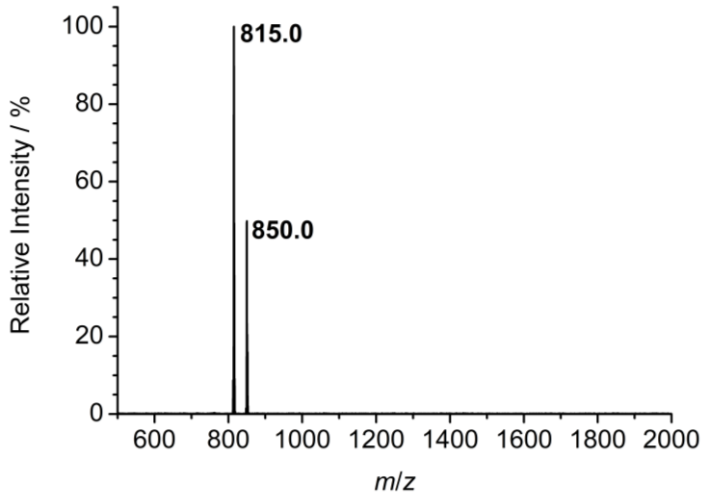

Figure 6.34. MALDI-TOF-MS spectrum of the green extract in CH_2Cl_2 (positive ion mode, solid matrix = anthracene).

6.7.4 X-Ray Structure of $[Fe_6O_2(\mu_5\text{-}O)H_3L_2]$ (**Fe$_6$L$_2$**)

The molecular structure of $[Fe_6O_2(\mu_5\text{-}O)H_3L_2]$ (**Fe$_6$L$_2$**) is displayed in Fig. 6.35. Crystal data and refinement parameters are gathered in Table 6.8, while relevant bond distances and angles are found in Table 6.9. This structure develops around a D_3 symmetry site, with a 3-fold axis and three 2-fold axes perpendicular to the triad. The organic skeleton of **Fe$_6$L$_2$** is composed by two tripodal ligands, with interpenetrating branches. All branches are helically wrapped around the 3-fold axis, with 25° angles between the mean planes of adjacent pyridine rings. The two ligands in each molecule have the same handedness, but the space group is centrosymmetric and the crystal contains both enantiomers in 1:1 proportions. The distance of the tertiary N atoms (N1 and $N1^{III}$) from the center of the structure is 6.738(9) Å and molecular size exceeds 1.6 nm.

Modelling the structure of the core was the most challenging part of this structural study (see experimental **Section 6.9.9**). The final model encompasses a central $Fe_5(\mu_5\text{-}O)$ cluster with a distorted square-pyramidal geometry (Fig. 6.36), disordered over three different positions by rotation around the 3-fold axis. Fe1 and Fe2 sites thus show partial occupancies of 2/3 and 1/3, respectively, while O1 has full occupancy, lies on the D_3 site and it is not disordered. On either side of the central core, two additional, full-occupancy O atoms (O2 and $O2^{III}$) lie on the 3-fold axis at 2.796(7) Å from O1.

The base of the pyramid is nonplanar, with internal angles $Fe1{-}Fe1^{II}{-}Fe1^{III}$ = 84.85(4)° and $Fe1^{II}{-}Fe1{-}Fe1^{IV}$ = 93.065(13)°. The length of the minor edge is 2.629(2) Å, suggesting a

possible M−M bond within the Fe1,Fe1^{II} and Fe1^{III},Fe1^{IV} pairs. This distance is in fact comparable with the mean Fe−Fe separation (2.64 Å) in a variety of carbonyl-containing polyiron complexes.[215] On the other hand, the Fe1···Fe1^{IV} and Fe1^{II}···Fe1^{III} distances are much longer (3.028(3) Å) and comparable with those found in [Fe_4(tpda)$_3$$Cl_2$] (**1Cl**),[20] indicating no M−M bond. Each Fe1 atom is five coordinated and forms coordination bonds with two N_{py} and one N_{am} donors (Fe1−N = 2.129−2.151 Å), as well as with O1 and O2 (Fe1−O = 1.997−2.133 Å). The coordination sphere of Fe1 is completed by one additional longer contact with the nearest symmetry-equivalent Fe1 center. The apical site of the pyramid is occupied by Fe2, whose distances to the other vertices (the four Fe1 atoms) are in the range 3.232−3.451 Å. Fe2 forms short coordination bonds with two N_{am} atoms and with O1 (Fe2−N_{am} = 2.019(5) Å, Fe2−O1 = 1.931(3) Å), along with two slightly longer ones with as many N_{py} atoms (Fe2−N_{py} = 2.331(5) Å). Fe2 has a square pyramidal geometry, with the metal lying ~0.86 Å from the mean plane defined by the four N donors.

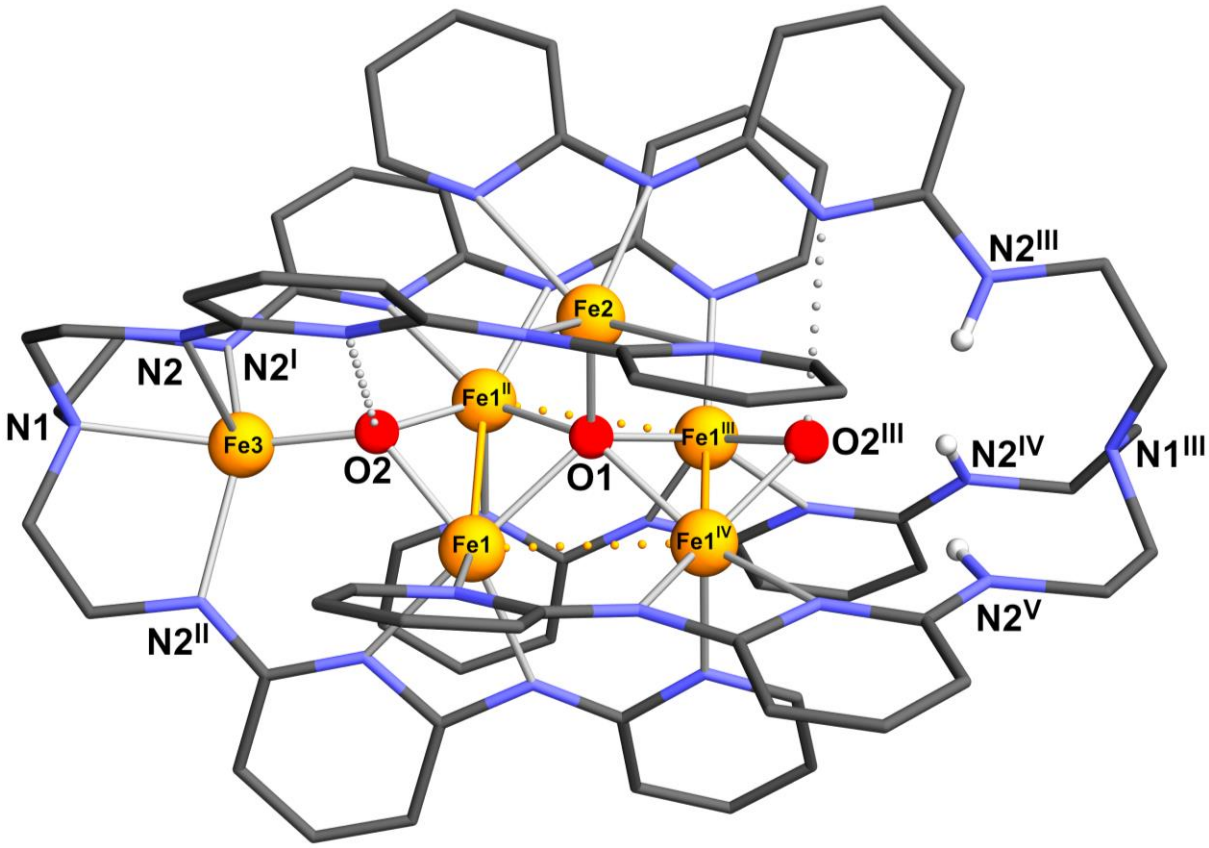

Figure 6.35. Molecular structure of **Fe_6L_2**. The organic ligands are represented with the wireframe model, while Fe and O atoms with ball-and-stick model. The orange dotted lines connecting Fe1···Fe1^{IV} and Fe1^{II}···Fe1^{III} ions do not correspond to chemical bonds, but provide a better representation only. The light grey dotted lines connecting O2 and O2^{III} with a N_{py} donor represent possible OH···N_{py} hydrogen bonds. Color code: orange, Fe; red, O; blue, N; dark gray, C; light gray, H. Only the hydrogen atoms bounded to N2^{III}, N2^{IV} and N2^{V} are displayed in the figure.

Table 6.8. Crystal data and refinement parameters for **Fe_6L_2**.

Empirical formula	$C_{72}H_{69}Fe_6N_{26}O_3$
Molecular formula	$[Fe_6O_2(\mu_5\text{-}O)H_3L_2]$
Formula weight (g/mol)	1681.63
T (K)	115(2)
Radiation	Mo-Kα (λ = 0.71073 Å)
Crystal system	trigonal
Space group	$P\bar{3}1c$
a (Å)	13.9467(7)
b (Å)	13.9467(7)
c (Å)	23.1917(13)
α (deg)	90
β (deg)	90
γ (deg)	120
V (Å^3)	3906.7(4)
Z	2
ρ_{calcd} (g cm^{-3})	1.430
$2\theta_{min}/2\theta_{max}$ (deg)	6.818/50.004
Reflections collected/independent	18337/2301
R_{int}	0.0763
No. of parameters/restraints	171/0
$R1/wR2$ (all data)	0.1351/0.2983
$R1/wR2$ ($I \geq 2\sigma(I)$)	0.0851/0.2453
GOF	1.049
Largest diff. peak/hole (e Å^{-3})	2.04/−0.81

Table 6.9. Selected interatomic distances (Å) and angles (°) in **Fe_6L_2**.

Distances (Å)		Angles (°)	
Fe1−Fe1^{II}	2.629(2)	Fe1−Fe1^{II}–Fe1^{III}	84.85(4)
Fe1···Fe1^{IV}	3.028(3)	Fe1^{II}–Fe1−Fe1^{IV}	93.065(13)
Fe1···Fe2	3.451(3)	Fe1−O1−Fe1^{II}	76.10(5)
Fe1^{II}···Fe2	3.232(3)	Fe1−O1−Fe1^{IV}	90.47(7)
Fe1−O1	2.1327(13)	Fe1−O1−Fe2	116.18(4)
Fe1−O2	1.997(4)	Fe1^{II}–O1−Fe2	105.25(4)
Fe1−N3	2.151(5)	Fe1−O2−Fe1^{II}	82.3(2)
Fe1−N4	2.129(5)	Fe1−O2−N1	130.53(15)
Fe1−N5	2.149(5)	N3−Fe1−N4	63.2(2)
Fe2−O1	1.931(3)	N3−Fe1−N5	97.1(2)
Fe2−N4	2.019(5)	N4−Fe1−N5	101.5(2)
Fe2−N5	2.331(5)	N4−Fe2−N5	62.3(2)
Fe3−O2	1.851(8)	N4−Fe2−N5^{III}	98.9(2)
Fe3−N1	2.162(10)	N1−Fe3−O2	158.4(3)
Fe3−N2	2.679(8)	N1−Fe3−N2	70.45(18)
Fe3−N2^{I}	2.180(12)	N1−Fe3−N2^{I}	81.1(3)
Fe3−N2^{II}	2.129(11)	N1−Fe3−N2^{II}	82.3(3)
O1···O2	2.796(7)		
O1···N1	6.738(9)		
O2···N3	2.979(5)		

The O^{2-} ion (O1) inside the $Fe_5(\mu_5\text{-}O)$ core is found at 0.75 Å from the mean plane defined by the four Fe1 ions. As mentioned above it forms short contacts with the four Fe1 atoms (2.1327(13) Å), and an even shorter one with Fe2 (1.931(3) Å). Similar $Fe_5(\mu_5\text{-}O)$ clusters were previously observed in the compounds $[Fe_5(\mu_5\text{-}O)(OEt)_{13}]$[216] (**17**) and $[Fe_5(\mu_5\text{-}O)(\mu\text{-}OPr^i)_8Cl_5]$[217] (**18**). The cores of **17** and **18** are almost identical to each other and are characterized by the presence of four additional O atoms (from $^-$OEt and $^-$OPr^i ions, respectively) surrounding Fe2, to give a cubic-like Fe_5O_4 cluster, which contains a $\mu_5\text{-}O^{2-}$ ion inside. The basal planes of these two cores are square-like (internal Fe···Fe···Fe angles = 89.7−90.3°) and feature Fe···Fe separations > 3 Å, indicating no M−M bonds. Therefore, to the best of our knowledge, **Fe_6L_2** is the first example of a complex with a distorted-square-pyramidal $Fe_5(\mu_5\text{-}O)$ core and M−M bonds.

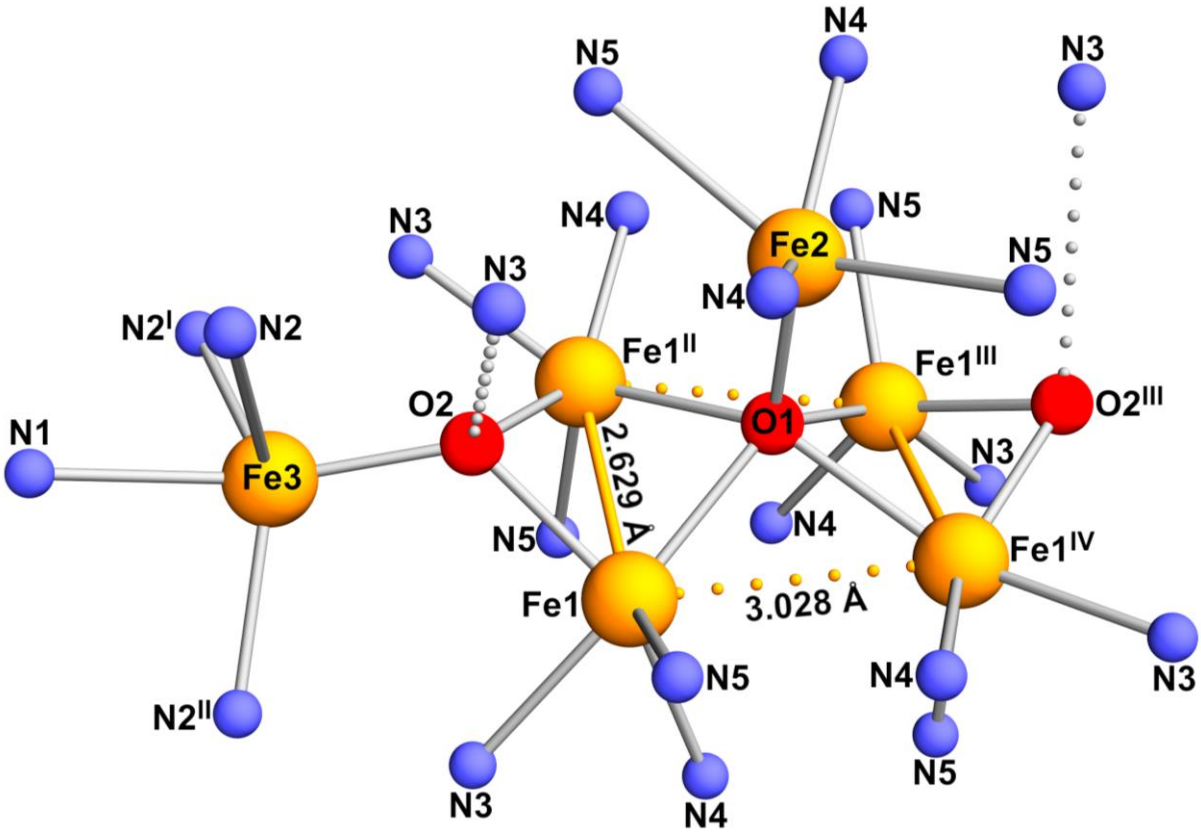

Figure 6.36. Coordination geometry of the Fe and O atoms in **Fe_6L_2** (ball-and-stick model), drawn using the same color code as in Fig. 6.35. The orange dotted lines connecting Fe1···Fe1^{IV} and Fe1^{II}···Fe1^{III} ions do not correspond to chemical bonds, but provide a better representation only. The light grey dotted line connecting O2 and O2^{III} with a N_{py} donor represent possible OH···N_{py} hydrogen bonds. The symmetry generated N atoms are indicated with the same label for simplicity (except N2, N2^I and N2^{II}).

The sixth Fe atom, Fe3, is found in the coordination pocket of the tren moiety, ~0.37 Å off the 3-fold axis and is consequently disordered over three position. It possesses distorted-trigonal-bypyramidal geometry, given by four short contacts with N1, O2 and two N_{am} donors,

and by a longer one with a third N_{am} atom (Fe3−N1 = 2.162(10) Å, Fe3−O2 = 1.851(8) Å, Fe−N_{am} = 2.129(11), 2.180(12) and 2.679(8) Å; N1−Fe3−O2 = 158.4(3)). Additionally, it is only half occupied, affording an average number of six Fe centers per molecule. Most likely, then, the crystal comprises Fe_6 molecules with a single tren pocket (N1,N2,$N2^{I}$,$N2^{II}$ in Fig. 6.35) deprotonated on its secondary amino nitrogen atoms and containing a metal ion, while the remaining tren pocket ($N1^{III}$,$N2^{III}$,$N2^{IV}$,$N2^{V}$ in Fig. 6.35) remains empty and retains its secondary amino hydrogen atoms (Fig. 6.35). Alternative scenarios cannot be excluded, like the occurrence of the molecular species [$Fe_5O_2(\mu_5\text{-}O)H_6L_2$] and [$Fe_7O_2(\mu_5\text{-}O)L_2$] mixed together in a 1:1 ratio inside the crystal. X-ray diffraction analysis cannot distinguish between these limiting situations and all the intermediate possibilities. Ionic species containing 5, 6, and 7 Fe centers were indeed detected by ESI-MS spectrometry (see **Section 6.7.3**). However, the signals of the hexairon species were by far the most intense, and it is likely that the Fe_6 complexes drawn in Fig. 6.35 and Fig. 6.36 are the dominant species. An intriguing feature of this structure is that, in spite of the severe disorder that affects both the $Fe_5(\mu_5\text{-}O)$ core and the sixth metal center, O2 is found exactly on the 3-fold axis and has no abnormal displacement ellipsoid. Worth noting is also the acute Fe1−O2−Fe1 angle of 82.3(2)°, which can be explained by the short Fe−Fe separation. A similar coordination geometry was recently observed in the hydroxo-bridged triosmium complex [$Os_3(CO)_8(\mu\text{-}OH)(\mu\text{-}H)(\mu\text{-}dppm)$] (**19**, where dppm = bis(diphenylphosphino)methane). In complex **19**, a OH^- ion coordinates two Os atoms engaged in a M−M bond (Os−Os = 2.7896(17) Å) and the Os−O−Os angle is as small as 81.1(2)°. Inspired by this report, we examined the possibility that O2 may be part of an hydroxo ligand. What makes this hypothesis realistic is the fact that O2 is surrounded by three N_{py} atoms almost exactly coplanar with it. The arrangement of these N_{py} atoms and the N_{py}−O2 distance of 2.979(5) Å are perfectly consistent with the presence of a OH···N_{py} hydrogen bond of moderate strength (according to the classification of Jeffrey).[218,219] In Fig. 6.35 and 6.36 these OH···N_{py} interactions are highlighted with light grey dotted bonds.

No counterions were detected in the X-Ray diffraction analysis and **Fe_6L_2** is a neutral complex. BVS calculations on the Fe centers suggest that Fe1, Fe2 and Fe3 are in a +2 oxidation state (Table 6.10). However, six Fe^{2+} ions would not afford a neutral complex for any of the formulations listed in Table 6.11 and differing in the number of OH^- ligands. Therefore, one, two or three Fe^{3+} ions must be present in the structure (see Table 6.11). Since BVS calculations gave similar results for all the Fe centers, predicting no Fe^{3+} ions, the most-likely scenario is the presence of five Fe^{2+} and one Fe^{3+} ions, where the positive extra-charge is probably delocalized. This situation implies that both O2 are OH^- ions (Table 6.11). However, since the molecular structure of **Fe_6L_2** is highly disordered (causing low-accuracy of bond distances), the

OH^- ions cannot be inserted in our model with good confidence, and we thus decided to not include them. Variable temperature Mössbauer spectroscopy measurements are required to directly probe the oxidation states of the Fe ions in this material.

Table 6.10. BVS calculations on **Fe_6L_2**.[a]

Atom	Fe^{2+}	Fe^{3+}
Fe1	1.898	2.143
Fe2	2.010	2.302
Fe3	1.840	2.087

[a]Bond-valence parameters (R_0; B) were taken from file bvparm2020.cif available at https://www.iucr.org/resources/data/datasets/bond-valence-parameters: Fe^{2+}–N^{3-} (1.76; 0.37), Fe^{3+}–N^{3-} (1.82; 0.37), Fe^{2+}–O^{2-} (1.734; 0.37), Fe^{3+}–O^{2-} (1.759; 0.37).

Table 6.11. Possible formulations of a neutral $[Fe_6O_x(OH)_yH_3L_2]$ complex with x = 1−3, y = 0−2 and $x+y$ = 3. $H_3L_2^{9-}$ moiety provides 9 negative charges (N. = number of ions).

N. O^{2-}	N. OH^-	−	N. Fe^{2+}	N. Fe^{3+}	+	N.	Total
3	0	6	3	3	15	1	0
2	1	5	4	2	14	1	0
1	2	4	5	1	13	1	0

6.8 Conclusions

In this Chapter a new tridecadentate tripodal ligand, H_3tren(Hdpa)$_3$ (H_6L) was designed, synthesized, and isolated with excellent purity (≥ 97%) and high-yield (65−70%), considering that a three-step reaction was involved. H_6L was prepared through the tri-arylation of the tren ligand, employing BrHdpa or FHdpa as arylating agents, and K_2CO_3 or Cs_2CO_3 as base, without the use of any solvent. The optimized synthesis involves FHdpa, which turned out to be more reactive than BrHdpa towards nucleophilic substitution reaction. FHdpa was not known prior this work and it was repeatedly prepared with 90−92% of yield from: F_2py, NH_2py and LiH (in py/toluene). Cs_2CO_3 was preferred over K_2CO_3, since the former has demonstrated to better promote the alkylation of primary amines (likewise tren), largely suppressing overalkylation reactions of the final product. In order to avoid chromatography, which caused high-loss of the product, a smarter purification method for the isolation of pure H_6L was developed and optimized. The acid properties of H_6L were tested with electronic spectroscopy, which indicates that a base stronger than ^{t}BuOK is required to achieve full deprotonation of the ligand. In fact, ^{t}BuOK is only able to remove the three more acidic protons, which turned out to be those attached to the secondary aromatic amines among the pyridines, as expected. The first structural data on H_3L^{3-} were obtained with the isolation of the monocobalt(II) complex K[CoH_3L] (**CoL**). **CoL** was obtained in THF from $CoCl_2$, KBn (or ^{t}BuOK) and H_6L, in two crystalline forms (**CoL** and **CoL**·THF), which both contain a distorted-octahedral Co^{2+} ion. The coordination mode of H_6L turned out to be strongly influenced by the base, whose exclusion from the reaction environment indicates tetrahedral coordination of the Co^{2+} ion, according to UV-Vis-NIR spectroscopy. After cobalt(II), the coordination chemistry of the tripodal ligand was investigated towards iron(II)-containing complexes. Preliminary studies have given evidence that mono- and diiron(II) compounds are likely to be synthetically feasible, following a similar approach to the one which led to **CoL**. This hypothesis was confirmed when crystals of [Fe_2ClH_3L]·0.36Et_2O (**Fe_2L**·0.36Et_2O) were accidentally obtained from [Fe_2(Mes)$_4$] and H_6L, which indeed systematically afford crystals of the polyiron complex [Fe_6O_2(μ_5-O)H_3L_2] (**Fe_6L_2**). Complex **Fe_6L_2** turned out to be exceedingly air-sensitive. Interestingly, when it is dissolved in THF solution and subsequently expose to the air, it converts in another species, which results then stable overtime. The molecular structure of **Fe_6L_2** features a Fe_5(μ_5-O) core which is likely to contain M−M bonds, that is embedded by two molecules of tripodal ligand which form a cage-like shell together.

In conclusion, the coordination chemistry of the novel tridecadentate tripodal ligand, H_6L, was explored towards cobalt(II) and iron(II). The optimized and reliable procedure for the synthesis of **CoL**, paved the way to the preparation of new mono- and polynuclear complexes of H_6L, based on cobalt(II), iron(II), and possibly on the other metal elements of the first transition series. In fact, although no crystalline iron(II)-based products were isolated so far with this method, it has to be considered that these were only very preliminary results, which were obtained towards the end of this work. Furthermore, mass spectrometry measurements afforded very encouraging results, and more efforts towards the synthesis of a mono- and diiron(II) complex of H_6L will follow this work. For example, the use of KBn instead of ^{t}BuOK may help to achieve pure microcrystalline material, or even XRD-quality single crystals, of new products (e.g. $K[FeH_3L]$, $[Fe_2ClH_3L]$), as it occurs during the synthesis of **CoL**. On the other hand, a similar procedure to that used in the preparation of tetrairon(II) EMACs (complexes **1Cl**[20] and **1Br**, see **Chapter 4**), afforded the following di- and polyiron complexes: **Fe_2L** (accidentally) and **Fe_6L_2**. The molecular structure of **Fe_2L** strongly resembles that of "half" complex **1Cl**, which feature a ferromagnetic Fe_2 dimer. Therefore, the study of the magnetic properties of **Fe_2L** are an intriguing perspective to better understand the magnetic behaviour of **1Cl**. Since **Fe_6L_2** contains six Fe centers and probably Fe−Fe bonds, another exciting oncoming outlook is the investigation of its magnetic properties, along with variable temperature Mössbauer spectroscopy measurements, which are necessary to experimentally determine the oxidation states of the Fe ions, and to get insight about their chemical environment. Furthermore, experimental observations suggest that new Fe^{2+}/Fe^{3+} MV systems can be prepared from the chemical oxidation of **Fe_6L_2**, which can be employed as starting material. Therefore, the study of the redox properties of **Fe_6L_2** appears significantly appealing, and its investigation will require CV measurements. Notably, the synthesis which afforded complex **Fe_6L_2** was originally tuned for the preparation of a triiron(II)-EMAC, which probably failed to assemble due to traces of oxygen and/or moisture in the reaction environment. Therefore, the synthesis of new iron(II)-EMACs based on H_6L remains one of the paramount ambitions of my future work, and it can be probably finalized by merely exercising a better control of the experimental conditions.

6.9 Experimental Section

6.9.1 Materials and Methods

All synthetic operations involving cobalt and iron complexes were carried out inside an MBraun UniLAB glovebox under an inert and controlled dinitrogen atmosphere, continuously purified over activated charcoal, molecular sieves and a copper oxygen scavenger (H_2O and O_2 < 1 ppm). All chemicals were of reagent grade and used as received, unless otherwise noted. Anhydrous dichloromethane, toluene and 1,4-dioxane were purchased and used exclusively for operation inside the glovebox. Tetrahydrofuran and Et_2O were pre-dried over KOH[125] and $CaCl_2$[126] respectively, and subsequently distilled from their sodium benzophenone ketyl solutions before use. Pyridine was distilled over KOH (115−116 °C) and stored over KOH pellets. All the solvents used inside the glovebox were deoxygenated through three freeze-pump-thaw cycles and stored over 4A molecular sieves. Compound BrHdpa was synthesized improving a known procedure.[188] The tren ligand was distilled over CaH_2 (10% in weight) under reduced pressure (137 °C, 17 mmHg). KBn was quantitatively prepared according to a well-known literature method, treating toluene with a 1:1 mixture of ^{t}BuOK and *n*-BuLi.[220] $[Fe_2(Mes)_4]$ was synthesized from $Fe_4Cl_8{\cdot}6THF$[82] and MesMgBr in THF/1,4-dioxane.[103,127]

Elemental analysis was performed using a ThermoFisher Scientific Flash 2000 analyzer, following brief exposure of the sample to the air (30-60 s). The molar concentration of the THF solution of $CoCl_2$ was determined by complexometric titration,[221] using xylenol orange and EDTA. The concentration of EDTA was established by titration with a standard solution of $Pb(NO_3)_2$. The Fe content in **Fe_6L_2** was determined similarly,[221] after digestion of the compound with HNO_3 and H_2O_2. All the other characterization data for **CoL** and **Fe_6L_2** were collected with strict exclusion of dioxygen and water, unless otherwise noted. ESI-MS measurements were conducted on a 6310A Ion Trap LC-MS(n) instrument (Agilent Technologies) by direct infusion of THF or CH_2Cl_2 solutions, in positive (or negative) ion mode. MALDI-TOF-MS measurements were performed at the University of Wisconsin-Madison with a Bruker ULTRAFLEX™ III (equipped with a SmartBeam™ laser), on a powdery sample finely milled with a large excess of pure anthracene, in positive ion mode. The *m*/*z* values in the MALDI-TOF-MS spectra are expressed by setting the isotopic peak of anthracene ($C_{14}H_{10}$) at *m*/*z* = 178.08. The electronic spectra in THF solution were recorded up

to 2000 nm on a double beam UV−Vis−NIR Jasco V-570 spectrometer, using a quartz cuvette sealed with an airtight Teflon® cap (optical path length l = 0.1 cm). The one- and two-dimensional NMR spectra (^{1}H, ^{13}C, ^{1}H–^{1}H COSY, ^{1}H–^{13}C HSQC and ^{1}H–^{13}C HMBC) were recorded at 298 K in CD_3CN or DMSO-d_6, using a Bruker FT-NMR Avance III HD 600 (600.13 MHz) or a Bruker Avance400 FT-NMR spectrometer (400.13 MHz). The chemical shifts are expressed in ppm downfield from Me_4Si as external standard, by setting the residual ^{1}H (^{13}C) signal of CD_3CN or DMSO-d_6 at 1.94 (1.32 ppm) and 2.50 ppm, respectively. Spectrum analysis was carried out with TopSpin 4.0.6 software.[86]

6.9.2 Synthesis of BrHdpa

In a three neck round bottom flask (1 L) equipped with a mechanical overhead stirrer and a condenser, NH_2py (5.2510 g, 55.796 mmol) and Br_2py (13.2155 g, 55.787 mmol) were dissolved in anhydrous toluene (500 mL) under nitrogen atmosphere. ^{t}BuOK (10.2110 g, 90.9990 mmol) was carefully added to the pale-yellow solution, which progressively darkened to dark blue/black. The dark solution was heated to 85 °C for three days. It is worth to note that during the initial heating a very dense solid mass formed around 70 °C. This mass was progressively dispersed into the suspension during the first 24 h, thanks to the mechanical stirrer. The suspension was allowed to cool to room temperature, and the solvent was evaporated under reduced pressure. The light-pink solid obtained was dissolved in CH_2Cl_2 (300 mL) and washed with water (150 mL + 2 × 50 mL). The inorganic phases were extracted with CH_2Cl_2 (2 × 50 mL). The extract was added to the main organic phase, and the red solution obtained was dried over $MgSO_4$ (90 min.). After filtration, the red organic solution was evaporated to dryness, to give a dark orange oil, which slowly crystallized into a solid under vacuum (~11.55 g). The product was obtained as pale-yellow solid (9.01 g, 36.0 mmol, yield = 64.6%), after purification through gradient-elution FC (eluent petroleum ether : Et_2O, from 1 : 0 to 1 : 1).

^{1}H NMR (DMSO-d_6, 400.13 MHz): δ_H (ppm) = 10.03 (3H, s, H*h*), 8.24 (3H, ddd, ^{3}J(*a*,*b*) = 5.0, ^{4}J(*a*,*c*) = 1.9, ^{5}J(*a*,*d*) = 0.8, H*a*), 7.92 (3H, dd, ^{3}J(*g*,*f*) = 8.3, ^{4}J(*g*,*e*) = 0.4, H*g*), 7.68 (3H, m, ^{3}J(*c*,*d*) = 8.4, ^{3}J(*c*,*b*) = 7.2, ^{4}J(*c*,*a*) = 2.0, H*c*), 7.59 (3H, pt, ^{3}J(*f*,*e*) ~ ^{3}J(*f*,*g*) ~ 7.9, H*f*), 7.48 (3H, m, ^{3}J(*d*,*c*) = 8.4, ^{4}J(*d*,*b*) ~ ^{5}J(*d*,*a*) ~ 0.9, H*d*), 7.05 (3H, dd, ^{3}J(*e*,*f*) = 7.5, ^{4}J(*e*,*g*) = 0.5, H*e*), 6.90 (3H, ddd, ^{3}J(*b*,*c*) = 7.2, ^{3}J(*b*,*a*) = 5.0, ^{4}J(*b*,*d*) = 1.0, H*b*).

6.9.3 Synthesis of FHdpa

In a three neck round bottom flask (250 mL) equipped with a condenser, NH_2py (1.3643 g, 14.496 mmol) and LiH (0.3940 g, 49.57 mmol) were added under nitrogen atmosphere. The two solids were stirred together and after five minutes F_2py (2.5050 g, 21.767 mmol) and py (7.5 mL) were added, to give a yellow suspension. The mixture was slowly heated until effervescence was produced (~90 °C) and color rapidly changed to orange. Then, anhydrous toluene (20 mL) was added from the top of the condenser, in order to slow down the reaction. When no more effervescence was observed, the temperature was carefully raised to 120 °C and the mixture heated for two hours, to give a dark red suspension. The mixture was allowed to cool to room temperature and then the solvent was evaporated under reduce pressure, to obtain a brown solid which was well pumped to dryness. The flask was placed into an ice-bath, and the excess of LiH was carefully quenched with small pieces of ice. When no more effervescence was observed, water (30 mL) was carefully added, and the suspension was stirred overnight at room temperature. The mixture was filtered on a fritted glass filter, to give a light-brown solid, which was washed with water (3 × 20 mL). Then, it was repeatedly extracted with CH_2Cl_2 (3 × 20 mL), to give a dark red solution, which was evaporated under reduced pressure. The solid was dissolved in CH_2Cl_2 (15 mL) and filtered over a very short silica plug (~2.0 g of SiO_2), placed over a layer of celite. After the filtration, additional CH_2Cl_2 (3 × 7 mL) was passed through the SiO_2. The filtrates were added together and evaporated to dryness, to give a light-brown solid, which was dried under vacuum for 3−4 hours, to give 2.5316 g of pure product (13.381 mmol, yield = 92.3%).

Anal. Calcd for FHdpa: C, 63.49; H, 4.26; N, 22.21. Found: C, 63.09; H, 4.63; N, 22.50. ^{1}H NMR (CD_3CN, 600.13 MHz): δ_H (ppm) = 8.24 (3H, ddd, ^3J(*a*,*b*) = 4.9, ^4J(*a*,*c*) = 1.9, ^5J(*a*,*d*) = 0.8, H*a*), 8.1 (3H, br, H*k*), 7.75 (3H, pq, ^3J(*h*,*g*) ~ ^3J(*h*,*i*) ~ 8.2, ^4J(*h*,F) = 8.2, H*h*), 7.67 (3H, m, ^3J(*c*,*d*) = 8.4, ^3J(*c*,*b*) = 7.2, ^4J(*c*,*a*) = 1.9, H*c*), 7.58 (3H, ddd, ^3J(*g*,*h*) = 8.0, ^5J(*g*,F) = 2.4, ^4J(*g*,*i*) = 0.4, H*g*), 7.55 (3H, m, ^3J(*d*,*c*) = 8.4, ^4J(*d*,*b*) ~ ^5J(*d*,*a*) ~ 0.9, H*d*), 6.92 (3H, ddd, ^3J(*b*,*c*) = 7.2, ^3J(*b*,*a*) = 4.9, ^4J(*b*,*d*) = 1.0, H*b*), 6.47 (3H, ddd, ^3J(*i*,*h*) = 7.8, ^3J(*i*,F) = 2.5, ^4J(*i*,*g*) = 0.4, H*i*). δ_C (ppm) = 163.2 (1C, d, ^1J(*j*,F) = 234.6, C*j*), 154.7 (1C, s, C*e*), 154.1 (1C, d, ^3J(*f*,F) = 16.2, C*f*), 148.7 (1C, s, C*a*), 143.6 (1C, d, ^3J(*h*,F) = 8.2, C*h*), 138.8 (1C, s, C*c*), 117.9 (1C, s, C*b*), 112.9 (1C, s, C*d*), 109.0 (1C, d, ^4J(*g*,F) = 4.2, C*g*), 100.3 (1C, d, ^2J(*i*,F) = 36.6, C*i*).

6.9.4 Synthesis of H_6L

Under nitrogen atmosphere, FHdpa (2.9992 g, 15.853 mmol) and Cs_2CO_3 (5.1647 g, 15.851 mmol) were introduced into a pear-shaped Schlenk. The tren ligand (0.7264 g, 4.967 mmol) was then added with a syringe, and the mixture was carefully heated to 130 °C with stirring. Between 85−100 °C the mixture progressively turned into a dark brown suspension due to the melting of FHdpa. The temperature was kept constant for three days, during which the mixture progressively hardened, to give a lighter brown solid. It is worth to note that after 24−30 h at 130 °C the magnetic stirring was blocked. This hard solid was allowed to cool down to room temperature, and then was dissolved in CH_2Cl_2 (30 mL) with the help of an ultrasonic bath. The dark red solution obtained was washed with a saturated solution of $NaHCO_3$ (3 × 6 mL) and subsequently with water (3 × 6 mL). The inorganic phases were extracted with CH_2Cl_2 (6 mL), and the extract was added to the main organic phase. The so-obtained CH_2Cl_2 solution was then dried over $MgSO_4$ (1 h), filtered over a fritted glass filter (porosity G3) and evaporated under reduce pressure. The afforded solid was dissolved in CH_2Cl_2 (7−8 mL) and filtered over a very short silica plug (~2.5 g of SiO_2), placed over a layer of celite. After the filtration, additional CH_2Cl_2 (7 mL) was passed through the SiO_2. The filtrates were combined and evaporated to dryness, to give a light-brown sticky solid. Afterwards, this solid was triturated for 24 h in Et_2O (25 mL). The solvent was subsequently removed with a narrow bore pipette. The yellow powder was finally admixed with *n*-hexane (15 mL). The suspension was stirred (20 min) and sonicated (10 min) alternately for 2 h, and then the solvent was removed with a narrow bore pipette. Finally, the solid was well dried in vacuum to afford the product as a yellow powder (2.17 g, 3.32 mmol, yield = 66.8%).

Anal. Calcd for $H_6L·0.44EtOH$: C, 65.72; H, 6.23; N, 27.01. Found: C, 65.48; H, 6.48; N, 27.33. UV-Vis-NIR (THF, $1.10·10^{-3}$ M): λ_{max} (ε) = 239 nm ($4.96·10^4$ M^{-1} cm^{-1}), 272 nm ($5.74·10^4$ M^{-1} cm^{-1}), 332 nm ($5.89·10^4$ M^{-1} cm^{-1}). ^{1}H NMR (CD_3CN, 600.13 MHz): δ_H (ppm) = 8.15 (3H, ddd, $^3J(a,b)$ = 4.9, $^4J(a,c)$ = 1.9, $^5J(a,d)$ = 0.9, H*a*), 7.77 (3H, br, H*k*), 7.73 (3H, m, $^3J(d,c)$ = 8.4, $^4J(d,b)$ ~ $^5J(d,a)$ ~ 0.9, H*d*), 7.53 (3H, m, $^3J(c,d)$ = 8.5, $^3J(c,b)$ = 7.1, $^4J(c,a)$ = 1.9, H*c*), 7.25 (3H, pq, $^3J(h,g)$ ~ $^3J(h,i)$ ~ 7.9, H*h*), 6.76 (3H, ddd, $^3J(b,c)$ = 7.2, $^3J(b,a)$ = 4.9, $^4J(b,d)$ = 1.0, H*b*), 6.60 (3H, ddd, $^3J(g,h)$ = 7.9, $^4J(g,i)$ = 0.5, H*g*), 5.94 (3H, ddd, $^3J(i,h)$ = 8.0, $^4J(i,g)$ = 0.6, H*i*), 5.21 (3H, pt, $^3J(n,l)$ = 5.6, H*n*), 3.37 (6H, q, $^3J(l,m)$ ~ $^3J(l,n)$ ~ 6.0, H*l*), 2.78 (6H, t, $^3J(m,l)$ = 6.2, H*m*). δ_C (ppm) = 159.1 (1C, C*j*), 155.6 (1C, C*e*), 154.2 (1C, C*f*), 148.6 (1C, C*a*), 139.7 (1C, C*h*), 138.4 (1C, C*c*), 116.6 (1C, C*b*), 112.5 (1C, C*d*), 100.4 (1C, C*i*), 99.7 (1C, C*g*), 54.5 (1C, C*m*), 40.8 (1C, C*l*).

6.9.5 Synthesis of K[CoH_3L] (**CoL**)

Inside a glovebox, H_6L (45.9 mg, 0.0702 mmol) was dissolved in THF (1 mL) to give a yellow solution, which was cooled down to −50 °C. KBn (31.2 mg, 0.240 mmol) was dissolved in cold THF (−50 °C, 1.5 mL) and the red solution obtained was slowly added under stirring to the ligand's solution, which rapidly turned green. A deep blue THF solution of $CoCl_2$ (0.0258 M, 2.70 mL, 0.0697 mmol) was then added dropwise, causing a color change to light brown/beige. The system was stirred for additional 30 minutes and then it was allowed to slowly reach room temperature. The dark red suspension obtained was filtered through a fritted glass funnel (porosity G4), in order to remove a very fine light grey solid, which was then washed with THF (1 mL). The solution was concentrated and layered with Et_2O. The crystallization afforded crystals of the product, which were separated by flotation from a powdery residue, washed with few drops of Et_2O, and stored under their mother liquor (38.4 mg, 0.0489 mmol, yield = 70.2% considering the average molecular weight of a 1:1 mixture of **CoL** and **CoL**·THF).

Anal. Calcd for K[CoH_3L]: C, 57.74; H, 4.85; N, 24.33. Found: C, 57.92; H, 5.29; N, 24.31. ESI-MS (THF:CH_2Cl_2 1:4, positive ion mode), *m*/*z*: 748.3 ($K[CoH_3L]^+$, 100); 692.4 ($K[H_6L]^+$, 8); 787.2 ($K_2[CoH_3L]^+$, 4). ESI-MS (THF:CH_2Cl_2 1:4, negative ion mode), *m*/*z*: 709.3 ($[CoH_3L]^-$, 100). UV-Vis-NIR (THF, $2.7\cdot10^{-4}$ M): λ_{max} (ε) = 237 nm ($8.11\cdot10^4$ M^{-1} cm^{-1}), 303 nm ($5.12\cdot10^4$ M^{-1} cm^{-1}), 362 nm ($6.50\cdot10^4$ M^{-1} cm^{-1}), ~450 nm (sh).

6.9.6 Synthesis of [$Fe_6O_2(\mu_5\text{-}O)H_3L_2$] (**$Fe_6L_2$**)

Inside a glovebox, [$Fe_2(Mes)_4$] (265.6 mg, 0.4514 mmol) and H_6L (184.8 mg, 0.2827 mmol) were admixed together in toluene (7 mL) and the suspension was heated to the reflux temperature for 3 h. During the reflux the suspension progressively turned from orange to dark red/brown. The reaction mixture was allowed to cool down to room temperature, and the solution was then eliminated by filtration through a fritted glass filter. The dark red solid was washed with fresh toluene (1 mL) and extracted with THF (4 × 10 mL). One additional overnight extraction was performed with 20 mL of THF. The red solution obtained was evaporated under vacuum, to give the product as a red solid (134 mg, 0.0797 mmol, yield = 56.4%). This red solid can be recrystallized from THF/Et_2O by slow liquid diffusion to afford small, very dark red, trapezoidal plates of **Fe_6L_2** (yield of the entire process = 48.1%). For all the following characterizations, these crystals were removed from the mother solution, washed with few drops of Et_2O, crushed and well dried under vacuum.

Anal. Calcd for $[Fe_6O_2(\mu_5\text{-}O)H_3L_2]$: C, 51.43; H, 4.14; N, 21.66. Found: C, 52.11; H, 4.12; N, 21.24. Fe content (%) for $[Fe_6O_2(\mu_5\text{-}O)H_3L_2]$: 19.93. Found: 19.7. ESI-MS (THF, positive ion mode), *m*/*z*: 1680.2−1681.2 ($[Fe_6O_3H_2L]^+$ and $[Fe_6O_3H_3L]^+$, 0.8:0.2 ratio, 100); 1626.3−1627.3 ($[Fe_5O_3H_4L]^+$ and $[Fe_5O_3H_5L]^+$, 0.9:0.1 ratio, 10); 850.1 ($[Fe_3ClL]^+$, 3). UV-Vis-NIR (THF, $1.4\cdot10^{-4}$ M): λ_{max} (ε) = 242 nm ($1.03\cdot10^5$ M^{-1} cm^{-1}), 268 nm (sh), 341 nm ($6.83\cdot10^4$ M^{-1} cm^{-1}), ~380 nm (sh), ~500 nm (sh).

6.9.7 X-Ray Crystallography of $K[CoH_3L]$ (**CoL**) and (**CoL**·THF)

Crystals of the compounds were removed from the mother solution under nitrogen, embedded in epoxy resin and mounted on a Bruker-Nonius X8APEX diffractometer equipped with Mo-Kα generator and area detector, for data collection at 298(2) K. Acquisition of matrix frames and data collection were carried out using APEX2 software[130] while data reduction used SAINT program.[130] Multi-scan absorption correction was applied with SADABS.[130] Programs SIR92[131] and SHELXL-2014/7,[132] both implemented in the WINGX v2014.1 suite,[133] were used for structure solution and refinement on F_o^2, respectively. Both compounds crystallize in the same space group ($P\bar{1}$).

In the structure of **CoL**, all atoms lie in general positions (Z = 2). The aliphatic part (NCH_2CH_2NH-) of one of the ligand's branches was found disordered over two different positions, with 0.63:0.37 occupancies. All non-hydrogen atoms were refined anisotropically. The conformation of the pyridyl rings (i.e. the correct assignment of C and N scattering factors) was firmly established by inspection of the pattern of displacement parameters within each ring. Restraints were introduced on geometry and displacement parameters of the disordered part using EXYZ, EADP, SAME and RIGU[183] instructions. Hydrogen atoms were set in idealized positions with IDPs constrained to those of the attached carbon atoms. Crystal data and refinement parameters are gathered in Table 6.1 while interatomic distances and angles are presented in Table 6.2.

In the structure of **CoL**·THF, all atoms lie in general positions (Z = 2). A crystallization THF molecule coordinates one K ion, and it was found disordered over two positions, which are present in a 0.63:0.37 ratio. All non-hydrogen atoms were refined anisotropically, excluding the disordered THF molecule. The conformation of the pyridyl rings (i.e., the correct assignment of C and N scattering factors) was firmly established by inspection of the pattern of

displacement parameters within each ring. Restraints were introduced on geometry and displacement parameters of disordered THF using EADP, SAME and SADI[183] instructions. Hydrogen atoms were set in idealized positions with IDPs constrained to those of the attached carbon and nitrogen atoms. Crystal data and refinement parameters are gathered in Table 6.1 while interatomic distances and angles are presented in Table 6.2.

6.9.8 X-Ray Crystallography of $[Fe_2ClH_3L]\cdot 0.36Et_2O$ ($\mathbf{Fe_2L}\cdot 0.36Et_2O$)

A crystal of the compound was removed from the mother solution under nitrogen, soaked in immersion oil, mounted on a MiTeGen MicroMount™ and transferred to a Bruker-Quazar SMART APEXII diffractometer, at the University of Wisconsin-Madison. The diffractometer is equipped with Mo-Kα generator, area detector, and Oxford Cryosystems low temperature device (model 700) for data collection at 100(2) K. Acquisition of matrix frames and data collection were carried out using APEX3 software[130] while data reduction used SAINT program.[130] Multi-scan absorption correction was applied with SADABS.[130] Programs SIR92[131] and SHELXL-2014/7,[132] both implemented in the WINGX v2014.1 suite,[133] were used for structure solution and refinement on F_o^2, respectively. The measured crystal, and likewise all tested samples, was weakly diffracting due to its very thin shape. Therefore, an exposure time of 200 s was set during the data collection, which was extended to a resolution of 0.80 Å ($2\theta_{max}$ = 52.74°) to give $\langle I/\sigma(I)\rangle$ = 7.62. Structure solution in the space group $P\bar{3}c1$ (trigonal crystal system) followed by a Fourier synthesis gave the positions of all non-hydrogen atoms. Molecules develop around a C_3 axis (Z = 4) and have crystallographically imposed threefold symmetry. A partially occupied Et_2O molecule develops around a D_3 special position, and is found disordered over two positions with 0.25 and 0.11 occupancies. Therefore, 0.36 molecules of solvent are present for each molecule of **Fe_2L**. All non-hydrogen atoms were refined anisotropically, excluding the crystallization Et_2O molecule. Additional restraints were introduced on geometry and displacement parameters of disordered Et_2O using EADP, SAME, DFIX and DANG[183] instructions. Hydrogen atoms were set in idealized positions with IDPs constrained to those of the attached carbon and nitrogen atoms. Crystal data and refinement parameters are gathered in Table 6.4 while interatomic distances and angles are presented in Table 6.5.

6.9.9 X-Ray Crystallography of $[Fe_6O_2(\mu_5\text{-}O)H_3L_2]$ (**Fe_6L_2**)

A plate-like crystal of the compound was covered with NVH immersion oil (Jena Bioscience), mounted on a MiTeGen Microloop™ and transferred to a Bruker-Nonius X8APEX diffractometer equipped with Mo-Kα generator, area detector and Kryoflex liquid nitrogen cryostat for data collection at 115(2) K. Acquisition of matrix frames and data collection were carried out using APEX2 software[130]. Data reduction used SAINT program[130] and was followed by multi-scan absorption correction applied with SADABS.[130] Programs SUPERFLIP[222,223] and SHELXL-2014/7,[132] implemented in the WINGX v2020.1 suite,[133] were used for structure solution and refinement on F_o^2, respectively. The measured crystal, and likewise all tested samples, was weakly diffracting and data collection was extended to a resolution of 0.84 Å ($2\theta_{max} = 50.0°$) to give $\langle I/\sigma(I)\rangle = 6.74$. The unit cell metrics and the symmetry of the diffraction pattern were consistent with trigonal crystal system, with R(merge) = 0.078, 0.073 and 0.048 in Laue classes $\bar{3}1m$ (hex), $\bar{3}$ (hex) and $\bar{1}$, respectively. Systematic absences were found to affect *hhl* reflections, which had $\langle I/\sigma(I)\rangle = -0.16$ for odd l (320 reflections) and 10.29 for even l (311 reflections), strongly suggesting extinction symbol *P*- - *c* and space groups *P*31c (noncentric) or $P\bar{3}1c$ (centric). Structure solution in the centric space group followed by a Fourier synthesis gave the positions of all non-hydrogen atoms. Molecules develop around a site with D_3 symmetry ($Z = 2$) and have crystallographic threefold symmetry. Two equivalent organic ligands encapsulate a central core whose structure, as resulting from a Fourier synthesis with phases based on the organic ligands alone, is depicted in Fig. 6.37. The six most intense peaks (Q1 = 10.75 eÅ^{-3}) define a slightly distorted trigonal prism, with the shortest Fe⋯Fe separations of 2.67 and 3.09 Å. Each longer edge of the prism is capped by an additional peak (Q2 = 7.89 eÅ^{-3}) lying exactly on a twofold axis at 1.59 Å from the vertices. Other significant electron density residuals are found on the threefold axis, namely at the center of the prism (Q3 = 5.66 eÅ^{-3}), in the tren-like pockets of the ligands (Q4 = 5.62 eÅ^{-3}) and in triangular-face capping positions (Q5 = 4.86 eÅ^{-3}). Refinement of Q1 and Q4 as full-occupancy Fe atoms and of Q2, Q3 and Q5 as full-occupancy O atoms gave IDPs of 0.053 (Q1), 0.178 (Q4), –0.001 (Q2), 0.017 (Q5) and 0.014 Å^2 (Q3). By comparing these values with the average IDP of ligand's nitrogen donors (0.027 Å^2), it can be inferred that, most likely, Q2 and Q4 are partially occupied metal sites. The Q1-Q2 distance is indeed unphysically short for a metal-metal contact and requires the central core to be disordered. Q1, Q2 and Q4 were then assigned as Fe1, Fe2 and Fe3, respectively, and the two remaining peaks as O1 and O2. Free refinement of both IDPs and site occupation factors (SOFs) gave IDPs in the range 0.020-0.040 Å^2 for all these atoms

with the exception of Fe3 (0.099 Å^2), with SOFs amounting to 0.59, 0.30, 0.44, 0.78 and 0.98. When Fe1 and Fe2 were refined anisotropically with complementary SOFs, the occupancies refined to 0.65 and 0.35, respectively, suggesting a pentairon core disordered by rotation around the trigonal axis, with a central μ_5-O ligand (O1) and a μ_3-O(H) group (O2) linking the central core to each Fe3 metal. Full anisotropic refinement gave *R*1 = 0.103 and occupancies of 0.65 (Fe1), 0.35 (Fe2), 0.39 (Fe3), 0.81 (O1) and 0.93 (O2). The anisotropic displacement parameter (ADP) of Fe3 was very oblate and the attached secondary N donors were distinctly elongated towards the metal, suggesting an off-axis Fe3 position. When Fe3 was allowed to move from the threefold axis and treated isotropically, its occupancy refined to 0.13 and *R*1 decreased slightly to 0.098. Fixed occupancies of 2/3, 1/3 and 1/6 were then assigned to Fe1, Fe2 and Fe3, respectively, while O1 and O2 were taken as fully occupied, affording practically unvaried *R*1 (0.100). Hydrogens were added in calculated positions with U(H) = 1.2U_{eq}(C), including the half-occupancy secondary NH hydrogens of the 50-% metalated tren-like pocket, which could be located in Δ*F* map. Final polishing with rejection of outliers and weighing gave w*R*2 = 0.298 (all data) and *R*1 = 0.085 ($I > 2\sigma(I)$).

Crystal data and refinement parameters are gathered in Table 6.8 while interatomic distances and angles are presented in Table 6.9.

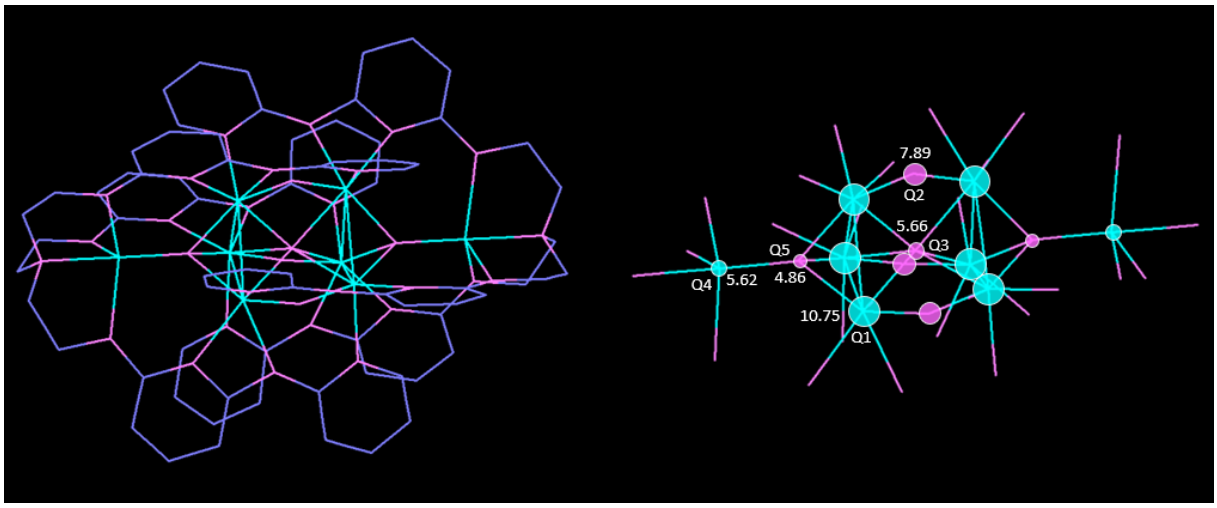

Figure 6.37. Molecular structure of **Fe$_6$L$_2$** (wireframe model). H atoms are omitted for clarity, along with C atoms in the structure on the right. The circles on the right represent the residual electron density (Q-peaks, in *e*Å^{-3}) resulting from a Fourier synthesis with phases based on the organic ligands alone.

Chapter 7

This Chapter contains a recently (2020) published paper I co-authored on a topic not directly related to my main project but relevant to the concepts covered in my Thesis. I have contributed to this paper with the preparation of one of the samples and with EPR spectroscopy measurements. Since it is a published manuscript, **Chapter 7** is self-consistent with references, abbreviations, etc…

The Origin of Magnetic Anisotropy and Single-Molecule Magnet Behavior in Chromium(II)-based Extended Metal Atom Chains

Andrea Cornia,[a] Anne-Laure Barra,[b] Vladimir Bulicanu,[c] Rodolphe Clérac,[c] Miguel Cortijo,[c] Elizabeth A. Hillard,[c]* Rita Galavotti,[a] Alessandro Lunghi,[d] Alessio Nicolini,[a,e] Mathieu Rouzières,[c] Lorenzo Sorace[f] and Federico Totti[f]**

[a]Department of Chemical and Geological Sciences, University of Modena and Reggio Emilia & INSTM, 41125 Modena, Italy

[b]Laboratoire National des Champs Magnétiques Intenses-CNRS, Université Grenoble-Alpes, 38042 Grenoble Cedex 9, France

[c]Univ. Bordeaux, CNRS, Centre de Recherche Paul Pascal, UMR 5031, 33600 Pessac, France

[d]School of Physics and CRANN Institute, Trinity College Dublin, Dublin 2, Ireland

[e]Department of Physics, Informatics and Mathematics, University of Modena and Reggio Emilia, 41125 Modena, Italy

[f]Department of Chemistry 'Ugo Schiff', University of Florence & INSTM, 50019 Sesto Fiorentino (FI), Italy

ABSTRACT

Chromium(II)-based Extended Metal Atom Chains have been the focus of considerable discussion regarding their symmetric vs. unsymmetric structure and magnetism. We have now investigated four complexes of this class, namely $[Cr_3(dpa)_4X_2]$ and $[Cr_5(tpda)_4X_2]$ with X = Cl^- and SCN^- [Hdpa = dipyridin-2-yl-amine; H_2tpda = N^2,N^6-di(pyridin-2-yl)pyridine-2,6-diamine]. By dc/ac magnetic techniques and EPR spectroscopy we found that all these complexes have easy-axis anisotropies of comparable magnitude in their S = 2 ground state ($|D|$ = 1.5-1.8 cm^{-1}) and behave as single-molecule magnets at low T. Ligand-field and DFT/CASSCF calculations were used to explain the similar magnetic properties of tri- vs. pentachromium(II) strings, in spite of their different geometrical preferences and electronic structure. For both X ligands, the ground structure is unsymmetric in pentachromium(II) species (i.e. with an alternation of long and short Cr-Cr distances), but symmetric in their shorter congeners. Analysis of the electronic structure using Quasi-Restricted Molecular Orbitals (QROs) showed that the four unpaired electrons in Cr_5 species are largely localized in four 3d-like QROs centered on the terminal, "isolated" Cr^{2+} ion. In Cr_3 complexes, they occupy four non-bonding combinations of 3d-like orbitals centered only on the two terminal metals. In both cases, then, QRO eigenvalues closely mirror the 3d-level pattern of the terminal ions, whose coordination environment remains quite similar irrespective of chain length. We conclude that the extent of unpaired-electron delocalization has little impact on magnetic anisotropy of these wire-like molecular species.

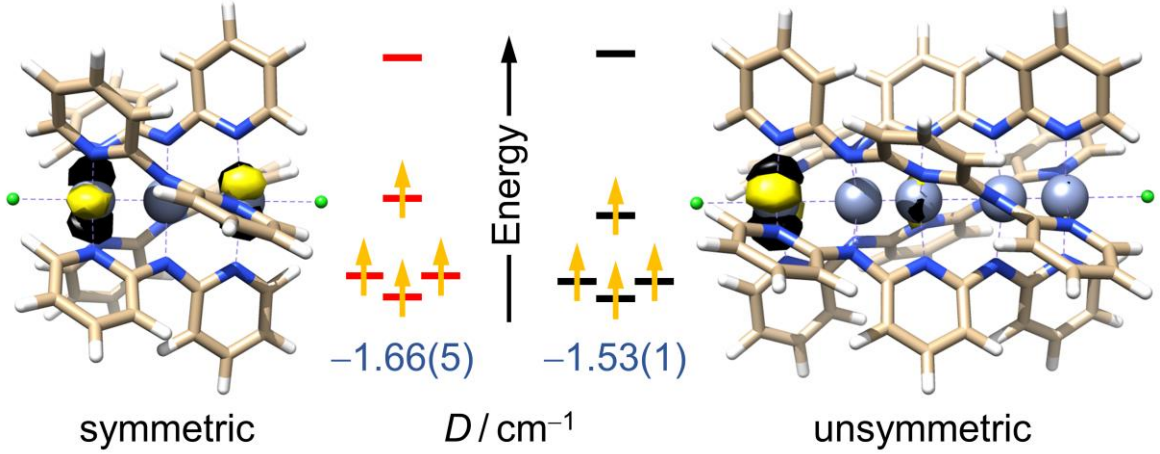

INTRODUCTION

Single-molecule magnets (SMMs) are molecules comprising one or more metal centers and showing slow relaxation of the magnetization below a characteristic temperature, referred to as the blocking temperature (T_B).[1,2] They are considered as the smallest chemically tunable components for spin-based devices and hold promise for applications in information storage[3–5] and quantum technologies.[6–9] A key ingredient for SMM behavior is magnetic anisotropy, which mainly originates from spin-orbit coupling and crystal-field effects.[10,11] Although cases of slow magnetic relaxation are known for predominantly easy-plane systems,[12,13] the vast majority of known SMMs have an easy-axis anisotropy in their ground

state. The reversal of the magnetic moment is then subject to an energy barrier, *U*, whose height is one of the important factors that rule magnetic relaxation.[14,15] A recent breakthrough in the field was the discovery that remarkably large energy barriers can be achieved even in mononuclear species.[13,16] Lanthanoid complexes of this type are indeed among the best SMMs known to date,[17–19] with U/k_B values approaching 2000 K[20–23] and record observable T_B's of up to 80 K.[22–24]

Examples of SMMs have been recently reported in polynuclear compounds containing metal-metal bonds and exhibiting, as a unique feature, a well-isolated high-spin ground state even at room temperature. The current record spin value is $S = 11$ for a mixed-valent hexa-iron complex with an octahedral metal topology.[25] Similar features are encountered in the so-called Extended Metal Atom Chains (EMACs), which have attracted attention as molecular analogues of macroscopic wires and benchmark systems for understanding metal-metal interactions.[26–29] EMACs consist of three or more metal centers forming a linear array supported by three or four deprotonated oligo-α-pyridylamine (or related) ligands, most often arranged in a helical fashion.[30–32] Their molecular wire-like structure has either rigorous or idealized axial symmetry and makes high-spin EMACs potential SMMs. In fact, the tri- and pentachromium(II) compounds $[Cr_3(dpa)_4Cl_2]\cdot CH_2Cl_2$ (**1a**·CH_2Cl_2)[33] and $[Cr_5(tpda)_4Cl_2]\cdot 4CHCl_3\cdot 2Et_2O$ (**2a**·$4CHCl_3\cdot 2Et_2O$)[34] have a well-isolated $S = 2$ state, display an easy-axis anisotropy of similar magnitude and behave as SMMs with energy barriers of 10.6(6) and 8.6(5) K, respectively (Hdpa = dipyridin-2-yl-amine; H_2tpda = N^2,N^6-di(pyridin-2-yl)pyridine-2,6-diamine; see Scheme 1).[35–37] The similarity in magnetic behavior is surprising since the electronic structure of the two string-like complexes is thought to be different. After considerable initial controversy,[38] there is now a general consensus that the abnormally elongated displacement ellipsoids of inner metal ions in the crystal structures of pentachromium(II) species reflect a disordered superposition of two unsymmetric structures with alternating short ($d_<$) and long ($d_>$) Cr-Cr distances (Scheme 1d). Resolution of the disorder afforded $d_<$ = 1.86-2.07 Å, $d_>$ = 2.50-2.66 Å and $\Delta d = d_> - d_< \sim 0.5$-0.8 Å in compounds $[Cr_5(tpda)_4X_2]\cdot$solv (X = Cl^-, SCN^-)[38] at 213 K, suggesting the presence of two pairs of quadruply-bonded [Cr_2] units *plus* one terminal Cr^{2+} ion. Density Functional Theory (DFT) indeed predicts the gas phase unsymmetric structure of **2a** to be more stable than the symmetric one by 2.9 kcal/mol (Scheme 1b,d, X = Cl^-).[39] As a result, the $S = 2$ state of **2a** is largely localized on one of the terminal five-coordinate high-spin Cr^{2+} ions. Other penta-[40] as well as hepta-[41] and nonachromium(II)[42] strings exhibit similar structural features, sometimes with attenuated Δd values. It should be mentioned that $^1H/^2H$ NMR signals from **2a** in dichloromethane solution reveal a symmetric configuration, suggesting fast switching between the two unsymmetric forms on the NMR timescale.[39]

Things are different in trichromium(II) EMACs, which exhibit greater structural diversity as a function of both axial and equatorial ligands.[33,43–45] The largest structural study so far available was performed by Cotton, Murillo *et al.*, who used X-ray crystallography to investigate fourteen compounds with the formula $[Cr_3(dpa)_4X_2]\cdot$solv (X = BF_4^-, NO_3^-, CH_3CN, Cl^-, Br^-, I^-, SCN^-, OCN^-, CN^-, $PhCC^-$) at the same temperature (213 K).[33,43,44] For all axial ligands, with the exception of the strongest σ donors (X = CN^- and $PhCC^-$), the central Cr^{2+} ion features an abnormally elongated displacement ellipsoid,

which was taken as evidence of an orientationally disordered unsymmetric structure (Scheme 1c). Refinement using a split-atom model was then undertaken,[43] which in the vast majority of cases gave Δd values of 0.22-0.32 Å, *i.e.* distinctly *smaller* than in the pentachromium(II) complexes. Only with very weak axial ligands (X = BF_4^-, NO_3^-) geometrical distortion reaches 0.6-0.7 Å, thereby approaching those observed in the higher-membered congeners and in $[Cr_3(dpa)_4XY]$ structures with two different axial groups (X = Cl^-; Y = BF_4^-, PF_6^-).[33]

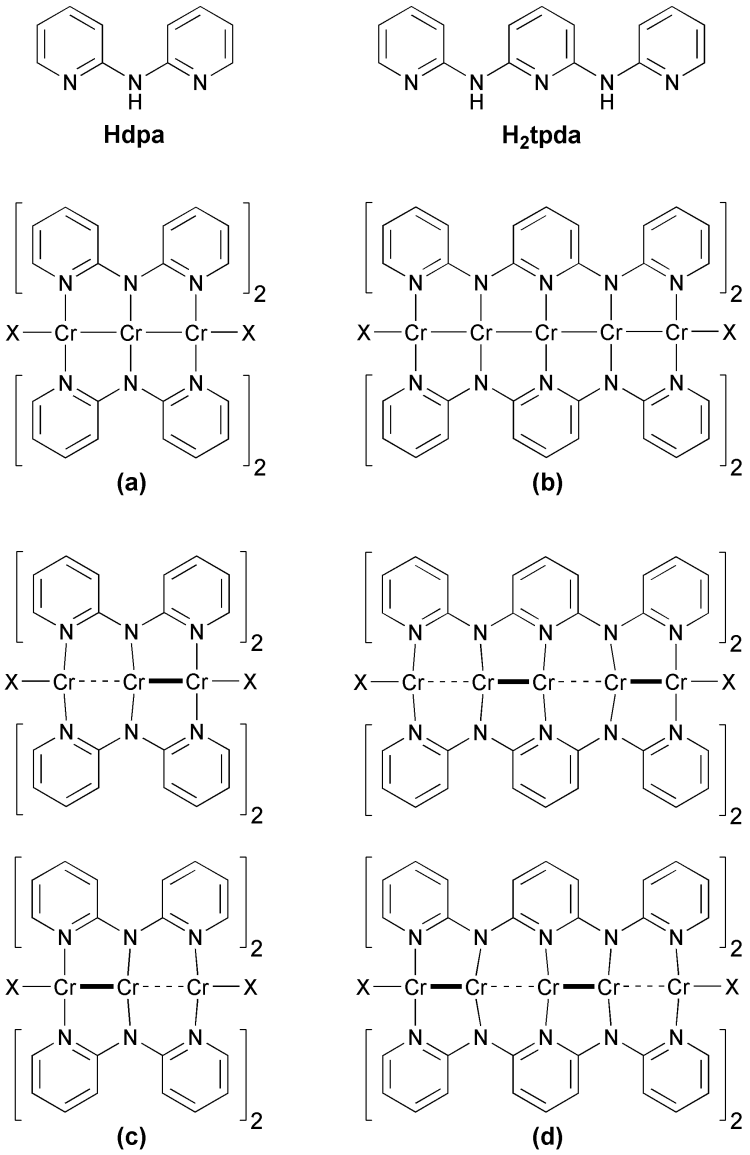

Scheme 1. Hdpa and H_2tpda ligands and structure of the $[Cr_3(dpa)_4X_2]$ (a,c) and $[Cr_5(tpda)_4X_2]$ (b,d) complexes in their symmetric (a,b) and unsymmetric (c,d) forms.

In 2014, an illuminating temperature-dependent structural study was published by Overgaard, Iversen *et al.* They showed that at 15 K the structure of **1a**·Et_2O is symmetric (Scheme 1a) within 0.002 Å and that at this temperature the vibrational amplitude of the central Cr^{2+} ion along the chain axis is only slightly larger than for the terminal ions ($\Delta U < 30 \cdot 10^{-4}$ Å^2). The difference becomes threefold larger at 100 K, indicating that the central metal is not positionally disordered but lies in a shallow

potential energy surface.[46] It was argued that the $S = 2$ state of **1a** is a delocalized molecular state in the temperature regime where SMM behavior manifests itself.[36] The observed low-temperature structure perfectly matches DFT theoretical predictions published in 2001 by Bérnard, Rohmer *et al.*[47] These authors first showed that **1a** has a quintet ground state in the gas phase, with a symmetric equilibrium structure supported by a 3-center-3-electron σ bond involving the metal $3d_{z^2}$ orbitals. The remaining π and δ orbitals contribute negligibly to the bonding and distortion of the symmetric structure is an energetically facile process (~1 and ~4 kcal/mol for $\Delta d = 0.106$ and 0.679 Å, respectively). More recent theoretical work on other $[Cr_3(dpa)_4X_2]$ derivatives depicted a similar scenario,[48–50] with very flat potential energy landscapes and a prominent role of thermal energy and crystal packing on molecular geometry.[51] This interpretation is also consistent with the fact that solutions of **1a**[52] and $[Cr_3(dpa)_4(N_3)_2]$[53] in dichloromethane show three ^{1}H NMR resonances, that is, only one less than expected for a symmetric structure over NMR timescale. The *ortho* protons of dpa^- ligands are most probably paramagnetically shifted and broadened beyond detection, as found in **2a**.[39]

We have now undertaken a wider magnetic and spectroscopic study on odd-membered chromium(II)-based EMACs, focusing on magnetic anisotropy and SMM behavior as a function of chain length and axial ligands. Our investigation covers chlorido derivatives **1a**·Et_2O and **2a**·$4CHCl_3$·$2Et_2O$ as well as the isothiocyanato adducts $[Cr_3(dpa)_4(NCS)_2]$·$0.4CH_2Cl_2$ (**1b**·$0.4CH_2Cl_2$) and $[Cr_5(tpda)_4(NCS)_2]$ (**2b**). We found that an easy-axis anisotropy and magnetic blocking observed under an applied magnetic field are general properties of these EMACs. With the aid of Angular Overlap Model (AOM) and DFT/CASSCF calculations, our findings throw new light on an old controversy concerning the amount of spin delocalization in these systems and give an explanation on the reason why similar magnetic properties arise in tri- and pentachromium(II) species despite their different structural preferences and electronic structure.

EXPERIMENTAL SECTION

Materials and Methods. Unless otherwise noted, reagents and solvents were of commercial origin and were used without further purification. Acetonitrile and dichloromethane were purified using an Inert Technologies solvent purification system, while anhydrous *n*-hexane (Sigma-Aldrich) was degassed by bubbling Ar before use. All reactions involving chromium(II) complexes were carried out under Ar or N_2 atmosphere using Schlenk techniques or glovebox methods. Compounds **1a**·Et_2O,[33,43,46,52] **2a**·$4CHCl_3$·$2Et_2O$[34] and **2b**[34,41] were prepared by literature procedures or slight modifications thereof (see Supporting Information and Table S1). Elemental analysis was carried out on a Thermofisher Scientific Flash EA1112 elemental analyzer by the PLACAMAT service (University of Bordeaux-CNRS UMS 3626). The IR spectra were measured on a Nicolet 6700 FT-IR spectrometer using a Smart iTR accessory between 600 and 4000 cm^{-1} with 4 cm^{-1} resolution.

Synthesis of $[Cr_3(dpa)_4(NCS)_2]\cdot 0.4CH_2Cl_2$ ($\mathbf{1b}\cdot 0.4CH_2Cl_2$). Preparation was accomplished by a modification of the literature procedure reported by Cotton, Murillo *et al.*[43] In a glovebox, $\mathbf{1a}\cdot Et_2O$ (100 mg, 0.102 mmol) and $TlBF_4$ (64 mg, 0.21 mmol) were dissolved in CH_3CN (15 mL). The mixture was stirred overnight and then filtered through a PTFE filter (0.2 μm porosity, VWR). To this solution a solution of KSCN (22 mg, 0.23 mmol) in CH_3CN (5 mL) was added and a dark green precipitate formed immediately. The mixture was filtered and the precipitate washed with CH_3CN and dissolved in CH_2Cl_2 (15 mL). The solution was filtered and layered with *n*-hexane in a Schlenk tube. After one week, the brownish-green rectangular platelets so obtained were collected in a glovebox and washed with *n*-hexane (65 mg, 64%). Anal. Calcd for $C_{42.4}H_{32.8}Cl_{0.8}Cr_3N_{14}S_2$ ($\mathbf{1b}\cdot 0.4CH_2Cl_2$, 986.89): C, 51.60; H, 3.35; N, 19.87. Found: C, 51.41; H, 3.45; N, 19.49. IR (ATR): $\tilde{\nu}_{max}$ (cm^{-1}) 2025m (C≡N), 1605m, 1595s, 1547w, 1463s sh, 1456s, 1420s, 1364s br, 1309m, 1277w, 1153s, 1106w, 1052w, 1013m, 917w, 880m, 856w, 800w, 761s, 737m, 644m.

Single-crystal X-ray diffraction. A single-crystal X-ray diffraction measurement on $\mathbf{1b}\cdot 0.4CH_2Cl_2$ was carried out using a Bruker Quazar SMART APEXII diffractometer with Mo-Kα radiation. The compound crystallized as brownish-green plates, which had the tendency to stack upon one another. This difficulty, compounded by the large unit cell, made it challenging to obtain a high quality structure. A small, thin plate suitable for X-ray diffraction was finally selected under immersion oil in ambient conditions and attached to a MiTeGen MicroLoop™. The crystal was mounted in a stream of cold N_2 at 120(2) K and centered in the X-ray beam using a video camera. The data were collected using a routine to survey reciprocal space, and reduction was performed using software included in Bruker Apex2 suite.[54] The structure was solved using direct methods and refined by least-squares cycles on F^2 followed by difference Fourier syntheses.[55] All hydrogen atoms were included in the final structure factor calculation at idealized positions and were allowed to ride on the neighboring atoms with relative isotropic displacement coefficients. Three independent Cr_3 complexes were found in the asymmetric unit. In all Cr_3 units the electron density associated with the central metal was invariably single peaked and was modelled in two different ways: as a single Cr atom undergoing anisotropic displacement (Model I or "unsplit atom" model)[33] or as a Cr atom disordered over two positions; in this case the two components were constrained to have the same isotropic displacement parameter and their occupancies were freely-refined but forced to sum up to unity (Model II, or "split atom" model).[43] As an outcome of Model I, the central metal atoms have significantly larger mean-square displacement amplitudes (U) along the Cr-Cr directions than the terminal metal atoms. ΔU values range from 87 to $164\cdot 10^{-4}$ Å^2 and are hence comparable to those found in $\mathbf{1a}\cdot Et_2O$ at 100 K (98-$110\cdot 10^{-4}$ Å^2).[46] By contrast the Cr-N(CS) bonds are much more rigid ($\Delta U \leq 30\cdot 10^{-4}$ Å^2). Since only in molecule Cr1-Cr2-Cr3 is the displacement ellipsoid of the central metal atom distinctly prolate along the chain axis, Model II was applied to Cr2 only. Crystal and refinement data (Model I) are available as Table S2, whereas selected geometrical parameters are gathered in Tables 1 and S3.

Magnetic measurements. The magnetic measurements were obtained with a Quantum Design MPMS-XL SQUID magnetometer and a PPMS-9 susceptometer. The MPMS-XL instrument works

between 1.8 and 400 K with applied direct current (dc) fields (*H*) ranging from –70 to 70 kOe. The alternating current (ac) susceptibility measurements were performed using an oscillating field of 3-5 Oe for frequencies from 1 to 1500 Hz (MPMS-XL) and an oscillating field of 1-6 Oe for frequencies from 10 Hz to 10 kHz (PPMS-9). Details on sample preparation are given in the Supporting Information. All magnetic data were corrected for the sample holder and for addenda (when used), and were reduced using the appropriate molar mass and a correction for diamagnetism.[56] The dc magnetic susceptibility (χ) was obtained as M/H from magnetization (M) measurements at 1 and 10 kOe in the temperature ranges 1.85-295 K (**1a**·Et_2O), 1.85-300 K (**1b**·0.4CH_2Cl_2 and **2b**), 1.85-320 K (**2a**), and 1.86-255 K (**2a**·4$CHCl_3$·2Et_2O). Isothermal magnetization data were also recorded between 1.8 and 10 K in fields up to 70 kOe for all samples. Above 1.8 K, no hysteresis effects were observed in the field dependence of the magnetization for field sweep rates between about 70 and 600 Oe/min. The ac susceptibility data were measured down to 1.8 K at frequencies up to 10 kHz, with applied dc fields of zero to 10 kOe. In the available temperature and frequency ranges, all samples displayed slow relaxation of the magnetization only observable in an applied dc field. The optimal dc field value was determined by variable-field ac studies at the lowest reachable temperature. All ac measurements were fitted to the generalized Debye model (using χ' and χ'' vs. ν data)[57,58] in order to extract the characteristic relaxation time (τ), the α parameter describing the width of the distribution of relaxation times, as well as the values of χ_0 and χ_∞. The α values at the lowest temperatures were ~0.07 (**1a**·Et_2O), ~0.3 (**1b**·0.4CH_2Cl_2), and ~0.2 (**2a**, **2a**·4$CHCl_3$·2Et_2O and **2b**) and decreased to ~0 upon heating. Detailed results of dc and ac magnetic characterization are presented in Figures S1-S30 and Table S4.

EPR spectroscopy. W-band EPR spectra were recorded using a Bruker Elexsys E600 spectrometer, equipped with a continuous ^{4}He flow CF935 Cryostat (Oxford Instruments). Microcrystalline powder samples were prepared by crushing single crystals of the different compounds in a glovebox. The sample was mixed with wax to avoid preferential orientation due to magnetic torque and to minimize the loss of crystallization solvent (when present) from the lattice. The resulting mixture was then inserted in an open-end quartz tube (0.80 mm outer diameter). To further reduce exposure to air, the tube was taken out of the glovebox in a sealed Schlenk, mounted on the sample holder rod under N_2 flux, pre-cooled in a bath of liquid N_2 and inserted in the spectrometer at 100 K.

High-Frequency EPR powder spectra were recorded on a multifrequency spectrometer operating in a double-pass configuration. A 110 GHz frequency source (Virginia Diodes Inc.), associated with either a doubler or a tripler, was used. The propagation of this exciting light was performed with a Quasi-Optical bridge (Thomas Keating) outside the cryostat and with a corrugated waveguide inside it. The detection was carried out with a hot electron InSb bolometer (QMC Instruments). The main magnetic field was supplied by a 16 T superconducting magnet associated with a VTI (Cryogenic). The sample was prepared in a glovebox by thoroughly grinding large crystals of **2a**·4$CHCl_3$·2Et_2O immersed in a mixture of Et_2O and $CHCl_3$ (5:1 v/v) in an EPR tube, which was subsequently flame sealed. The presence of the solvent allowed to preserve crystallinity and to prevent torqueing effects at low temperature. This preparation technique led to somewhat imperfect powder averaging, which however

did not preclude a straightforward interpretation of the spectra. The powder spectra were simulated using parameters obtained through the fitting of the resonance positions.[59,60] Details on EPR experiments are given in Figures S31-S35.

Angular Overlap Model (AOM) calculations. Ligand-field (LF) calculations within AOM[61] were performed using *B, C,* ζ_{3d} and *k* values reported in Refs.[62,63] LF parameters were also taken from Ref.[62] and adapted to provide a reasonable reproduction of the electronic spectra reported in the literature for $[Cr(4\text{-Mepy})_4Cl_2]$.[62,64] This was achieved by considering a completely anisotropic π-interaction for the pyridine-type ligands, and a completely isotropic π-interaction for the axial ligands X. Angular coordinates were either made to correspond to idealized C_4 point-group symmetry to study the dependency of the calculated *D* on axial and equatorial LF strength, or taken directly from X-ray structures. In the first case, the pyridine-type ligands were oriented so as to form a dihedral angle $\psi = 18°$ with the X-Cr-N_{py} planes, in agreement with the structure of **2a**.

DFT/CASSCF calculations. DFT calculations were performed with the ORCA[65] program package, version 3.0.3.33 (see Figures S36-S38 for further information). The same computational setup used to optimize **2a** in the gas-phase[39] was applied to **1a**, **1b** and **2b**. In detail, the PBE[66] functional with D3 dispersion[67] correction scheme was used. Scalar relativistic re-contracted versions of the Ahlrichs triple-ζ basis set, def2-TZVP, were chosen for Cr, N, and Cl atoms while single-ζ basis set, def2-SVP, was chosen for S, C and H atoms.[68,69] Resolution of identity (RI) was used to approximate two-electron integrals. Considering the possibility to face very flat potential energy surfaces, symmetric and unsymmetric arrangements of the Cr atoms were imposed as guess geometries. However, all geometries were fully optimized with no constraints on symmetry[47] or on the position of any Cr atom.[50] All the calculations were performed on a Broken Symmetry (BS) state with $S = 2$. A tight convergence threshold was also used (TightOpt). The SCF calculations were tightly converged (TightSCF) with unrestricted spin (UKS). Numerical integrations during all DFT calculations were done on a dense grid (ORCA grid4) while the final run was also performed on a denser one (ORCA grid5). Second-order anisotropy parameters (*D*, *E*) for the optimized unsymmetric structures of pentachromium(II) species **2a** and **2b** (**2a**$_{\mathbf{unsym}}$ and **2b**$_{\mathbf{unsym}}$) were computed at *post*-HF (CASSCF) level. The use of *post*-HF approach is needed since the anisotropy tensor calculations at the UDFT level require the electronic spin density of the system to be consistent with an $\hat{\mathbf{S}}^2$ eigenstate. Unfortunately, this is not the case since the value of $\langle\hat{\mathbf{S}}^2\rangle$ from DFT significantly deviates from the expected spin-only value of 6 for a quintet state.[39] However, due to hardware computational limits *post*-HF methods can be applied to systems with a couple of magnetic centers and a reduced number of non-magnetic atoms. For such a reason we chose a *divide et impera* approach by extrapolating two subunits from **2a**$_{\mathbf{unsym}}$ and **2b**$_{\mathbf{unsym}}$: the monomer Cr1 and the dimer Cr2-Cr3, which represent the two basic units present in the lowest energy structure of pentachromium(II) strings. The Cr1 and Cr2-Cr3 models were obtained from optimized structures by simplifying the ligands to four pyridines and four (*E*)-*N*,*N'*-diethenylmethanimidamido anions, respectively (Figure S38). Since the geometry of Cr2-Cr3 fragment shows only negligible differences in **2a**$_{\mathbf{unsym}}$ and **2b**$_{\mathbf{unsym}}$, Cr2-Cr3 model was based on **2a**$_{\mathbf{unsym}}$. CASSCF calculations were done employing

a def2-TZVP basis set for chromium(II) ions and their first neighbors, while def2-SVP basis set was used for all the other atoms. The RI-J approximation along with the def2-TZVP/J auxiliary basis set for all the elements was used. Grids were set to 5 and VeryTightSCF. Using def2-TZVP for all atoms showed no significant differences on the energy ladder of the excited states, thus supporting the choice of our computational setup.

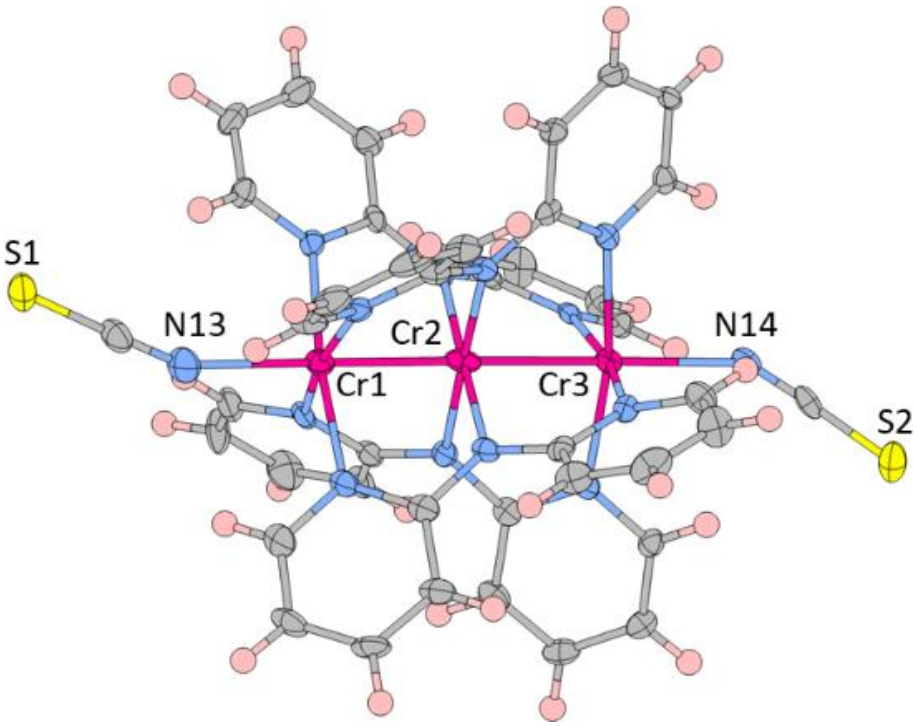

Figure 1. Structure of one of the independent molecules in **1b**·0.4CH_2Cl_2 (molecule A), in which the thermal ellipsoid of the central Cr^{2+} ion is distinctly prolate along the chain axis.

RESULTS AND DISCUSSION

Synthesis and Structures. Trichromium(II) compounds **1a**·Et_2O and **1b**·0.4CH_2Cl_2, and pentachromium(II) compounds **2a**·4$CHCl_3$·2Et_2O and **2b** were synthesized by following (or by slight modification of) literature procedures.[33,34,41,43,46,52] Only **1b**·0.4CH_2Cl_2 is a new crystal phase and is the fourth published solvatomorph of **1b**, after **1b**·2C_6H_6,[43] **1b**·2C_7H_8[43] and **1b**·2$C_2H_4Cl_2$.[70] It was prepared by first reacting **1a**·Et_2O with $TlBF_4$ in CH_3CN to replace the axial chlorido ligands with CH_3CN, then precipitating the isothiocyanato derivative with KSCN and finally recrystallizing it from CH_2Cl_2/*n*-hexane. The new method does not require isolation of a $[Cr_3(dpa)_4(NCCH_3)_2]X_2$ intermediate but results in comparable overall yield with respect the published two-step synthesis of the benzene and toluene solvates.[43] The structure contains two-and-a-half trichromium(II) complexes and one disordered interstitial molecule of dichloromethane per asymmetric unit.

Table 1. Selected bond distances (Å) and angles (°) in **1b**·0.4CH_2Cl_2 resulting from Model I.[a]

	molecule A	molecule B	molecule C
Cr_{T1}–Cr_C	2.3060(12)	2.3446(13)	2.3527(8)
Cr_C–Cr_{T2}	2.3526(11)	2.3565(13)	2.3527(8)
Cr_{T1}–N_{eq}	2.115[4]	2.115[4]	2.108[5]
Cr_C–N_{eq}	2.026[4]	2.024[5]	2.032[6]
Cr_{T2}–N_{eq}	2.109[4]	2.110[5]	2.108[5]
Cr_{T1}–N_{ax}	2.200(4)	2.226(5)	2.216(5)
Cr_{T2}–N_{ax}	2.208(4)	2.197(5)	2.216(5)
Cr_{T1}–Cr_C–Cr_{T2}	179.14(5)	177.73(5)	179.32(8)
Cr_{T1}–N_{ax}–C	153.4(4)	147.6(4)	165.1(5)
Cr_{T2}–N_{ax}–C	144.2(4)	155.8(5)	165.1(5)
(Cr_{T1}–)N_{ax}–C–S	178.7(5)	177.6(6)	179.2(6)
(Cr_{T2}–)N_{ax}–C–S	177.6(5)	179.1(6)	179.2(6)

[a] Cr_C = central Cr^{2+} ion, Cr_{T1} and Cr_{T2} = terminal Cr^{2+} ions, N_{eq} = equatorial nitrogen donor from dpa^-, N_{ax} = axial nitrogen donor from isothiocyanate.

Two [Cr_3] moieties [molecule A: Cr1,Cr2,Cr3 (Figure 1); molecule B: Cr4,Cr5,Cr6] are entirely in general positions; the third one (molecule C: Cr7,Cr8,Cr7′) lies with its central metal site (Cr8) and two amido N atoms on a twofold axis and consequently has crystallographically imposed C_2 symmetry. When the central metal atom is modelled as a single, full-occupancy anisotropic scatterer (Model I), the three independent molecules in **1b**·0.4CH_2Cl_2 show a more or less symmetric arrangement of metal atoms, with Cr-Cr distances ranging from 2.31 to 2.36 Å (Table 1). Splitting of Cr2 in molecule A (Model II) gave Δd values typical of trichromium(II) strings (0.23-0.30 Å).[43] The Cr-Cr-Cr moieties are linear within 2.5°, whereas the Cr-NCS units are bent at the N atom, with Cr-N_{ax}-C angles ranging from 144 to 165° (Table 1).

As a final remark, it is important to stress that the four EMACs under investigation have either idealized (**1a**·Et_2O, **1b**·0.4CH_2Cl_2, **2a**·4$CHCl_3$·2Et_2O) or crystallographic (**2b**) fourfold symmetry. The analysis of the terminal chromophores (CrN_4Cl or CrN_4N) using program SHAPE v2.1[71] indeed indicates very small deviations from square-pyramidal (SPY-5) and vacant-octahedral (vOC-5) geometries, both of which have C_{4v} symmetry (Table S3). In chlorido derivatives the coordination spheres are closer to SPY-5, with shape measures ranging from 0.30 to 0.51, whereas in isothiocyanato-terminated strings deviation is minimal from vOC-5 (0.29-0.34).

Magnetic Measurements and EPR spectra. The dc and ac magnetic measurements were performed on polycrystalline samples of **1a**·Et_2O, **1b**·0.4CH_2Cl_2 and **2b**. Compound **2a**·4$CHCl_3$·2Et_2O was studied both in solvated crystalline form and after solvent removal under vacuum. The solvated and unsolvated samples display very similar static and dynamic magnetic properties (see below). In an applied field of 1 kOe, the χT product of all compounds remains constant at 2.9-3.1 cm^3 K mol^{-1} between room

temperature and 10-15 K, signaling a well-isolated $S = 2$ ground state. At lower temperatures, χT rapidly drops as expected from magnetic anisotropy effects. Isothermal molar magnetization (M) vs. H data do not saturate at 70 kOe and 1.8-1.9 K, although the highest obtained values (ca. 3.8 $N_A\mu_B$) are close to the expected saturation value for an $S = 2$ state ($4N_A\mu_B$ with $g = 2$). When plotted vs. H/T, the magnetization curves display a pronounced nesting, suggesting deviation from the Brillouin function and the presence of magnetic anisotropy. The quantitative analysis of M vs. H data (see Supporting Information for details) was based on zero-field-splitting (zfs) *plus* Zeeman Hamiltonian in Eq. (1):

$$\hat{H} = D\left[\hat{S}_Z^2 - S(S+1)/3\right] + E\left(\hat{S}_X^2 - \hat{S}_Y^2\right) + \mu_B \mathbf{B} \cdot \bar{\bar{\mathbf{g}}} \cdot \hat{\mathbf{S}} \qquad (1)$$

where D and E are the axial and rhombic zfs parameters, respectively. **S** is the total spin vector, with component S_Z along the anisotropy axis (Z) (*XYZ* label here the principal magnetic axes; as molecular symmetry is approximately fourfold, Z must be close to the chain axis). For simplicity, rhombic anisotropy was disregarded ($E = 0$) and an isotropic Landé factor was assumed, i.e. $\bar{\bar{\mathbf{g}}} = g\bar{\bar{\mathbf{I}}}$, where $\bar{\bar{\mathbf{I}}}$ is the identity matrix. The best-fit anisotropy parameters so obtained (Table 2) confirm an easy-axis anisotropy ($D < 0$) for all compounds, with $|D| = 1.5\text{-}1.7$ cm^{-1} (the complete set of best-fit parameters is provided as Table S4).

Table 2. Magnetic parameters of chromium(II)-based EMACs with different nuclearity (n) and axial ligands (X), as determined by EPR spectroscopy and dc/ac magnetic measurements.

Compound	n	X	D (cm^{-1})[a]	$\lvert E/D\rvert$[a]	$g_{X,Y}$[a]	g_Z[a]	D (cm^{-1})[b]	U_{eff}/k_B (K)[c]	τ_0 (μs)[c]	Ref.
1a·CH_2Cl_2	3	Cl^-	–1.640[d]	0.021[d]	1.998[d]	1.981[d]		10.6(6)[e]	2.9(5)[e]	[36,37]
1a·Et_2O	3	Cl^-	–1.66(5)	0.020(5)	2.000(5)	1.995(5)	–1.656(16)	10.5(5)[e]	3.1(5)[e]	this work
1b·0.4CH_2Cl_2	3	SCN^-	–1.78(5)	0.000(3)	1.998(3)	1.970(2)	–1.711(12)	12.4(5)[f]	0.26(5)[f]	this work
2a·4$CHCl_3$·2Et_2O	5	Cl^-	–1.53(1)	0.006(2)	1.990(3)	1.975(2)	–1.507(2)	8.6(5)[g]	11(5)[g]	[35]
2a	5	Cl^-					–1.510(6)	9.2(5)[g]	2.2(5)[g]	[35]
2b	5	SCN^-	–1.61(5)	0.003(2)	2.000(5)	1.985(2)	–1.696(4)	10.2(5)[g]	3.3(5)[g]	this work

[a] From W-band EPR, unless otherwise noted. [b] From isothermal M vs. H data. [c] From ac susceptometry. [d] From high-frequency EPR (240 GHz). [e] Under an applied dc field of 2.0 kOe. [f] Under an applied dc field of 3.5 kOe. [g] Under an applied dc field of 2.5 kOe.

For a more accurate, state-of-the-art determination of D and E, as well as of the principal components of the $\bar{\bar{\mathbf{g}}}$ matrix, we used W-band ($\nu \sim 94$ GHz) EPR spectroscopy. In spite of the difficulties in obtaining pure powder pattern spectra, the low temperature W-band EPR traces (Figure 2) provide an unequivocal picture over the trend of D values in the studied series of complexes. Because of the condition $|D| \sim h\nu$, the analysis of the spectra using Eq. (1) is not straightforward and requires careful consideration of the angular dependence of the transitions.[59] Most of them are actually occurring at off-axis turning points, the most intense one being close to 25 kOe, and as looping transitions (Figure S31). Only a couple of signals, expected to occur at 16 and 60 kOe for $D = -1.6$ cm^{-1}, $g = 1.99$ and $\nu = 94.27$ GHz, can be attributed to perpendicular transitions (Figure S32). The separation between these two lines (or the position of the first one, when the second exceeds the field range of the spectrometer, as occurring in

1b·0.4CH_2Cl_2) shows that $|D|$ is slightly larger for tri- as compared to pentachromium(II) complexes, and for isothiocyanato as compared to chlorido derivatives. On the other hand, the EPR transition observed around 25 kOe is essentially independent of the D value but can be used to obtain a more accurate estimate of $g_{X,Y}$, since it arises from microcrystallites oriented with their main anisotropy axes at $55° < \theta < 90°$ from the applied field (Figure S31).

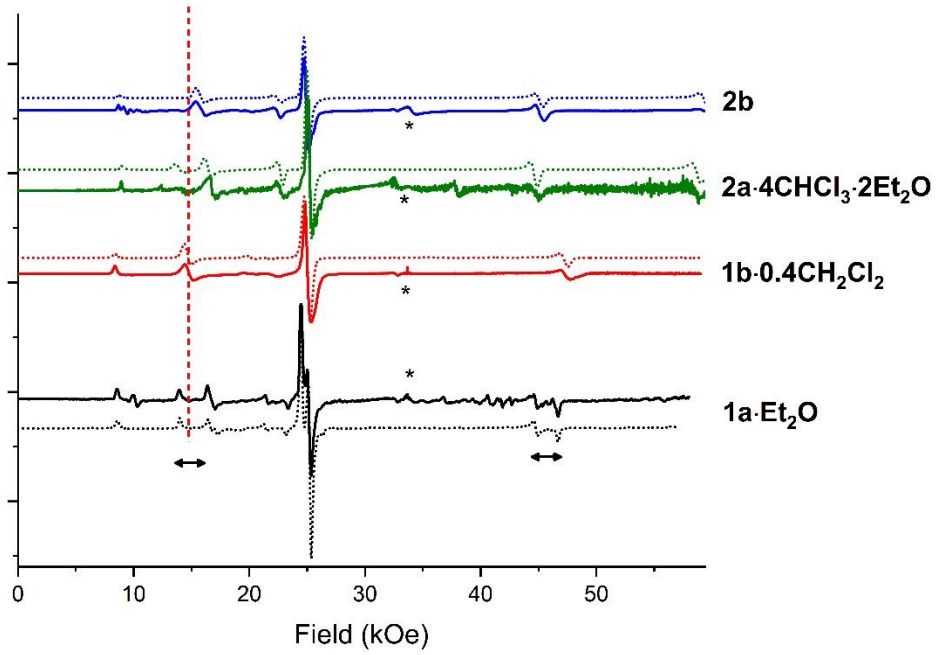

Figure 2. W-band (94.27 GHz) EPR spectra recorded at 6 K for **1a**·Et_2O, **1b**·0.4CH_2Cl_2, **2a**·4$CHCl_3$·2Et_2O and **2b**. Continuous lines: experimental spectra; dotted lines: best simulations obtained using the parameters reported in the text. The double arrows evidence the splitting of the transitions due to the non-negligible rhombicity of **1a**·Et_2O. The vertical dashed line is centered on the perpendicular transition occurring furthest from the center of the spectrum, indicating the largest $|D|$ value in the series. The asterisk indicates a signal from an impurity in the cavity walls. The spectrum of **2a**·4$CHCl_3$·2Et_2O and the corresponding simulation were originally reported in Ref.[35].

With one exception, the observed experimental spectra indicate very weak rhombicity ($|E/D| \sim 0$), consistent with the idealized or crystallographic fourfold molecular symmetry. In **1a**·Et_2O, the twofold splitting of both perpendicular and looping transitions points to significant deviation from axiality. Following these considerations the spectra were simulated[72] to obtain the best-fit parameters gathered in Table 2 (an axial $\tilde{\tilde{\mathbf{g}}}$ matrix was assumed to reduce the number of parameters). We stress that the evolution of the spectra at higher temperatures is only compatible with a negative D parameter (Figure S33), consistent with previous literature reports.[35–37] As for the rhombicity of **1a**·Et_2O, best simulations were obtained with $|E/D| = 0.020(5)$, i.e. the same value reported for the dichloromethane solvate.[36,37] Unexpectedly, the inclusion of a small rhombic term was necessary to accurately reproduce the spectra of **2b**, suggesting that the actual molecular symmetry is lower than the reported crystallographic

symmetry.[34] The $g_{X,Y}$ values are always very close to the free electron value, indicating a negligible effect of spin-orbit coupling over this parameter, whereas g_Z is always unequivocally smaller. Finally, the spectra of **1b**·0.4CH_2Cl_2 could be reproduced with a single set of spin Hamiltonian parameters. The structural differences among the three crystallographically independent molecules are thus undetectable by EPR.

For derivative **2a**·4$CHCl_3$·2Et_2O, the accuracy of the spin Hamiltonian parameters obtained from W-band EPR spectra was confirmed by a high-frequency EPR study at 220.8 and 331.2 GHz. The spectra show the pattern expected for an $S = 2$ spin system but some lines are split (Figures S34-S35). For instance, at 331.2 GHz the signal observed close to 7 T ($M_S = -2 \rightarrow -1$ transition for the Z orientation) comprises a dominant and a satellite component at 6.93 and 6.96 T, respectively. The dominant peaks are consistent with the spin Hamiltonian parameters extracted from W-band spectra; their positions and those of the W-band signals were simultaneously fitted to give: $D = -1.534(12)$ cm^{-1}, $E = 0.008(5)$ cm^{-1}, $g_X = 1.995(3)$, $g_Y = 1.993(3)$, $g_Z = 1.985(11)$. The weaker signals, some of which *exceed* the highest fields of the dominant set, are attributed to a minority species (~20% molar fraction) with slightly different anisotropy parameters ($D = -1.55$ cm^{-1}, $E = 0.011$ cm^{-1}, $g_X = 1.98$, $g_Y = 1.97$, $g_Z = 1.98$), which remains unresolved in W-band spectra. The uncertainty on this second parameter set is larger because signals are weaker and less resonances can be identified; especially, no W-band signal could be introduced in the fit, thereby limiting the frequency range explored.

The ac magnetic susceptibility studies on all compounds revealed no out-of-phase component in zero dc field within the available range of temperature (down to 1.8 K) and frequency (up to 10 kHz). Application of a static field was however effective to reveal the magnetization relaxation leading to the appearance of an out-of-phase signal. The optimal field value (2.0-3.5 kOe) was located in a preliminary scan from 0 to 10 kOe at 1.8-1.9 K and was used for subsequent temperature and frequency dependent studies. Plots of $\ln\tau$ vs. $1/T$ were found to be linear in **1b**·0.4CH_2Cl_2, **2a** and **2a**·4$CHCl_3$·2Et_2O, while a slight curvature was detected in **1a**·Et_2O and **2b**. Linear fits to all the data (or to the linear, high-temperature region) gave the effective anisotropy barriers (U_{eff}) and the attempt times (τ_0) gathered in Table 2. For all derivatives but **1b**·0.4CH_2Cl_2 the value of U_{eff} is, within uncertainty, coincident with the total splitting of the $S = 2$ multiplet ($U = |D|S^2$), as calculated from the D parameter determined by EPR and when accounting for an external dc field. We note in this respect that **1b**·0.4CH_2Cl_2 shows the widest distribution of relaxation times (α) at the measuring field. This has recently been shown[73] to result in a large uncertainty on the actual relaxation time and thus on the parameters of the relaxation process. We can then conclude that all the data lend support to an overbarrier Orbach mechanism for magnetic moment reversal.

In spite of the small S value, all chromium(II)-based EMACs considered in this and previous works[35,36] behave as SMMs, although the observation of magnetic bistability by ac susceptibility measurements requires the application of a dc magnetic field. In this respect, their magnetic properties are similar to those of the mononuclear square planar complexes [$Cr(N(SiMe_3)_2)_2(py)_2$] and

$[Cr(N(SiMe_3)_2)_2(THF)_2]$, which also feature a negative *D* value, very weak rhombicity and slow relaxation of their magnetization observed under dc field.[74]

Angular Overlap Model Calculations. The Angular Overlap Model (AOM)[61] proved remarkably successful in predicting the anisotropy of **2a**·$4CHCl_3$·$2Et_2O$ starting from the coordination environment of its structurally-isolated terminal ion.[35] We herein show that the same approach offers a straightforward explanation of the slightly enhanced anisotropy observed in the isothiocyanato derivative **2b**. Calculations were performed starting from the experimental atomic coordinates of **2a**·$4CHCl_3$·$2Et_2O$ and **2b** and using the same Ligand-Field (LF) parameters as reported in Ref.[35] (except for a larger *Dq* value for SCN^- compared to Cl^-, in agreement with their relative position in the spectrochemical series). The calculated *g* values are in accordance with EPR spectra, with $g_{X,Y}$ very close to 2.00 and g_Z always around 1.98 (Table 3). More important, the resulting *D* parameters quantitatively agree with experiment, including the larger |*D*| value of **2b**. The role of excited triplet states emerges clearly from side calculations in which triplets are disregarded: in this case the |*D*| parameters are dramatically underestimated (ca. 0.6 vs. 1.4-1.6 cm^{-1}) and the differences between the two complexes become negligible (Table 3).

Table 3. Magnetic parameters for terminal ion (Cr1) in chromium(II)-based EMACs with different nuclearity (*n*) and axial ligands (X), evaluated within the AOM.[a]

	n, X	*D* (cm^{-1})[b]	*D* (cm^{-1})[c]	*E* (cm^{-1})[b]	g_X[b]	g_Y[b]	g_Z[b]	Ref.
1a·Et_2O	3, Cl^-	–1.42	–0.61	0.010	1.998	1.998	1.978	this work
1b·$0.4CH_2Cl_2$[d]	3, SCN^-	–1.55	–0.61	$5\cdot10^{-3}$	1.998	1.998	1.977	this work
2a·$4CHCl_3$·$2Et_2O$	5, Cl^-	–1.44	–0.61	$6\cdot10^{-3}$	1.998	1.998	1.978	this work,[35]
2b	5, SCN^-	–1.60	–0.64	0	1.998	1.998	1.976	this work

[a] LF parameters: B = 800 cm^{-1}, C = 3300 cm^{-1}, ζ_{3d} = 235 cm^{-1}, k = 0.82, $10Dq(N)$ = 16500 cm^{-1}, $10Dq(Cl^-)$ = 5000 cm^{-1}, $10Dq(SCN^-)$ = 8000 cm^{-1}, $(e_{\pi c}+e_{\pi s})/e_\sigma$ = 0.3 for all ligands, $e_{\pi c}(N)/e_{\pi s}(N)$ = 0.0, $e_{\pi c}(X)/e_{\pi s}(X)$ = 1.0 (X = Cl^-, SCN^-). [b] Calculated by including all the states arising from $3d^4$ configuration. [c] Calculated by considering only states arising from ^5D term. [d] Calculated for molecule C (Cr7,Cr8,Cr7′) with crystallographic C_2 symmetry.

These results are easily rationalized by analyzing idealized tetragonal structures containing four equatorial pyridine-type ligands and two weaker axial ligands (i.e. $Dq_{ax} < Dq_{eq}$). When the LF parameters of equatorial sites are held fixed, the *D* value is crucially determined by the global LF strength of the two axial coordination sites, i.e. by the sum of their *Dq* values. In particular, as the average *Dq* of axial ligands is increased towards that of equatorial ligands, i.e. on lowering distortions from octahedral symmetry, the AOM predicts a more negative *D* value (Figure 3a). While this might look counterintuitive, one has to consider that the $3d^4$ configuration in octahedral symmetry is characterized by a ^5E_g ground state, which cannot be mapped on a simple spin Hamiltonian such as Eq. (1), even including higher-order terms. However, as soon as the octahedral degeneracy is lifted by

tetragonal elongation, the spin Hamiltonian formalism can be applied: in a perturbative approach the magnitude of $|D|$ is then inversely dependent on the distortion.[75] This effect is triggered primarily by the strength of the σ interaction with the axial ligand(s) (see Figure 3b). Furthermore, it crucially depends on the contribution of excited triplet states, which takes the form:[76,77]

$$D' = -\frac{\zeta_{3d}^2/4}{6B+5C-\Delta E} \quad (2)$$

where ζ_{3d} is the single 3d-electron spin-orbit coupling constant, B and C are Racah parameters and

$$\Delta E = 2e_\sigma^{ax} + e_\sigma^{eq} - 2e_\pi^{ax} - 2e_\pi^{eq} \quad (3)$$

is the energy difference between the $3d_{z^2}$ orbital and the $3d_{xz}, 3d_{yz}$ pair [please note that Eq. (2) was misprinted in Ref.[78]]. From Eq. (3), it follows that ΔE increases with increasing σ donor strength of the axial ligands, causing D' to become more negative (Eq. (2)). By contrast, the contribution of quintet states is smaller[79] and independent of e_σ^{ax}, while singlets essentially do not contribute to the anisotropy.

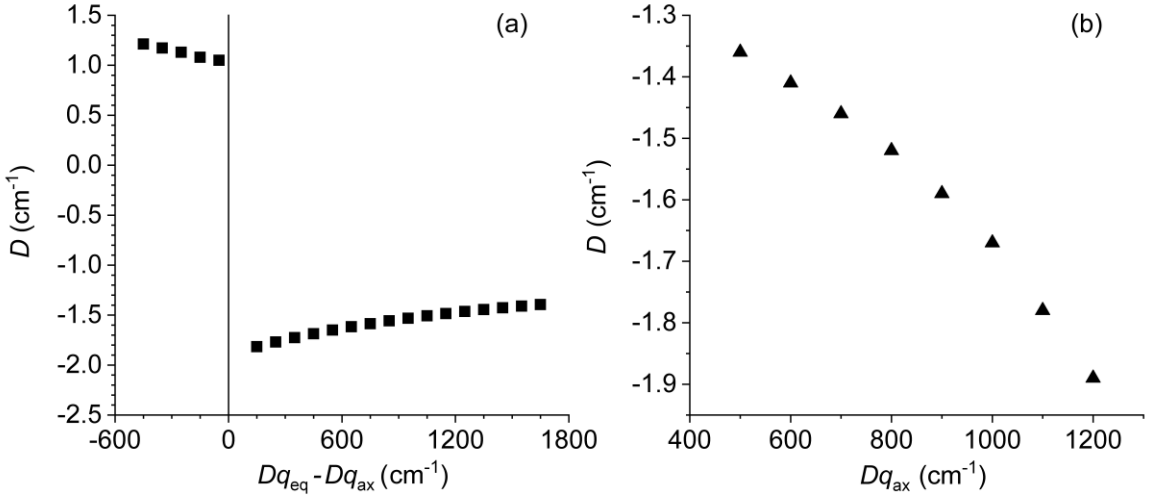

Figure 3. Calculated D value for a $3d^4$ ML_4X_2 system in D_{4h} symmetry: (a) as a function of the difference between equatorial and axial LF strength [$(e_{\pi c} + e_{\pi s})/e_\sigma$ = 0.3 for all ligands]; (b) as a function of axial LF strength for constant $e_{\pi c}^{ax} = e_{\pi s}^{ax}$ = 312.5 cm^{-1}. For both plots the other parameters were: B = 800 cm^{-1}, C = 3300 cm^{-1}, ζ_{3d} = 235 cm^{-1}, k = 0.82, Dq_{eq} = 1650 cm^{-1}.

In trichromium(II) strings (**1a** and **1b**), the coordination environment of terminal ions remains quite similar to their longer congeners and, rather unsurprisingly, AOM predicts comparable single-ion anisotropies and g factors (Table 3). Based on the available experimental and theoretical knowledge, however, the origin of magnetic anisotropy in **1a** and **1b** is much less straightforward. While chlorido derivative **2a** entails a fairly isolated Cr1 center and two formally diamagnetic chromium(II) pairs,[39] the ground structure of **1a** is symmetric.[46] Therefore, contributions to magnetic anisotropy potentially arise from both terminal ions as well as from central ion. One might reason that three localized s = 2 spins with strong antiferromagnetic coupling would also yield a well-isolated S = 2 ground state, whose D parameter relates to projected single-ion anisotropies.[80] At this stage, shedding light on the origin of magnetic anisotropy clearly requires a more accurate electronic description of these EMACs based on

ab initio methods. The DFT/CASSCF calculations described in next section indeed disprove a spin-localized model of trichromium(II) strings, while providing a simple explanation as to why the two types of strings have similar magnetic anisotropy.

DFT Structure Optimization. In our *ab initio* investigation of **1a**, **1b**, **2a** and **2b**, the Cr centers were numbered as Cr1, Cr2,...Cr5 along the chain, with Cr1 representing the formally "isolated" metal center in the unsymmetric structures. The results of structural optimization on **2a** were published in Ref.,[39] where we probed the two different energy minima corresponding to a symmetric (**2a**$_{\mathbf{sym}}$) and an unsymmetric (**2a**$_{\mathbf{unsym}}$) structure (these data are collected in Table 4 for convenience). In agreement with the structural model proposed by Cotton *et al.*,[38,81] the unsymmetric structure was found more stable by 2.9 kcal mol^{-1}.[39] The same calculation protocol applied to **2b** gave a similar energy profile, with **2b**$_{\mathbf{unsym}}$ more stable than **2b**$_{\mathbf{sym}}$ by 1.7 kcal mol^{-1}, and overall geometrical parameters in close agreement with the experimental structure (including perfectly linear Cr-NCS units). These results confirm the occurrence of a shallow potential energy surface in both pentachromium(II) species. Furthermore, terminal ligands have little influence on the geometry of both symmetric and unsymmetric structures. For instance, the two inner Cr-Cr distances in **2a**$_{\mathbf{sym}}$ (Cr2-Cr3 and Cr3-Cr4) are shorter (2.21-2.22 Å) than Cr1-Cr2 and Cr4-Cr5 (2.31-2.32 Å) (see Table 4).[39] The pattern is similar in **2b**$_{\mathbf{sym}}$, albeit with a smaller difference between the two sets of distances (2.25 Å for inner and 2.28 Å for outer Cr-Cr separations). Notice that a Cr-Cr distance of ~2.2 Å corresponds to a multiple bond.[82]

Table 4. Computed Cr-Cr distances (in Å) in the symmetric and unsymmetric structures of **2a** and **2b** (BS S = 2 state).

	X	Cr1-Cr2	Cr2-Cr3	Cr3-Cr4	Cr4-Cr5	Ref.
2a$_{\mathbf{sym}}$	Cl^-	2.319	2.207	2.221	2.308	[39]
2b$_{\mathbf{sym}}$	SCN^-	2.285	2.246	2.246	2.285	this work
2a$_{\mathbf{unsym}}$	Cl^-	2.550	1.862	2.606	1.904	[39]
2b$_{\mathbf{unsym}}$	SCN^-	2.547	1.865	2.604	1.908	this work

In the unsymmetric structures, the C_2 symmetry element located on Cr3 is lost and an alternation of short and long distances is found, with $d_<$ = 1.86-1.91 Å and $d_>$ = 2.55-2.61 Å (see Table 4). It is worth to mention that Cr-Cr distances of 1.8-1.9 Å are in agreement with a third/fourth-order Cr-Cr bond[82] while a very weak Cr-Cr interaction is expected for distances longer than ~2.5 Å. Such results strongly suggest that one of the terminal Cr^{2+} ions in the most stable, unsymmetric structure of pentachromium(II) strings can be considered as "isolated" and with a square-pyramidal coordination environment featuring the Cl^- or SCN^- ligands in apical position.

The computed spin densities (Löwdin analysis) and expectation values $\langle \hat{\mathbf{S}}^2 \rangle$ for the BS S = 2 state, reported in Table 5, are very similar for corresponding structures of **2a** and **2b**. On average, the spin densities in **2b** are slightly reduced as compared with **2a** while $\langle \hat{\mathbf{S}}^2 \rangle$ is practically unchanged.

Table 5. Computed spin densities (in unpaired electrons) and $\langle \hat{\mathbf{S}}^2 \rangle$ values in the symmetric and unsymmetric structures of **2a** and **2b** (BS S = 2 state).

	X	Cr1	Cr2	Cr3	Cr4	Cr5	$\langle \hat{\mathbf{S}}^2 \rangle$	Ref
$\mathbf{2a_{sym}}$	Cl^-	3.10	–2.45	2.50	–2.44	3.12	10.46	[39]
$\mathbf{2b_{sym}}$	SCN^-	3.01	–2.39	2.60	–2.37	3.01	10.41	this work
$\mathbf{2a_{unsym}}$	Cl^-	3.40	–1.40	1.60	–1.54	1.73	8.04	[39]
$\mathbf{2b_{unsym}}$	SCN^-	3.31	–1.40	1.62	–1.52	1.71	8.03	this work

The alternating signs and the magnitudes of the spin densities support the goodness of the BS solution obtained for S = 2 and, in addition, evidence the impact of an unsymmetric vs. symmetric configuration on the electronic structure. Indeed, in the symmetric structures the spin densities are almost homogeneous in absolute value among the five metal centers (3.0-3.1 unpaired electrons on Cr1 and Cr5; 2.4-2.6 unpaired electrons on Cr2, Cr3 and Cr4). On the contrary, in the unsymmetric structures 3.3-3.4 unpaired electrons are localized on Cr1 while only 1.4-1.7 unpaired electrons are present on each of the remaining metal centers. The amount of spin density left on Cr2, Cr3, Cr4 and Cr5 suggests that a bond order larger than three is unlikely to occur within the formally quadruply-bonded Cr2-Cr3 and Cr4-Cr5 pairs, while a practically isolated Cr1 is confirmed. Therefore, a bond localization is clearly evident compared to the symmetric case.

The expectation value $\langle \hat{\mathbf{S}}^2 \rangle$ calculated by DFT gives an indication of the closeness of the spin ground state of a molecule to the multi-spin picture suggested by the atomic spin density values.[83,84] The latter suggest the presence of antiferromagnetically coupled spins along the chain. In an unrestricted DFT formalism this should correspond to an $\langle \hat{\mathbf{S}}^2 \rangle$ calculated value of 10.81 (10.69) for $\mathbf{2a_{sym}}$ ($\mathbf{2b_{sym}}$) and 8.83 (8.78) for $\mathbf{2a_{unsym}}$ ($\mathbf{2b_{unsym}}$).[83,84] In all cases, the calculated values reported in Table 5 are underestimated. This points to a deviation from a multi-spin picture and the presence of significant overlap between the orbitals bearing the unpaired spins. Moreover, this effect is stronger in the unsymmetric case, further supporting the previous analysis in terms of spin densities and bond-lengths.

The structure optimization procedure was extended to trichromium(II) species **1a** and **1b** (Table 6). In agreement with previous studies,[46–51] the energy difference between $\mathbf{1a_{unsym}}$ and $\mathbf{1a_{sym}}$ is now 5.4 kcal mol^{-1}, but in favor of the symmetric structure. Unfortunately, it was not possible to fully converge on an unsymmetric structure for isothiocyanato derivative **1b** because the optimization procedure kept on converging on a symmetric one. At any rate, such behavior hints to symmetric and unsymmetric structures of very similar energy, with a slight preference for the symmetric one.

The spin densities and $\langle \hat{\mathbf{S}}^2 \rangle$ values are also presented in Table 6. Also in this case, the DFT calculated $\langle \hat{\mathbf{S}}^2 \rangle$ values deviate from those expected from multi-spin picture (8.44, 8.46 and 7.41 for $\mathbf{1a_{sym}}$, $\mathbf{1b_{sym}}$ and $\mathbf{1a_{unsym}}$, respectively) confirming that trichromium(II) strings cannot be described as three localized, exchange-coupled s = 2 spins.[83,84] To further support our analysis, we calculated the exchange-coupling constants between Cr^{2+} ions in $\mathbf{1a_{sym}}$ at the BS-DFT level (see Supporting

Information for more details).[83] Use of the spin Hamiltonian $\hat{H} = J_1(\hat{\mathbf{s}}_1 \cdot \hat{\mathbf{s}}_2 + \hat{\mathbf{s}}_2 \cdot \hat{\mathbf{s}}_3) + J_2 \hat{\mathbf{s}}_1 \cdot \hat{\mathbf{s}}_3$, where $\mathbf{s}_i$ is the spin vector localized on Cr*i*, gives large antiferromagnetic interactions between nearest neighbors (J_1 = 1635 cm^{-1}) and next-nearest neighbors (J_2 = 606 cm^{-1}), clearly indicating the presence of a delocalized bond all over the three Cr ions. We conclude that, in the gas phase, the preferred geometry of tri- and pentachromium(II) species with terminal Cl^- or SCN^- ligands is symmetric and unsymmetric, respectively.

Table 6. Computed Cr-Cr distances (in Å), spin densities (in unpaired electrons) and $\langle \hat{\mathbf{S}}^2 \rangle$ values in the symmetric and unsymmetric structures of **1a** and **1b** (BS S = 2 state).

	X	Cr1-Cr2	Cr2-Cr3	Cr1	Cr2	Cr3	$\langle \hat{\mathbf{S}}^2 \rangle$
$\mathbf{1a_{sym}}$	Cl^-	2.335	2.335	3.17	–2.54	3.17	8.38
$\mathbf{1b_{sym}}$	SCN^-	2.337	2.337	3.18	–2.56	3.18	8.41
$\mathbf{1a_{unsym}}$	Cl^-	2.686	1.886	3.50	–1.52	1.79	7.08
$\mathbf{1b_{unsym}}$	SCN^-	-	-	-	-	-	-

Electronic Structures. We analyzed in greater detail the electronic structures of the chlorido derivatives **1a** and **2a** through the use of Quasi-Restricted Molecular Orbitals (QROs), computed at the DFT level.[85] Figures 4 and 5 depict the singly-occupied QROs (SOMOs) for the optimized unsymmetric and symmetric structures of **2a** and **1a**, respectively (from now on, the principal quantum number will be dropped from orbital symbols, unless when strictly necessary). In $\mathbf{2a_{unsym}}$, these four frontier QROs have strong d-like character (d_{xy}, d_{xz}, d_{yz} and d_{z^2}) and are well localized on Cr1 (Figure 4). The $d_{x^2-y^2}$-like orbital is found at higher energy and is empty (VIRTUAL). Such a result suggests that the unsymmetric structures can be considered as the superposition of two sub-units, Cr1 and Cr2-Cr3-Cr4-Cr5, marginally interacting with each other. Indeed, only the d_{z^2}-like QRO on Cr1 is slightly delocalized over the Cr2-Cr3-Cr4-Cr5 fragment, as expected since the d_{z^2} metal orbitals have the most efficient overlap along the metal chain. Turning now to the Cr2-Cr3-Cr4-Cr5 fragment, the σ(σ∗) interactions are delocalized over the four ions, whereas π(π∗) and δ(δ∗) interactions are pretty localized on the Cr2-Cr3 and Cr4-Cr5 pairs, as suggested by the computed short Cr-Cr distances (Figure S36).

Considering a symmetric structure ($\mathbf{2a_{sym}}$) of the complex, a completely different picture would result (Figure S37). The unpaired electrons would now be found in four QROs (SOMOs) which can be described as one σ, two π and one δ non-bonding linear combinations of metal d orbitals. Nodal planes are present on Cr2 and Cr4 in all four QROs except for σ molecular orbital, where some electron density is still present on Cr2 and Cr4. A fifth δ-type non-bonding combination, with contributions from odd sites only, remains unoccupied (VIRTUAL); it was included in Figure S37 for consistency with the composition of SOMOs, although it is not the LUMO. The four unpaired electrons in $\mathbf{2a_{sym}}$ are thus *shared* among Cr1, Cr3 and Cr5, whereas they are *localized* on Cr1 in $\mathbf{2a_{unsym}}$. However, the presence

of a nodal plane on Cr2 and Cr4 makes each terminal Cr^{2+} ion in **2a**$_{sym}$ almost equivalent to Cr1 in **2a**$_{unsym}$ *in terms of electronic structure*.

A scenario similar to **2a**$_{sym}$ occurs in trichromium(II) string **1a**$_{sym}$. The four unpaired electrons are in one σ, two π and one δ non-bonding linear combinations of d orbitals centered on Cr1 and Cr3 (SOMOs), with a nodal plane now located on central metal Cr2 (Figure 5). A fifth δ-type molecular orbital also delocalized on Cr1 and Cr3 is found at higher energy and is empty (VIRTUAL); although it is not the LUMO, it was included in our analysis for symmetry consistency with the composition of the SOMOs.

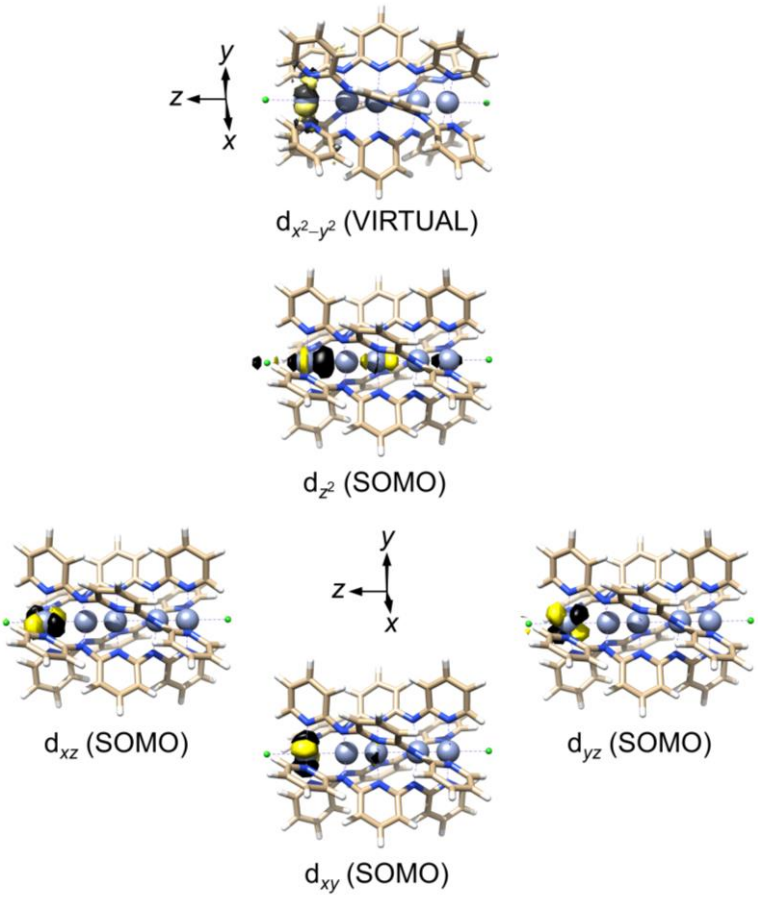

Figure 4. Frontier QROs in **2a**$_{unsym}$. The given reference frame is used to label the d-like QROs, which are almost completely localized on the leftmost Cr^{2+} ion (Cr1). A slightly different molecular orientation is used for a better representation of the $d_{x^2-y^2}$-like QRO. Positive and negative signs of the wave function are plotted in yellow and black, respectively.

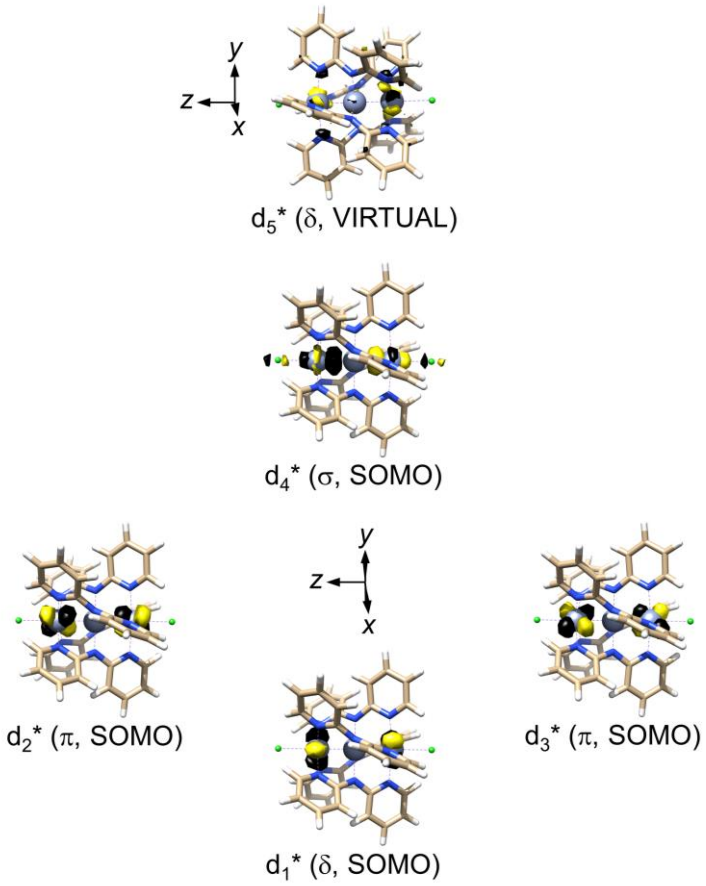

Figure 5. Frontier QROs in **1a**$_{\mathbf{sym}}$. The reference frame is defined by the coordination environment of Cr1 and is used to label the d-like contributions to QROs, as given by Eqs. (4a-e). A slightly different molecular orientation is used for a better representation of d_5*. Positive and negative signs of the wave function are plotted in yellow and black, respectively.

Since the $Cr1N_4$ and $Cr3N_4$ basal planes are twisted by ~45° with respect to each other along the chain axis, the wave function composition in terms of d orbitals can be worked out by simple inspection of Figure 5:

$$d_1^* = 2^{-1/2}\left(d_{xy}^{Cr1} - d_{x^2-y^2}^{Cr3}\right) \quad (4a)$$

$$d_2^* = 2^{-1/2}\left(d_{yz}^{Cr1} - d_{yz}^{Cr3}\right) \quad (4b)$$

$$d_3^* = 2^{-1/2}\left(-d_{xz}^{Cr1} + d_{xz}^{Cr3}\right) \quad (4c)$$

$$d_4^* = 2^{-1/2}\left(-d_{z^2}^{Cr1} + d_{z^2}^{Cr3}\right) \quad (4d)$$

$$d_5^* = 2^{-1/2}\left(-d_{x^2-y^2}^{Cr1} - d_{xy}^{Cr3}\right) \quad (4e)$$

Notice that d orbitals on Cr1 and Cr3 are expressed in two collinear reference frames, whose orientation is defined by the coordination environment of Cr1 (see Figure 5 and Supporting Information for more details). These results provide a starting point to explain the similar magnetic behavior observed in tri- and pentachromium(II) derivatives, in spite of their different structural preferences and electronic structure.

The Origin of Magnetic Anisotropy. The "isolated" Cr^{2+} ion (Cr1) in the ground, unsymmetric structures of pentachromium(II) strings (**2a**$_{\mathbf{unsym}}$ and **2b**$_{\mathbf{unsym}}$) displays a square-pyramidal coordination environment, with the metal only slightly out of the basal plane. Calculations at CASSCF(4,5) level on truncated Cr1 models (Figure S38a,b) afford an easy-axis anisotropy in the ground quintet state, with D = –1.513 and –1.592 cm^{-1} in **2a**$_{\mathbf{unsym}}$ and **2b**$_{\mathbf{unsym}}$, respectively (see Table 7).

Table 7. Magnetic parameters (cm^{-1}) determined by CASSCF calculations on Cr1 and $Cr1Zn_4$ models of **2a**$_{\mathbf{unsym}}$ and **2b**$_{\mathbf{unsym}}$.

	2a$_{\mathbf{unsym}}$ (X = Cl^-)		**2b**$_{\mathbf{unsym}}$ (X = SCN^-)	
Model	D	E/D	D	E/D
Cr1	–1.513	0.000	–1.592	0.000
$Cr1Zn_4$	–1.441	0.000	–1.248	0.000

These CASSCF results compare well with the experimental data gathered in Table 2 and with the predictions of AOM (Table 3), and correctly reproduce the larger axial anisotropy of the isothiocyanato (**2b**) vs. chlorido (**2a**) derivative.

To check the validity of the truncated models, we also calculated the magnetic properties of the neighboring Cr2-Cr3 pair (Figure S38c). As suggested by the short Cr-Cr distance and confirmed by the computed Unrestricted Natural Orbitals (UNOs), the two chromium(II) ions are strongly coupled and for this reason both static and dynamic correlations are supposed to be relevant. Therefore, CASSCF(8,8) was used to determine the electronic structure for this fragment. The active space was built with σ; π; π; δ and σ*; π*; π*; δ* orbitals (derived from the combination of d orbitals except for $d_{x^2-y^2}$) and the wave function was allowed to converge on both the first triplet and singlet CI solutions. As expected, the singlet state was found more stable by 3927.95 cm^{-1}, indicating that the Cr2-Cr3 unit can be regarded as a diamagnetic fragment. UNO analysis gave a bond order of 2.27 for the singlet ground state solution, which significantly deviates from the expected value of 4. As reported in the literature,[50] this is due to the partial occupation of antibonding orbitals as an effect of electron correlation. The twist of neighboring equatorial N_4 planes results in a deviation from a perfectly eclipsed configuration,[86] which reduces the overlap between d_{xz}, d_{yz}, and d_{xy} orbitals, i.e. the ones responsible for π and δ interactions. In turn, this effect leads to a lower energy splitting between their bonding and antibonding combinations, causes a larger spread of electron occupation numbers all over the Fermi energy region and reduces the effective bond order of the chromium pair. According to the above considerations, the Cr2-Cr3-Cr4-Cr5 unit is expected to behave as a diamagnetic fragment and to only

marginally affect the electronic structure of Cr1. Moreover, the long Cr1-Cr2 distance and the almost complete separation between UNOs of the two different fragments strongly suggest that the magnetic behavior of these unsymmetric EMACs is ruled *only by the Cr1 fragment*.

To further evaluate the effect of the Cr2-Cr3-Cr4-Cr5 fragment on the *D* value of Cr1, we performed a CASSCF calculation replacing the four Cr^{2+} with Zn^{2+} ions, without any structural relaxation ($Cr1Zn_4$ model). Such a choice was necessary since the explicit inclusion of the four Cr^{2+} ions would be computationally too demanding. The magnetic anisotropy parameters for Cr1 and $Cr1Zn_4$ models based on the structures of $\mathbf{2a_{unsym}}$ and $\mathbf{2b_{unsym}}$ are compared in Table 7. The Zn^{2+} ions have a limited impact on calculated *D* values, which become somewhat less negative. We can therefore conclude that an axial "diamagnetic substitution" approach does not significantly alter the main contributions to the anisotropy, which originate almost totally from the N_4Cl or $N_4N(CS)$ coordination environments.

Unfortunately, CASSCF calculations cannot be applied to the symmetric structure of trichromium(II) complexes; for a correct representation of their electronic structure, the CAS space should be extended over the 3d sets of the three Cr^{2+} ions, and this would be unmanageable in terms of computational resources.

A unified treatment of both types of complexes can however rely on an approach devised by Neese *et al.*,[85,87,88] in which the electronic structure is described in terms of QROs. For simplicity, we herein limit our analysis to the d-like molecular orbitals that are depicted in Figures 4 and 5 and whose energies, as provided by DFT/PBE calculations, are reported in Table 8. As discussed above, in $\mathbf{2a_{unsym}}$ and $\mathbf{2b_{unsym}}$ these frontier QROs essentially correspond to the d orbitals of Cr1 (Figure 4). Notice that their energy ordering for α spin components is consistent with the square-pyramidal coordination geometry of Cr1, namely:

$$\varepsilon^{\alpha}\left(\mathrm{d}_{xy}^{\mathrm{Cr1}}\right)^{1} < \varepsilon^{\alpha}\left(\mathrm{d}_{xz}^{\mathrm{Cr1}}\right)^{1} = \varepsilon^{\alpha}\left(\mathrm{d}_{yz}^{\mathrm{Cr1}}\right)^{1} < \varepsilon^{\alpha}\left(\mathrm{d}_{z^2}^{\mathrm{Cr1}}\right)^{1} < \varepsilon^{\alpha}\left(\mathrm{d}_{x^2-y^2}^{\mathrm{Cr1}}\right)^{0} \qquad (5)$$

where we have included information on electronic occupation as superscript. The contribution of quintet and triplet excited states to the axial zfs parameter (*D*) of the ground $S = 2$ state is then described in terms of single-particle α → α (SOMO → VIRTUAL) and α → β (SOMO → SOMO) spin excitations, respectively (details are available in the Supporting Information). The values of $D_{\alpha\to\alpha}$, $D_{\alpha\to\beta}$ and $D = D_{\alpha\to\alpha} + D_{\alpha\to\beta}$ obtained by setting the 3d spin-orbit coupling constant (ζ_{3d}) for Cr^{2+} to the free-ion value are presented in Table 9. Such results are only semi-quantitative since several other excitations involving doubly-occupied and empty orbitals, as well as spin-spin contributions, were not included.[88]

Table 8. Calculated frontier d QRO eigenvalues (eV) for **1a$_{sym}$**, **1b$_{sym}$**, **2a$_{unsym}$** and **2b$_{unsym}$**.

	1a$_{sym}$		**1b$_{sym}$**	
	ε^{α}	ε^{β}	ε^{α}	ε^{β}
d_1^* (SOMO)	–4.694	–1.769	–4.915	–2.032
d_2^* (SOMO)	–4.422	–1.460	–4.605	–1.759
d_3^* (SOMO)	–4.422	–1.460	–4.605	–1.759
d_4^* (SOMO)	–3.429	–1.294	–3.501	–1.334
d_5^* (VIRTUAL)	–1.628	_ [a]	–1.918	_ [a]
	2a$_{unsym}$		**2b$_{unsym}$**	
	ε^{α}	ε^{β}	ε^{α}	ε^{β}
d_{xy}^{Cr1} (SOMO)	–4.705	–1.828	–4.846	–2.031
d_{xz}^{Cr1} (SOMO)	–4.495	–1.334	–4.595	–1.587
d_{yz}^{Cr1} (SOMO)	–4.494	–1.333	–4.594	–1.586
$d_{z^2}^{Cr1}$ (SOMO)	–3.649	–1.618	–3.662	–1.651
$d_{x^2-y^2}^{Cr1}$ (VIRTUAL)	–1.583	_ [a]	–2.019	_ [a]

[a] Not reported since not needed in calculations.

Table 9 clearly shows that spin-forbidden ($\alpha \rightarrow \beta$) LF excitations can by no means be neglected. From the relevant equations reported in the Supporting Information, it is seen that the $D_{\alpha\rightarrow\alpha}$ contribution becomes more negative as d_{xy} and $d_{x^2-y^2}$ get closer in energy. Considering σ interactions as dominant, this condition is fulfilled on lowering the σ LF contributions of the equatorial ligands. On the other hand, $D_{\alpha\rightarrow\beta}$ contribution becomes more negative if the α (β) component of d_{z^2} and the β (α) component of d_{xz}/d_{yz} pair get closer in energy, i.e. on increasing the axial LF strength given by the terminal ligand and by the Cr2-Cr3-Cr4-Cr5 fragment. All these considerations are in agreement with the results obtained in AOM section and with previous work on other isoelectronic systems.[75–79,89]

In the case of **1a$_{sym}$** and **1b$_{sym}$**, frontier QROs are no longer single-center d orbitals, although they exhibit a similar energy pattern to pentachromium(II) strings (Table 8). With the wave functions given by Eqs. (4a-e) and the corresponding spin-resolved energies (Table 8), Neese's approach yields the $D_{\alpha\rightarrow\alpha}$, $D_{\alpha\rightarrow\beta}$ and overall D parameters also presented in Table 9 (details are available in the Supporting Information).

Table 9. Calculated values of $D_{\alpha\rightarrow\alpha}$, $D_{\alpha\rightarrow\beta}$ and overall D (in cm^{-1}) with ζ_{3d}= 230 cm^{-1}.

	1a$_{sym}$	**1b$_{sym}$**	**2a$_{unsym}$**	**2b$_{unsym}$**
$D_{\alpha\rightarrow\alpha}$	–0.46	–0.47	–0.38	–0.42
$D_{\alpha\rightarrow\beta}$	–1.18	–1.25	–1.30	–1.36
D	–1.64	–1.72	–1.68	–1.79

These data give numerical support to the similar anisotropy displayed by tri- and pentachromium(II) derivatives, primarily because frontier MOs with dominant d character follow a similar energy pattern. The ultimate reason is that frontier orbitals in trichromium(II) chains are non-bonding linear combinations of d orbitals of Cr1 and Cr3 and their energy thus largely reflects the d-level pattern of

terminal ions. Furthermore our treatment also accounts for the slightly enhanced anisotropy of isothiocyanato vs. chlorido derivatives.

CONCLUSION

The present work is the first systematic attempt to extend magnetic studies on odd-membered (n = 3, 5) chromium(II)-based EMACs beyond S-value determination. As a first important result, we found that both tri- and pentachromium(II) strings have a negative zfs parameter D ($|D|$ = 1.5-1.8 cm^{-1}), weak rhombicity ($|E/D| \leq 0.02$) and display slow relaxation of their magnetization. These properties are only marginally affected by the axial ligands (X = Cl^-, SCN^-), with the isothiocyanato derivatives slightly more anisotropic than the chlorido complexes. Such similarities in electronic structure over remarkably small energy scales are surprising in light of the different structural preferences as chain length is varied. Confirming previous experimental and theoretical investigations,[39,46–51] our DFT calculations showed that the preferred structure is symmetric (D_4) for n = 3 but unsymmetric (C_4) for n = 5. The subsequent step of our work then consisted in investigating the impact of a symmetric vs. unsymmetric structure on the distribution of unpaired electrons and on the zfs of the S = 2 state. DFT studies on pentachromium(II) complexes clearly showed the occurrence of a structurally-isolated terminal Cr^{2+} ion (Cr1), whose d orbitals provide the leading contribution to the four SOMOs. CASSCF-level calculations on terminal $Cr1N_4Cl$ and $Cr1N_4N(CS)$ chromophores in fact yielded D and E parameters in remarkable agreement with experiment and with elementary LF arguments based on the spectrochemical series.

Such a structural confinement is absent in the symmetric structure of trichromium(II) strings, whose terminal metals are equivalent by symmetry. However, a major simplification arises from the fact that, to a good approximation, the four SOMOs are non-bonding linear combination of d orbitals centered on terminal metals (Cr1 and Cr3), with no contribution from Cr2. For this reason, their energies closely mirror the pattern of LF-split d orbitals of terminal metals, whose coordination environment is only weakly affected by chain length. To achieve an estimate of the zfs in both symmetric and unsymmetric structures at the same level of theory, we followed the quasi-restricted DFT approach devised by Neese *et al*.[85,87,88] We found that, in spite of the very different extent of unpaired electron delocalization, in both tri- and pentachromium(II) species the D parameter is expected to be negative and of similar magnitude, with SCN^- axial ligands triggering a slightly higher anisotropy.

In conclusion, the similar S value, magnetic anisotropy and spin dynamics of tri- and pentachromium(II) EMACs implies by no means a similar pattern of Cr-Cr distances, i.e. the occurrence of a structurally confined Cr^{2+} ion plus one or two diamagnetic [Cr_2] pairs. In both cases, the d orbitals of terminal ions are invariably the most important contributors to the four SOMOs, at the same time explaining why axial ligands have a small but detectable impact on magnetic anisotropy. However, it should be mentioned that the LF strengths of the axial ligands studied here are quite similar, and therefore the influence of the axial ligand may be more clearly revealed by comparing complexes with strong (e.g. CN^-) and weak (e.g. BF_4^-) donors. A series of Cr_3 compounds with a variety of axial ligands

is currently under examination to confirm the degree of their influence on the magnitude of the relaxation barrier.

ASSOCIATED CONTENT

Supporting Information. The Supporting Information is available free of charge on the ACS Publications website at https://pubs.acs.org/doi/10.1021/acs.inorgchem.9b02994.

Additional synthetic procedures, crystallographic and structural tables, details of dc/ac magnetic analyses, EPR diagrams and spectra, additional DFT figures, details of BS-DFT calculation of exchange-coupling constants, description of the quasi-restricted DFT approach to the *D* value in tri- and pentachromium(II) EMACs (.pdf), DFT (.docx) and CASSCF (.txt) input files.

Accession codes. CCDC 1953230 contains the supplementary crystallographic data for this paper. These data can be obtained free of charge via www.ccdc.cam.ac.uk/data_request/cif, or by emailing data_request@ccdc.cam.ac.uk, or by contacting The Cambridge Crystallographic Data Centre, 12 Union Road, Cambridge CB2 1EZ, UK; fax: +44 1223 336033.

AUTHOR INFORMATION

Corresponding Author

*Email for A.C.: acornia@unimore.it.

Author contributions

The manuscript was written through contributions of all authors. All authors have given approval to the final version of the manuscript.

Notes

The authors declare no competing financial interest.

While our manuscript was close to submission, an *ab initio* investigation of **1a** was published by Sakaki *et al*.[90] They report a similar composition of SOMOs, although their study is unrelated to magnetic anisotropy.

ACKNOWLEDGMENTS

We thank the University of Bordeaux, the CNRS, the Conseil Régional de Nouvelle Aquitaine, the MOLSPIN COST Action (CA15128) and the GdR MCM-2: Magnétisme et Commutation Moléculaires. We acknowledge the financial contributions of the European Research Council through the Advanced Grant MolNanoMaS (267746), of Italian MIUR through FIRB projects RBAP117RWN and RBFR10OAI0, and of University of Modena and Reggio Emilia through a FAR2014 (Fondo di Ateneo per la Ricerca 2014) project. A. C. is grateful to S. Boccedi and L. Rigamonti for their contributions to the synthesis and spectroscopic characterization of the compounds. E. A. H. and R. C. thank L. Falvello for crystallographic advice.

REFERENCES

(1) Gatteschi, D.; Sessoli, R.; Villain, J. *Molecular Nanomagnets*; Oxford University Press: Oxford, 2006.

(2) *Molecular Nanomagnets and Related Phenomena - Structure and Bonding Series, Vol. 164*; Gao, S., Ed.; Springer-Verlag: Berlin Heidelberg, 2015.

(3) Mannini, M.; Pineider, F.; Danieli, C.; Totti, F.; Sorace, L.; Sainctavit, P.; Arrio, M.-A.; Otero, E.; Joly, L.; Cezar, J. C.; Cornia, A.; Sessoli, R. Quantum tunnelling of the magnetization in a monolayer of oriented single-molecule magnets. *Nature* **2010**, *468* (7322), 417–421.

(4) Malavolti, L.; Lanzilotto, V.; Ninova, S.; Poggini, L.; Cimatti, I.; Cortigiani, B.; Margheriti, L.; Chiappe, D.; Otero, E.; Sainctavit, P.; Totti, F.; Cornia, A.; Mannini, M.; Sessoli, R. Magnetic bistability in a submonolayer of sublimated Fe_4 single-molecule magnets. *Nano Lett.* **2015**, *15* (1), 535–541.

(5) Wäckerlin, C.; Donati, F.; Singha, A.; Baltic, R.; Rusponi, S.; Diller, K.; Patthey, F.; Pivetta, M.; Lan, Y.; Klyatskaya, S.; Ruben, M.; Brune, H.; Dreiser, J. Giant Hysteresis of Single-Molecule Magnets Adsorbed on a Nonmagnetic Insulator. *Adv. Mater.* **2016**, *28* (26), 5195–5199.

(6) Katoh, K.; Komeda, T.; Yamashita, M. The Frontier of Molecular Spintronics Based on Multiple-Decker Phthalocyaninato Tb^{III} Single-Molecule Magnets. *Chem. Rec.* **2016**, *16* (2), 987–1016.

(7) Moreno-Pineda, E.; Godfrin, C.; Balestro, F.; Wernsdorfer, W.; Ruben, M. Molecular spin qudits for quantum algorithms. *Chem. Soc. Rev.* **2018**, *47* (2), 501–513.

(8) Cornia, A.; Seneor, P. Spintronics: The molecular way. *Nat. Mater.* **2017**, *16* (5), 505–506.

(9) Gaita-Ariño, A.; Luis, F.; Hill, S.; Coronado, E. Molecular spins for quantum computation. *Nat. Chem.* **2019**, *11* (4), 301–309.

(10) Gómez-Coca, S.; Aravena, D.; Morales, R.; Ruiz, E. Large magnetic anisotropy in mononuclear metal complexes. *Coord. Chem. Rev.* **2015**, *289–290*, 379–392.

(11) Atanasov, M.; Aravena, D.; Suturina, E.; Bill, E.; Maganas, D.; Neese, F. First principles approach to the electronic structure, magnetic anisotropy and spin relaxation in mononuclear 3d-transition metal single molecule magnets. *Coord. Chem. Rev.* **2015**, *289–290*, 177–214.

(12) Gómez-Coca, S.; Urtizberea, A.; Cremades, E.; Alonso, P. J.; Camón, A.; Ruiz, E.; Luis, F. Origin of slow magnetic relaxation in Kramers ions with non-uniaxial anisotropy. *Nat. Commun.* **2014**, *5* (1), 4300.

(13) Feng, M.; Tong, M.-L. Single Ion Magnets from 3d to 5f: Developments and Strategies. *Chem. Eur. J.* **2018**, *24* (30), 7574–7594.

(14) Lunghi, A.; Totti, F.; Sessoli, R.; Sanvito, S. The role of anharmonic phonons in under-barrier spin relaxation of single molecule magnets. *Nat. Commun.* **2017**, *8*, 14620.

(15) Escalera-Moreno, L.; Baldoví, J. J.; Gaita-Ariño, A.; Coronado, E. Spin states, vibrations and spin relaxation in molecular nanomagnets and spin qubits: a critical perspective. *Chem. Sci.* **2018**, *9* (13), 3265–3275.

(16) Bunting, P. C.; Atanasov, M.; Damgaard-Møller, E.; Perfetti, M.; Crassee, I.; Orlita, M.; Overgaard, J.; van Slageren, J.; Neese, F.; Long, J. R. A linear cobalt(II) complex with maximal orbital angular momentum from a non-Aufbau ground state. *Science (80-.).* **2018**, *362* (6421), eaat7319.

(17) Bar, A. K.; Kalita, P.; Singh, M. K.; Rajaraman, G.; Chandrasekhar, V. Low-coordinate mononuclear lanthanide complexes as molecular nanomagnets. *Coord. Chem. Rev.* **2018**, *367*, 163–216.

(18) Gupta, S. K.; Murugavel, R. Enriching lanthanide single-ion magnetism through symmetry and axiality. *Chem. Commun.* **2018**, *54* (30), 3685–3696.

(19) Liu, J.-L.; Chen, Y.-C.; Tong, M.-L. Symmetry strategies for high performance lanthanide-based single-molecule magnets. *Chem. Soc. Rev.* **2018**, *47* (7), 2431–2453.

(20) Ding, Y.-S.; Chilton, N. F.; Winpenny, R. E. P.; Zheng, Y.-Z. On Approaching the Limit of Molecular Magnetic Anisotropy: A Near-Perfect Pentagonal Bipyramidal Dysprosium(III) Single-Molecule Magnet. *Angew. Chem. Int. Ed.* **2016**, *55* (52), 16071–16074.

(21) Chilton, N. F. Design criteria for high-temperature single-molecule magnets. *Inorg. Chem.* **2015**, *54* (5), 2097–2099.

(22) Guo, F.-S.; Day, B. M.; Chen, Y.-C.; Tong, M.-L.; Mansikkamäki, A.; Layfield, R. A. A Dysprosium Metallocene Single-Molecule Magnet Functioning at the Axial Limit. *Angew. Chem. Int. Ed.* **2017**, *56* (38), 11445–11449.

(23) Goodwin, C. A. P.; Ortu, F.; Reta, D.; Chilton, N. F.; Mills, D. P. Molecular magnetic hysteresis at 60 kelvin in dysprosocenium. *Nature* **2017**, *548* (7668), 439–442.

(24) Guo, F.-S.; Day, B. M.; Chen, Y.-C.; Tong, M.-L.; Mansikkamäki, A.; Layfield, R. A. Magnetic hysteresis up to 80 kelvin in a dysprosium metallocene single-molecule magnet. *Science (80-.).* **2018**, *362* (6421), 1400–1403.

(25) Hernández Sánchez, R.; Betley, T. A. Thermally Persistent High-Spin Ground States in Octahedral Iron Clusters. *J. Am. Chem. Soc.* **2018**, *140* (48), 16792–16806.

(26) Majumdar, M.; Bera, J. K. Transition-Metal-Based Linear Chain Compounds. In *Macromolecules Containing Metal and Metal-like Elements, Volume 9: Supramolecular and Self-Assembled Metal-Containing Materials*; Abd-El Aziz, A. S., Carraher, C. E., Pittman, C. U., Zeldin, M., Eds.; John Wiley & Sons, Inc.: Hoboken, NJ, 2009; pp 181–253.

(27) Berry, J. F. Metal–Metal Bonds in Chains of Three or More Metal Atoms: From Homometallic to Heterometallic Chains. *Struct. Bond.* **2010**, *136*, 1–28.

(28) Hua, S.-A.; Cheng, M.-C.; Chen, C.; Peng, S.-M. From Homonuclear Metal String Complexes to Heteronuclear Metal String Complexes. *Eur. J. Inorg. Chem.* **2015**, *2015* (15), 2510–2523.

(29) Chen, P.-J.; Sigrist, M.; Horng, E.-C.; Lin, G.-M.; Lee, G.-H.; Chen, C.; Peng, S.-M. A ligand design with a modified naphthyridylamide for achieving the longest EMACs: the 1st single-molecule conductance of an undeca-nickel metal string. *Chem. Commun.* **2017**, *53* (34), 4673–4676.

(30) Srinivasan, A.; Cortijo, M.; Bulicanu, V.; Naim, A.; Clérac, R.; Sainctavit, P.; Rogalev, A.; Wilhelm, F.; Rosa, P.; Hillard, E. A. Enantiomeric resolution and X-ray optical activity of a tricobalt extended metal atom chain. *Chem. Sci.* **2018**, *9* (5), 1136–1143.

(31) Yu, C.; Kuo, M.; Chuang, C.; Lee, G.; Hua, S.; Jin, B.; Peng, S. Chirality Control of Quadruple Helixes of Metal Strings by Peripheral Chiral Ligands. *Chem. Asian J.* **2014**, *9* (11), 3111–3115.

(32) Nicolini, A.; Galavotti, R.; Barra, A.-L.; Borsari, M.; Caleffi, M.; Luo, G.; Novitchi, G.; Park, K.; Ranieri, A.; Rigamonti, L.; Roncaglia, F.; Train, C.; Cornia, A. Filling the Gap in Extended Metal Atom Chains: Ferromagnetic Interactions in a Tetrairon(II) String Supported by Oligo-α-pyridylamido Ligands. *Inorg. Chem.* **2018**, *57* (9), 5438–5448.

(33) Clérac, R.; Cotton, F. A.; Daniels, L. M.; Dunbar, K. R.; Murillo, C. A.; Pascual, I. Linear Trichromium Complexes with Direct Cr to Cr Contacts. 1. Compounds with Cr_3(dipyridylamide)$_4^{2+}$ Cores. *Inorg. Chem.* **2000**, *39* (4), 748–751.

(34) Chang, H.; Li, J.; Wang, C.; Lin, T.; Lee, H.-C.; Lee, G.; Peng, S. Linear Five-Centred Chromium Multiple Bonds Bridged by Four tpda^{2-} Ligands [tpda^{2-} = tripyridyldiamido dianion] – Synthesis and Structural Studies. *Eur. J. Inorg. Chem.* **1999**, *1999* (8), 1243–1251.

(35) Cornia, A.; Rigamonti, L.; Boccedi, S.; Clérac, R.; Rouzières, M.; Sorace, L. Magnetic blocking in extended metal atom chains: A pentachromium(II) complex behaving as a single-molecule magnet. *Chem. Commun.* **2014**, *50* (96), 15191–15194.

(36) Christian, J. H.; Brogden, D. W.; Bindra, J. K.; Kinyon, J. S.; van Tol, J.; Wang, J.; Berry, J. F.; Dalal, N. S. Enhancing the Magnetic Anisotropy of Linear Cr(II) Chain Compounds Using Heavy Metal Substitutions. *Inorg. Chem.* **2016**, *55* (13), 6376–6383.

(37) Wang, J.; Wang, Z.; Clark, R. J.; Ozarowski, A.; van Tol, J.; Dalal, N. S. A high-frequency EPR characterization of the *S*=2 linear tri-atomic chain in $Cr_3(dpa)_4Cl_2 \cdot CH_2Cl_2$. *Polyhedron* **2011**, *30* (18), 3058–3061.

(38) Berry, J. F.; Cotton, F. A.; Fewox, C. S.; Lu, T.; Murillo, C. a; Wang, X. Extended metal atom chains (EMACs) of five chromium or cobalt atoms: Symmetrical or unsymmetrical? *Dalton Trans.* **2004**, No. 15, 2297–2302.

(39) Dirvanauskas, A.; Galavotti, R.; Lunghi, A.; Nicolini, A.; Roncaglia, F.; Totti, F.; Cornia, A. Solution structure of a pentachromium(II) single molecule magnet from DFT calculations, isotopic labelling and multinuclear NMR spectroscopy. *Dalton Trans.* **2018**, *47* (2), 585–595.

(40) Wang, W.-Z.; Ismayilov, R. H.; Lee, G.-H.; Huang, Y.-L.; Yeh, C.-Y.; Fu, M.-D.; Chen, C.; Peng, S.-M. Fine tuning of pentachromium(II) metal string complexes through elaborate design of ligand. *New J. Chem.* **2012**, *36* (3), 632–637.

(41) Ismayilov, R. H.; Wang, W.-Z.; Lee, G.-H.; Chien, C.-H.; Jiang, C.-H.; Chiu, C.-L.; Yeh, C.-Y.; Peng, S.-M. Redox Modification of EMACs Through the Tuning of Ligands: Heptametal(II) Complexes of Pyrazine-Modulated Oligo-α-pyridylamido Ligands. *Eur. J. Inorg. Chem.* **2009**, *2009* (14), 2110–2120.

(42) Ismayilov, R. H.; Wang, W.-Z.; Wang, R.-R.; Yeh, C.-Y.; Lee, G.-H.; Peng, S.-M. Four quadruple metal–metal bonds lined up: linear nonachromium(II) metal string complexes. *Chem. Commun.* **2007**, No. 11, 1121–1123.

(43) Berry, J. F.; Cotton, F. A.; Lu, T.; Murillo, C. A.; Roberts, B. K.; Wang, X. Molecular and electronic structures by design: Tuning symmetrical and unsymmetrical linear trichromium chains. *J. Am. Chem. Soc.* **2004**, *126* (22), 7082–7096.

(44) Berry, J. F.; Cotton, F. A.; Murillo, C. A.; Roberts, B. K. An Efficient Synthesis of Acetylide/Trimetal/Acetylide Molecular Wires. *Inorg. Chem.* **2004**, *43* (7), 2277–2283.

(45) Ismayilov, R. H.; Wang, W.-Z.; Lee, G.-H.; Wang, R.-R.; Liu, I. P.-C.; Yeh, C.-Y.; Peng, S.-M. New versatile ligand family, pyrazine-modulated oligo-α-pyridylamino ligands, from coordination polymer to extended metal atom chains. *Dalton Trans.* **2007**, No. 27, 2898–2907.

(46) Wu, L.-C.; Thomsen, M. K.; Madsen, S. R.; Schmoekel, M.; Jørgensen, M. R. V.; Cheng, M.-C.; Peng, S.-M.; Chen, Y.-S.; Overgaard, J.; Iversen, B. B. Chemical Bonding in a Linear Chromium Metal String Complex. *Inorg. Chem.* **2014**, *53* (23), 12489–12498.

(47) Benbellat, N.; Rohmer, M.-M.; Bénard, M. Electronic origin of the structural versatility in linear trichromium complexes of dipyridylamide. *Chem. Commun.* **2001**, *3* (22), 2368–2369.

(48) Georgiev, V. P.; McGrady, J. E. Influence of Low-Symmetry Distortions on Electron Transport through Metal Atom Chains: When Is a Molecular Wire Really "Broken"? *J. Am. Chem. Soc.* **2011**, *133* (32), 12590–12599.

(49) Georgiev, V. P.; Mohan, P. J.; DeBrincat, D.; McGrady, J. E. Low-symmetry distortions in Extended Metal Atom Chains (EMACs): Origins and consequences for electron transport. *Coord. Chem. Rev.* **2013**, *257* (1), 290–298.

(50) Spivak, M.; Arcisauskaite, V.; López, X.; McGrady, J. E.; de Graaf, C. A multiconfigurational approach to the electronic structure of trichromium extended metal atom chains. *Dalton Trans.* **2017**, *46* (19), 6202–6211.

(51) Spivak, M.; Arcisauskaite, V.; López, X.; de Graaf, C. Backbone flexibility of extended metal atom chains. Ab initio molecular dynamics for $Cr_3(dpa)_4X_2$ (X = NCS, CN, NO_3) in gas and crystalline phases. *Dalton Trans.* **2017**, *46* (44), 15487–15493.

(52) Berry, J. F.; Cotton, F. A.; Murillo, C. A.; Chan, Z.-K.; Yeh, C.-W.; Chen, J.-D. Linear Trichromium, Tricobalt, Trinickel, and Tricopper Complexes of 2,2′-Dipyridylamide. *Inorg. Syn.* **2014**, *36*, 103–110.

(53) Turov, Y.; Berry, J. F. Synthesis, characterization and thermal properties of trimetallic N_3–Cr≡Cr···M–N_3 azide complexes with M = Cr, Mn, Fe, and Co. *Dalton Trans.* **2012**, *41* (26), 8153–8161.

(54) *APEX2, SADABS, and SAINT Software Reference Manuals*; Bruker-AXS, Inc.: Madison, Wisconsin, USA, 2009.

(55) Sheldrick, G. M. Crystal structure refinement with *SHELXL*. *Acta Crystallogr. Sect. C Struct. Chem.* **2015**, *71* (1), 3–8.

(56) Bain, G. A.; Berry, J. F. Diamagnetic Corrections and Pascal's Constants. *J. Chem. Educ.* **2008**, *85* (4), 532–536.

(57) Cole, K. S.; Cole, R. H. Dispersion and Absorption in Dielectrics I. Alternating Current Characteristics. *J. Chem. Phys.* **1941**, *9* (4), 341–351.

(58) Dekker, C.; Arts, A. F. M.; de Wijn, H. W.; van Duyneveldt, A. J.; Mydosh, J. A. Activated dynamics in a two-dimensional Ising spin glass: $Rb_2Cu_{1-x}Co_xF_4$. *Phys. Rev. B* **1989**, *40* (16), 11243–11251.

(59) Mossin, S.; Weihe, H.; Barra, A.-L. Is the Axial Zero-Field Splitting Parameter of Tetragonally Elongated High-Spin Manganese(III) Complexes Always Negative? *J. Am. Chem. Soc.* **2002**, *124* (30), 8764–8765.

(60) Jacobsen, C. J. H.; Pedersen, E.; Villadsen, J.; Weihe, H. ESR characterization of *trans*-$V^{II}(py)_4X_2$ and *trans*-$Mn^{II}(py)_4X_2$ (X = NCS, Cl, Br, I; py = pyridine). *Inorg. Chem.* **1993**, *32* (7), 1216–1221.

(61) Bencini, A.; Ciofini, I.; Uytterhoeven, M. G. Angular overlap calculations of the spin Hamiltonian parameters of transition metal ions in low symmetry environments. High spin iron(II), iron(III) and manganese(III). *Inorg. Chim. Acta* **1998**, *274* (1), 90–101.

(62) Lever, A. B. P. *Inorganic Electronic Spectroscopy*, 2nd ed.; Elsevier: Amsterdam, The Netherlands, 1986.

(63) Bencini, A.; Benelli, C.; Gatteschi, D. The angular overlap model for the description of the paramagnetic properties of transition metal complexes. *Coord. Chem. Rev.* **1984**, *60*, 131–169.

(64) Khamar, M. M.; Larkworthy, L. F.; Nelson-Richardson, M. H. O. Complexes of chromium(II) halides with methylpyridines. *Inorg. Chim. Acta* **1978**, *28*, 245–250.

(65) Neese, F. The *ORCA* program system. *Wiley Interdiscip. Rev. Comput. Mol. Sci.* **2012**, *2* (1), 73–78.

(66) Segall, M. D.; Shah, R.; Pickard, C. J.; Payne, M. C. Population analysis of plane-wave electronic structure calculations of bulk materials. *Phys. Rev. B* **1996**, *54* (23), 16317–16320.

(67) Grimme, S.; Antony, J.; Ehrlich, S.; Krieg, H. A consistent and accurate ab initio parametrization of density functional dispersion correction (DFT-D) for the 94 elements H-Pu. *J. Chem. Phys.* **2010**, *132* (15), 154104.

(68) Pantazis, D. A.; Chen, X.-Y.; Landis, C. R.; Neese, F. All-Electron Scalar Relativistic Basis Sets for Third-Row Transition Metal Atoms. *J. Chem. Theory Comput.* **2008**, *4* (6), 908–919.

(69) Weigend, F.; Ahlrichs, R. Balanced basis sets of split valence, triple zeta valence and quadruple zeta valence quality for H to Rn: Design and assessment of accuracy. *Phys. Chem. Chem. Phys.* **2005**, *7* (18), 3297–3305.

(70) Lin, S.-Y.; Chen, I.-W. P.; Chen, C.; Hsieh, M.-H.; Yeh, C.-Y.; Lin, T.-W.; Chen, Y.-H.; Peng, S.-M. Effect of Metal−Metal Interactions on Electron Transfer: an STM Study of One-Dimensional Metal String Complexes. *J. Phys. Chem. B* **2004**, *108* (3), 959–964.

(71) M. Llunell, D. Casanova, J. Cirera, P. Alemany, S. A. *SHAPE v2.1 - Continuous Shape Measures calculation*; Universitat de Barcelona, Spain, 2013.

(72) Stoll, S.; Schweiger, A. *EasySpin*, a comprehensive software package for spectral simulation and analysis in EPR. *J. Magn. Reson.* **2006**, *178* (1), 42–55.

(73) Reta, D.; Chilton, N. F. Uncertainty estimates for magnetic relaxation times and magnetic relaxation parameters. *Phys. Chem. Chem. Phys.* **2019**, *21* (42), 23567–23575.

(74) Deng, Y.-F.; Han, T.; Wang, Z.; Ouyang, Z.; Yin, B.; Zheng, Z.; Krzystek, J.; Zheng, Y.-Z. Uniaxial magnetic anisotropy of square-planar chromium(II) complexes revealed by magnetic and HF-EPR studies. *Chem. Commun.* **2015**, *51* (100), 17688–17691.

(75) Gatteschi, D.; Sorace, L.; Sessoli, R.; Barra, A.-L. High-frequency EPR: An occasion for revisiting ligand field theory. *Appl. Magn. Reson.* **2001**, *21* (3–4), 299–310.

(76) Krzystek, J.; Telser, J.; Pardi, L. A.; Goldberg, D. P.; Hoffman, B. M.; Brunel, L.-C. High-

Frequency and -Field Electron Paramagnetic Resonance of High-Spin Manganese(III) in Porphyrinic Complexes. *Inorg. Chem.* **1999**, *38* (26), 6121–6129.

(77) Telser, J.; Pardi, L. A.; Krzystek, J.; Brunel, L.-C. EPR Spectra from "EPR-Silent" Species: High-Field EPR Spectroscopy of Aqueous Chromium(II). *Inorg. Chem.* **2000**, *39* (8), 1834–1834.

(78) Barra, A.-L.; Gatteschi, D.; Sessoli, R.; Abbati, G. L.; Cornia, A.; Fabretti, A. C.; Uytterhoeven, M. G. Electronic structure of manganese(III) compounds from high-frequency EPR spectra. *Angew. Chem. Int. Ed.* **1997**, *36* (21), 2329–2331.

(79) Telser, J. A perspective on applications of ligand-field analysis: inspiration from electron paramagnetic resonance spectroscopy of coordination complexes of transition metal ions. *J. Braz. Chem. Soc.* **2006**, *17* (8), 1501–1515.

(80) Bencini, A.; Gatteschi, D. *EPR of Exchange Coupled Systems*; Springer-Verlag: Berlin, 1990.

(81) Cotton, F. A.; Daniels, L. M.; Murillo, C. A.; Wang, X. Getting the right answer to a key question concerning molecular wires. *Chem. Commun.* **1999**, *5* (24), 2461–2462.

(82) Cotton, F. A. Chromium Compounds. In *Multiple Bonds between Metal Atoms*; Cotton, F. A., Murillo, C. A., Walton, R. A., Eds.; Springer Science & Business Media, Inc.: New York, 2005; pp 35–68.

(83) Bencini, A.; Totti, F. A Few Comments on the Application of Density Functional Theory to the Calculation of the Magnetic Structure of Oligo-Nuclear Transition Metal Clusters. *J. Chem. Theory Comput.* **2009**, *5* (1), 144–154.

(84) Bencini, A.; Totti, F. DFT description of the magnetic structure of polynuclear transition-metal clusters: The complexes $[\{Cu(bpca)_2(H_2O)_2\}\{Cu(NO_3)_2\}_2]$, (bpca = Bis(2-pyridylcarbonyl)amine), and $[Cu(DBSQ)(C_2H_5O)]_2$, (DBSQ = 3,5-di- tert -butyl-semiquinonato). *Int. J. Quantum Chem.* **2005**, *101* (6), 819–825.

(85) Neese, F. Calculation of the zero-field splitting tensor on the basis of hybrid density functional and Hartree-Fock theory. *J. Chem. Phys.* **2007**, *127* (16), 164112.

(86) Cotton, F. A.; Felthouse, T. R. Pyridine and pyrazine adducts of tetrakis(acetato)dichromium. *Inorg. Chem.* **1980**, *19* (2), 328–331.

(87) Neese, F.; Solomon, E. I. Calculation of Zero-Field Splittings, g-Values, and the Relativistic Nephelauxetic Effect in Transition Metal Complexes. Application to High-Spin Ferric Complexes. *Inorg. Chem.* **1998**, *37* (26), 6568–6582.

(88) Neese, F. Importance of Direct Spin−Spin Coupling and Spin-Flip Excitations for the Zero-Field Splittings of Transition Metal Complexes: A Case Study. *J. Am. Chem. Soc.* **2006**, *128* (31), 10213–10222.

(89) Liakos, D. G.; Ganyushin, D.; Neese, F. A Multiconfigurational ab Initio Study of the Zero-Field Splitting in the Di- and Trivalent Hexaquo−Chromium Complexes. *Inorg. Chem.* **2009**, *48* (22), 10572–10580.

(90) Nakagaki, M.; Nakatani, N.; Sakaki, S. How to understand very weak Cr–Cr double bonds and negative spin populations in trinuclear Cr complexes: theoretical insight. *Phys. Chem. Chem. Phys.* **2019**, *21* (41), 22976–22989.

Chapter 8

General Conclusions and Future Perspectives

In this Thesis we succeeded in the challenging synthesis of polynuclear transition metal compounds, belonging to the family of EMACs and exhibiting magnetic ground states and prevalent ferromagnetic interactions. We were able to prepare new homometallic iron(II)-based EMACs, in spite of the exceedingly elusive behavior of this family of compounds, which proved to be synthetically accessible only in strictly anaerobic and anhydrous conditions. Moreover, two very uncommon MV Fe^{2+}/Fe^{3+} EMACs were isolated and characterized.

Complex $[Fe_4(tpda)_3Cl_2]$ (**1Cl**), the first-reported iron(II)-EMAC based on oligo-*α*-pyridylamido ligands, was widely studied at the beginning of this work, laying the foundation of this Thesis.[20] **1Cl** features two ferromagnetic Fe_2 units, weakly antiferromagnetically coupled with each other at low temperature. It exhibits weak SMM behavior when a small static field is applied. Particularly appealing was the possibility of manipulating its magnetic properties through chemical design.

First, the replacement of axial Cl^- with Br^- ligands in **1Cl** was investigated in order to probe the effect of softer capping ligands. Complex $[Fe_4(tpda)_3Br_2]$ (**1Br**) was prepared following the same synthetic route used for **1Cl**. The solution and solid-state properties of the two derivatives were widely analyzed and compared. Mössbauer spectroscopy showed that both **1Cl** and **1Br** only contain HS iron(II) ions, demonstrating that our working conditions are properly tuned to handle such air- and moisture-sensitive compounds. This is a non-trivial achievement, since iron(II)-based EMAC proved to be very difficult to synthesize in the past, even with strict exclusion of oxygen and water. The magnetic properties of **1Br** were close to those of **1Cl**, with some relevant differences. The most important one is that, although **1Br** shows weaker

ferromagnetic interactions, it displays SMM behavior in zero static field also. A detailed analysis of the magnetic properties and of the low-lying spin levels in **1Cl** and **1Br** was undertaken. Our approach consisted in evaluating the single-ion properties of each Fe center through *ab-initio* calculations (CASSCF-NEVPT2-SO), assuming a local site model. The resulting CF parameters and *g*-values were then held fixed in the treatment of DC magnetic data, which provided the super-exchange coupling constants between spins. This method proved to be extremely effective for analyzing the magnetic behavior of complicated polynuclear compounds, such as the tetrairon(II) EMACs reported in this work. The four non-equivalent HS iron(II) ions turned out to possess large and noncollinear anisotropies, which compete with super-exchange interactions between the Fe centers (ferromagnetic within the Fe1,Fe2 and Fe3,Fe4 pairs and antiferromagnetic between Fe2 and Fe3). This competition leads to a weakly magnetic ground state, which is nevertheless sufficient for **1Cl** and **1Br** to exhibit SMM properties.

Another important observation was that **1Cl** and **1Br** undergo four consecutive quasi-reversible one-electron oxidations in dichloromethane solution. As expected, **1Br** was more difficult to oxidize than its congener, while the one-electron oxidized form of **1Cl** proved to be much more thermodynamically stable towards disproportionation than its bromo analogue. These Fe^{2+}/Fe^{3+} MV EMACs are attractive synthetic targets due to the possible occurrence of double-exchange interactions, which usually strengthen ferromagnetic coupling between ions in different oxidation states. Therefore, we decided to attempt the chemical oxidation of **1Cl** with $FcPF_6$, which afforded two MV systems, namely the one- and two-electron oxidized species $[Fe_2^{II}Fe^{III}(tpda)_3]PF_6$ (**3**) and $[Fe^{II}Fe_2^{III}(tpda)_3Cl]PF_6$ (**3a**, obtained as by-product during the synthesis of **3**). Interestingly, the partial oxidation of **1Cl** causes a structural rearrangement which leads to the extrusion of a $FeCl_2$ or FeCl moiety. For both compounds SC-XRD analysis indicates localized valence states at 115 K. However, the width of the IVCT band in the room-temperature electronic spectrum of **3** suggests that **3** is on the threshold of Robin-Day Class II and Class III classification over the timescale of electronic absorption spectroscopy. Variable-temperature Mössbauer spectroscopy suggests that the most appropriate classification is Robin-Day Class II at 294 K, while it confirms that **3** does not exhibit electron delocalization at lower temperatures (77 and 10 K). The magnetic behavior of **3** was analyzed following a similar approach to that employed for **1Cl** and **1Br** (single-ion parameters evaluated with CASSCF/RASSI-SO *ab-initio* calculations), modelling isotropic and anisotropic exchange interactions between the metals. Again, ferromagnetic interactions turned out to be prevalent in **3**, especially within the Fe^{2+}–Fe^{2+} pair, which features a shorter iron-iron distance (2.73 Å) than in **1Cl**/**1Br** (2.94–2.99 Å) and in complex **6** (2.78 Å).[80] In spite of the

hard-axis anisotropies predicted by *ab-initio* calculations for both Fe^{2+} ions, the competition with super-exchange interactions leads to overall easy-axis anisotropy in complex **3**, a property that was experimentally confirmed by micro-SQUID measurements. The latter technique also revealed an opening of the hysteresis loop below 0.5 K, with a small remanent magnetization. Consistent with this, when **3** was tested for SRM by AC susceptometry zero-field SMM behavior was detected. Hence, both the replacement of Cl^- with Br^- capping ligands *and* the one-electron oxidation of **1Cl** afford similar results in terms of SRM. On the contrary, a further one-electron oxidation of **3** to give **3a** causes the complete loss of SRM and the closure of magnetic hysteresis loop. Since both MV complexes were only obtained as triiron chains, the synthesis of tetrairon MV derivatives of **1Cl** is still an open challenge, and we will work towards this direction in the future.

In order to attempt stabilizing these chain-like structures, a new tridecadentate tripodal ligand based on three covalently linked oligo-*α*-pyridylamine units, $N(CH_2CH_2NH\text{-}py\text{-}NH\text{-}py)_3$ (H_6L), was designed and synthesized. H_6L was prepared via tris-arylation of the tren ligand, employing FHdpa as arylating agent and Cs_2CO_3 as base. Use of the cesium base proved to be essential for the success of the synthesis, in that it prevents the formation of overarylated by-products. The novel tripodal ligand was synthesized with excellent purity and high-yield (65−70%), considering the three consecutive arylations involved. A smart purification method was also developed in order to avoid chromatographic separation, which causes a significant loss of product when polyamines such as H_6L are involved. With its versatile structure, H_6L can potentially host metal ions in tetrahedral, octahedral, and trigonal coordination pockets. Its coordination chemistry was thus tested towards cobalt(II) and iron(II). These preliminary studies led to the isolation of a variety of compounds in crystalline form: $K[CoH_3L]$ (**CoL**), **CoL**·THF, $[Fe_2ClH_3L]$ (**Fe_2L**) and $[Fe_6O_2(\mu_5\text{-}O)H_3L_2]$ (**Fe_6L_2**). The first X-ray diffraction data on the new ligand were provided by **CoL** (obtained from $CoCl_2$, ^{t}BuOK and H_6L), which contains an octahedrally-coordinated Co^{2+} ion. Interestingly, a tetrahedral Co^{2+} complex is formed when the base is not used for ligand deprotonation. In **Fe_2L**, one of the two iron(II) ions occupies the same octahedral coordination pocket as the cobalt(II) ion in **CoL**, while the second one is coordinated by the three terminal N_{py} donors and by one axial Cl^- ligand. This molecular structure directly mimics "half" **1Cl**, and **Fe_2L** is expected to display intramolecular ferromagnetic coupling, an appealing target for future investigation. Finally, **Fe_6L_2** features a $Fe_5O_2(\mu_5\text{-}O)$ core with two short Fe−Fe separations (2.63 Å) and an additional metal center in one of the tren-like coordination pockets. The metal core is entrapped by two molecules of tripodal ligand which form a cage-like shell. The isolation of **Fe_6L_2**, which contains adventitious oxygen atoms, was unexpected and opens the way for further studies, starting from

the investigation of its magnetic properties and its further characterization by Mössbauer spectroscopy and CV. The redox behavior, preliminarily probed by UV-Vis-NIR spectroscopy, suggests that **Fe_6L_2** could be used as a starting material for the preparation of new MV compounds.

In conclusion, the results reported in this Thesis confirm that iron(II)-based EMACs are chemically versatile and magnetically appealing molecules, since they tend to exhibit predominant ferromagnetic interactions and SMM behavior. However, the formation of M−M bonds seems to be an essential prerogative for stabilizing well-isolated ground spin states in this family of compounds. The formation of MV iron-based EMACs is an interesting alternative to achieve better SMM behavior. Certainly, although no new EMACs were obtained so far, the coordination chemistry of H_6L proved to be exceedingly interesting and versatile, paving the way for a manifold of possible future studies.

Acknowledgments

First of all, I want to thank my supervisor Prof. Andrea Cornia, who guided me during these years. I have learned a lot thanks to his knowledge and his patience. This work would not be possible without him. A special thank goes to the Master student Biagio Anderlini, for his massive contribution regarding the work on the tripodal ligand and on the cobalt complexes, and for being an incredibly funny labmate. I would also like to thank all the amazing people, friends, and co-workers of the Department of Chemical and Geological Science. In particular, thank you Mirko for being the best travel mate I could have, and thank you Manuel for being an awesome friend since the first time I stepped my foot into this University.

Many thanks to all the scientists I have collaborated with during these years, in particular: from the University of Modena and Reggio Emilia, Prof. Marco Borsari, Prof. Antonio Ranieri, and graduating student Matteo Caleffi (now PhD student) for the electrochemical characterization, and Prof. Marco Affronte for DC and AC magnetic measurements; Prof. Alessandro Soncini and Dr. Simone Calvello from the University of Melbourne, and Dr. Benjamin Cahier (Max-Planck-Institut für Kohlenforschung), for performing the *ab-initio* calculations; Dr. Tobias Rüffer (Institute of Chemistry, Chemnitz) for his contribution in the determination of some molecular structures by SC-XRD; Prof. Wolfgang Wernsdorfer and PhD student Michael Schulze (Karlsruhe Institute of Technology) for the micro-SQUID measurements. Last, but not least, a very special thanks goes to Prof. John F. Berry and his amazing research group, at the Department of Chemistry of the University of Wisconsin-Madison (USA). They kindly host me in the Berry Group for half a year, always helping me and providing everything I needed, making me feel at home. In addition, I also want to thank Prof. Berry and Daniel J. SantaLucia for performing the Mössbauer characterizations.

My deep gratitude goes to Jeannine and Ed Desautels, for welcoming me with open arms in their house, but more importantly for giving me a new American family. Thank you Jeannine, for all the cups of tea at late hours, and for always correcting my English!

Finally, I would like to thank my family, Mum, Dad, Mattia, and Linda, who always believed in me, encouraging and inspiring me in so many different ways. Thank you so much.

Appendix

1) Synthesis and Solution Studies

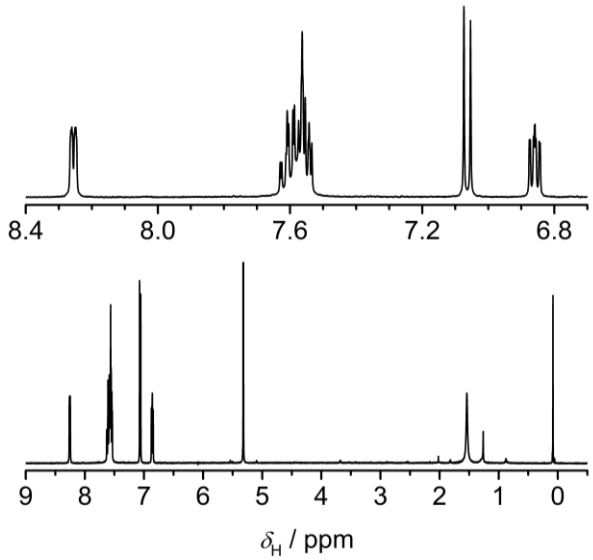

Figure A.1. ^{1}H NMR spectrum of H_2tpda in CD_2Cl_2 (298 K, 400.13 MHz) up to δ_H = 9 ppm (bottom) and for δ_H = 6.7−8.4 ppm (above). Processing parameters (TopSpin 4.0.6[86]): SI = TD, LB = 0.30 Hz. δ_H (ppm) = 0.08 (silicone grease, CH_3, s), 0.9 (H grease, CH_3, m), 1.26 (H grease, CH_2, br s), 1.54 (water, OH, s), 5.32 (residual signal of CD_2Cl_2).

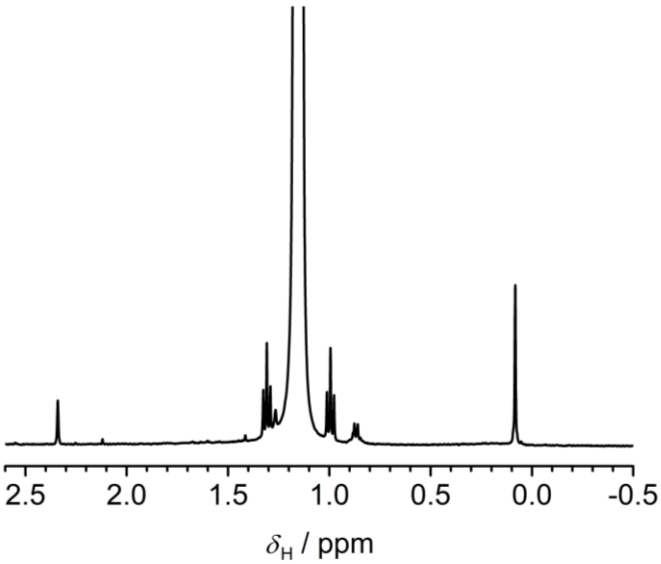

Figure A.2. ^{1}H NMR spectrum of **1Br** in CD_2Cl_2 (298 K, 400.13 MHz) in the 0−2.6 ppm region. Processing parameters (TopSpin 4.0.6[86]): SI = TD, LB = 1.00 Hz. δ_H (ppm) = 0.08 (silicone grease, CH_3, s), 0.9 (H grease, CH_3, m), 1.15 (diethyl ether, CH_3, t, ^3J = 7 Hz), 1.27 (H grease, CH_2, br s), 2.12 (acetone, CH_3, s), 2.34 (toluene, CH_3, s).

2) Single Crystal X-Ray Diffraction

Supplementary Note 1: minority crystal phases. The described synthetic procedure affords minor amounts of other crystal phases, which are easily removed by flotation. These include:

a) small, yellow parallelogram-shaped plates, as-yet unidentified with certainty;

b) (occasionally) yellow elongated plates, identified as a second solvatomorph of **1Br**. Preliminary crystal data at 298(2): **1Br**·0.62CH_2Cl_2·0.38Et_2O, triclinic, $P\bar{1}$, a = 13.8989(8), b = 17.5023(8), c = 23.1212(13) Å, α = 95.9578(17), β = 101.9550(19), γ = 113.2249(16)°, V = 4947.8(5) $Å^3$, Z = 4, $R1$ ($I \geq 2\sigma(I)$) = 6.21%.

Supplementary Note 2: details of structural analysis for 1Br·2.3CH_2Cl_2·Et_2O. Indexing of intense peaks in the diffraction pattern gave a monoclinic P unit cell very similar to that of chloro derivative,[20] with a = 19.6801(16), b = 16.4420(14), c = 18.6092(14) Å, β = 104.979(3)°, V = 5817.0(8) $Å^3$, Z = 4, R_{merge} = 2.4% at 115(2) K. Systematic absences also hinted to the same space group ($P2_1/c$) although many violations were observed. Weak superstructure reflections were indeed detected at half-integer reciprocal-lattice points (h+1/2, k+1/2, l+1/2), with average intensity > 20 times lower than for substructure reflections. The complete diffraction pattern could be indexed using a metrically monoclinic C-centered cell with the same b-axis orientation as the monoclinic P cell, but a fourfold-larger volume (e.g.: **a**′ = 2**c**, **b**′ = 2**b**, **c**′ = –**a**–**c**, or alternative settings with a different choice of supercell vectors in the ac-plane; R_{merge} = 3.4%). Systematic absences however revealed that a c-type glide plane is not present in this supercell, thus restricting possible space groups to $C2$, Cm or $C2/m$. Since these space groups are inconsistent with the known crystal structure of the chloro derivative,[20] we argue that the structure cannot be monoclinic. This conclusion is supported by group-subgroups relations explorable with the program SUBGROUPS at the Bilbao Crystallographic Server (www.cryst.ehu.es). Application of a commensurate modulation with wave-vector q = (1/2, 1/2, 1/2) to the 13 monoclinic space groups affords superstructures that are either triclinic or belong to space groups $C2$, Cm or $C2/m$. In particular, monoclinic space groups compatible with the crystal structure of the chloro derivative (i.e. $P2_1/c$, $P2_1$ and Pc) give triclinic superstructures with doubled unit-cell volume [a = 23.3208(20), b = 24.8162(20), c = 24.8374(20) Å, α = 82.930(3), β = 64.239(3), γ = 64.270(3)°, V = 11623.9(17) $Å^3$, Z = 8, R_{merge} = 2.9%]. Unfortunately, refinement in space-group $P\bar{1}$ proved very difficult due to the four independent and partially disorderd tetrairon(II) molecules in the asymmetric unit and to the extensively disordered lattice solvent. The results suggested that the observed superstructure arises from a commensurate modulation of lattice solvent. On the contrary, refinement on substructure

reflections converged well and was regarded as completely satisfactory for the purposes of the present study. The actual superstructure was therefore not further investigated. A second data collection at 115(2) K was carried out on a crystal from another synthetic batch and afforded a very similar diffraction pattern and an identical structure. *Five* additional prismatic crystals were screened, coming from both syntheses, and afforded the same unit-cell parameters.

Table A.1. Interatomic distances (Å) and angles (deg) for **1Br**·2.3CH_2Cl_2·Et_2O.

Fe1−Fe2	2.9747(12)	Fe1A−Fe2A	2.890(10)
Fe2−Fe3	2.9711(11)	Fe2A−Fe3A	3.026(10)
Fe3−Fe4	2.9551(12)	Fe3A−Fe4A	2.954(11)
Fe1−Br1	2.5314(11)	Fe1A−Br1A	2.525(8)
Fe4−Br2	2.5100(12)	Fe4A−Br2A	2.499(8)
Fe1−N1	2.089(4)	Fe1A−N1	2.096(13)
Fe1−N2	2.067(4)	Fe1A−N2	2.293(12)
Fe1−N3	2.096(4)	Fe1A−N3A	2.04(2)
Fe2−N4	2.108(4)	Fe2A−N4	2.238(7)
Fe2−N5	1.993(4)	Fe2A−N5	2.176(7)
Fe2−N6	2.011(4)	Fe2A−N6A	2.05(2)
Fe2−N7	2.175(4)	Fe2A−N9A	2.198(19)
Fe2−N8	2.492(4)	Fe3A−N8	2.103(8)
Fe3−N8	2.500(4)	Fe3A−N9A	2.77(2)
Fe3−N9	2.234(4)	Fe3A−N10	1.946(9)
Fe3−N10	2.042(4)	Fe3A−N11	1.963(9)
Fe3−N11	2.036(4)	Fe3A−N12A	2.03(2)
Fe3−N12	2.087(4)	Fe4A−N13	2.065(17)
Fe4−N13	2.088(4)	Fe4A−N14	2.010(16)
Fe4−N14	2.088(4)	Fe4A−N15A	2.10(3)
Fe4−N15	2.071(5)		
Br1−Fe1−Fe2	177.01(6)	Br1A−Fe1A−Fe2A	176.2(6)
Fe1−Fe2−Fe3	172.08(4)	Fe1A−Fe2A−Fe3A	168.5(4)
Fe2−Fe3−Fe4	167.67(6)	Fe2A−Fe3A−Fe4A	169.9(5)
Fe3−Fe4−Br2	178.62(8)	Fe3A−Fe4A−Br2A	176.1(7)
Br1−Fe1−N1	95.07(11)	Br1A−Fe1A−N1	94.8(5)
Br1−Fe1−N2	97.96(11)	Br1A−Fe1A−N2	97.9(4)
Br1−Fe1−N3	98.44(13)	Br1A−Fe1A−N3A	94.7(7)
N13−Fe4−Br2	98.45(12)	N13−Fe4A−Br2A	97.4(5)
N14−Fe4−Br2	97.84(12)	N14−Fe4A−Br2A	94.5(5)
N15−Fe4−Br2	96.91(13)	N15A−Fe4A−Br2A	99.1(8)
N1−Fe1−N2	121.12(15)	N1−Fe1A−N2	111.0(5)
N1−Fe1−N3	110.87(16)	N1−Fe1A−N3A	125.7(10)
N2−Fe1−N3	123.32(16)	N2−Fe1A−N3A	120.3(11)
N13−Fe4−N14	112.63(17)	N13−Fe4A−N14	117.1(8)
N13−Fe4−N15	116.27(18)	N13−Fe4A−N15A	123.7(11)
N14−Fe4−N15	125.75(19)	N14−Fe4A−N15A	114.8(11)

3) Mössbauer Spectroscopy

Supplementary Note 3: alternative fits to the 77 K dataset.

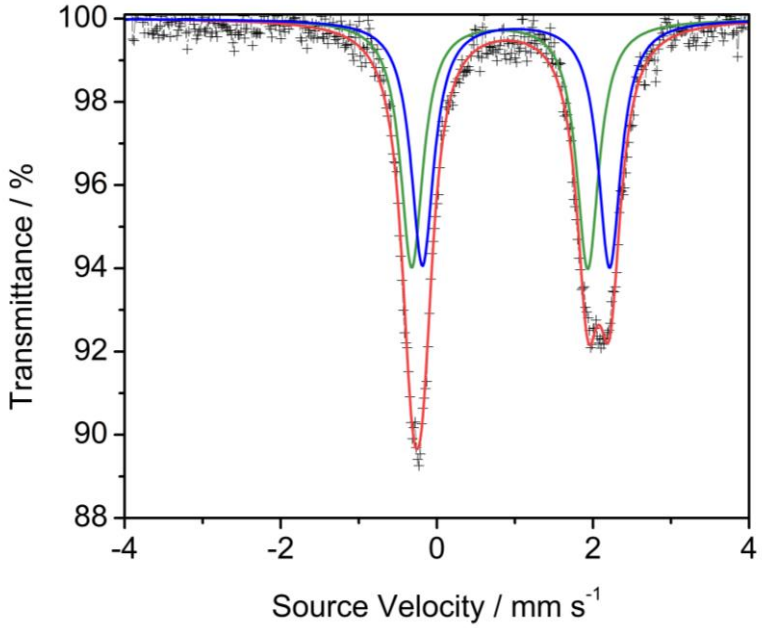

Figure A.3. Alternative fit to the 77 K dataset for **1Br**. Same color code as in Fig. 4.13. Best-fit parameters: δ_1 = 0.81 mm/s, ΔE_{Q1} = 2.25 mm/s, $FWHM_1$ = 0.35 mm/s, δ_2 = 1.01 mm/s, ΔE_{Q2} = 2.40 mm/s, and $FWHM_2$ = 0.35 mm/s; reduced χ^2 = 0.577.

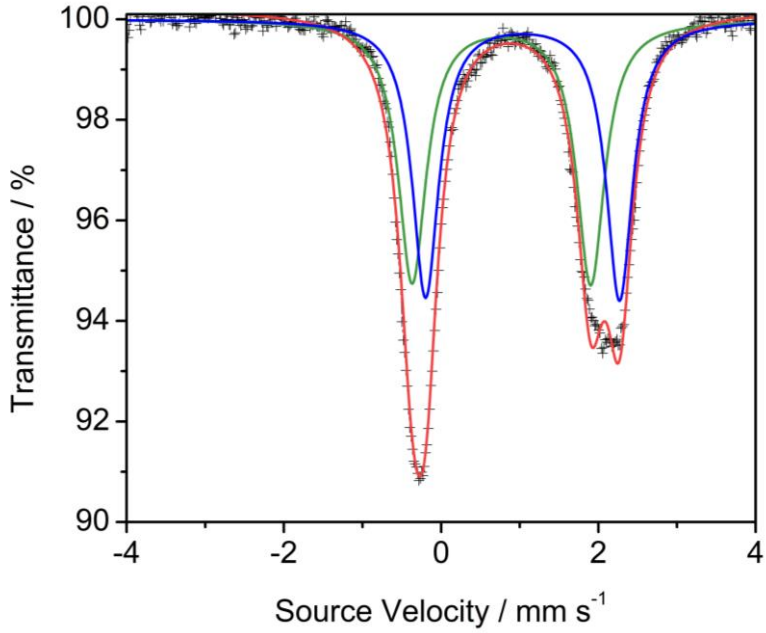

Figure A.4. Alternative fit to the 77 K dataset for **1Cl**. Same color code as in Fig. 4.13. Best-fit parameters: δ_1 = 0.77 mm/s, ΔE_{Q1} = 2.27 mm/s, $FWHM_1$ = 0.43 mm/s, δ_2 = 1.04 mm/s, ΔE_{Q2} = 2.47 mm/s, and $FWHM_2$ = 0.41 mm/s; reduced χ^2 = 1.697.

4) Ab-initio Calculations

Table A.2. Lowest lying states for the four iron(II) ions in **1Cl** as determined by CASSCF-NEVPT2-SO calculations.

Fe1

Eigenvalues:	cm^{-1}	eV	Boltzmann population at T = 300.000 K
0:	0.00	0.0000	1.90e-01
1:	0.75	0.0001	1.90e-01
2:	27.33	0.0034	1.67e-01
3:	39.31	0.0049	1.58e-01
4:	48.48	0.0060	1.51e-01
5:	350.24	0.0434	3.55e-02
6:	360.14	0.0447	3.38e-02
7:	395.35	0.0490	2.86e-02
8:	437.06	0.0542	2.34e-02
9:	439.83	0.0545	2.31e-02

Fe2

Eigenvalues:	cm^{-1}	eV	Boltzmann population at T = 300.000 K
0:	0.00	0.0000	2.20e-01
1:	4.88	0.0006	2.15e-01
2:	16.55	0.0021	2.03e-01
3:	39.57	0.0049	1.82e-01
4:	40.74	0.0051	1.81e-01

Fe3

Eigenvalues:	cm^{-1}	eV	Boltzmann population at T = 300.000 K
0:	0.00	0.0000	2.15e-01
1:	6.42	0.0008	2.09e-01
2:	9.39	0.0012	2.06e-01
3:	31.35	0.0039	1.85e-01
4:	31.44	0.0039	1.85e-01

Fe4

Eigenvalues:	cm^{-1}	eV	Boltzmann population at T = 300.000 K
0:	0.00	0.0000	1.85e-01
1:	0.30	0.0000	1.84e-01
2:	49.00	0.0061	1.46e-01
3:	55.55	0.0069	1.41e-01
4:	81.05	0.0100	1.25e-01
5:	239.82	0.0297	5.84e-02
6:	260.42	0.0323	5.29e-02
7:	303.87	0.0377	4.30e-02
8:	362.40	0.0449	3.24e-02
9:	364.00	0.0451	3.22e-02

Table A.3. Lowest lying states for the four iron(II) ions in **1Br** as determined by CASSCF- NEVPT2-SO calculations.

Fe1

Eigenvalues:	cm^{-1}	eV	Boltzmann population at T = 300.000 K
0:	0.00	0.0000	1.93e-01
1:	0.98	0.0001	1.92e-01
2:	28.63	0.0036	1.68e-01
3:	42.18	0.0052	1.58e-01
4:	51.85	0.0064	1.51e-01
5:	359.79	0.0446	3.44e-02
6:	371.09	0.0460	3.26e-02
7:	408.02	0.0506	2.73e-02
8:	454.42	0.0563	2.19e-02
9:	457.17	0.0567	2.16e-02

Fe2

Eigenvalues:	cm^{-1}	eV	Boltzmann population at T = 300.000 K
0:	0.00	0.0000	2.20e-01
1:	4.70	0.0006	2.15e-01
2:	17.00	0.0021	2.03e-01
3:	39.72	0.0049	1.82e-01
4:	41.02	0.0051	1.81e-01

Fe3

Eigenvalues:	cm^{-1}	eV	Boltzmann population at T = 300.000 K
0:	0.00	0.0000	2.15e-01
1:	6.26	0.0008	2.09e-01
2:	9.30	0.0012	2.06e-01
3:	30.84	0.0038	1.85e-01
4:	30.93	0.0038	1.85e-01

Fe4

Eigenvalues:	cm^{-1}	eV	Boltzmann population at T = 300.000 K
0:	0.00	0.0000	1.93e-01
1:	0.45	0.0001	1.92e-01
2:	44.44	0.0055	1.56e-01
3:	54.25	0.0067	1.49e-01
4:	73.75	0.0091	1.35e-01
5:	298.72	0.0370	4.60e-02
6:	316.67	0.0393	4.22e-02
7:	357.13	0.0443	3.48e-02
8:	416.22	0.0516	2.62e-02
9:	418.09	0.0518	2.60e-02

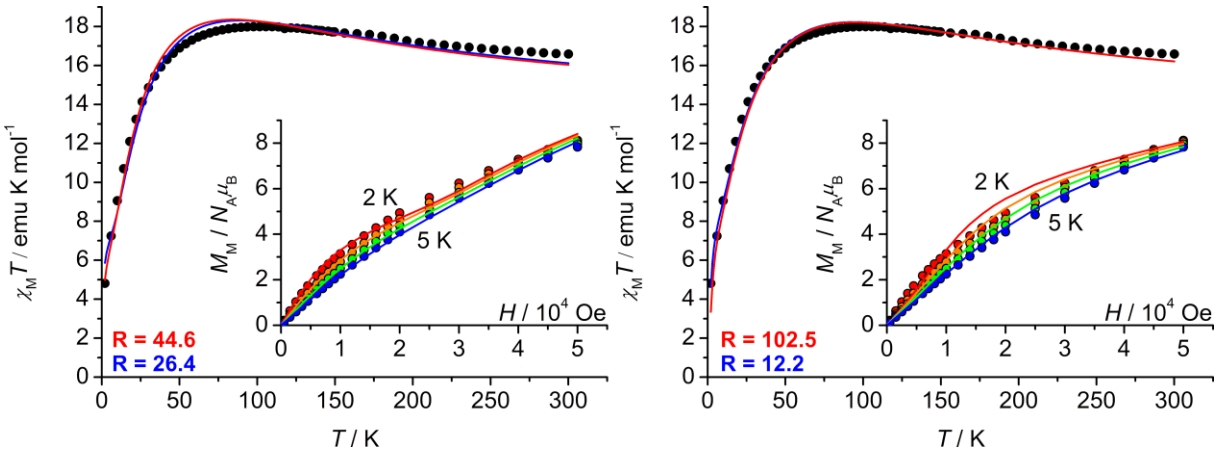

Figure A.5. Best-fit curves to the experimental data in Fig. 4.14(b) based on model m**1Cl**B (left) and model m**1Cl**C (right) (see Table A.4). The blue lines in the main panels are the best-fit curves from the treatment of $\chi_M T$ vs T data only, based on model m**1Cl**B' (left) and model m**1Cl**C' (right) (see Table A.6).

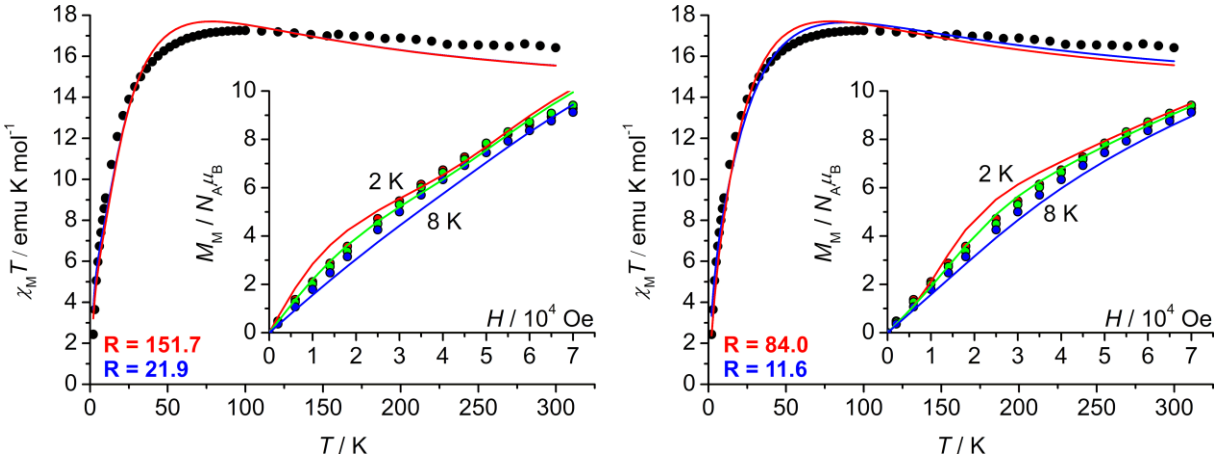

Figure A.6. Best-fit curves to the experimental data in Fig. 4.14(a) based on model m**1Br**B (left) and model m**1Br**C (right) (see Table A.5). The blue lines in the main panels are the best-fit curves from the treatment of $\chi_M T$ vs T data only, based on model m**1Br**B' (left) and model m**1Br**C' (right) (see Table A.6).

Table A.4. Best-fit parameters from the simultaneous treatment of $\chi_M T$ vs T and M_M vs H data for **1Cl**·2.6CH_2Cl_2·0.84Et_2O.[a]

Model	J_{12}	J_{34}	J_{23}	$J' = J_{13} = J_{24}$	TIP	R
m**1Cl**A	−14.0(2)		4.404(17)	/	$8.0(2)\cdot10^{-3}$	322.4
m**1Cl**B	−23.74(14)		−3.31(3)	3.863(19)	/	44.6
m**1Cl**C	−26.11(15)		9.52(10)	−2.19(4)	/	102.5
m**1Cl**D	−51.4(10)	−9.43(5)	4.319(7)	/	$1.9(15)\cdot10^{-4}$	19.1
m**1Cl**E	−4.87(13)	−35.1(10)	4.48(3)	/	$5.7(2)\cdot10^{-3}$	325.8
m**1Cl**F	−51.6(4)	−10.53(10)	−3.29(4)	3.86(2)	/	6.5
m**1Cl**G	−52.0(3)	−9.76(10)	4.56(6)	−0.11(3)	/	18.6
m**1Cl**H	−7.32(15)	−55.7(6)	−2.44(4)	3.06(3)	/	22.0
m**1Cl**I	−13.87(15)	−46.4(4)	8.54(7)	−1.76(3)	/	45.3

[a] J values are in cm^{-1}, with $J > 0$ ($J < 0$) for antiferromagnetic (ferromagnetic) coupling; TIP is in emu mol^{-1}.

Table A.5. Best-fit parameters from the simultaneous treatment of $\chi_M T$ vs T and M_M vs H data for **1Br**·2.3CH_2Cl_2·Et_2O.[a]

Model	J_{12}	J_{34}	J_{23}	$J' = J_{13} = J_{24}$	TIP	R
m**1Br**A	−9.31(16)		4.11(3)	/	$8.9(3)\cdot10^{-3}$	54.2
m**1Br**B	−18.7(4)		−4.48(15)	4.47(8)	/	151.7
m**1Br**C	−18.7(5)		7.5(2)	−1.47(10)	/	84.0
m**1Br**D	−26.8(14)	−4.61(15)	4.19(3)	/	$4.7(4)\cdot10^{-3}$	25.4
m**1Br**E	−3.61(3)	−38.6(11)	4.292(13)	/	$2.5(2)\cdot10^{-3}$	4.9
m**1Br**F	−54.6(10)	−2.2(3)	−1.7(2)	2.66(12)	/	122.3
m**1Br**G	−47.2(16)	−5.2(3)	4.59(16)	−0.14(7)	/	33.0
m**1Br**H	0.81(17)	−63.1(17)	−1.43(7)	2.17(4)	/	28.1
m**1Br**I	−4.25(14)	−52.4(6)	4.76(10)	−0.18(4)	/	6.8

[a] J values are in cm^{-1}, with $J > 0$ ($J < 0$) for antiferromagnetic (ferromagnetic) coupling; TIP is in emu mol^{-1}.

Table A.6. Best-fit parameters from the treatment of $\chi_M T$ vs T data for **1Cl**·2.6CH_2Cl_2·0.84Et_2O and **1Br**·2.3CH_2Cl_2·Et_2O.[a]

Model	$J_{12} = J_{34}$	J_{23}	$J' = J_{13} = J_{24}$	TIP	R
m**1Cl**A’	−16.6(3)	4.33(3)	/	$5.7(2)\cdot10^{-3}$	31.4
m**1Cl**B’	−24.91(19)	−4.93(17)	4.79(9)	/	26.4
m**1Cl**C’	−26.16(15)	10.20(12)	−2.56(5)	/	12.2
m**1Br**A’	−9.4(2)	3.70(5)	/	$8.3(4)\cdot10^{-3}$	8.3
m**1Br**B’	−18.8(8)	−5.2(5)	4.8(3)	/	21.9
m**1Br**C’	−21.2(7)	10.9(6)	−2.8(2)	/	11.6

[a] J values are in cm^{-1}, with $J > 0$ ($J < 0$) for antiferromagnetic (ferromagnetic) coupling; TIP is in emu mol^{-1}.

Bibliography

(1) Reinsel, D.; Gantz, J.; Rydning, J. The Digitization of the World. *An IDC White Pap.* **2018**, *#US4441331*, 1–28.

(2) Žutić, I.; Fabian, J.; Das Sarma, S. Spintronics: Fundamentals and Applications. *Rev. Mod. Phys.* **2004**, *76* (2), 323–410. https://doi.org/10.1103/RevModPhys.76.323.

(3) Gatteschi, D.; Sessoli, R.; Villain, J. *Molecular Nanomagnets*; Oxford University Press: New York, USA, 2006. https://doi.org/10.1093/acprof:oso/9780198567530.001.0001.

(4) *Molecular Nanomagnets and Related Phenomena - Structure and Bonding Series*; Gao, S., Ed.; Springer-Verlag: Berlin Heidelberg, Germany, 2015; Vol. 164. https://doi.org/10.1007/978-3-662-45723-8.

(5) Caneschi, A.; Gatteschi, D.; Sangregorio, C.; Sessoli, R.; Sorace, L.; Cornia, A.; Novak, M. A.; Paulsen, C.; Wernsdorfer, W. The Molecular Approach to Nanoscale Magnetism. *J. Magn. Magn. Mater.* **1999**, *200* (1–3), 182–201. https://doi.org/10.1016/S0304-8853(99)00408-4.

(6) Sessoli, R.; Gatteschi, D.; Caneschi, A.; Novak, M. A. Magnetic Bistability in a Metal-Ion Cluster. *Nature* **1993**, *365* (6442), 141–143. https://doi.org/10.1038/365141a0.

(7) Gatteschi, D.; Sessoli, R. Quantum Tunneling of Magnetization and Related Phenomena in Molecular Materials. *Angew. Chem., Int. Ed. Engl.* **2003**, *42* (3), 268–297. https://doi.org/10.1002/anie.200390099.

(8) Thomas, L.; Lionti, F.; Ballou, R.; Gatteschi, D.; Sessoli, R.; Barbara, B. Macroscopic Quantum Tunnelling of Magnetization in a Single Crystal of Nanomagnets. *Nature* **1996**, *383* (6596), 145–147. https://doi.org/10.1038/383145a0.

(9) Friedman, J. R.; Sarachik, M. P.; Tejada, J.; Ziolo, R. Macroscopic Measurement of Resonant Magnetization Tunneling in High-Spin Molecules. *Phys. Rev. Lett.* **1996**, *76*, 3830–3833. https://doi.org/https://doi.org/10.1103/PhysRevLett.76.3830.

(10) Moreno-Pineda, E.; Godfrin, C.; Balestro, F.; Wernsdorfer, W.; Ruben, M. Molecular Spin Qudits for Quantum Algorithms. *Chem. Soc. Rev.* **2018**, *47* (2), 501–513. https://doi.org/10.1039/C5CS00933B.

(11) Gaita-Ariño, A.; Luis, F.; Hill, S.; Coronado, E. Molecular Spins for Quantum Computation. *Nat. Chem.* **2019**, *11* (4), 301–309. https://doi.org/10.1038/s41557-019-0232-y.

(12) Chappert, C.; Fert, A.; Van Dau, F. N. The Emergence of Spin Electronics in Data Storage. In *Nanoscience and Technology*; Co-Published with Macmillan Publishers Ltd: London, UK, 2009; Vol. 6, pp 147–157. https://doi.org/10.1142/9789814287005_0015.

(13) Sanvito, S. Molecular Spintronics. *Chem. Soc. Rev.* **2011**, *40* (6), 3336–3355. https://doi.org/10.1039/c1cs15047b.

(14) Jiang, S.-D.; Goß, K.; Cervetti, C.; Bogani, L. An Introduction to Molecular Spintronics. *Sci. China: Chem.* **2012**, *55* (6), 867–882. https://doi.org/10.1007/s11426-012-4628-4.

(15) Cornia, A.; Seneor, P. Spintronics: The Molecular Way. *Nat. Mater.* **2017**, *16* (5), 505–506. https://doi.org/10.1038/nmat4900.

(16) Bogani, L.; Wernsdorfer, W. Molecular Spintronics Using Single-Molecule Magnets. In *Nanoscience and Technology*; Co-Published with Macmillan Publishers Ltd: London, UK, 2009; Vol. 7, pp 194–201. https://doi.org/10.1142/9789814287005_0020.

(17) Katoh, K.; Komeda, T.; Yamashita, M. The Frontier of Molecular Spintronics Based on Multiple-Decker Phthalocyaninato Tb^{III} Single-Molecule Magnets. *Chem. Rec.* **2016**, *16* (2), 987–1016. https://doi.org/10.1002/tcr.201500290.

(18) Cornia, A.; Mannini, M. Single-Molecule Magnets on Surfaces. In *Molecular Nanomagnets and Related Phenomena - Structure and Bonding Series*; Gao, S., Ed.; Springer-Verlag: Berlin Heidelberg, Germany, 2015; Vol. 164, pp 293–330. https://doi.org/10.1007/430_2014_150.

(19) Malavolti, L.; Lanzilotto, V.; Ninova, S.; Poggini, L.; Cimatti, I.; Cortigiani, B.; Margheriti, L.; Chiappe, D.; Otero, E.; Sainctavit, P.; Totti, F.; Cornia, A.; Mannini, M.; Sessoli, R. Magnetic Bistability in a Submonolayer of Sublimated Fe_4 Single-Molecule Magnets. *Nano Lett.* **2015**, *15* (1), 535–541. https://doi.org/10.1021/nl503925h.

(20) Nicolini, A.; Galavotti, R.; Barra, A.-L.; Borsari, M.; Caleffi, M.; Luo, G.; Novitchi, G.; Park, K.; Ranieri, A.; Rigamonti, L.; Roncaglia, F.; Train, C.; Cornia, A. Filling the Gap

in Extended Metal Atom Chains: Ferromagnetic Interactions in a Tetrairon(II) String Supported by Oligo-*α*-Pyridylamido Ligands. *Inorg. Chem.* **2018**, *57* (9), 5438–5448. https://doi.org/10.1021/acs.inorgchem.8b00405.

(21) Cornia, A.; Barra, A.-L.; Bulicanu, V.; Clérac, R.; Cortijo, M.; Hillard, E. A.; Galavotti, R.; Lunghi, A.; Nicolini, A.; Rouzières, M.; Sorace, L.; Totti, F. The Origin of Magnetic Anisotropy and Single-Molecule Magnet Behavior in Chromium(II)-Based Extended Metal Atom Chains. *Inorg. Chem.* **2020**, *59* (3), 1763–1777. https://doi.org/10.1021/acs.inorgchem.9b02994.

(22) Lis, T. Preparation, Structure, and Magnetic Properties of a Dodecanuclear Mixed-Valence Manganese Carboxylate. *Acta Crystallogr., Sect. B: Struct. Sci., Cryst. Eng. Mater.* **1980**, *36* (9), 2042–2046. https://doi.org/10.1107/S0567740880007893.

(23) Caneschi, A.; Gatteschi, D.; Sessoli, R.; Barra, A.-L.; Brunel, L. C.; Guillot, M. Alternating Current Susceptibility, High Field Magnetization, and Millimeter Band EPR Evidence for a Ground $S = 10$ State in $[Mn_{12}O_{12}(CH_3COO)_{16}(H_2O)_4]\cdot 2CH_3COOH\cdot 4H_2O$. *J. Am. Chem. Soc.* **1991**, *113* (15), 5873–5874. https://doi.org/10.1021/ja00015a057.

(24) Sessoli, R.; Tsai, H.-L.; Schake, A. R.; Wang, S.; Vincent, J. B.; Folting, K.; Gatteschi, D.; Christou, G.; Hendrickson, D. N. High-Spin Molecules: $[Mn_{12}O_{12}(O_2CR)_{16}(H_2O)_4]$. *J. Am. Chem. Soc.* **1993**, *115* (5), 1804–1816. https://doi.org/10.1021/ja00058a027.

(25) Coronado, E. Molecular Magnetism: From Chemical Design to Spin Control in Molecules, Materials and Devices. *Nat. Rev. Mater.* **2020**, *5* (2), 87–104. https://doi.org/10.1038/s41578-019-0146-8.

(26) Kahn, O. *Molecular Magnetism*; VCH: New York, USA, 1993.

(27) Layfield, R. A. Organometallic Single-Molecule Magnets. *Organometallics* **2014**, *33* (5), 1084–1099. https://doi.org/10.1021/om401107f.

(28) Gómez-Coca, S.; Aravena, D.; Morales, R.; Ruiz, E. Large Magnetic Anisotropy in Mononuclear Metal Complexes. *Coord. Chem. Rev.* **2015**, *289–290*, 379–392. https://doi.org/10.1016/j.ccr.2015.01.021.

(29) Guo, F.-S.; Day, B. M.; Chen, Y.-C.; Tong, M.-L.; Mansikkamäki, A.; Layfield, R. A. A Dysprosium Metallocene Single-Molecule Magnet Functioning at the Axial Limit. *Angew. Chemie Int. Ed.* **2017**, *56* (38), 11445–11449. https://doi.org/10.1002/anie.201705426.

(30) Guo, F.-S.; Day, B. M.; Chen, Y.-C.; Tong, M.-L.; Mansikkamäki, A.; Layfield, R. A. Magnetic Hysteresis up to 80 Kelvin in a Dysprosium Metallocene Single-Molecule Magnet. *Science* **2018**, *362* (6421), 1400–1403. https://doi.org/10.1126/science.aav0652.

(31) Goodwin, C. A. P.; Ortu, F.; Reta, D.; Chilton, N. F.; Mills, D. P. Molecular Magnetic Hysteresis at 60 Kelvin in Dysprosocenium. *Nature* **2017**, *548* (7668), 439–442. https://doi.org/10.1038/nature23447.

(32) *Lanthanides and Actinides in Molecular Magnetism*; Layfield, R. A., Murugesu, M., Eds.; Wiley-VCH Verlag GmbH & Co. KGaA: Weinheim, Germany, 2015. https://doi.org/10.1002/9783527673476.

(33) Hernández Sánchez, R.; Betley, T. A. Meta-Atom Behavior in Clusters Revealing Large Spin Ground States. *J. Am. Chem. Soc.* **2015**, *137* (43), 13949–13956. https://doi.org/10.1021/jacs.5b08962.

(34) Miller, D. L.; Siedschlag, R. B.; Clouston, L. J.; Young, V. G.; Chen, Y.-S.; Bill, E.; Gagliardi, L.; Lu, C. C. Redox Pairs of Diiron and Iron–Cobalt Complexes with High-Spin Ground States. *Inorg. Chem.* **2016**, *55* (19), 9725–9735. https://doi.org/10.1021/acs.inorgchem.6b01487.

(35) Kramers, H. A. Théorie Générale de La Rotation Paramagnétique Dans Les Cristaux. *Proc. − Acad. Sci. Amsterdam* **1930**, *33*, 959–972.

(36) *Molecular Magnetism: From Molecular Assemblies to the Devices*; Coronado, E., Delhaès, P., Gatteschi, D., Miller, J. S., Eds.; Springer Netherlands: Dordrecht, Netherlands, 1996. https://doi.org/10.1007/978-94-017-2319-0.

(37) Slater, J. C. *Quantum Theory of Matter*; Mcgraw-Hill: New York, USA, 1968.

(38) *Mixed-Valence Compounds*; Brown, D. B., Ed.; Springer Netherlands: Dordrecht, Netherlands, 1980. https://doi.org/10.1007/978-94-009-9076-0.

(39) Zener, C. Interaction between the *d*-Shells in the Transition Metals. II. Ferromagnetic Compounds of Manganese with Perovskite Structure. *Phys. Rev.* **1951**, *82* (3), 403–405. https://doi.org/10.1103/PhysRev.82.403.

(40) Gaudette, A. I.; Jeon, I.-R.; Anderson, J. S.; Grandjean, F.; Long, G. J.; Harris, T. D. Electron Hopping through Double-Exchange Coupling in a Mixed-Valence Diiminobenzoquinone-Bridged Fe_2 Complex. *J. Am. Chem. Soc.* **2015**, *137* (39),

12617–12626. https://doi.org/10.1021/jacs.5b07251.

(41) Atanasov, M.; Aravena, D.; Suturina, E.; Bill, E.; Maganas, D.; Neese, F. First Principles Approach to the Electronic Structure, Magnetic Anisotropy and Spin Relaxation in Mononuclear 3d-Transition Metal Single Molecule Magnets. *Coord. Chem. Rev.* **2015**, *289–290*, 177–214. https://doi.org/10.1016/j.ccr.2014.10.015.

(42) Gómez-Coca, S.; Urtizberea, A.; Cremades, E.; Alonso, P. J.; Camón, A.; Ruiz, E.; Luis, F. Origin of Slow Magnetic Relaxation in Kramers Ions with Non-Uniaxial Anisotropy. *Nat. Commun.* **2014**, *5* (1), 4300. https://doi.org/10.1038/ncomms5300.

(43) Feng, M.; Tong, M.-L. Single Ion Magnets from 3d to 5f: Developments and Strategies. *Chem. – Eur. J.* **2018**, *24* (30), 7574–7594. https://doi.org/10.1002/chem.201705761.

(44) Gatteschi, D.; Barra, A.-L.; Caneschi, A.; Cornia, A.; Sessoli, R.; Sorace, L. EPR of Molecular Nanomagnets. *Coord. Chem. Rev.* **2006**, *250* (11–12), 1514–1529. https://doi.org/10.1016/j.ccr.2006.02.006.

(45) Barra, A.-L.; Caneschi, A.; Gatteschi, D.; Sessoli, R. Very High Field EPR Study of a Molecular Nanomagnet. *J. Magn. Magn. Mater.* **1998**, *177–181*, 709–710. https://doi.org/10.1016/S0304-8853(97)00716-6.

(46) Caciuffo, R.; Amoretti, G.; Murani, A.; Sessoli, R.; Caneschi, A.; Gatteschi, D. Neutron Spectroscopy for the Magnetic Anisotropy of Molecular Clusters. *Phys. Rev. Lett.* **1998**, *81* (21), 4744–4747. https://doi.org/10.1103/PhysRevLett.81.4744.

(47) Atanasov, M.; Ganyushin, D.; Sivalingam, K.; Neese, F. A Modern First-Principles View on Ligand Field Theory Through the Eyes of Correlated Multireference Wavefunctions. In *Molecular Electronic Structures of Transition Metal Complexes II - Structure and Bonding Series*; Mingos, D. M. P., Day, P., Dahl, J. P., Eds.; Springer Berlin Heidelberg: Berlin, Heidelberg, Germany, 2011; Vol. 143, pp 149–220. https://doi.org/10.1007/430_2011_57

(48) Lang, L.; Atanasov, M.; Neese, F. Improvement of Ab Initio Ligand Field Theory by Means of Multistate Perturbation Theory. *J. Phys. Chem. A* **2020**, *124* (5), 1025–1037. https://doi.org/10.1021/acs.jpca.9b11227.

(49) Bencini, A.; Ciofini, I.; Uytterhoeven, M. G. Angular Overlap Calculations of the Spin Hamiltonian Parameters of Transition Metal Ions in Low Symmetry Environments. High Spin Iron(II), Iron(III) and Manganese(III). *Inorganica Chim. Acta* **1998**, *274* (1), 90–101. https://doi.org/10.1016/S0020-1693(97)05985-9.

(50) Freedman, D. E.; Harman, W. H.; Harris, T. D.; Long, G. J.; Chang, C. J.; Long, J. R. Slow Magnetic Relaxation in a High-Spin Iron(II) Complex. *J. Am. Chem. Soc.* **2010**, *132* (4), 1224–1225. https://doi.org/10.1021/ja909560d.

(51) Harman, W. H.; Harris, T. D.; Freedman, D. E.; Fong, H.; Chang, A.; Rinehart, J. D.; Ozarowski, A.; Sougrati, M. T.; Grandjean, F.; Long, G. J.; Long, J. R.; Chang, C. J. Slow Magnetic Relaxation in a Family of Trigonal Pyramidal Iron(II) Pyrrolide Complexes. *J. Am. Chem. Soc.* **2010**, *132* (51), 18115–18126. https://doi.org/10.1021/ja105291x.

(52) Cornia, A.; Rigamonti, L.; Boccedi, S.; Clérac, R.; Rouzières, M.; Sorace, L. Magnetic Blocking in Extended Metal Atom Chains: A Pentachromium(II) Complex Behaving as a Single-Molecule Magnet. *Chem. Commun.* **2014**, *50* (96), 15191–15194. https://doi.org/10.1039/c4cc06693f.

(53) Novak, M. A.; Sessoli, R. AC Susceptibility Relaxation Studies on a Manganese Organic Cluster Compound: $Mn_{12}Ac$. In *Quantum Tunneling of Magnetization — QTM '94. NATO ASI Series (Series E: Applied Sciences)*; Gunther, L., Barbara, B., Eds.; Springer Netherlands: Dordrecht, Netherlands, 1995; Vol. 301, pp 171–188. https://doi.org/10.1007/978-94-011-0403-6_10.

(54) Berry, J. F. Metal–Metal Bonds in Chains of Three or More Metal Atoms: From Homometallic to Heterometallic Chains. In *Structure and Bonding*; Parkin, G., Ed.; Springer Berlin Heidelberg: Berlin, Heidelberg, Germany, 2010; Vol. 136, pp 1–28. https://doi.org/10.1007/978-3-642-05243-9_1.

(55) Berry, J. F. Extended Metal Atom Chains. In *Multiple Bonds Between Metal Atoms*; Cotton, F. A., Murillo, C. A., Walton, R. A., Eds.; Springer-Verlag: Boston, USA, 2005; pp 669–706. https://doi.org/10.1007/0-387-25829-9_15.

(56) Hua, S.-A.; Cheng, M.-C.; Chen, C.-h.; Peng, S.-M. From Homonuclear Metal String Complexes to Heteronuclear Metal String Complexes. *Eur. J. Inorg. Chem.* **2015**, *2015* (15), 2510–2523. https://doi.org/10.1002/ejic.201403237.

(57) Hua, S.-A.; Tsai, Y.-C.; Peng, S.-M. A Journey of Metal-Metal Bonding beyond Cotton's Quadruple Bonds. *J. Chinese Chem. Soc.* **2014**, *61* (1), 9–26. https://doi.org/10.1002/jccs.201300417.

(58) Chipman, J. A.; Berry, J. F. Paramagnetic Metal-Metal Bonded Heterometallic Complexes. *Chem. Rev.* **2020**, *120*, 2409–2447.

https://doi.org/10.1021/acs.chemrev.9b00540.

(59) Liu, I. P.-C.; Wang, W.-Z.; Peng, S.-M. New Generation of Metal String Complexes: Strengthening Metal–Metal Interaction *via* Naphthyridyl Group Modulated Oligo-α-Pyridylamido Ligands. *Chem. Commun.* **2009**, No. 29, 4323–4331. https://doi.org/10.1039/b904719k.

(60) Yeh, C.-Y.; Wang, C.-C.; Chen, C.-h.; Peng, S.-M. Molecular Metal Wires Built from a Linear Metal Atom Chain Supported by Oligopyridylamido Ligands. In *Redox Systems Under Nano-Space Control*; Hirao, T., Ed.; Springer-Verlag: Berlin Heidelberg, Germany, 2006; pp 85–117. https://doi.org/10.1007/3-540-29580-1_5.

(61) Chen, P.-J.; Sigrist, M.; Horng, E.-C.; Lin, G.-M.; Lee, G.-H.; Chen, C.-h.; Peng, S.-M. A Ligand Design with a Modified Naphthyridylamide for Achieving the Longest EMACs: The 1st Single-Molecule Conductance of an Undeca-Nickel Metal String. *Chem. Commun.* **2017**, *53* (34), 4673–4676. https://doi.org/10.1039/C7CC01831B.

(62) Majumdar, M.; Bera, J. K. Transition-Metal-Based Linear Chain Compounds. In *Macromolecules Containing Metal and Metal-like Elements, Volume 9: Supramolecular and Self-Assembled Metal-Containing Materials*; Abd-El Aziz, A. S., Carraher, C. E., Pittman, C. U., Zeldin, M., Eds.; John Wiley & Sons, Inc.: Hoboken, USA, 2009; pp 181–253.

(63) Tanaka, Y.; Kiguchi, M.; Akita, M. Inorganic and Organometallic Molecular Wires for Single-Molecule Devices. *Chem. – Eur. J.* **2017**, *23* (20), 4741–4749. https://doi.org/10.1002/chem.201604812.

(64) Ting, T.-C.; Hsu, L.-Y.; Huang, M.-J.; Horng, E.-C.; Lu, H.-C.; Hsu, C.-H.; Jiang, C.-H.; Jin, B.-Y.; Peng, S.-M.; Chen, C.-h. Energy-Level Alignment for Single-Molecule Conductance of Extended Metal-Atom Chains. *Angew. Chemie Int. Ed.* **2015**, *54* (52), 15734–15738. https://doi.org/10.1002/anie.201508199.

(65) Georgiev, V. P.; Mohan, P. J.; DeBrincat, D.; McGrady, J. E. Low-Symmetry Distortions in Extended Metal Atom Chains (EMACs): Origins and Consequences for Electron Transport. *Coord. Chem. Rev.* **2013**, *257* (1), 290–298. https://doi.org/10.1016/j.ccr.2012.05.025.

(66) Christian, J. H.; Brogden, D. W.; Bindra, J. K.; Kinyon, J. S.; van Tol, J.; Wang, J.; Berry, J. F.; Dalal, N. S. Enhancing the Magnetic Anisotropy of Linear Cr(II) Chain Compounds Using Heavy Metal Substitutions. *Inorg. Chem.* **2016**, *55* (13), 6376–6383.

https://doi.org/10.1021/acs.inorgchem.5b02545.

(67) Brogden, D. W.; Berry, J. F. Coordination Chemistry of 2,2'-Dipyridylamine: The Gift That Keeps on Giving. *Comments Inorg. Chem.* **2016**, *36* (1), 17–37. https://doi.org/10.1080/02603594.2015.1079522.

(68) Ismayilov, R. H.; Wang, W.-Z.; Lee, G.-H.; Yeh, C.-Y.; Hua, S.-A.; Song, Y.; Rohmer, M.-M.; Bénard, M.; Peng, S.-M. Two Linear Undecanickel Mixed-Valence Complexes: Increasing the Size and the Scope of the Electronic Properties of Nickel Metal Strings. *Angew. Chem., Int. Ed.* **2011**, *50* (9), 2045–2048. https://doi.org/10.1002/anie.201006695.

(69) Shieh, S.-J.; Chou, C.-C.; Lee, G.-H.; Wang, C.-C.; Peng, S.-M. Linear Pentanuclear Complexes Containing a Chain of Metal Atoms: $[Co_5^{II}(\mu_5\text{-tpda})_4(NCS)_2]$ and $[Ni_5^{II}(\mu_5\text{-tpda})_4Cl_2]$. *Angew. Chem. Int., Ed. Engl.* **1997**, *36* (1–2), 56–59. https://doi.org/10.1002/anie.199700561.

(70) Dirvanauskas, A.; Galavotti, R.; Lunghi, A.; Nicolini, A.; Roncaglia, F.; Totti, F.; Cornia, A. Solution Structure of a Pentachromium(II) Single Molecule Magnet from DFT Calculations, Isotopic Labelling and Multinuclear NMR Spectroscopy. *Dalton Trans.* **2018**, *47* (2), 585–595. https://doi.org/10.1039/C7DT03931J.

(71) Tsao, T.-B.; Lo, S.-S.; Yeh, C.-Y.; Lee, G.-H.; Peng, S.-M. Novel Multi-Spin-State Linear Hexanickel Complexes and Their Singly Oxidized Products with 1,8-Naphthyridine-Based Ligands: Tuning the Redox Properties of the Metal String. *Polyhedron* **2007**, *26* (14), 3833–3841. https://doi.org/10.1016/j.poly.2007.04.036.

(72) Hernández Sánchez, R.; Betley, T. A. Thermally Persistent High-Spin Ground States in Octahedral Iron Clusters. *J. Am. Chem. Soc.* **2018**, *140* (48), 16792–16806. https://doi.org/10.1021/jacs.8b10181.

(73) Craig, G. A.; Murrie, M. 3d Single-Ion Magnets. *Chem. Soc. Rev.* **2015**, *44* (8), 2135–2147. https://doi.org/10.1039/c4cs00439f.

(74) Szarek, P.; Wegner, W.; Grochala, W. Ferromagnetic Ground State for a Hypothetical Iron-Based Extended Metal Atom Chain. *J. Mol. Model.* **2016**, *22* (3), 63. https://doi.org/10.1007/s00894-016-2928-x.

(75) Nippe, M.; Berry, J. F. Introducing a Metal−Metal Multiply Bonded Group as an "Axial Ligand" to Iron: Synthetic Design of a Linear Cr−Cr···Fe Framework. *J. Am. Chem. Soc.* **2007**, *129* (42), 12684–12685. https://doi.org/10.1021/ja076337j.

(76) Nippe, M.; Wang, J.; Bill, E.; Hope, H.; Dalal, N. S.; Berry, J. F. Crystals in Which Some Metal Atoms Are More Equal Than Others: Inequalities From Crystal Packing and Their Spectroscopic/Magnetic Consequences. *J. Am. Chem. Soc.* **2010**, *132* (40), 14261–14272. https://doi.org/10.1021/ja106510g.

(77) Nippe, M.; Bill, E.; Berry, J. F. Group 6 Complexes with Iron and Zinc Heterometals: Understanding the Structural, Spectroscopic, and Electrochemical Properties of a Complete Series of M≡M···M′ Compounds. *Inorg. Chem.* **2011**, *50* (16), 7650–7661. https://doi.org/10.1021/ic2011315.

(78) Nippe, M.; Turov, Y.; Berry, J. F. Remote Effects of Axial Ligand Substitution in Heterometallic Cr≡Cr···M Chains. *Inorg. Chem.* **2011**, *50* (21), 10592–10599. https://doi.org/10.1021/ic2011309.

(79) Turov, Y.; Berry, J. F. Synthesis, Characterization and Thermal Properties of Trimetallic N_3–Cr≡Cr···M–N_3 Azide Complexes with M = Cr, Mn, Fe, and Co. *Dalton Trans.* **2012**, *41* (26), 8153–8161. https://doi.org/10.1039/c2dt30150d.

(80) Cotton, F. A.; Murillo, C. A.; Wang, X. Trinuclear Complexes of Copper, Cobalt and Iron with N,N′-Di(2-Pyridyl) Formamidinate Ligands, $[M_3(DPyF)_4][PF_6]_2$. *Inorg. Chem. Commun.* **1998**, *1* (8), 281–283. https://doi.org/10.1016/S1387-7003(98)00063-X.

(81) Cotton, F. A.; Daniels, L. M.; Jordan, G. T.; Murillo, C. A.; Pascual, I. Structural Variations in the Ligands around a Simple Oxo-Centered Building Block, the Tetrahedral $[M_4O]^{6+}$ Unit, M=Mn and Fe. *Inorganica Chim. Acta* **2000**, *297* (1–2), 6–10. https://doi.org/10.1016/S0020-1693(99)00252-2.

(82) Zhao, H.; Clérac, R.; Sun, J.-S.; Ouyang, X.; Clemente-Juan, J. M.; Gomez-Garcia, C. J.; Coronado, E.; Dunbar, K. R. A Comparative Structural and Magnetic Study of Three Compounds Based on the Cluster Unit $M_4Cl_8(THF)_6$ (M = Mn, Fe, Co). *J. Solid State Chem.* **2001**, *159* (2), 281–292. https://doi.org/10.1006/jssc.2001.9157.

(83) Sundberg, J.; Vad, M. S.; McGrady, J. E.; Björemark, P. M.; Håkansson, M.; McKenzie, C. J. Accessing Iron Amides from Dimesityliron. *J. Organomet. Chem.* **2015**, *786*, 40–47. https://doi.org/10.1016/j.jorganchem.2015.03.015.

(84) Cole, R. B.; Zhu, J. Chloride Anion Attachment in Negative Ion Electrospray Ionization Mass Spectrometry. *Rapid Commun. Mass Spectrom.* **1999**, *13* (7), 607–611. https://doi.org/10.1002/(SICI)1097-0231(19990415)13:7<607::AID-RCM530>3.0.CO;2-2.

(85) Zhu, J.; Cole, R. B. Formation and Decompositions of Chloride Adduct Ions, $[M + Cl]^-$, in Negative Ion Electrospray Ionization Mass Spectrometry. *J. Am. Soc. Mass Spectrom.* **2000**, *11* (11), 932–941. https://doi.org/10.1016/S1044-0305(00)00164-1.

(86) Bruker. *TopSpin 4.0.6*; Bruker AXS Inc.: Madison, Wisconsin, USA.

(87) Clérac, R.; Cotton, F. A.; Daniels, L. M.; Dunbar, K. R.; Murillo, C. A.; Wang, X. Structural and Magnetic Properties of $Co_3(dpa)_4Br_2$. *J. Chem. Soc. Dalton Trans.* **2001**, No. 4, 386–391. https://doi.org/10.1039/b007876j.

(88) Berry, J. F.; Cotton, F. A.; Lu, T.; Murillo, C. A.; Roberts, B. K.; Wang, X. Molecular and Electronic Structures by Design: Tuning Symmetrical and Unsymmetrical Linear Trichromium Chains. *J. Am. Chem. Soc.* **2004**, *126* (22), 7082–7096. https://doi.org/10.1021/ja049055h.

(89) Clérac, R.; Cotton, F. A.; Daniels, L. M.; Dunbar, K. R.; Kirschbaum, K.; Murillo, C. A.; Pinkerton, A. A.; Schultz, A. J.; Wang, X. Linear Tricobalt Compounds with Di(2-pyridyl)amide (dpa) Ligands: Temperature Dependence of the Structural and Magnetic Properties of Symmetrical and Unsymmetrical Forms of $Co_3(dpa)_4Cl_2$ in the Solid State. *J. Am. Chem. Soc.* **2000**, *122* (26), 6226–6236. https://doi.org/10.1021/ja000515q.

(90) Berry, J. F.; Cotton, F. A.; Lei, P.; Murillo, C. A. Further Structural and Magnetic Studies of Tricopper Dipyridylamido Complexes. *Inorg. Chem.* **2003**, *42* (2), 377–382. https://doi.org/10.1021/ic025957c.

(91) Wu, L.-P.; Field, P.; Morrissey, T.; Murphy, C.; Nagle, P.; Hathaway, B.; Simmons, C.; Thornton, P. Crystal Structure and Electronic Properties of Dibromo- and Dichloro-Tetrakis[μ_3-Bis(2-Pyridyl)Amido]Tricopper(II) Hydrate. *J. Chem. Soc., Dalton Trans.* **1990**, No. 12, 3835–3840. https://doi.org/10.1039/DT9900003835.

(92) Maddock, L. C. H.; Borilovic, I.; McIntyre, J.; Kennedy, A. R.; Aromí, G.; Hevia, E. Synthetic, Structural and Magnetic Implications of Introducing 2,2′-Dipyridylamide to Sodium-Ferrate Complexes. *Dalton Trans.* **2017**, *46* (20), 6683–6691. https://doi.org/10.1039/C7DT01319A.

(93) Guillet, G. L.; Arpin, K. Y.; Boltin, A. M.; Gordon, J. B.; Rave, J. A.; Hillesheim, P. C. Synthesis and Characterization of a Linear Triiron(II) Extended Metal Atom Chain Complex with Fe–Fe Bonds. *Inorg. Chem.* **2020**, *59* (16), 11238–11243. https://doi.org/10.1021/acs.inorgchem.0c01625.

(94) Wang, C.-C.; Lo, W.-C.; Chou, C.-C.; Lee, G.-H.; Chen, J.-M.; Peng, S.-M. Synthesis, Crystal Structures, and Magnetic Properties of a Series of Linear Pentanickel(II) Complexes: $[Ni_5(\mu_5\text{-tpda})_4X_2]$ (X = Cl^-, CN^-, N_3^-, NCS^-) and $[Ni_5(\mu_5\text{-tpda})_4(CH_3CN)_2](PF6)_2$ ($tpda^{2-}$ = the Tripyridyldiamido Dianion). *Inorg. Chem.* **1998**, *37* (16), 4059–4065. https://doi.org/10.1021/ic971608k.

(95) Cotton, F. A.; Daniels, L. M.; Murillo, C. A.; Wang, X. Getting the Right Answer to a Key Question Concerning Molecular Wires. *Chem. Commun.* **1999**, *5* (24), 2461–2462. https://doi.org/10.1039/a906727b.

(96) Cotton, F. A.; Daniels, L. M.; Lu, T.; Murillo, A.; Wang, X. A Chain of Five Chromium(II) Atoms: A Desired Compound with an Undesired, Unsurprising, but Important Structure. *J. Chem. Soc., Dalton Trans.* **1999**, 517–518.

(97) Yeh, C.-Y.; Chou, C.-H.; Pan, K.-C.; Wang, C.-C.; Lee, G.-H.; Su, Y. O.; Peng, S.-M. Linear Pentacobalt Complexes: Synthesis, Structures, and Physical Properties of Neutral and One-Electron Oxidation Compounds. *J. Chem. Soc., Dalton Trans.* **2002**, No. 13, 2670–2677. https://doi.org/10.1039/b111462j.

(98) Yin, C.; Huang, G.-C.; Kuo, C.-K.; Fu, M.-D.; Lu, H.-C.; Ke, J.-H.; Shih, K.-N.; Huang, Y.-L.; Lee, G.-H.; Yeh, C.-Y.; Chen, C.-h.; Peng, S.-M. Extended Metal-Atom Chains with an Inert Second Row Transition Metal: $[Ru_5(\mu_5\text{-tpda})_4X_2]$ ($tpda^{2-}$ = Tripyridyldiamido Dianion, X = Cl and NCS). *J. Am. Chem. Soc.* **2008**, *130* (31), 10090–10092. https://doi.org/10.1021/ja8016818.

(99) Clérac, R.; Cotton, F. A.; Dunbar, K. R.; Murillo, C. A.; Pascual, I.; Wang, X. Further Study of the Linear Trinickel(II) Complex of Dipyridylamide. *Inorg. Chem.* **1999**, *38* (11), 2655–2657. https://doi.org/10.1021/ic990006t.

(100) Berry, J. F.; Cotton, F. A.; Murillo, C. A. Making Connections with Molecular Wires: Extending Tri-Nickel Chains with Axial Cyanide, Dicyanamide, and Phenylacetylide Ligands. *Dalton Trans.* **2003**, No. 15, 3015–3021. https://doi.org/10.1039/B305258C.

(101) Kuo, C.-K.; Liu, I. P.-C.; Yeh, C.-Y.; Chou, C.-H.; Tsao, T.-B.; Lee, G.-H.; Peng, S.-M. Oxidation of Linear Trinuclear Ruthenium Complexes $[Ru_3(dpa)_4Cl_2]$ and $[Ru_3(dpa)_4(CN)_2]$: Synthesis, Structures, Electrochemical and Magnetic Properties. *Chem. − Eur. J.* **2007**, *13* (5), 1442–1451. https://doi.org/10.1002/chem.200601219.

(102) Zhao, Q.; Harris, T. D.; Betley, T. A. $[(^{H}L)_2Fe_6(NCMe)_m]^{n+}$ (m = 0, 2, 4, 6; n = −1, 0, 1, 2, 3, 4, 6): An Electron-Transfer Series Featuring Octahedral Fe_6 Clusters Supported by

a Hexaamide Ligand Platform. *J. Am. Chem. Soc.* **2011**, *133* (21), 8293–8306. https://doi.org/10.1021/ja2015845.

(103) Zhao, Q.; Betley, T. A. Synthesis and Redox Properties of Triiron Complexes Featuring Strong Fe-Fe Interactions. *Angew. Chem., Int. Ed.* **2011**, *50* (3), 709–712. https://doi.org/10.1002/anie.201005198.

(104) Richardson, D. E.; Taube, H. Determination of E20-E10 in Multistep Charge Transfer by Stationary-Electrode Pulse and Cyclic Voltammetry: Application to Binuclear Ruthenium Ammines. *Inorg. Chem.* **1981**, *20* (4), 1278–1285. https://doi.org/10.1021/ic50218a062.

(105) Santi, S.; Bisello, A.; Cardena, R.; Donoli, A. Key Multi(Ferrocenyl) Complexes in the Interplay between Electronic Coupling and Electrostatic Interaction. *Dalton Trans.* **2015**, *44* (12), 5234–5257. https://doi.org/10.1039/C4DT03581J.

(106) Ludi, A. Descriptive Chemistry of Mixed-Valence Compounds. In *Mixed-Valence Compounds: Theory and Applications in Chemistry, Physics, Geology, and Biology*; Brown, D. B., Ed.; D. Reidel Publishing Company: Dordrecht, Netherlands, 1980; pp 25–47. https://doi.org/10.1007/978-94-009-9076-0_2.

(107) Brodsky, C. N.; Hadt, R. G.; Hayes, D.; Reinhart, B. J.; Li, N.; Chen, L. X.; Nocera, D. G. In Situ Characterization of Cofacial Co(IV) Centers in Co_4O_4 Cubane: Modeling the High-Valent Active Site in Oxygen-Evolving Catalysts. *Proc. Natl. Acad. Sci. U. S. A.* **2017**, *114* (15), 3855–3860. https://doi.org/10.1073/pnas.1701816114.

(108) Gütlich, P.; Eckhard, B.; Trautwein, A. X. *Mössbauer Spectroscopy and Transition Metal Chemistry: Fundamentals and Applications*; Springer-Verlag: Berlin Heidelberg, Germany, 2011. https://doi.org/10.1007/978-3-540-88428-6.

(109) Tereniak, S. J.; Carlson, R. K.; Clouston, L. J.; Young, V. G.; Bill, E.; Maurice, R.; Chen, Y.-S.; Kim, H. J.; Gagliardi, L.; Lu, C. C. Role of the Metal in the Bonding and Properties of Bimetallic Complexes Involving Manganese, Iron, and Cobalt. *J. Am. Chem. Soc.* **2014**, *136* (5), 1842–1855. https://doi.org/10.1021/ja409016w.

(110) Adamsky, H. (with contributions from Hoggard, P. E.; Atanasov, M.; Eifert, K.). AOMX; http://www.aomx.de/docs/html/aomxeh.html (accessed May 2020).

(111) Bencini, A.; Benelli, C.; Gatteschi, D. The Angular Overlap Model for the Description of the Paramagnetic Properties of Transition Metal Complexes. *Coord. Chem. Rev.* **1984**, *60*, 131–169. https://doi.org/10.1016/0010-8545(84)85064-X.

(112) Little, B. F.; Long, G. J. Moessbauer, Electronic, and Structural Properties of Several Bis- and Tetrakis(Pyridine)Iron(II) Complexes. *Inorg. Chem.* **1978**, *17* (12), 3401–3413. https://doi.org/10.1021/ic50190a021.

(113) Forgan, R.; Tasker, P.; White, F. CCDC 1408270: Experimental Crystal Structure Determination. **2015**. https://doi.org/10.5517/cc1j8f29.

(114) Gerloch, M.; McMeeking, R. F.; White, A. M. Paramagnetic Ellipsoids and π Bonding in Dithiocyanatotetrapyridine-Cobalt(II) and -Iron(II). *J. Chem. Soc., Dalton Trans.* **1975**, No. 22, 2452–2459. https://doi.org/10.1039/dt9750002452.

(115) Long, G. J.; Clarke, P. J. Crystal and Molecular Structures of Trans-Tetrakis(Pyridine)Dichloroiron(II), -Nickel(II), and -Cobalt(II) and Trans-Tetrakis(Pyridine)Dichloroiron(II) Monohydrate. *Inorg. Chem.* **1978**, *17* (6), 1394–1401. https://doi.org/10.1021/ic50184a002.

(116) Lever, A. B. P. *Inorganic Electronic Spectroscopy*, 2nd ed.; Elsevier, Ed.; Elsevier: Amsterdam, Netherlands, 1984.

(117) Chilton, N. F.; Anderson, R. P.; Turner, L. D.; Soncini, A.; Murray, K. S. PHI: A Powerful New Program for the Analysis of Anisotropic Monomeric and Exchange-Coupled Polynuclear d- and f-Block Complexes. *J. Comput. Chem.* **2013**, *34* (13), 1164–1175. https://doi.org/10.1002/jcc.23234.

(118) Lines, M. E. Orbital Angular Momentum in the Theory of Paramagnetic Clusters. *J. Chem. Phys.* **1971**, *55* (6), 2977–2984. https://doi.org/10.1063/1.1676524.

(119) Atanasov, M.; Ganyushin, D.; Pantazis, D. A.; Sivalingam, K.; Neese, F. Detailed Ab Initio First-Principles Study of the Magnetic Anisotropy in a Family of Trigonal Pyramidal Iron(II) Pyrrolide Complexes. *Inorg. Chem.* **2011**, *50* (16), 7460–7477. https://doi.org/10.1021/ic200196k.

(120) Bartolomé, J.; Filoti, G.; Kuncser, V.; Schinteie, G.; Mereacre, V.; Anson, C. E.; Powell, A. K.; Prodius, D.; Turta, C. Magnetostructural Correlations in the Tetranuclear Series of $\{Fe_3LnO_2\}$ Butterfly Core Clusters: Magnetic and Mössbauer Spectroscopic Study. *Phys. Rev. B* **2009**, *80* (1), 014430. https://doi.org/10.1103/PhysRevB.80.014430.

(121) Langley, S. K.; Ungur, L.; Chilton, N. F.; Moubaraki, B.; Chibotaru, L. F.; Murray, K. S. Structure, Magnetism and Theory of a Family of Nonanuclear $Cu^{II}_5Ln^{III}_4$-Triethanolamine Clusters Displaying Single-Molecule Magnet Behaviour. *Chem. − Eur. J.* **2011**, *17* (33), 9209–9218. https://doi.org/10.1002/chem.201100218.

(122) Cole, K. S.; Cole, R. H. Dispersion and Absorption in Dielectrics I. Alternating Current Characteristics. *J. Chem. Phys.* **1941**, *9* (4), 341–351. https://doi.org/10.1063/1.1750906.

(123) Dekker, C.; Arts, A. F. M.; de Wijn, H. W.; van Duyneveldt, A. J.; Mydosh, J. A. Activated Dynamics in a Two-Dimensional Ising Spin Glass: $Rb_2Cu_{1-x}Co_xF_4$. *Phys. Rev. B* **1989**, *40* (16), 11243–11251. https://doi.org/10.1103/PhysRevB.40.11243.

(124) Greer, S. M.; Gramigna, K. M.; Thomas, C. M.; Stoian, S. A.; Hill, S. Insights into Molecular Magnetism in Metal–Metal Bonded Systems as Revealed by a Spectroscopic and Computational Analysis of Diiron Complexes. *Inorg. Chem.* **2020**, *59* (24), 18141–18155. https://doi.org/10.1021/acs.inorgchem.0c02605.

(125) Simas, A. B. C.; Pereira, V. L. P.; Barreto, C. B. J.; de Sales, D. L.; de Carvalho, L. L. An Expeditious and Consistent Procedure for Tetrahydrofuran (THF) Drying and Deoxygenation by the Still Apparatus. *Quim. Nov.* **2009**, *32* (9), 2473–2475. https://doi.org/10.1590/S0100-40422009000900042.

(126) Armarego, W. L. F. *Purification of Laboratory Chemicals*, 8th ed.; Elsevier, Ed.; Butterworth-Heinemann: Oxford, UK, 2017.

(127) Klose, A.; Solari, E.; Floriani, C.; Chiesi-Villa, A.; Rizzoli, C.; Re, N. Magnetic Properties Diagnostic for the Existence of Iron(II)-Iron(II) Bonds in Dinuclear Complexes Which Derive from Stepwise Insertion Reactions on Unsupported Iron-Aryl Bonds. *J. Am. Chem. Soc.* **1994**, *116* (20), 9123–9135. https://doi.org/10.1021/ja00099a030.

(128) Alberico, E.; Sponholz, P.; Cordes, C.; Nielsen, M.; Drexler, H. J.; Baumann, W.; Junge, H.; Beller, M. Selective Hydrogen Production from Methanol with a Defined Iron Pincer Catalyst under Mild Conditions. *Angew. Chem., Int. Ed.* **2013**, *52* (52), 14162–14166. https://doi.org/10.1002/anie.201307224.

(129) Mund, G.; Vidovic, D.; Batchelor, R. J.; Britten, J. F.; Sharma, R. D.; Jones, C. H. W.; Leznoff, D. B. Unusual Iron(III) Ate Complexes Stabilized By Li-π Interactions. *Chem. − Eur. J.* **2003**, *9* (19), 4757–4763. https://doi.org/10.1002/chem.200305014.

(130) Bruker. *APEX2, SADABS, SAINT*; Bruker AXS Inc.: Madison, Wisconsin, USA, 2008.

(131) Altomare, A.; Cascarano, G.; Giacovazzo, C.; Guagliardi, A. Completion and Refinement of Crystal Structures with SIR 92. *J. Appl. Crystallogr.* **1993**, *26* (3), 343–350. https://doi.org/10.1107/S0021889892010331.

(132) Sheldrick, G. M. Crystal Structure Refinement with SHELXL. *Acta Crystallogr., Sect. C: Struct. Chem.* **2015**, *71* (1), 3–8. https://doi.org/10.1107/S2053229614024218.

(133) Farrugia, L. J. WinGX and ORTEP for Windows: An Update. *J. Appl. Crystallogr.* **2012**, *45* (4), 849–854. https://doi.org/10.1107/S0021889812029111.

(134) Meneses, A. B.; Antonello, S.; Arévalo, M. C.; Maran, F. Double-Layer Correction for Electron-Transfer Kinetics at Glassy Carbon and Mercury Electrodes in *N*,*N*-Dimethylformamide. *Electroanalysis* **2006**, *18* (4), 363–370. https://doi.org/10.1002/elan.200503419.

(135) Antonello, S.; Arrigoni, G.; Dainese, T.; De Nardi, M.; Parisio, G.; Perotti, L.; René, A.; Venzo, A.; Maran, F. Electron Transfer through 3D Monolayers on Au_{25} Clusters. *ACS Nano* **2014**, *8* (3), 2788–2795. https://doi.org/10.1021/nn406504k.

(136) Nicholson, R. S. Theory and Application of Cyclic Voltammetry for Measurement of Electrode Reaction Kinetics. *Anal. Chem.* **1965**, *37* (11), 1351–1355. https://doi.org/10.1021/ac60230a016.

(137) Bain, G. A.; Berry, J. F. Diamagnetic Corrections and Pascal's Constants. *J. Chem. Educ.* **2008**, *85* (4), 532–536. https://doi.org/10.1021/ed085p532.

(138) Prisecaru, I. WMOSS4 Mössbauer Spectral Analysis Software. www.wmoss.org, 2009-2016 2013.

(139) Dennis, J. E.; Gay, D. M.; Walsh, R. E. An Adaptive Nonlinear Least-Squares Algorithm. *ACM Trans. Math. Softw.* **1981**, *7* (3), 348–368. https://doi.org/10.1145/355958.355965.

(140) Taylor, J. *Introduction to Error Analysis, the Study of Uncertainties in Physical Measurements*, 2nd ed.; University Science Books: New York, USA, 1997.

(141) Neese, F. Software Update: The ORCA Program System, Version 4.0. *WIREs Comput. Mol. Sci.* **2018**, *8* (1). https://doi.org/10.1002/wcms.1327.

(142) Maurice, R.; Bastardis, R.; Graaf, C. de; Suaud, N.; Mallah, T.; Guihéry, N. Universal Theoretical Approach to Extract Anisotropic Spin Hamiltonians. *J. Chem. Theory Comput.* **2009**, *5* (11), 2977–2984. https://doi.org/10.1021/ct900326e.

(143) Guo, Y.; Sivalingam, K.; Valeev, E. F.; Neese, F. SparseMaps—A Systematic Infrastructure for Reduced-Scaling Electronic Structure Methods. III. Linear-Scaling Multireference Domain-Based Pair Natural Orbital N-Electron Valence Perturbation

Theory. *J. Chem. Phys.* **2016**, *144* (9), 094111. https://doi.org/10.1063/1.4942769.

(144) Neese, F. Efficient and Accurate Approximations to the Molecular Spin-Orbit Coupling Operator and Their Use in Molecular *g*-Tensor Calculations. *J. Chem. Phys.* **2005**, *122* (3), 034107. https://doi.org/10.1063/1.1829047.

(145) Weigend, F.; Ahlrichs, R. Balanced Basis Sets of Split Valence, Triple Zeta Valence and Quadruple Zeta Valence Quality for H to Rn: Design and Assessment of Accuracy. *Phys. Chem. Chem. Phys.* **2005**, *7* (18), 3297–3305. https://doi.org/10.1039/b508541a.

(146) Weigend, F. Hartree–Fock Exchange Fitting Basis Sets for H to Rn. *J. Comput. Chem.* **2008**, *29* (2), 167–175. https://doi.org/10.1002/jcc.20702.

(147) Singh, S. K.; Rajaraman, G. Deciphering the Origin of Giant Magnetic Anisotropy and Fast Quantum Tunnelling in Rhenium(IV) Single-Molecule Magnets. *Nat. Commun.* **2016**, *7* (1), 10669. https://doi.org/10.1038/ncomms10669.

(148) Edén, M.; Levitt, M. H. Computation of Orientational Averages in Solid-State NMR by Gaussian Spherical Quadrature. *J. Magn. Reson.* **1998**, *132* (2), 220–239. https://doi.org/10.1006/jmre.1998.1427.

(149) ZHEEV LAPACK Driver Routine (Version 2.0), Univ. of Tennessee, Univ. of California Berkeley, NAG Ltd., Courant Institute, Argonne National Lab, and Rice University. USA 1994.

(150) Day, P.; Hush, N. S.; Clark, R. J. Mixed Valence: Origins and Developments. *Phil. Trans. R. Soc. A.* **2008**, *366* (1862), 5–14. https://doi.org/10.1098/rsta.2007.2135.

(151) Allen, G. C.; Hush, N. S. Intervalence-Transfer Absorption. Part 1. Qualitative Evidence for Intervalence-Transfer Absorption in Inorganic Systems in Solution and in the Solid State. In *Progress in Inorganic Chemistry*; Cotton, F. A., Ed.; John Wiley & Sons, Inc., 1967; Vol. 8, pp 357–389. https://doi.org/10.1002/9780470166093.ch6.

(152) Hush, N. S. Intervalence-Transfer Absorption. Part 2. Theoretical Considerations and Spectroscopic Data. In *Progress in Inorganic Chemistry*; Cotton, F. A., Ed.; John Wiley & Sons, Inc., 1967; Vol. 8, pp 391–444. https://doi.org/10.1002/9780470166093.ch7.

(153) Hofmann, K. A.; Höschele, K. Das Magnesiumchlorid Als Mineralisator. II.: Das Urancerblau Und Das Wesen Der Konstitutiven Färbung. Das Magnesiarot Und Das Magnesiagrün. *Berichte der Dtsch. Chem. Gesellschaft* **1915**, *48* (1), 20–28. https://doi.org/10.1002/cber.19150480106.

(154) Robin, M. B.; Day, P. Mixed Valence Chemistry-A Survey and Classification. *Adv. Inorg. Chem. Radiochem.* **1968**, *10* (C), 247–422. https://doi.org/10.1016/S0065-2792(08)60179-X.

(155) Creutz, C. Mixed Valence Complexes of d^5-d^6 Metal Centers. In *Progress in Inorganic Chemistry*; Lippard, S. J., Ed.; John Wiley & Sons, Inc., 1983; pp 1–73. https://doi.org/10.1002/9780470166314.ch1.

(156) Launay, J.-P. Mixed-Valent Compounds and Their Properties - Recent Developments. *Eur. J. Inorg. Chem.* **2020**, *2020* (4), 329–341. https://doi.org/10.1002/ejic.201901180.

(157) Anderson, P. W.; Hasegawa, H. Considerations on Double Exchange. *Phys. Rev.* **1955**, *100* (2), 675–681. https://doi.org/10.1103/PhysRev.100.675.

(158) Blondin, G.; Girerd, J. J. Interplay of Electron Exchange and Electron Transfer in Metal Polynuclear Complexes in Proteins or Chemical Models. *Chem. Rev.* **1990**, *90* (8), 1359–1376. https://doi.org/10.1021/cr00106a001.

(159) Gamelin, D. R.; Bominaar, E. L.; Kirk, M. L.; Wieghardt, K.; Solomon, E. I. Excited-State Contributions to Ground-State Properties of Mixed-Valence Dimers: Spectral and Electronic-Structural Studies of $[Fe_2(OH)_3(Tmtacn)_2]^{2+}$ Related to the $[Fe_2S_2]^{+}$ Active Sites of Plant-Type Ferredoxins. *J. Am. Chem. Soc.* **1996**, *118* (34), 8085–8097. https://doi.org/10.1021/ja9536633.

(160) Day, P. Spectra and Constitution of Antimony(III) Antimony(V) Hexahalide Salts and Related Compounds. *Inorg. Chem.* **1963**, *2* (3), 452–456. https://doi.org/10.1021/ic50007a006.

(161) Culpin, D.; Day, P.; Edwards, P. R.; Williams, R. J. P. Charge Transfer in Solid Chlorocuprates(I, II). *Chem. Commun.* **1965**, No. 19, 450. https://doi.org/10.1039/c19650000450.

(162) Robin, M. B. The Color and Electronic Configurations of Prussian Blue. *Inorg. Chem.* **1962**, *1* (2), 337–342. https://doi.org/10.1021/ic50002a028.

(163) Woodward, J. Præparatio Cærulei Prussiaci Ex Germaniâ Missa Ad. *Philos. Trans. R. Soc. London* **1724**, *33* (381), 15–17. https://doi.org/10.1098/rstl.1724.0005.

(164) Fultz, B. Mössbauer Spectrometry. In *Characterization of Materials*; Kaufmann, E. N., Ed.; John Wiley & Sons, Inc.: Hoboken, USA, 2012. https://doi.org/10.1002/0471266965.com069.pub2.

(165) Drüeke, S.; Chaudhuri, P.; Pohl, K.; Wieghardt, K.; Ding, X.-Q.; Bill, E.; Sawaryn, A.; Trautwein, a X.; Winkler, H.; Gurman, S. J. The Novel Mixed-Valence, Exchange-Coupled, Class III Dimer $[L_2Fe_2(\mu\text{-}OH)_3]^{2+}$ (L = *N*,*N*′,*N*″-Trimethyl-1,4,7-Triazacyclononane). *J. Chem. Soc., Chem. Commun.* **1989**, *509* (1), 59–62. https://doi.org/10.1039/C39890000059.

(166) Dutta, S. K.; Ensling, J.; Werner, R.; Flörke, U.; Haase, W.; Gütlich, P.; Nag, K. Valence-Delocalized and Valence-Trapped $Fe^{II}Fe^{III}$ Complexes: Drastic Influence of the Ligands. *Angew. Chem., Int. Ed. Engl.* **1997**, *36* (12), 152–155. https://doi.org/10.1002/anie.199701521.

(167) Lee, D.; Krebs, C.; Huynh, B. H.; Hendrich, M. P.; Lippard, S. J. Valence-Delocalized Diiron(II,III) Cores Supported by Carboxylate-Only Bridging Ligands. *J. Am. Chem. Soc.* **2000**, *122* (20), 5000–5001. https://doi.org/10.1021/ja994448f.

(168) Lee, D.; DuBois, J. L.; Pierce, B.; Hedman, B.; Hodgson, K. O.; Hendrich, M. P.; Lippard, S. J. Structural and Spectroscopic Studies of Valence-Delocalized Diiron(II,III) Complexes Supported by Carboxylate-Only Bridging Ligands. *Inorg. Chem.* **2002**, *41* (12), 3172–3182. https://doi.org/10.1021/ic011050n.

(169) Cohen, J. D.; Payne, S.; Hagen, K. S.; Sanders-Loehr, J. Raman Evidence for a Trapped-Valence Fe^{II}–O–Fe^{III} Complex Formed from an Outer-Sphere Reaction of Diiron(II) with Dioxygen. *J. Am. Chem. Soc.* **1997**, *119* (12), 2960–2961. https://doi.org/10.1021/ja9638871.

(170) Hagadorn, J. R.; Que, L.; Tolman, W. B.; Prisecaru, I.; Münck, E. Conformational Tuning of Valence Delocalization in Carboxylate-Rich Diiron Complexes. *J. Am. Chem. Soc.* **1999**, *121* (41), 9760–9761. https://doi.org/10.1021/ja992038l.

(171) Stubna, A.; Jo, D.-H.; Costas, M.; Brenessel, W. W.; Andres, H.; Bominaar, E. L.; Münck, E.; Que, L. A Structural and Mössbauer Study of Complexes with $Fe_2(\mu\text{-}O(H))_2$ Cores: Stepwise Oxidation from $Fe^{II}(\mu\text{-}OH)_2Fe^{II}$ through $Fe^{II}(\mu\text{-}OH)_2Fe^{III}$ to $Fe^{III}(\mu\text{-}O)(\mu\text{-}OH)Fe^{III}$. *Inorg. Chem.* **2004**, *43* (10), 3067–3079. https://doi.org/10.1021/ic030296k.

(172) Ding, X.; Bominaar, E. L.; Bill, E.; Winkler, H.; Trautwein, A. X.; Drüeke, S.; Chaudhuri, P.; Wieghardt, K. Mössbauer and Electron Paramagnetic Resonance Study of the Double-exchange and Heisenberg-exchange Interactions in a Novel Binuclear Fe(II/III) Delocalized-valence Compound. *J. Chem. Phys.* **1990**, *92* (1), 178–186.

https://doi.org/10.1063/1.458460.

(173) Parthey, M.; Kaupp, M. Quantum-Chemical Insights into Mixed-Valence Systems: Within and beyond the Robin–Day Scheme. *Chem. Soc. Rev.* **2014**, *43* (14), 5067–5088. https://doi.org/10.1039/C3CS60481K.

(174) Saal, C.; Mohanta, S.; Nag, K.; Dutta, S. K.; Werner, R.; Haase, W.; Duin, E.; Johnson, M. K. Magnetic Investigations on a Valence-Delocalized Dinuclear Fe(II)-Fe(III) Complex. *Berichte der Bunsengesellschaft für Phys. Chemie* **1996**, *100* (12), 2086–2090. https://doi.org/10.1002/bbpc.19961001228.

(175) Glaser, T.; Beissel, T.; Bill, E.; Weyhermüller, T.; Schünemann, V.; Meyer-Klaucke, W.; Trautwein, A. X.; Wieghardt, K. Electronic Structure of Linear Thiophenolate-Bridged Heterotrinuclear Complexes $[LFeMFeL]^{n+}$ (M = Cr, Co, Fe; n = 1−3): Localized vs Delocalized Models. *J. Am. Chem. Soc.* **1999**, *121* (10), 2193–2208. https://doi.org/10.1021/ja982898m.

(176) Pandelia, M.-E.; Bykov, D.; Izsak, R.; Infossi, P.; Giudici-Orticoni, M.-T.; Bill, E.; Neese, F.; Lubitz, W. Electronic Structure of the Unique [4Fe-3S] Cluster in O_2-Tolerant Hydrogenases Characterized by ^{57}Fe Mossbauer and EPR Spectroscopy. *Proc. Natl. Acad. Sci.* **2013**, *110* (2), 483–488. https://doi.org/10.1073/pnas.1202575110.

(177) Dong, T.-Y.; Lai, X.-Q.; Lin, Z.-W.; Lin, K.-J. Effects of Environment on Intramolecular Electron Transfer in Mixed-Valence 1′,1‴-Dinaphthylmethyl(Biferrocenium) Triiodide: Structural and ^{57}Fe Mössbauer Characteristics. *Angew. Chem., Int. Ed. Engl.* **1997**, *36* (18), 2002–2004. https://doi.org/10.1002/anie.199720021.

(178) Aquilante, F.; Autschbach, J.; Carlson, R. K.; Chibotaru, L. F.; Delcey, M. G.; De Vico, L.; Fdez. Galván, I.; Ferré, N.; Frutos, L. M.; Gagliardi, L.; Garavelli, M.; Giussani, A.; Hoyer, C. E.; Li Manni, G.; Lischka, H.; Ma, D.; Malmqvist, P. Å.; Müller, T.; Nenov, A.; Olivucci, M.; Pedersen, T. B.; Peng, D.; Plasser, F.; Pritchard, B.; Reiher, M.; Rivalta, I.; Schapiro, I.; Segarra-Martí, J.; Stenrup, M.; Truhlar, D. G.; Ungur, L.; Valentini, A.; Vancoillie, S.; Veryazov, V.; Vysotskiy, V. P.; Weingart, O.; Zapata, F.; Lindh, R. Molcas 8: New Capabilities for Multiconfigurational Quantum Chemical Calculations across the Periodic Table. *J. Comput. Chem.* **2016**, *37* (5), 506–541. https://doi.org/10.1002/jcc.24221.

(179) Moreno-Pineda, E.; Taran, G.; Wernsdorfer, W.; Ruben, M. Quantum Tunnelling of the Magnetisation in Single-Molecule Magnet Isotopologue Dimers. *Chem. Sci.* **2019**, *10*

(19), 5138–5145. https://doi.org/10.1039/C9SC01062A.

(180) *Molecular Magnets*; Bartolomé, J., Luis, F., Fernández, J. F., Eds.; NanoScience and Technology; Springer Berlin Heidelberg: Berlin, Heidelberg, Germany, 2014. https://doi.org/10.1007/978-3-642-40609-6.

(181) Moreno-Pineda, E.; Klyatskaya, S.; Du, P.; Damjanović, M.; Taran, G.; Wernsdorfer, W.; Ruben, M. Observation of Cooperative Electronic Quantum Tunneling: Increasing Accessible Nuclear States in a Molecular Qudit. *Inorg. Chem.* **2018**, *57* (16), 9873–9879. https://doi.org/10.1021/acs.inorgchem.8b00823.

(182) Taran, G.; Bonet, E.; Wernsdorfer, W. The Role of the Quadrupolar Interaction in the Tunneling Dynamics of Lanthanide Molecular Magnets. *J. Appl. Phys.* **2019**, *125* (14), 142903. https://doi.org/10.1063/1.5079453.

(183) Thorn, A.; Dittrich, B.; Sheldrick, G. M. Enhanced Rigid-Bond Restraints. *Acta Crystallogr., Sect. A: Found. Crystallogr.* **2012**, *68* (4), 448–451. https://doi.org/10.1107/S0108767312014535.

(184) Zall, C. M.; Clouston, L. J.; Young, V. G.; Ding, K.; Kim, H. J.; Zherebetskyy, D.; Chen, Y.-S.; Bill, E.; Gagliardi, L.; Lu, C. C. Mixed-Valent Dicobalt and Iron–Cobalt Complexes with High-Spin Configurations and Short Metal–Metal Bonds. *Inorg. Chem.* **2013**, *52* (16), 9216–9228. https://doi.org/10.1021/ic400292g.

(185) Hohloch, S.; Pankhurst, J. R.; Jaekel, E. E.; Parker, B. F.; Lussier, D. J.; Garner, M. E.; Booth, C. H.; Love, J. B.; Arnold, J. Benzoquinonoid-Bridged Dinuclear Actinide Complexes. *Dalton Trans.* **2017**, *46* (35), 11615–11625. https://doi.org/10.1039/c7dt02728a.

(186) Tsai, Y.-J.; Lee, U. H.; Zhao, Q. Synthesis and Characterization of Two Polydentate Pyridylamines, Their Acidified Salts and Late First-Row Transition Metal Complexes. *Polyhedron* **2017**, *124*, 206–214. https://doi.org/10.1016/j.poly.2016.12.021.

(187) Wu, J. *N*-(6-Bromopyridin-2-Yl)Pyridin-2-Amine. *Acta Crystallogr., Sect. E: Struct. Rep. Online* **2007**, *63* (11), 67–70. https://doi.org/10.1107/S1600536807051860.

(188) Deng, Y.; Cheng, Y. Y.; Liu, H.; Mack, J.; Lu, H.; Zhu, L. G. Asymmetrical Aza-Boron-Dipyridomethene Derivatives with Large Stokes Shifts: Synthesis and Spectroscopic Properties. *Tetrahedron Lett.* **2014**, *55* (28), 3792–3796. https://doi.org/10.1016/j.tetlet.2014.05.066.

(189) Hartwig, J. F. Palladium-Catalyzed Amination of Aryl Halides and Related Reactions. In *Handbook of Organopalladium Chemistry for Organic Synthesis*; John Wiley & Sons, Inc.: New York, USA, 2002; pp 1051–1096. https://doi.org/10.1002/0471212466.ch42.

(190) Wolfe, J. P.; Wagaw, S.; Marcoux, J.-F.; Buchwald, S. L. Rational Development of Practical Catalysts for Aromatic Carbon−Nitrogen Bond Formation. *Acc. Chem. Res.* **1998**, *31* (12), 805–818. https://doi.org/10.1021/ar9600650.

(191) Nakamura, I.; Yamamoto, Y. Transition-Metal-Catalyzed Reactions in Heterocyclic Synthesis. *Chem. Rev.* **2004**, *104* (5), 2127–2198. https://doi.org/10.1021/cr020095i.

(192) Hasanov, H.; Tan, U.-K.; Wang, R.-R.; Lee, G. H.; Peng, S.-M. Synthesis of Long-Chained Oligo-α-Aminopyridines by Tandem Pd-Catalyzed Cross-Coupling Aminations and Their Helical Dinuclear Complexes. *Tetrahedron Lett.* **2004**, *45* (41), 7765–7769. https://doi.org/10.1016/j.tetlet.2004.08.066.

(193) Ismayilov, R. H.; Wang, W.-Z.; Wang, R.-R.; Yeh, C.-Y.; Lee, G.-H.; Peng, S.-M. Four Quadruple Metal–Metal Bonds Lined up: Linear Nonachromium(II) Metal String Complexes. *Chem. Commun.* **2007**, No. 11, 1121–1123. https://doi.org/10.1039/B614597C.

(194) Leung, M.; Mandal, A. B.; Wang, C.-C.; Lee, G.-H.; Peng, S.-M.; Cheng, H.-L.; Her, G.-R.; Chao, I.; Lu, H.-F.; Sun, Y.-C.; Shiao, M.-Y.; Chou, P.-T. Self-Complementarity of Oligo-2-Aminopyridines: A New Class of Hydrogen-Bonded Ladders. *J. Am. Chem. Soc.* **2002**, *124* (16), 4287–4297. https://doi.org/10.1021/ja011679p.

(195) Ismayilov, R. H.; Wang, W.-Z.; Lee, G.-H.; Peng, S.-M. One-, Two- and Three-Dimensional Cu(II) Complexes Built via New Oligopyrazinediamine Ligands: From Antiferromagnetic to Ferromagnetic Coupling. *Dalton Trans.* **2006**, No. 3, 478–491. https://doi.org/10.1039/B507485A.

(196) Hua, S.-A.; Liu, I. P.-C.; Hasanov, H.; Huang, G.-C.; Ismayilov, R. H.; Chiu, C.-L.; Yeh, C.-Y.; Lee, G.-H.; Peng, S.-M. Probing the Electronic Communication of Linear Heptanickel and Nonanickel String Complexes by Utilizing Two Redox-Active $[Ni_2(Napy)_4]^{3+}$ Moieties. *Dalton Trans.* **2010**, *39* (16), 3890–3896. https://doi.org/10.1039/b923125k.

(197) Berry, J. F.; Cotton, F. A.; Lei, P.; Lu, T.; Murillo, C. A. Additional Steps toward Molecular Scale Wires: Further Study of $Ni_5^{10/11+}$ Chains Embraced by Polypyridylamide Ligands. *Inorg. Chem.* **2003**, *42* (11), 3534–3539.

https://doi.org/10.1021/ic034071l.

(198) Wang, C.-J.; Ma, H.-R.; Wang, Y.-Y.; Liu, P.; Zhou, L.-J.; Shi, Q.-Z.; Peng, S.-M. Subtle Structural Changes in Coordination Chains: Influence of the Flexibility of the Precursor Ligands and of the Solvent. *Cryst. Growth Des.* **2007**, *7* (9), 1811–1817. https://doi.org/10.1021/cg070246g.

(199) Yin, C.-X.; Su, J.; Huo, F.-J.; Ismayilov, R.-H.; Wang, W.-Z.; Lee, G.-H.; Yeh, C.-Y.; Peng, S.-M. Synthesis, Structure, Magnetism, and Electrochemical Properties of a Linear Pentanuclear Ni_5 Compound Derived from an Oligo-α-Pyridylamino Ligand: $Ni_5(\mu\text{-Dmpdda})_4(NCS)_2$. *J. Coord. Chem.* **2009**, *62* (18), 2974–2982. https://doi.org/10.1080/00958970902988837.

(200) Yang, M.; Lin, T.-W.; Chou, C.-C.; Lee, H.-C.; Chang, H.-C.; Lee, G.-H.; Leung, M.; Peng, S.-M. New Oligo-α-Pyridylamino Ligands and Their Metal Complexes. *Chem. Commun.* **1997**, No. 23, 2279–2280. https://doi.org/10.1039/A706439J.

(201) Ho, K.; Yu, W.; Cheung, K.; Che, C. Blue Luminescent Zinc(II) Complexes with Polypyridylamine Ligands: Crystal Structures and Luminescence Properties. *J. Chem. Soc., Dalton Trans.* **1999**, *14* (10), 1581–1586. https://doi.org/10.1039/a900504h.

(202) Wuts, P. G. M.; Greene, T. W. *Greene's Protective Groups in Organic Synthesis*; John Wiley & Sons, Inc.: Hoboken, USA, 2006. https://doi.org/10.1002/0470053488.

(203) Yao, B.; Wang, D.-X.; Gong, H.-Y.; Huang, Z.-T.; Wang, M.-X. Synthesis, Structure, and Reactions of NH-Bridged Calix[*m*]Arene[*n*]Pyridines. *J. Org. Chem.* **2009**, *74* (15), 5361–5368. https://doi.org/10.1021/jo900826n.

(204) Rawal, V. H.; Jones, R. J.; Cava, M. P. Photocyclization Strategy for the Synthesis of Antitumor Agent CC-1065: Synthesis of Dideoxy PDE-I and PDE-II. Synthesis of Thiophene and Furan Analogs of Dideoxy PDE-I and PDE-II. *J. Org. Chem.* **1987**, *52* (1), 19–28. https://doi.org/10.1021/jo00377a004.

(205) Wang, J.; Liang, Y. L.; Qu, J. Boiling Water-Catalyzed Neutral and Selective N-Boc Deprotection. *Chem. Commun.* **2009**, No. 34, 5144–5146. https://doi.org/10.1039/b910239f.

(206) Zinelaabidine, C.; Souad, O.; Zoubir, J.; Malika, B.; Nour-Eddine, A. A Simple and Efficient Green Method for the Deprotection of N-Boc in Various Structurally Diverse Amines under Water-Mediated Catalyst-Free Conditions. *Int. J. Chem.* **2012**, *4* (3), 73–79. https://doi.org/10.5539/ijc.v4n3p73.

(207) Salvatore, R. N.; Nagle, A. S.; Schmidt, S. E.; Jung, K. W. Cesium Hydroxide Promoted Chemoselective *N*-Alkylation for the Generally Efficient Synthesis of Secondary Amines. *Org. Lett.* **1999**, *1* (12), 1893–1896. https://doi.org/10.1021/ol9910417.

(208) Salvatore, R. N.; Nagle, A. S.; Kyung, W. J. Cesium Effect: High Chemoselectivity in Direct N-Alkylation of Amines. *J. Org. Chem.* **2002**, *67* (3), 674–683. https://doi.org/10.1021/jo010643c.

(209) Ferguson, J. Crystal Spectra of Metal Coordination Compounds. I. Tetrahedral Cobalt(II). *J. Chem. Phys.* **1960**, *32* (2), 528–532. https://doi.org/10.1063/1.1730729.

(210) Allan, J. R.; Baillie, G. M.; Bowley, H. J.; Gerrard, D. L. The Spectral and Magnetic Properties of Some Chloro and Thiocyanato Transition Metal Complexes of the Aminopyridines and a Study of Their Performance as Colouring Materials for Poly(Vinyl Chloride). *Eur. Polym. J.* **1988**, *24* (12), 1149–1153. https://doi.org/10.1016/0014-3057(88)90101-2.

(211) Cotton, F. A.; Goodgame, D. M. L.; Goodgame, M. The Electronic Structures of Tetrahedral Cobalt(II) Complexes. *J. Am. Chem. Soc.* **1961**, *83* (23), 4690–4699. https://doi.org/10.1021/ja01484a002.

(212) Fine, D. A. Halide Complexes of Cobalt(II) in Acetone Solution. *J. Am. Chem. Soc.* **1962**, *84* (7), 1139–1144. https://doi.org/10.1021/ja00866a016.

(213) Csöregh, I.; Kenessey, G.; Wadsten, T.; Liptay, G.; Carson, B. R. Pyridine Type Complexes of Transition-Metal Halides XI. Structural, Thermal and Spectroscopic Studies of Aminopyridine Complexes of Cobalt(II) Halides. *Zeitschrift für Krist. - Cryst. Mater.* **2000**, *215* (9). https://doi.org/10.1524/zkri.2000.215.9.547.

(214) Kotsinaris, A.; Kyriacou, G.; Lambrou, C. Electrochemical Reduction of Dichloromethane to Higher Hydrocarbons. *J. Appl. Electrochem.* **1998**, *28* (6), 613–616. https://doi.org/10.1023/A:1003202203067.

(215) Pauling, L. Metal-Metal Bond Lengths in Complexes of Transition Metals. *Proc. Natl. Acad. Sci.* **1976**, *73* (12), 4290–4293. https://doi.org/10.1073/pnas.73.12.4290.

(216) O'Keefe, B. J.; Monnier, S. M.; Hillmyer, M. A.; Tolman, W. B. Rapid and Controlled Polymerization of Lactide by Structurally Characterized Ferric Alkoxides. *J. Am. Chem. Soc.* **2001**, *123* (2), 339–340. https://doi.org/10.1021/ja003537l.

(217) Reis, D. M.; Nunes, G. G.; Sá, E. L.; Friedermann, G. R.; Mangrich, A. S.; Evans, D. J.;

Hitchcock, P. B.; Leigh, G. J.; Soares, J. F. Iron(III) and Titanium(IV) Oxoalkoxide Chemistry: Synthetic, Structural, Magnetochemical and Spectroscopic Studies of $[Ti_3(\mu_3\text{-}OPr^i)_2(\mu\text{-}OPr^i)_3(OPr^i)_6][FeCl_4]$ and $[Fe_5(\mu_5\text{-}O)(\mu\text{-}OPr^i)_8Cl_5]$. *New J. Chem.* **2004**, *28* (9), 1168–1176. https://doi.org/10.1039/B403899A.

(218) Steiner, T. The Hydrogen Bond in the Solid State. *Angew. Chem., Int. Ed.* **2002**, *41* (1), 48–76. https://doi.org/10.1002/1521-3773(20020104)41:1<48::AID-ANIE48>3.0.CO;2-U.

(219) Jeffrey, G. A. *An Introduction to Hydrogen Bonding*; Oxford University Press, New York, USA; 1997.

(220) Bailey, P. J.; Coxall, R. A.; Dick, C. M.; Fabre, S.; Henderson, L. C.; Herber, C.; Liddle, S. T.; Loroño-González, D.; Parkin, A.; Parsons, S. The First Structural Characterisation of a Group 2 Metal Alkylperoxide Complex: Comments on the Cleavage of Dioxygen by Magnesium Alkyl Complexes. *Chem. – Eur. J.* **2003**, *9* (19), 4820–4828. https://doi.org/10.1002/chem.200305053.

(221) Jeffery, G. H.; Basset, J.; Mendham, J.; Denney, R. C. *Vogel's Textbook of Quantitative Chemical Analysis*, 5th ed.; Technical, L. S., Essex, UK, 1989.

(222) Palatinus, L.; Chapuis, G. SUPERFLIP – a Computer Program for the Solution of Crystal Structures by Charge Flipping in Arbitrary Dimensions. *J. Appl. Crystallogr.* **2007**, *40* (4), 786–790. https://doi.org/10.1107/S0021889807029238.

(223) Palatinus, L.; Prathapa, S. J.; van Smaalen, S. EDMA : A Computer Program for Topological Analysis of Discrete Electron Densities. *J. Appl. Crystallogr.* **2012**, *45* (3), 575–580. https://doi.org/10.1107/S0021889812016068.